ORNL/FEDC-83/9

OAK RIDGE NATIONAL LABORATORY LIBRARY
3 4456 0039826 4

MFTF-α+T PROGRESS REPORT

W.D. NELSON

OAK RIDGE NATIONAL LABORATORY
CENTRAL RESEARCH LIBRARY
CIRCULATION SECTION
4500N ROOM 175
LIBRARY LOAN COPY
DO NOT TRANSFER TO ANOTHER PERSON
If you wish someone else to see this report, send in name with report and the library will arrange a loan.
UCN-7969 (3 9-77)

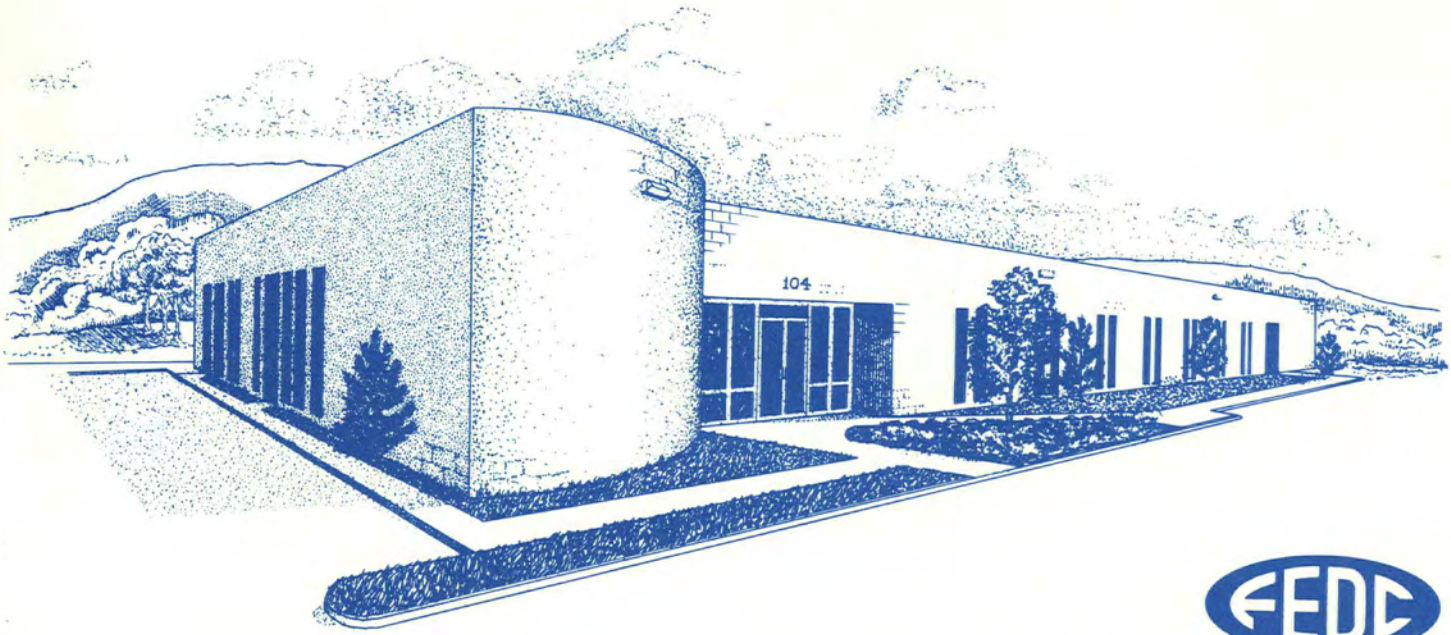

FUSION ENGINEERING DESIGN CENTER
Oak Ridge National Laboratory * Oak Ridge, Tennessee

Printed in the United States of America. Available from
National Technical Information Service
U.S. Department of Commerce
5285 Port Royal Road, Springfield, Virginia 22161
NTIS price codes—Printed Copy: A99 Microfiche A01

This report was prepared as an account of work sponsored by an agency of the United States Government. Neither the United States Government nor any agency thereof, nor any of their employees, makes any warranty, express or implied, or assumes any legal liability or responsibility for the accuracy, completeness, or usefulness of any information, apparatus, product, or process disclosed, or represents that its use would not infringe privately owned rights. Reference herein to any specific commercial product, process, or service by trade name, trademark, manufacturer, or otherwise, does not necessarily constitute or imply its endorsement, recommendation, or favoring by the United States Government or any agency thereof. The views and opinions of authors expressed herein do not necessarily state or reflect those of the United States Government or any agency thereof.

ORNL/FEDC-83/9
Dist. Category UC-20 c,d

ORNL Fusion Program

MFTF-α+T PROGRESS REPORT

The Fusion Engineering Design Center Staff
Chief scientific editor: W. Donald Nelson

Date Published - April 1985

Prepared by
OAK RIDGE NATIONAL LABORATORY
Oak Ridge, Tennessee 37831
operated by
MARTIN MARIETTA ENERGY SYSTEMS, INC.
for the
U.S. DEPARTMENT OF ENERGY
under Contract No. DE-AC05-84OR21400

OAK RIDGE NATIONAL LABORATORY LIBRARY
3 4456 0039826 4

CONTENTS

ACKNOWLEDGMENTS vii
ABSTRACT ix
EXECUTIVE SUMMARY 1
BACKGROUND 3
PHYSICS PARAMETERS 4
MFTF-α+T DESIGN FEATURES 5
REFERENCES 14

1. INTRODUCTION 1-1
1.1 MISSION 1-3
1.2 BASELINE CONCEPT 1-4
1.3 PRINCIPAL DESIGN GUIDELINES 1-4
1.4 PHYSICS PARAMETERS 1-4
1.5 ORGANIZATION OF THIS REPORT 1-5
REFERENCES 1-6

2. PHYSICS AND PLASMA ENGINEERING 2-1
2.1 INTRODUCTION 2-3
2.2 GOALS 2-7
2.3 PHYSICS DESCRIPTION 2-9
REFERENCES 2-24

3. CONFIGURATION 3-1
3.1 OVERVIEW 3-3
3.2 FACILITY MODIFICATIONS 3-8
3.3 D-T AXICELL AND CENTRAL CELL 3-10
3.4 END CELLS 3-17
3.5 FUTURE WORK 3-28
REFERENCE 3-29

4. MAGNET SYSTEMS 4-1
4.1 DESIGN REQUIREMENTS 4-3
4.2 SYSTEM DESCRIPTION 4-7
4.3 COMPONENT DESIGN DESCRIPTIONS 4-22
4.4 CRYOGENIC SYSTEM 4-65
4.5 TRADE STUDIES 4-68
REFERENCES 4-91

5. HEATING, FUELING, AND DRIFT PUMPING 5-1
5.1 INTRODUCTION 5-3
5.2 SUMMARY OF STUDY RESULTS 5-3
5.3 SYSTEM REQUIREMENTS 5-4

5.4 DESIGN DESCRIPTIONS 5-11
5.5 PERFORMANCE ANALYSES 5-37
5.6 TRADE STUDIES 5-60
REFERENCES 5-86

6. HALO SCRAPER, DIRECT CONVERTER, AND VACUUM PUMPING SYSTEM 6-1
6.1 INTRODUCTION 6-3
6.2 HALO SCRAPER 6-5
6.3 DIRECT CONVERTER 6-22
6.4 VACUUM PUMPING SYSTEM 6-32
REFERENCES 6-36

7. TRITIUM SYSTEMS 7-1
7.1 INTRODUCTION 7-3
7.2 KEY PARAMETERS 7-3
7.3 SELECTION OF DISPOSAL METHOD 7-4
7.4 SYSTEM DESCRIPTIONS 7-7
7.5 ACCIDENT SCENARIOS 7-20
7.6 OPERATING CONSIDERATIONS 7-22
7.7 KEY ISSUES 7-27
REFERENCES 7-28

8. VACUUM VESSEL, SUPPORT STRUCTURE, AND NUCLEAR SHIELDING 8-1
8.1 INTRODUCTION 8-3
8.2 REQUIREMENTS AND GUIDELINES 8-3
8.3 DESIGN DESCRIPTION 8-4
8.4 STRUCTURAL ANALYSIS 8-28
8.5 TRADE STUDIES 8-31

9. SHIELDING AND MATERIALS STUDIES 9-1
9.1 INTRODUCTION 9-3
9.2 SHIELDING CRITERIA 9-3
9.3 MATERIALS CONSIDERATIONS 9-6
9.4 DESIGN ANALYSES AND TRADE-OFF STUDIES 9-8
9.5 ACTIVATION ANALYSES 9-27
REFERENCES 9-40

10. ELECTRICAL SYSTEMS 10-1
10.1 INTRODUCTION 10-3
10.2 AC POWER SYSTEM 10-3
10.3 POWER CONVERSION SYSTEM 10-13
10.4 PROCESS CONTROL AND DISPLAY SYSTEM 10-22

10.5 PLASMA CONTROL AND DISPLAY SYSTEM 10-49
10.6 PLASMA DIAGNOSTIC SYSTEM 10-56
10.7 DATA ACQUISITION SYSTEM 10-76
REFERENCE 10-82

11. TESTING AND OPERATIONS 11-1
11.1 INTRODUCTION 11-3
11.2 SYSTEM CHECKOUT 11-4
11.3 DEVICE PERFORMANCE EVALUATION 11-7
11.4 ADVANCED SYSTEMS TESTING 11-7
11.5 TEST SCENARIO 11-14
REFERENCES 11-16

12. MAINTENANCE 12-1
12.1 INTRODUCTION 12-3
12.2 MAINTENANCE PHILOSOPHY 12-3
12.3 MAINTENANCE APPROACH 12-4
12.4 MAINTENANCE OPERATIONS 12-12
12.5 MAINTENANCE EQUIPMENT 12-22
REFERENCES 12-28

13. PLANT FACILITIES 13-1
13.1 INTRODUCTION 13-3
13.2 REQUIREMENTS AND CRITERIA 13-3
13.3 DESIGN DESCRIPTION 13-4

14. SAFETY AND SITING 14-1
14.1 INTRODUCTION 14-3
14.2 SAFETY CRITERIA AND REQUIREMENTS 14-3
14.3 POTENTIAL RADIOLOGICAL HAZARDS AND CONSEQUENCES 14-6
14.4 SAFETY FEATURES 14-10
14.5 SITING 14-11
14.6 SUMMARY 14-11
REFERENCES 14-12

Appendix A. ASSESSMENT OF MFTF-α+T SEISMIC CAPABILITY A-1

LIST OF ABBREVIATIONS AND ACRONYMS B-1

ACKNOWLEDGMENTS

A report of this size and magnitude is accomplished only through the hard work of many individuals. Those who have contributed to this report bring great credit to the organizations they represent. I thank all of them for their contributions.

I wish to make special note of the extra effort put forth by two individuals. Joe O'Toole (Fusion Engineering Design Center/Grumman Aerospace Corporation) provided major input to the overall machine design as part of his job. In addition, he worked countless hours reviewing and improving the work of others. He edited, created, sketched, and was, in short, invaluable. The second person deserving special credit is Patricia Powell (Fusion Engineering Design Center/General Electric Company). All of the secretarial staff of the Design Center are noteworthy for the quantity and quality of their work. Patricia has gone well beyond her job description in managing the artwork interface between the physicists and the engineers and the publications staff. In addition, she has maintained and updated a baseline copy of the report throughout its preparation and has been a superb expediter.

As preparation for the publication of this report reached its final stages, it became more and more clear that special acknowledgment is also due the staff of the Fusion Energy Division Publications Office—in particular, the graphics group leader, Jane Parrott, and the publication editor, Bonnie Nestor Johnson. Without Bonnie's extra attention to this report, it would still be "in process."

W. Donald Nelson
Fusion Engineering Design Center/General Electric Company

ABSTRACT

Early in FY 1983, several upgrades of the Mirror Fusion Test Facility (MFTF-B) at Lawrence Livermore National Laboratory (LLNL) were proposed to the fusion community. The one most favorably received was designated MFTF-α+T. The engineering design of this device, guided by LLNL, has been a principal activity of the Fusion Engineering Design Center during FY 1983. This interim progress report represents a "snapshot" of the device design, which was begun in FY 1983 and will continue for several years.

The report is organized as a complete design description. Because it is an interim report, some parts are incomplete; they will be supplied as the design study proceeds.

As described in this report, MFTF-α+T uses existing facilities, many MFTF-B components, and a number of innovations to improve on the physics parameters of MFTF-B. It burns deuterium-tritium and has a central-cell Q of 2, a wall loading Γ_n of 2 MW/m^2 (with a central-cell insert module), and an availability of 10%. The machine is fully shielded, allows hands-on maintenance of components outside the vacuum vessel 24 h after shutdown, and has provisions for repair of all operating components.

EXECUTIVE SUMMARY

W. D. Nelson
Fusion Engineering Design Center/General Electric Company

J. N. Doggett
Lawrence Livermore National Laboratory

CONTENTS

BACKGROUND 3
Mission 3
Baseline Concept 3
Principal Design Guidelines 3
PHYSICS PARAMETERS 4
MFTF-α+T DESIGN FEATURES 5
Configuration 6
Magnet System 6
Heating, Fueling, and Drift Pumping 7
Halo Scraper, Direct Converter, and Vacuum Pumping 8
Tritium Systems 10
Vacuum Vessel, Support Structure, and Shielding 10
Electrical Systems 11
Testing and Operations 11
Maintenance 12
Plant Facilities 12
Safety and Siting 13
REFERENCES 14

EXECUTIVE SUMMARY

The MFTF-α+T is an upgrade of the Mirror Fusion Test Facility (MFTF-B) at Lawrence Livermore National Laboratory (LLNL). The engineering design of this device has been a principal design activity of the Fusion Engineering Design Center (FEDC) during FY 1983. Guided by LLNL, the Design Center initiated a number of trade studies with the goal of producing a complete design description of the MFTF-α+T device. This interim progress report represents a "snapshot" of the device design.

BACKGROUND

Mission

The mission of the MFTF-α+T is to provide a useful step in the orderly progression from MFTF-B to the next major experimental mirror machine. As such, MFTF-α+T will advance the physics database and verify the technology required for the Fusion Power Demonstration (FPD) that is to follow. The physics issues addressed for this purpose are

- alpha particle physics in a tritium-burning system,
- physics of a reactor geometry based on the Mirror Advanced Reactor Study (MARS),[1]
- halo physics, and
- drift pumping physics.

Technology issues include

- tritium processing and cleanup in a reactorlike mode,
- negative-ion-based neutral-beam injection,
- tritium-breeding blankets,
- power-producing blankets,
- operation of high-field magnets in a nuclear environment,
- operation of control systems in a reactorlike mode,
- maintenance of an activated system, and
- response of materials to irradiation at reactor-level fluxes.

Baseline Concept

The baseline concept proposed by LLNL includes the use of end plugs like those described for MARS,[1] direct conversion, halo pumping, negative-ion-based neutral-beam injectors to produce sloshing ion beams, and full neutron shielding. The expected performance of MFTF-α+T is summarized in Table 1.

Principal Design Guidelines

The following constraints were imposed on the MFTF-α+T design.

- The device is to be housed in the MFTF-B vault space.
- The MFTF-B hardware systems are to be used as fully as possible.

Table 1. MFTF-α+T performance parameters

	Operating mode	
	High Q	High Γ
Effective Q Q_{eff}	2.4	1.2
Average beta, %	40	31
Field B_0, T	1.6	4.5
Ion confinement parameter $n\tau$, $cm^{-3}\cdot s$	1×10^{14}	4.7×10^{13}
Density n, cm^{-3}	1.9×10^{14}	4.75×10^{14}
Fusion power density, W/cm^2	1.93	55.2
Total fusion power, MW	7	17
Γ., MW/m^2	0.11	2.0
Plasma radius r_p, m	0.25	0.15
Cell length, m	20	4.0

- The technology is limited to modest extrapolation of existing systems or that scheduled to be produced by existing programs.
- The experimental run length is to be 100 h (steady state).
- A high-flux nuclear testing region is to be included.
- The capital cost will be low.

PHYSICS PARAMETERS

As described in ref. 2, the MFTF-α+T device will operate in two distinctly different modes. In the high-Q mode (Q = fusion power produced/power input to the plasma), confinement is improved and a central-cell Q of 2 is achieved. In the high-Γ mode, a nuclear test station insert is placed in the central-cell region, the device is operated in a Kelley mode,[3] the neutron wall loading Γ_n is 2 MW/m^2, and pulses last up to 100 h. The fluence is expected to be more than 2 $MW\cdot year/m^2$ over the 10-year device lifetime. Deuterium-tritium (D-T) fuel is used in both modes.

The MARS end plug design[1] is used for MFTF-α+T because it leads to substantial improvements in tandem mirror physics. The increased magnetic field level and sloshing beam energy provide a plugging potential twice that of MFTF-B, so that the confinement parameter $n\tau \approx 10^{14}$ $cm^{-3}\cdot s$ and operation is at $Q \sim 2$ (compared to $Q \sim 0.2$ to 0.4, as expected in MFTF-B). End plugging is good enough that radial losses dominate (MARS regime), the central-cell heating and power losses dominate over plug power, the central-cell population is more nearly isotropic than in MFTF-B, and alpha heating is significant. With the improved magnetohydrodynamic (MHD) design of the end plugs, the central-cell beta is double that in MFTF-B (average beta is 40%), and $\beta_c B_c^2$ increases five-fold during operation at 1.6 T in the central cell.

The Q value is further improved by the use of drift pumping, which also removes impurities (necessary for long-pulse or steady-state operation), instead of beam charge-exchange pumping in the MFTF-α+T end cells. Another feature is the addition of a

region of good curvature in the transition region. This region becomes the MHD anchor and adds to the MHD damping of the plug region—the other region of good curvature with high plasma pressure. The additional region of good curvature is also a feature of MFTF-B; it was emphasized in the MARS design to very good effect, as it is in the MFTF-α+T design.

MFTF-α+T DESIGN FEATURES

Using the mission statement, baseline concept, design guidelines, and physics parameters provided by LLNL, the Design Center initiated trade studies addressing key issues for MFTF-α+T. These studies, many of which are still in progress, have resulted in the design shown in Fig. 1. This design meets the requirements derived from the mission statement, makes use of the technologies suggested in the baseline concept, and adheres to the design guidelines.

The MFTF-α+T design incorporates existing hardware and modifies existing components wherever possible to maximize the contribution of MFTF-B to the upgrade. It also incorporates some totally new systems. The most technologically innovative additions are the continuous 80- and 200-keV neutral beams, the high-field, unshielded copper coils, and the drift pumping system. Aggressive development programs will be needed to make

ORNL–DWG 83-4006 FED

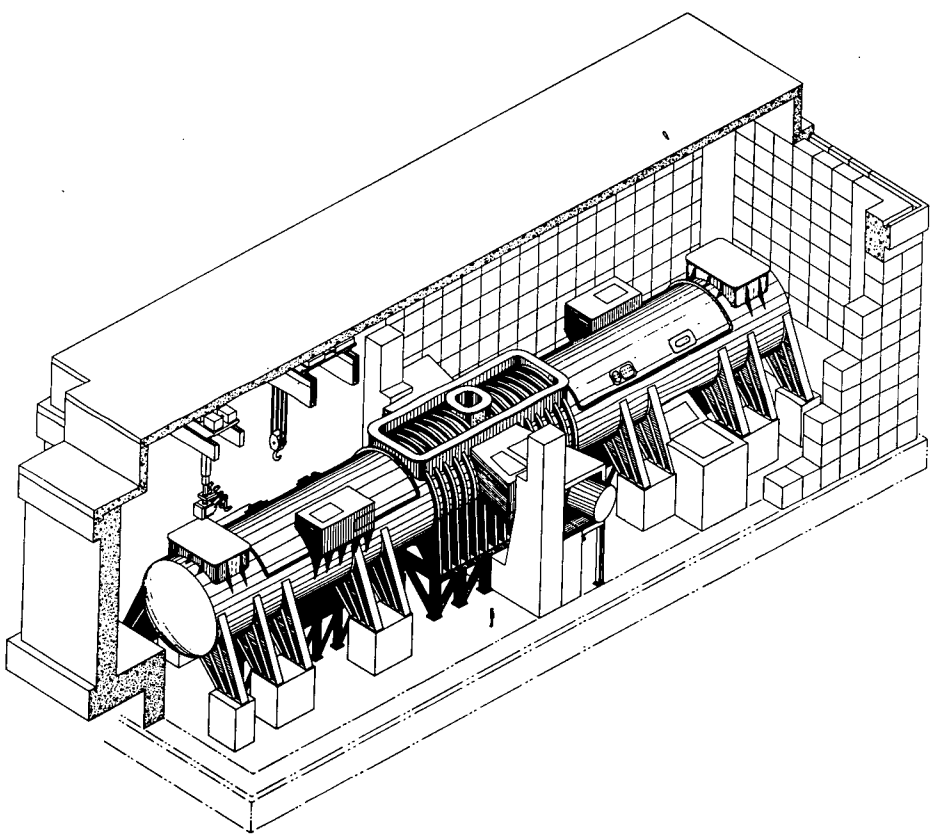

Fig. 1. The MFTF-α+T device.

these items available in time. The most critical new technology on MFTF-α+T is the tritium fuel cycle and cleanup system.

Configuration

As shown in Fig. 1, the external configuration of MFTF-α+T is basically a circular cylinder 8.3 m in diameter and 65 m long. (By comparison, MFTF-B has an end-cell diameter of 11.6 m and is 58 m long.) The major systems and components of MFTF-α+T are shown in Fig. 2. In this cutaway plan view, the components have been rotated into a plane for the sake of clarity. All of the end-cell components (and the halo plasma outline) are actually oriented at 45° to the plane of the drawing.

For engineering purposes, the device can be divided into three areas: the D-T axicell, the central cell, and the end cells. The D-T axicell consists of a new structure that accommodates one central background-field copper coil, two 12-T choke coils, two positive-ion-based neutral-beam injectors, and a nuclear test module. The test module is located at the midpoint of the machine between the 12-T choke coils, and its background field is provided by large superconducting coils. The central cell extends for 8 m on either side of the D-T axicells and ends at the 18-T choke coils. Each half of the central cell contains five MFTF-B solenoid coils. The end cells contain all of the systems required for plugging and stabilizing the plasma, vacuum pumping, impurity removal, and potential control.

Magnet System

The magnet system of MFTF-α+T differs significantly from that of MFTF-B. Major additions are the MARS-like end cells and the central-cell nuclear test module.

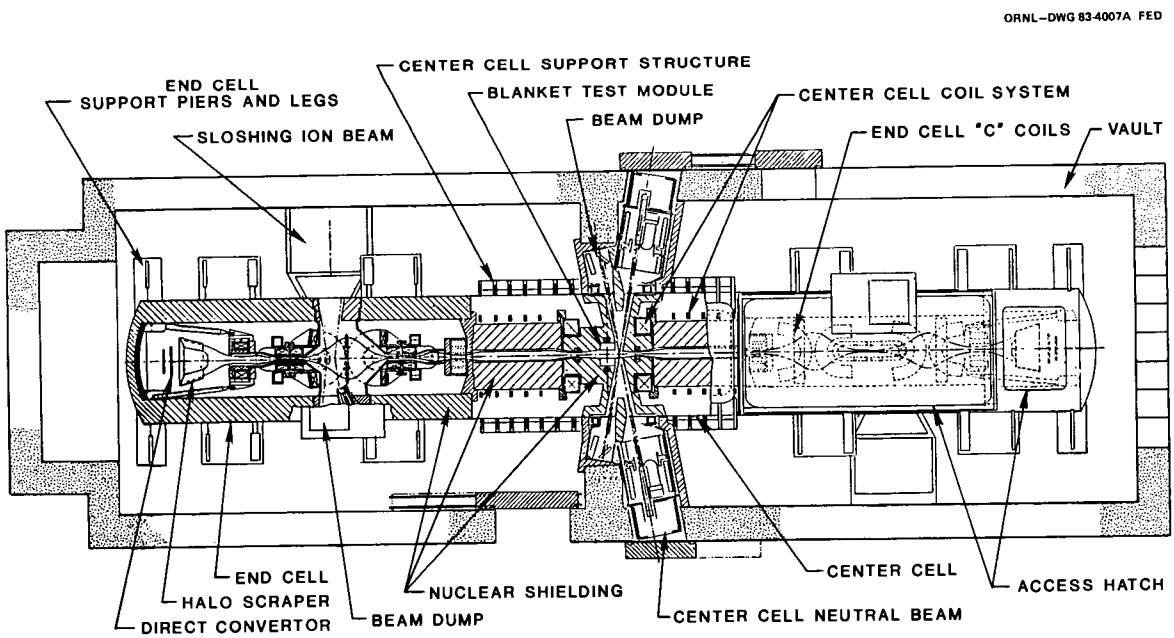

Fig. 2. Cutaway plan view of MFTF-α+T.

The superconducting magnet technology is extrapolated from MFTF-B, and 12 of the 24 superconducting coils on MFTF-α+T will be taken from MFTF-B, as shown in Fig. 3.

The entire magnet set—24 superconducting coils and 5 copper coils—will be shielded from the D-T neutron environment. In addition, all of the superconducting coils are removable, and the copper coils are accessible for repair or replacement.

Of the five copper coils, four are inserts to superconducting coils and are used to provide background fields. These coils will produce fields on axis of 12 and 18 T and represent significant extensions of the state of the art. The fifth copper coil is located in the D-T axicell region, where its use should help to lower the cost of the nuclear test module magnets.

Heating, Fueling, and Drift Pumping

On MFTF-α+T, radio-frequency (rf) power is used for almost all heating and particle pumping functions. Neutral beam injection is used in the central cell to fuel the plasma and in the end cells to maintain a high-energy sloshing ion population (see Fig. 4).

Electron-cyclotron resonance heating (ECRH) is used to provide thermal and potential barriers in the end plugs. Most of the equipment needed is available on MFTF-B.

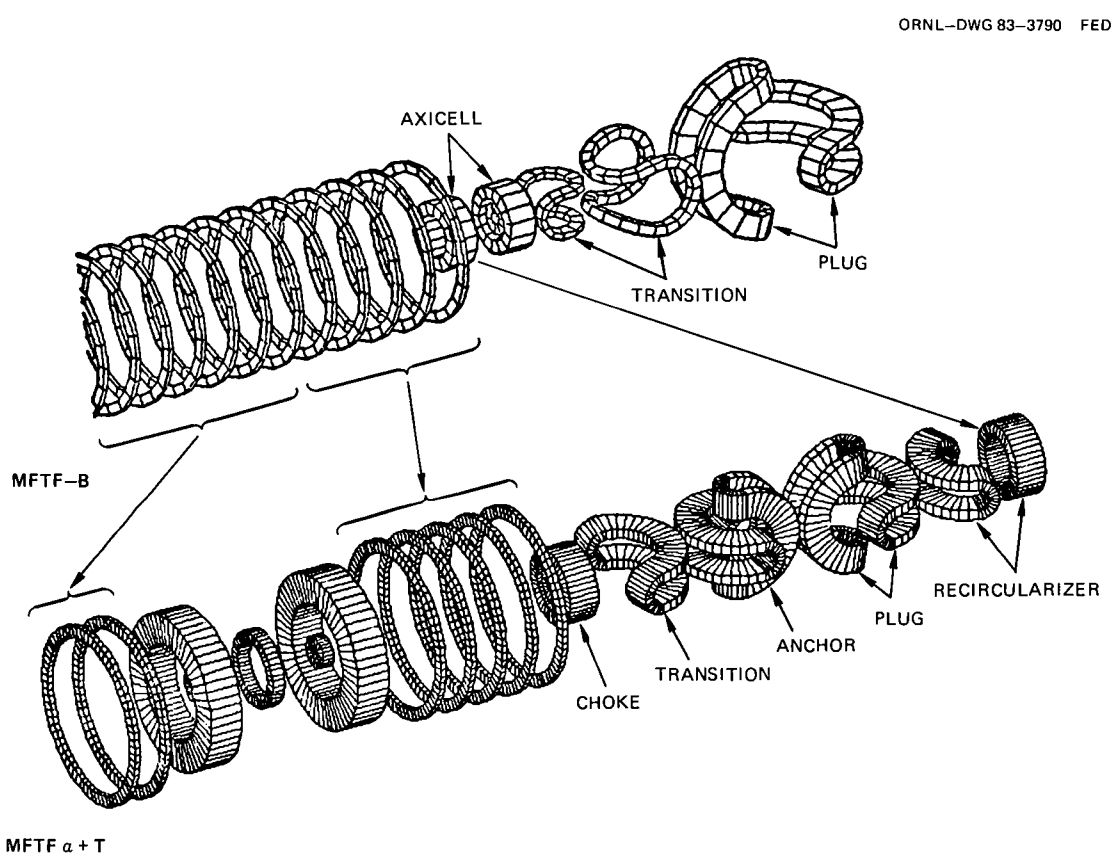

Fig. 3. Magnet configurations of MFTF-B and MFTF-α+T, showing how existing coils will be used in the new device.

ORNL–DWG 83-4016A FED

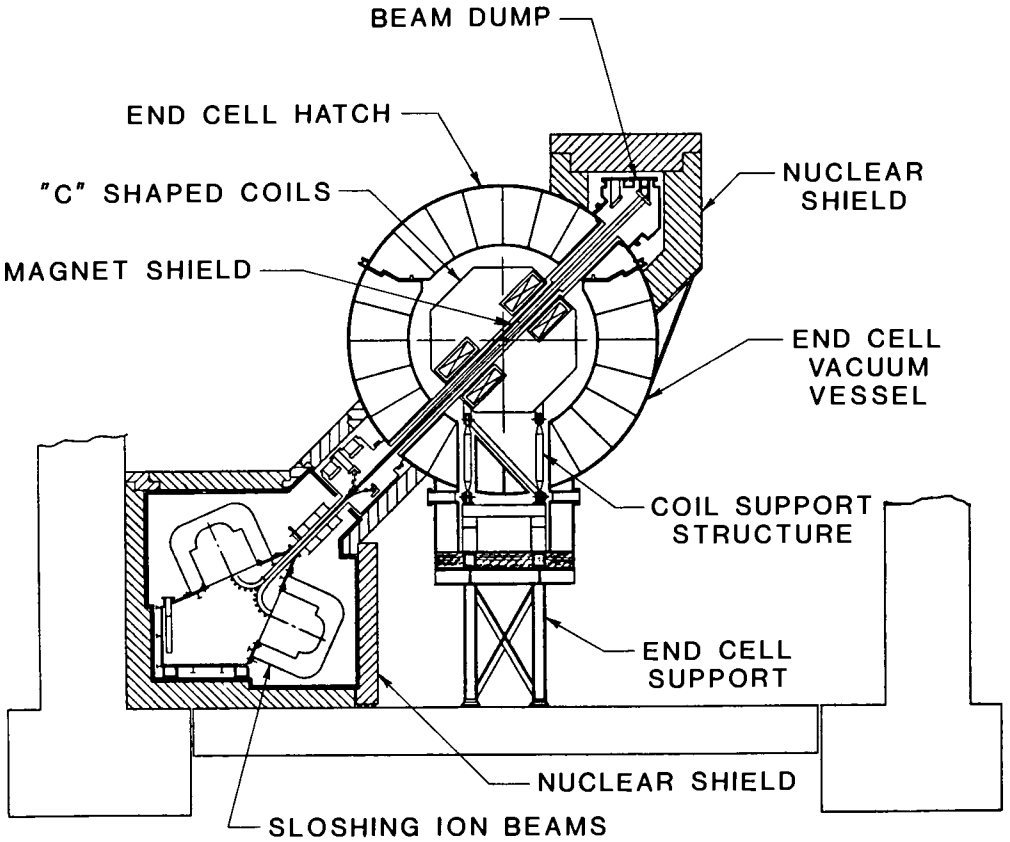

Fig. 4. Sloshing ion beam and end dump configuration.

Ion-cyclotron resonance heating (ICRH) is used in the anchor cells to control beta in place of transition pumping beams. The MFTF-B central-cell equipment is to be converted to 25 MHz; two additional systems, with frequencies of 25 and 50 MHz, are required.

For rf drift pumping, very low frequency, high-current signals are used to excite coils placed in the anchor and end cells (see Fig. 5). The flux created by these coils perturbs the end-cell magnetic fields, which increases the ion radial transport. This allows the direct converter to function as an electron device.

Halo Scraper, Direct Converter, and Vacuum Pumping

The MFTF-α+T device will be the first to feature a halo scraper for impurity removal. The materials and the location of the scraper, selected through trade studies, are expected to allow this component to last for the life of the device. A gridless direct converter, to control the plasma potential and to extract heat and electrical energy from the plasma, is included in the MFTF-α+T design. (To keep capital costs low, no provision for processing this energy is included.) Vacuum pumping during the plasma burn can be done

ORNL-DWG 83-4005 FED

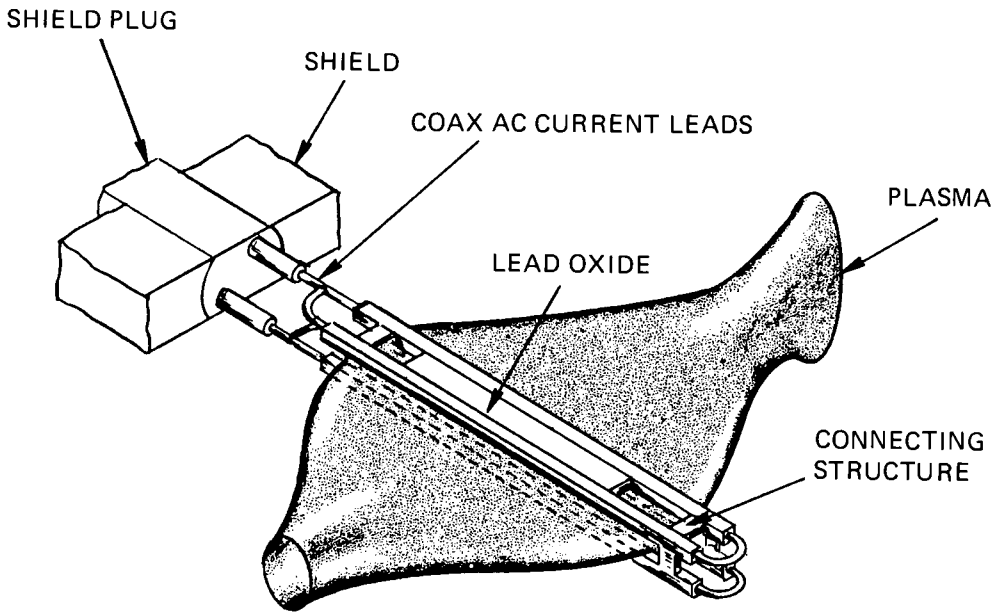

Fig. 5. Drift pump antenna arrangement.

at much higher pressure than would be possible without the halo scraper, which allows the use of turbomolecular pumps rather than cryopumps. This in turn reduces the tritium inventory. The halo scraper and direct converter are shown in Fig. 6.

ORNL-DWG 83-4009 FED

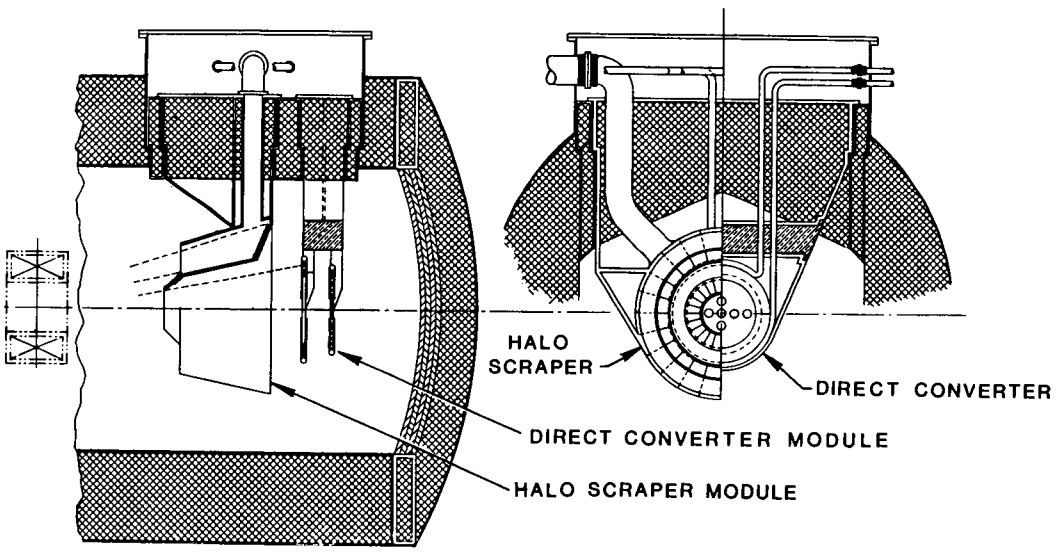

Fig. 6. Halo scraper and direct converter.

Tritium Systems

The fueling requirements of MFTF-α+T, which will produce 17 MW of fusion power with a burn fraction of 0.02 and pulses lasting over 100 h, make it highly desirable to include a continuous tritium processing system. Without reprocessing, a tritium inventory of 2–3 kg would be needed; with the complete fuel cycle designed for MFTF-α+T, less than 450 g is required. The cost of tritium over the device lifetime is reduced by a factor of 10 or more, even when the capital cost of the reprocessing system is taken into account. The lower inventory is also a safety factor. The system includes components for processing and storage, secondary containment, atmospheric tritium recovery, waste processing, accountability analysis, and safety.

Vacuum Vessel, Support Structure, and Shielding

Cost, ease of maintenance, and machine availability were important factors in the selection of concepts for the MFTF-B vacuum vessel and support structure. For example, the central cells and the end cells have the same diameter, which lowers tooling and fabrication costs; the existing end-cell support piers are used; and the integrated vacuum vessel/shield design of the end cells is an efficient use of structurally required material. An indication of the approach is given by Fig. 7.

To support the philosophy of hands-on maintenance of components outside the vacuum vessel 24 h after shutdown, the bulk shielding is located inside the vacuum vessel.

ORNL–DWG 83-4008A FED

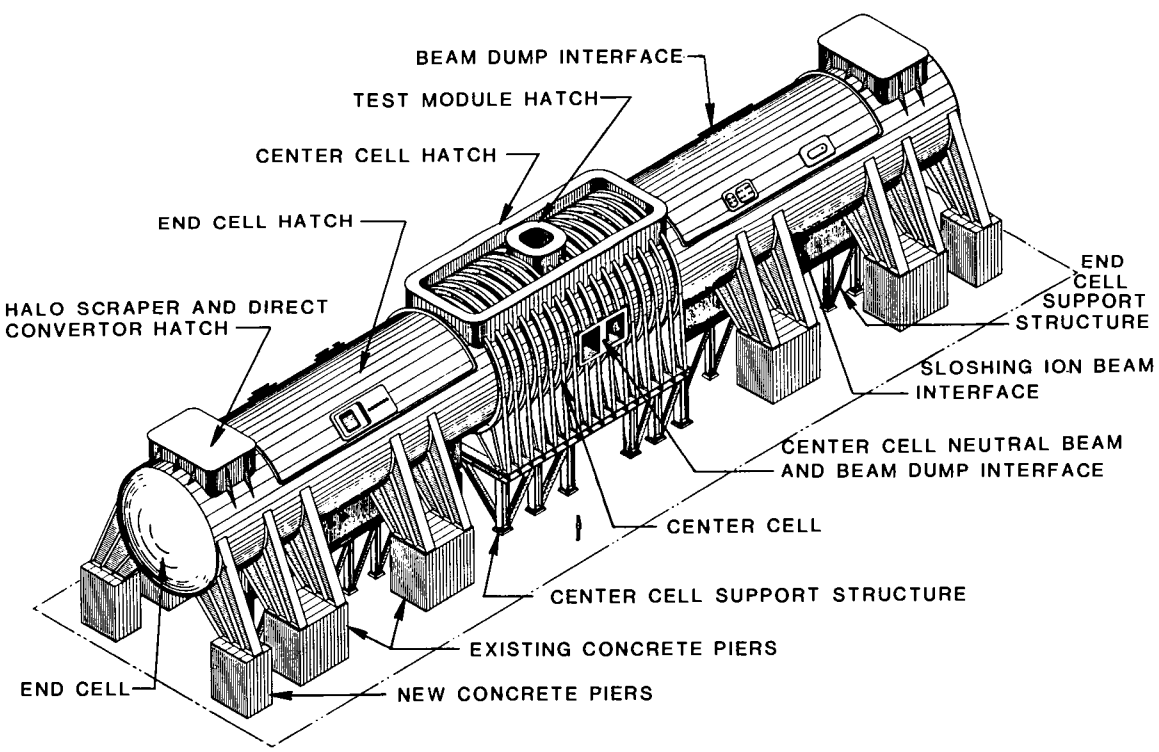

Fig. 7. External view of vacuum vessel and support structure.

Low-cost shielding materials (water and concrete) are used wherever possible. The shielding is sufficient to allow 10% availability and to keep radiation at the end of the machine lifetime to 0.5 mrem/h after the machine has been shut down for 24 h.

Electrical Systems

The MFTF-α+T electrical systems include the ac power system, the power conversion system, the instrumentation and control (I&C) system, and the data acquisition and processing system. The cost of these systems is minimized by using much of the existing MFTF-B equipment.

Two ac power substations that provide power to MFTF-B are to be upgraded, and four diesel generators to provide backup power for tritium and safety systems will be added. Power for the MFTF-α+T magnets is provided by 17 MFTF-B magnet supplies and by 6 new power supplies (needed to meet the higher current requirements of the copper choke coils and the center background-field coil).

The MFTF-B neutral beam power supplies are to be modified as required and used to provide dc power to the MFTF-α+T neutral beam injectors and rf systems. The cooling system will be modified as needed to allow continuous operation of these supplies at reduced current.

The primary controls for MFTF-α+T use reliable process measurements that are compatible with the I&C on MFTF-B. Considerably more I&C is required for the rf power systems on MFTF-α+T. The primary control system accommodates some secondary controls for plasma trim feedback control. All systems are designed to be flexible enough to cope with the limited physics understanding of the end cells and to accommodate experiments.

Much of the equipment used for diagnostic signal conditioning and data acquisition on MFTF-B external to the vacuum vessel can be used for MFTF-α+T. The diagnostics for MFTF-α+T are designed to provide information about the problems of operation in a highly radioactive environment, about the D-T axicell plasma despite limited access, and about real-time feedback control. Plasma measurements must be reported reliably (with an accuracy of $\pm 5\%$ or better). The need for data on both the D-D and D-T phases of operation (including tritium, neutron, and alpha particle diagnostics, which are not available on MFTF-B) is addressed.

The MFTF-B data acquisition system will be expanded to accommodate additional measurements of neutral beam injection, ECRH, ICRH, and drift pumping. Measurements must also be taken from the shield and structure, the fueling processing systems, the water cooling systems, the direct converter, and the test module. Several thousand additional data channels will be installed for MFTF-α+T.

Testing and Operations

The MFTF-α+T device is envisioned as one of the first fusion devices to be used as both an engineering facility and a nuclear test facility. Over its 10-year lifetime, the systems integration aspects of MFTF-α+T, its unique plasma characteristics, its large nuclear test volume, and its relatively long burn times and high availability will lend

themselves to tests of a number of issues. Test categories include system checkout tests to determine the operating behavior and reliability of individual systems under reactor conditions; device performance tests to explore the integrated performance in terms of plasma operation, neutron production, and impurity removal; and advanced systems tests to investigate the performance of systems (e.g., tritium-breeding blankets) that may be used in future reactors. The test scenario currently proposed for MFTF-α+T is as follows:

- one year of preoperation and online checkouts of individual systems,
- two years of operation in the high-Q mode for device performance tests, and
- seven years of operation in the high-Γ mode to collect engineering reliability data and to test blanket designs for the FPD.

The selection of tests to be performed depends on the relationship of MFTF-α+T to the rest of the fusion program, in particular other test devices.

Maintenance

The maintenance philosophy for MFTF-α+T is a four-fold approach based on providing operational flexibility for this near-term device and accomplishing numerous maintenance tasks between operating runs. The MFTF-α+T design meets the following maintenance requirements.

- Contact operations at the shield boundary are permitted 24 h after device shutdown.
- Major maintenance and disassembly operations can be accomplished remotely under both normal and emergency conditions.
- Modularized component installations are arranged for independent disassembly procedures.
- Proven remote-equipment technology is used.

The design of the vacuum vessel and support structure takes into account needs for maintenance and high availability. Hatches and access ports are provided to allow direct removal of major components where possible, as illustrated in Fig. 8.

The equipment needed to maintain MFTF-α+T is generally available or under development in other programs. A necessary constituent of the success of this approach is a mockup facility, which will be used over the lifetime of the device to improve and verify equipment use, assess component design, and train operators.

Plant Facilities

The MFTF-α+T meets design guidelines in making maximum use of the MFTF-B facility at LLNL. Building 431 and the reactor vault are used in their entirety, as are existing buildings for MFTF source testing and space formerly used to house an experimental test accelerator (see Fig. 9). Modifications of the reactor vault are needed to make it meet MFTF-α+T seismic requirements and to provide remote maintenance facilities. A hot cell facility and a tritium processing facility are to be added, and some modifications to the power supply and cooling systems are required.

ORNL–DWG 83–4025 FED

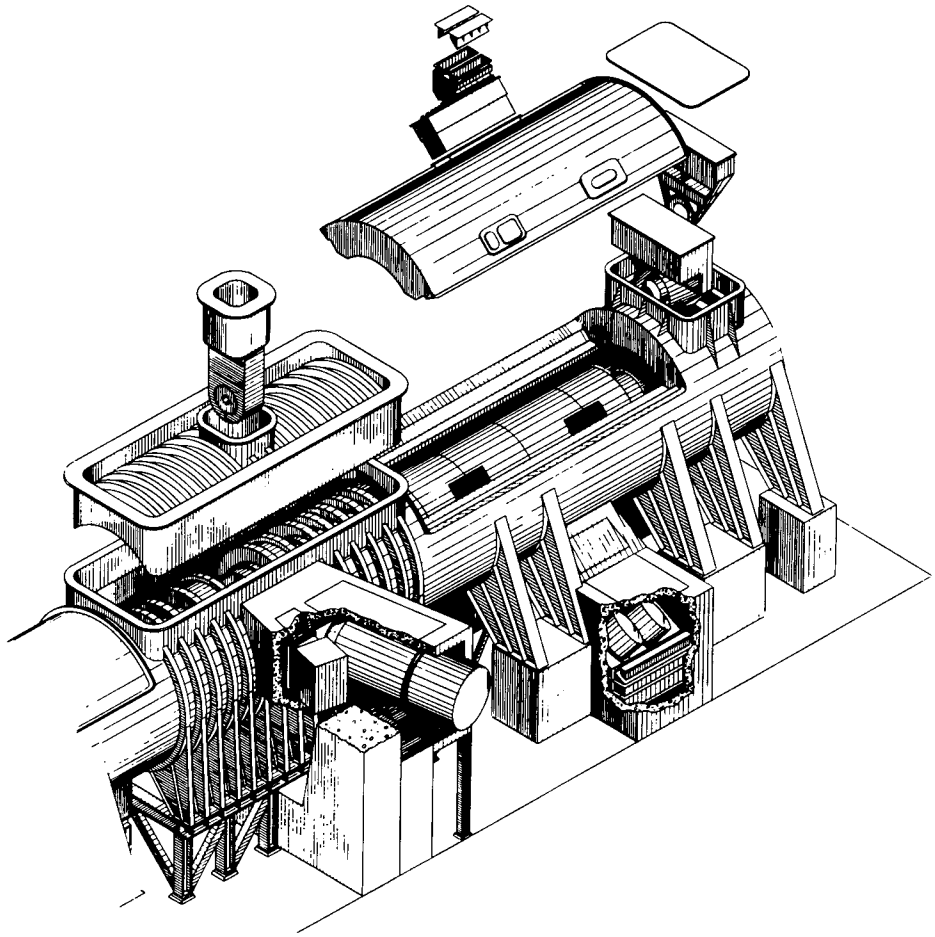

Fig. 8. Test station assembly and access to major components.

Safety and Siting

One objective of MFTF-α+T is to demonstrate safe operation of a D-T–burning fusion facility with minimum environmental impact. A preliminary assessment of the effects of normal operation, component failure, and failure induced by natural phenomena indicates that a major release of tritium — the primary source of environmental and safety concern — is highly improbable ($<10^{-6}$ per year), given the multiple levels of confinement barriers to all major sources of tritium.

Major siting considerations for MFTF-α+T include the seismicity of the LLNL site, the location of the site boundary, and the location of population zones outside the site boundary. All safety-related structures are to be designed to accommodate maximum credible seismic forces. The site boundary is located 0.5 km from the MFTF-α+T facility. Preliminary estimates indicate that, for normal operation or for conditions following an accident, an individual at the site boundary or a member of the general public residing in the nearest population zone will receive a radiation dose far lower (by several orders of magnitude) than the limits allowed by the Department of Energy.

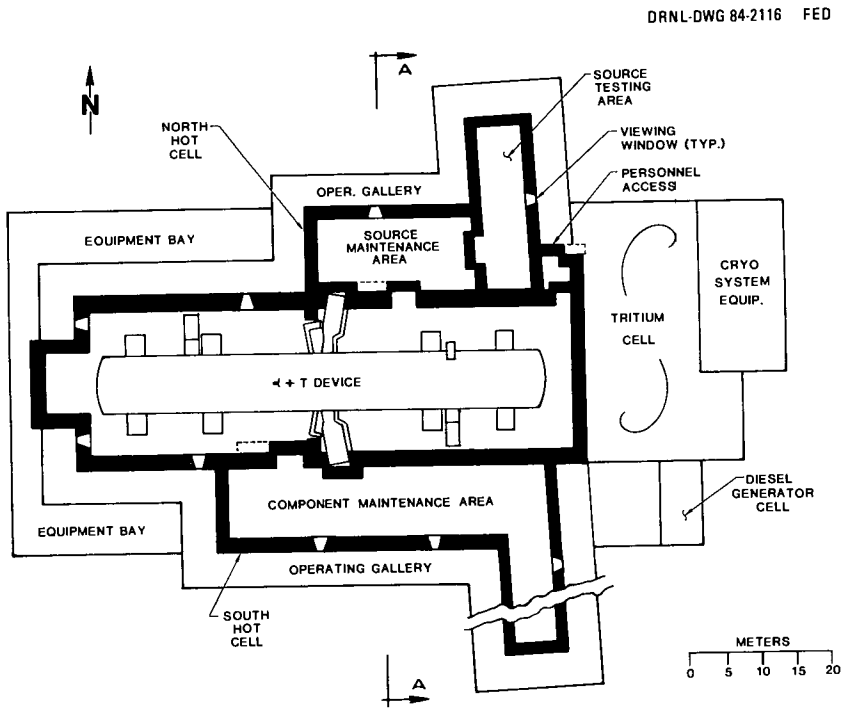

Fig. 9. Use of space for MFTF-α+T.

REFERENCES

1. *Mirror Advanced Reactor Study—Interim Report*, UCID-53333, Univ. California, Lawrence Livermore Natl. Lab., Livermore, Calif., 1983.

2. K. I. Thomassen and J. N. Doggett, *Options to Upgrade the Mirror Fusion Test Facility*, UCID-19743, Univ. California, Lawrence Livermore Natl. Lab., Livermore, Calif., April 1983.

3. "Kelley mode" refers to the two-component ion distribution in the central cell; the hot, magnetically trapped ions constitute the majority species. The mode is named for George G. Kelley, who first described different modes of operation in mirror devices.

1. INTRODUCTION

Fusion Engineering Design Center Staff

Oak Ridge National Laboratory

CONTENTS

1.1 MISSION 1-3
1.2 BASELINE CONCEPT 1-4
1.3 PRINCIPAL DESIGN GUIDELINES 1-4
1.4 PHYSICS PARAMETERS 1-4
1.5 ORGANIZATION OF THIS REPORT 1-5
REFERENCES 1-6

1. INTRODUCTION

The objective of mirror fusion research is to produce energy from the fusion of light ions through the confinement of high-temperature plasmas in magnetic mirror systems. Achieving this objective requires the successful development of a series of machines with ever-increasing performance.[1] The MFTF-α+T device, an upgrade of the Mirror Fusion Test Facility (MFTF-B) at Lawrence Livermore National Laboratory (LLNL), is a major step in this series of machines. It will serve both to advance the physics data base needed in predicting with confidence the behavior of mirror containment systems and to verify the technology needed for future fusion reactors.

The mission of MFTF-α+T, a baseline concept for the device, a set of principal design guidelines, and the physics parameters were evolved by LLNL staff. Using this information, the Fusion Engineering Design Center (FEDC) initiated a number of trade studies with the goal of producing a complete design description of the MFTF-α+T device. This interim report presents a "snapshot" of the device design that is being carried out by the Design Center under the guidance of LLNL.

The input provided by LLNL is summarized in Sects. 1.1 through 1.4; the organization of the remainder of the report is outlined in Sect. 1.5.

1.1 MISSION

The MFTF-α+T is intended to provide a useful step in the orderly progression from MFTF-B to the next major experimental machine, the Fusion Power Demonstration (FPD). The physics issues to be addressed by MFTF-α+T for this purpose are:

- alpha particle physics in a tritium-burning system,
- physics of a reactor geometry based on the Mirror Advanced Reactor Study (MARS),[2]
- physics of the plasma halo, and
- physics of drift pumping.

Key technology issues for fusion reactors that will be developed and tested on MFTF-α+T include:

- tritium processing and cleanup in a reactorlike mode,
- negative-ion-based neutral beam injection,
- tritium-breeding blankets,
- power-producing blankets,
- operation of high-field magnets in a nuclear environment,
- operation of control systems in a reactorlike mode,
- maintenance of an activated system, and
- response of materials to irradiation at reactor-level fluxes.

1.2 BASELINE CONCEPT

The baseline concept for MFTF-α+T incorporates proven technologies, recent design developments, and new concepts to fulfill the mission objectives. Positive-ion-based neutral beams heat the central cell; negative-ion-based beam injectors are used to produce the sloshing-ion beams that improve plasma microstability. The magnetic fields will be provided by a combination of existing coils from MFTF-B and new coils built for MFTF-α+T. The end-plug design developed in the MARS[2] design work is used. The conversion to electric power of energy that would otherwise be lost is demonstrated with the gridless direct converters in each end cell (although there are no provisions for processing this energy). Impurities are removed with a halo scraper; MFTF-α+T is the first device to feature this method of impurity control. Full neutron shielding is provided and protects device components and personnel so that hands-on maintenance is possible in the reactor vault. Remote maintenance techniques developed for MFTF-α+T will serve as a basis for future reactor operations.

1.3 PRINCIPAL DESIGN GUIDELINES

Because the MFTF-α+T is an upgrade of an existing system, a number of constraints were imposed on the design process to meet the budget and schedule for the upgrade and to ensure that the requirements of the mission are met.

The device is to be housed in the MFTF-B vault space, and all MFTF-B systems are to be used as fully as possible. Technology must be scheduled to be produced by existing programs or must result from modest extrapolation of existing systems, so that no major development is necessary. The experimental run length is to be 100 h; that is, the device will operate in an essentially steady state. A high-flux nuclear testing region is to be included. In this region, tests of blanket modules can be carried out to fulfill the mission objectives. Finally, the capital cost must be low.

1.4 PHYSICS PARAMETERS

A complete description of the physics parameters of MFTF-α+T is given in Chap. 2. Briefly, the MFTF-α+T device will operate in two distinctly different modes, as described in ref. 3. In the high-Q mode (Q = fusion power produced/power input to the plasma), confinement is improved and a central-cell Q of 2 is achieved. In the high-Γ mode, a nuclear test module insert is placed in the central-cell region, the device is operated in a Kelley mode,[4] the neutron wall loading Γ_n is 2 MW/m^2, and pulses last up to 100 h. The fluence is expected to be more than 2 MW·year/m^2 over the 10-year device lifetime. Deuterium-tritium (D-T) fuel is used in both modes.

The MARS end plug design[2] leads to substantial improvements in tandem mirror physics. Operation is at $Q \sim 2$ (compared to $Q \sim 0.2$ to 0.4, as expected in MFTF-B). End plugging is good enough that radial losses dominate (MARS regime), the central-cell heating and power losses dominate over plug power, the central-cell population is more nearly isotropic than in MFTF-B, and alpha heating is significant. The central-cell beta is double that in MFTF-B (average beta is 40%), and $\beta_c B_c^2$ increases five-fold during operation at 1.6 T in the central cell.

The Q value is further improved by the use of drift pumping, which also removes impurities (necessary for long-pulse or steady-state operation), instead of beam charge-exchange pumping in the MFTF-α+T end cells. A region of good curvature is added in the transition region. This region becomes the MHD anchor and adds to the MHD damping of the plug region—the other region of good curvature with high plasma pressure. The additional region of good curvature is also a feature of MFTF-B; it was emphasized in the MARS design to very good effect, as it is in the MFTF-α+T design.

1.5 ORGANIZATION OF THIS REPORT

Using the mission statement, baseline concept, design guidelines, and physics parameters provided by LLNL, the Design Center initiated extensive trade studies for MFTF-α+T beginning in FY 1983. This report presents a design description of MFTF-α+T based on these studies. Issues relating to all aspects of the MFTF-α+T device are being examined in detail, and studies are expected to continue for several years. Some topics are discussed only in general terms or are not addressed; as information becomes available, it will be presented in future reports.

The description begins with a detailed discussion of the physics of MFTF-α+T in Chap. 2. The overall device configuration is described in Chap. 3. Magnet systems are described in Chap. 4; heating, fueling, and drift pumping systems in Chap. 5. The two systems to be used for the first time on MFTF-α+T, the halo scraper and the direct converter, are discussed in Chap. 6. The tritium processing system for MFTF-α+T is described in Chap. 7. Chapter 8 addresses the requirements of the vacuum vessel, support structure, and nuclear shielding necessary for MFTF-α+T. Studies of shielding and materials are described in Chap. 9. The electrical systems for device operation are evaluated in Chap. 10. Testing and operations are discussed in Chap. 11, maintenance needs in Chap. 12, and plant facilities in Chap. 13. Chapter 14 contains a discussion of safety needs and precautions, including an evaluation of the suitability of the LLNL site. A table of contents is provided at the beginning of each chapter, and a list of acronyms and abbreviations is provided on a foldout page at the end of the report.

REFERENCES

1. R. R. Borchers and C. M. VanAtta, eds., *The National Mirror Fusion Program Plan*, UCAR-10042-80, Univ. California, Lawrence Livermore Natl. Lab., Livermore, Calif., January 1980.

2. *Mirror Advanced Reactor Study—Interim Report*, UCID-53333, Univ. California, Lawrence Livermore Natl. Lab., Livermore, Calif., 1983.

3. K. I. Thomassen and J. N. Doggett, *Options to Upgrade the Mirror Fusion Test Facility*, UCID-19743, Univ. California, Lawrence Livermore Natl. Lab., Livermore, Calif., April 1983.

4. "Kelley mode" refers to the two-component ion distribution in the central cell; the hot, magnetically trapped ions constitute the majority species. The mode is named for George G. Kelley, who first described different modes of operation in mirror devices.

2. PHYSICS AND PLASMA ENGINEERING

K. E. Thomassen

Lawrence Livermore National Laboratory

CONTENTS

2.1 INTRODUCTION 2-3
2.2 GOALS 2-7
2.2.1 Physics Issues 2-7
2.2.2 Plasma Technology Development 2-8
2.3 PHYSICS DESCRIPTION 2-9
2.3.1 The High-Q Mode 2-14
2.3.2 The High-Γ Mode 2-20
REFERENCES 2-24

2. PHYSICS AND PLASMA ENGINEERING

2.1 INTRODUCTION

Part of the mission of the MFTF-α+T device, an upgrade of the Mirror Fusion Test Facility (MFTF-B) at Lawrence Livermore National Laboratory (LLNL), is to advance the physics database required for the eventual demonstration of fusion power. The physics parameters of MFTF-B, MFTF-α+T, the Fusion Power Demonstration (FPD), and the Mirror Advanced Reactor Study (MARS) are compared in Tables 2.1 and 2.2. These tables indicate that MFTF-α+T comes impressively close to reactor conditions in its physics and nuclear engineering parameters.

The upgrade of both the central cell and the end cells of MFTF-B will permit MFTF-α+T to operate in two major modes, one emphasizing better confinement and higher Q (= fusion power produced/power input to the plasma), the other emphasizing high fusion power production in the central cell. In the high-Q mode, particle confinement is improved and the overall physics is extended to achieve a central-cell $Q \sim 2$ in a deuterium-tritium (D-T) plasma. At this point, about one-third of the central-cell heating comes from the alpha particles. In the high-Γ mode, a central-cell insert operating in a Kelley mode will yield reactorlike parameters of several hours per shot at a neutron wall loading Γ_n of 2 MW/m^2 over a length of 4 m. The physics of these modes is described in detail in Sects. 2.3.1 and 2.3.2.

Located within the central cell, the MFTF-α+T D-T axicell is a shielded cylindrical region approximately 4 m long (mirror to mirror) and 8.3 m in diameter. A complete tandem mirror reactor would consist of a line of many such cylindrical sections. The axicell of MFTF-α+T represents, in all respects, a working section of a tandem mirror reactor, at full magnetic field and full fusion power density. The main difference is that the plasma radius of the MFTF-α+T axicell is smaller. To compensate for the smaller plasma radius and still obtain reactor-level power densities in the inner blanket region, the first wall radius must also be reduced. However, the overall diameter of the MFTF-α+T axicell is still about the same as that of the MARS central cell, and a relatively high fluence is provided for high-flux nuclear testing. The superconducting coils and long-pulse-capable power systems make it possible to extend any "shot" to 100 h or more to achieve steady-state conditions in the blanket and auxiliary systems.

The insertion of a complete power-producing reactor section into MFTF-α+T is possible because of the linear geometry of the tandem mirror. Mirror coils are used to isolate a short section of the central cell from the rest of the machine. Because of its small volume, this isolated section can be kept at a high plasma density and temperature by intense auxiliary heating. In MFTF-α+T, the heating is supplied by the MFTF-B 80-keV neutral beam system, upgraded for steady-state operation with tritium. These beams also fuel the central cell.

The end cells of MFTF-α+T play an important role in attaining high fusion power density by "anchoring" the high-beta central-cell plasma to provide magnetohydrodynamic (MHD) stability. In addition, the improved end cells allow the electrostatic potential to be increased from ~70 kV (relative to ground) in MFTF-B to ~140 kV in MFTF-α+T (in the high-Q mode). This is about half the potential required to reach ignition in the central

Table 2.1. Physics parameters for tandem mirror facilities

Parameter	MFTF-B[a]	MFTF-α+T High-Q	MFTF-α+T High-Γ	FPD[b] FPD-II	FPD[b] FPD-III	MARS
Central-cell length,[c] m	15.8	20	4.0	75	75	130
Central-cell plasma radius, m	0.30	0.25	0.15	0.54	0.6	0.49
Central-cell field,[d] T	1.0	1.6	4.5	2.5	3.5	4.7
Central-cell density, cm^{-3}	0.39×10^{14}	1.9×10^{14}	4.75×10^{14}	1.5×10^{14}	2.85×10^{14}	3.26×10^{14}
Average ion temperature, keV	15	25[e]	27	28.5	30.2	28.6
Electron temperature, keV	9	12	7	24.3	24.8	24.0
Central-cell average beta %	20	40[f]	31[g]	47	47	28
Ion confinement parameter $n\tau$,[h] $cm^{-3} \cdot s$	2.2×10^{13}	1×10^{14}	4.7×10^{13}	4.8×10^{14}	4.9×10^{14}	5.15×10^{14}
Ion lifetime,[h] s	0.57	1.06	0.26	3.2	1.72	1.6
Ion confining potential, kV	30	62	22	153	160	156
Total plug potential, kV	66	141	69	322	335	329
Q in the central cell[i] (Q_c)	0.62	1.7	1.0	4.73	4.95	5.08
Effective Q_c[j] $(Q_c)_{eff}$	0.62	2.4	1.2	∞[k]	∞[k]	∞[k]
Global Q[l]	0.23	1.5	1.1	7.14	18.2	25.6

[a]Parameters for the axicell MFTF-B are taken from K. I. Thomassen and R. A. Jong, *MFTF-B Performance Calculations*, UCID-19621, Univ. California, Lawrence Livermore Natl. Lab., Livermore, Calif., December 1982.

[b]FPD-II and FPD-III (Demo) refer to different phases of operation in the same facility.

[c]Distance between the first mirror peaks at the ends of the central cell, except for MFTF-α+T. There the 4-m length for the high-Γ mode is the test module insert length; the 20-m length for the high-Q mode is the distance between the 18-T choke coils.

[d]Axicell field in the high-Γ mode, central-cell field in the high-Q mode. MFTF-B is designed for 1.6 T; FPD, for 3.5 T.

[e]With axicell.

[f]Central cell.

[g]Axicell.

[h]Includes radial and axial losses; averaged over hot and warm species.

[i]Ratio of fusion power and power losses from the central cell. For MFTF-B, the equivalent value for D-T is given. No credit is taken for alpha heating makeup of the losses.

[j]Full alpha heating is used to reduce the central-cell losses.

[k]Ignited.

[l]Ratio of fusion power and total plasma power losses.

Source: Adapted with permission from K. I. Thomassen and J. N. Doggett, *Options to Upgrade the Mirror Fusion Test Facility*, UCID-19743, Univ. California, Lawrence Livermore Natl. Lab., Livermore, Calif., April 1983.

Table 2.2. Parameters of the power-producing regions of MARS, FPD, and MFTF-α+T (per meter of length)

Parameter	MFTF-α+T		FPD[a]		MARS
	High-Q[b]	High-Γ	FPD-II	FPD-III	
Plasma radius, m	0.25	0.15	0.54	0.6	0.49
Plasma density, cm^{-3}	1.1×10^{14}	4.75×10^{14}	1.5×10^{14}	2.85×10^{14}	3.26×10^{14}
Fusion power density, W/cm^3	1.93	55.2	5.8	20.6	26.5
Fusion power P_{fusion} per unit length, MW/m	0.38	3.9	5.3	23.3	20.0
Γ, MW/m^2	0.11	2.0	0.96	3.57	4.24
First wall radius, m	0.45	0.25	0.7	0.83	0.6
Blanket thickness, m	0.5	0.5[c]	0.41	0.41	0.41
Reflector thickness, m	0.5	0.5[c]	0.42	0.42	0.42
B_0, T	1.6	4.5	2.5	3.5	4.7
Mean coil diameter, m	5.0	5.0	5.6	5.6	5.6
Coil spacing, m	1.25	5.3	3.2	3.2	3.2
Tritium production, g/day	0.06	0.6	0.8	3.5	3.0

[a]FPD-II and FPD-III (Demo) refer to different phases of operation of the same facility.

[b]Central-cell parameters are used because the axicell is not the primary power-producing region in this mode.

[c]Available.

Source: Adapted with permission from K. I. Thomassen and J. N. Doggett, *Options to Upgrade the Mirror Fusion Test Facility*, UCID-19743, Univ. California, Lawrence Livermore Natl. Lab., Livermore, Calif., April 1983.

cell. In a tandem mirror, ignition means that the alphas heat the central cell so that the only power input is that required to sustain the plugs. Thus, Q is directly proportional to the length of the central cell. The alphas in MFTF-α+T supply about 30% of the central-cell heating ($Q = 2$). Demonstration of ignition in MFTF-α+T is desirable, but there are limitations on the field strength and plasma length in the end-cell region, which set the upper limit on adiabatic confinement and thus on ion energies (sloshing and passing ions). This in turn sets limits on the potential levels. [This is an issue of cost, however, and not of technical readiness. For example, a full MARS yin-yang anchor is only 30% larger (linear dimensions) than the MFTF yin-yang coil that has been built and tested, and it could use NbTi conductor. The cost differences lie in the use of He_{II} (at 1.8 K) to achieve 10-T fields in the conductor and in the additional ampere-meters of conductor needed in the MARS coils.]

Microstability

The microstability of both electrons and ions is of special concern in open systems because of the non-Maxwellian nature of the distribution function of one or both species. Both loss-cone and anisotropy-driven modes have been observed for ions in previous experiments, and in thermal barriers the ion distribution may be susceptible to streaming-type modes as well. Loss-cone and anisotropy-driven modes have been observed for hot electrons in selected nonbarrier experiments and can occur in thermal barriers. In theory, it is possible to design high-performance machines that are stable to all these modes or that have fluctuation levels less than the corresponding classical rates. Microstability has been achieved in TMX-U, a major accomplishment for the program. Verifying this theory and augmenting the database constitute an important mission for each new generation of experiments.

Low-frequency stability

Equilibrium and low-frequency stability requirements have the most direct impact on magnetic field design. Both depend on the details of the magnetic field line curvature, and both are affected by radial electric fields. For equilibrium, the principal issue is minimizing the flux-tube distortion in the central cell that results from currents parallel to the magnetic field B generated in the end cells. For stability, it is necessary to maintain separate regions of favorable and unfavorable magnetic curvature. The problem is further complicated by added destabilization caused by a rotation of the central cell driven by radial electric fields. Stability is thus dependent on localizing the perturbations to unstable regions. This localization can be accomplished either by magnetic field line bending, as is the case in MHD balloon modes, or by the electrostatic ballooning caused by trapped particles. Ultimately, the plasma pressure that an unstable region can hold stably is limited by both MHD and electrostatic ballooning modes; the communicating density is limited by the trapped particle modes. These modes are strong functions of the magnetic design and device configuration, and the theoretical tools for this design must be calibrated.

As demonstrated in the ELMO Bumpy Torus (EBT), kinetic effects can dramatically alter the low-frequency behavior of hot electrons. Low-frequency stability will be affected by the behavior of the hot electrons in the thermal barrier, where they contribute a majority of the local pressure. The issues for tandem mirrors range from describing the hot electrons correctly to finding active ways to capitalize on their increased stability.

Thermal barriers

Thermal barriers and potential enhancement introduce entirely new physics issues. Simply stated, the potential profiles are generated by controlling the electron distribution and the ion distribution simultaneously. The added means of control is selective ion heating, initially via electron-cyclotron resonance heating (ECRH) but possibly by other means in some applications. This raises questions of wave penetration and deposition, avoidance of runaways, and instability. Ion distribution in MFTF-α+T will initially be controlled by charge exchange on injected neutral beams. However, assessments of this technique in reactor conditions point out the need for alternative means of control (e.g., rf fields), particularly to prevent the accumulation of impurities and alpha particles in the thermal barrier.

2.2 GOALS

The physics and technology database needed to design a thermal-barrier tandem mirror fusion reactor will be provided by the operation of four machines during the 1980s. Experiments in the Tandem Mirror Experiment Upgrade (TMX-U) at LLNL, TARA at the Massachusetts Institute of Technology, and GAMMA-10 in Japan will substantially verify the basic physics design of the thermal-barrier tandem mirror reactor concept. Experiments in MFTF-B (scheduled to begin operations in 1986) will

- demonstrate scaling to plasma conditions nearer those of a full-scale reactor,
- provide definitive information for long-time-scale processes,
- provide information on transport at reduced collisionality in the central-cell plasma, and
- advance the development of technologies that must be demonstrated with a confined plasma at energy and power levels near those of a reactor.

Information gained from the 4-year operating period of MFTF-B will be fully exploited to resolve issues critical to a tandem mirror reactor.

The MFTF-α+T device will build on the results from all four of these experiments. It will verify scalings established in MFTF-B by demonstrating predicted performance. In addition, MFTF-α+T will demonstrate improved radial and axial confinement with the central-cell Q increasing to 2. The central-cell plasma will provide definitive data on alpha heating and reactorlike D-T plasmas. Plasma containment experiments will demonstrate the development of impurity control (halo pumping and drift pumping), fueling, direct conversion, and active feedback control. Operation of MFTF-α+T is expected to provide answers to all of the physics questions critical to the development of a mirror FDP.

2.2.1 Physics Issues

The physics issues addressed by MFTF-α+T are categorized under the following broad headings:

1. microstability,
2. low-frequency stability,
3. thermal barriers and potential enhancement,
4. axial confinement,
5. radial confinement,
6. radio-frequency (rf) heating, and
7. startup.

Each of these categories encompasses a set of questions fundamental to the operation of any tandem mirror device in a thermal-barrier mode and a set of questions that only becomes important as the parameter regime of reactors is approached. The current experiments (TMX-U, TARA, GAMMA-10) will provide information on the fundamental questions, and MFTF-B will provide confirmation of scaling to near-reactor parameters. The second set of questions can only be addressed by MFTF-B because of its field configuration and parameter regime. The MFTF-α+T device will confirm the MFTF-B scaling and demonstrate solutions to additional physics and technology issues.

Axial confinement

In reactors, the ion confinement time must be 50 to 100 times the ion 90° scattering time; this requires a net confining potential of about $2.5T_i$. Possible means of developing the required plugging potential include thermal barriers, potential enhancement, and negative operation. Each one requires different types and amounts of applied power and thus implies different performance parameters, such as the system's overall nuclear power gain (Q). The method selected to improve axial confinement and the stability and technology requirements that accompany it will ultimately dictate the detailed operating mode of a tandem mirror reactor.

Radial confinement

The radial ion and electron heat confinement must be comparable to the axial confinement. The radial ion step size is controlled by the average geodesic curvature, as seen by an ion transiting the end cells. Therefore, the step size depends on the magnet design and alignment. However, ion drift also affects the average curvature, so ion transport is a sensitive function of the radial electric field in the transition region. Electron heat diffusivity in a reactor must be $<800\ \mathrm{cm}^2/\mathrm{s}$. This is lower than in existing tokamaks and would be masked by axial electron power flow in current machines.

The dependence of ion radial transport (and of equilibrium and low-frequency stability) on details of the radial electric field strongly suggests that some form of radial potential control may be needed. Possible techniques include segmentation of the end-wall potentials, like that employed in the rotating plasmas in Novosibirsk;[1] radial variation of the power; and particle deposition in the plasma.

RF heating

For ion heating, rf power can supplement or replace neutral beams. It may be useful in manipulating the electric potential. At low frequency it may be useful for preventing ion accumulation in thermal barriers (i.e., pumping).

Startup

Startup of a thermal barrier requires initiation of a plasma with low collisionality that satisfies conditions of MHD stability and microstability. The plasma is formed in the central cell and allowed to flow out axially. Dump tanks reduce contact between the barriers and the end walls to allow high electron temperature. Gas control (discussed in Sect. 2.2.2) is critical during startup, when neutral beam coupling is weak and microwave coupling is poor.

2.2.2 Plasma Technology Development

Technology issues critical to the development of a mirror reactor include the following:

- impurity control,
- fueling,
- gas control,

- alternative ion pumps,
- direct conversion, and
- active feedback control.

Impurities in energetic plasmas cause radiative cooling and, in thermal barrier regions, also enhance the trapping rate of passing particles, which increases the required ion pumping and lowers Q. Effective impurity control includes minimizing the impurity content of the neutral beams and effectively preventing radial inward diffusion of impurities.

The central-cell plasmas in TMX-U, TARA, and GAMMA-10 are fueled by gas penetration in the radially thin fan regions. It is unlikely that this method will be satisfactory for larger, denser, more energetic reactor plasmas. Fueling by injection of solid pellets, which has been demonstrated in tokamaks,[2] may be required in future mirror machines. However, because plasma containment in linear devices differs from that in tokamaks, a demonstration of pellet fueling in an operating mirror device is necessary.

Neutral gas incident on the plasma leads to energy and particle losses and must be kept at low density. Methods of doing this include reduction of all gas sources to minimum levels, high-speed pumping by actively gettered panels or cryopanels, reduction of streaming gas from the neutral beams, and reduction of desorption and recycling from the walls. Pellet fueling may reduce unwanted gas associated with gas penetration fueling.

Cool trapped ions must be removed from both the anchor and the transition regions of a tandem mirror system. Neutral beams injected at small angles to the magnetic field lines are used for this purpose in TMX-U, TARA, GAMMA-10, and MFTF-B. However, this method is not effective in removing impurities. Alternative pumping methods that remove both impurities and cool ions and may also improve power efficiency have been proposed.

Direct conversion of the energy carried by the plasma lost from the ends of a linear system is a standard feature of mirror reactors. Successful small-scale tests have verified the basic concept, but full-scale integration at high power levels in an actual containment experiment must be demonstrated. Direct conversion may be the preferred energy removal option in future facilities.

Finally, it is anticipated that active feedback control will be needed to maintain the operating point parameters in long-pulse and continuously operating reactors. Control systems must be demonstrated.

2.3 PHYSICS DESCRIPTION

For D-T operation, MFTF-α+T includes a shielded axicell with a high field ($B_{\text{midplane}} = 4.5$ T) and continuous neutral beam injection (>100 h, E_{inj} = 60-keV D^0,T^0) in the central cell; end plug magnets (see Figs. 2.1 and 2.2) that are geometrically similar to those of the MARS design; 200-keV sloshing-ion beam injection; ion-cyclotron resonance heating (ICRH); and drift pumping. The combination of the central-cell and end-cell elements meets the objectives of improving the confinement of a D-T plasma to provide significant alpha heating ($Q \sim 2$) in the high-Q mode and economical blanket testing ($\Gamma_n \simeq 2$ MW/m^2) in the high-Γ mode.

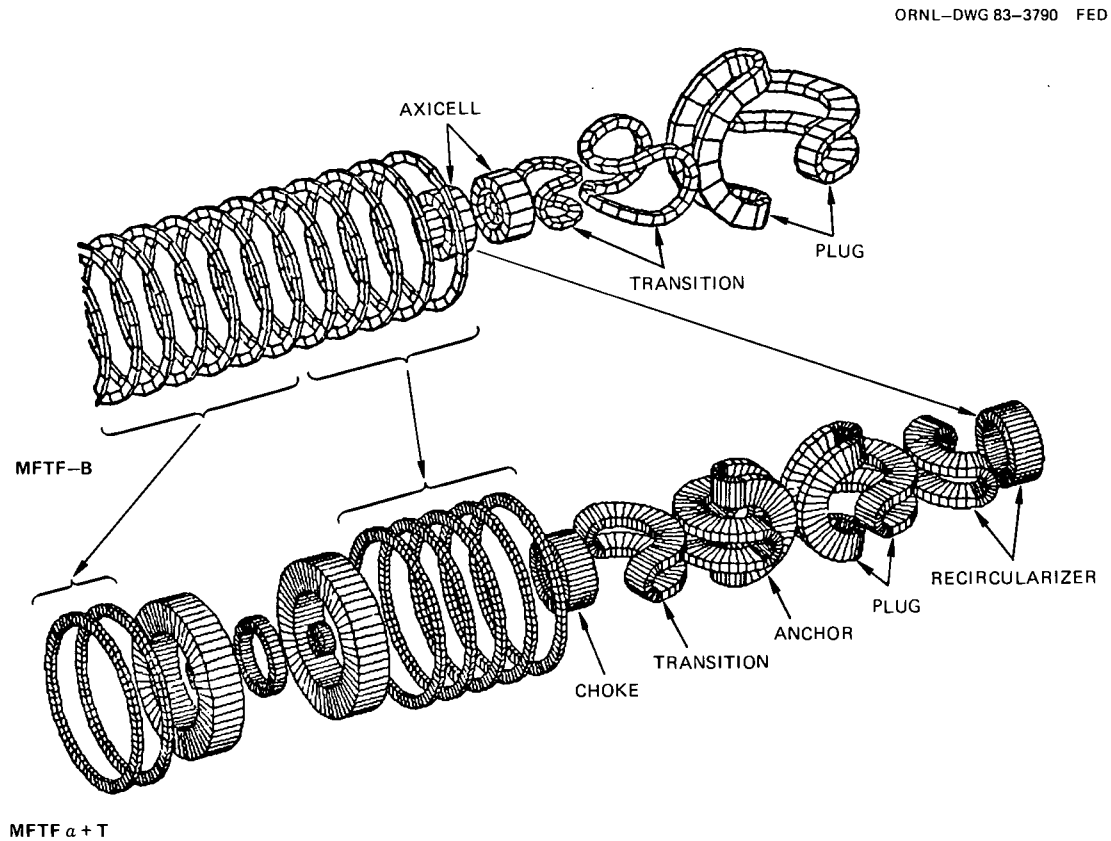

Fig. 2.1. Magnet configurations for MFTF-B and MFTF-α+T.

As demonstrated in the Technology Demonstration Facility (TDF) study,[3] it is not necessary to create large end-plug confining potentials in a small beam-injected mirror cell to produce interesting levels of 14-MeV neutron production. In fact, the 2XIIB device[4] produced $n > 10^{14}\,\mathrm{cm}^{-3}, T_i > 10\,\mathrm{keV}$ at $\beta \simeq 1$, which would have generated a fusion power density of $>1\ \mathrm{W/cm}^3$ in a few liters of volume with D-T fuel. Because such plasmas are anisotropic, high densities and neutron fluxes can be generated with manageable beam powers in a small mirror-cell volume even at low $(Q_c)_{\mathrm{eff}}$, the ratio of fusion power to injection power. Since the injection power equals the central-cell losses minus the alpha heating power P_α,

$$(Q_c)_{\mathrm{eff}} \simeq \frac{0.25 n_{\mathrm{DT}}^2 \langle \sigma v \rangle_{\mathrm{DT}} \times 17{,}600\,\mathrm{keV}}{[n_{\mathrm{DT}}^2/(n\tau)_c][(E_i)_{\mathrm{loss}} + \phi_e + T_{ec}] - P_\alpha}, \tag{2.1}$$

where the alpha heating power P_α is in units of $\mathrm{keV \cdot cm^{-3} \cdot s}$, and

$$(n\tau)_c^{-1} \simeq (n\tau)_{\mathrm{mirror}}^{-1} \sim [2(n\tau)_{90}\log_{10}R]^{-1} + \{(n\tau)_{\mathrm{drag}}\ln[E_{\mathrm{inj}}/(E_i)_{\mathrm{loss}}]\}^{-1} \tag{2.2}$$

ORNL-DWG 83-3491 FED

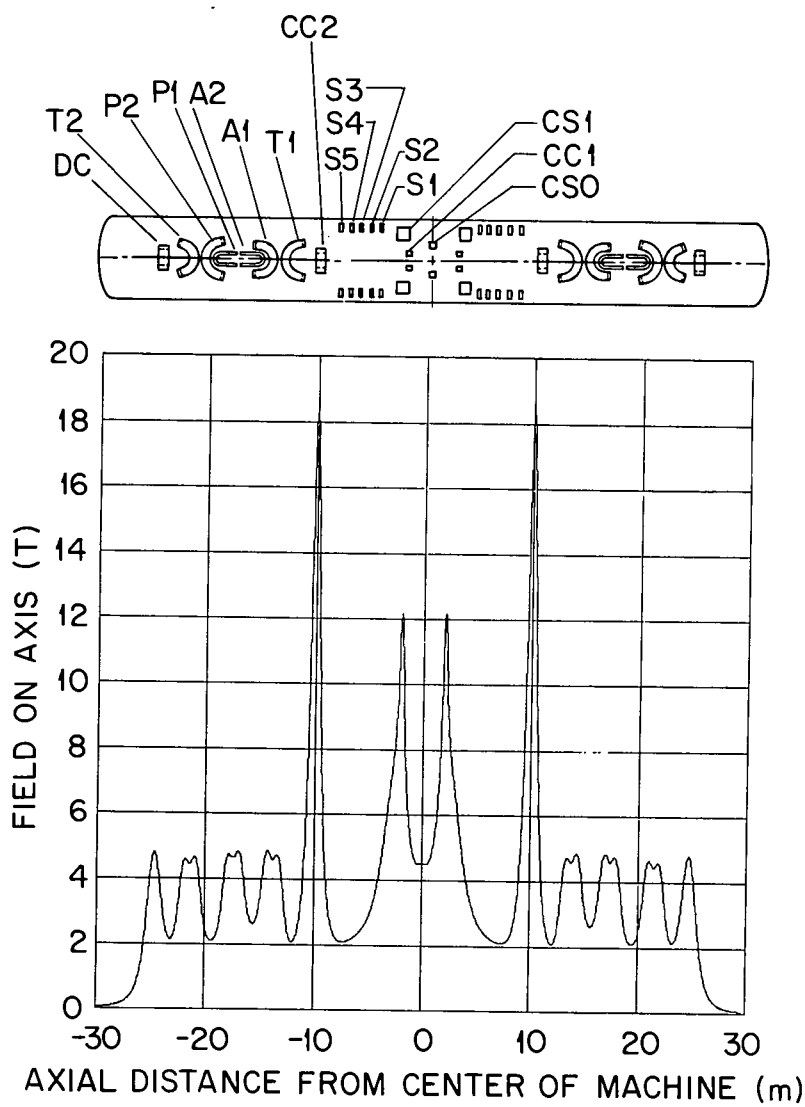

Fig. 2.2. MFTF-α+T magnet configuration and field on axis.

would be a mirror ion confinement parameter limited by ion-ion scattering and electron drag.

Although mirror confinement alone may be adequate for neutron production, much better confinement is needed to ignite the central cell in a tandem mirror reactor, where P_α equals the central-cell energy losses and $(Q_c)_{\text{eff}} \rightarrow \infty$. Because the required confinement time for ignition is many ion-ion scattering times, the central-cell pressure tends to become isotropic; that is, the mirror throat density approaches the midplane density. In MFTF-α+T the maximum mirror throat density that can be electrostatically plugged with

thermal barriers (10^{14} cm^{-3} Maxwellian density, limited in part by ECRH absorption) is less than the peak midplane density that can be supported with 15 MW of beam power in the most compactly designed mirror D-T axicell. Thus, in the MFTF-α+T maximum $(Q_c)_{eff}$ and maximum Γ_n are achieved in two different operating modes. The central-cell and end-plug components are designed for compatibility with both modes of operation so that switching from one mode of operation to the other can be done as quickly and easily as possible. The coils, magnetic fields, and plug heating equipment are the same for both modes.

While the maximum plugging potentials of the high-Q mode may not be needed in the high-Γ mode, the end-plug design combined with the central-cell design provides a healthy margin in plugging potential generation for the high-Γ mode. The end-plug design also provides an extra anchor cell, which increases the MHD beta limit and improves the thermal barrier pumping (drift pumping). This allows the high-Γ mode to be extended to 2 MW/m^2, significantly higher than the maximum (1.3 MW/m^2) possible in MFTF-B. The plasma parameters in the D-T axicell, the central cell, the transition region, the anchors, and the end plugs are shown in Table 2.3 for both modes of operation.

Table 2.3. Plasma parameters for high-Q and high-Γ modes of operation

Parameter	High-Q mode	High-Γ mode
DT axicell		
Magnetic field B_x, T	4.5	4.5
Maximum magnetic field B_{mx}, T	12	12
Average ion energy $\overline{E}_{ix}$, keV	50	40
Electron temperature T_{ec}, keV	12	7
Density $\hat{n}_x$, cm^{-3}	1.9×10^{14}	4.75×10^{14}
Peak beta $\hat{\beta}_x$, %	28[a]	46[a]
Volume-averaged beta $\langle\hat{\beta}_x\rangle$, %	19[a]	31[a]
Electron plugging potential ϕ_e, kV	79	47
Ion plugging potential ϕ_c, kV	62	22
Local mirror $n\tau$, cm^{-3}·s	2.5×10^{13}	2.0×10^{13}
Fusion reaction rate $\langle\sigma v\rangle_{DT}$, cm^3/s	6.6×10^{-16}	6.6×10^{-16}
Fusion power P_{fusion}, MW	2.25	11
Plasma radius r_x, cm	15	15
Wall radius r_w, cm	25	25
Axicell length L_x, m	4.0	4.0
Effective axicell length $(L_x)_{eff}$, m	3.5	2.8
Neutron wall loading Γ_n (at r_w = 25 cm), MW/m^2	0.33	2.0
Central cell		
Magnetic field B_c, T	1.6	1.6
Maximum magnetic field B_{mc}, T	18	18
Electron density n_{ec}, cm^{-3}	1.1×10^{14}	1.6×10^{14}
Warm ion density $(n_{ic})_w$, cm^{-3}	1.0×10^{14}	1.3×10^{14}
Hot ion density $(n_{ic})_h$, cm^{-3}	1.0×10^{13}	3×10^{13}

Table 2.3 (continued)

Parameter	High-Q mode	High-Γ mode
Central cell (continued)		
Warm ion temperature $(T_{ic})_w$, keV	20	15
Hot ion temperature $(T_{ic})_h$, keV	30	20
Electron temperature T_{ec}, keV	12	7
Beta $\hat{\beta}_c$ (total), %	60[a]	60[a]
Volume-averaged beta $\langle\beta_c\rangle$, %	40[a]	40[a]
Current I_c (Pastukhov), A	4.4	90
Confinement parameter $(n\tau)_{Pastukhov}$, $cm^{-3}\cdot s$	5.5×10^{14}	4.7×10^{13}
Ion plugging potential ϕ_{ic}, kV	68	30
Electron plugging potential ϕ_{ec}, kV	73	39
Plasma radius r_c, cm	25	25
Wall radius r_w, cm	45	45
Central-cell length L_c, m	20	20
Effective central-cell length $(L_c)_{eff}$, m	12	12
Fusion power P_{fusion}, MW	4.55	5.9
Neutron wall loading Γ_n (at $r_w = 45$ cm), MW/m^2	0.11	0.14
Anchor		
Passing particle density $n_{pass}(B_A)$, cm^{-3}	5×10^{12}	7.75×10^{12}
Hot ion density $(n_i)_h(B_A)$, cm^{-3}	2.4×10^{13}	2.4×10^{13}
Electron density $n_e(B_A)$, cm^{-3}	3.4×10^{13}	3.7×10^{13}
Magnetic field B_A, T	2.6[b]	2.6[b]
B_{res}, T	3.3[c]	3.3[b]
Maximum magnetic field B_{mA}, T	4.8	4.8[c]
Peak beta $\hat{\beta}_A$	60[a]	60[a]
Volume-averaged beta $\langle\beta_A\rangle$	40[a]	40[a]
Hot ion energy, keV	400[d]	400[d]
Anchor-cell length L_A, m	2.7	2.7
Effective anchor-cell length $(L_A)_{eff}$, m	1.3	1.3
Radius r_A, cm	20	0.2
Transition[e]		
Trapping current I_{trap}, A	21	97
Neoclassical current I_{neo}, A	5.6	3
$\overline{\delta\phi_t}$, kV	15	10
Passing-particle density n_{pass} (at 3 T), cm^{-3}	8×10^{12}	1.2×10^{13}
Ion density ratio g_b	2.0	1.7
Plug region		
Passing-particle density n_{pass} (at point b')	2×10^{12}	3×10^{12}
Density n_b (point b')	1.0×10^{13}	1.2×10^{13}
Ion density ratio g_b	2.0	1.7
Ion density ratio G_b	5.0	4
Density n_a (point a')	1.65×10^{13}	2.3×10^{13}
Magnetic field B_a, T	1.65[g]	2.2[f]
B_p (point b'), T	2.0[b], 1.25[g]	2.0[g], 1.25[g]
$B_{a'}$ (injection point), T	2.7[g]	2.7[f]

Table 2.3 (continued)

Parameter	High-Q mode	High-Γ mode
Plug region (continued)		
Hot electron energy, keV	580	475
Warm-electron temperature $(T_e)_w$, keV	100	60
Peak beta $\hat{\beta}_p$, %	60[a]	60[a]
Volume-averaged beta $\langle\beta_p\rangle$, %	40[a]	40[a]
$\delta\phi_{a'\to a}$, kV	78	37
$\delta\phi_a$, kV	125	60
$\hat{n}_{slosh}/n_s(b)$	2.75	3.3

[a]Quartic radial profile.
[b]In vacuum.
[c]With plasma.
[d]With D^+.
[e]Choke to $\hat{\phi}$.
[f]The locations of points a and b are shown in Figs. 2.2 and 2.3.
[g]Beta-depressed value.

2.3.1 The High-Q Mode

The axial profiles of the magnetic field, the potential, and the density along the axis of MFTF-α+T in the high-Q mode are shown in Fig. 2.3. Table 2.4 lists heating system parameters, and Table 2.5 summarizes performance parameters.

The potential profiles shown in Fig. 2.3 are plotted with respect to end-wall plates biased to a negative voltage that is sufficient, with proper radial tailoring of the pumping ECRH and wall potentials, to hold the central-cell radial electric field E_r to a small fraction of T_{ec}/r_c, the ratio of the electron temperature to the plasma radius. This minimizes resonant transport due to $\mathbf{E} \times \mathbf{B}$ drifts, which would otherwise reduce the radial ion confinement to much less than the value required to achieve $Q = 2$, $n\tau = 10^{14}$ cm^{-3}·s. Even with $E_r = 0$ in the central cell, there is still a residual neoclassical radial transport for central-cell ions passing to the plugs. However, the geodesic curvature components in the quadrupole transition fields are smaller than those in the MFTF-B transition coil by nearly a factor of 3, which increases $(n\tau)_{neo}$ by almost an order of magnitude to an estimated 5×10^{14} cm^{-3}·s.

The dominant radial loss of central-cell ions is expected to occur as a result of collisional trapping in the transition regions, followed by radial loss induced by bounce-resonance drift pumping. This type of central-cell loss, which is required to maintain low-density thermal barriers in the ends, scales roughly as

$$(n\tau)_{pump} \simeq 10 n\tau_{ii}(B_{max}/B_c)[(L_c)_{eff}2L_t] \simeq 1.8 \times 10^{14}\ \mathrm{cm}^{-3}\cdot\mathrm{s}\ , \tag{2.3}$$

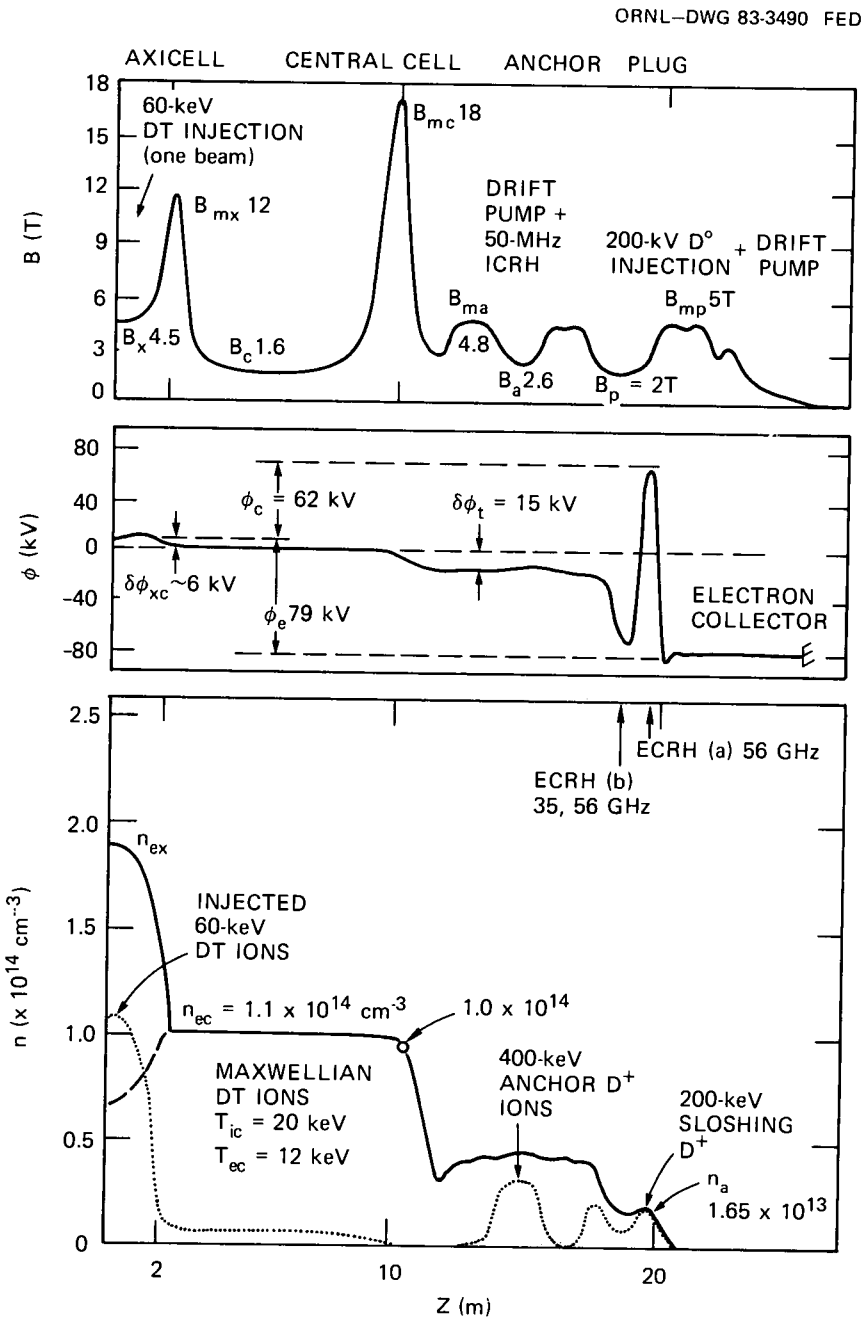

Fig. 2.3. Profiles of field, potential, and density in the high-Q mode.

where $n\tau_{ii}$ is the 90° ion-ion scattering time at a temperature T_{ic} = 20 keV, B_{max} = 18 T is the peak mirror field, and L_t = 10 m is the transition length over which pumping is required. The length of a uniform cylinder with radius r_c = 25 cm, having the same volume as the central-cell plasma, is $(L_c)_{eff}$ = 12 m. The factor of 10 in Eq. (2.3) comes from matching Fokker-Planck calculations. With central-cell ion plugging potentials of ϕ_c = 62 keV (see Fig. 2.3), which is sufficient to give an axial confinement

Table 2.4. Heating systems parameters

	High Q	High Γ
	Axicell beams	
Trapped power	1.86 MW at 31 A	11.4 MW at 190 A
Incident power	2.7 MW at 45 A	14.4 MW at 240 A
Energy	$E_{inj} = 60$ keV at $\theta_{inj} \geqslant 75°$	$E_{inj} = 60$ keV at $\theta_{inj} \geqslant 75°$
	Anchor drift pumps	
Trapped power	15 kW (antenna dissipation) + 50 kW (plasma dissipation) at each anchor	80 kW (antenna dissipation) + 150 kW (plasma dissipation) at each anchor
Incident power	0.66 MW reactive (each anchor), $I_{antenna} \simeq 1.3$ kA rms for each of four loops	3 MW reactive (each anchor), $I_{antenna} \sim 3$ kA rms for each of four loops
Frequency	$f_0 = 160$ kHz, $\Delta f_0 = \pm 32$ kHz ($N = 12$ oscillators 5.3 kHz apart)	$f_0 = 140$ kHz, $\Delta f_0 = \pm 28$ kHz ($N = 10$ oscillators 5.6 kHz apart)
	Plug drift pumps	
Trapped power	1.5 kW (antenna dissipation) + 65 kW (plasma dissipation) at each plug	1.5 kW (antenna dissipation) + 24 kW (plasma dissipation) at each plug
Incident power	0.2 MW reactive (each plug), $I_{antenna} \simeq 0.4$ kA rms for each of four loops	0.2 MW reactive (each plug), $I_{antenna} \simeq 0.4$ kA rms for each of four loops
Frequency	$f_0 = 1.2$ MHz, $\Delta f_0 = \pm 84$ kHz (1 FM oscillator with 0.1-s sweeptime)	$f_0 = 1.2$ MHz, $\Delta f_0 = \pm 84$ kHz (1 FM oscillator with 0.1-s sweeptime)
	Anchor ICRH	
Trapped power	(1) 350 kW absorbed at each anchor (2) 67 kW absorbed at each anchor	(1) 400 kW absorbed at each anchor (2) 170 kW absorbed at each anchor
Incident power	(1) 700 kW (antenna) (2) 130 kW (antenna)	(1) 800 kW (antenna) (2) 340 kW (antenna)
Frequency	(1) 25 MHz (ω_0, fundamental) (2) 50 MHz ($2\omega_0$, for beta control)	(1) 25 MHz (ω_0, fundamental) (2) 50 MHz ($2\omega_0$, for beta control)
	Plug ECRH	
Trapped power	(1) 320 kW at each plug (point b) (2) 300 kW at each plug (point b) (3) 60 kW at each plug (point b)	(1) 500 kW at each plug (point b) (2) 400 kW at each plug (point b) (3) 100 kW at each plug (point b)
Incident power	(1) 384 kW (2) 360 kW (3) 72 kW	(1) 600 kW (2) 480 kW (3) 120 kW
Frequency	(1) 35 GHz (2) 56 GHz (3) 56 GHz	(1) 35 GHz (2) 56 GHz (3) 56 GHz
	Plug sloshing beam	
Trapped power	125 kW at 0.63 A (each plug, point a')	85 kW at 0.42 A (each plug, point a')
Incident power	0.84 MW at 4.2 A (each plug, point a')	0.44 MW at 2.2 A (each plug, point a')
Energy	200 keV (D^0)	200 keV (D^0)

Table 2.5. Composite confinement parameters for high-Q and high-Γ modes

	High-Q	High-Γ
Radial and axial ion particle containment[a]		
$(n\tau)_{DT}$, $cm^{-3}\cdot s$	1.0×10^{14}	4.7×10^{13}
τ_{DT}, s	1.06	0.26 s
Radial and axial ion energy confinement[a]		
$(n\tau)_{energy}$, $cm^{-3}\cdot s$	4.2×10^{13}	2.2×10^{13}
τ_{energy}, s	0.42	0.11
Q values		
$\left[\dfrac{P_{fusion}(\text{axicell}) + P_{fusion}(\text{cell})}{\text{Axicell energy losses} + \text{central cell energy losses}}\right]$, Q_c	1.7	1.0
$\left[\dfrac{P_{fusion}(\text{axicell}) + P_{fusion}(\text{cell})}{\text{Energy losses} - \alpha\text{ heating}}\right]$, $(Q_c)_{eff}$	2.4	1.2
$\left[\dfrac{P_{fusion}(\text{axicell}) + P_{fusion}(\text{cell})}{\text{Total central-cell power plus injected power}}\right]$, global Q	1.5	1.1

[a]Values for $n\tau$ are (n^2V) weighted; τ values are (nV) weighted (V = volume).

$(n\tau)_{axial} = (n\tau)_{Pastukhov} = 5 \times 10^{14}$ $cm^{-3}\cdot s$, the equivalent radial ion losses due to transition drift pumping exceed the axial electrostatic ion losses. So

$$(n\tau)_{radial} = [(n\tau)_{pump}^{-1} + (n\tau)_{neo}^{-1}]^{-1} = 1.4 \times 10^{14}\,cm^{-3}\cdot s$$

and

$$(n\tau)_{total} = [(n\tau)_{radial}^{-1} + (n\tau)_{axial}^{-1}]^{-1} = 1.0 \times 10^{14}\,cm^{-3}\cdot s\ .$$

The scaling for $(n\tau)_{pump}$ given by Eq. (2.3) motivated the development of higher field (18-T) choke coils placed a maximum of 20 m apart, as shown in Fig. 2.3, to maximize $n\tau$ and Q. The estimated neoclassical transport for electrons is much smaller than that for ions, so all electron losses are taken as axial losses to the negative electron collectors at each end of the device. The situation of mainly radial ion loss and mainly axial electron loss is the same as that in the MARS reactor, in which collection of the electron losses at $-\phi_e$ potential on a biased, gridless plate constitutes a simple and efficient direct conversion. Although end plugging was not sufficient to stem all the axial ion loss in the Tandem Mirror Experiment (TMX), a net electron current was collected in the ends, consistent with the predictions of neoclassical theory.[5]

For sloshing ions to be confined by the plug mirrors, they must be injected with an energy above a cutoff,

$$E_{\text{cutoff}} > (\phi_c + \phi_e)/(B_{\text{mirror}}/B_{\text{inj}}) - 1 \ , \tag{2.4}$$

which, for a total potential drop $\phi_c + \phi_e \simeq 140$ kV, requires approximately 200 keV of negative-ion-based neutral beams. These ion energies are within but not far from the adiabatic energy limit for conservation of μ of deuterium ions,

$$E_{\text{adiabatic}} < 250 B_p^2 (1 - \beta_p) L_m^2 \tag{2.5}$$

(where B_p is in tesla and L_m is in meters). For $B_p = 2$ T and $\beta_p = 0.6$, with a magnetic doubling scale length $L_m = 0.9$ m in the plugs, $E_{\text{adiabatic}} < 320$ keV. In other words, the potentials shown in Fig. 2.3 are near the maximum consistent with the adiabatic sloshing-ion energy limits in the end-cell magnets. Because the central-cell ion temperature, the electrostatic potential, and the sloshing-ion energy tend to scale together, the adiabaticity limit sets an upper limit on the end-plugging capability, given a negative-ion beam that matches the adiabatic limits. With the limits on radial confinement set pumping [Eq. (2.3)], which depend on basic machine parameters such as mirror ratios ana the ratio of central-cell length to end-cell length, and the energy limits, $Q \simeq 2$ may be the maximum that can be achieved in MFTF-α+T.

A particularly significant improvement in the MFTF-α+T end-plug magnet design (in addition to the higher fields, which raise the adiabatic energy limits compared to MFTF-B) is the inclusion of an extra yin-yang anchor in the transition region between the choke coil and the plug. The MFTF-B transition baseball coil[6] is replaced with a yin-yang pair, and the local fields and mirror ratio are raised to provide a local mirror cell in which beams or ICRH can be used to add anisotropic ion pressure in a region of good curvature. Present thinking favors ICRH for this purpose, but energetic negative-ion beams may be used as an alternative. The extra anchor cells more than double the MHD beta limit in the central cell because the fields (higher than the MFTF-B transition fields) reduce the magnitude of the bad curvature in the connecting flux-tube fans and add more good curvature in the anchor wells. (Reduced geodesic curvature also accompanies reduced normal curvature, thus creating neoclassical transport.)

The density profiles shown in Fig. 2.3 represent the maximum value in the central-cell region consistent with a calculated MHD beta limit of $\langle \beta_c \rangle \simeq 0.4$, where the angle brackets denote a volume average. For a given beta limit, the central-cell density could be raised by proportionally lowering all temperatures, potentials, and beam energies. However, because both central-cell and end-cell losses are dominated by Coulomb collision processes, $n\tau$ would decrease proportional to $T^{3/2}$. Moreover, the fusion reaction rate $\langle \sigma v \rangle_{DT}$ would decrease, so that $Q \sim n\tau \langle \sigma v \rangle$ would drop on both counts. On the other hand, maintaining the temperatures specified in Fig. 2.3 while lowering all the densities and betas would have little effect on Q because the value of $n\tau$ is limited by the collision rate and is independent of density. Thus, only the maximum neutral wall loading depends

strongly on the beta limit in the high-Q mode. It is limited to 0.33 MW/m^2 in the axicell and 0.11 MW/m^2 in the central cell for the maximum densities and betas in Fig. 2.3. In addition to the beta limits (0.6 on axis in the central-cell, anchor, and plug midplanes), the maximum central-cell density would be constrained by the maximum plug density for ECRH heating, together with the relationship between plug and central-cell densities for pumped thermal barriers:

$$n_p \simeq n_c \frac{B_p}{B_{max}} \left[\frac{T_{ic}}{\pi(\phi_c - \phi_p)} \right]^{1/2} \frac{n_{trap} + n_{pass}}{n_{pass}} \sim n_c(B_p/B_{max}) \ , \tag{2.6}$$

where n_c is the Maxwellian density at the throat of the $B_{max} = 18$ T choke coil. Again we see the motivation to increase B_{max} to as high a field as is practical, either by increasing n_c for a given plug density (increased fusion power) or by reducing n_p and the plug ECRH power (which is proportional to n_p^2) for a given n_c. For $B_p \simeq 2$ T ($f_{ce} = 56$ GHz), the maximum useful density for ECRH would be four times that of TMX-U (in which $B_p \simeq 1$ T, $f_{ce} = 28$ GHz, and $n \simeq 5 \times 10^{12}$ cm^{-3}), or $(n_p)_{max} \simeq 2 \times 10^{13}$ cm^{-3}. This would produce $(n_c)_{max} \simeq 1.8 \times 10^{14}$ cm^{-3} in Eq. (2.6), which is not much higher than the beta-limited value, 1.1×10^{14} cm^{-3}.

If the fueling (30-A equivalent D-T) and auxiliary heating (1.8 MW) required to sustain the central-cell losses in the high-Q mode with one 30-A, 60-keV (trapped) neutral beam injected into the D-T axicell are provided, then Fokker-Planck calculations indicate that the local peaking of injected ion density in the axicell will be less than a factor of 2 over the Maxwellian density in the central cell. If an alternative combination of 30-A equivalent fueling by pellet injection and an equal power (1.8 MW) of ICRH were used, then Fokker-Planck models indicate that the local density peak would be even smaller. From these considerations, we conclude that for this maximized Q mode the maximum neutron wall loading is probably below 0.1 MW/m^2.

In terms of the relative importance of alpha heating to the central-cell energy balance, the high-Q mode is about a factor of 3.5 away from ignition. The central-cell energy losses consist of the following: 21 A (pump radial ion loss) + 5.6 A (neoclassical radial ion loss) = 26.6 A $\times (3/2)T_{ic} = 0.4$ MW; 4.4 A (axial ion loss) $\times (\phi_c + {}_{ic}) = 0.4$ MW; and 31 A (axial electron loss) $\times (\phi_e + T_{ec}) = 2.8$ MW; thus, the total power loss is 4.0 MW. The fusion power in the central cell is 4.55 MW and that in the axicell (the source of central-cell heating and fueling) is 2.25 MW, for a total power $P_{fusion} = 6.8$ MW. Thus, the alpha power generated is $6.8 \times 0.2 = 1.36$ MW, of which 85% (1.16 MW) is defined as mirror-trapped and transferred to the central-cell ions and electrons according to Fokker-Planck calculations. Thus, fusion alpha heating makes up 1.16/4.0 = 29% of the central-cell energy losses. This is certainly enough to be measured, and experiments to determine the fractional energy transfer of the alpha energy to the plasma, which could then be compared with the Fokker-Planck calculations, are a goal of MFTF-α+T in the high-Q mode.

In terms of $n\tau$, the high-Q mode is about a factor of 5 away from central-cell ignition; $(n\tau)_{DT} \simeq 1 \times 10^{14}$ cm^{-3}·s in MFTF-α+T vs 5×10^{14} cm^{-3}·s for ignition in

MARS and FPD. The ignition $n\tau$ is more than $(0.29)^{-1} \times 10^{14}\,\mathrm{cm}^{-3}$ (where the alpha heating is 29%) because the energy losses per ion-electron pair, $(E_i)_{loss} + \phi_c + T_{ec} + \phi_e$ in Eq. (2.1), must increase as $n\tau$ increases, since both the ion and the electron potentials increase as $\ln(n\tau/n\tau_{scat})$. In spite of the "ignition gap" in $n\tau$, the high-Q mode can operate in the same physics confinement regime as MARS and FPD, where the relative importance of pumping and neoclassical radial ion losses would be nearly the same.

Another important alpha physics issue to be addressed during high-Q operation is the accumulation of thermal alphas and the efficiency of their removal by neoclassical radial transport and bounce-resonant drift pumping. Fokker-Planck calculations show that without such radial loss mechanisms equilibrium thermal alpha fractions could build up to very high levels:

$$\frac{n_\alpha(\text{thermal})}{n_{DT}} \simeq f_{\text{thermal}} f_{\text{burnup}} \frac{\exp \phi_c/T_{ic}}{Z_\alpha^2} , \tag{2.7}$$

where $f_{\text{thermal}} \simeq 0.7$ is the fraction of alphas thermalized to the D-T temperature and $f_{\text{burnup}} \simeq 1/2(n\tau)_{DT}\langle\sigma v\rangle_{DT}$ is the D-T burnup fraction. For MARS and FPD, with $f_{\text{burnup}} = 0.15$ and $\phi_c/T_{ic} = 5$, Eq. (2.7) predicts a disastrous $n_\alpha = 4n_{DT}$, but even for MFTF-α+T with $f_{\text{burnup}} = 0.02$ and a lower $\phi_c/T_{ic} = 3.4$, Eq. (2.7) still predicts a significant concentration, $n_\alpha = 0.1$. Consequently, n_{DT} is 20% higher than n_e, and there is a 40% increase in the D-T ion collision rate. Determining radial loss rates in MFTF-α+T is both possible, since the consequences of factors of 2 in radial loss rates would have significant effects on n_e/n_i and on scattering rates, and valuable in pinpointing ignition conditions for FPD. We could, of course, inject helium into the central cell to simulate part of the thermal alpha physics, but only D-T operation will confirm the actual thermalization fraction f_{thermal} originating from 3.5-MeV alphas and produce the radial profiles on which the transport rates depend.

2.3.2 The High-Γ Mode

Figure 2.4 shows axial profiles of magnetic field, potential, and density along the axis of MFTF-α+T in the high-Γ mode. Plasma parameters, heating system parameters, and performance parameters are listed in Tables 2.3–2.5. The major differences between the high-Γ mode and the high-Q mode are the amount of beam power injected into the D-T axicell and the amount of plug ECRH. Six axicell beams are used in the high-Γ mode, compared with one in the high-Q mode, and the total absorbed ECRH power in the high-Γ mode is 2.0 MW, compared with 1.36 MW in the high-Q mode.

The sixfold increase in neutral beam injection into the D-T axicell increases the peak density of mirror-trapped ions in the test cell to the maximum set by MHD beta limits. This maximizes the local 14-MeV neutron flux ($\Gamma_n = 2\ \mathrm{MW/m^2}$) for blanket testing purposes. The maximum axicell beta in the high-Γ mode, $\langle\beta_x\rangle = 0.31$, is moderately higher than that in the high-Q mode, $\langle\beta_x\rangle = 0.19$, because the pressure of the Maxwellian plasma in the central cell and passing through the transitions is 11% lower in the

ORNL–DWG 83-3959 FED

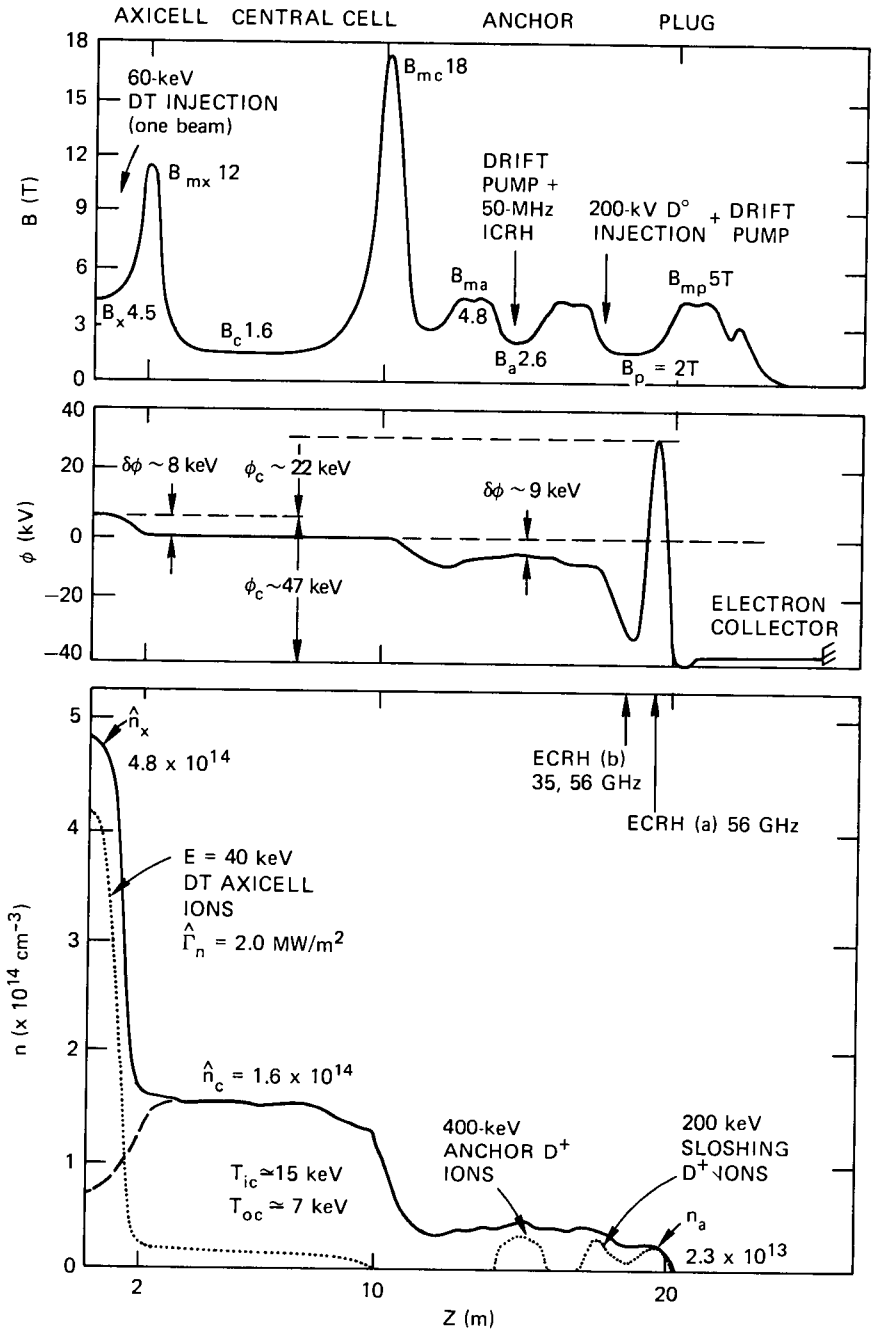

Fig. 2.4. Profiles of field, potential, and density in the high-Γ mode.

high-Γ mode than in the high-Q mode due to lower values of T_{ic} (15 keV vs 20 keV) and T_{ec} (7 keV vs 12 keV) in the high-Γ mode. The MHD stability allows pressure in one bad curvature region to be traded off with pressure in another bad curvature region, although this is limited to some extent by ballooning.

Because some of the bad curvature drive in the central cell could, as an option, be reduced by drift-pumping the Maxwellian component down to the density of the passing ions in both the central cell and the transition regions, the allowed beta in the axicell could be raised beyond $\langle\beta_x\rangle = 0.31$ and, correspondingly, Γ_n could be increased beyond 2 MW/m^2, provided enough neutral beams were added (to match the increase in n_x^2 and to compensate for a 20% to 30% reduction in $n\tau_{local}$ caused by the central-cell pumping). However, because six to eight neutral beams are a reasonable match to the space available for beam lines in the D-T axicell region of MFTF-α+T, it was decided to forego the option of beam pumping to remove pressure from the central-cell region. Thus, significant fusion power (5.9 MW) is generated between the 12- and 18-T mirrors of the central cell in the high-Γ mode as well as in the high-Q mode. Aside from the benefit that an additional 1 MW of alpha heating provides to the central-cell power balance, keeping a long Maxwellian plasma column in the central cell permits the acquisition of almost as much plasma information during high-Γ mode operation as during high-Q mode operation. Therefore, blanket testing operations need not conflict with the time needed to diagnose fusion physics in the central cell.

However, some quantitative reductions in $(n\tau)_{DT}$ and $(Q_c)_{eff}$ are required in changing from the high-Q to the high-Γ mode. Increasing the injected beam current from 30 to 190 A produces about a sixfold increase in n_x^2 in the axicell because in the axicell $n\tau_{local}$ is mostly a mirror-scattering $n\tau$ [see Eq. (2.2)] and E_{inj} is held fixed at 60 keV. Because the 18-T mirror field is significantly higher than the 12-T axicell mirror field, most of the injected axicell current will be transferred to the Maxwellian central-cell plasma. If $n\tau$ in the central cell is held to its high-Q mode value (i.e., $T_{ic} = 20$ keV and $\phi_c = 62$ kV), then the six axicell beams of the high-Γ mode would cause the central-cell density to rise by the same factor as in the axicell ($\sqrt{6}$). The increase in the central-cell density allowed by the MHD stability is smaller, $(n_c)_w \simeq 1.3 \times 10^{14}$ cm^{-3} (Maxwellian). This is permitted because of the decrease in T_{ic} and T_{ec} in the high-Γ mode. Therefore, the local $(n\tau)_c$ for the central-cell ions must drop by a factor of almost 4, from 1×10^{14} cm^{-3}·s to 2.5×10^{13} cm^{-3}·s, to accommodate the sixfold increase in current. This is accomplished with a lower $(n\tau)_{pump} \sim 5 \times 10^{13}$ cm^{-3}·s [caused by lower T_{ic} and a smaller transition $g_b = (n_{trap}+n_{pass})/n_{pass}$, which reduces the coefficient in Eq. (2.3) to less than 10] and a lower $(n\tau)_{pump}$ Pastukhov (axial) $\sim 5 \times 10^{13}$ cm^{-3}·s, due to the lowering of ϕ_{ic} from 68 to 30 keV.

Because the same D-T ions spend time in both the high- and low-field portions of the central cell, a composite $(n\tau)_{DT}$, defined by an n^2-weighted average

$$(n\tau)_{DT} = \frac{(16/30)(n_x^2 V_x + n_c^2 V_c)}{I/q} , \tag{2.8}$$

and an average time in the system, defined as

$$\tau_{DT} = \frac{(2/3)(n_x V_x + n_c V_c)}{I_{beam}/q} , \tag{2.9}$$

will always be larger than the local values of $n\tau$ and τ obtained by dividing the current into a local cell alone. However, using the weighted averages allows us to make a better judgment of the sensitivity of the whole system to unknown loss processes (those other than the ones included in this analysis). In Eqs. (2.8) and (2.9), the factors 16/30 and 2/3 are radial profile factors appropriate for the quartic radial profiles

$$n(r) = n\left[1 - \left(\frac{r}{r_p}\right)^4\right] \tag{2.10}$$

assumed in this report. For energy confinement, we similarly define

$$(n\tau)_{energy} = \frac{(16/30)\left[n_x^2 V_x\left(E_{ix} + \frac{3}{2}T_{ec}\right) + n_c^2 V_c\left(\frac{3}{2}T_{ic} + \frac{3}{2}T_{ec}\right)\right]}{I_{inj}[(E_i)_{loss} + \phi_e + T_{ec}]} \tag{2.11}$$

and

$$\tau_{energy} = \frac{(2/3)\left[n_x V_x\left(E_{ix} + \frac{3}{2}T_{ec}\right) + n_c V_c\left(\frac{3}{2}T_{ic} + \frac{3}{2}T_{ec}\right)\right]}{I_{inj}[(E_i)_{loss} + \phi_e + T_{ec}]} , \tag{2.12}$$

where

$$(E_i)_{loss} = \frac{I_{radial}\left(\frac{3}{2}T_{ic}\right) + I_{axial}\left(\phi_c + T_{ic}\right)}{I_{inj}} , \tag{2.13}$$

$$V_x = \pi r_x^2 (L_x)_{eff} , \tag{2.14}$$

$$V_c = \pi r_c^2 (L_c)_{eff} , \tag{2.15}$$

and

$$L_{\text{eff}} = \int_{\text{mirror}}^{\text{mirror}} \left[\frac{n(z)}{n}\right]^2 \left[\frac{B_0}{B(z)}\right] dz \ . \tag{2.16}$$

When we compare the confinement parameters in Table 2.5, we see that the high-Γ mode requires about a factor of 2 less $n\tau$ (both particle and energy) and about a factor of 2 less τ (both particle and energy) than the high-Q mode. Thus, the high-Γ mode is "safer" with respect to unknown losses, which is useful for blanket testing, and the high-Q mode pushes confinement with "known" loss processes to their limits and is thus better for testing the importance of any "unknown" losses.

REFERENCES

1. A. A. Bekhtenev et al., "Problems of a Thermonuclear Reactor with a Rotating Plasma," *Nucl. Fusion* **20**, 579–98 (1980).

2. S. L. Milora et al., "Pellet Injection into PDX Diverted Plasmas," *Nucl. Fusion* **22**, 1263 (1982).

3. *A Tandem Mirror Technology Demonstration Facility*, UCID-19328, Univ. California, Lawrence Livermore Natl. Lab., Livermore, Calif., Oct. 1983.

4. T. C. Simonen et al., "2XIIB Confinement Experiments," pp. 389–99 in *Proceedings of the 7th International Conference on Plasma Physics and Controlled Nuclear Fusion Research*, Int. Atomic Energy Association, Vienna, 1978.

5. T. C. Simonen, ed., *Summary of Results from the Tandem Mirror Experiment (TMX)*, UCRL-53120, Univ. California, Lawrence Livermore Lab., Livermore, Calif., 1981.

6. *Final Design Review for the A-Cell, Transition, and Solenoid Coils for the Mirror Fusion Test Facility-B (MFTF-B)*, GDC-MFTF-B-81-04, General Dynamics Corp., San Diego, 1982, p. 5-7.

3. CONFIGURATION

J. A. O'Toole

Grumman Aerospace Corporation/Fusion Engineering Design Center

CONTENTS

3.1 OVERVIEW 3-3
3.2 FACILITY MODIFICATIONS 3-8
3.2.1 Vault 3-8
3.2.2 Hot Cells 3-10
3.2.3 Tritium Processing Facility 3-10
3.3 D-T AXICELL AND CENTRAL CELL 3-10
3.4 END CELLS 3-17
3.5 FUTURE WORK 3-28
REFERENCE 3-29

3. CONFIGURATION

3.1 OVERVIEW

The MFTF-α+T configuration meets the stipulated mission and conforms to the principal design guidelines, including the direction to make maximum use of the existing Mirror Fusion Test Facility (MFTF-B). The configuration described here has evolved over the past year, with emphasis on minimizing capital cost.

The MFTF-α+T device will be installed in the existing MFTF-B Experimental Facility, located in Bldg. 431 at Lawrence Livermore National Laboratory (LLNL). A site map is shown in Fig. 3.1. The MFTF-B vault will be extensively modified to accommodate the new device, and two hot cells and a tritium processing facility will be added (see Figs. 3.2 and 3.3). The MFTF-α+T device and its location in the vault are shown in Figs. 3.4 and 3.5. (In Fig. 3.5, the end-cell coils have been rotated into the plane of the drawing for clarity. All of the end-cell components are actually oriented at 45° to the plane of the drawing.)

To describe the configuration, we divide the device into three areas: the deuterium-tritium (D-T) axicell, the central cell, and the end cells. Figure 3.6 shows these areas and the nomenclature of the coil sets.

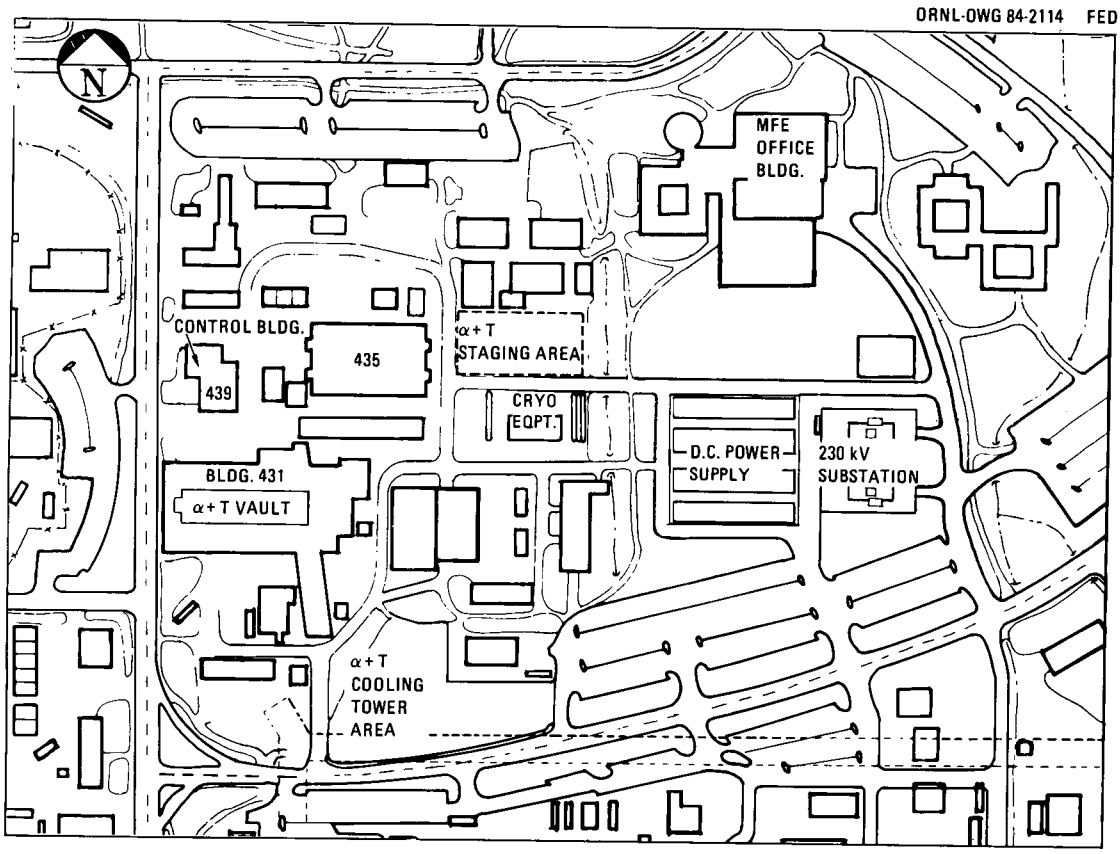

Fig. 3.1. Location of MFTF-α+T at LLNL.

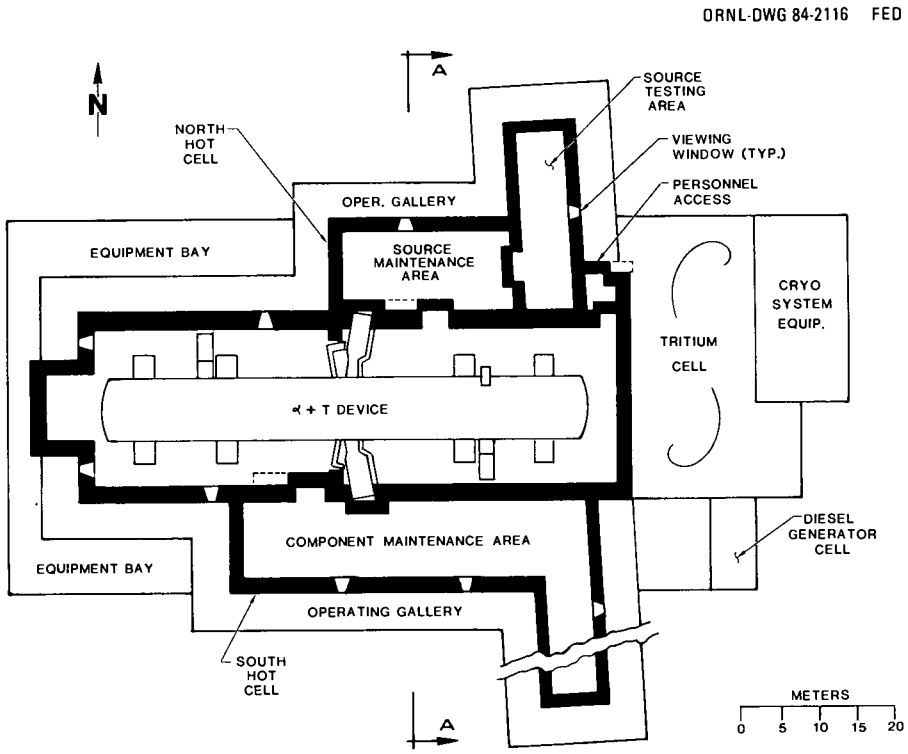

Fig. 3.2. First floor of MFTF-α+T vault in Bldg. 431.

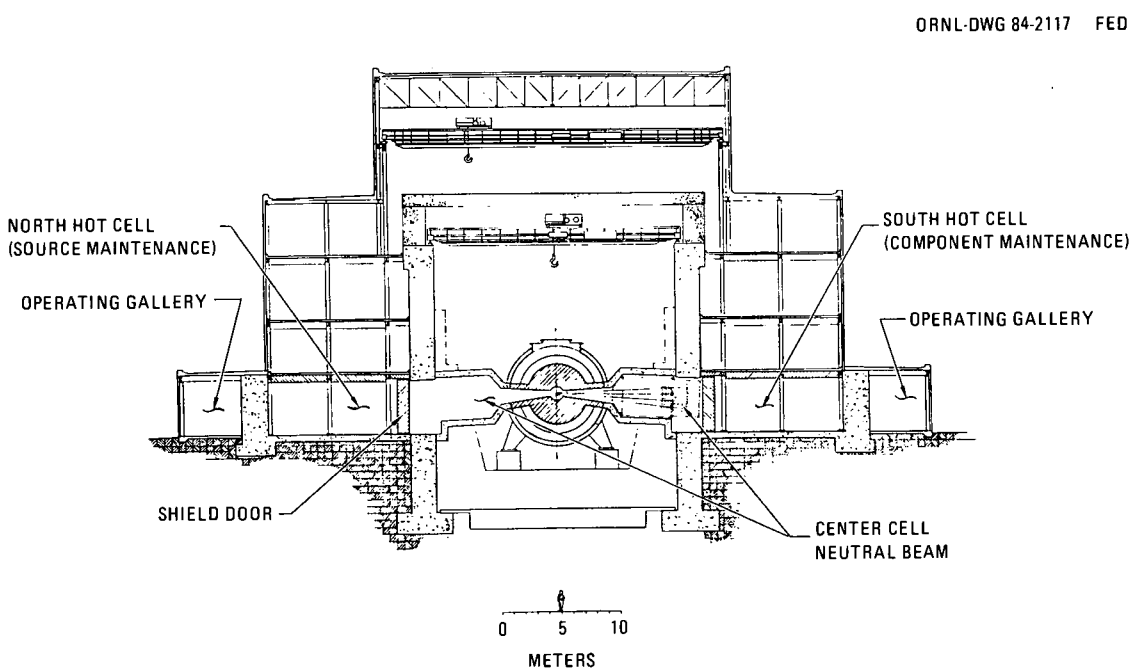

Fig. 3.3. Elevation of MFTF-α+T vault in Bldg. 431.

ORNL–DWG 83-4006 FED

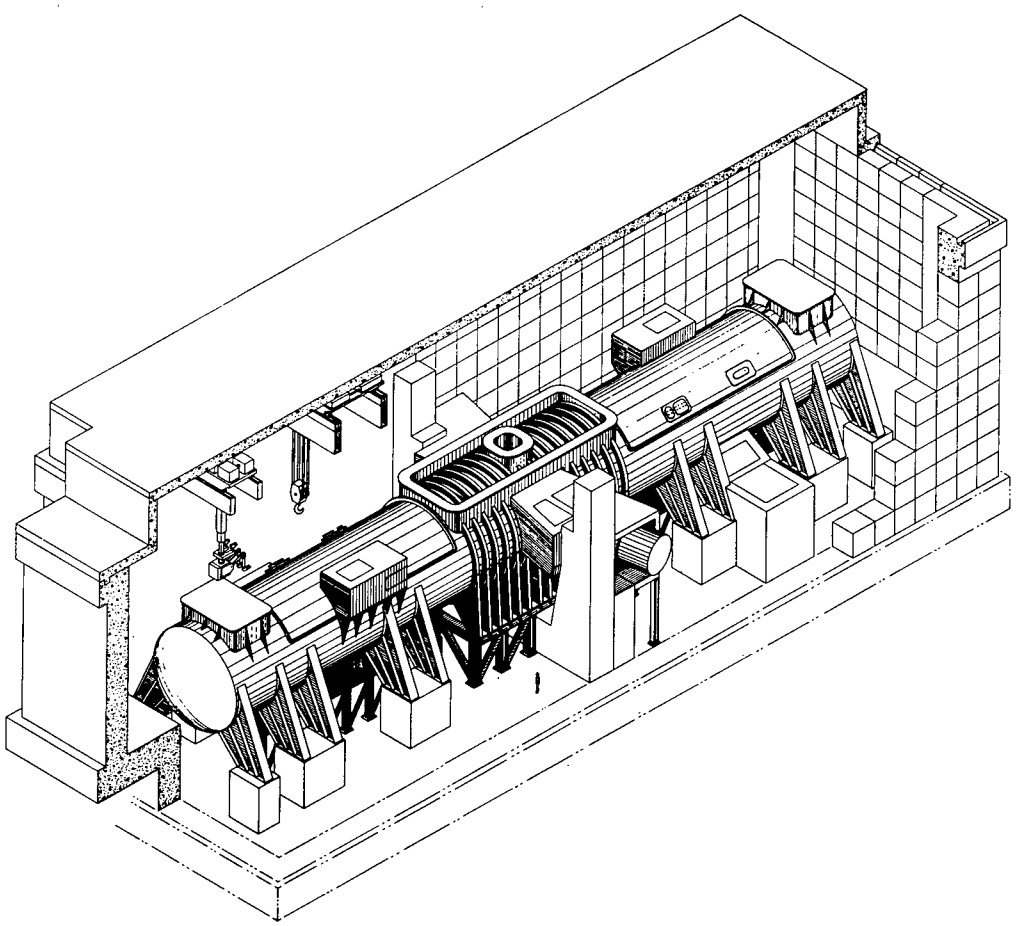

Fig. 3.4. The MFTF-α+T device.

The D-T axicell includes the 12-T choke coils, two positive-ion-based beam lines and their dumps, nuclear shielding, and the blanket test module. The central cell extends on either side of the D-T axicell from the 12-T coils to the 18-T choke coils. This area includes two sets of five solenoid coils and their nuclear shielding.

The end cells start at the 18-T choke coils and consist of eight coils configured as described in the Mirror Advanced Reactor Study (MARS).[1] Each end cell has an anchor ion cyclotron resonance heating (ICRH) system, two electron cyclotron resonance heating (ECRH) systems, and a negative-ion-based beam line. A drift pumping system, a halo scraper (which also intercepts the drift-pumped ions), and a direct converter (which intercepts the electrons) are located in each end cell. Turbomolecular pumps provide steady-state pumping of the ions collected by the halo scraper. Nuclear shielding within the coil set limits nuclear damage of the coils and reduces the heat load on the cryogenic system; a biological shield outside the coil set is an integral part of the end-cell vacuum vessel.

ORNL-DWG 83-4007A FED

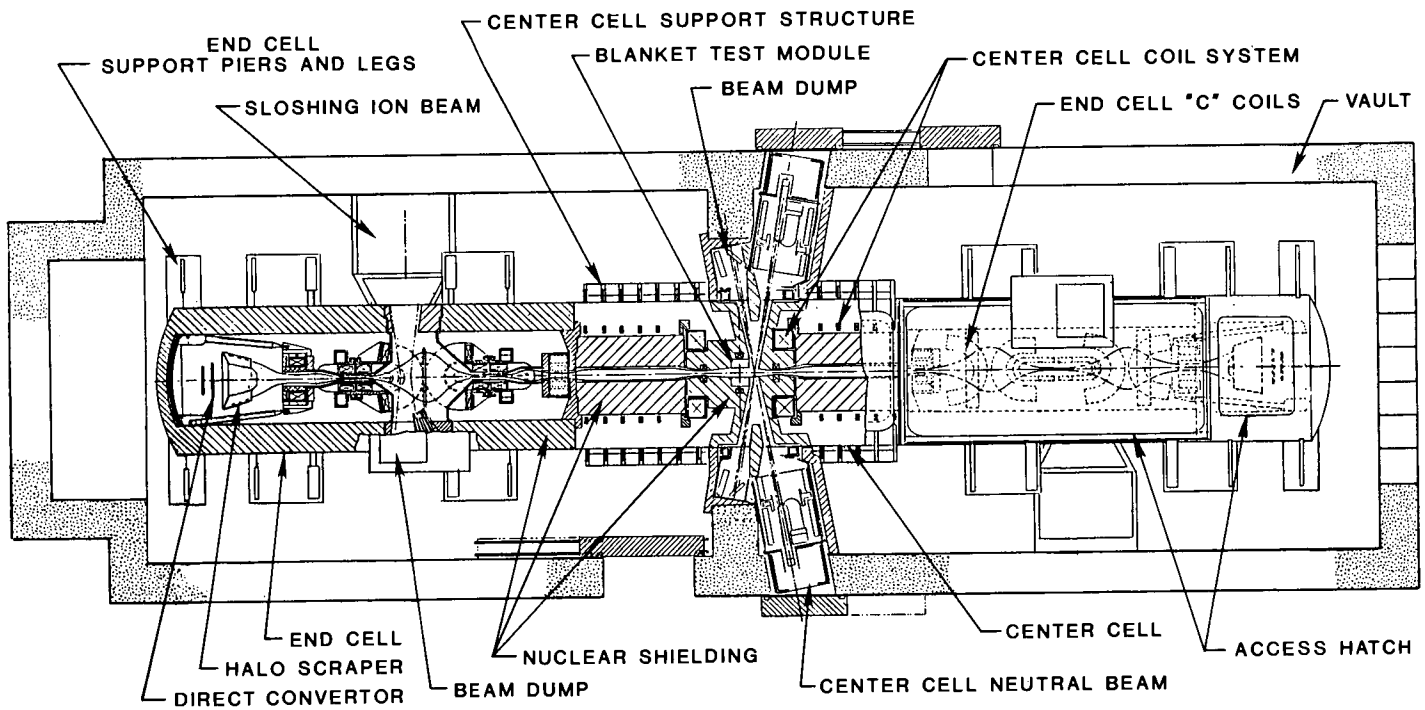

Fig. 3.5. Plan view of MFTF-α+T (components rotated into plane).

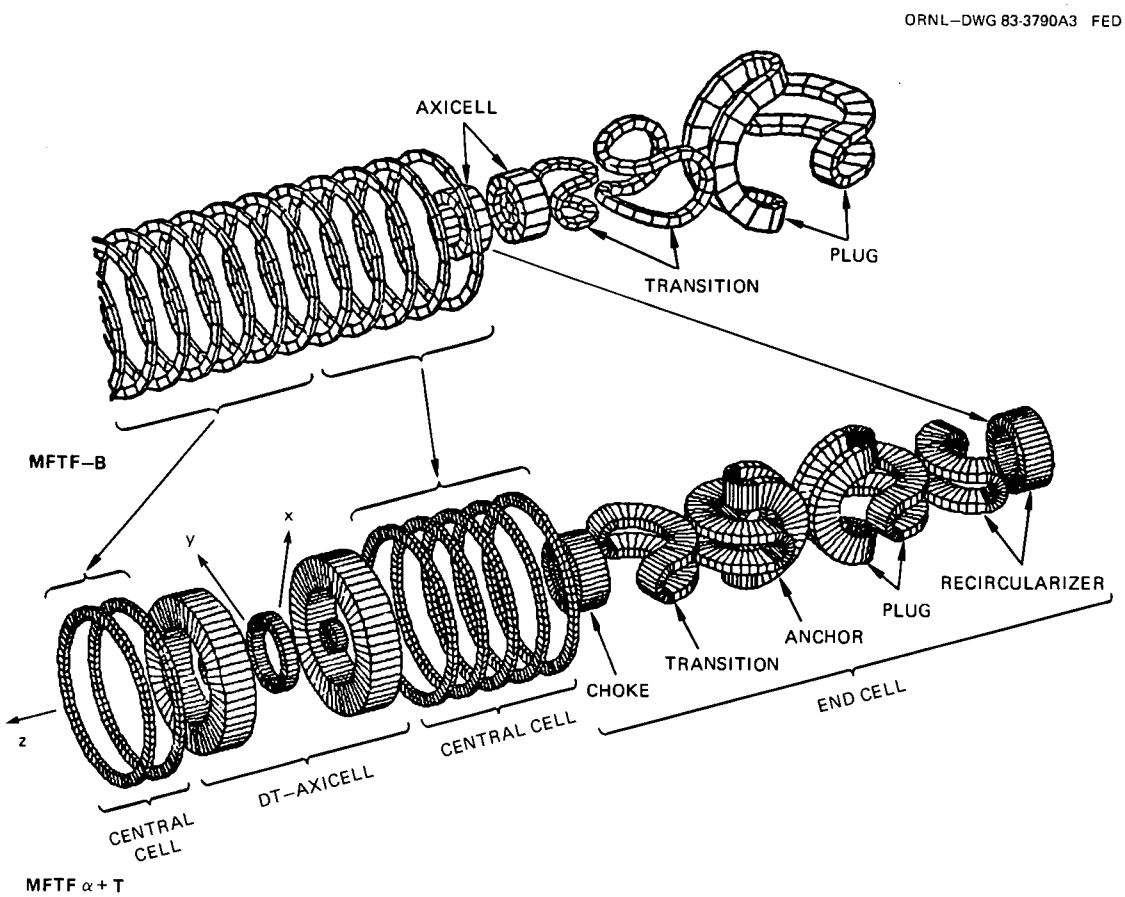

Fig. 3.6. Nomenclature of coils and areas of MFTF-α+T and definition of coordinate system.

The maintenance philosophy adopted for MFTF-α+T calls for the performance of both routine and unscheduled maintenance on a schedule that will achieve 10% availability while minimizing personnel exposure. The configuration is designed to carry out this philosophy. All nuclear shielding is located inside the vacuum vessel so that access cover attachments and utility connections are accessible for hands-on maintenance. Once the cover is removed, personnel leave the vault and the component module is remotely removed for replacement, as shown in Fig. 3.7. To allow for removal of lifetime components (because of premature failure or for decommisioning), the large access hatches shown in Fig. 3.8 are attached and seal-welded into place. The seals are outside the vacuum surface so that personnel can use an automatic cutting/welding machine, and the attachments consist of primary pins used with holes and slotted holes so that the hatches are not part of the primary vessel structure. This approach, which minimizes the number of structural connections, is made possible through the double-wall construction of the end-cell vessel and through the support of the central-cell magnetic loads entirely by cold structure.

The necessary modifications to the MFTF-B facilities are described in Sect. 3.2. The configuration of the D-T axicell and central-cell regions is described in Sect. 3.3; that of the end cells, in Sect. 3.4. Section 3.5 contains a brief listing of issues for future work.

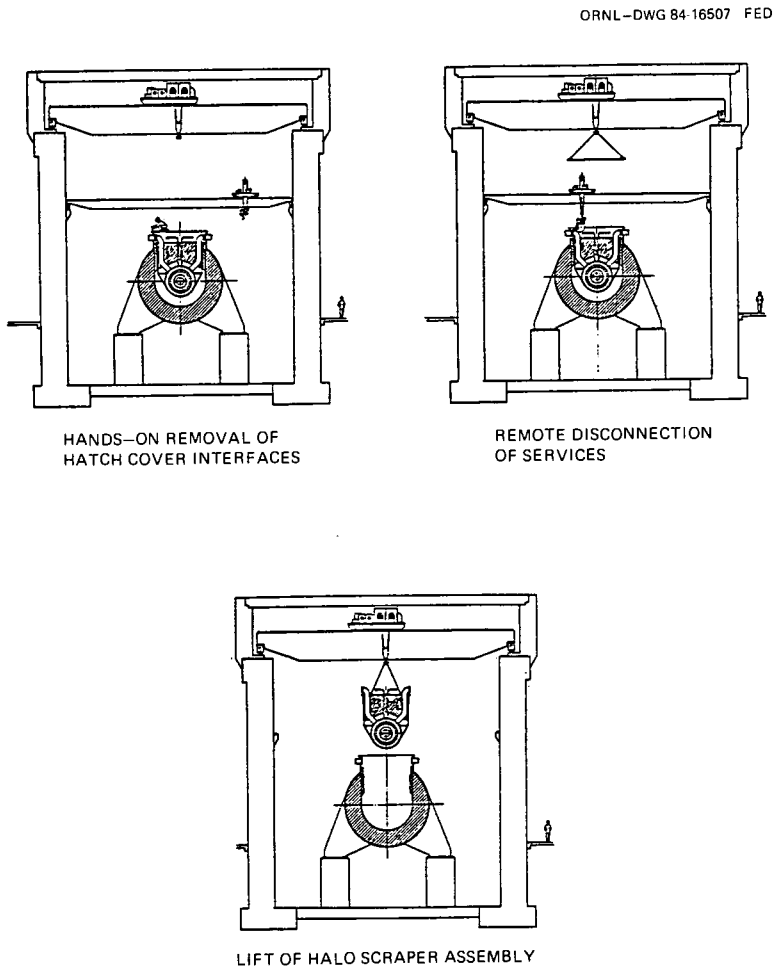

Fig. 3.7. Removal of a system module for maintenance.

3.2 FACILITY MODIFICATIONS

3.2.1 Vault

The existing MFTF-B vault is rectangular, as shown by Figs. 3.4 and 3.5, with an east wall made up of 7-ft cubes of concrete and a poured concrete west end wall. All of the walls are prestressed with embedded steel tendons. The vault must be modified significantly to accommodate the MFTF-α+T device.

Penetrations will be required for access to the central-cell beam lines and to the vault, for in-vault air conditioning, for tritium cleanup ducting to the tritium processing facility, and for piping, wiring, and viewing ports. Existing ventilation penetrations will be sealed.

The MFTF-α+T vacuum vessel is longer than that of MFTF-B, and more room is needed at the west end of the vault for diagnostic equipment. A portion of the west end wall that is built up of cubes will be modified to allow for these changes. The modified wall will be poured concrete prestressed with internal tendons to meet standards for contamination containment, tritium compatibility, and seismic events.

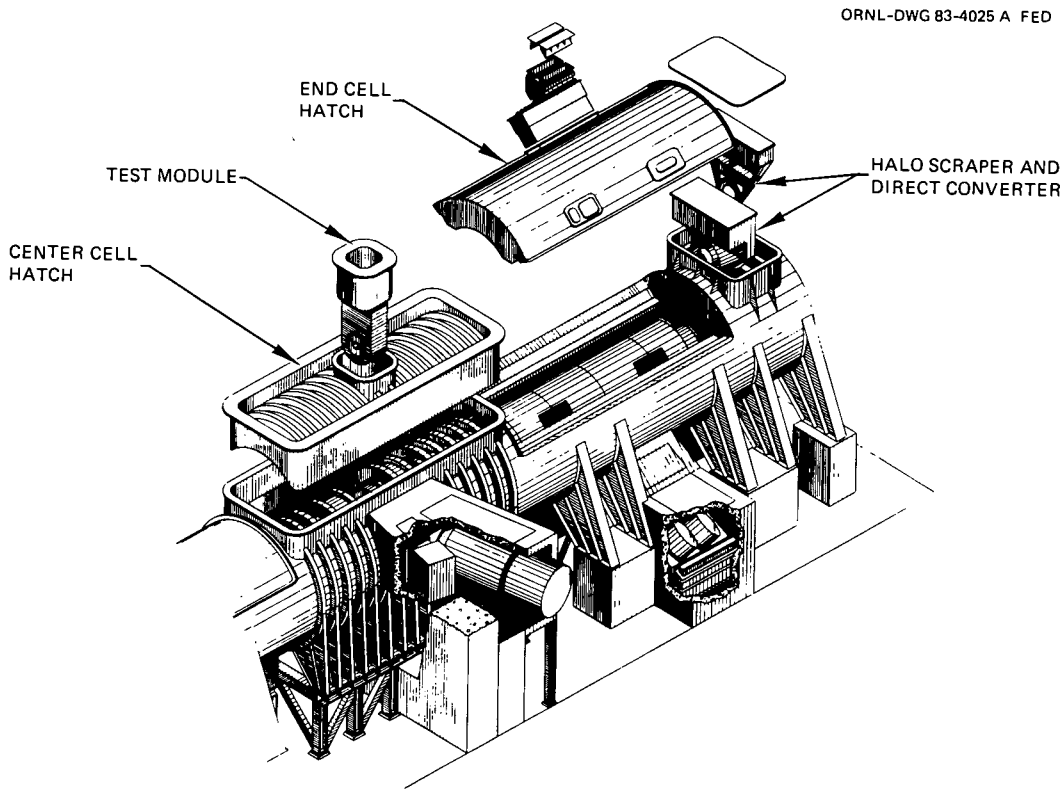

Fig. 3.8. Access to major end-cell components through large access hatches.

The roof of the existing vault will be replaced with a 1-m-thick roof of prestressed concrete planks. Stub walls will raise the new roof 16 ft higher than the existing one to make room for a 150-ton bridge crane; the crane rails will be mounted on the existing vault sidewall caps, as shown in Fig. 3.3. A 20-ton bridge crane mounted lower down will carry a bridge-mounted manipulator and viewing system (Fig. 3.4). The cranes will not be significantly activated, so no shielded storage bay is provided.

The vault foundation will be modified to accommodate the central-cell supports. Two concrete support piers will be added at each end of the machine.

The vault interior (floor, walls, and roof) must be prepared for the possible tritium environment. Penetrations and cracks between wall cubes must be sealed. Epoxy paint will be used to seal the concrete surfaces. A new in-vault fire protection system will be installed.

The vault must be able to withstand a 5-g seismic event without permanent deformation or loss of containment. An analysis of the existing vault was performed and is included as Appendix A of this report. Possible modifications include adding buttresses at the one-quarter and three-quarter points along the outside of the side walls and reinforcing the foundations. Further study is required to fully define the necessary modifications.

3.2.2 Hot Cells

The locations of the two hot cells are shown in Figs. 3.2 and 3.3. The hot cells are used to move components into and out of the main vault. Contaminated components are disassembled and their subcomponents loaded into casks for shipment to decontamination and disposal facilities.

The north hot cell services the central-cell beam line on that side of the device and provides a servicing and test facility for beam line sources. The larger south hot cell services the central-cell beam line on that side of the device and the device components located within the vault.

3.2.3 Tritium Processing Facility

The tritium processing facility is located in the east end of Bldg. 431's high bay area, near personnel and local control room facilities (see Fig. 3.2). The tritium facility is a self-contained processing facility that cleans the exhaust gas and separates it into usable tritium and deuterium. Air and water cleanup units will service the experimental facility in normal and off-normal operating conditions, and emergency diesel generators ensure continuous power to all required systems.

3.3 D-T AXICELL AND CENTRAL CELL

The D-T axicell region (Fig. 3.9) includes the two 12-T choke coils, the two positive-ion-based beam lines and their dumps, the nuclear shielding, and the blanket test module. The central cell extends on both sides of the axicell and includes the ten solenoid coils and their nuclear shielding.

The vacuum vessel is 8.3 m in diameter, the same size as the MFTF-B central-cell vessel, to accommodate the solenoid coils and their supports. A 5.6-m-wide hatch cover extends the length of the central cell (Fig. 3.10). The vessel is supported against the side-wall pressure loading by the action of the cover sill beam, the circumferential stiffeners, and the leg frames (Fig. 3.11). The hatch allows access to the internal components of the central cell during initial assembly and decommissioning, and it would provide access for replacement of components if this should be necessary. A smaller hatch cover in the middle of the main hatch cover (Fig. 3.10) is used in replacing the blanket test module and the 12-T normal-conducting choke coils. Its construction is similar to that of the main hatch.

The vessel leg frames are supported by a structure consisting of box beams, legs, and crossbracing (shown in Figs. 3.12 and 3.13), which is secured to concrete footings. At the axial midpoint of the machine, a series of axial shear panels (Fig. 3.14) supports the machine against the overall axial loading that would be generated by a seismic event. The length and stiffness of the central-cell leg frames allow for the small axial deformation caused by thermal strain and by the compression loading produced by the end-cell coil sets.

The D-T axicell region contains three normal copper coils. One is located at the center of the machine and is sized to fit around the blanket test module. It helps to maintain a 4.5-T field at the center of the machine. The other two are located at $Z = +2.0$ m and $Z = -2.0$ m and help to maintain a 12.0-T field at the choke points. All three

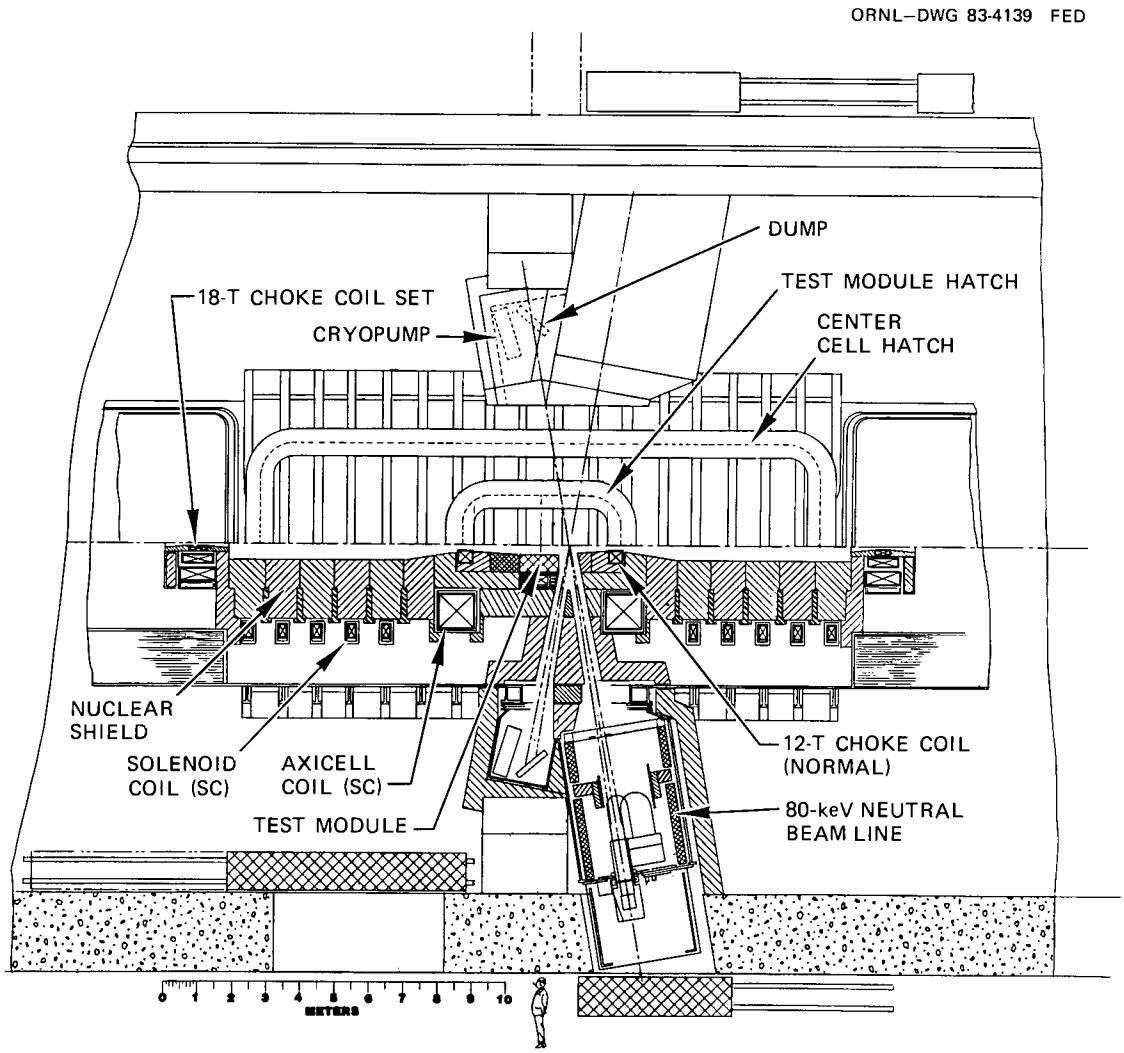

Fig. 3.9. Plan view of central cell.

coils are water cooled, made of hollow conductor, and encased in stainless steel. These coils are not expected to be lifetime components; they will be replaced during planned major shutdowns. The center coil will probably be replaced when the test module is replaced, and the 12-T coils will be replaced every 27 months.

The superconducting coil set consists of two large coils that are part of the D-T axicell and ten MFTF-B solenoid coils, five on each side of the D-T axicell. Each coil is hung by a pair of struts (Fig. 3.15) attached to the vessel sill beam. To minimize the refrigeration load, the superconducting coils, their cold support structure, and their supporting struts are surrounded by a cold wall cooled with liquid nitrogen (LN_2). The cold wall is supported by thermal isolation standoffs on the structure, which is cooled with liquid helium (LHe). In addition, the cold mass supporting struts have LN_2-cooled sections. All superconducting coils are expected to be lifetime components (although they can be replaced if necessary).

ORNL-DWG 84-16508 FED

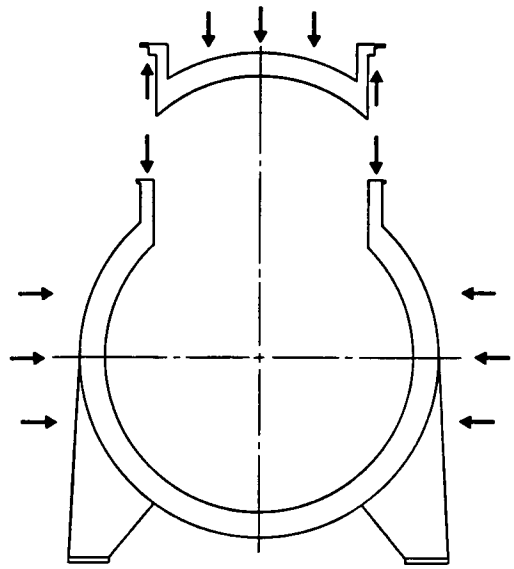

Fig. 3.10. Balancing of pressure loads.

ORNL-DWG 84-18339 FED

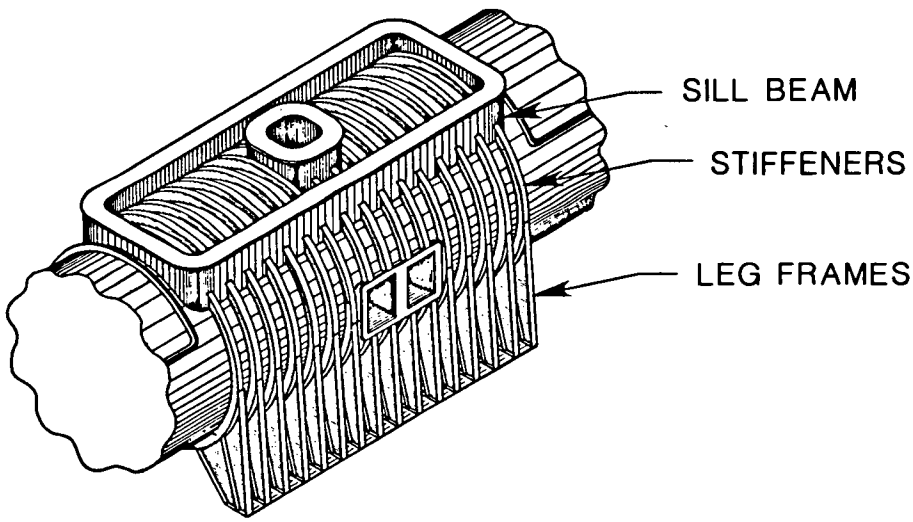

Fig. 3.11. Support structure for central cell.

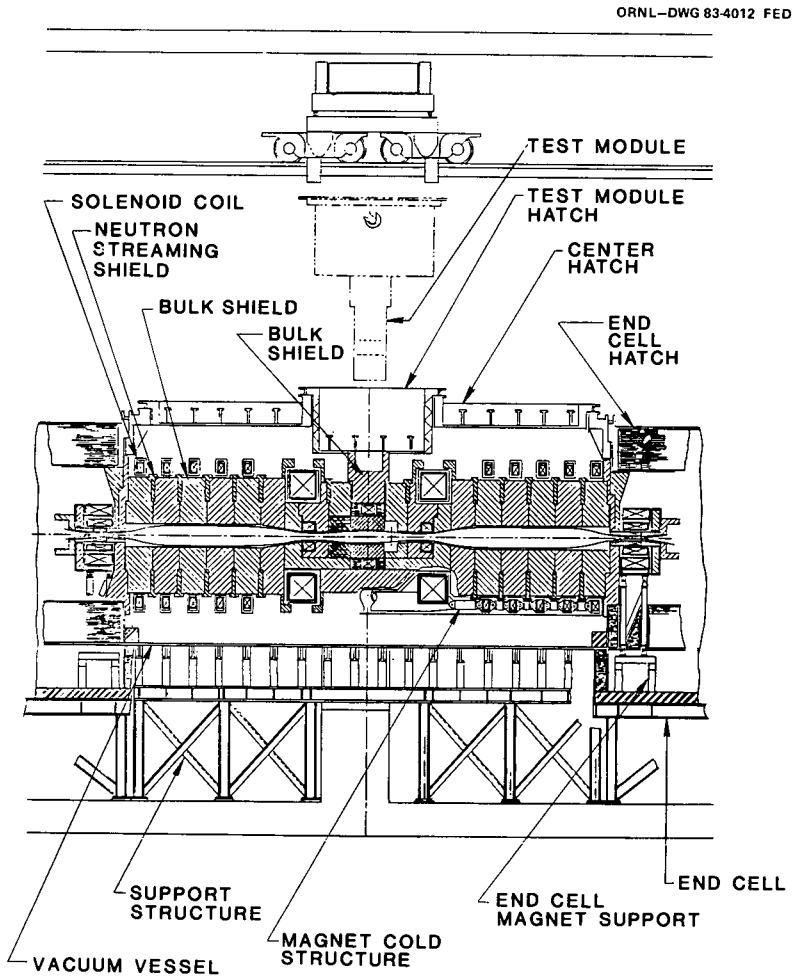

Fig. 3.12. Solenoid coil/shield support structure.

Nuclear shielding is needed in four areas: the central cell, the bores of the superconducting D-T axicell coils, the 12-T coil supports, and the center of the D-T axicell.

In the central cell, a shield module is centered on each solenoid coil, and pairs of C-shaped shield segments prevent streaming at the interfaces between the shield modules (Fig. 3.15). Shield modules are hung on two pairs of struts (Fig. 3.16), which are accessible for remote disassembly and installation. Modules contain an integral water-cooled steel shield nearest the plasma, a water shield outboard, and layers of boron carbide (B_4C) and lead. They limit nuclear damage to the magnets, provide biological shielding to achieve the 0.5-mrem/h dose criterion 24 h after shutdown, and reduce the refrigeration load. The central-cell shield is considered a lifetime component.

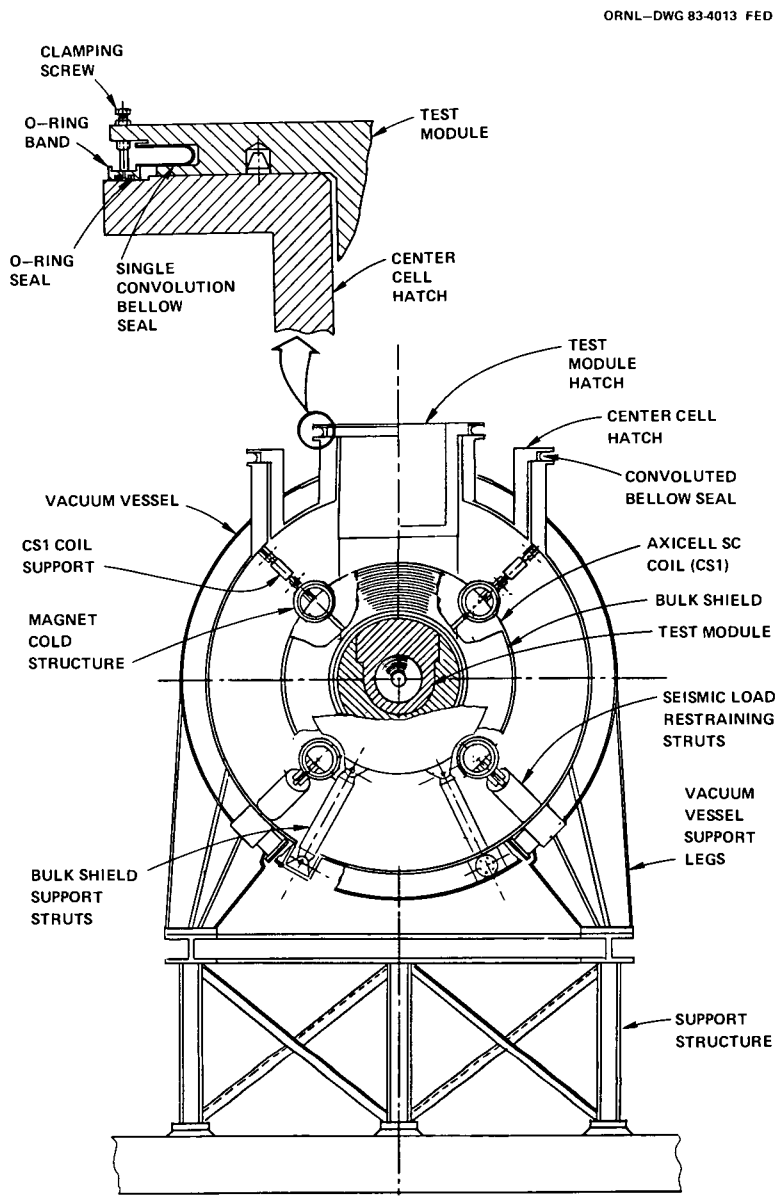

Fig. 3.13. Elevation through D-T axicell.

The shield within the bore of the D-T axicell superconducting coils (see Fig. 3.13) protects the coils and reduces the refrigeration load. The radial thickness of the shield was chosen to fit the space between the first wall and the magnet bore; with the shielding provided by the coil itself, the biological shielding is more than adequate. The shield module is made of water-cooled steel with an integral water-cooled steel first wall and outer layers of boron carbide and lead. It is considered a lifetime component.

In the area between the coils, the first shield module is similar to a large washer with the 12-T coil fastened to it (see Figs. 3.10, 3.12, and 3.17). The shield supports the coil's weight and is in turn supported by the center shield module on a pair of shoulder support

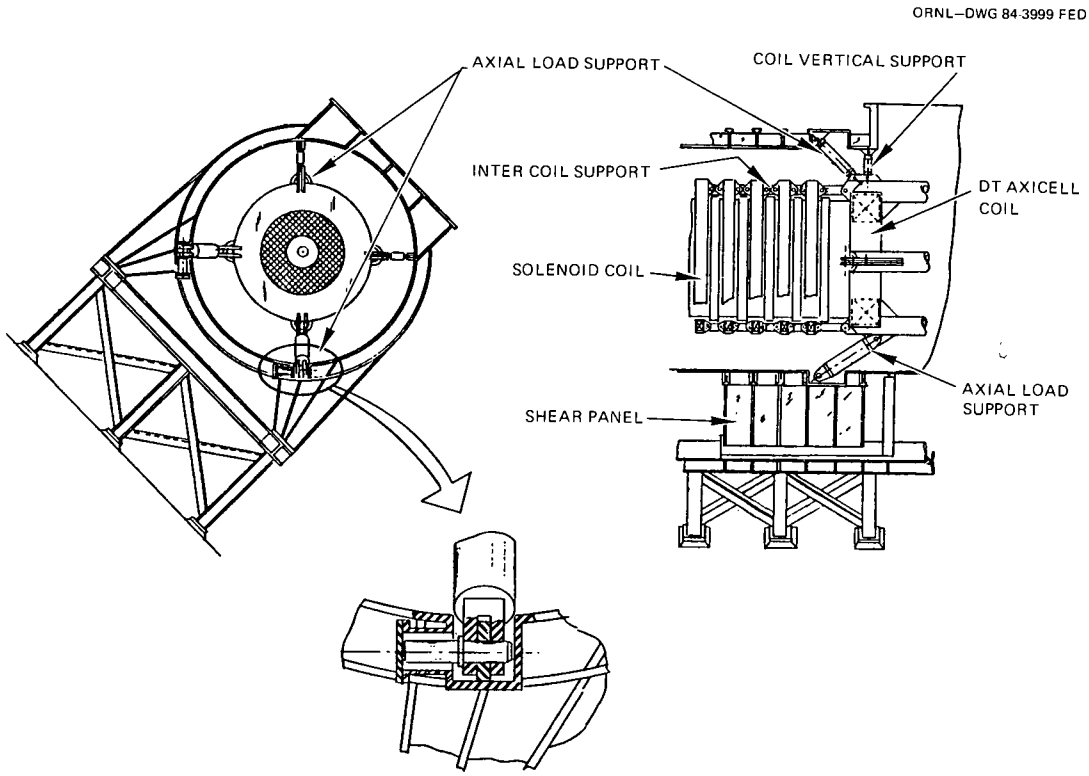

Fig. 3.14. D-T axicell coil supports.

structures (Fig. 3.18). The axial magnetic load that tries to move the coils toward the center of the machine is taken in compression by a set of wedging pads, which transfer the load so that it can be balanced through the central shield modules in bulk compression.

The center shield assembly is constructed with a pair of penetrations for the central-cell beams and an opening for the blanket test module and its plug shield. The area west of the blanket test module is reserved for coolant piping and/or for small nuclear test modules (to be installed when blanket test modules are replaced). The first wall of the shield is made of water-cooled steel and can tolerate high heat fluxes. It lines the inside of the shield module from the 12-T choke coil to the test module, from the blanket test module to the beam penetrations, and then to the other 12-T choke coil. The shield module is also made of water-cooled steel. The center shield system is restrained from axial motion by a set of struts.

The beam line ducts (Fig. 3.19) in the central cell have first walls and nuclear shielding of water-cooled steel. These ducts are installed before the center shield module and are supported by brackets on the vessel side wall and pins on the center shield module.

The blanket test module (Figs. 3.12 and 3.19), its companion coils, and the nuclear shield plug are installed through the vessel access hatch into the center shield module. Coolant lines and instrumentation cabling are preinstalled in the test module subassembly. This subassembly hangs from the hatch and is supported axially by pins holding it to the center shield module. As part of the test program, the blanket test module will be

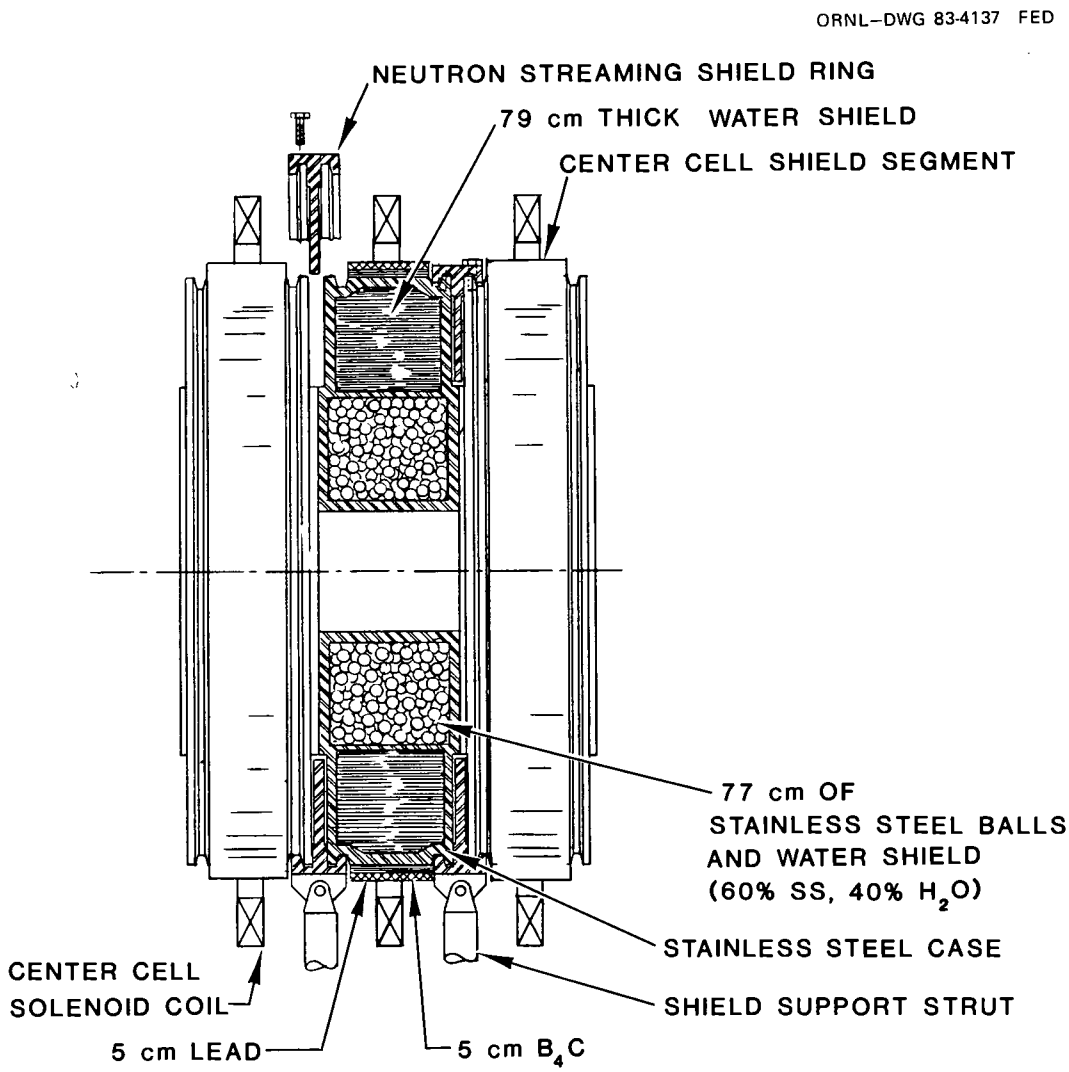

Fig. 3.15. Central-cell solenoid coil shielding.

replaced every 12 to 18 months. It is expected that a new coil and shield plug will be installed with each test subassembly.

The two central-cell beam lines (Figs. 3.10 and 3.19) are patterned after those of the Technology Demonstration Facility (TDF), but the MFTF-α+T design uses four sources instead of three; the fourth source provides an on-line spare. The design features a vacuum isolation valve for each source to be used during source replacement. The beam line is attached to the vessel access port by a bellows, which allows for manufacturing tolerances and decouples the mass of the beam line from the vessel.

The central-cell beam line dumps (Figs. 3.10 and 3.19) are placed in vacuum enclosures outside the main vacuum vessel to accommodate their cryopumps. The dump enclosures are designed for remote replacement of either the dump or the cryopump; both components are mounted on port covers for vertical removal. The concrete nuclear shield enclosure around the dump enclosure has a removable roof with a shield plug over the access ports.

ORNL–DWG 83-4140 FED

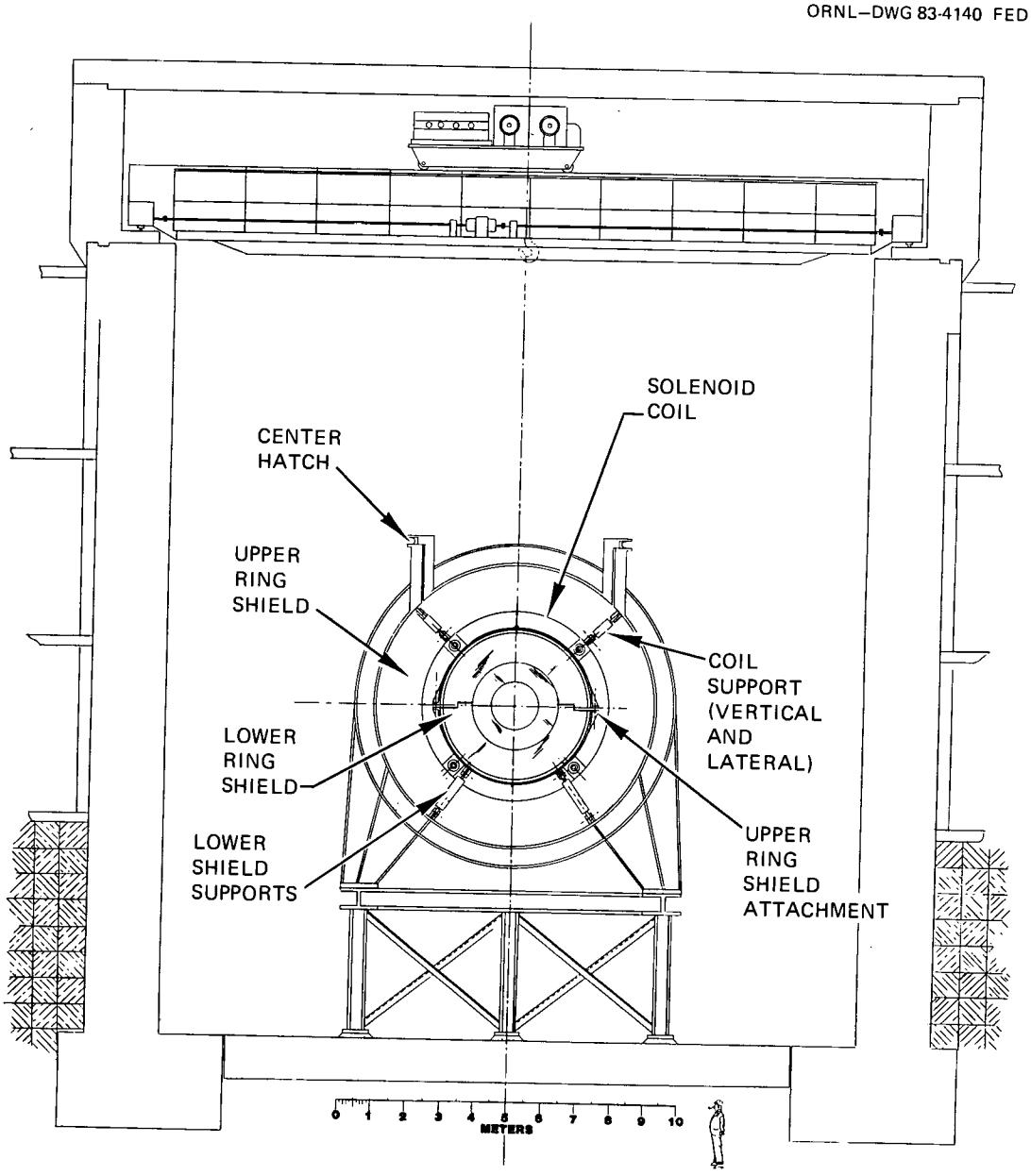

Fig. 3.16. Central-cell configuration and supports.

3.4 END CELLS

Each end cell (Fig. 3.20) includes the vacuum vessel with its nuclear shielding, an 18-T choke coil, six C coils, a recirculating coil, a pair of drift pumping subsystems, ICRH subsystems, ECRH subsystems, a sloshing-ion beam line with a dump, a halo scraper, and a direct converter.

The double-walled internally framed vessel (Figs. 3.20 and 3.21) has an outer wall diameter of 8.3 m and an inner wall diameter of 5.0 m. The inner diameter provides

ORNL-DWG 83-4026 FED

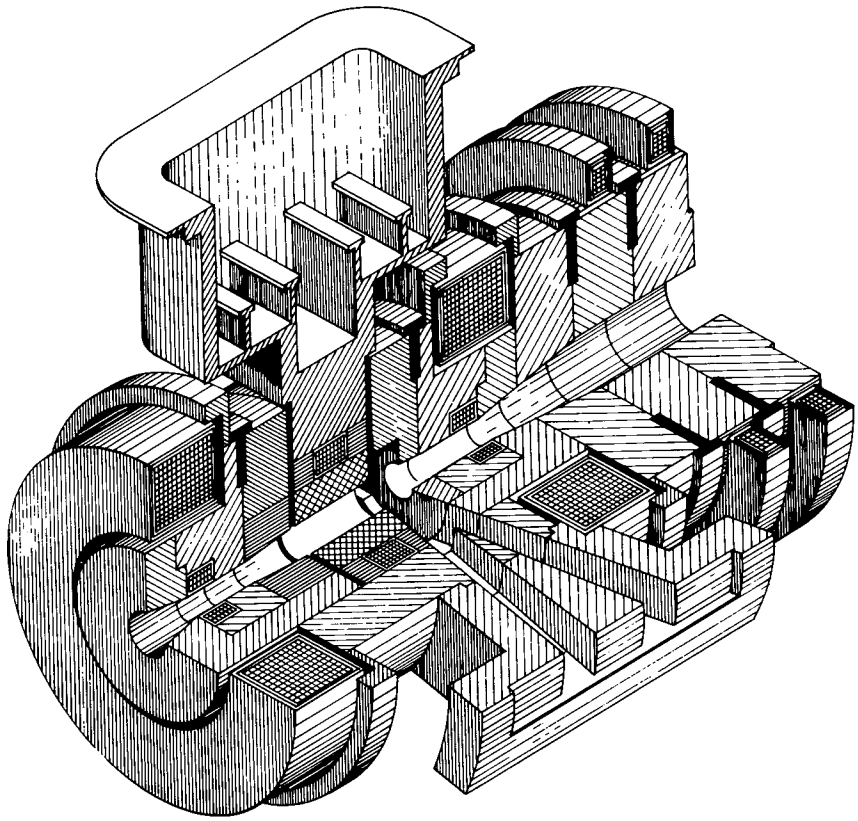

Fig. 3.17. D-T axicell design, showing accommodation of choke coil replacement and test module changeout. A modular set of shield sections can be removed through the test module access hatch.

clearance between the vessel and the end-cell magnets with their cold wall. The outer diameter was selected so that the space between the outer and the inner walls (1.6 m) would satisfy the allowable biological dose rate criteria with a water shield. The outer surface of the inner wall is lined with a layer of boron carbide, and the outside of the outer wall is lined with a layer of boron carbide followed by a layer of lead. The vessel's internal framing allows draining of the water. Support legs at the same axial locations as on the MFTF-B vessel allow the use of the existing concrete piers. Another pair of legs and piers (Fig. 3.20) is added to support the ends of the vessels, which are slightly longer than the MFTF-B vessels and much heavier because of their shielding. The end dome of the vessel is also a double-walled water shield design, except that the inner steel wall is thicker to provide the required shielding.

A set of ports provides access to the device internal components. A large hatch in the top of the end-cell vessel (Fig. 3.20) provides access to the end-cell coils during initial assembly and decommissioning. This cover is a double-walled, water-shielded design, as is

ORNL–DWG 83–4027 FED

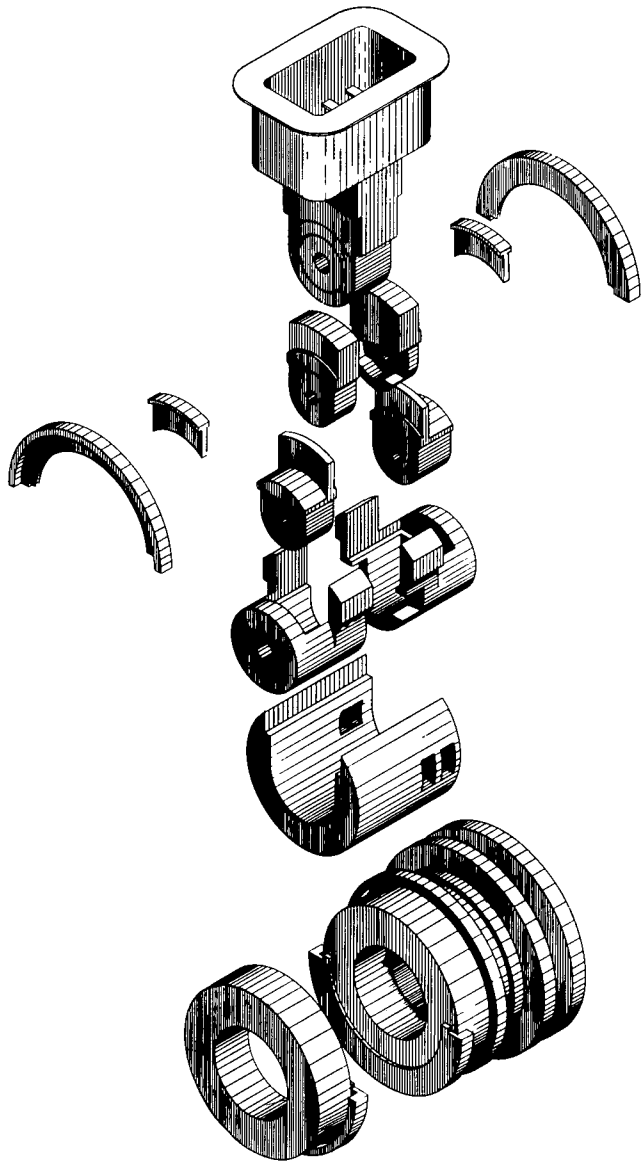

Fig. 3.18. Exploded view of central cell.

the main vessel (Fig. 3.21). The cover carries only its own weight, possible seismic loading, and the atmospheric load. A welded, single-convoluted bellows vacuum seal is used around the cover.

A hatch (Figs. 3.20 and 3.22) is provided at the end of the vessel for removal of the halo scraper and direct convertor. The nuclear shield is inside the cover and is not attached to it. This allows hands-on removal of the welded, single-convoluted bellows seal by an automatic welder/cutter and hands-on disconnection of utility connections.

ORNL-DWG 83-4028 FED

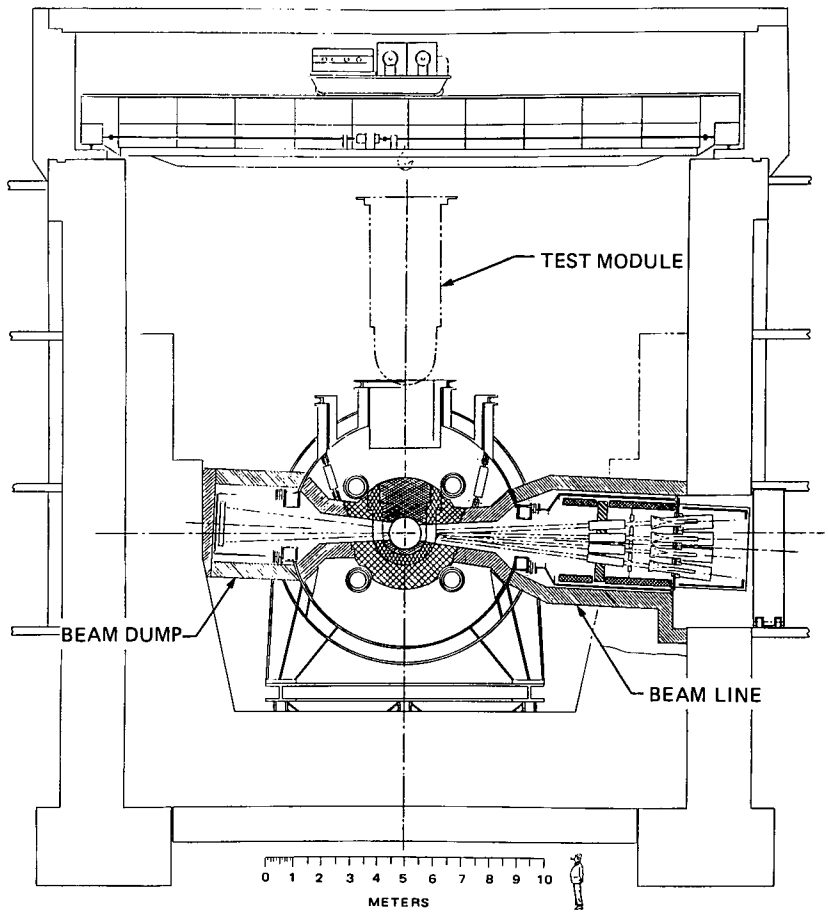

Fig. 3.19. Elevation through D-T axicell showing neutral beam line and dump.

The end-cell coil set is shown in Fig. 3.6. The 18-T choke coil set consists of a normal copper insert coil and an outer superconducting coil enclosed in an LN_2-cooled cold wall. Each coil is separately supported. The T1 coil is superconducting and encased by a structure that supports the coil's major lobe-opening force. A strongback box beam structure is located on each side of the coil. The ends of these two box beam structures are tied together by a pair of tension straps. This structure is designed to support the coil's minor lobe-opening force. The next two coils form the anchor coil set, and the following two the plug coil set. Each coil has a steel structural case to support its major lobe-opening magnetic forces and contain the LHe coolant. A set of four identical structures (Fig. 3.23) is used to support the coil minor lobe-opening forces. These collars provide a load path to the mating coil, which then acts to restrain the opening force (Fig. 3.24).

The direct convertor (DC) coil and the T2 coil recircularize the plasma as it approaches the halo scraper and DC collector. The T2 coil is similar to the T1 coil. The DC coil is an MFTF-B coil with G10-CR fiberglass insulation, which is more easily damaged by radiation than the polyimide insulation used by the new coils; therefore, the internal nuclear shield protecting this coil is 35 cm thick.

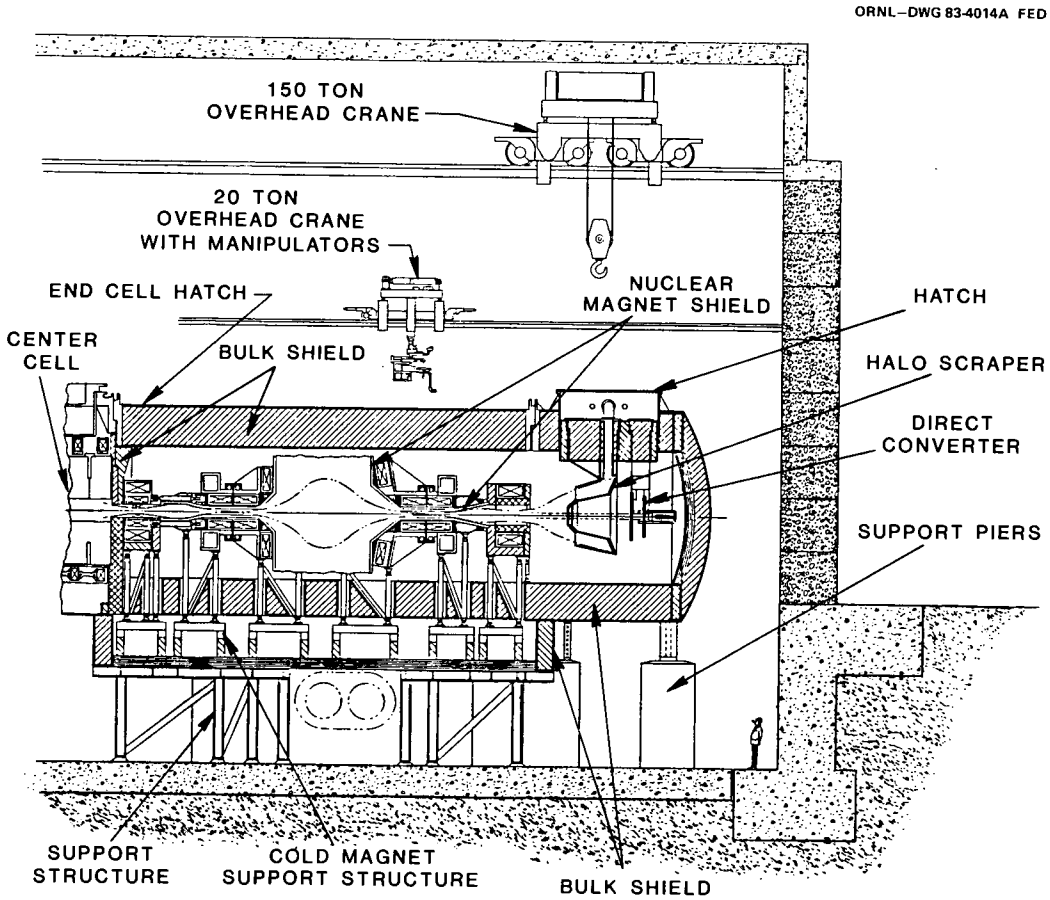

Fig. 3.20. End-cell longitudinal elevation.

The superconducting coil of the 18-T coil set is supported by a cradle structure supported by a set of struts (Fig. 3.20) attached to a support table. The table is supported on four roller assemblies mounted on box leg structures. This design is also used for all of the C coils. The roller assemblies allow axial motion during cooldown of the LHe-cooled coil set.

The T1, anchor, plug, and T2 coils are supported by struts and cold tables mounted on roller assemblies with box legs. This design is similar to that used for the 18-T coil set, except that the legs are attached to the cold tables by pinned connections, which can be remotely withdrawn for coil replacement should any of these coils prematurely fail.

The end-cell magnets produce a total tension load of 2.3 million lb, and the DC coil has a centering force of 1.5 million lb. The sum of these two loads is carried to the vessel by two drag struts attached to the DC coil support cradle (Fig. 3.25). The C coils are axially linked by a series of struts (Fig. 3.24), as are the 18-T superconducting coil and the T2 coil case. This system provides a direct load path for the axial loading and lends itself to the remote replacement of any of the coil assemblies, should this prove necessary.

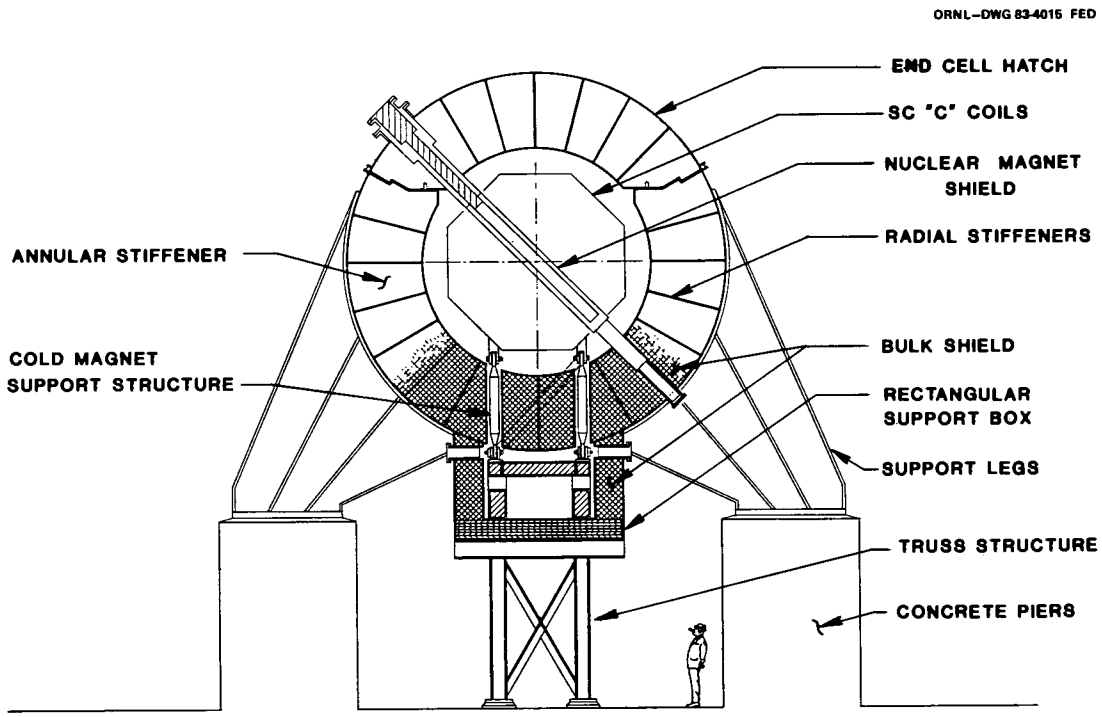

Fig. 3.21. Typical cross section of the end cell.

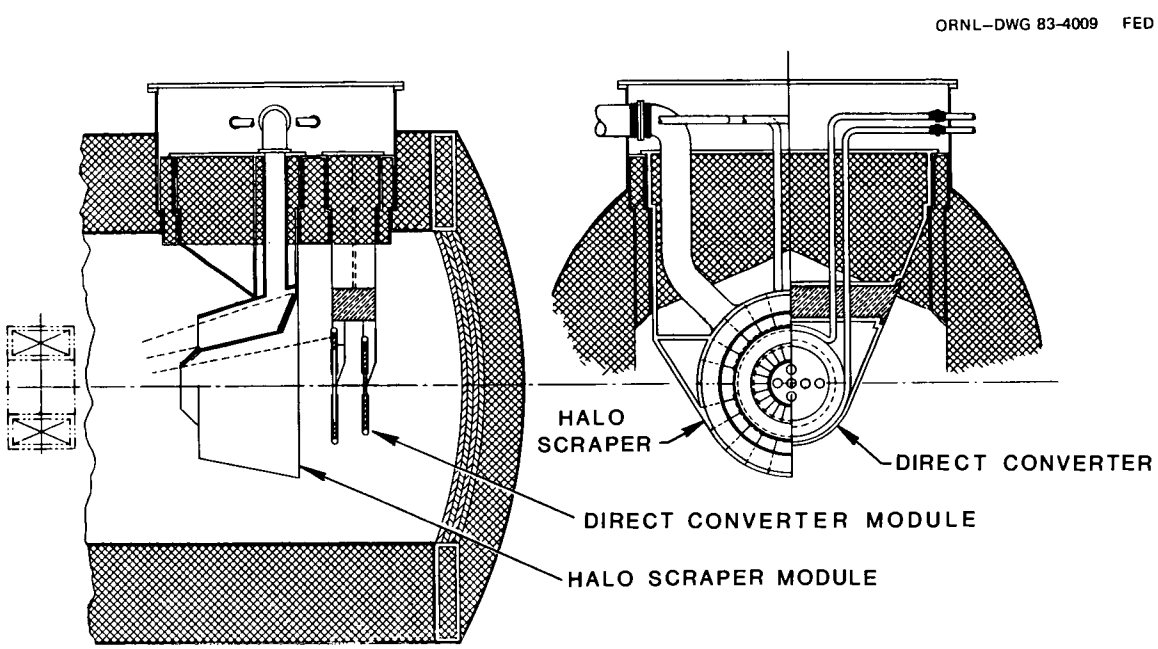

Fig. 3.22. Halo scraper and direct converter assemblies.

ORNL-DWG 83-4021 FED

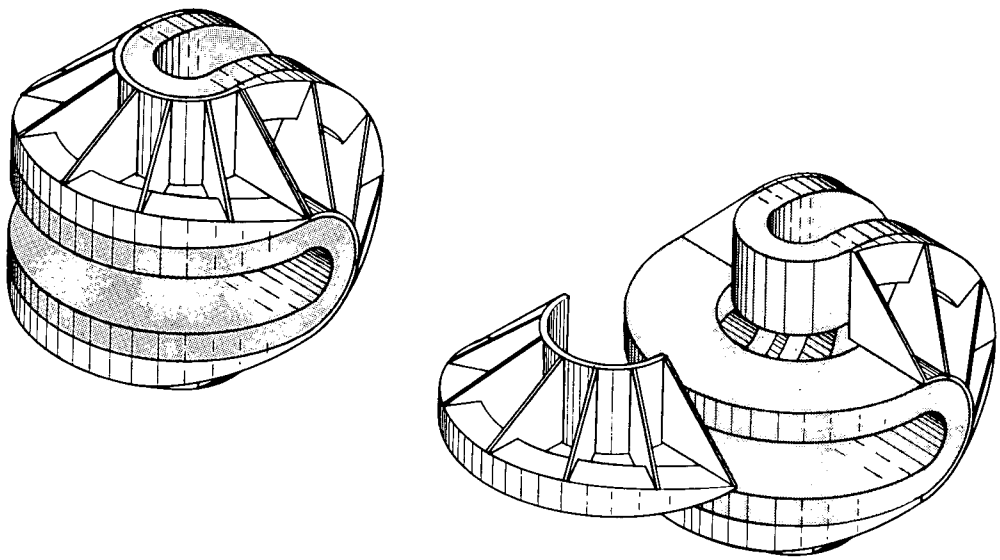

Fig. 3.23. Anchor and plug coil set support structure.

A water-cooled steel neutron shield that protects the end-cell magnets and reduces the refrigeration load is located within the end-cell coil set and surrounds the plasma (Fig. 3.24). It extends from the end of the 18-T coil to the end of the DC coil. The shield is at least 10 cm thick; within the bore of the DC coil, it is 35 cm thick. It is segmented so that it can be removed without disturbing the coil set.

A drift pumping system is located between the T1 and the A1 coils (Fig. 3.26). This system is operated at a center frequency of 70 kHz. The two drift pumping coil subassemblies are located on opposite sides of the plasma. The coil subassembly consists of a pair of water-cooled, hollow copper coils (Fig. 3.27). Their central sections of lead oxide, which are encased in a 1-cm-thick layer of aluminum oxide insulation, can be withdrawn from between the magnets. A similar drift pumping system is located between the A2 and the P1 coils (Fig. 3.28). This system operates at a center frequency of 600 kHz.

An ICRH subsystem is located in the A1 coil area (Fig. 3.26). The launcher array consists of two pairs of loop antennas located on opposite sides of the plasma. The pair toward the machine center operates at a frequency of 50 MHz, and the other pair operates at 25 MHz. The assembly can be withdrawn through its dedicated port on a pair of rails embedded in the lower shield.

At point *a* ($Z = \pm 20.2$ m) and point *b* ($Z = \pm 18.6$ m) ECRH is applied. Point *b* is also the target for the sloshing beams. At point *a*, one ECRH horn operates at a frequency of 56 GHz (Fig. 3.26) at an angle of 90° to the *z*-axis. At point *b*, three horns operate at 56 GHz and three at 35 GHz (Fig. 3.28). Collectively, they are at an angle of 45° to the *z*-axis. Each ECRH launcher consists of a long, cylindrical receptacle

ORNL–DWG 83-4030A FED

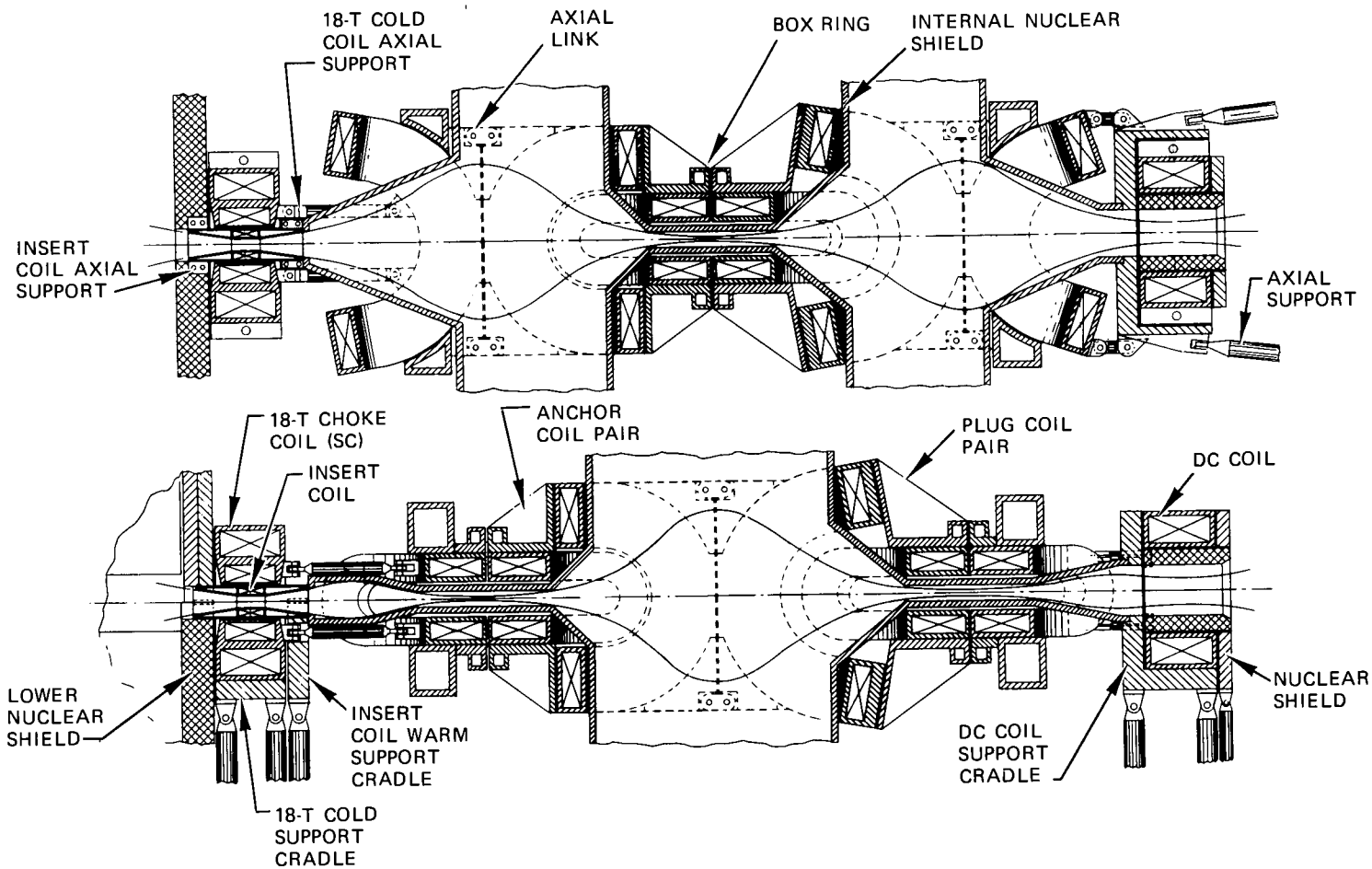

Fig. 3.24. End-cell structural support.

ORNL–DWG 84-3998 FED

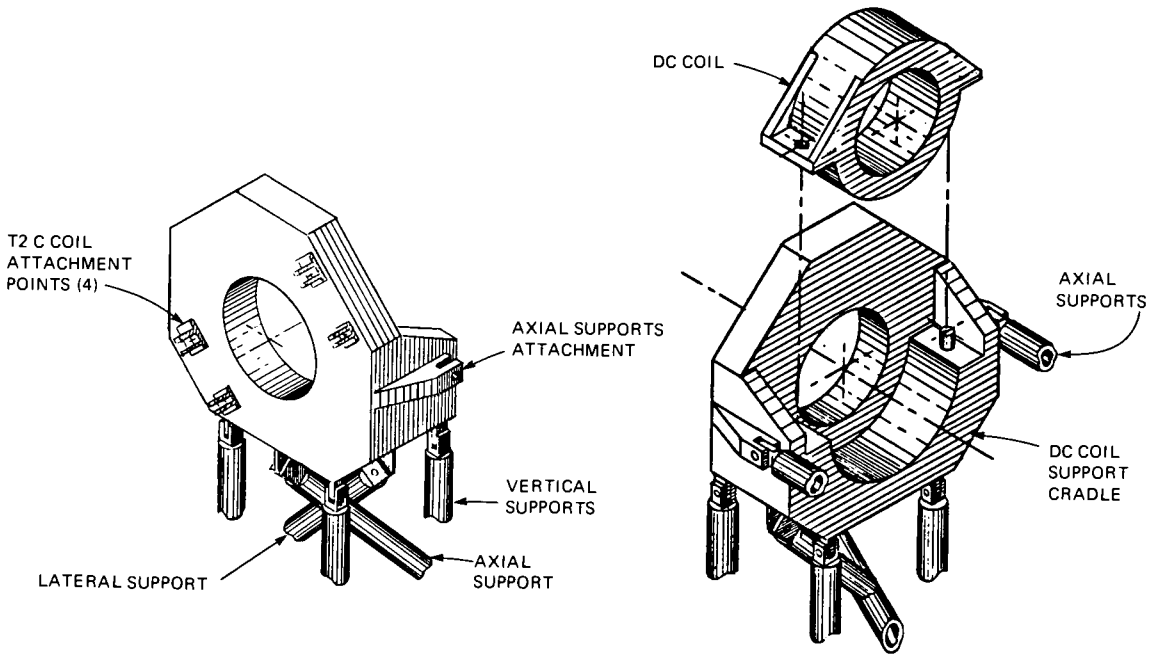

Fig. 3.25. DC coil support cradle.

ORNL–DWG 83-4032A FED

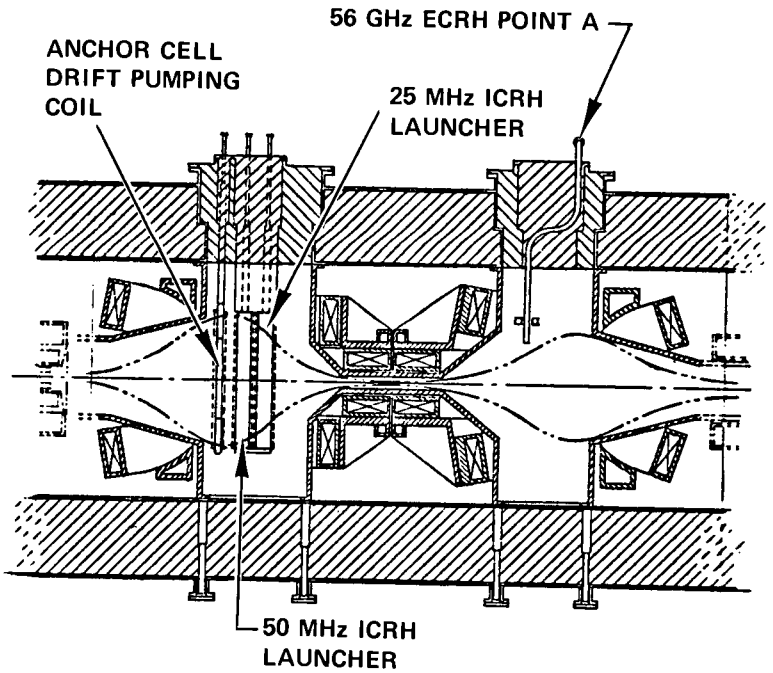

Fig. 3.26. End-cell rf systems.

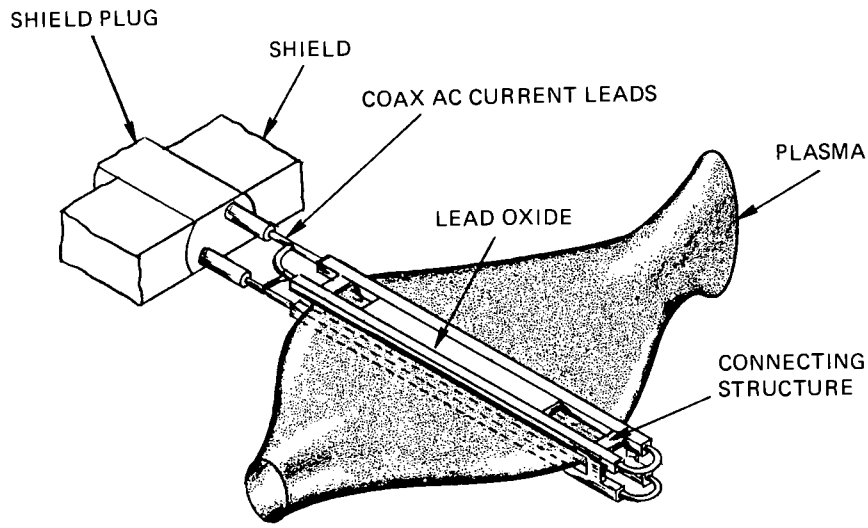

Fig. 3.27. Drift pumping coil installation.

into which the horn subassembly is inserted. An extension of the sloshing-ion beam dump shield encloses the ECRH and drift pumping ports to shield against neutron streaming (Fig. 3.28). Shield plugs are provided for access.

Each end cell has a negative-ion neutral beam injector (NBI) operating at −200 keV (Fig. 3.29). Each injector has four sources that produce 0.5-m-wide ribbon beams (Fig. 3.28). One source is an on-line spare. The sources are mounted in a vacuum enclosure with vacuum gate valves that permit source changeout without loss of primary machine vacuum. Two sources are mounted on the upper surface of the enclosure and two on the lower surface. The sources are located so that their beams feed virtual sources that are 9 m from the plasma centerline. Each beam travels from its source to its virtual source through a transverse-field-focusing (TFF) beam transport system, which causes the negative beam to curve through a radius of 0.5 m. The TFF and lower end of the neutralizer are pumped by cryopanels, which can be vertically removed for servicing.

The sources are far enough apart that they will not arc to each other when one is at 200 keV and the other is at ground. The distance required is reduced by enclosing the pair of sources with a cover filled with SF_6 gas.

A box structure contains the beam line dumps and two continuously pumping cryopumps. The cryopumps are attached to an access cover for removal. The dumps are joined at their ends and attached to a dedicated access cover. The dumps may be removed without disturbing the cryopumps. The cryopumps are removed with the dump assembly. The beam line is enclosed by a concrete nuclear shield lined with ferritic iron. This lining acts as a magnetic shield and ends on either side of the end of the neutralizer, so that the charged part of the beam curves into the dumps. Shield plugs in the enclosure permit servicing of the beam line. A rolling shield door allows the two lower sources to be serviced by specialized remote equipment.

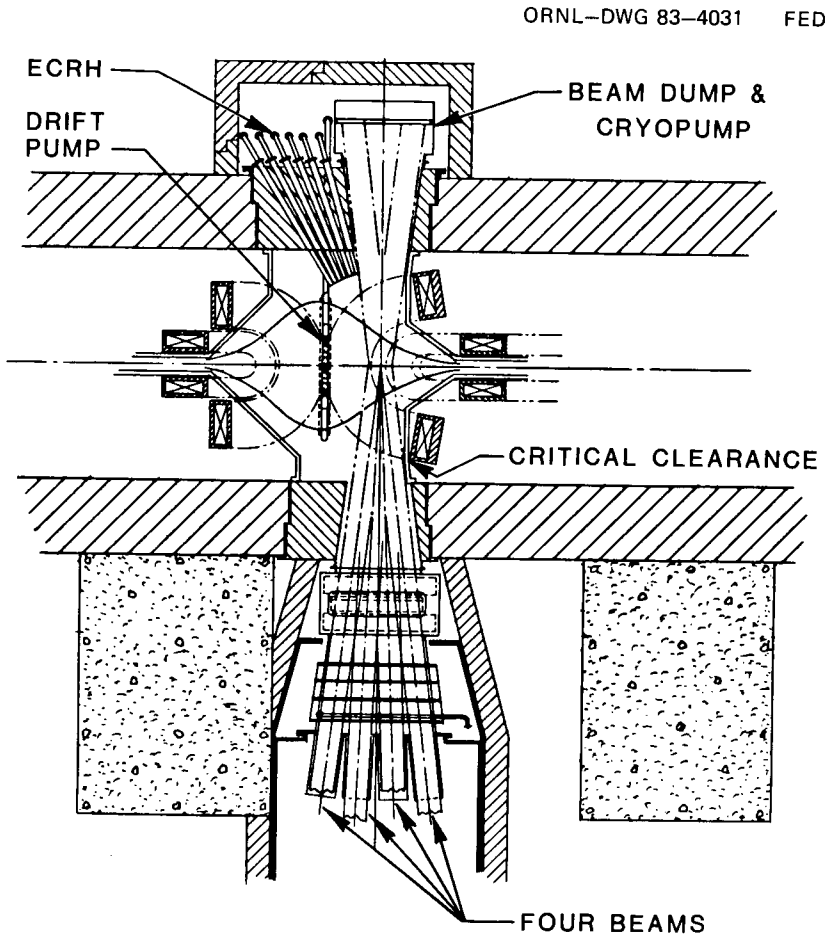

Fig. 3.28. End-cell drift pumping and negative-ion neutral beam injection systems.

The halo scraper assembly is positioned near the end of the end cell just after the DC coil (Fig. 3.22) with its leading edge at $Z = \pm 27$ m. The halo scraper intercepts and pumps away the cold outer halo plasma and intercepts the drift-pumped ions that form the inner halo. Ions entering the halo scraper and striking the outer halo plate are pumped by a pair of turbomolecular pumps. The halo scraper, including its inner halo plate, is expected to be a lifetime component. However, the halo scraper connections are designed for remote disassembly in the hot cell, where a new inner halo plate assembly can be installed if necessary.

The DC system has a center collector plate located at $Z = \pm 30.0$ m and an outer collector plate located at $Z = \pm 29.5$ m. The center collector plate is a water-cooled copper plate maintained at the desired potential. The outer collector plate, also a water-cooled copper plate, is washer shaped and overlaps the edge of the inner collector plate to ensure interception of the incoming ions and electrons. It is maintained at a potential between that of the inner collector and the ground potential of the halo scraper. The distances between the halo scraper, the outer collector, and the inner collector were chosen to prevent arcing. The DC collector module is considered a lifetime component but can be

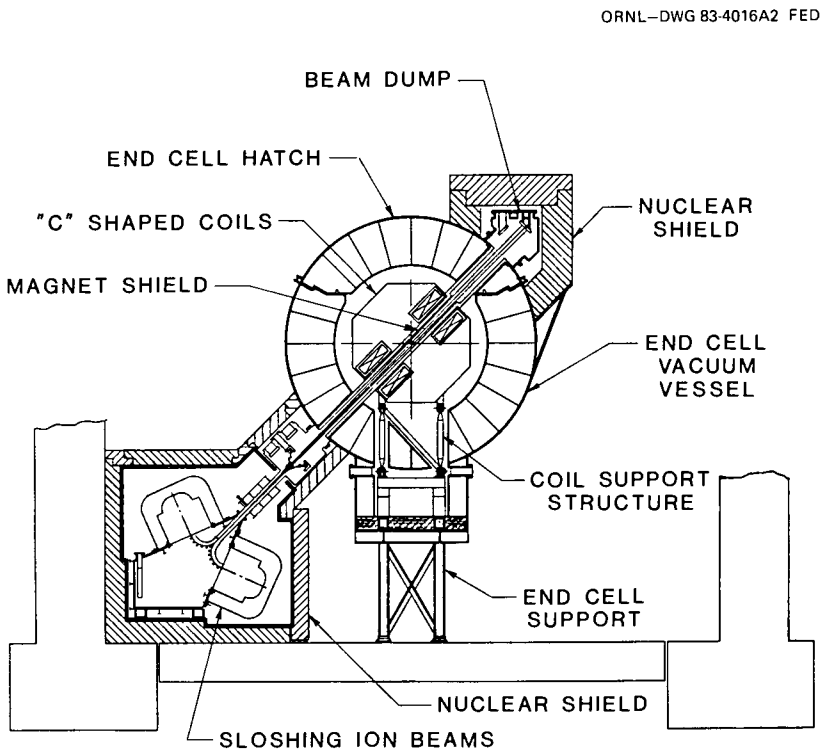

Fig. 3.29. Sloshing-ion beam configuration.

replaced if necessary. The shield within the access cover is also designed to be removable. This feature is used during initial assembly for access to the end-cell coil set drag struts and would be used during decommissioning. It also allows repositioning and replacement of the halo scraper and the DC modules by updated designs, should this prove desirable.

3.5 FUTURE WORK

The current MFTF-α+T configuration is a feasible design that satisfies the program objectives and design criteria. Some future work will be directed toward resolving the issues in areas considered important to the device design. These areas are (1) relationship of the sloshing beam and the plug coil throat size, (2) nuclear shielding thickness required to protect the plug coil at the sloshing beam, (3) design of the 18-T choke coil set, (4) structural analysis of the anchor and plug coil sets, (5) development of representative blanket test modules and their interface with the machine, (6) refined analysis of drift pumping and plasma parameters in the radial direction, and (7) further development of the startup scenario and incorporation of the required startup subsystems in the configuration.

REFERENCE

1. *Mirror Advanced Reactor Study—Interim Report*, UCID-53333, Univ. California, Lawrence Livermore Natl. Lab., Livermore, Calif., 1983.

4. MAGNET SYSTEMS

S. S. Kalsi
V. C. Srivastava
B. L. Hunter
J. A. O'Toole

Fusion Engineering Design Center

J. Schultz

Massachusetts Institute of Technology

CONTENTS

4.1 DESIGN REQUIREMENTS 4-3
4.1.1 Functional Requirements 4-3
4.1.2 Design Criteria 4-4
4.1.3 Neutronic Environment 4-6
4.1.4 Seismic Loading 4-6
4.2 SYSTEM DESCRIPTION 4-7
4.2.1 Magnetic Fields 4-7
4.2.2 Magnetic Forces During Normal Operation 4-11
4.2.3 Magnetic Forces During Off-Normal Operation 4-14
4.3 COMPONENT DESIGN DESCRIPTIONS 4-22
4.3.1 D-T Axicell Coils 4-22
4.3.2 Central-Cell Solenoid Coils 4-31
4.3.3 Superconducting Background Portion of 18-T Choke Coil 4-34
4.3.4 Resistive Insert Portion of 18-T Choke Coil 4-43
4.3.5 End-Cell C Coils 4-45
4.3.6 Direct Converter Coils 4-53
4.3.7 Coil Supports 4-56
4.8.3 LN_2-Cooled Cold Shield 4-65
4.4 CRYOGENIC SYSTEM 4-65
4.4.1 Summary of Cryogenic Loads 4-65
4.4.2 Refrigeration Configuration 4-67
4.5 TRADE STUDIES 4-68
4.5.1 D-T Axicell Configuration 4-68
4.5.2 Central-Cell Configuration 4-72
4.5.3 C Coil Operating Current 4-73
4.5.4 Helium Vapor Clearing 4-74
4.5.5 End-Cell Magnet Shield Thickness 4-75
4.5.6 Resistive Insert for 18-T Choke Coil 4-78
4.5.7 End-Cell Anchor and Plug Coil Support System 4-84
REFERENCES 4-91

4. MAGNET SYSTEMS

The MFTF-α+T magnet systems include a deuterium-tritium (D-T) axicell at the center of the machine; end plugs at each end to plug the machine and provide magnetohydrodynamic (MHD) stability; and a central cell, which provides a transition between the axicell and the end plugs. These systems must provide the field on axis required to achieve the optimum plasma performance.

The design requirements are described in detail in Sect. 4.1. Section 4.2 describes the development of a magnet system to meet these requirements. Design descriptions of system components are presented in Sect. 4.3, and the cryogenic system is discussed in Sect. 4.4. Trade studies performed during the design effort are described in Sect. 4.5.

4.1 DESIGN REQUIREMENTS

The magnet system must be sized and arranged to provide the field on axis required to achieve optimum plasma performance. The resulting field-on-axis profile must be evaluated and adjusted as necessary to ensure MHD stability. The system arrangement must be compatible with a variety of access and clearance constraints. The magnetic forces (in normal and fault modes), deadweight, and seismic loads of the system must be supported for the life of the device. The magnets must be adequately cooled and ventilated to ensure cryostable operation. The cryogenic system must provide cryogenic coolants [liquid helium (LHe) and liquid nitrogen (LN_2)] at required temperatures and rates not only for the magnets, but also for other components.

4.1.1 Functional Requirements

Field on axis

The desired field characteristics along the axis of the machine are illustrated in Fig. 4.1. Significant requirements are a field of 4.5 T in the test space ($Z = 0$ m) to provide the desired neutron generating capability; a 12-T choke field at the ends of the axicell ($Z \pm 2.0$ m) for ion confinement; a field dip in the central cell to no less than 2 T (i.e., the same as the minimum end-plugging field); an 18-T choke field at the ends of the central cell for particle confinement; and end plugs with a peak field of 5 T and a mirror ratio of about 2.5:1 to provide the thermal barrier function. In addition, the field on axis must be verified to provide MHD stability. A further requirement related to field is a circular plasma leaving the end plug regions for compatibility with a circular direct converter.

Access and clearance requirements

The magnets must be sized and located to accommodate several arrangement constraints. These include access for heating [neutral beams and electron-cyclotron resonance heating (ECRH) horns]; access to the test space; and sufficient clear bore to accommodate the plasma, including the plasma halo, with space for magnet shielding.

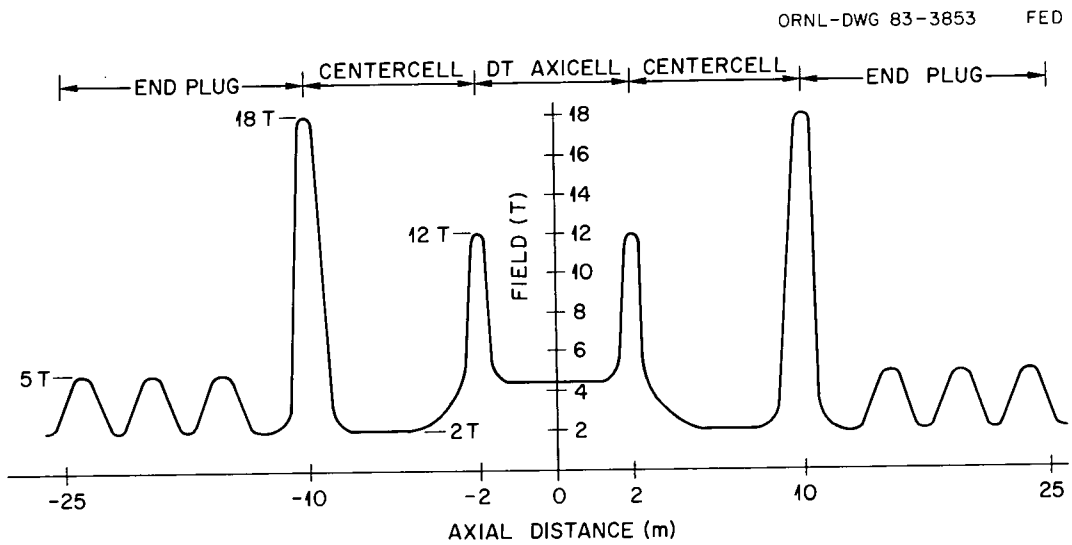

Fig. 4.1. Desired field on axis.

Design life and number of cycles

The machine is being designed for ten years of operation at a 10% duty factor. The resistive magnets are designed for 12,000 energization-deenergization cycles (maximum of 100 shots per month). The superconducting magnets are designed to withstand 120 cycles of cooldown, energization, deenergization, and warmup and 11,880 cycles of energization and deenergization during which the magnets are kept cold.

Maintainability

The superconducting magnets are designed to last for the device lifetime. However, they must be designed and supported so that they could be replaced if necessary. The normal water-cooled coils may have shorter lifetimes and must be designed to be replaceable.

4.1.2 Design Criteria

Superconducting coils

Cryostability of conductor and winding. All of the superconducting coils are designed to be cryostable. A static stability analysis is performed and an operating current is selected to ensure that the surface flux required to remove the heat deposited in a short normal zone is no more than 80% of the critical recovery heat flux. The heat deposited includes neutronic heating, resistive heating, and heat conducted from the coil case. The operating current must be ≤80% of the conductor critical current when the conductor is energized along the magnet load line. Finally, the vapor content of the helium exiting the superconducting magnets is limited to 10% by volume, which is consistent with Lawrence Livermore National Laboratory (LLNL) design practice on the magnets for the Mirror Fusion Test Facility (MFTF-B).

Allowable stress. For this design, type 316 LN stainless steel was selected for the coil cases. Limits are placed on primary stresses (those necessary to equilibrate applied mechanical loads, which do not include the effects of structural discontinuities or stress concentrations) to prevent gross distortion or burst-type ductile fracture and on peak tensile stress to prevent brittle fracture or fracture due to crack growth.

1. Primary stress limits: Limits are stated in terms of the primary membrane stress intensity S_m, defined as 0.66 times the yield stress (0.2% offset) or 0.33 times the ultimate stress (measured in uniaxial tension or compression tests at room temperature), whichever is less. For type 316 LN stainless steel at 4.2 K, $S_m = 460$ MPa; for copper stabilizer at 4.2 K, $S_m = 160$ MPa. Under normal operating conditions [those arising as the plant fulfills its function or those expected to occur, although not by design (e.g., quench)] the limits provide a safety factor of 1.5 against yielding of a section and a safety factor of 3 against rupture:

- primary membrane stress intensity $\leqslant S_m$,
- primary membrane-plus-bending stress intensity $\leqslant 1.5S_m$,
- average shear stress $\leqslant 0.6S_m$.

Under abnormal operating conditions (e.g., loads due to off-normal coil currents, seismic loads), the limits provide a safety factor of 1.0 against yielding of a section and a safety factor of 2.0 against rupture; each of the limits for normal operating conditions is divided by 1.5.

2. Fatigue and fracture mechanics limits: The allowable peak tensile stress is derived from the Paris crack growth law and from fundamental fracture mechanics principles. For type 316 LN stainless steel, a fully cyclic load, and 12,000 load cycles, the allowable stress is 370 MPa. This limit incorporates a safety factor of 3 on stress.

Additional limits. The maximum allowable discharge voltage for superconducting coils is 1000 V. The maximum allowable hot-spot temperature rise in their windings is 200 K.

Resistive coils

Both water and LN_2 have been considered as coolants for the copper coils. The coil cases are made of A286. The structural design of the resistive coils is in accordance with the criteria for the superconducting coils. Primary stress limits are expressed in terms of the 0.2% offset yield strength and the ultimate strength of the material at operating temperature, as they are for the superconducting coils.

Companion structural criteria that address potential failure due to cyclic crack growth and brittle fracture are based on empirical crack growth data (da/dN vs ΔK) supplied by testing organizations such as the National Bureau of Standards. While some data on da/dN are available for A286 at 4 K, none were available for A286 at room temperature or higher, and none at all were available for copper. Consequently, a limit on peak tensile stress was derived from the limited available fatigue data (stress range vs cycles to failure). A safety factor of about 8 was introduced by using the failure stress at 100,000 cycles as the limiting peak tensile stress (the coils are expected to go through 12,000 load cycles). The value thus obtained for A286 at 80 K was in good agreement with the value obtained from the crack growth–fracture formalism using data for A286 at 4 K.

4.1.3 Neutronic Environment

In contrast to previous tandem mirror machines, MFTF-α+T will experience a significant radiation environment. The magnets must be shielded as necessary to meet the established limits described here.

Integrated dose

The central-cell solenoids, the direct converter (DC) coils, and the outer sections of the central-cell choke coils are all existing MFTF-B coils with G-10 epoxy insulation. The maximum integrated dose to these coils is 1×10^8 rad, which is the upper limit for epoxy insulation.

The new superconducting coils can be designed to use polyimide insulation. The upper limit for this material is 1×10^{10} rad.

The maximum integrated dose for resistive coils with ceramic insulation is 1×10^{12} rad. Tests at the Massachusetts Institute of Technology (MIT) have shown that polyimide insulation can withstand this dose if the insulator is used in the compression mode.

Damage to copper stabilizer

The maximum allowable damage to copper in the superconducting coils is 1.1×10^{-4} dpa. This amount of radiation damage will result in a resistivity increase of about 25%. This damage limit may be achieved by shielding or by a combination of shielding and periodic annealing of the magnets. If the superconducting magnets are warmed up each time the test module is replaced (which is the approach currently under consideration), then this limit may not apply.

Neutronic heating

Neutronic heating in the superconducting magnets affects performance and is an important cost consideration, since it is heat that must be removed at 4 K. Heat deposited in the resistive coils is of much less concern; it does not affect performance, and the cost of removing this heat (via the plant process water system) is not a major consideration.

Superconducting coils. During normal operation, the percentage (by volume) of helium that leaves the coil as vapor depends on the integrated heat load in the coil. Table 4.1 shows peak neutronic heating and integrated heat loads in the three magnet systems. These loads can be handled by forced helium circulation through the windings.

Normal coils. The copper coils for the 12-T and 18-T choke coils are designed to operate with coil cases ~1 cm thick but without additional shielding. The magnet cooling systems must be designed to handle Joule and nuclear heating loads. Nuclear heating loads for the axicell 12-T choke coils are ~270 kW; for the central-cell 18-T choke coils, ~400 kW.

4.1.4 Seismic Loading

The natural frequencies of the massive structures characteristic of fusion plants are typically in the peak response portion of the design response spectra for seismic loads (i.e.,

Table 4.1. Neutronic heating in MFTF-α+T

Location	Peak heating, mW/cm^3	Total integrated heat load, kW
Axicell	1.0	
Central cell	1.0	0.3
End cell	18	2.6

1 to 10 cps). Consequently, magnet supports are sized for the peak amplification of 4 associated with the 2% structural damping characteristic of welded structures. Ground motion acceleration is specified to be 0.5 g for MFTF-α+T and, multiplying by 4, we use 2 g laterally and vertically as the equivalent static load.

4.2 SYSTEM DESCRIPTION

The MFTF-α+T magnet system is shown in Fig. 4.2, which also identifies the MFTF-B magnets to be used on the new device. Coil locations and currents are listed in Table 4.2. This system satisfies the functional requirements described in Sect. 4.1 (i.e., field on axis and clear bore for plasma and shielding).

4.2.1 Magnetic Fields

In addition to the field on axis, the maximum fields in the magnets themselves (Table 4.3) and the stray fields in various locations (e.g., at the neutral-beam sources) (Fig. 4.3) are important, because they affect the detailed design of the system components. The EFFI computer program has been used to calculate the magnetic fields, with the coils modeled as a series of circular arcs with finite, uniform current density.

The field on axis is plotted in Fig. 4.4. Comparison with Fig. 4.1 shows that the desired field will be achieved. Calculations by R. Bulmer of LLNL using the TABASCO computer code with the baseline MFTF-α+T field-on-axis profile have verified MHD stability.

Figure 4.5 shows projections of the plasma and the plasma halo in the x-y and x-z planes. The edges of the hot plasma and of the plasma halo are defined by the flux bundles at radii of 15.0 cm and 21.6 cm, respectively, in the center the machine ($Z = 0$).

The central-cell superconducting coils (CS1) are sized to accommodate about 100 cm of shielding between the coils and the plasma. At the 12-T choke coil (CC1), the halo is pinched to a radius of 13.1 cm, which determines the clear bore required for this coil. At the 18-T choke coil (CC2), the halo is pinched to a 10.6-cm radius. The central-cell solenoid coils (S1 through S5) accommodate 165 cm of steel and concrete shielding between the magnets and the plasma. The end-cell C coils (T1, T2, P1, P2, A1, and A2) accommodate a 10-cm-thick stainless-steel shield between the magnets and the plasma.

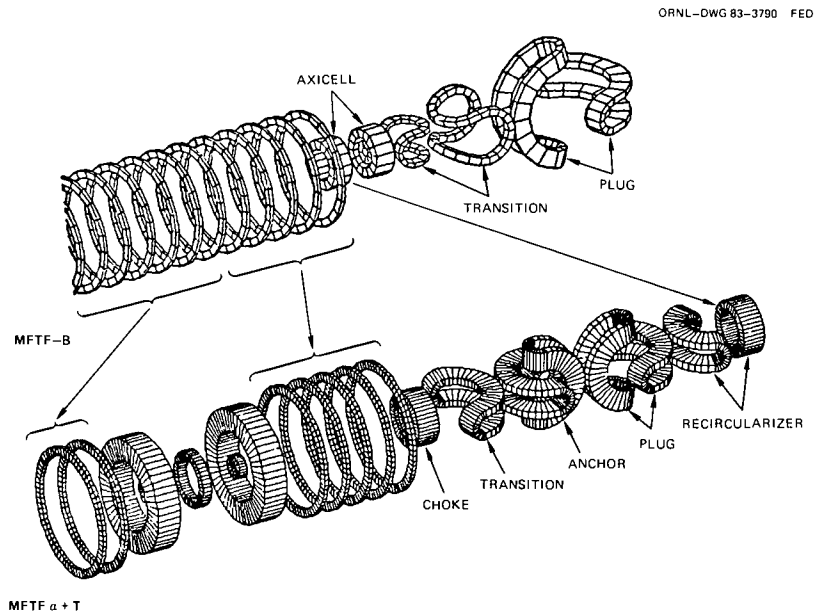

Fig. 4.2. MFTF-α+T magnet system.

Table 4.2. Coil parameters

Coil	Axial location Z, m	Diameter (solenoids) or major/minor radius (C coils), m	Sweep angle, deg	Coil current, MA·turns	Winding dimensions $W1/W2$,[a] m	Operating current, kA	Winding current density, A/cm^2
CC1	±2.0	0.64		2.83	0.4/0.34	130.0	2140
CC2	±10.0	2.9		18.6	1.4/0.61	25.0	2160
		1.5		10.7	1.2/0.45	20.5	1980
		0.5		2.3	0.8/0.30	57.5	960
CS0	0.0	2.0		1.7	0.4/0.3	77.0	1417
CS1	±2.4	3.8		19.8	0.9/1.0	18.50	2200
S1	±4.5	5.0		1.64	0.163/0.336	2.73	2994
S2	±5.5	5.0		1.64	0.163/0.336	2.73	2994
S3	±6.5	5.0		1.64	0.163/0.336	2.73	2994
S4	±7.5	5.0		1.64	0.163/0.336	2.73	2994
S5	±8.5	5.0		1.64	0.163/0.336	2.73	2994
T1	±11.811	1.5/0.5	80	5.6	0.869/0.298	5.0	2162
A1	±15.611	1.3/0.5	90	5.6	0.869/0.298	5.0	2162
A2	±15.611	1.3/0.5	90	5.6	0.869/0.298	5.0	2162
P1	±19.411	1.5/0.5	80	5.6	0.869/0.298	5.0	2162
P2	±19.411	1.5/0.5	80	5.6	0.869/0.298	5.0	2162
T2	±23.211	1.3/0.5	71	5.6	0.869/0.298	5.0	2162
DC	±24.711	1.856		7.0	0.94/0.41	3.41	1785

[a]Winding dimensions are defined as follows:

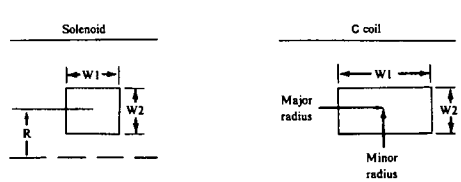

Table 4.3. Maximum magnetic fields

Coil	B_{max}, T	Radius R, m	Axial location Z, m
CC1	12.4	0.15	2.0
CC2	18.5	0.10	10.0
CS0	5.4	0.85	0.0
CS1	10.8	1.45	2.4
S1	3.2	2.3	4.5
S2	3.1	2.3	5.5
S3	3.0	2.3	6.5
S4	2.9	2.3	7.5
S5	2.7	2.3	8.5
T1	6.0	1.4	11.7
A1	5.7	1.1	16.0
A2	5.8	1.2	15.3
P1	6.0	1.5	19.5
P2	6.0	1.4	19.3
T2	5.8	1.1	23.2
DC	6.1	0.72	24.7

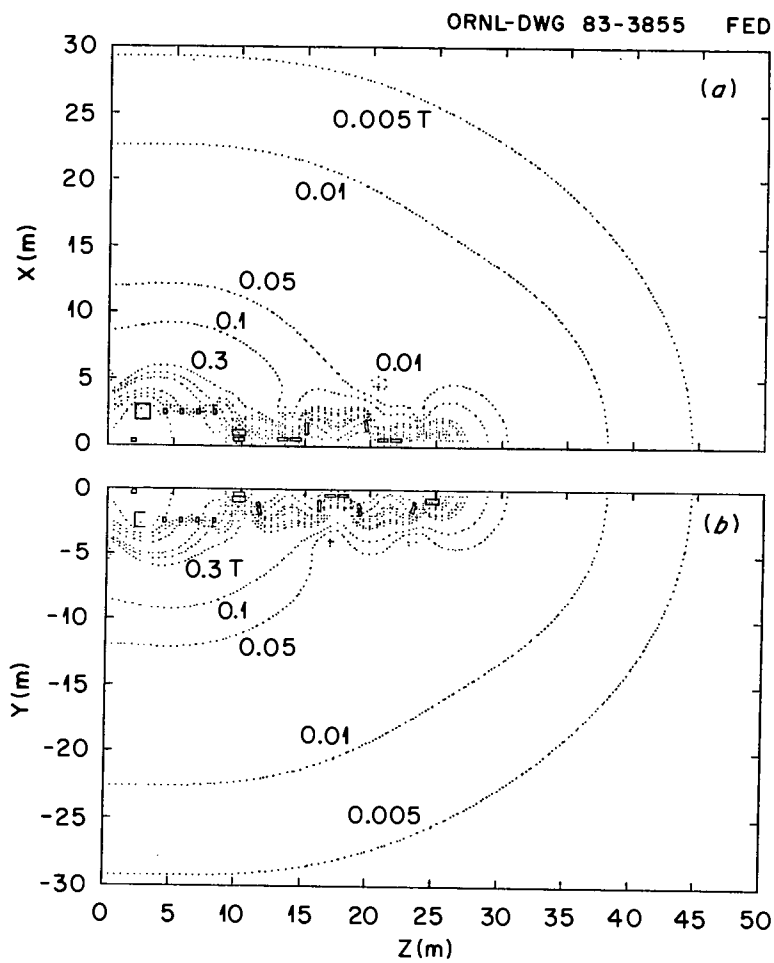

Fig. 4.3. External fields (a) in x-z plane and (b) in y-z plane.

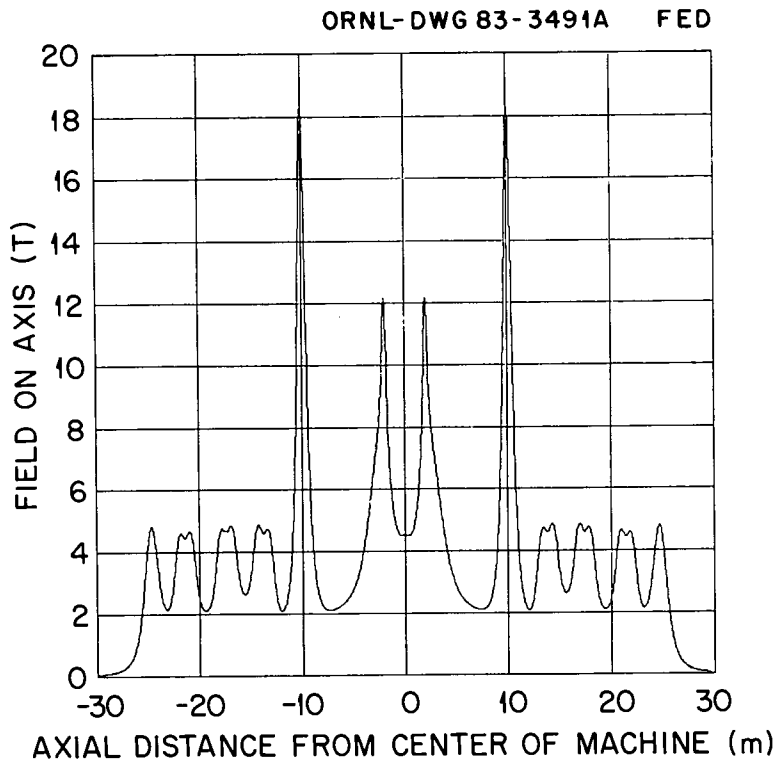

Fig. 4.4. Axial field profile for MFTF-α+T.

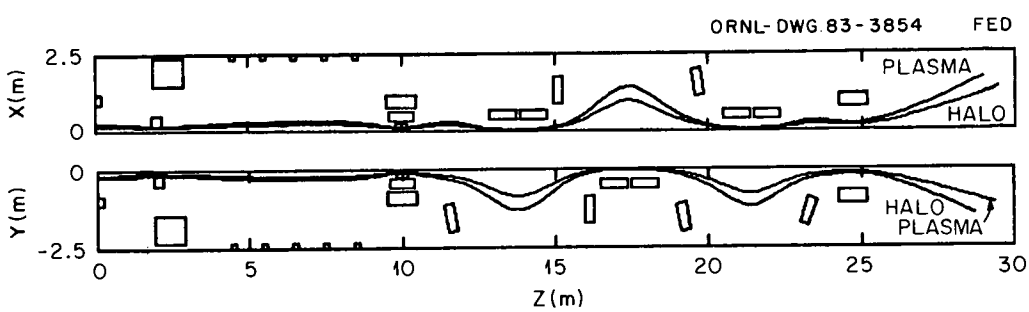

Fig. 4.5. Plasma and plasma halo boundaries in the x-z (θ = 0°) and y-z (θ = 90°) planes.

The function of the DC coils is closely related to the plasma halo. Without the DC coil, the second transition coil (T2) "overcircularizes" the plasma; that is, the elliptical plasma fan leaving the mouth of the second plug coil (P2) is reshaped by the T2 coil so that it is slightly elliptical in the other direction. The DC coil recircularizes the plasma and projects a nearly circular cross section onto the DC plate.

4.2.2 Magnetic Forces During Normal Operation

The EFFI computer program was used to calculate the magnetic forces on the coils. Results of this computation are presented for three categories of loading:

- running loads (rated force per unit length both in and out of the plane of circular coil segments), which are used to calculate winding stresses;
- resulting axial loads on each coil, which are used for sizing cold mass supports for all coils and for sizing the structural cases of the axicell and central-cell solenoid coils;
- resulting lobe forces and maximum lobe bending moments on C coils, which are important in sizing the structural cases for these coils.

Running loads

The interaction of the coil current and the local magnetic field produces running loads (force per unit length) on every circular coil arc. The running load on an arc may be decomposed into an in-plane and an out-of-plane component. A typical solenoid and a typical C coil are shown in Fig. 4.6, indicating the positive sense of the in-plane and out-of-plane running loads, f_i and f_o. The positive sense of the in-plane load is in a direction to dilate the arc. The out-of-plane load on a solenoid is positive in the positive z-direction, and on a C coil the out-of-plane load is considered positive if it acts in a direction to cause spreading of the lobe on which it acts.

The maximum values of the in-plane and out-of-plane running loads on each solenoid and on the major lobe (the lobe having the major radius as radius of curvature) and minor lobe of each C coil are given in Table 4.4.

Axial forces

Because of the inherent symmetry in the MFTF-α+T machine, the integral of the magnetic running loads f_i and f_o over any coil is statically equivalent to an axial force F_z. The resultant axial force on each coil is given in Table 4.4.

C coil lobe forces and bending moments

The integral of the running loads acting on any half of a C coil produces forces in two of the three principal directions of the C coil. For example, the action of the running loads f_o and f_i on the upper half of the C coils in Fig. 4.6b produces forces in the x- and z-directions. (The net force in the y-direction on the upper half of the coil will be zero because of symmetry.) The force in the x-direction acts to spread the major lobes. Similarly, when the right-hand half of the C coil is considered, a minor lobe spreading force can be calculated. The C coil major and minor lobe spreading forces are given in Table 4.5.

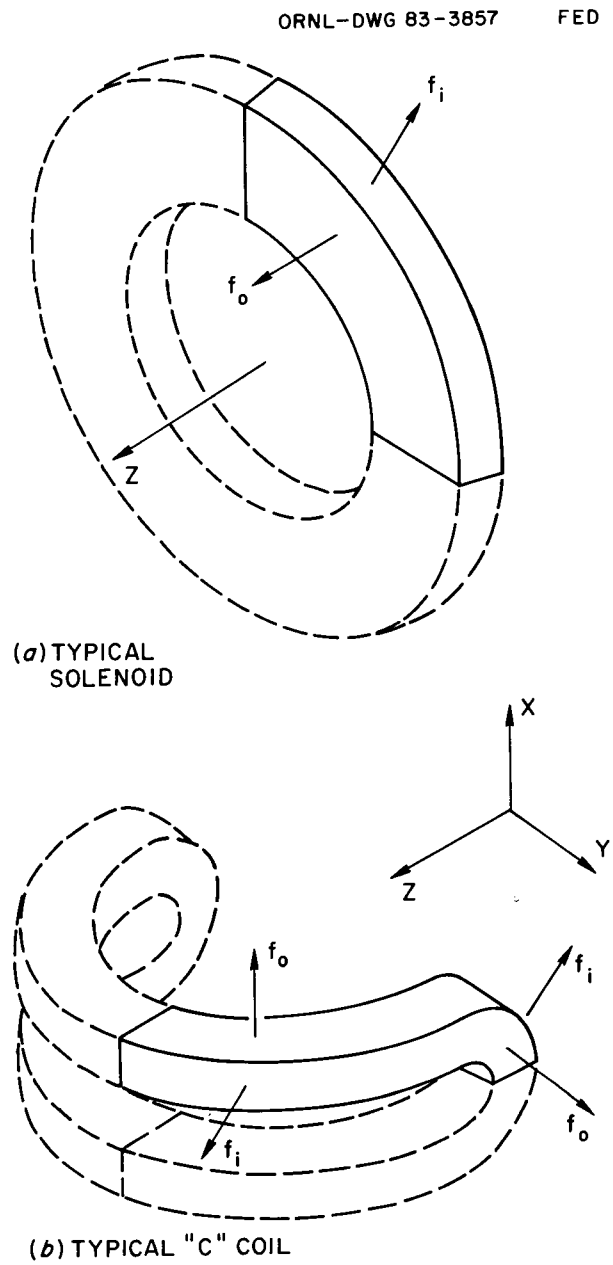

Fig. 4.6. Running loads in (a) a typical solenoid and (b) a typical C coil.

The critical locations for bending stress are the centers of the major and minor lobes. For example, the major lobe spreading forces produce bending moments that are maximum on a section through the centers of the minor lobes, as shown in Fig. 4.7. The bending moments in the centers of the C coil major and minor lobes due to the magnetic running loads are given in Table 4.5.

Table 4.4. Coil running loads and axial forces under normal operating conditions

Coil	Maximum running load, MN/m		Axial force, MN
	In-plane	Out-of-plane	
CC1	24.34	0.8536	1.716
CC2-A	22.80	−0.7192	−3.965
CC2-B	82.35	−0.2859	−0.764
CC2-C	20.98	−0.01759	−0.0183
CS0	5.848	0	0
CS1	64.23	0.2213	2.629
S1	1.887	−0.7480	−11.75
S2	1.872	−0.4457	−6.994
S3	1.740	−0.3044	−4.770
S4	1.560	−0.3006	−4.701
S5	1.233	−0.5820	−9.099
T1	5.670/11.48[a]	10.06/4.028[a]	3.018
A1	5.783/13.29	11.18/2.280	4.486
A2	5.808/13.332	11.14/2.344	−4.544
P1	5.594/11.31	10.30/2.077	−1.943
P2	5.435/11.44	9.899/2.048	1.013
T2	6.033/11.13	9.660/3.016	−3.741
DC	22.03	−1.260	−6.968

[a]Major lobe/minor lobe.

Table 4.5. C coil stress due to magnetic running loads

Coil	Lobe spreading forces, MN		Lobe bending moments, MN·m	
	Major lobe	Minor lobe	Center of major lobe	Center of minor lobe
T1	46.4	13.1	10.1	0.4
A1	52.4	10.0	8.0	−2.6
A2	52.5	10.0	1.4	−5.0
P1	47.8	11.36	1.7	−12.4
P2	47.4	11.1	10.1	0.4
T2	37.5	12.8	5.5	−2.2

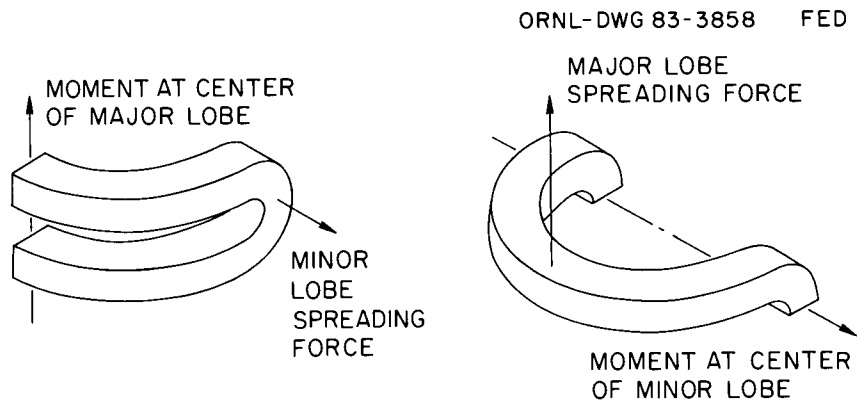

Fig. 4.7. Bending moments and spreading forces in the C coils.

4.2.3 Magnetic Forces During Off-Normal Operation

(Early in 1983, before MFTF-α+T was identified, plans were made to determine peak loads in the magnets of mirror machines. The peak loads were to be identified by exciting all the coils under normal operating conditions and by exciting them discretely, as may be required during startup and shakedown of a device. Since this analysis involved a number of time-consuming calculations, it was decided to study the MFTF-B+T option. After MFTF-α+T was identified, it was decided not to modify the guidelines for this study because the study's objective was to develop a methodology. This methodology will be applied to MFTF-α+T as the system design progresses.)

Magnet systems consisting of multiple inductively coupled coils can experience substantial changes in their usual operating load patterns in the event of a fault condition (such as a short circuit) followed by a rapid system discharge. The methods for determining the load changes are straightforward but time-consuming, and the number of cases that must be considered grows as the number of coils and circuits in a system increases. Efficient codes have been devised for studying this problem, and a format for presenting a large number of cases has been developed. The codes were developed using the coil system of the MFTF-B+T device, which has 24 coils connected in 9 circuits (Fig. 4.8). Results[1] are discussed in this section and are indicative of the types of load changes that can occur in MFTF-α+T.

Definition of off-normal conditions

Estimating the severity of a fault condition requires a well-defined set of usual operating conditions for comparison. The latter is defined here as the extreme maximum or minimum values of the selected critical parameters for any combination of circuits in a fully "on" or "off" condition. Thus, this definition includes any possible scenario for the entire system or partial system at full operating current as a "usual" condition.

Figure 4.8 shows the MFTF-B+T 24-coil set, which includes 2 large central solenoids, 2 high-field choke coils, and 12 identical solenoids in the central cell. Each of

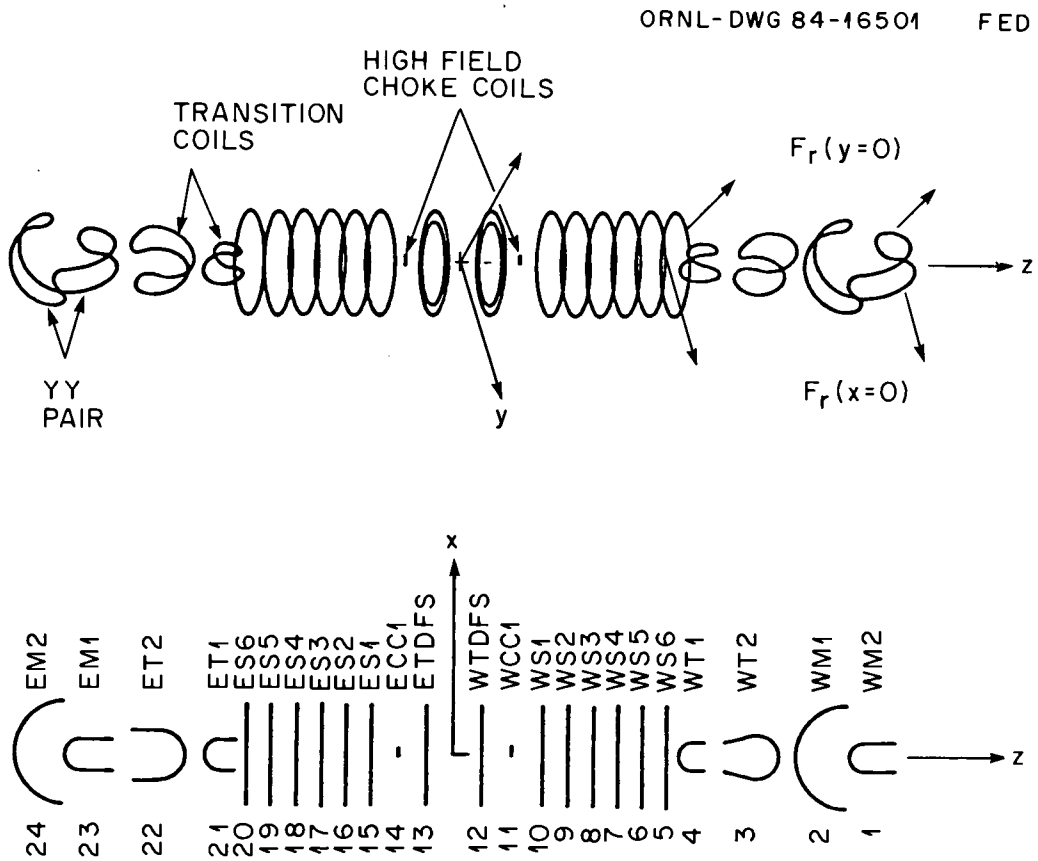

Fig. 4.8. MFTF-B+T coil centerlines, numbers, and nomenclature.

the machine ends has four coils; two transition coils and a yin-yang pair. The coils are numbered consecutively from the coil with the largest positive axial (z) coordinate (coil 1) to the one with the largest negative coordinate (coil 24). Table 4.6 lists the coils by number, name, circuit number, and operating current. The circuit numbering is arbitrary, but each of the four yin-yang coils is in an independent circuit, whereas similar coils are in series in the same circuit. Results may change considerably for different current levels or circuit configurations.

In itself, the magnetostatic analysis is nontrivial in a complex system. For example, for the 9 circuits in MFTF-B+T, there are 512 (2^9) usual operating conditions. It should be emphasized that these represent feasible conditions, since it is conceivable that any combination of circuits could be fully charged during shakedown tests or system operation.

Table 4.7 summarizes the peak values of the net axial force that can act on each coil from all of the possible normal operating conditions. The largest positive and negative loads are given, along with the current scenarios that produce these forces. Except for the two end coils, the worst-case loadings do not occur when all coils are at full operating

Table 4.6. MFTF-B+T coil and circuit numbering and nomenclature

Coil number	Coil name	Circuit number	Operating current, A
1	WM2	1	4,403
2	WM1	2	3,872
3	WT2	3	5,206
4	WT1	4	2,328
5	WS6	5	1,823
6	WS5	5	1,823
7	WS4	5	1,823
8	WS3	5	1,823
9	WS2	5	1,823
10	WS1	5	1,823
11	WCC1	6	107,190
12	WTDFS2	7	8,000
13	ETDFS2	7	8,000
14	ECC1	6	107,190
15	ES1	5	1,823
16	ES2	5	1,823
17	ES3	5	1,823
18	ES4	5	1,823
19	ES5	5	1,823
20	ES6	5	1,823
21	ET1	4	2,328
22	ET2	3	5,206
23	EM1	8	3,872
24	EM2	9	4,403

Table 4.7. Peak axial loads under normal operating conditions

Coil number	Coil name	Peak positive load, MN	Current scenario[a]	Peak negative load, MN	Current scenario[a]
1	WM2	0		−5.27	111111111
2	WM1	4.75	110000000	−5.02	011111111
3	WT2	4.96	111000000	−1.51	001111111
4	WT1	1.04	111100000	−0.48	000111111
5	WS6	0		−4.44	000011111
6	WS5	0		−2.17	000011111
7	WS4	0		−1.63	000011111
8	WS3	0.43	111110000	−1.84	000011111
9	WS2	1.41	111110000	−2.80	000011111
10	WS1	3.91	111110000	−4.82	000011111
11	WCC1	0.21	111111000	−1.68	000001111
12	WTDFS2	0		−102.00	000000111
13	ETDFS2	102.0	110000100	0	
14	ECC1	1.68	110001100	−0.21	001111011
15	ES1	4.82	110011100	−3.91	001110011
16	ES2	2.80	110011100	−1.41	001110011
17	ES3	1.84	110011100	−0.43	001110011
18	ES4	1.63	110011100	0	
19	ES5	2.17	110011100	0	
20	ES6	4.44	110011100	0	
21	ET1	0.48	110111100	−1.04	001100011
22	ET2	1.51	111111100	−4.96	001000011
23	EM1	5.02	111111110	−4.75	000000011
24	EM2	5.27	111111111	0	

[a]Each digit represents a circuit on (1) or off (0). For example, 110011100 means circuits 1, 2, 5, 6, and 7 are on and circuits 3, 4, 8, and 9 are off.

current. Similarly, none of the cases of a single circuit on (all others off) generates maximum or minimum forces. In general, the worst-case loading occurs when as many coils as possible to one side of the coil under consideration have zero current and as many as possible on the other side have full current. Because of the connection symmetry of most circuits, the worst-case load does not correspond to all coils on one side on and all coils on the other side off.

Forces are listed as 0 when no scenario gives a significant force of that sign on that coil. For example, WS6 (coil 5) has a zero maximum (positive) force. This means that there is no possible combination of circuits completely on or off that produces a net force on WS6 that is away from the machine center. However, there are several combinations that produce a net force on WS6 toward the machine center. The worst-case load is −4.44 MN and occurs when circuits 1–4 are off and circuits 5–9 are on.

Table 4.8 summarizes the peak radial loading per unit length acting on each coil for normal operating conditions. In a solenoid, the forces per unit length are indeed radial.

Table 4.8. Peak radial loads per unit length under normal operating conditions

Coil number	Coil name	$x = 0$ plane F_r, MN/m	Current scenario[a]	$y = 0$ plane F_r, MN/m	Current scenario[a]
1	WM2	4.95	111111111	5.41	111111111
2	WM1	6.03	111111111	3.99	111111111
3	WT2	0.80	101111111	1.34	111111111
4	WT1	0.87	111111111	0.66	111111111
5	WS6	0.67	111011111	0.65	110111111
6	WS5	0.75	111011111	0.75	111111111
7	WS4	0.82	111111111	0.83	111111111
8	WS3	0.90	111111111	0.90	111111111
9	WS2	1.01	111111111	1.01	111111111
10	WS1	1.16	111110111	1.16	111110111
11	WCC1	34.0	111111111	34.0	111111111
12	WTDFS2	28.1	111110111	28.1	111110111
13	ETDFS2	28.1	111110111	28.1	111110111
14	ECC1	34.0	111111111	34.0	111111111
15	ES1	1.16	111110111	1.16	111110111
16	ES2	1.01	111111111	1.01	111111111
17	ES3	0.90	111111111	0.90	111111111
18	ES4	0.83	111111111	0.82	111111111
19	ES5	0.75	111111111	0.75	111011111
20	ES6	0.65	110111111	0.67	111011111
21	ET1	0.66	111111111	0.87	111111111
22	ET2	1.34	111111111	0.80	111111101
23	EM1	3.99	111111111	6.03	111111111
24	EM2	5.41	111111111	4.95	111111111

[a]Each digit represents a circuit on (1) or off (0). For example, 110011100 means circuits 1, 2, 5, 6, and 7 are on and circuits 3, 4, 8, and 9 are off.

For C-shaped coils, these forces are local running loads (N/m), which contribute to the lobe-opening forces. For this study, these forces were denoted as radial (F_r) for all coils. Two values are presented: the first in the $x = 0$ plane, the second in the $y = 0$ plane. The two radial force directions are illustrated in Fig. 4.6 for a typical C-shaped magnet and for a typical solenoid. Note that the force in the $x = 0$ plane is y-directed and the force in the $y = 0$ plane is x-directed. In a purely solenoidal system, these two forces would be equal. The lack of equality is a function of the nonsolenoidal fields produced by the C-shaped magnets. The radial forces are positive for all cases and are usually extreme when all circuits are on. However, some coils (e.g., WT2) experience the worst-case radial loading when an adjacent coil is off and unable to hold the axial flux from the system away from the winding in question. The forces computed should be considered "bell-wether" parameters, which allow rapid comparison of cases and are expected to indicate those circuit conditions that lead to worst-case loads. Once these are identified, more detailed load distributions must be determined for structural analysis.

Effects of off-normal conditions

For this study, the fault conditions assume that all circuits are charged to their operating levels, a short circuit occurs across one coil, and a discharge of the entire system follows. Each case requires a transient circuit analysis followed by electromagnetic load determination as a function of time because the extreme loads do not necessarily occur when a discharge current in a circuit passes through its maximum value.

Tables 4.9 and 4.10 list the worst-case loadings for each coil from all the usual and fault current scenarios investigated. If the load is from a usual operating condition, the nine-digit number is given to describe which circuits are charged and which are not. If the worst case arises during a coil short-circuit transient, the number of the coil being shorted is given. Only the first 12 coils are listed. The peak forces on the other coils will have the expected symmetry or antisymmetry. These worst-case loadings are also shown in Figs. 4.9 and 4.10. This presentation format shows not only the large relative differences in these loads among the coils, but also the load reversals that are possible under different current conditions.

Results such as those in Fig. 4.9 are particularly important in designing the structural supports between coils and the gravitational support struts for coils or groups of coils. Depending on their distribution among coils, the struts may be required to withstand load reversals as well as changes in load magnitude. Because of the rapid change in magnetic load as a function of displacement, the struts must be stiff enough to ensure mechanical stability and carry the expected load.

Another class of faults involves system behavior during a discharge with a section of one of the superconducting coils in the resistive state. Even though the coils are designed to be stable under usual conditions, (i.e., complete LHe coolant immersion), a resistive (low-coolant) region is possible in the event of a fault. The temperature rise in a resistive region that is not immersed in coolant is strongly dependent on the coupled discharge character of the circuits and on the operating current and dump voltage selected.

Substantial progress has been made in the ability to reverse certain classes of fault conditions, as evidenced by the cases treated in this section. However, other classes of

Table 4.9. Peak axial loads under all conditions

Coil number	Coil name	Peak positive load, MN	Current scenario[a]	Peak negative load, MN	Current scenario[a]
1	WM2	0		−5.27	111111111
2	WM1	4.75	110000000	−5.02	011111111
3	WT2	4.96	111000000	−1.51	001111111
4	WT1	1.04	111100000	−0.48	000111111
5	WS6	0+[b]	Short 4	−4.44	000011111
6	WS5	0.56	Short 5	−2.29	Short 6
7	WS4	0.75	Short 6	−1.86	Short 8
8	WS3	0.89	Short 7	−2.10	Short 8
9	WS2	1.41	111110000	−2.80	000011111
10	WS1	3.91	111110000	−4.83	Short 10
11	WCC1	0.21	111111000	−1.68	000001111
12	WTDFS2	0.90	Short 10	−102.0	000000111

[a]Each digit represents a circuit on (1) or off (0). For example, 110011100 means circuits 1, 2, 5, 6, and 7 are on and circuits 3, 4, 8, and 9 are off.

[b]Denotes a small force (on the order of kilonewtons).

Table 4.10. Peak radial loads per unit length under all conditions

Coil number	Coil name	$x = 0$ plane F_r, MN/m	Current scenario[a]	$y = 0$ plane F_r, MN/m	Current scenario[a]
1	WM2	4.95	111111111	5.41	111111111
2	WM1	6.03	111111111	4.13	Short 2
3	WT2	0.80–0.03[b]	101111111	1.34	111111111
4	WT1	0.87	111111111	0.66	111111111
5	WS6	1.15	Short 5	1.15	Short 5
6	WS5	1.53	Short 6	1.53	Short 6
7	WS4	1.78	Short 7	1.78	Short 7
8	WS3	2.05	Short 8	2.05	Short 8
9	WS2	2.46	Short 9	2.46	Short 9
10	WS1	3.23	Short 10	3.23	Short 10
11	WCC1	49.0	Short 11	49.0	Short 11
12	WTDFS2	30.4	Short 12	30.4	Short 12

[a]Each digit represents a circuit on (1) or off (0). For example, 110011100 means circuits 1, 2, 5, 6, and 7 are on and circuits 3, 4, 8, and 9 are off.

[b]Force reversal for short 2.

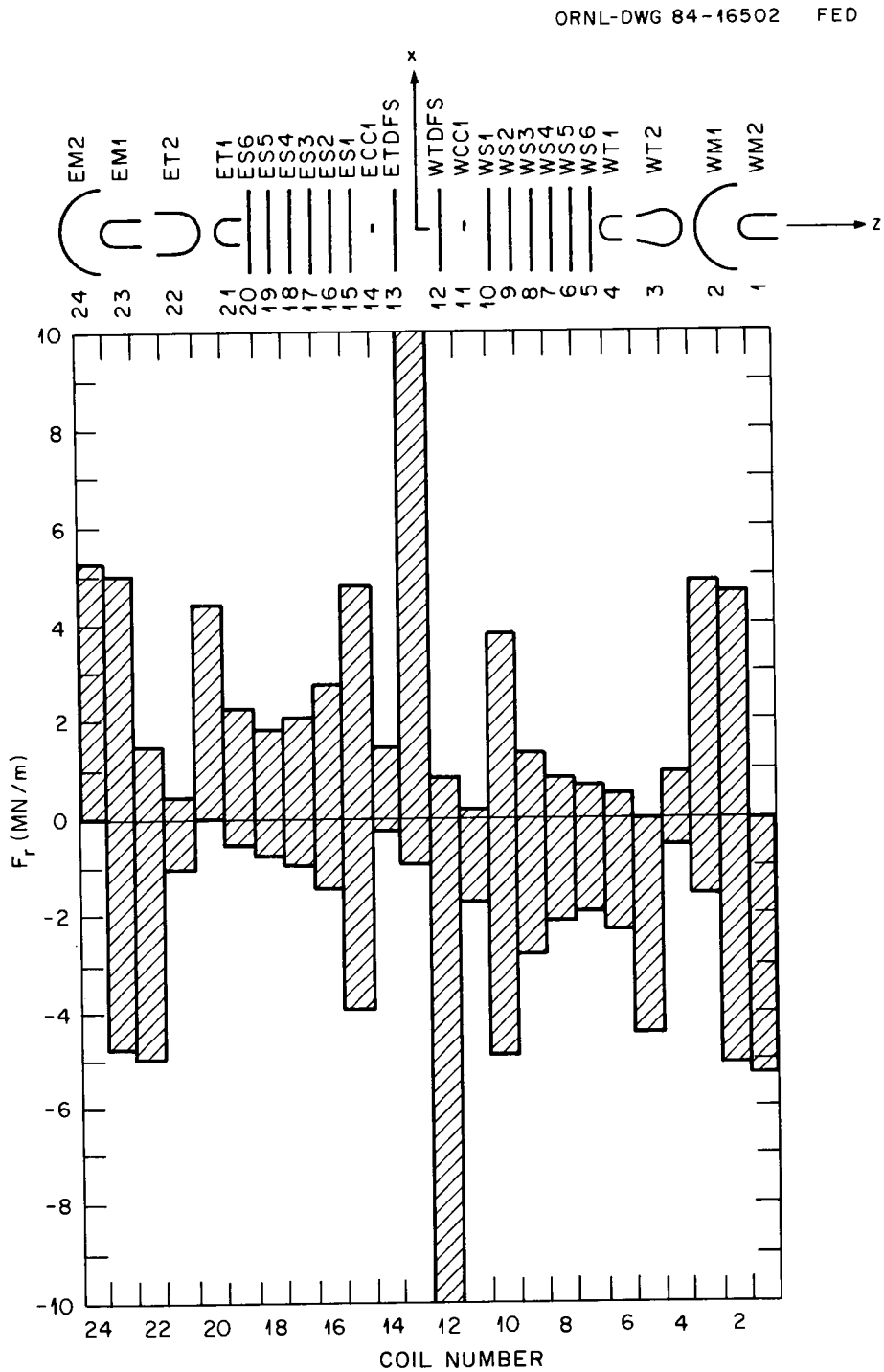

Fig. 4.9. Peak axial loads for all MFTF-B+T current scenarios.

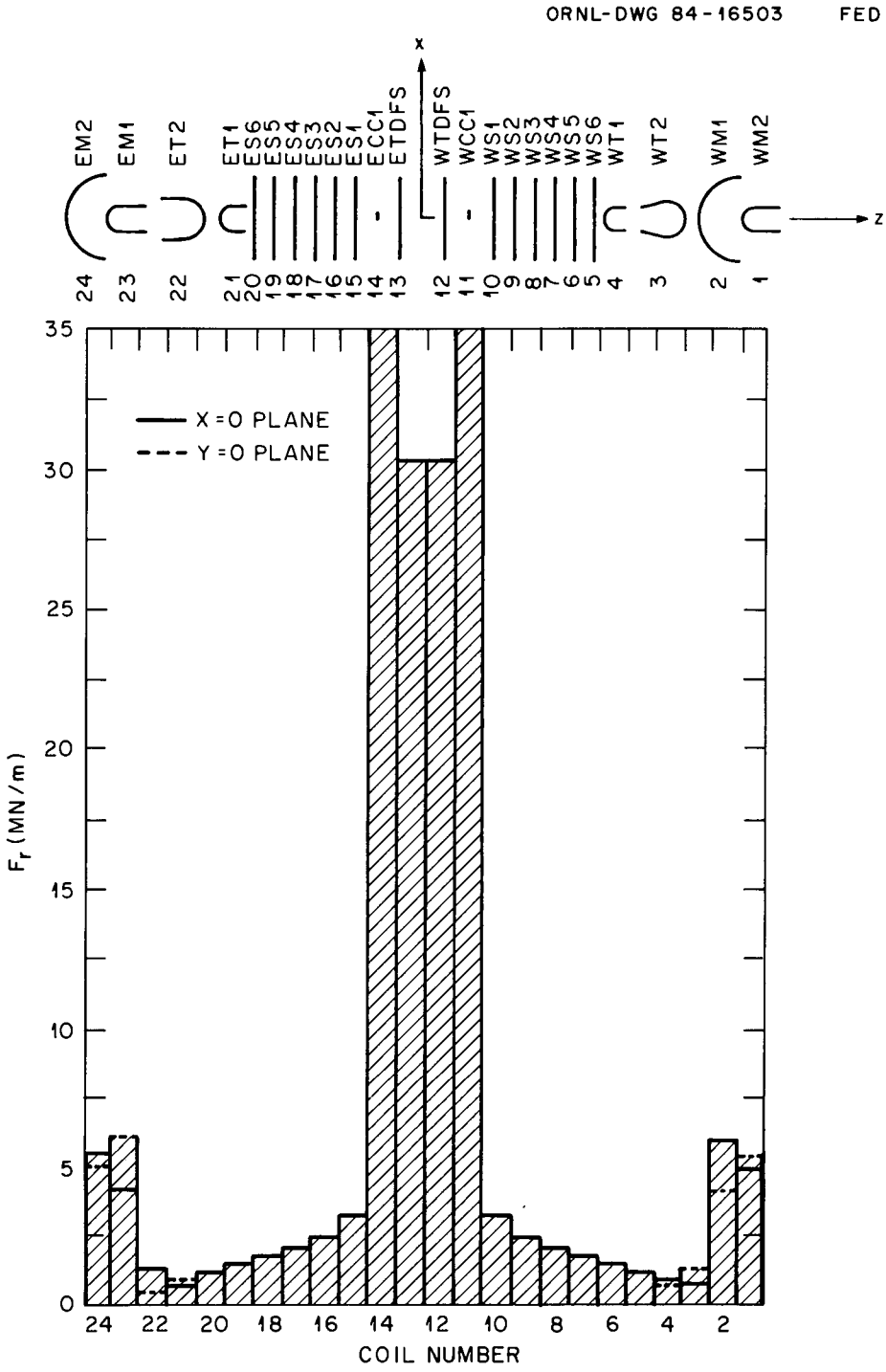

Fig. 4.10. Peak radial loads per unit length for all MFTF-B+T current scenarios.

severe conditions exist, and method development for rapid reversal of these cases should continue.

Effect of construction misalignments

The construction and assembly of a system of this scale will lead to less-than-ideal field characteristics because of cumulative fabrication tolerances. These may affect machine physics or structural requirements. In a future design phase, the possible assembly tolerances should be estimated so that error fields can be considered from the physics standpoint and so that intercoil and gravitational structural elements can be reviewed for magnetoelastic stability to alterations in forces between coils. Typical errors should include pitch, roll, and yaw of individual coils relative to the machine axis, as well as axial or radial misplacement of coil centers.

4.3 COMPONENT DESIGN DESCRIPTIONS

4.3.1 D-T Axicell Coils

Superconducting background coils (CS1)

The D-T axicell superconducting background coils (designated CS1) are new coils with a peak field at the winding of 10.8 T (see Table 4.3). The hybrid coil windings (NbTi from 0 to 8 T, Nb_3Sn from 8 to 12 T) are designed for cryostability. The double-pancake windings are cooled by pool boiling in 4.2 K helium at atmospheric pressure.

Choice of conductor and operating current. The NbTi and Nb_3Sn are shown in Fig. 4.11 and described in Table 4.11. This conductor was originally proposed for use in 12-T toroidal field coils;[2] a short length of the Nb_3Sn conductor has been manufactured and is to be tested at the Oak Ridge National Laboratory (ORNL). The conductor consists of cables of triplets of strands co-wound in a U-shaped, stainless steel channel and is ideal for the CS1 coil windings, which have high hoop loads. The conductor can be graded to increase the overall winding current density ($\sim$2 kA/cm^2); it is rated for 16.5 kA.

Static stability and conductor performance. Within the conductor cross section, 42% of the cable space is occupied by liquid helium. The superconducting strands are in direct contact with the helium, which facilitates heat transfer and cryostable operation. To ensure cryostability, the heat flux at the conductor surface must not exceed a critical value[2,3] of 0.24 W/cm^2. The conductor operating current is chosen so that the surface heat flux is no more than 80% of the critical recovery heat flux (see Sect. 4.1.2).

The peak nuclear heating load occurs in the winding at the inner diameter. The 11-T grade Nb_3Sn conductor is used here. The nuclear heating in the coil case is conducted to the winding, but this component is small. The heat loads in the Nb_3Sn conductor at the coil inside radius are given in Table 4.12. The estimated critical heat flux (0.24 W/cm^2) will be verified experimentally.[3]

The critical currents for the Nb_3Sn conductor as a function of magnetic field are shown in Fig. 4.12. The magnet load line and the operating point are also shown. For this study the operating current should be no more than 80% of the critical current along the load line. The selected operating current is approximately 82% of the critical current.

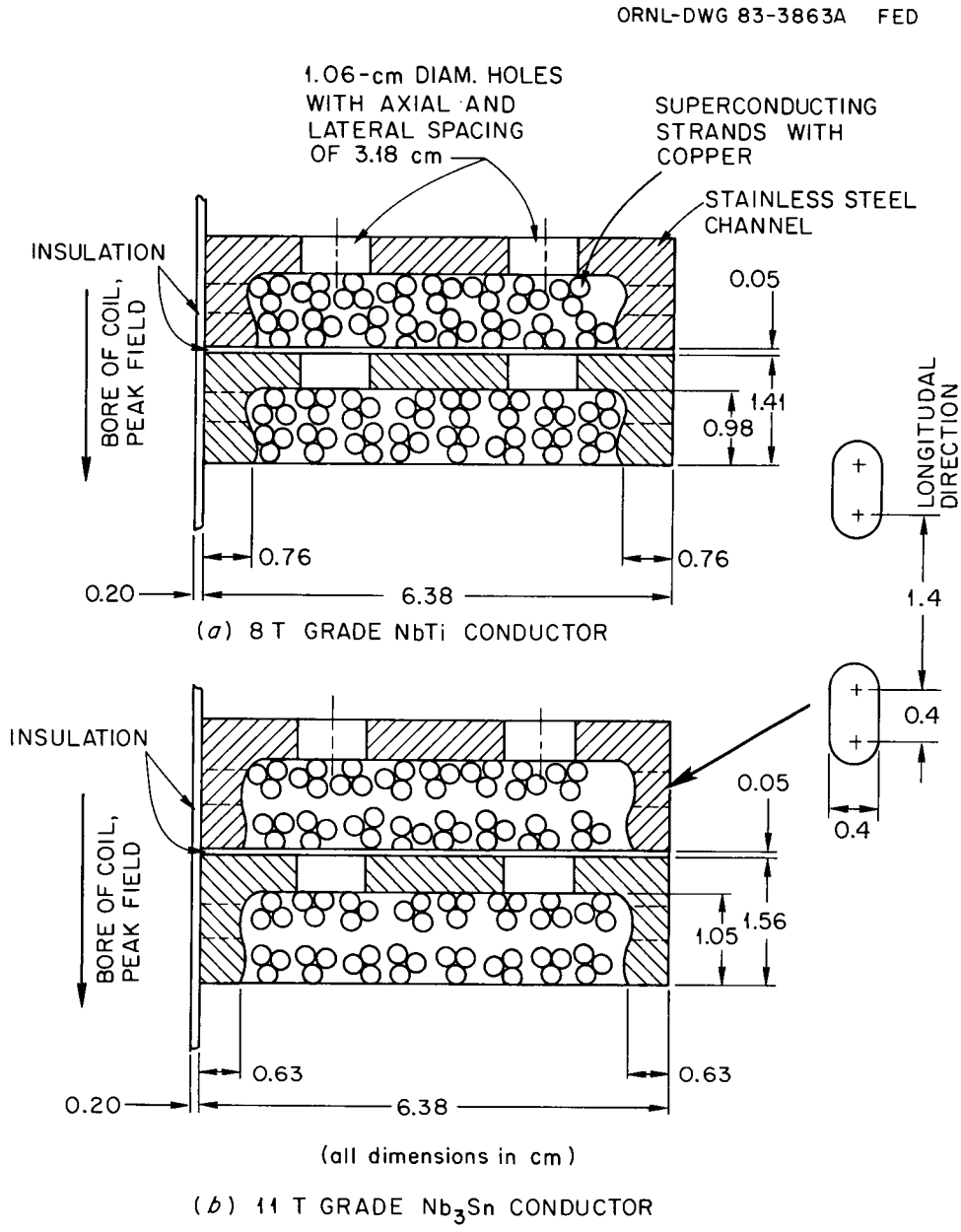

Fig. 4.11. (a) NbTi and (b) Nb_3Sn conductor for CS1 coils.

Table 4.11. Parameters of CS1 coil conductor

	Nb_3Sn	NbTi
Operating current, kA	16.5	16.5
Channel		
Width, cm	6.38	6.38
Side thickness, cm	0.63	0.76
Hole D, axial and lateral spacing, cm	1.06	3.18
Plate thickness, cm	0.51	0.43
Overall height, cm	1.56	1.41
Cable		
Number of triplets	16	16
Number of strands	48	48
Strand diameter, cm	0.288	0.268
Helium in channel groove, %	42	42
Superconductor area/cable, cm^2	0.525	0.329
Copper stabilizer (annealed)		
RRR	150	150
Area/cable, cm^2	2.60	2.37
Fully normal heat transfer (watts/unoccluded surface), W/cm^2	~0.24	~0.24

Table 4.12. Peak heat loads and stability considerations for the CS1 coil winding

Parameter	Winding	Coil case	Total
Peak heat loads in 11-T grade conductor			
Nuclear heating, W/cm	0.013	0.021	0.034
Joule heating in normal zone, W/cm	6.830	0	6.830
Total	6.843	0.021	6.864
Peak heat flux at conductor surface, W/cm^2			0.19
Critical recovery heat flux, W/cm^2			0.24

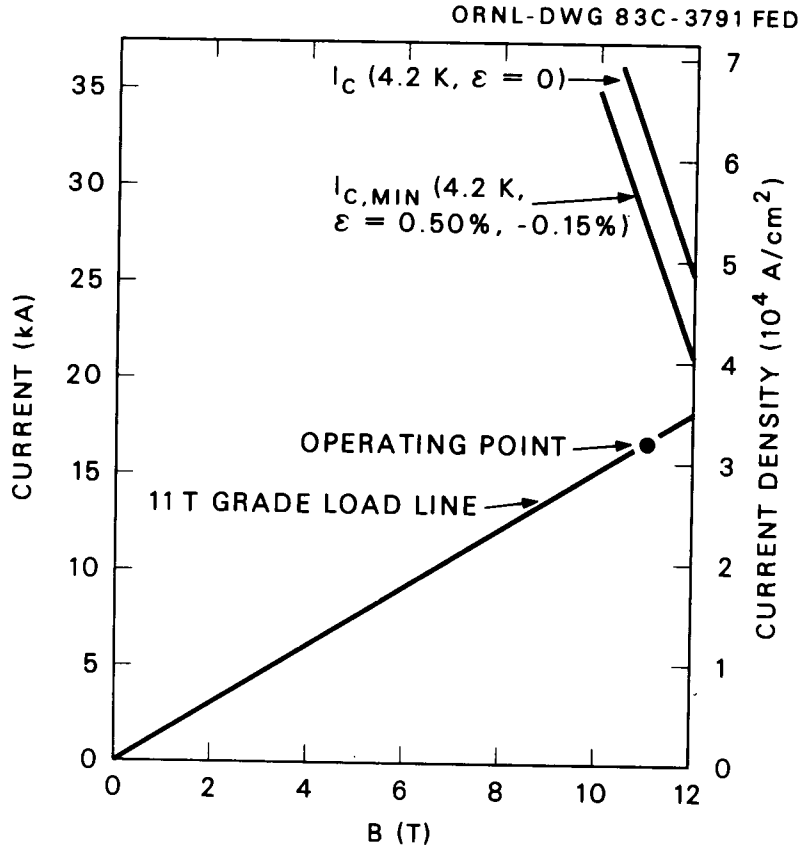

Fig. 4.12. Critical currents for Nb_3Sn conductor.

Quench analysis. As noted in Sect. 4.1.2, the discharge voltage and the hot-spot temperature are limited to less than 1000 V and 200 K, respectively. The corresponding discharge characteristics with an external dump resistor are shown in Fig. 4.13 and listed in Table 4.13. Discharge data were computed using the Thermal Analysis for Stability and Safety (TASS) code for pool-boiling magnets.[4]

Winding layout. The winding layout for the CS1 coil is shown in Fig. 4.14; key parameters are listed in Table 4.14. The pancake winding approach was selected to facilitate grading of the conductor to achieve ~2000-A/cm^2 winding current density. Each pancake consists of three grades of conductor. The conductor in the high field region has more superconductor and a relatively thick stainless steel channel; that in the low field region has less superconductor and a relatively thin stainless steel channel. Graded conductors are optimized for local field and force requirements within the coil winding.

The three grades are of different thicknesses but the same width. The windings consist of 14 pancakes with 86 turns each for a total of 1204 turns, which will provide the required 19.8 MA·turns per coil (see Table 4.14). The 0.5-mm-thick turn-to-turn insulation has holes to provide bubble percolation. The pancake-to-pancake insulation is 2 mm thick. The integrated radiation dose to the insulation is 10^{10} rad, so polyimide insulation

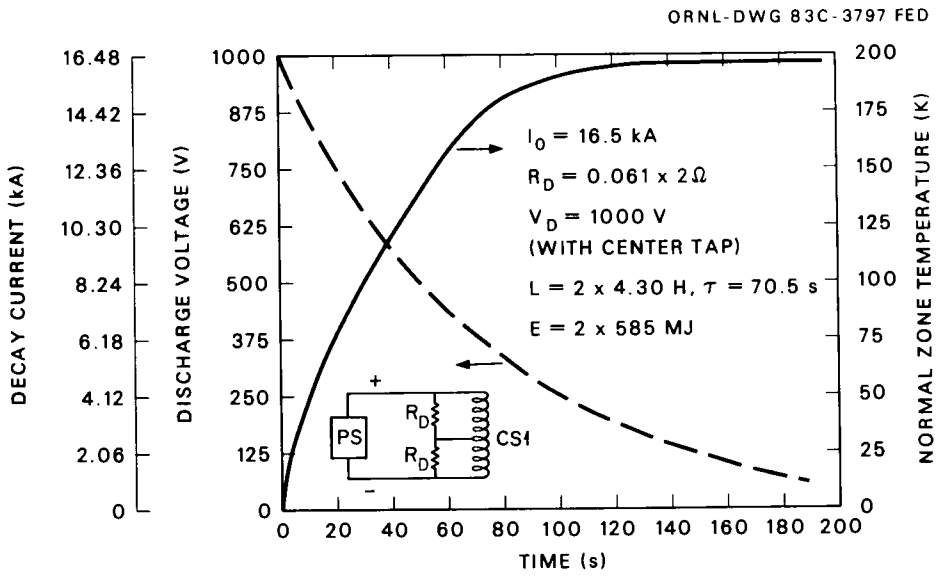

Fig. 4.13. Quench characteristics of CS1 coil.

Table 4.13. CS1 coil discharge parameters

Stored energy per coil, MJ	1170
Self-inductance of each coil, H	8.60
Operating current, kA	16.5
Maximum temperature rise in the winding, K	200
Area of copper conductor, cm^2	2.37
External dump resistance, Ω	0.061
Time constant of dump resistor, s	70
Maximum discharge voltage, kV	1.0

is specified. Conductor splices are made[5] by soldering strands with an adequate lap joint length (~50 cm) to reduce the joint resistance. The joints are supported by stainless steel back plates with shimming immediately before and after each joint.

Winding pack stresses. The in-plane running load on the CS1 coil is 64.23 MN/m; the out-of-plane running load is 0.2213 MN/m. The in-plane running loads are equilibrated by hoop stress in the winding and in the case; out-of-plane loads are equilibrated by bending stress in the case. The hoop stress in the conductor is σ_θ = 324 MPa and the bearing stress is σ_{brg} = 2 MPa, both of which are less than the allowable stress of 370 MPa.

ORNL-DWG 83C-3864 FED

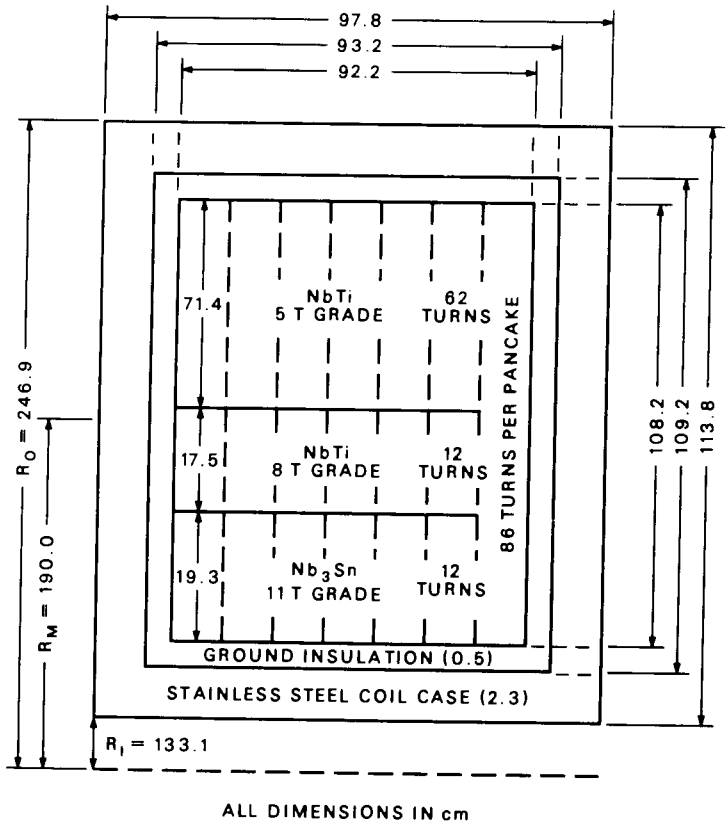

Fig. 4.14. CS1 coil winding layout.

Table 4.14. CS1 coil parameters

Electromagnetic	
Ampere-turns, MA·turns	19.8
Peak field, T	10.8
Operating current, kA	16.5
Conductor current density, A/cm^2	2050
Winding current density, A/cm^2	1990
Overall current density (including structure), A/cm^2	1800
Geometric	
Mean radius, m	1.90
Mean axial position Z, m	±2.40
Radial width ΔR, m	1.138
Axial width ΔZ, m	0.978
Number of pancakes	14
Number of turns per pancake	86
Total number of turns	1204
Cryogenic	
Operating temperature, K	4.2
Stability margin, mJ/cm^3	100

To assess design margins, stresses were calculated at critical points throughout the winding and compared with stress limits. The maximum channel web bending stress due to the Lorentz load appears in the 11-T grade conductor (the effect of ventilating holes on the conductor stress is included). The results of stress analyses on winding pack are summarized in Table 4.15. All the stresses are within design limits (see Sect. 1.2).

Table 4.15. Summary of winding pack stresses

	Actual stress, MPa	Allowable stress, MPa
Interturn insulation compression	241	276
Interpancake insulation compression	1	276
Dilational tensile stress		
Channel	252	
Copper	114	159
Bending stress in web of channel	262	
Tresca membrane stress in channel	490	517
Tresca membrane stress plus bending stress in channel	503	776

Coil case/cold structure stresses. The out-of-plane axial load on the winding produces a uniform pressure on the 2.3-cm-thick side wall of the coil case (see Fig. 4.14), which must be equilibrated in plate bending. The stresses in the side wall are calculated for a simply supported plate, with the maximum out-of-plane load of 0.2213 MN/m uniformly distributed to produce a bending stress of 345 MPa. This is less than the allowable bending stress of 370 MPa.

The coils are supported at four axial locations (similar to the arrangement for the S1 to S5 coils) around the coil periphery by intercoil supports that carry the resultant axial force. The section of the coil between supports must carry the axial running loads in beam bending. The combined stress in the coil case due to plate bending and beam bending is 351 MPa, which is less than the allowable stress of 370 MPa.

Cryogenic heat loads. The neutronic heat load at the coil inner surface is estimated to be 0.4 mW/cm^2, based on a one-dimensional (1-D) shielding analysis (Chap. 9). The total integrated heat load is obtained by attenuating the peak heat load by an e-folding distance of 7 cm through the winding radial build. On this basis, the neutronic heat load in the winding is 105 W/coil. The neutronic heat load in the coil case (similarly calculated) is 80 W/coil, so the total heat load to be removed from each coil is 185 W.

Normal copper coil (CS0)

The normal copper CS0 coil provides a significant portion of the field at the center of the device ($Z = 0$). Its location and dimensions are listed in Table 4.2. The coil bore is small so that the corrective field will be produced only at $Z = 0$; the field contribution of

this coil at $Z = \pm 2$ m is minor. The coil's axial length is constrained by the neutral beams. There is not enough space for adequate shielding, so water-cooled windings are used. The coil requires 17 MA·turns.

The copper conductor is similar to that used for the Joint European Torus (JET). The conductor and winding configurations are shown in Fig. 4.15. Briefly, the conductor is 2.4 cm by 1.8 cm and has four 1.2-cm-diam cooling holes. The 0.5-cm-thick ground wall insulation is made of S-glass impregnated with polyimide epoxy. There is a stainless steel jacket over the ground wall insulation. Overall, the insulated conductor is 3 cm by 20 cm. The cross section of a double pancake is 33 cm by 40 cm; each pancake has 11 turns. The cooled path length is equal to one-half turn. The temperature rise of the cooling water is 17°C. The overall current density of the coil is 1300 A/cm^2, and the conductor (lead) current is 77 kA. The power consumption of this coil is 7.5 MW.

12-T choke coils (CC1)

The CC1 coils generate a 12-T peak field at $Z = \pm 2.0$ m (in conjunction with the CS1 coils located at $Z = \pm 2.4$ m). The coil locations and dimensions are listed in Table 4.2. Each coil requires 2.83 MA·turns.

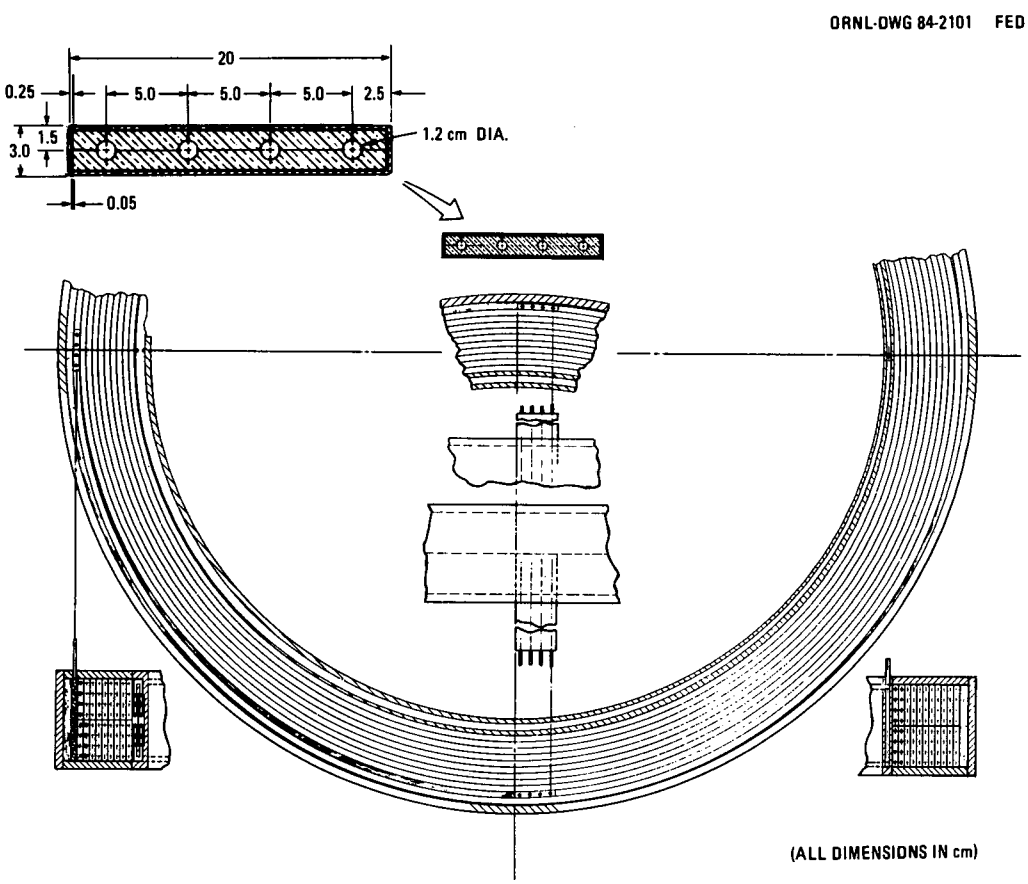

Fig. 4.15. Cross section of the CS0 coil.

Trade studies for the Technology Demonstration Facility (TDF) showed that these coils must use water-cooled normal windings to achieve a minimum life-cycle cost. The conductor used is like that proposed for JET (Fig. 4.15). As noted, this conductor is wrapped with ground wall insulation and encased in a stainless steel jacket. Tests at MIT have confirmed that this insulation can withstand very high radiation fluences with no degradation in its mechanical strength in compression. The coil configuration is shown in Fig. 4.16. The winding pack consists of a double pancake; each pancake has 11 turns. The winding cross section is 40 cm by 33 cm.

The total coil heat is 6.7 MW (Joule heating of 5.13 MW and nuclear heating of 1.56 MW). The nuclear heating is calculated on the basis of an 8-cm e-folding distance

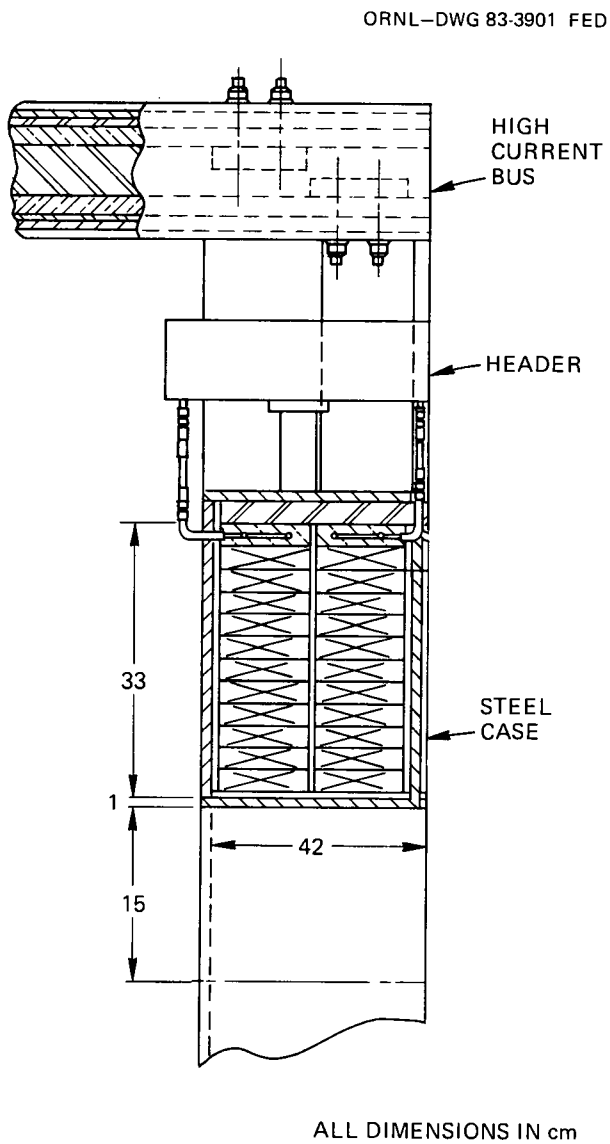

Fig. 4.16. 12-T choke coil configuration.

for copper containing water. The peak nuclear heating of 35 W/cm^3 occurs at the highest field turn, and cooling calculations are based on this turn. The cooled path length is one-half turn. Water enters the turn on one side and exits from the other. The heat load in the hottest turn is 235 kW (Joule heating of 100 kW and nuclear heating of 135 kW). Calculations indicate that the conductor resistivity increases because of the elevated temperature of the conductor (120°C) and because of neutronic damage in the conductor. The temperature of the cooling water rises 15°C in the hottest turn, and the pressure drop is 6 psig for a water flow velocity of 6.1 m/s. The hottest spot in the conductor is at the midpoint between adjacent holes, where the temperature is 80°C above the water temperature. The coil performance parameters are summarized in Table 4.16.

The power consumption for each coil is 5.1 MW, the terminal voltage is 38 V, and the total pumping power is 7.4 kW. The peak stress in the conductor is 90 MPa.

4.3.2 Central-Cell Solenoid Coils

The MFTF-B solenoid coils will be used as the central-cell solenoid coils designated S1 through S5. Cross sections of the coil and the conductor are shown in Fig. 4.17. The

Table 4.16. CC1 coil performance

Ampere-turn requirement, MA·turns	2.83
Conductor current, kA	128.6
Peak nuclear heating, W/cm^3	35
Inside radius of winding, cm	16
Outside radius of winding, cm	49
Axial length of winding, cm	40
Number of turns	22
Current density over winding pack, A/cm^3	2140
Resistivity of copper at 100°C, $\mu\Omega\cdot$cm	2.23
Increase in resistivity due to dpa, $\mu\Omega\cdot$cm	0.4
Heat load in the hottest turn, kW	
Joule heating	110
Nuclear heating	135
Total	245
Water flow velocity, m/s	6.1
Water temperature, °C	
Inlet	38
Outlet	43
Conductor hot spot temperature, °C	103
Coil heat load, MW	
Joule heating	5.1
Nuclear heating	1.6
Total	6.7
Voltage drop, V	38

ORNL-DWG 83-3859 FED

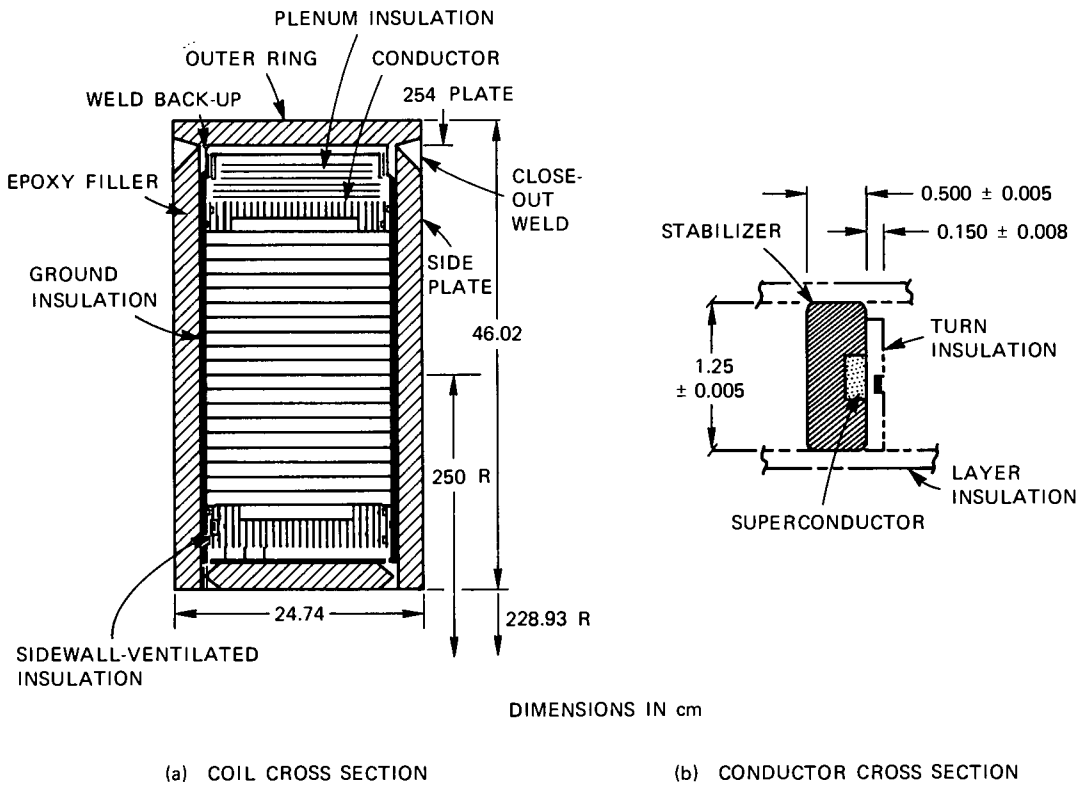

Fig. 4.17. Configuration of central-cell solenoid (S1–S5) coils.

conductor is constructed of a monolithic NbTi superconductor soldered into a copper stabilizer. Key parameters are listed in Table 4.17. Each coil will carry 1.64 MA·turns, and with 600 turns the conductor current will be 2.73 kA.

Static stability

The static stability was analyzed to compute the heat flux required to remove the heat deposited in a normal zone. The selected operating current limits the required heat flux to

Table 4.17. Solenoid coil conductor parameters

Copper-to-superconductor ratio	
Core	2:1
Overall	28.8:1
Quarter-hard copper stabilizer tensile yield, ksi	34
Minimum RRR (stabilizer)	110
Cross-sectional area, cm^2/cm	0.6
Wetted area, cm^2/cm	2.42
Critical heat flux, W/cm^2	0.22

less than 80% of the critical recovery heat flux for the conductor. Irradiation damage is assumed to cause a 25% increase in the resistivity of the copper. However, this damage will be annealed out if the coils are warmed up once a year (as proposed in the current testing approach).

The conductor surface heat flux is calculated as 0.17 W/cm^2 at the operating current of 2730 A, which meets the selected goal. The operating heat flux includes the effects of the increase in resistivity due to irradiation, the effect of nuclear heating induced in the conductor, and the effect of heat conduction from the coil case. Thus, these coils are expected to operate in a cryostable mode.

Margin against critical current

A plot of critical current vs field is shown in Fig. 4.18 for the central-cell solenoid conductor. The operating points for the five solenoid coils are indicated. The stability criterion is to limit the operating current to 80% of the critical current (determined by the magnet load line). This criterion is violated to some degree in all of the central-cell

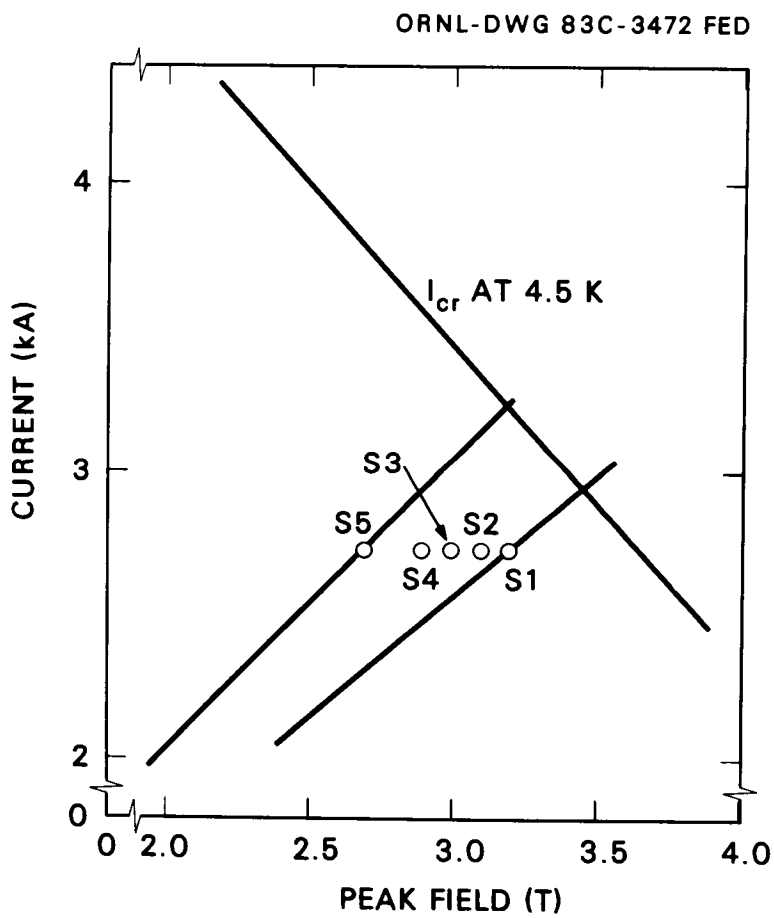

Fig. 4.18. Operating currents in the S1–S5 coils.

solenoid coils. As shown in Fig. 4.18, the operating current (expressed as a percentage of critical current) is different for each coil. The S1 coil undergoes the most severe combination of field and current, with an operating current that is 91% of the critical current. For the S5 coil, which has the least severe combination, the operating current is 84% of the critical current. Further evaluation, with different coil spacing and axial locations, is needed to meet the desired current margin.

Structural evaluation

The S1 coil is the most severely loaded of the five solenoid coils (see Table 4.4), with in-plane running loads of 1.887 MN/m and out-of-plane loads of 0.748 MN/m. The in-plane running loads are equilibrated by hoop stress in the conductor, and out-of-plane loads are equilibrated by bearing against the case side wall. The hoop stress σ_θ and bearing stress σ_{brg} in the conductor have been calculated; σ_θ = 140 MPa and σ_{brg} = 2.5 MPa, both of which are less than the allowable stress of 159 MPa.

The axial load produces a uniform pressure on the 2.54-cm-thick side wall that must be equilibrated in plate bending. The side wall is evaluated as a simply supported plate, with the maximum out-of-plane load of 0.748 MN/m uniformly distributed and producing a bending stress of 357 MPa, which is less than the allowable 372 MPa.

Each coil is supported at four equally spaced locations around its periphery by inter-coil supports that carry the resultant axial forces. The section of coil between the supports must carry the axial running load in beam bending. The maximum axial running load of 0.748 MN/m produces a bending stress in the coil case of 370 MPa, which is less than the allowable 372 MPa.

The plate bending and beam bending stresses calculated here act in orthogonal directions. The case side wall, against which the winding bears, is thus in tension on one side and in compression on the other (due to plate bending) and is in nearly uniform tension in the orthogonal direction (due to beam bending). The combined Tresca stress (stress intensity) from these two components is 664 MPa, which is within the 690-MPa limit for primary membrane-plus-bending stress intensity.

Cryogenic load

The peak neutronic heat load at the inner surface of the coil case is estimated to be 4.1×10^{-6} W/cm^3. The integrated heat load on the winding and the coil case is estimated by attenuating this peak heat load by an e-folding distance of ~7 cm. In both the winding and the coil case the total integrated heat load is calculated to be 0.5 W, for a total heat load of ~1.0 W/coil.

4.3.3 Superconducting Background Portion of 18-T Choke Coil

The 18-T choke coil assembly is shown in Figs. 4.19 and 4.20. This assembly consists of an 18-T normal insert coil (discussed in Sect. 4.3.4) and a 15-T superconducting background coil. The superconducting portion of the assembly is further divided into two subcoils, each with a separate conductor and coil case: the outer or background 8-T coil provides 7.36 T to the field on axis, and the inner or "15-T insert" coil provides 7.0 T to the

ORNL-DWG 84-2102 FED

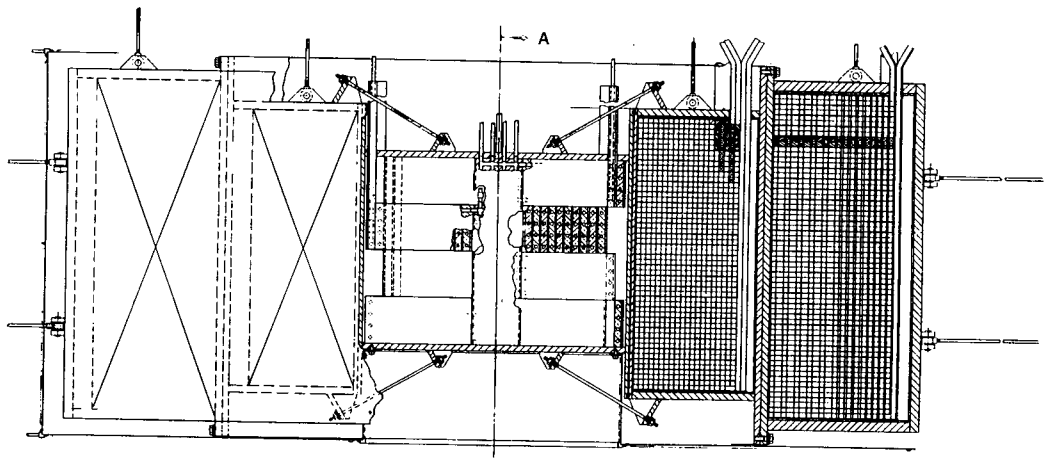

Fig. 4.19. Cross section of the 18-T choke coil.

ORNL-DWG 84-2103 FED

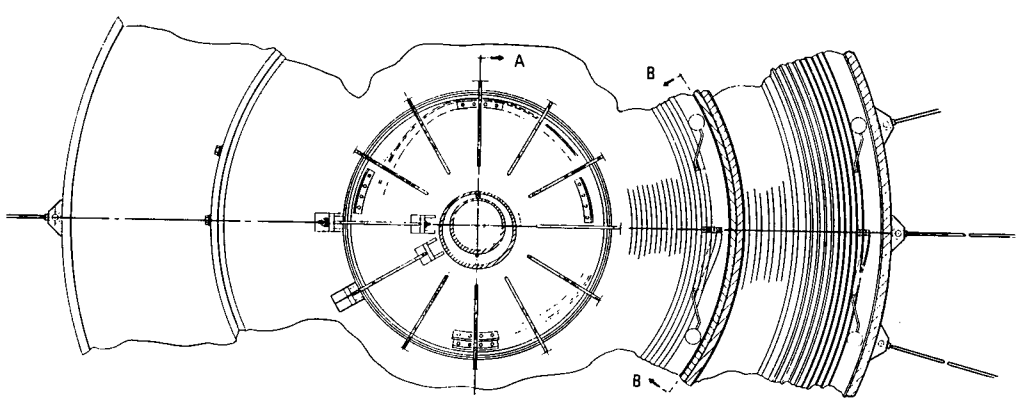

Fig. 4.20. Side elevation view of the 18-T choke coil.

field on axis. Major parameters are given in Table 4.18 for the background coil and in Table 4.19 for the 15-T insert coil.

These coil are designed for a peak neutronic heat load of 65 mW/cm^3 at the 15-T coil case. However, the revised neutronic analysis calculations suggest that the peak heat load may be less than 46 mW/cm^3. The design of the 18-T choke coil, especially the normal and superconducting coil proportions, will be reevaluated later in the design process.

8-T background coil

Choice of conductor and operating current. The 8-T background coil is the least difficult of the three modules making up the 18-T choke coil, but it still is a high-performance, state-of-the-art magnet. Each coil will have a self-energy of 412 MJ.

Table 4.18. Parameters of 8-T background coil for 18-T choke magnet

Axial field contribution B_0, T	7.36
Maximum field at the conductor B_{max}, T	9.4
Average current density over the winding pack λJ, A/cm^2	2160
Total number of ampere-turns, MA·turns	18.6
Conductor current I_{cond}, kA	25
Stand-alone stored energy W_m, MJ	410
Peak voltage on coil discharge V_{peak}, kV	4

Table 4.19. Parameters of 15-T superconducting insert for 18-T choke magnet

Axial field contribution B_0, T	7.0
Maximum field at the conductor B_{max}, T	16.2
Average current density over the winding pack λJ, A/cm^2	1980
Total number of ampere-turns, MA·turns	10.7
Conductor current I_{cond}, kA	20.5
Stand-alone stored energy W_m, MJ	190

Traditionally, NbTi has been selected for use at 8 T and below. However, some recent studies of the Nb_3Sn cable-in-conduit conductor suggest that this selection is no longer optimal; Nb_3Sn is cost-effective at all fields in a large magnet. Since a relatively high overall current density is demanded for the background coil, a high-current-density conductor will aid in satisfying coil structural requirements. A partial list of measured critical currents of candidate conductors is shown in Table 4.20. The most attractive is Nb_3Sn prepared with the internal tin method, which has double the critical current density in the noncopper of the other superconductors, according to advertised, "guaranteed" performance specifications.[6] Since the amount of noncopper is less than half the amount of NbTi that would be needed, the selection of the more advanced conductor would free valuable space for structure, and the cable itself would probably cost less.

Stability. The approach to ensuring stability in the 8-T background coil is the same as that used for the 15-T insert (described later in this section). Because the strain sensitivity of Nb_3Sn is lower at 8 T than it is at 15 T, the strain reduction techniques should be effective at 8 T. The conductor is designed to an operating current of half the short-sample, uncompacted, critical current density reported in Table 4.20. The stability margin, then, is expected to be above 500 mJ/cm^3, by analogy with similar designs, such as the 10-T coil design for Alcator DCT.[7]

Table 4.20. Critical current density of superconductors at 8 T and 4.2 K

Conductor	Description	Critical current density, A/mm^2
NbTi	Published data by Iwasa	600
Nb_3Sn–Ti	Furukawa conductor with titanium insert	640
Nb_3Sn	External bronze method, Large Coil Program (LCP) conductor	850
Nb_3Sn	Internal tin method, Intermagnetics General Corporation	2000

Winding layout. The winding layout of the 8-T background coil is shown in Fig. 4.19. The winding is similar in concept to that of the 15-T insert, consisting of 31 double pancakes connected electrically in series. Heat is removed through channels in insulating sheets between double pancakes, as in Alcator DCT.[7] Winding pack parameters are shown in Table 4.21.

Winding pack stresses. Each layer of the solenoid is self-supporting against both hoop and axial forces. Structural strength is provided by co-winding the magnet with a steel reinforcing support strip. Because of the high average thickness of the reinforcing support strip, the strip and jacket would probably be at least partially preformed before winding.

The hoop and axial stresses in the winding pack are shown in Figs. 4.21 and 4.22, with the winding pack treated as a homogeneous, orthotropic material. The hoop forces vary widely, from 285 MPa in tension in the inner layer to 137 MPa in compression in the outer layer, requiring the use of grading in the structural steel strip. Since the allowable Tresca membrane stress for thick strips of a high-strength steel (such as A286) is 550 MPa at 120 cycles at 4.2 K, the allowable multiplier on the inside layer is 550/(285, hoop tension, + 49, axial compression)=1.65. This can be achieved by co-winding with a strip that is 3.35 cm thick. If all 13 grades were this thick, the winding would have a

Table 4.21. Winding pack parameters for 8-T background coil

Inside radius R_1, m	1.13
Outside radius R_2, m	1.74
Smaller axial position Z_1, m	9.3
Larger axial position Z_2, m	10.7
Total number of turns	775
Number of layers	13
Number of pancakes	62

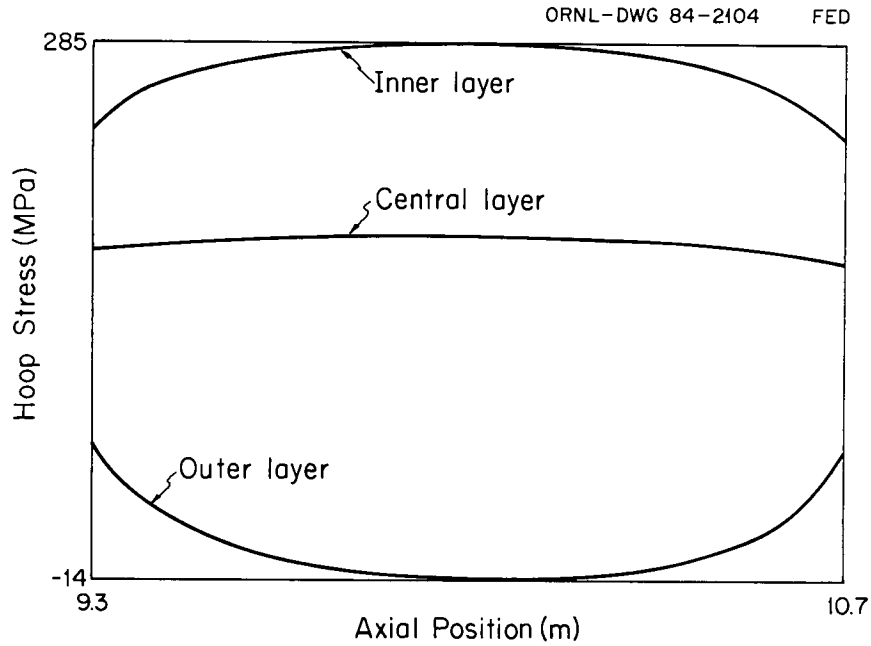

Fig. 4.21. Hoop stress in the 8-T background coil, averaged over the local winding envelope.

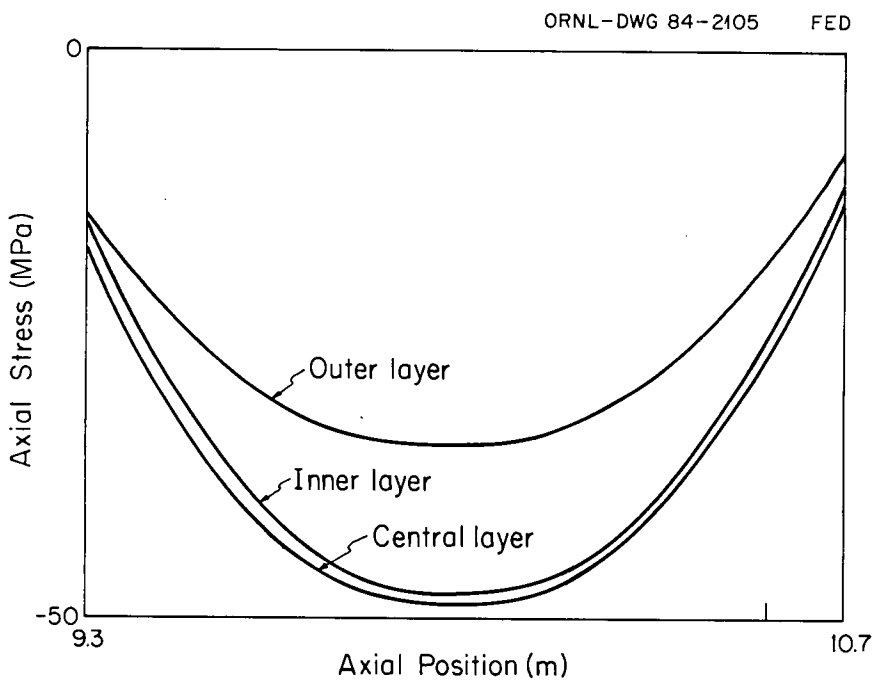

Fig. 4.22. Axial stresses in the 8-T background coil, averaged over the local winding envelope.

total radial build of 72 cm, so grading of the reinforcing structure is necessary. In the central layer, the allowable stress multiplier is 550 MPa/(133 MPa, hoop tension, + 46 MPa, axial compression)=3.1, which can be achieved by a 1.0-cm-thick strip. In the outer layer, the allowable stress multiplier is 550/(137, hoop compression, − 34.7, axial compression)=5.4, which can be achieved by a 0.495-cm-thick reinforcing strip, at which point one might design so that the cable conduit strength is adequate to support the loads. When the three grades are used, the average reinforcing strip thickness is 1.6 cm, giving a total winding pack build of 49 cm. This leaves another 10 cm for making the coil more compact on further design iterations or for adding more structure for greater conservatism.

15-T insert

Choice of conductor and operating current. Very few commercially available superconductors can operate at 16 T. All of the candidates considered for this coil are Nb_3Sn because of its high critical field. The two most advanced forms at this time are Nb_3Sn with titanium inserts, which was selected for the 12-T insert in MFTF-B,[8] and Nb_3Sn produced by the internal tin method, which has been selected for use in accelerator magnets at Berkeley. The internal tin method appears to be preferred over the titanium inserts at fields below about 12 T, although the best attainable current densities with either method are rapidly changing and improving.

Stability. The superconductor is chosen to operate at half the short-sample critical current. This is a frequently used conservative design principle with Nb_3Sn and corresponds closely to the design decisions for the MFTF-B 12-T insert coil and the Westinghouse 8-T Large Coil Program (LCP) coil. Recent unpublished data[9] on conductor samples from Furukawa indicated a critical current density of 290 A/mm^2 at 16 T and 4.2 K in Nb_3Sn multifilamentary strands. This is considerably better than the performance of any other commercially available conductor at this time and was selected as the reference for this design.

The selection of half the critical current is based partly on historical precedent and partly on consideration of the mechanisms by which an actual magnet may be inferior to a short sample (decomposition into a desired energy margin and predictable degradation due to strain in the superconductor).

At operating temperatures that are high in comparison with subcooled or superfluid operation (i.e., 4.2 K and above), operation at 70% of critical current guarantees a high energy margin against sudden energy deposition for a cable-in-conduit conductor. In the 15-T insert coil, the temperature in the superconductor ranges from 4.35 K to a peak of 4.5 K. The helium void fraction of the conduit is 0.3, similar to that of the LCP and Alcator DCT coils. The available enthalpy to the current-sharing temperature is 600 mJ/cm^3. This is much larger than the typical energy deposition of 20 mJ/cm^3 or less of a stick-slip event and allows for margins of error due to manufacturing tolerances in a relatively new process or uncertainties in neutronics calculations.

The second degradation factor of 70% is that due to strain degradation. At 8 T in LCP, this degradation is due to intrinsic compressive stress in the superconductor due to cooldown in a compacted JBK-75 jacket, added to bending stress during winding. The MFTF-α+T Nb_3Sn coils follow the approach of Alcator DCT, reacting the superconductor after winding[7] thus eliminating bending-induced strain in the superconductor.

Further reduction of strain is important because the strain sensitivity of the critical current density in Nb_3Sn increases with magnetic field. For a compressive strain of 0.4% at 8 T, the degradation of critical current from an ideal zero strain condition is about 1.4, roughly corresponding to the design point of the Westinghouse LCP conductor; at 16 T, a 0.4% compressive strain would cause a degradation (assuming symmetry in Ekin's curves about the maximum[10]) of a factor of 6.1, which is clearly unacceptable. Fortunately, if the intrinsic strain can be halved to 0.2%, the degradation of critical current is greatly improved to a factor of 1.3. Recent experiments by Steeves and Hoenig[11] indicate that if a high-strength material with a better match in thermal contraction to that of Nb_3Sn is used for the conduit material, then the intrinsic strain in the superconductor is reduced, causing large, measurable improvements in the conductor critical current. In particular, Incoloy 903, a high-strength alloy, has little effect on the cooldown strain in Nb_3Sn at any conduit compaction. This alloy is being considered for use in the toroidal field magnets of Alcator DCT and is proposed here as a reference conduit for MFTF-α+T. Cooldown of Nb_3Sn at a compaction of 0.3 in Incoloy 903 should leave the superconductor at a residual compression of approximately 0.1% strain. The strains induced by Lorentz forces are relatively constant throughout the winding, ranging from a low of 0.17% tensile strain to a high of 0.2% tensile strain. Thus, since the magnet is stress relieved after winding, the intrinsic strain in the conductor is expected to be everywhere less than 0.1%, which should permit a conservative design at half the short-sample critical current.

Winding layout. The 15-T insert is wound in double pancakes; the conductor current is 20.5 kA. Interpancake channels that remove heat from the magnet are graded so that twice as much nuclear heat can be removed from the channel closest to the machine center as from the average channel. The overall winding pack has 26 double pancakes and 10 layers of co-wound conduit and steel strip. The winding pack parameters are given in Table 4.22.

Winding pack stresses. The winding pack support concept in the superconducting coils of the 18-T hybrid coil is to equalize stresses throughout a pancake winding by grading co-wound, high-strength steel strips. In the 15-T coil, this concept is the least necessary, because the field and radius vary almost inversely throughout the winding pack, so that the variation in stress is not very high ($\pm 15\%$) without grading. However, since the overall size of the co-wound strips is the same as that in the 8-T background coil, which has three grades, two grades of co-wound strip are used in the 15-T insert.

Table 4.22. Winding pack parameters for 15-T insert for 18-T choke magnet

Inside radius R_1, m	0.532
Outside radius R_2, m	0.982
Smaller axial position Z_1, m	9.4
Larger axial position Z_2, m	10.6
Total number of turns	520
Number of layers	10
Number of pancakes	52

The average stresses in the solenoid (considered as a homogeneous, orthotropic material) are shown in Figs. 4.23 and 4.24. The peak Tresca membrane stress in the outer layer, combining radial and axial stresses, is 258 MPa, implying that the geometry-related multiplying factor must be <2.1, for an allowable stress at 4.2 K of 550 MPa at 120 cycles. This can be accomplished by using a 2.2-cm-thick strip on the outside. At the inside layer, the peak Tresca membrane stress in the homogeneous model is 229 MPa, implying that the geometry-related multiplying factor must be less than 2.4. This can be accomplished with a 1.6-cm-thick strip on the outside. If the average radial build of the supporting strip is 1.9 cm, the radial build of 10 turns is 41 cm, which allows a slightly smaller winding pack than the reference design. If it is possible to wind a double pancake without intermediate welds in the reinforcing strip, then only one grade, 2.3 cm thick, would be used, requiring the reference radial build of 45 cm. Since the reinforcing strip would be thick, it would be preformed before winding to minimize bending stresses.

Cooling requirements. The overall cooling requirements of the 15-T insert magnets are dominated by neutron gamma heating, which requires 10.1 kW of refrigeration in each of the two insert magnets. Cooling requirements for a 15-T insert magnet are summarized in Table 4.23.

Neutron and gamma heating at the surface of the 15-T insert magnet has an estimated peak value of 46 mW/cm^3, which is much higher than previously considered values for superconducting magnets. The first consideration in designing a cooling system is to define a strategy to prevent the temperature in the intense heating zone from locally exceeding the critical temperature of the superconductor.

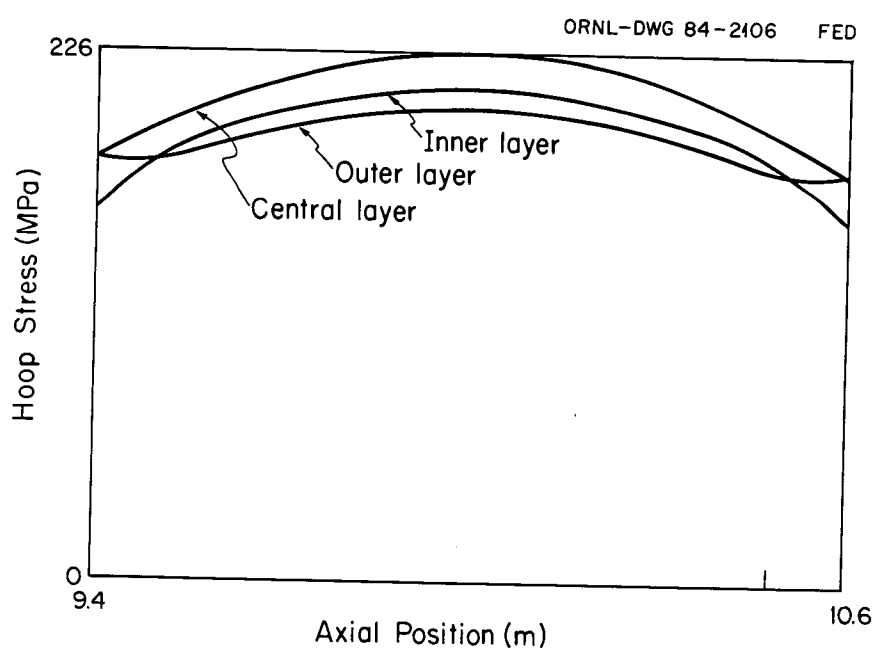

Fig. 4.23. Hoop stress in the 15-T superconducting insert coil, averaged over the local winding envelope.

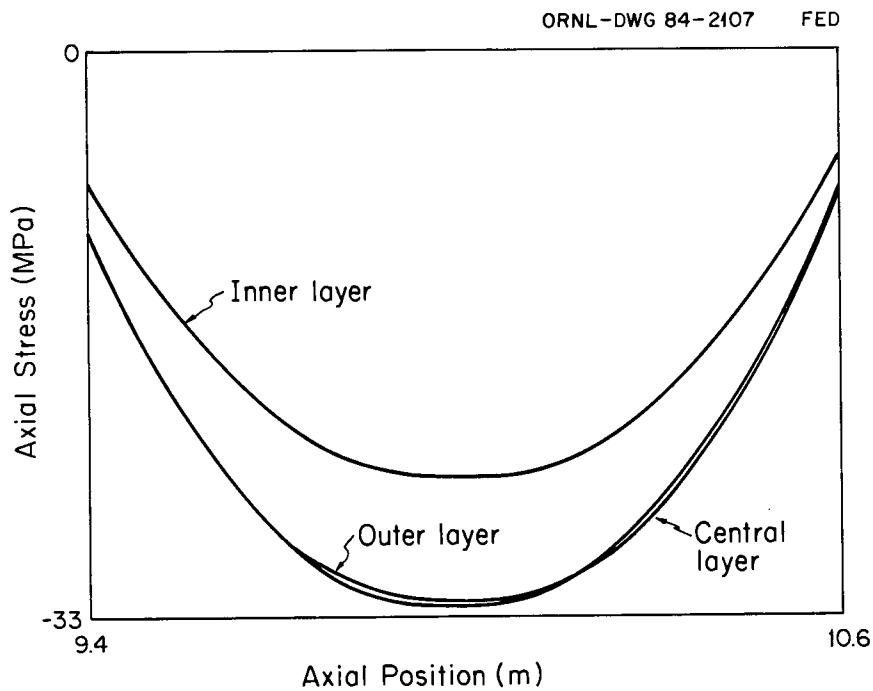

Fig. 4.24. Axial stresses in the 15-T superconducting insert coil, averaged over the local winding envelope.

Table 4.23. 15-T insert cooling requirement (per coil)

Total heating rate $P_{n,\lambda}$, kW	10.1
Peak local heat deposition Q''', mW/cm^3	46
ΔT_{sheath}, K	0.01
Maximum helium quality (top of coil) $Q_{He,max}$, W	0.14
Maximum heat removal per channel $Q_{max,channel}$, W	860
Average heat removal per channel $Q_{av,channel}$, W	388

Cooling design. Heat is removed from the winding pack by thermal conduction through the conductor conduit, followed by bubble flow in small radial paths in the interpancake sheets. Holes in the insulating ground wrap around each conductor are spaced every 4 cm on the face of the conduit directly facing the channel in the sheet between double pancakes to ensure good thermal conductivity, independent of bond integrity. Radial bubble rise is enhanced by including an LHe reservoir above the magnet system, in order to allow natural circulation of the coolant.

At a neutron and gamma heating rate as high as 46 mW/cm^3, it is not possible to use a high-strength steel as the conduit material. For example, if the conduit thickness is 0.173 cm (e.g., Westinghouse LCP and Alcator DCT coils), the inner height of the conductor sheath is 1.734 cm, and the thermal conductivity of the steel is 0.3 W/m·K, then

the temperature rise in the steel across a bare conduit would be 4.3 K. If the multiplying factor, due to only partial baring of the insulation and partial coverage by coolant channels, were as low as 4, the temperature rise would be 17.2 K. However, the temperature of OFE copper is as high as 500 W/m·K at 4.2 K and 1000 W/m·K at 10 K, so that the rise in copper with a temperature multiplier of 4 would be only 0.01 K, leaving a large margin for degradation of copper's thermal properties by neutron irradiation. Since the co-wound steel strip is the principal structural element of the conductor, the lesser strength of a copper conduit is not a first-order disadvantage, so this option is selected.

4.3.4 Resistive Insert Portion of 18-T Choke Coil

The innermost solenoid of the 18-T choke coil is a normal insert that provides 3.0 T of the total 18-T field. Even the most advanced superconductors suffer a severe degradation of their critical current between 15 and 18 T. In addition, a resistive magnet can operate closer to the plasma than a superconducting magnet, which must be shielded against neutron and gamma irradiation at the flux levels expected in MFTF-α+T. The normal insert coil dimensions are given in Fig. 4.25. This coil requires 2.30 MA·turns.

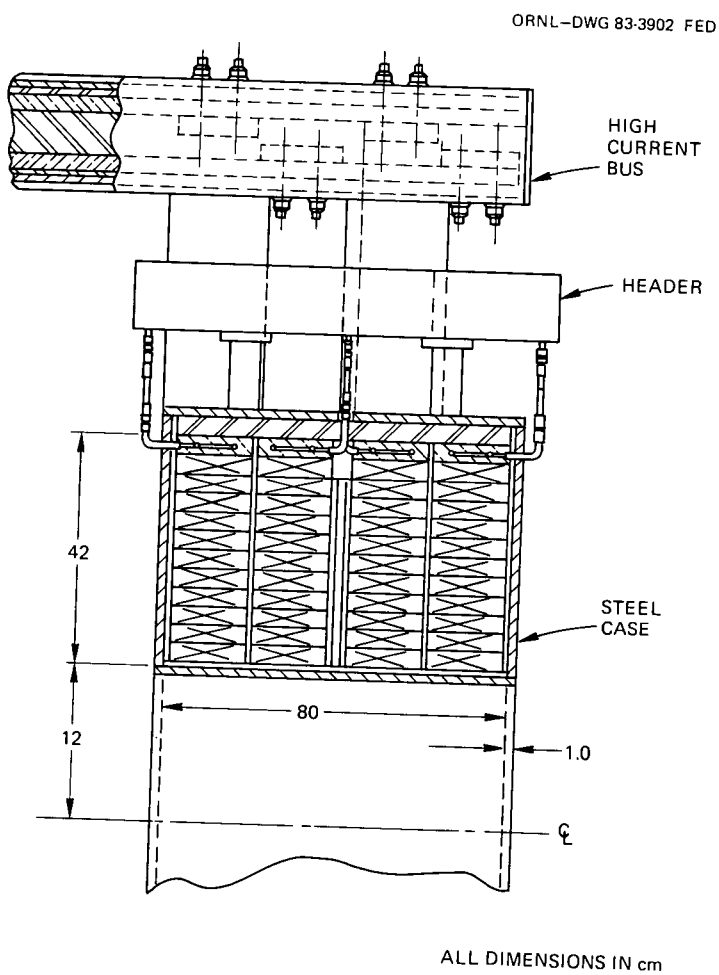

Fig. 4.25. 18-T choke coil normal insert.

Like the other normal MFTF-α+T coils, this coil uses the JET-type conductor illustrated in Fig. 4.15. The winding pack consists of two double pancakes, and each pancake has ten turns. The winding cross section is 80 cm by 33 cm. The total coil heat load is 2 MW (Joule heating of 1.8 MW and nuclear heating of 0.2 MW). The nuclear heating is calculated on the basis of an 8-cm e-folding distance for copper containing water. The peak nuclear heating at the coil inside radius is 3 W/cm^3 (from nuclear analysis calculations).

The coil configuration is shown in Fig. 4.25. All ten turns of a pancake are cooled in series. The temperature rise of the cooling water is 35°C, and the total pressure drop is 150 psig. If the inlet water temperature rise is 35°C, the peak conductor temperature would be 130°C, which is acceptable. The coolant temperature rise can be reduced if pancakes are wound with two conductors in hand. The pumping power is 12 kW. The coil performance parameters are summarized in Table 4.24. The coil terminal voltage is 16 V.

The peak hoop stress in copper, which occurs in the low-field turn at 15 T, is 13 ksi. Since this stress is too high for copper, AMAX-MZC alloy is proposed. This alloy is composed of 99.27% Cu, 0.1% Zr, 0.03% Mg, and 0.6%Cr. The electrical resistivity is

Table 4.24. Performance of resistive insert for 18-T choke magnet

Ampere-turn requirement, MA·turns	2.3
Peak nuclear heating, W/cm^3	3
Inside radius of winding, cm	12
Outside radius of winding, cm	42
Axial length of winding, cm	80
Number of turns	40
Current density over winding pack, A/cm^3	960
Conductor current, kA	57.5
Resistivity of copper at 100°C, $\mu\Omega\cdot$cm	2.23
Increase in resistivity due to dpa, $\mu\Omega\cdot$cm	0.4
Heat load in the hottest turn, kW	
Joule heating	19
Nuclear heating	9
Total	28
Water flow velocity, m/s	6.1
Water temperature, °C	
Inlet	35
Outlet	80
Conductor hot spot temperature, °C	140
Coil heat load, MW	
Joule heating	1.8
Nuclear heating	0.2
Total	2
Voltage drop, V	32
Pumping power, kW	12

2.2 $\mu\Omega\cdot$cm, which is 30% higher than that of electrical-grade copper. The coil design calculations used a resistivity value of 2.4 $\mu\Omega\cdot$cm. At 200°C, the yield strength is 365 MPa and the ultimate strength is 407 MPa. The 90-MPa peak stress on the conductor is within the selected design stress criteria; that is, it is less than 0.66 times the yield stress and 0.33 times the ultimate stress. The impact of a neutronic environment on this alloy's strength and resistivity is not known.

Since the inside radius of this coil is small compared with the conductor height, the copper conductor with cooling holes will be wrapped with S-glass and then encased in a stainless steel jacket. Holes in the steel jacket allow later impregnation with polyimide. The coil will be wound using this conductor. The completed winding will then be impregnated with polyimide epoxy. This process will bond the copper conductor to its jacket and will also bond the jacket of a conductor to its neighboring conductors. Some development work will be required to qualify this winding approach.

4.3.5 End-Cell C Coils

The winding centerline dimensions and winding pack cross sections for the end-cell C coils are given in Table 4.2. A more detailed description of these coils is given here.

Choice of conductor and operating current

The MFTF-B grade I yin-yang conductor (Fig. 4.26) was selected for the end-cell C coils. The operating current is 5 kA. The conductor has been successfully fabricated,

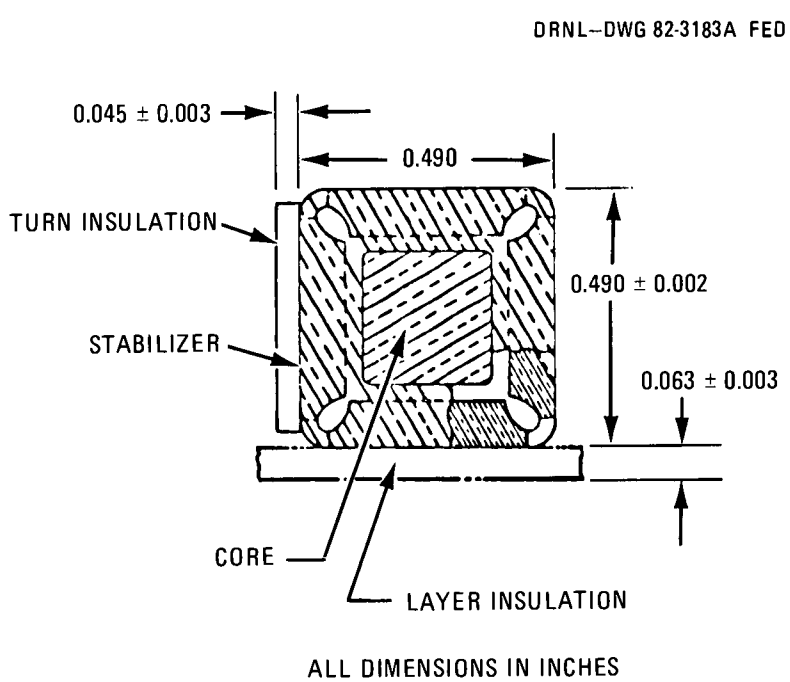

Fig. 4.26. MFTF-B yin-yang conductor.

tested, and operated in an application similar to MFTF-α+T, giving a high degree of confidence to its use. Key parameters for the conductor are listed in Table 4.25. The conductor has a monolithic core with wrapped copper stabilizer, and the NbTi superconductor contains (46.5 ± 1.5)% titanium. Solder with a 50:50 ratio of lead to tin is used. The turn and layer insulation is G-10CR epoxy.

Table 4.25. MFTF-B yin-yang conductor parameters

Copper-to-superconductor ratio	
Core	
Grade I	1.7:1
Grade II	6:11
Overall	
Grade I	6.4:1
Grade II	18.7:1
RRR	
Core	150
Stabilizer	220
ICR at 4.5 K and 5.1 T, kA	
Grade I	8.93
Grade II	7.20
Copper area, cm^2	
Grade I	1.074
Grade II	1.168
Wetted area, cm^2/cm	8.17
Quarter-hard copper stabilizer tensile yield, ksi	34
Operating current, kA	5

Static stability

The static stability was analyzed to compute the heat flux required to remove the heat deposited in a normal zone. The operating heat flux includes the effects of the increase in resistivity due to radiation, the effect of nuclear heating in the conductor, and the effect of heat conduction from the coil case.

Irradiation damage is assumed to cause a 25% increase in the resistivity of copper. However, this damage will be annealed out if the coils are warmed up once a year (as proposed in the current testing approach). The calculation for heat conduction from the coil case took into account the neutronic heating of the case and the heat radiated to the case from the cold shield; the latter effect was found to be negligible compared to neutronic heating. (A detailed discussion of the calculation is contained in Sect. 4.5.3). The selected operating current limits the required heat flux to less than 80% of the critical recovery heat flux for the conductor (0.19 W/cm^2).

Margin against critical current

A plot of critical current vs field is shown in Fig. 4.27 for the C coil conductor. The operating point for these coils is indicated. The criterion for stability is to limit the operating current to 80% of the critical current (determined by the magnet load line). As shown, the operating current is only 73% of the critical current.

Helium bubble ventilation

The helium bubble ventilation has been evaluated for the coil cross section shown in Fig. 4.28. (Details of the evaluation are given in Sect. 4.5.4.) With the 10-cm-thick shielding between the plasma and the C coils, the maximum heat load on any coil is 2.6 MW. For this load, the vapor content of the helium exiting the coil is 9.4%, which is within the design limit of 10%.

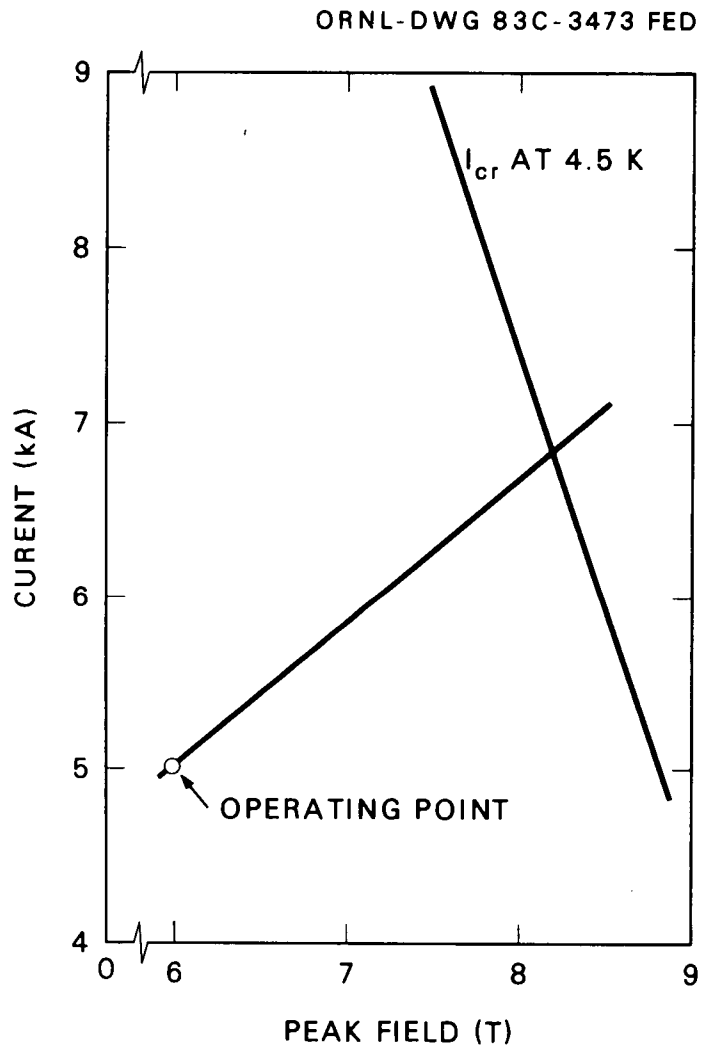

Fig. 4.27. C coil stability margin.

ORNL-DWG 83C-3471 FED

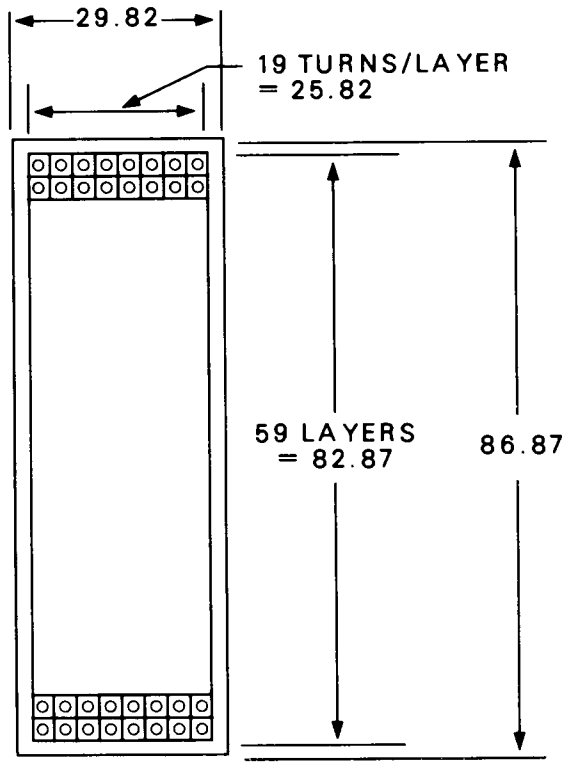

ALL DIMENSIONS IN cm

Fig. 4.28. C coil winding layout.

Winding layout

With a 5-kA operating current, 1120 turns are needed to provide the 5.6-MA·turn coil currents for the C coils. The winding layout shown in Fig. 4.28 has a total of 1121 turns.

Conductor stresses

Out-of-plane running loads accumulate from turn to turn and are transmitted in bearing to the coil case. In-plane loads are equilibrated by hoop membrane stress in each turn. The bearing stress σ_{brg} and hoop stress σ_θ in the conductor are computed as follows. For the major lobe,

$$\sigma_{brg} = f_o/N_L h$$

and

$$\sigma_\theta = f_i R_M / NA \ ;$$

for the minor lobe,

$$\sigma_{brg} = f_o / N_T h$$

and

$$\sigma_\theta = f_i R_m / NA \ .$$

Here f_o and f_i are the running loads identified in Sect. 4.2.3; R_M and R_m are the major and minor radii, respectively; N_L is the number of layers, N_T is the number of turns per layer, and N ($= N_T N_L$) is the total number of turns; h is the height of the conductor; and A is the conductor cross-sectional copper area. The computed stresses are compared with the 159-MPa allowable primary membrane stress in quarter-hard copper. The maximum σ_{brg} is 17.0 MPa in the minor lobe of the A2 coil; the maximum σ_θ is 70.6 MPa in the major lobe of the T1 coil. These stresses are obviously well within the allowable limit.

Coil case and cold structure stresses

The support structure described here for the C coils was selected following studies of several concepts (see Sect. 4.5.7). Each of the 12 C coils (6 in each end of the device) has a structural case of type 316 LN stainless steel that supports the magnet winding and acts as a Dewar flask to contain the LHe coolant. The minor lobe opening force is supported by the coil case.

The major lobe opening force is supported by a strongback and tension tie structure for each of the two transition coils (Fig. 4.29) and by a set of four identical collars for each of the plug and anchor coils (Fig. 4.30). (Because the two plug coils have a half-angle of 80°, a short flat must be built into the side of the minor radius area of their cases to permit all four collars to be identical.) Each coil in a pair acts as a C-clamp to support the greater part of its mate's major lobe opening force (Fig. 4.31). Thus, the critical section through each coil case (located midway along the minor lobe) is subjected to the axial load and bending moment that is the sum of the coil's minor lobe opening force P_A and its mate's major lobe opening force P_B.

Structural analysis of the transition coil support structure was limited to feasibility checking. The strongback structure was compared with the MFTF-B A-cell coil structure (Fig. 4.32), which was analyzed in some detail.[12]

The major lobe opening force on the T1 coil is 46.4×10^6 N; that on the T2 coil is 37.5×10^6 N (see Table 4.5). The total span of the strongback for each transition coil is $\simeq 3.4$ m. The strongback for the A-cell coil supports a load of 45.8×10^6 N and has a total span of 7.62 m (see Fig. 4.33). It was concluded that with a similar load but a

ORNL–DWG 84-16509 FED

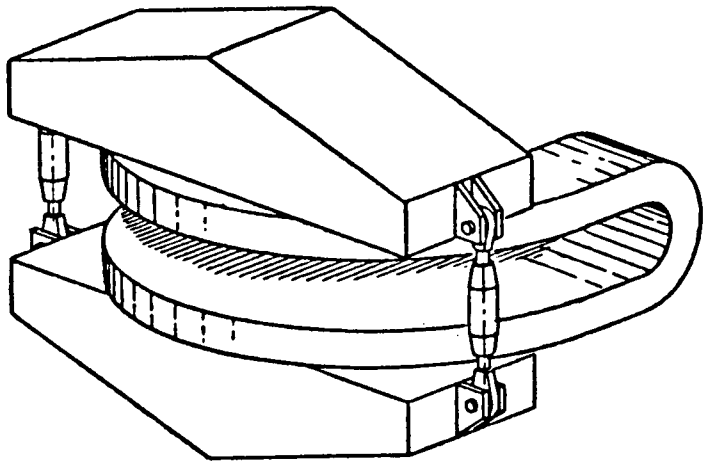

Fig. 4.29. Transition coil with strongback support structure.

ORNL-DWG 83-4021 FED

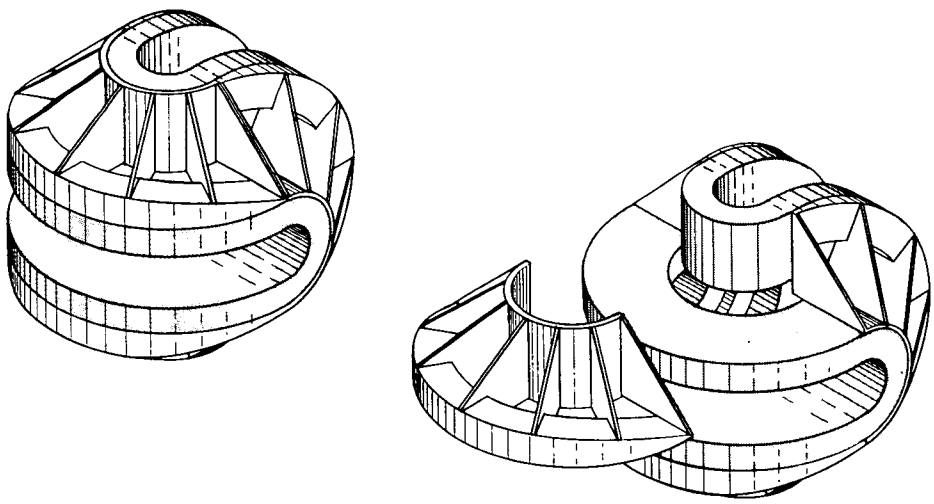

Fig. 4.30. Anchor and plug coil support structure.

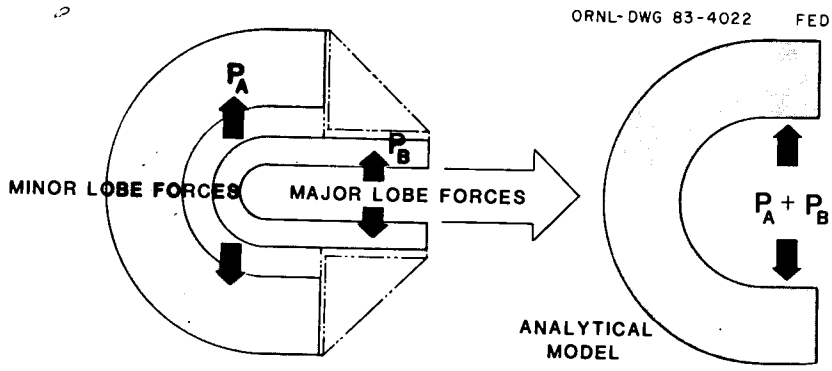

Fig. 4.31. Load path for support of anchor and plug coils.

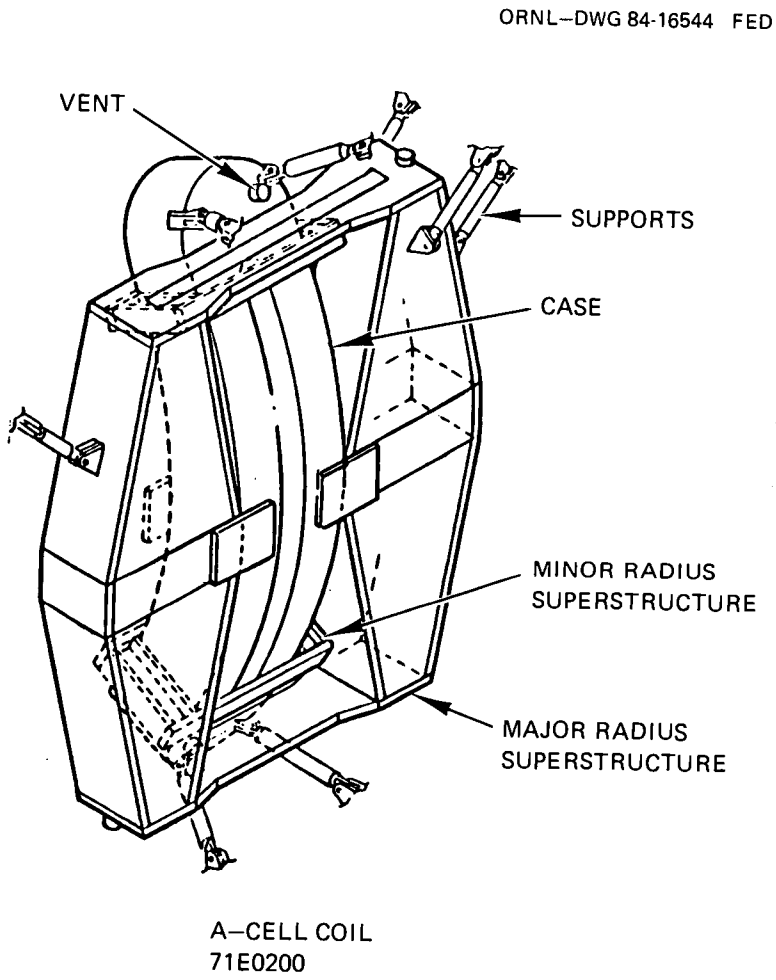

Fig. 4.32. MFTF-B A-cell.

span about half that of the A-cell strongback, a structure to support the transition coils could have a smaller depth and still prove feasible.

A minor radius superstructure was needed on the A-cell strongback to prevent part of the spreading load from entering the minor radius area of the coil (Fig. 4.33). The transition coil support structure does not include such a superstructure because (1) the transition coil half-angle is much larger than that of the A-cell coil (see Fig. 4.34), which moves the minor radius region out of the central region and decreases its relative stiffness to the

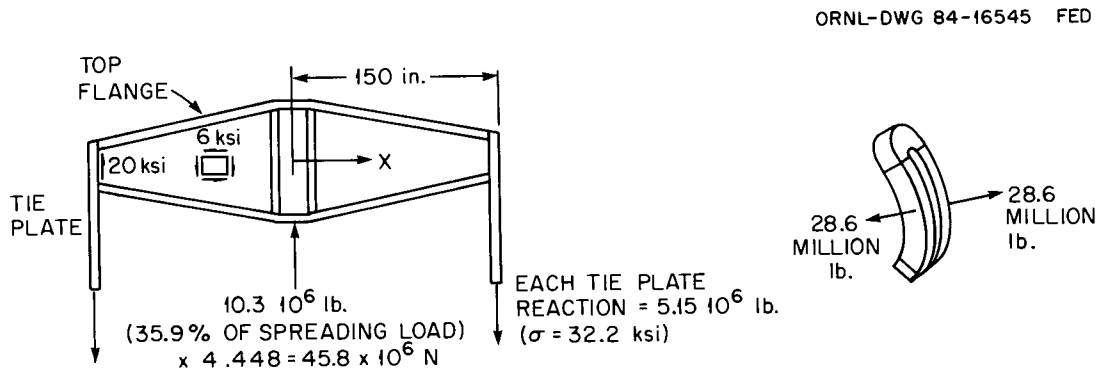

Fig. 4.33. The A-cell major radius superstructure.

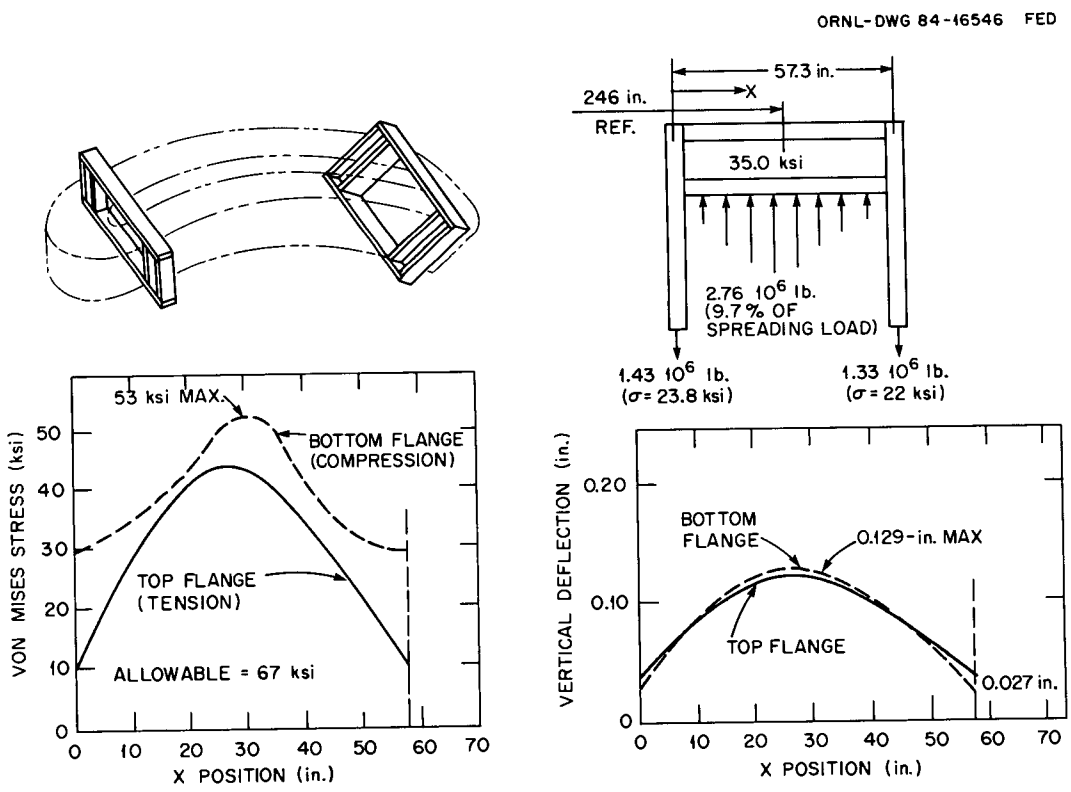

Fig. 4.34. The A-cell minor radius superstructure.

strongback in regard to support of the major lobe opening force, and (2) the span of the transition coil strongback is less than half that of the A-cell coil strongback, which greatly increases the stiffness of the strongback. An analysis of the total support system is expected to show that a minor radius clamping superstructure is unnecessary for the transition coils.

Structural analysis for the anchor and plug coils was limited to sizing the coil cases and support structure at the critical cross section (midway along the minor lobe). The stress limit was 345 MPa for combined tension and bending stress. The material needed at the outer ring was too thick and interfered with the adjacent coil structure. Because the space between coil winding cavities is used to adjust for MHD equilibrium and cannot easily be changed, the coil case structure was reconfigured. The coil minor lobe opening force P_A and the bending moment are supported by the coil case; the complementary coil's major lobe opening force P_B and its bending moment are supported by the coil case and the collar structure. Major lobe opening forces are introduced into the case, and the moment is introduced by a compression load at the outer region of the coil minor radius. This load is carried in bulk compression through a set of wedges used to accommodate manufacturing tolerances (including radius mismatch) and to ensure a tight fit. The complementary tension load is carried through the collar 1 structure into the collar 2 structure through a welded or bolted connection. The collar 2 structure carries the load into the coil through bulk compression of wedges along two areas of each major lobe. The wedges accommodate manufacturing tolerances and ensure a tight fit.

Each set of coils is assembled by locating the coils with respect to each other and installing first the collar structures and then the wedges. If necessary, a shim can be installed over the major lobe surface of the coils to allow for manufacturing tolerances. This shim could be a bladder constructed of thin stainless steel sheets and injected to conform the coil case structure to any collar structure gaps. This design is used for the MFTF-B yin-yang coil set. This system will allow alignment of the coils to produce the proper magnetic geometry.

Cryogenic load

A 1-D shielding analysis has determined maximum heating in the coil cases and windings of the end-cell coils. To compute the cryogenic load on a coil, the maximum rate from the shielding analysis was assumed to be distributed uniformly over the surface of the mouth of the coil and was integrated to yield a heat load of 2.6 kW at 4.2 K. The heat load due to radiation from the cold shield is negligible by comparison.

The 2.6-kW heat load is multiplied by 12 to account for all end-cell coils. The resulting value, 31.2 kW at 4.2 K, is conservative because it is assumed that the peak neutronic heating applies over the entire mouth of each coil and that every coil is heated equally. A three-dimensional (3-D) shielding analysis of the end-cell coils is in progress, and more realistic estimates of cryogenic loading will be made when this analysis is complete.

4.3.6 Direct Converter Coil

The DC coil will use the background (low-field) portion of the high-field axicell coil on MFTF-B, as shown in Fig. 4.2. A coil cross section is shown in Fig. 4.35.

ORNL-DWG 83-3861 FED

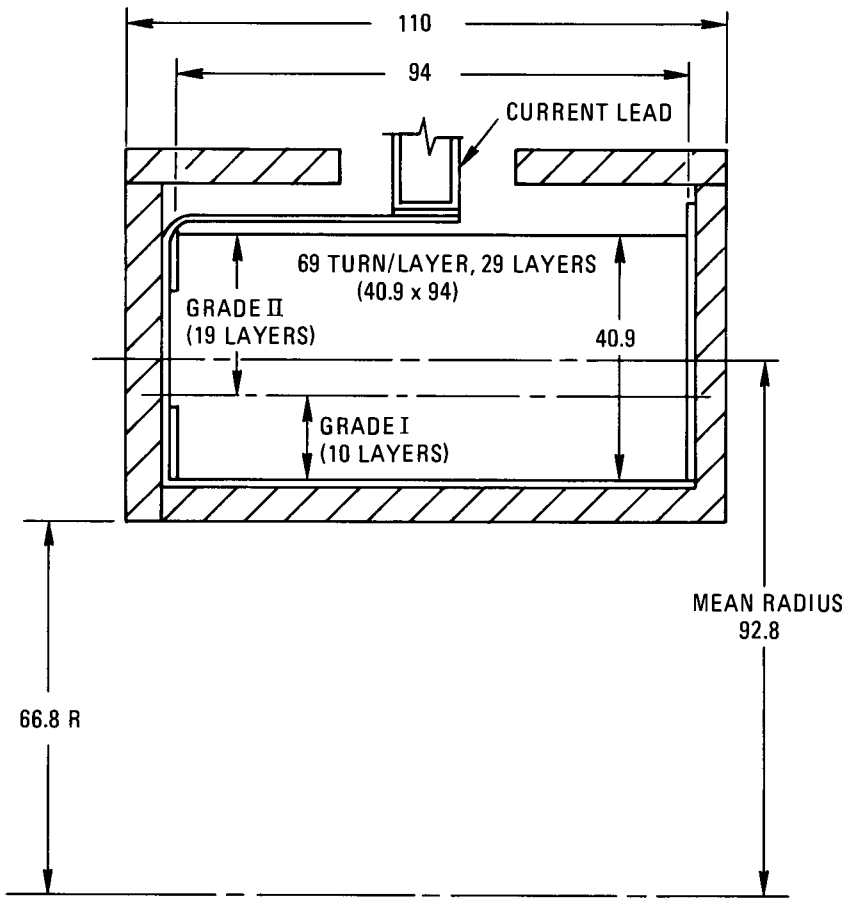

Fig. 4.35. DC coil cross section.

Choice of conductor and operating current

The winding is graded, with an MFTF-B yin-yang type I conductor in the first 10 layers (high-field portion) and a type II conductor in the other 19 layers. The operating current is 3.41 kA. Conductor cross-section dimensions are shown in Fig. 4.26, and key parameters are listed in Table 4.25.

Static stability and conductor performance

The conductor/winding must operate in a cryostable mode. The design goal is to limit the peak conductor surface heat flux at the selected operating current to two-thirds of the critical heat flux (0.19 W/cm^2). The peak heat load occurs in the high-field turns and consists of normal-zone I^2R heating, nuclear heating, and heat conducted from the coil case. Heat conducted from the coil supports is negligible. A summary of peak heat loads is presented in Table 4.26; the peak design heat flux is 0.07 W/cm^2, which is 37% of the critical heat flux.

Table 4.26. Peak heat loads and stability considerations for DC coil winding

	Winding	Coil case	Total
Peak heat loads in grade I conductor, W/cm			
Nuclear heating	0.001	0.001	0.002
Joule heating in normal zone	0.524	0	0.524
Total	0.537	0.015	0.552
Peak heat flux at the conductor surface, W/cm^2			0.07
Critical recovery heat flux, W/cm^2			0.19

Margin against critical current

The operating current is 3.41 kA, which is 75% of the operating current in MFTF-B. The peak field for the DC coils is 6.0 T, compared to 7.5 T in MFTF-B. The DC coils should therefore have a satisfactory margin against critical current, provided the stabilizer resistivity does not increase significantly.

Quench analysis

Because these coils will be operated at a lower current in MFTF-α+T than in MFTF-B, the existing dump resistor circuitry will be used. Discharge characteristics are given in Table 4.27. The discharge voltage is limited to 1000 V, and the hot-spot temperature is limited to 200 K.

Winding pack and coil case stresses

Because the DC coil will be operating at lower current and peak field in MFTF-α+T than in MFTF-B, the winding pack and coil case stresses should be acceptable.

Table 4.27. Discharge parameters for DC coils

Stored energy per coil, MJ	36
Self-inductance of each coil, H	6.04
Operating current, kA	3.41
Maximum temperature rise in the winding, K	$\leq$200
Area of copper in the conductor, cm^2	1.07
External dump resistance, Ω	0.055
Time constant with dump resistor, s	110
Maximum discharge voltage, kV	$\leq$1.0

Cryogenic load

The neutronic heat load at the inner surface of the coil case is 2 mW/cm^3. The total integrated heat load in the winding is 41 W; that in the coil case is 40 W. The total heat load is thus ~82 W/coil. These loads are calculated by attenuating the 0.16-mW/cm^3 peak load at the coil case by an e-folding distance of ~7 cm.

4.3.7 Coil Supports

The principal loading on the coil set is the axial magnetic load on each coil. In addition, the coils must be supported for any possible seismic loading. The axial force on each coil is listed in Table 4.4. No analysis of possible magnetic fault loads or of seismic loads has been carried out. The support structure discussed here is based on the MFTF-B design and on estimates of the critical loads.

The nominal axial magnetic loads and the optimum coil groupings were studied, taking into account the effects on configuration and vessel design. In the baseline design, the superconducting central-cell coils are tied together axially (Fig. 4.36), as are the superconducting end-cell coils (Fig. 4.37). A set of axial struts ties the superconducting central-cell coil set to the vessel; these struts nominally carry no load but would restrain axial motion caused by a magnetic fault condition or a seismic event. Each superconducting

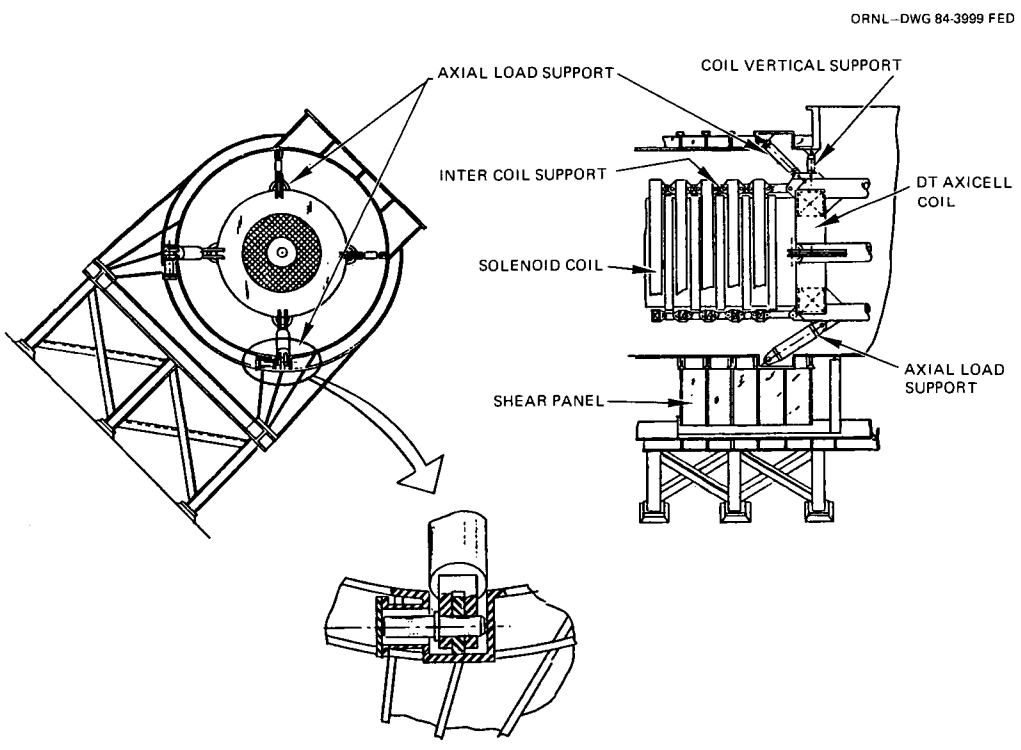

Fig. 4.36. Axicell coil supports.

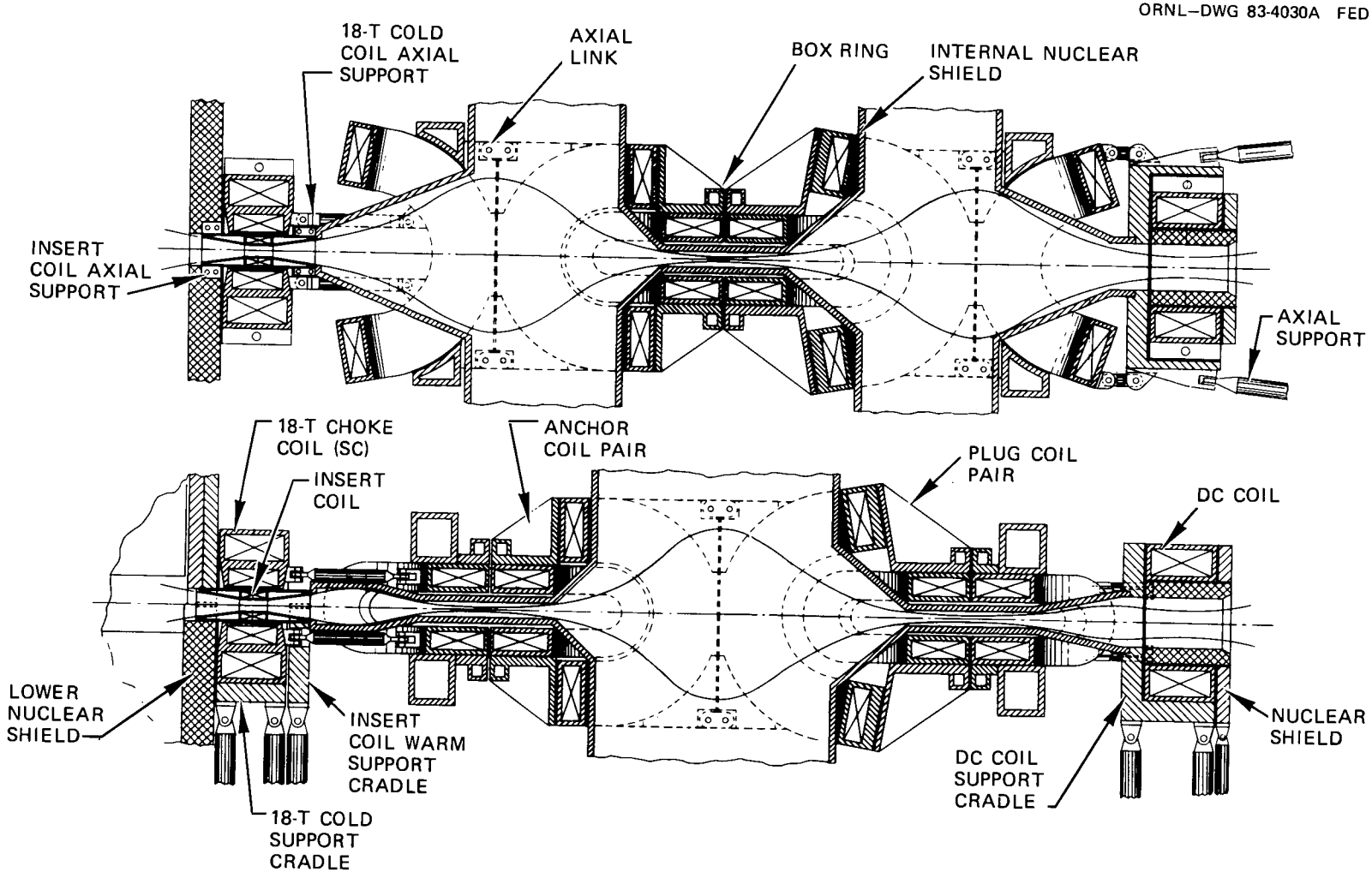

Fig. 4.37. End-cell structural support.

end-cell coil set is restrained by a pair of axial struts that carry the net axial load to the vessel; the vessel balances the complementary loads at either end of the machine. These struts also provide axial support for a fault or a seismic event.

The two D-T axicell superconducting solenoid coils are attached to each other with four corner beams (Fig. 4.38). The two lower beams are bolted to the coil cases after the coils are installed; the two upper beams are bolted into place after the central shield module is installed. The central-cell solenoids are linked to each other and to the D-T axicell solenoid coil assembly by sets of struts (each set consists of four struts). The entire central-cell and D-T axicell superconducting coil set is axially restrained by a set of four struts that attach the west wall of the D-T axicell superconducting solenoid coil to the vessel (Fig. 4.36). The axial loading is transmitted to the ground by a set of shear panels and by the vessel support frame. The D-T axicell coils are hung from the vessel sill beam

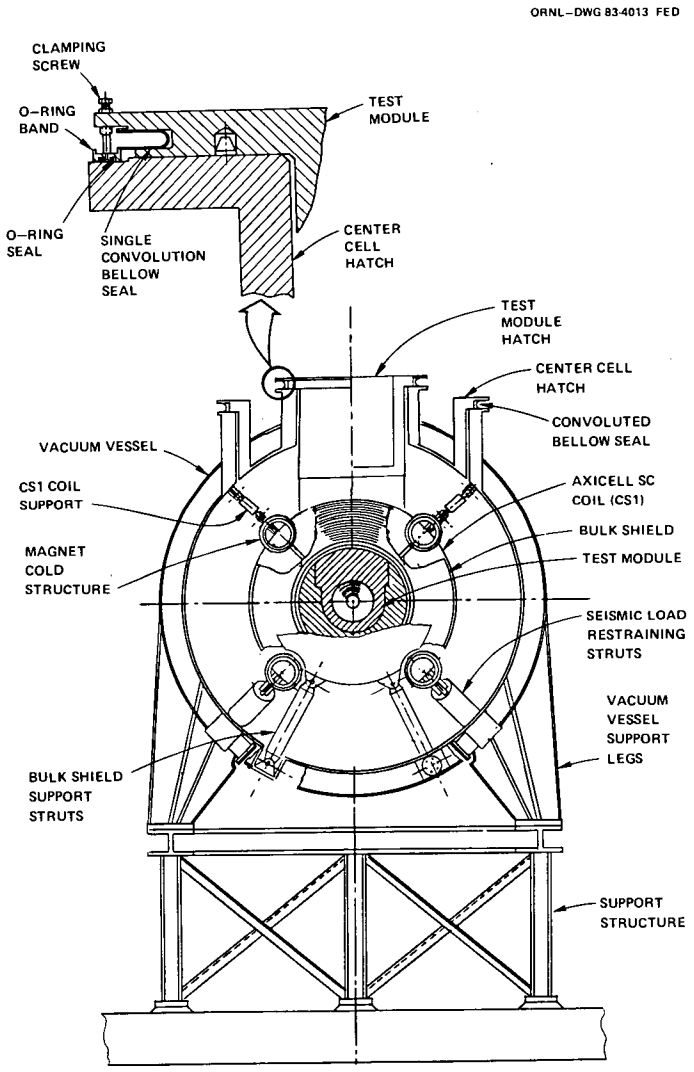

Fig. 4.38. Elevation through D-T axicell.

by a pair of struts that provide vertical and lateral support (Fig. 4.36); this system is also used for the central-cell superconducting coil set (Fig. 4.39).

The alignment of the superconducting coils can be corrected by adjusting the hanger and axial struts, and the spread of the two D-T axicell coils can be ensured by machining and/or shimming the ends of the four beams. To measure the relative position of the coils, optical techniques like those routinely used to align major airframe subassemblies [e.g., for the space shuttle and the Tokamak Fusion Test Reactor (TFTR)] may be used. Optical targets can be placed on a coil in a known location with respect to the coil's current center (which can be determined with eddy current loops) and used to locate the coil very accurately to ensure the correct magnetic geometry.

The two normal conducting 12-T coils are supported by the nuclear shielding in the D-T axicell. The adjacent shield module, which is similar to a large washer with the coil secured to it, is made to support the coil (Fig. 4.40). The coil's coolant piping is routed

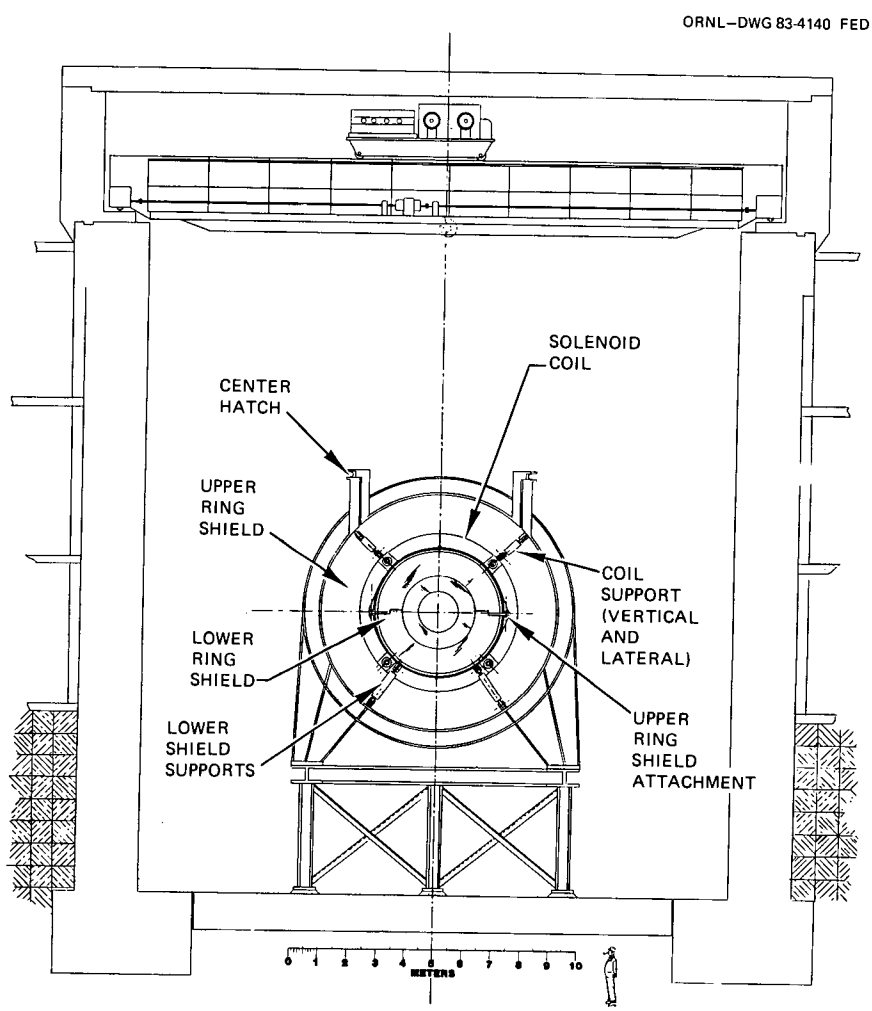

Fig. 4.39. Central-cell configuration and supports.

ORNL–DWG 83-4026A FED

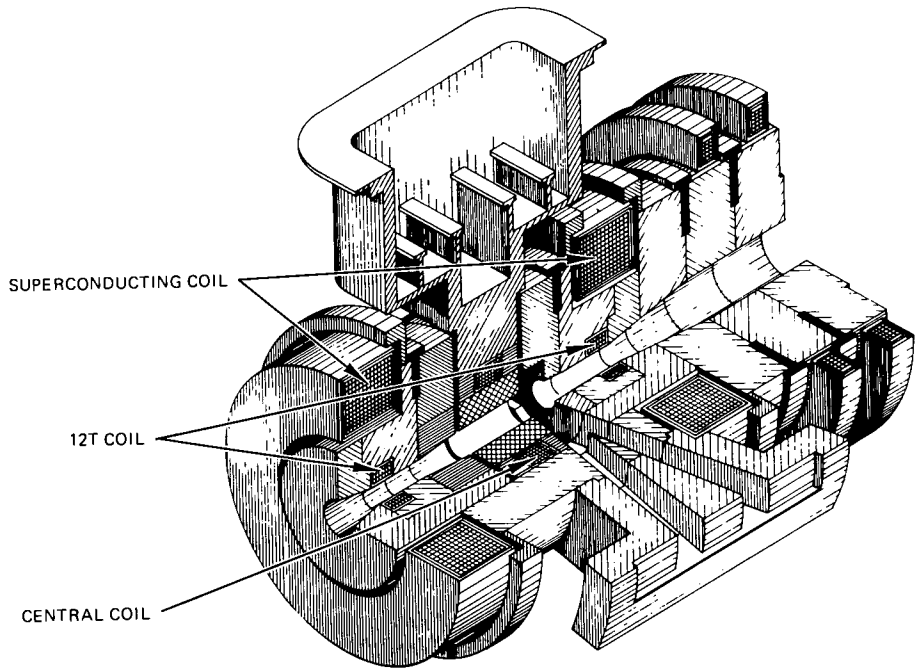

Fig. 4.40. D-T axicell normal conducting coil support.

within the shield to the top of the machine. The axial magnetic load of 1.716×10^6 N, which tries to move the coils toward the center of the machine, is taken in compression by a set of wedging pads that transfers the load so that it can be balanced in bulk compression from the 12-T coil module to the inner shield module. The axial coil load is then carried by a set of pins into the outer shield module and similarly into the central shield module. The wedging pads are adjustable to ensure a tight fit. Magnets are aligned by adjusting the shoulder connections (Fig. 4.41) that attach the coil/shield module to the center shield module. The pads on the end of the shield section, which is positioned inside the superconducting coil, are preadjusted to ensure axial alignment.

The coil/shield module assembly is installed and removed with a remotely actuated handling fixture positioned on a set of pins at the center of the machine. The fixture rests on a set of rails that are permanently attached to the bottom of the center shield module. The fixture moves to the coil/shield assembly, where a set of remotely activated pins attaches the assembly to the fixture. The fixture then moves the assembly to a place beneath the access cover so that it can be lifted by the overhead crane. To replace the shield/module assembly (e.g., after installation of a new coil in the hot cell), the process is reversed. The fixture moves the module until it rests against the preadjusted support pads on the adjacent central shield module. The handling fixture can be lifted and rotated 180° so that it can service both 12-T coils. This coil replacement method is similar to the method used for blanket assembly replacement in the Mirror Advanced Reactor Study

ORNL–DWG 83-4027A FED

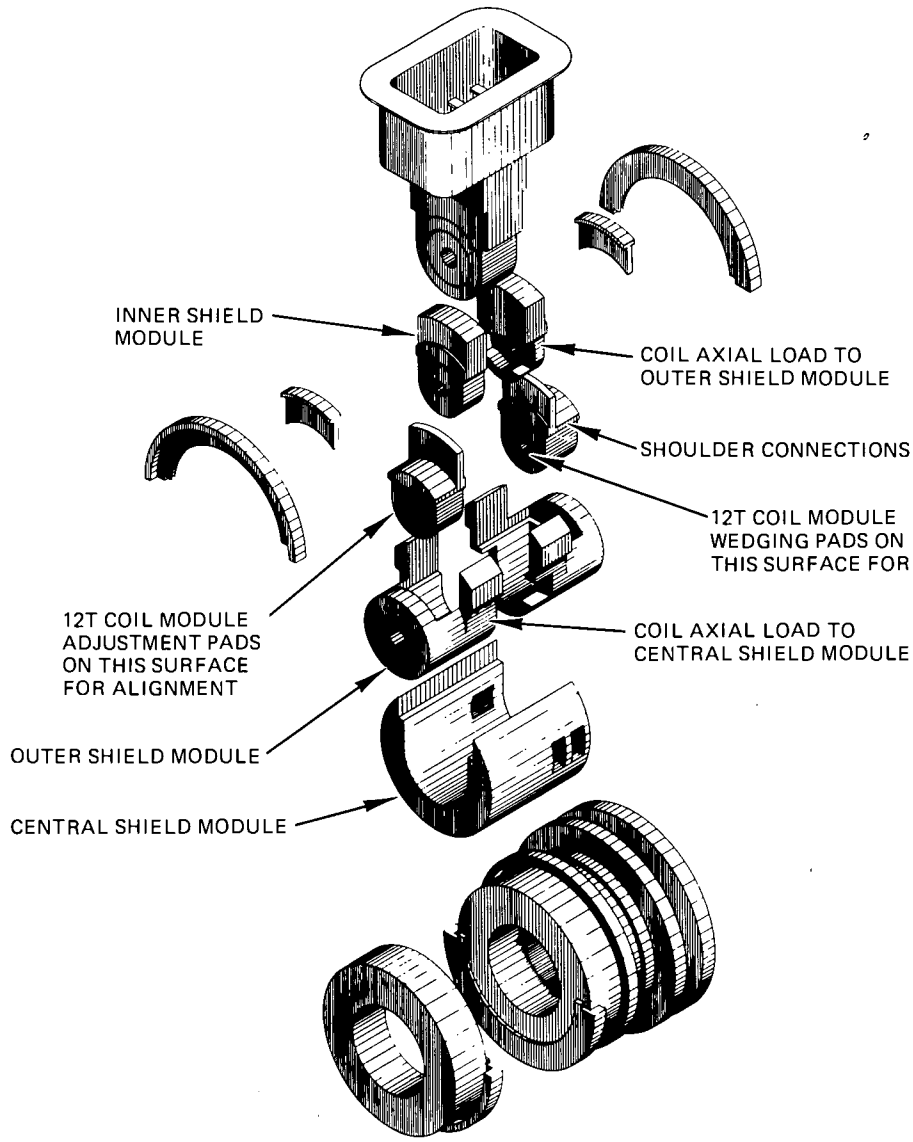

Fig. 4.41. Exploded view of central cell.

(MARS) design. The development of this technique in MFTF-α+T will be useful for future devices.

The normal conducting central coil is supported as an integral part of the blanket test module (Fig. 4.40). It is expected that, because each test module will be unique, a new central coil will be provided whenever the test module is replaced.

The 18-T choke coil consists of a normal copper insert coil and an outer superconducting coil. These coils are supported separately. The superconducting coil is held by a cradle structure, which is supported by a set of struts (Figs. 4.37 and 4.42). The struts are

ORNL–DWG 83-4014A2 FED

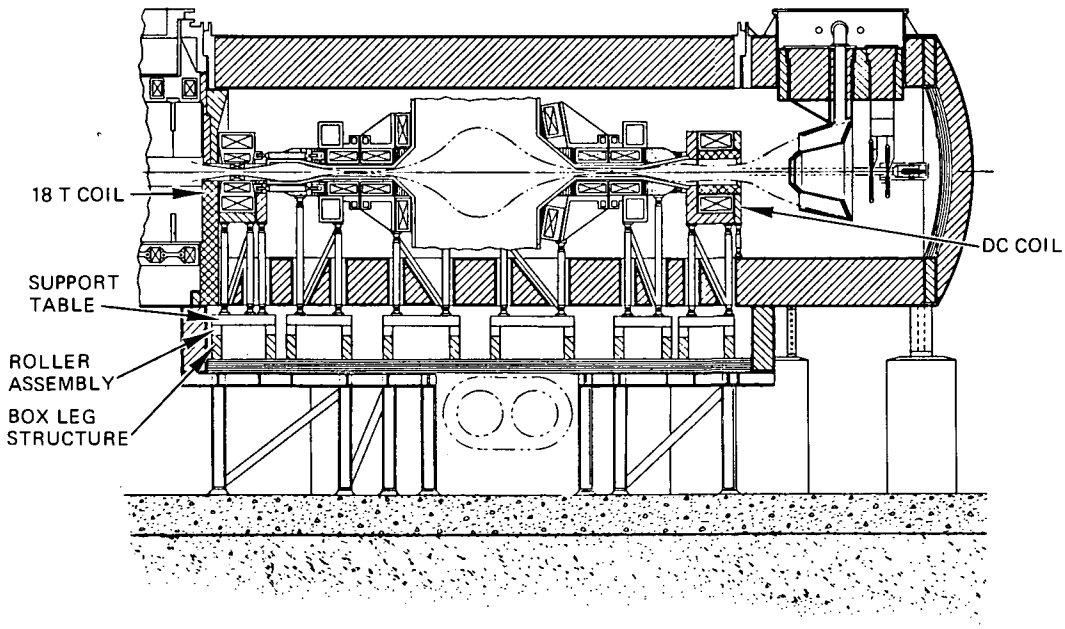

Fig. 4.42. End-cell longitudinal elevation.

attached to a special support table, which is dedicated to the support of the 18-T coil and mounted on a set of four special roller assemblies attached to box leg structures. This design is also used for all of the C coils. The roller assemblies allow axial motion during cooldown of the LHe-cooled coil set but restrain vertical and lateral motion. They are based on the Large Coil Test Facility (LCTF) spider-frame support structure, with the table replacing the spider frame. The cradle and struts are considered permanent and are not removed with the coil. The struts also reduce the refrigeration load. The superconducting coil has two shoulder structures that rest on the cradle. The coil is secured to the cradle by a pin and a pair of bolts at each shoulder. The LHe-cooled coil and its supporting structures are surrounded by an LN_2-cooled cold wall. The design is similar to that of the DC coil support described below.

The normal conducting coil of the 18-T coil set will be axially prepositioned so that its position with respect to the superconducting coil will be correct after cooldown of the superconducting coil set. This is necessary because the superconducting coils are all linked together and restrained at the DC coil, and a small but significant axial shrinking will result upon cooldown.

The insert coil has extensions on each end that project out of the superconducting coil. Each extension has a pair of shoulder structures that rest on a warm cradle structure. The coils are attached to the cradle by a pin and a pair of bolts at each shoulder. The cradle on the side of the coil toward the center of the machine is a boxlike structure filled with steel shielding and supported by the vessel (Fig. 4.37). The 18,300-N axial load on the insert coil is carried to the vessel by this structure.

The insert coil in the 18-T choke coil will probably require replacement every 30 months. The coil support system was designed to allow the coil to be replaced via remote maintenance. The normal conducting portion of the 18-T coil rests on a set of pads within the superconducting coil's bore. The pads prevent crushing of the cold wall within the bore. The shoulders of the inner coil bottom out on their support cradles after the aligning pins engage as the coil assembly is lowered. Then the coil lifts off the pads. The outer superconducting coil shoulders bottom out on their support cradle. Finally, the superconducting coil's axial struts are swung into position, and pins are inserted.

The transition, anchor, and plug coils are all supported by struts and cold tables mounted on roller assemblies with box legs (Fig. 4.42). The design is similar to that for the 18-T coil, except that the legs are attached to the cold tables by pinned connections that can be remotely withdrawn, so any coil that fails prematurely can be replaced (Fig. 4.43). Remotely activated pin pullers can be installed through a set of ports in the vessel trough structure.

The DC coil is supported on a cold cradle mounted on a set of struts attached to the vessel (Fig. 4.42). This structure is considered permanent. Shoulder structures on the coil rest on the cradle and are attached with pins and bolts (Fig. 4.44). The T2 coil case is attached to the highback structure of the DC coil cradle (Fig. 4.45) by four struts that are sized to support the axial magnetic load and any seismically induced axial load from the superconducting portion of the 18-T coil and the C coils. The magnetic loading produces a

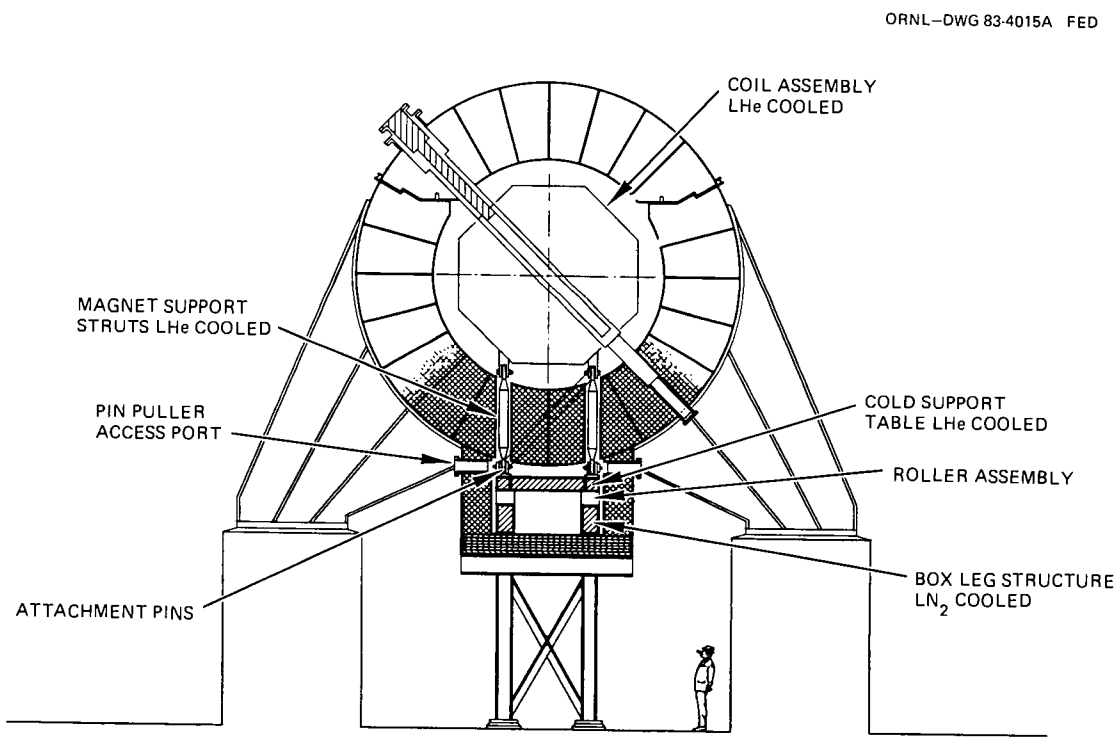

Fig. 4.43. C coil support.

ORNL–DWG 84-3997 FED

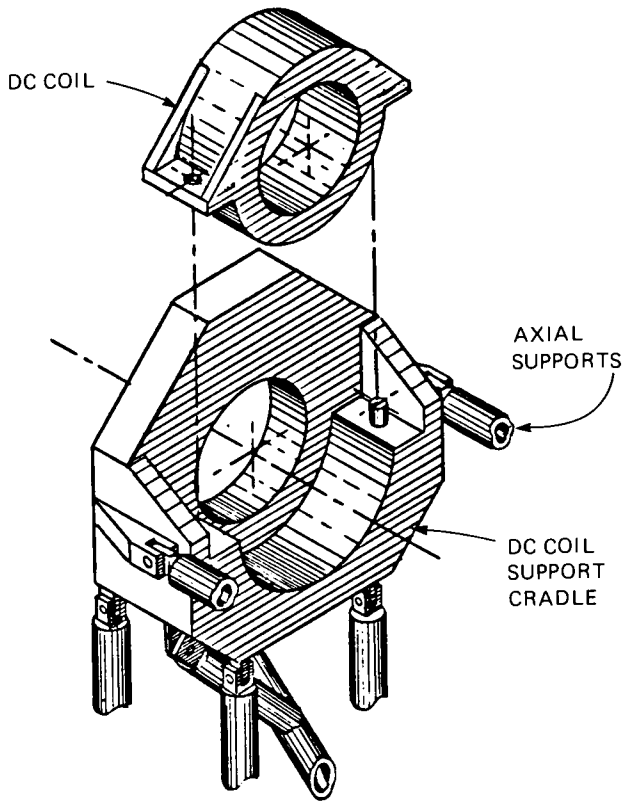

Fig. 4.44. DC coil support structure.

ORNL–DWG 84-3996 FED

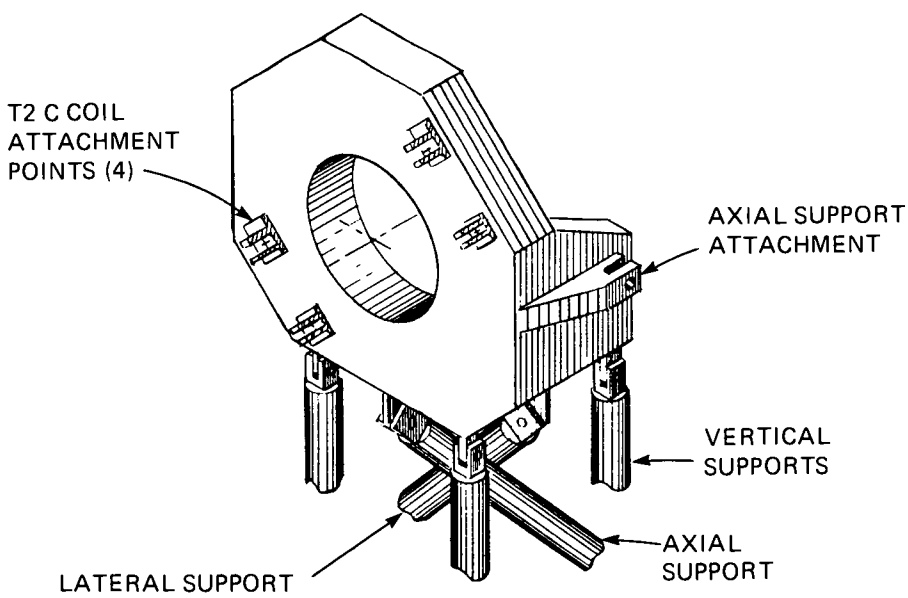

Fig. 4.45. Support for T2 coil case on DC coil support structure.

total tension load of 6.44×10^6 N, and the DC coil has a centering force of 6.97×10^6 N. The sum of these two loads is carried to the vessel by two axial struts attached to the DC coil support cradle. These struts are attached to the vessel attachment fittings, and the vessel shears this load to its outer wall by internal shear panels. The kick loads are balanced by an internal vessel ring beam. The outer vessel wall balances the two axial strut loads with the complementary loads at the opposite end of the machine. The DC coil cradle and the two axial struts are considered permanent. Because the C coil loading is carried directly to the axial struts through the cradle structure, the DC coil case and its attachment pins can be sized for the loading of this coil only. The C coils are axially tied together by a set of links (Fig. 4.37), as are the 18-T superconducting coil and the T1 coil case. This system provides a direct load path for the axial loading and lends itself to the remote replacement of any of the coil assemblies, if necessary.

The entire set of superconducting coils, their cold support structure, and their supporting struts are surrounded by an LN_2-cooled cold wall. This thermal radiation shield is supported on thermal isolation standoffs, which are located on the LHe-cooled structure. The cold mass box leg structures also have LN_2-cooled sections to further reduce the refrigeration load.

4.3.8 LN_2-Cooled Cold Shield

An LN_2-cooled cold shield around each of the LHe-cooled superconducting magnets will shield the helium vessels from radiation heat load and from room-temperature surfaces. A 10-cm envelope has been reserved next to all LHe-cooled magnet cases to accommodate the cold shield and clearances. In areas where space is restricted (e.g., at the corners of the case and next to neutral beam penetrations), the envelope has been reduced to 5 cm. In these areas, flat copper bars or sheets can be used instead of actively cooled panels to conserve space. Cooling in these areas is provided by conduction in the plane of the copper insert to its actively cooled edges. It has been estimated that the surface area of the cold shield will be approximately 1410 m^2 and that the radiation heating of the cold shield from warm surfaces will be 322 kW at 77 K.

4.4 CRYOGENIC SYSTEM

The cryogenic system of MFTF-B must be upgraded to meet the requirements for MFTF-α+T. In this section, these requirements are summarized and the necessary modifications to the system are described.

4.4.1 Summary of Cryogenic Loads

Without the neutron and gamma heating, the cryogenic load of the MFTF-α+T device would require only a moderate upgrade of the MFTF-B facility, corresponding to the addition of a few new magnets and the neutral beam heating systems. However, the neutron and gamma heating of the superconducting magnets, supports, and cryopanels will be the dominant load on the system as it is now understood. This load is comparable to all

other cryogenic refrigeration loads combined, but it is the least well understood of all the cryogenic loads because of physics uncertainties, lack of time to perform 3-D neutronics analyses, and lack of opportunity to redesign the shielding for the increased refrigeration load. The refrigeration system described here is thus based on a best estimate of the load but highlights the need for further work to calculate and reduce the integrated load.

As shown in Table 4.28, the total helium load is 25.5 kW at 4.35 K, dominated by 13.9 kW of neutron and gamma heating. The coil heat loads include a 3.2-kW component for the superconducting coils in the 18-T choke coil. The size of the 18-T copper insert must be iterated in the future to reduce this load to a more reasonable value. If a reserve capacity of 6.3 kW is included and credit is taken for the existing 11.1-kW facility for MFTF-B, the amount of new refrigeration needed is 20.9 kW. This is comparable in overall size to the refrigerator procured for the Isabelle project.[13]

The nitrogen cooling requirements are approximately one-third larger than those for MFTF-B[14] and are not proportionally as affected by neutron and gamma heating as are the helium loads. As shown in Table 4.29, the nitrogen refrigeration load is estimated to be 555 kW. With a reserve capacity of 120 kW and the existing capacity of 500 kW at MFTF-B, the new nitrogen refrigeration required is 175 kW.

Table 4.28. Summary of helium cryogenic loads

Load type	Load, kW	Temperature, K
Radiation	1.42	4.35–77
Cold mass supports	1.97	4.35–77
Neutron and gamma heating	13.9	4.35
Main cryopanels	5.2	4.35
Neutral beam cryopanels	1.0	4.35
Miscellaneous	2.0	4.35
Total helium load	25.5	4.35
Refrigeration reserve	6.3	
Total capacity required	32.0	4.35
Existing MFTF-B capacity	11.1	
New refrigeration required	20.9	

Table 4.29. Summary of nitrogen cooling requirements

Load type	Load, kW	Temperature, K
Radiation and conduction	220	85
Cryopanel shields	185	85
Neutron and gamma	50	85
Miscellaneous	100	85
Total nitrogen load	555	85
Refrigeration reserve	120	85
Total capacity required	675	85

The neutron and gamma heating of the magnets, their supports, and the neutral beam cryopanels is shown in Table 4.30. The total of 13.9 kW includes several moderately high loads, precluding the simple solution of overshielding a single dominant load. The largest single load is that of the CC2 superconducting insert coil, which constitutes 20% of the total.

Table 4.30. Neutron and gamma heating cryogenic refrigeration loads

	Surface load from case, mW/cm^3	Surface load from winding, mW/cm^3	Total load from case, W	Total load from winding, W
DC	0.16	0.07	7	30
T2	5	2.1	4	7
P2	5	2.1	4	7
P1	5	2.1	4	7
A2	5	2.1	4	7
A1	5	2.1	4	7
T1	5	2.1	4	7
CC2[a]	46	27	970	3,200
S1–S5	0.004	0.003	0.39	0.43
CS1	0.32	0.14	8.3	20
Supports				2,000
Cryopanels				3,000
Total, E+W				13,900

[a]Superconducting portion.

4.4.2 Refrigerator Configuration

Despite the dominance of neutron and gamma heating, the refrigeration loads presented in MFTF-α+T are not significantly different from those in MFTF-B. Thus, the most obvious approach to the refrigerator configuration is simply to purchase two new refrigerator units identical to the MFTF-B system, providing the economies associated with a repeat purchase. A variation on this would be to separate the nitrogen cooling loop and purchase only one new nitrogen cooling system, since the nitrogen requirements are less than double those of MFTF-B.

The basic refrigerator configuration of MFTF-B has been described by Van Sant,[14,15] Cornish,[16] and Sterbentz.[17] Its principal features include the provision of liquid helium at 4.35 K to all magnets and cryopanels, nitrogen refrigeration at 85 K, liquefaction and LHe storage, closed-loop recovery, and purification of helium gas. Liquid helium flow from the supply Dewar flasks to the load is by natural convection. The Dewar flasks are located about 15 m above the load inlets, allowing rapid flow in response to high neutron and gamma loads without mechanical pumps. The refrigerator configuration, as described by Van Sant,[14] is shown in Fig. 4.46.

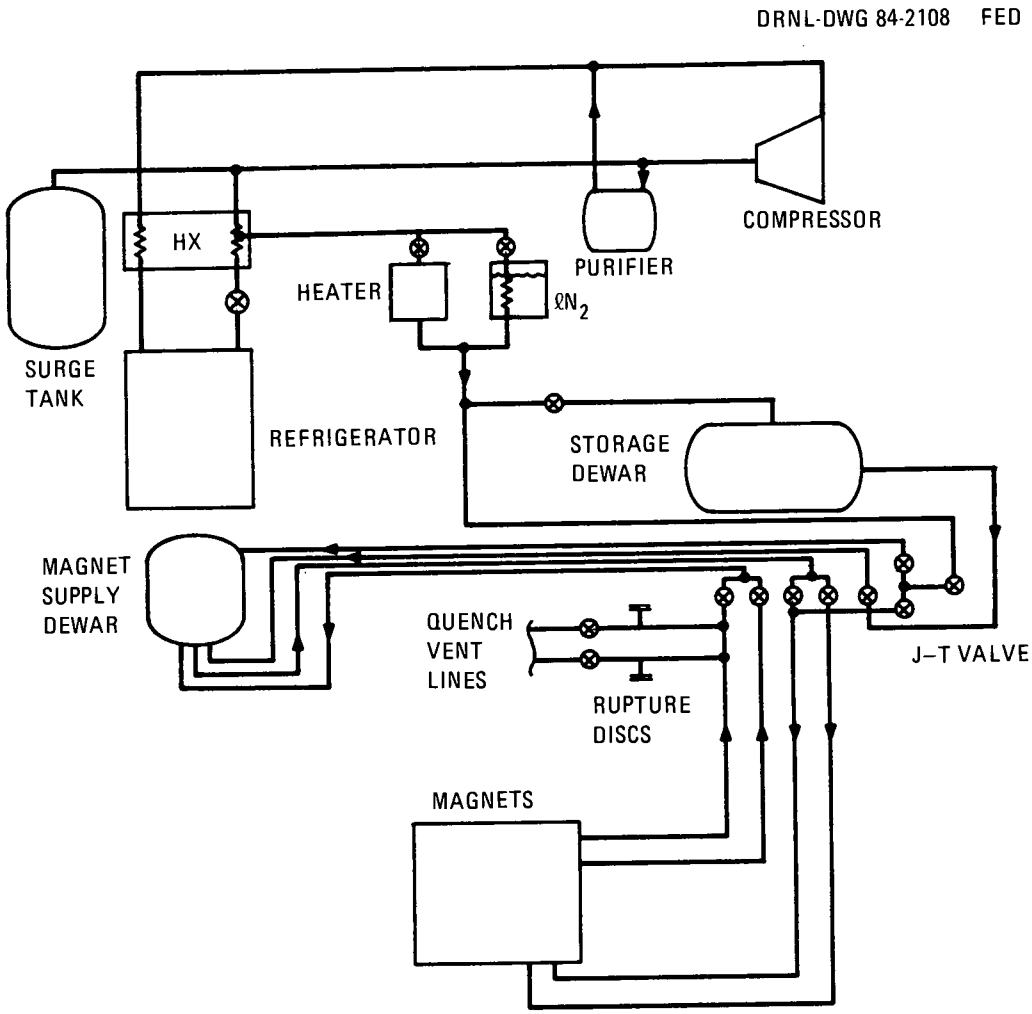

Fig. 4.46. MFTF-α+T refrigerator system. (Courtesy of J. H. Van Sant.)

A 90,000-L storage Dewar flask would provide enough helium for 2.5 h of steady-state operation, without refrigeration. It would also allow final fill from 20 K of the magnets and cryopanels.

The refrigerator can operate in several different modes, including cooldown, D-T operation, hydrogen operation, and recovery from quench. The mass flow requirements for D-T operation and hydrogen operation are shown in Fig. 4.47.

4.5 TRADE STUDIES

4.5.1 D-T Axicell Configuration

The D-T axicell comprises the CS0, CS1, and CC1 coils. The baseline configuration of these coils (see Table 4.2) evolved through a trade study that evaluated several alternatives, with emphasis on reducing cost.

ORNL-DWG 84-2109 FED

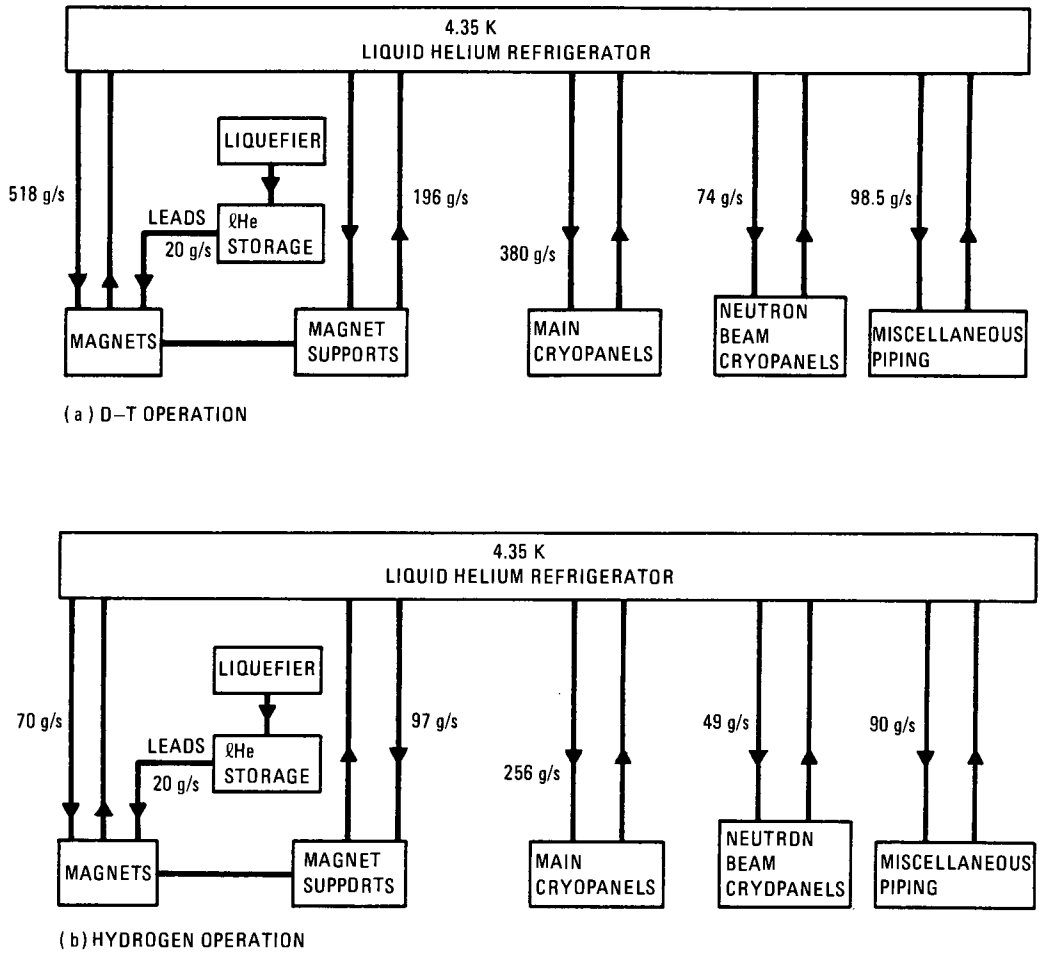

Fig. 4.47. Mass flow requirements. (Courtesy of J. H. Van Sant.)

The axicell design requirements (see Sect. 4.1.1) are a field on axis of 4.5 T at Z = 0 and 12 T at Z = ±2 m, superconducting coils that clear the neutral beam ducts with 25-cm-thick shielding, a coil case and cold wall that take up ~10 cm of radial space (the remaining ~90 cm can be used for shielding), and clear access to the blanket test module.

In addition to the functional requirements, the following criteria and objectives apply.

- Ripple: The field on axis must provide satisfactory MHD stability. The field ripple must be within an acceptable limit; it is estimated that a 10% ripple will be acceptable.
- Peak fields: The peak fields in the windings of the superconducting coils should not exceed 12 T, and an 8-T limit is preferred to avoid the need for Nb_3Sn conductor (a less mature technology than NbTi).

- Power requirements: To avoid upgrading the feeder line to the site, the ac power should be limited to 10 MW in the axicell.
- Number of coils: All else being equal, the system with the fewest coils is preferred.

The simplest approach to meeting the functional requirements is a simple mirror. A single pair of coils, each carrying 26.2 MA·turns with a radius of 1.442 m and located at $Z = \pm 2$ m, would meet the field-on-axis requirements. The peak field would be 15 T. If these coils were resistive, however, their power requirement would be ~200 MW, which is clearly unacceptable.

The next possibility considered was a set of three coils: a single resistive coil at $Z = 0$ with a 1-m radius (so that it would fit around the test module) that would produce 4.5 T on axis at this point and a pair of resistive choke coils at $Z = \pm 2.0$ m with a 0.32-m radius that would produce the 12-T choke field. Because these coils were so close to the axis, the field dipped to a minimum of 1.7 T at $Z = \pm 1.2$ m. This is an unacceptable ripple.

As a result of these studies, three configurations (shown in Fig. 4.48) were considered in detail. It was concluded that a minimum of four axicell coils is required—a pair of background coils (superconducting to reduce ac power requirements) on either side of the machine center, in order to clear the beam ducts, that will provide the 4.5-T field on axis

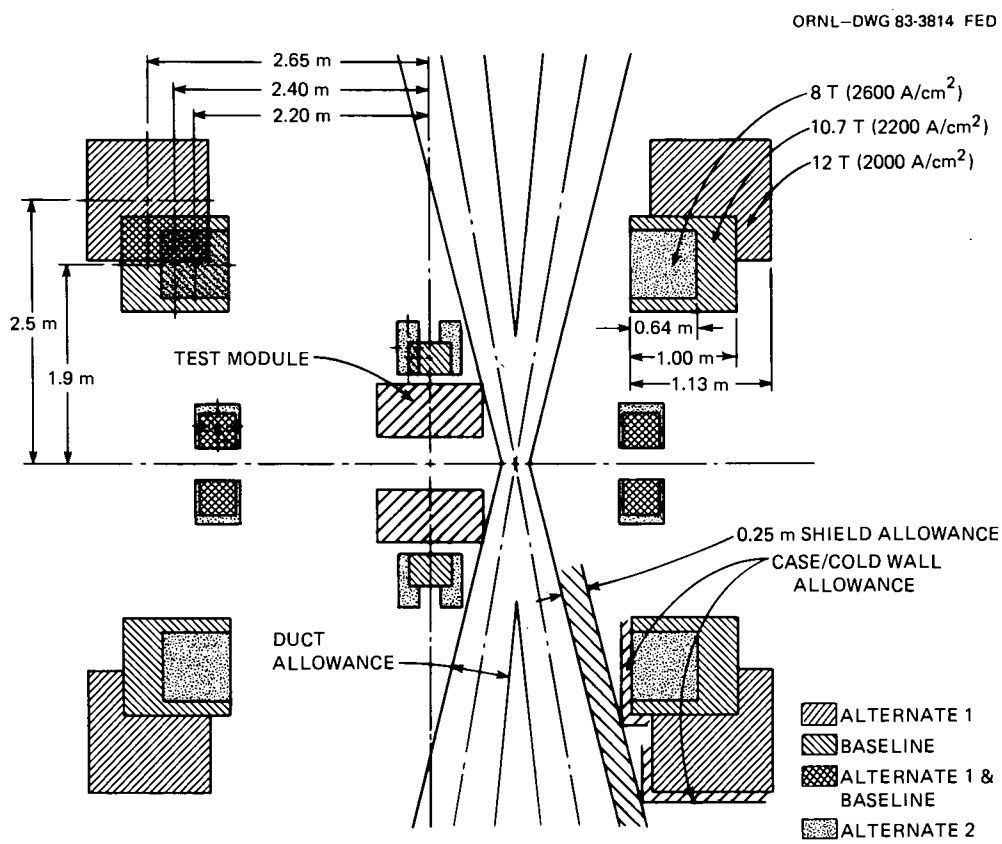

Fig. 4.48. Composite of baseline, alternative 1, and alternative 2 configurations.

at $Z = 0$ and a pair of resistive choke coils at $Z = \pm 2$ m that augment the field of the background coils to produce the 12-T choke field. A coil set with these features is designated alternative 1 in Fig. 4.48. Two other configurations, designated baseline and alternative 2 in the figure, vary the four-coil set by placing a resistive coil or coils at $Z = 0$ in the shadow of the test module to provide some of the 4.5-T field on axis at this point.

The three configurations are compared in Tables 4.31 and 4.32. Table 4.32 clearly illustrates the cost advantage of placing the resistive coil or coils in the shadow of the test module. Alternative 1, which has no coils in this location, is nearly twice as expensive as

Table 4.31. Coil configurations for the D-T axicell

Coil	Mean axial position Z_m, m	Mean radial position R_m, m	Axial build ΔZ, m	Radial build ΔR, m	Winding current density, A/cm^2	Ampere-turns, MA·turns
			Baseline			
CC1	±2.00	0.32	0.34	0.34	2450	2.83
CS1	±2.40	1.90	1.00	0.90	2200	19.80
CS0	0.00	1.0	0.40	0.30	1420	1.70
			Alternative 1			
CC1	±2.00	0.32	0.34	0.34	2450	2.83
CS1	±2.65	2.50	1.13	1.13	2000	25.53
			Alternative 2			
CC1	±2.00	0.36	0.42	0.42	2750	4.85
CS1	±2.20	1.90	0.64	0.64	2600	10.65
CS0	±0.20	1.10	0.20	0.59	1950	1.95

Table 4.32. Comparison of axicell configurations

	Baseline	Alternative 1	Alternative 2
Cost,[a] millions of dollars			
Capital	21.8	44.9	10.1
Operating[b]	7.1	4.8	13.4
Ripple, %	3.5	0	8.5
Peak field in superconducting coils, T	10.7	12.0	8.0
AC power, MW	9.5	4.9	19.0

[a]Based on a 10-year life at a 10% duty factor.

[b]Based on electrical power cost of \$0.05/kWh and demand charge of \$2.50·kWh/month.

the next most costly option. Introducing coils at $Z = 0$ reduces the required ampere-turns from 25.5 MA·turns (alternative 1) to 19.8 MA·turns (baseline) or 10.7 MA·turns (alternative 2). In addition, the radius of the background coils can be reduced from 2.5 m to 1.9 m. Both effects reduce the capital cost of the superconducting coils, which is a major system cost driver. Introducing coils at $Z = 0$ also makes it possible to reduce the peak field in the winding of the superconducting background coils.

Although alternative 2 is the most economical and has a low enough field to obviate the need for Nb_3Sn technology, the 8.5% ripple of this configuration is close to the design limit, and the 10-MW limit on ac power is exceeded. The baseline configuration has a ripple of almost zero, and its ac power requirements are within the design limit. The baseline was the selected configuration based on these considerations.

4.5.2 Central-Cell Configuration

(During FY1983 activities on MFTF-α+T, a trade study was conducted that later proved to be largely academic because of changes in the magnet system configuration. It is documented here because it is somewhat relevant and because it dealt with a problem that is to some degree generic to the insertion of a high-field axicell into a low-field solenoid.)

During baseline definition of the central-cell configuration, a potential problem was discovered with the axial forces on the central-cell solenoid coils. A magnet system configuration (designated alternative 1 in Sect. 4.5.1) was selected in February 1983 as a point of departure for trade studies. This configuration incorporated four solenoid coils in each central-cell region, located at $Z = \pm 4.375$ m, ± 5.625 m, ± 6.875 m, and ± 8.125 m. These coils were to be MFTF-B solenoid coils, which have a mean radius of 5 m and (on MFTF-B) carry 1.7 MA·turns in a peak field of ~ 3.0 T. Calculation of fields and forces revealed that the out-of-plane (axial) magnetic running load on these coils in the February 1983 baseline would be much higher than the loads in MFTF-B. The projected loads ranged from 0.65 MN/m to 3.2 MN/m, with the largest load on the solenoid closest to the axicell; on MFTF-B, the largest axial running load is 0.038 MN/m.

The greatly increased axial load results from the proximity of the background (CS1) coils, which carry a very high current, and in particular from the radial component of field attributable to these coils. There are three areas of concern about the effect of this loading on the MFTF-B coils. The first is overstressing the conductors. Axial forces on each turn of the conductor accumulate from turn to turn and are borne by the side wall of the case in bearing. Preliminary evaluation indicated that this would not be a problem, because conductor bearing stresses are quite low, even for the greatly increased side wall load. A second concern is plate bending of the coil case side wall as the result of winding pack bearing load. Preliminary evaluation indicated that the side wall would need to be stiffened (e.g., with doubler plates or stiffening ribs). The third concern is beam bending of the coil case. Coils are supported against axial loads by intercoil struts at four evenly spaced locations around the coil periphery. The coil case must bridge the gaps between support locations, transmitting the axial running load to the supports in beam bending. Preliminary evaluation indicated a need for additional intercoil support structure (e.g., compression panels around the circumference of the coils).

An effort was made to reduce the running loads, first by reducing the coil currents as much as possible, consistent with the requirement that the field in the central cell dip to no less than 2 T on axis, without changing the number or axial locations of the coils. In the February 1983 baseline, all coil currents were 1.7 MA·turns. If the currents are reduced to 0.864, 1.33, 1.51, and 1.6 MA·turns (with the lowest current in the coil closest to the CS1 coil), the axial running loads are reduced to levels from 0.50 to 1.7 MN/m. Again, the coil closest to the axicell is the most severely loaded. This set of reduced coil currents was optimized to minimize the maximum axial running load for four solenoid coils in each central cell, located at the February 1983 baseline locations and with a minimum field on axis of 2 T in the central cell.

Following the axicell trade study described in Sect. 4.5.1, the baseline D-T axicell configuration was changed; the February 1983 baseline became alternative 1. Although currents in the solenoid coils have not been optimized for the present baseline, the changes in the axicell configuration have significantly ameliorated problems with the central-cell magnet system.

In the present baseline, the background axicell (CS1) coils carry a lower current than before (19.8 vs 25.5 MA·turns), which reduces the background field. The diameter of the CS1 coils has been reduced from 5.0 m to 3.8 m, which locates them farther from the central-cell solenoid coils and therefore diminishes their effect on the S1 coil. The S1 coil (the coil closest to CS1) is at $Z = \pm 4.5$ m rather than ± 4.0 m, which further tends to decouple the S1 and CS1 coils. Finally, the present baseline has five, rather than four, solenoid coils spaced at 1 m, rather than 1.25 m. The current in each coil is less than that in the February 1983 baseline, and this also contributes to lower axial force on the central-cell solenoids. In the present baseline, the largest axial running load is 0.58 MN/m.

4.5.3 C Coil Operating Current

Once a conductor configuration is defined, pertinent parameters (i.e., area of superconductor, area of copper stabilizer, wetted perimeter, relative resistance ratio, and critical recovery heat flux) are fixed. The designer has some freedom, however, in the choice of conductor current. By increasing the thickness of the neutronic shield between the magnet and the plasma, the designer can reduce the neutronic heating, increase the operating current, and still maintain the same margin against critical recovery surface heat flux.

For the MFTF-α+T end-cell plasma conditions, the peak neutronic heating rates in the winding and steel case of the superconducting coils are given in Table 4.33. Values

Table 4.33. Neutronic heating in C coils vs shield thickness

Amount of stainless steel shielding, cm	Peak neutronic heating, mW/cm^3	
	Outside surface of case	Surface of of winding
0	25	13
15	3	1.3

are given for no shield and for a 15-cm-thick stainless steel shield (the thickness of the end-cell shield in the February 1983 baseline, chosen as the point of departure for MFTF-α+T design studies). The heating rates in Table 4.33 include the shielding provided by the 5-cm-thick steel coil case.

In a static stability analysis of the C coil conductor described in Sect. 4.3.5, it was found that the permissible operating current is not significantly affected by neutronic heating or, therefore, by the shield thickness. With no shielding at all, the operating current can be 5 kA; at the other extreme, an infinitely thick shield that prevents any neutronic heating, the operating current can be 5.25 kA. Therefore, 5 kA is chosen as the operating current in the C coils, ensuring that they will be locally cryostable even with no shielding. The operating current is limited by heat transfer rather than by critical current, as the peak field on the winding of the C coils is 6 T.

This does not mean, of course, that shielding is not required, because local cryostability is not the only design requirement related to neutronic heating. The neutronic heating, integrated over the coil, must produce no more than 10% (by volume) of vapor in the helium exiting the coil. (This is the LLNL design criterion for MFTF-B magnets.) Furthermore, the cryogenic heat load of unshielded magnets would result in excessive operating costs. Thus, shielding the magnets is both necessary (to meet the helium quality requirement) and desirable (to reduce costs). However, it is deemed appropriate to choose the operating current as if there were no shielding, because the penalty in operating current density is small and the choice ensures that streaming paths or local thinning of the shield will not compromise local cryostability.

The conductor for the C coils is the same as that used for the MFTF-B yin-yang magnets. However, the MFTF-α+T coils are smaller and have much less stored energy than the MFTF-B coils. It is therefore concluded that it would be possible to discharge these magnets without exceeding the dump voltage or the peak conductor temperature of the MFTF-B yin-yang magnets.

4.5.4 Helium Vapor Clearing

One of the design objectives is to limit the vapor content in the helium exiting the superconducting coils to 10% by volume. This criterion was evaluated in some detail for the C coils.

Individual LHe supply Dewar flasks for each C coil will be located on top of the vacuum vessel. Helium in the Dewar flask is assumed to be at 4.35 K and at the saturation pressure. The helium inlet to the C coil is at the bottom. Because of static head, the helium is subcooled at the inlet, receives heat as it passes through the magnet, and exits at the top of the coil. The exit conditions depend on the amount of heat added to the coil. However, because of heating, the helium exiting the coil is less dense than the supply helium. The difference in density between the supply and return lines produces a finite pressure difference and a net flow in this nominally static system.

A thermal-hydraulic analysis of the coil and its supply systems was performed to determine flow rates and exit quality of the coolant. A plot of vapor content by volume as a function of integrated heat load is given in Fig. 4.49. As may be seen from the figure, subcooling the helium permits a heat load of 1.5 kW before boiling is initiated. Vapor

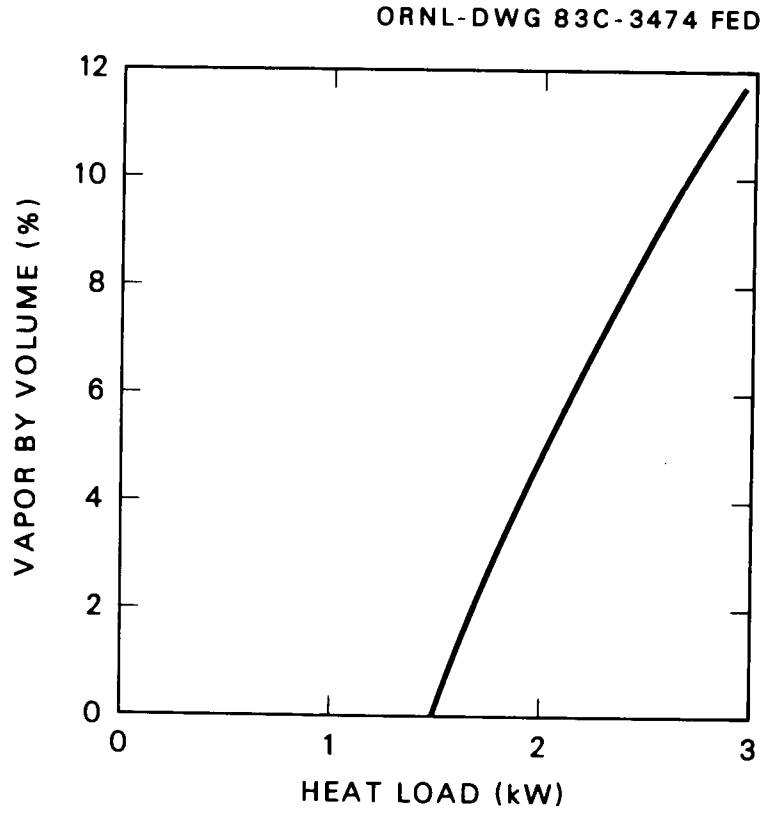

Fig. 4.49. Vapor content by volume vs heat load.

content increases with increasing heat load; 10% vapor by volume is reached at a heat load of 2.7 kW.

Another important result of the analysis is that the flow through the magnet resulting from the difference in density between the supply and return lines is large compared to the free-rise velocity of vapor bubbles in liquid helium. For a 2-kW heat load, for example, the mass velocity flow through the magnet is 34 cm/s, compared to a free-rise velocity of 2 cm/s. This ensures that bubbles will be swept out by the bulk helium flow and will not percolate through the winding to pocket on the upper surface of the case.

4.5.5 End-Cell Magnet Shield Thickness

A trade study was undertaken to determine the optimum thickness of the shield between the end-cell C coils and the plasma. The thicker the shield, the greater the capital cost of the end-cell magnets, vacuum vessel, and external shield. On the other hand, the capital cost of the cryoplant and the operating cost of cooling the coils decrease as shield thickness increases. A functional constraint on the optimization is the requirement that the integrated heat load on a coil must produce no more than 10% vapor by volume in the helium exiting the coil.

The trade study was conducted for the February 1983 baseline configuration. The end-cell C coil parameters for that configuration are given in Table 4.34. It was determined that nominally 15 cm of water-cooled stainless steel shielding could be accommodated in the arrangement after allowances were made for the plasma and plasma halo, drift pumping coils, cold wall, clearances, and coil cases.

Table 4.34. February 1983 configuration for end-cell C coils

Coil current = 5.6 MA·turns

Winding pack = 0.2 m × 0.8 m

Coil	Axial location Z, m	Major radius, m	Minor radius, m
T1	±11.811	1.5	0.5
A1	±15.611	1.3	0.5
A2	±15.611	1.3	0.5
P1	±19.411	1.5	0.5
P2	±19.411	1.5	0.5
A2	±23.211	1.3	0.5

The system life-cycle cost was calculated as a function of shield thickness, which was varied about the baseline value of 15 cm. The clear width in the mouth of the magnet was adjusted to conform to shield thickness. A consistent set of winding centerline dimensions and coil currents was derived based on the assumption that, at least to first order, centerline dimensions and coil current can be scaled proportionately up or down with no detrimental effect on field on axis. Operating costs were based on a 10-year life and a 10% duty factor. The system cost is plotted in Fig. 4.50.

The results suggested that system cost could be reduced by decreasing the shield thickness and the size of the magnets. This was not done, however, because of a serious problem in the February 1983 baseline that was discovered as a result of the C coil conductor current study (described in Sect. 4.5.3). As discussed in Sect. 4.5.3, an operating current of 5 kA was selected for the C coils. For this operating current, the 20- by 80-cm (0.16-m^2) winding space for the C coils in the February 1983 baseline is insufficient; a 0.26-m^2 winding area is required.

A new baseline was defined with a winding cavity of 30 cm by 87 cm, with no change in C coil centerline dimensions. The long dimension of the winding was increased as much as deemed prudent without necessitating an increase in the spacing of the C coils along the axis of the machine. The revised winding size provides the 0.26-m^2 required winding area with minor impact on system cost and machine size. With the revised winding dimensions, the clear space between windings where the centers of the major lobes abut (see Fig. 4.51) is reduced to 13 cm. This is judged to be about the minimum space required for coil cases and tolerance.

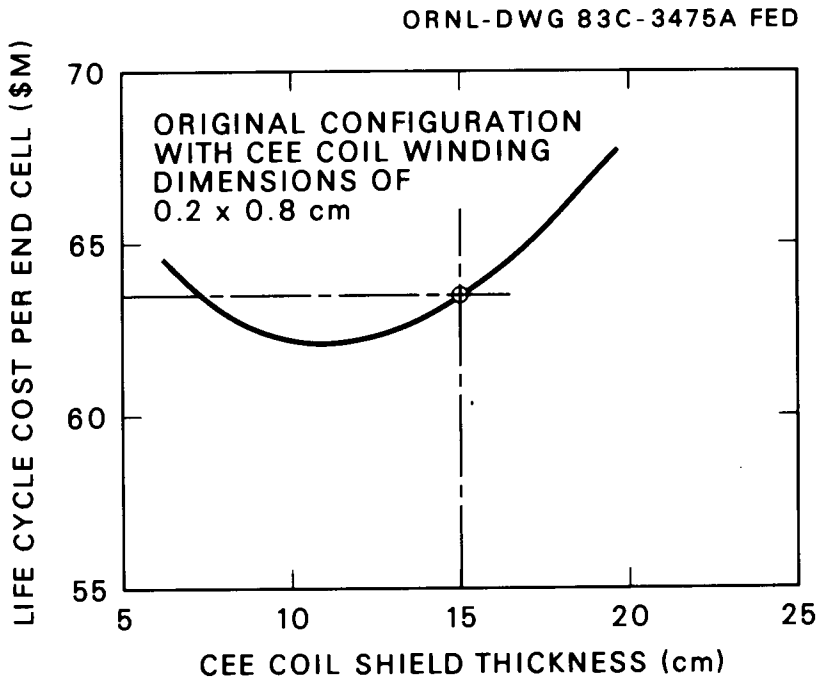

Fig. 4.50. Life-cycle cost per end cell vs shield thickness.

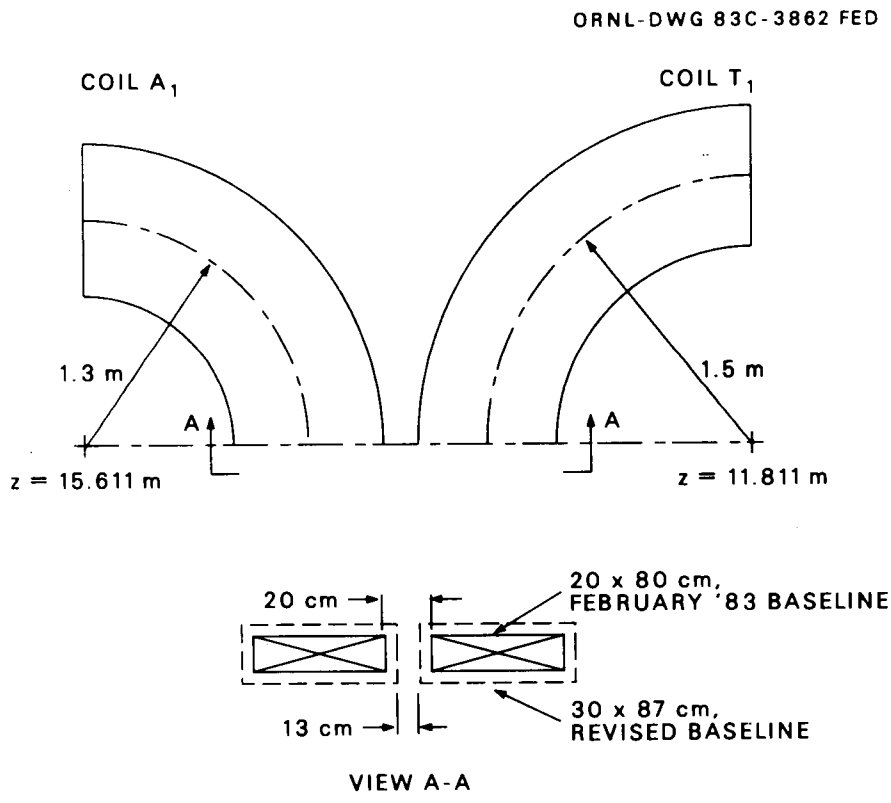

Fig. 4.51. Clear bore between major lobes of windings.

The revised baseline winding dimensions result in a system cost of $65 million per end cell compared to the February 1983 baseline cost of $63.4 million per end cell. Although cost calculations were not performed for different C coil spacing along the machine axis, it is judged that accommodating the increased winding size by axial spreading of the coils would have a greater impact on cost.

Reducing the shield thickness from 15 cm to 10 cm results in an integrated heat load of 2.59 kW on the C coil with the greatest neutronic heating. This means that the vapor content exiting the coil will be 9.4% by volume, which is less than the limit of 10%.

4.5.6 Resistive Insert for 18-T Choke Coil

The innermost solenoid of the 18-T choke coil is a normal insert that provides 3.0 T of the total 18-T field. Even the most advanced superconductors suffer a severe degradation of their critical current between 15 T and 18 T. In addition, a resistive magnet can operate closer to the plasma than a superconducting magnet, which must be shielded against neutron and gamma irradiation at the flux levels expected in MFTF-α+T.

The principal trade-off for normal magnets is between room-temperature and cryoresistive magnets. Because of the neutron and gamma irradiation and because of increased copper resistivity due to that irradiation, the overall power balance favors a water-cooled, room-temperature magnet. However, a cryoresistive magnet has several attractive features in this application that are far more important than possible savings in power supply cost. Probably the most important advantage of cryocooled coils is the absence of electrochemical failure mechanisms, such as corrosion, radiolysis, and electrolysis, that limit the lifetime of water-cooled, room-temperature magnets. Corrosion of copper and insulation by purified water routinely destroys unirradiated high-field magnets after a few hundred hours of operation. Internally cooled magnets have been destroyed in accelerators by irradiation-catalyzed copper erosion.[18] Corrosion mechanisms can probably be defeated by using steel claddings like those used and qualified for fission reactors, but these will inevitably give a less-than-optimal thermal performance, because of higher temperature drops across the cladding and its bond to the copper conductor.

Both helium and nitrogen are inert with respect to copper, and any chemistry due to impurities is greatly reduced by cryogenic temperature. Nitrogen is preferred because it can be circulated as a liquid at 77 K, without requiring high pumping powers. However, nitrogen is activated by neutron irradiation, requiring a separate processing plant, and presents a danger to reliability because of vapor lock under intense irradiation. Helium was selected as the basis for design of this magnet, but nitrogen should not be ruled out. An attractive option is to flow nitrogen radially through split copper Bitter plates, thus providing a small enough flow path that vapor lock can be avoided. The only disadvantage of this approach compared with the internal helium-cooled conductors selected here is that the Bitter coils cannot grade the hoop stress as conveniently as a pancake-wound coil with graded steel reinforcing strip.

Choice of conductor and operating current

The basic constraints on the conductor in a highly irradiated magnet are as follows. The current should be as high as possible because the rate of any electrical failure

mechanism will probably be an exponential function of the electrical field in the magnet and because the difficulty of cooling a magnet will be a first-order function of the hydraulic path length, which is linearly related to the number of turns. Against this is the fact that at high current and low voltage, the cost of buswork and power supplies increases almost linearly with current, becoming almost independent of total power. It is also believed that there is a manufacturing limit on the size of the conductor. A well-cooled conductor with as high a current as desired could be created simply by taking two slabs of copper, milling multiple slots in them, and brazing the two halves together. Copper-copper brazes should probably be avoided, if possible, in a high-stress magnet. For instance, the toroidal field magnet conductors for JET are extruded with two cooling holes. The JET conductors are about as large as possible for extrusions with multiple holes. JET researchers reported a manufacturing limitation of 4000 mm^2 for copper with two internal coolant channels from Kabelmetal of Osnabrück.[19] Thus, conductors with dimensions similar to those of JET were selected.

The reference conductors are 2.3 cm high by 17 cm wide. Each conductor has four coolant holes, each 1.2 cm in diameter and interconnected axially at the hydraulic connections to the inlet and outlet headers. The current in the conductor is 57.5 kA, which is less than that in the JET conductors but must be carried steady state.

Winding layout

Each of the two 18-T normal insert coils is wound in two double pancakes. Each pancake has 11 turns and is wound two-in-hand. Since two turns are lost at each crossover, each coil has 40 turns. Conductor cooling by the forced flow of helum requires at least eight parallel hydraulic paths through the winding. This is accomplished with inlet and outlet headers at the radial inside and outside of the magnet, respectively, and with two-in-hand winding. Helium flows through a cylindrical plenum at the radial inside of the winding pack to a plenum on the radial outside of the winding pack. Access to the innermost winding in the two-in-hand wound pancake is obtained by joggling the crossovers at different angular positions on the inside and by terminating the windings at different angular positions on the outside. Thus, each hydraulic channel for helium consists of only five turns, with eight hydraulic channels in parallel. The winding pack layout is shown in Fig. 4.52.

Each of the two-in-hand windings is connected in series with its partner and in series with the other double pancake. Central jumpers connect the double pancakes, while an axial bus across the top of the winding connects the upper with the lower two-in-hand winding. A second axial bus across the top of the winding allows the forward and return leads to be taken out of the magnet in a single mechanical package. Even with the double-pancake and two-in-hand windings in series, the steady-state terminal voltage is only 6.0 V, while the charging voltage may be 10 V. If the coil were designed with above-room-temperature, irradiated conductors, the steady-state voltage would be approximately 30 V, which is still a very low voltage. However, as the organic insulation degrades, this voltage is still high enough for an arc to be physically possible or for insulator impurity atoms to migrate across a material interface. At 6.0 V, arcs are impossible and any chemical degradation of the copper or insulation surfaces will be extremely slow, since this voltage is lower than most surface potentials.

ORNL-DWG 84-2110 FED

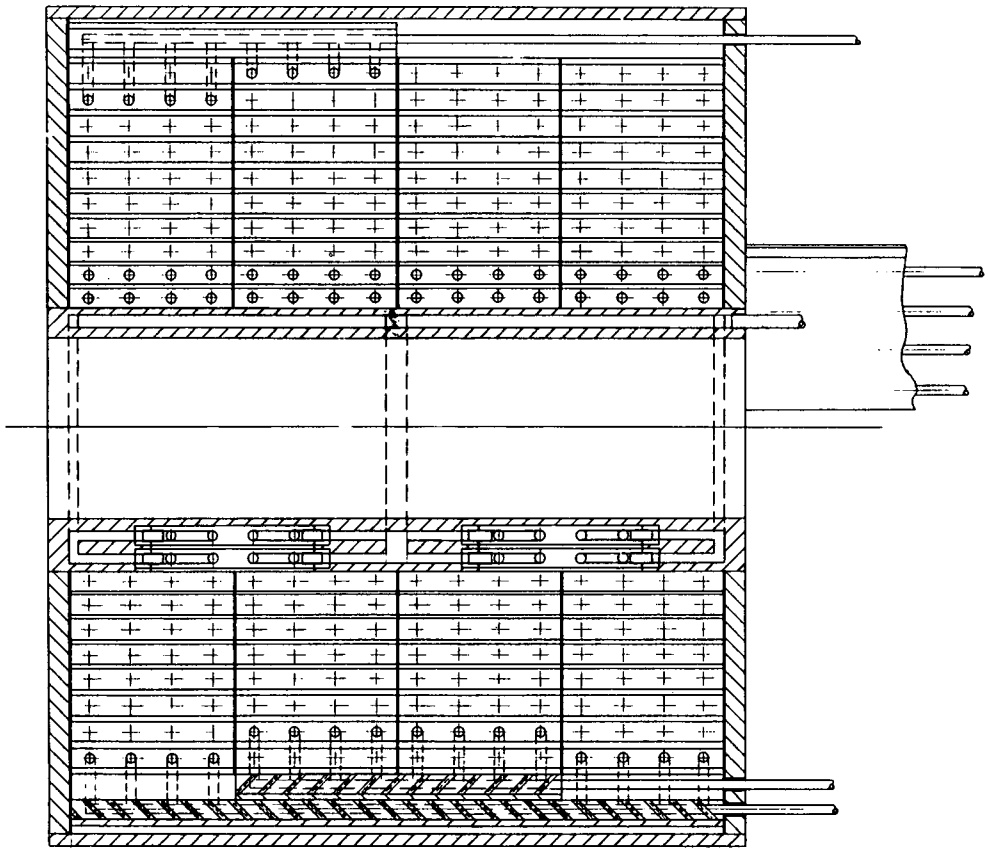

Fig. 4.52. Cross section of 18-T insert coil.

Winding pack stresses

The structural concept used to support the winding pack is to co-wind pancakes with graded, stainless steel strip. Grading the steel strip so that each layer has only as much steel as it needs is the optimum structural concept. It can approach the uniform stress distribution of a polyhelical magnet without the possibly unsolvable problems associated with the support of leads and independent layer-wound structures in a high-irradiation environment. In the design reported here, the steel strip is divided into three grades of 9 mm, 6 mm, and 3 mm.

Stresses in the winding pack have been calculated by assuming that each turn is self-supporting against hoop stresses and that each layer is self-supporting through the case and external support structure. The Lorentz load on each turn is calculated individually and converted to a stress in a homogeneous, anisotropic material, as shown in Figs. 4.53 and 4.54. Under the conservative assumption that all hoop and axial losses are supported through the co-wound steel strip, the stress multiplying factors in the steel are 3.67 in the outer layer, 5.0 in the center, and 9.0 in the inner layer. The peak stresses in the strip

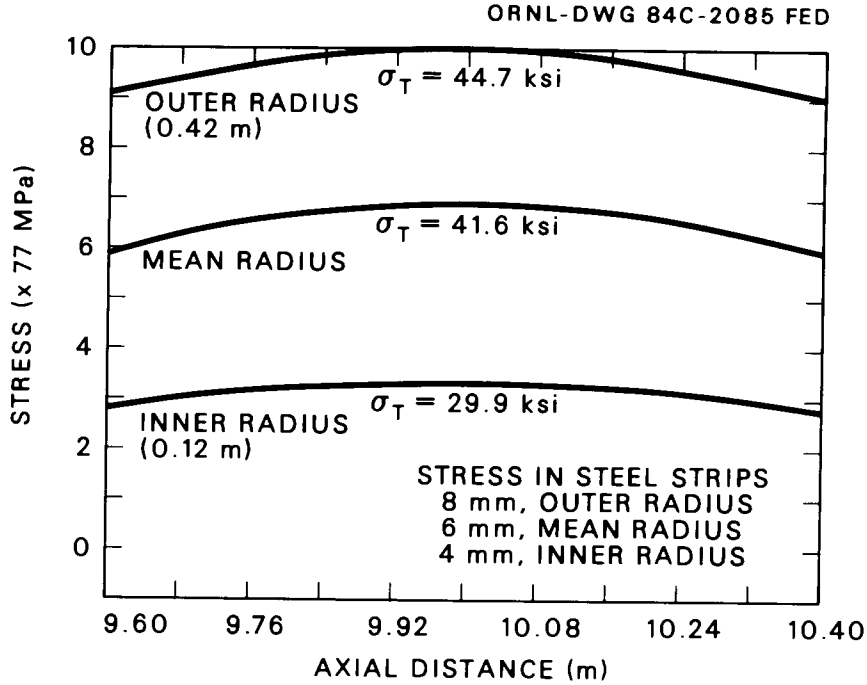

Fig. 4.53. Hoop stress in the 18-T normal insert coil, averaged over the local winding envelope.

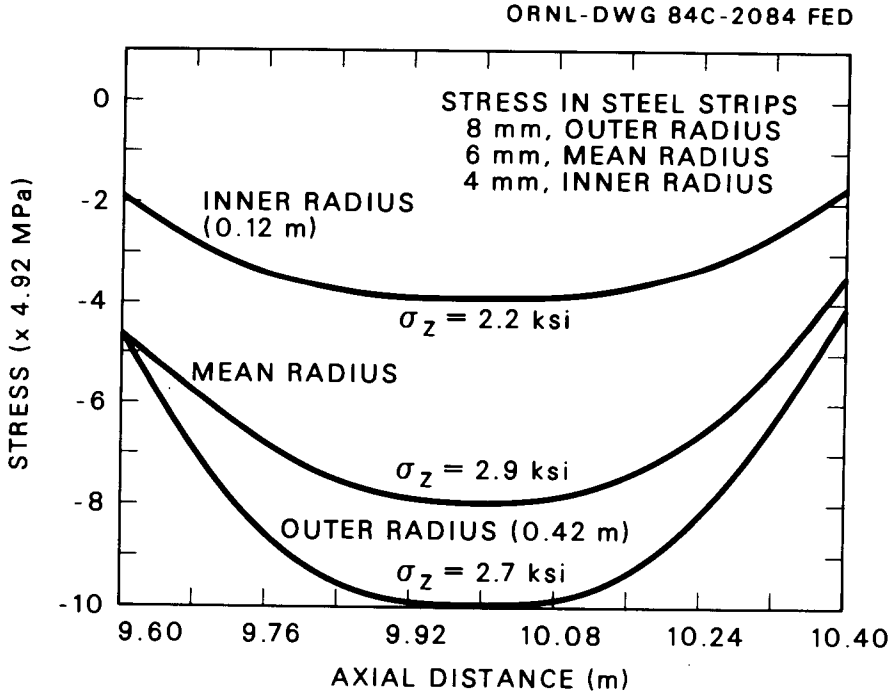

Fig. 4.54. Axial stresses in the 18-T normal insert coil, averaged over the local winding envelope.

would occur near the center of the coil and are listed in Table 4.35. The peak Tresca membrane stresses in the strip range from 80% of the 376-MPa allowable stress in the outer layer to 65% of the allowable stress in the inner layer. Without grading, the stress in the strip would vary by a factor of 3. The grading could be adjusted so that the 19% difference between the inner and outer layer peak stresses would be eliminated, but the practical differences for a magnet that must also support fault loads do not warrant another iteration at this time. The peak axial bearing stress of 4.9 MPa is well below the 200-MPa allowable compression stress in polyimide S-glass–reinforced epoxy, allowing stress risers for penetrations.

Table 4.35. Peak stresses in outer, central, and inner layers of steel strip

	Outer layer	Central layer	Inner layer
Hoop stress, MPa	283	266	229
Axial stress, MPa	18	19.7	17.3
Tresca membrane stress, MPa	301	286	247
Fraction of allowable stress, %	80	76	65

Insulation requirements

In a highly irradiated environment, it is best that to require only that the insulation stay in one place. If the insulation is required to bear any part of the structural load, it must be as thin sheets in compression. The estimated radiation parameters are shown in Table 4.36.

Table 4.36. Radiation parameters of the resistive insert

Peak neutron and gamma heating in steel Q'''_{peak}, W/cm^3	2.94
Average neutron and gamma heating over inner surface Q'''_{av}, W/cm^3	1.47
Average surface heat flux Q''_{av}, W/cm^2	9.5
Total neutron and gamma heating per coil Q_{tot}, kW	52
Peak integrated energy absorbed by insulation, rad	3.7×10^{12}

Conductor cooling

The conductor is cooled internally by helium flowing through four symmetrically spaced, extruded cooling passages. To keep the average surface temperature at about 80 K, the helium enters at 38.8 K and exits at 120 K. The outlet pressure is 3 atm. These temperatures and pressures were selected based on a helium refrigeration trade study for the LITE reactor by Cohn and Bromberg,[20] which showed them to be close to an overall minimum for refrigerator power consumption, taking into account the trade-offs between Joule heating and cold recirculator loop power consumption.

For the selected winding pack layout, the internally cooled conductor configuration is rather tightly constrained. If there were only four parallel coolant passages, a straightforward sizing of the mass flow would require an outlet velocity higher than the speed of sound in helium. A three-in-hand winding with 12 parallel coolant passages would require altering the number of turns and would significantly increase the complexity of the hydraulic fittings. Therefore, eight parallel coolant passages through two-in-hand windings were selected. The additional entropy generated by the 8-atm drop across the winding pack is not an excessive refrigeration burden. The inlet-outlet header drops were calculated to add 0.3 atm to the drop across the magnet. Hydraulic parameters are shown in Table 4.37.

Table 4.37. Hydraulic parameters of the resistive insert

Helium inlet temperature T_{in}, K	38.8
Helium outlet temperature T_{out}, K	120
Helium inlet pressure P_{in}, atm	11.2
Helium outlet pressure P_{out}, atm	3
Mass flow through conductor, g/s	120
Total mass flow through coils, kg/s	1.92
Total entropy generation in load, kW/K	18.1
Helium outlet velocity v_{out}, m/s	220
Outlet Reynold's number Re	294,300
Friction factor f	0.018
Pressure drop per unit length p/L, atm/m	1

Resistive losses

The steady-state resistive losses in each magnet have a steady-state value of 350 kW or 700 kW for an east-west pair. These can be provided by one power supply, with the coils fed in series and grounded between the coils. The two coils would then draw 57.5 kA with a steady-state terminal voltage of ± 6 V and a charging voltage of ± 10 V. Electrical parameters of the resistive inserts are shown in Table 4.38.

Table 4.38. Electrical parameters of the resistive insert

Steady-state power per coil, kW	350
Conductor current, kW	57.5
Steady-state terminal voltage, V	6
Peak terminal voltage, V	10
Copper resistivity (design value), nΩ·m	5.5

Helium pumping requirements

The thermal load that must be removed by forced circulation of gaseous helium consists of the Joule heating of the copper and the neutron and gamma heating of all magnet materials. This thermal load is estimated at 350 kW per coil of Joule heating and 50 kW of neutron and gamma heating, for a total thermal load on the helium cold compressor loop of 800 kW. This can be compared with the estimated 675 kW of nitrogen cooling required primarily for vacuum vessel thermal radiation shields.

In order to force 1.92 kg/s of helium through the magnets, a three-stage cold compressor circuit is required. The pumping requirements of the load itself are shown in Table 4.37. The entropy flow in the load is 18.1 kW/K. Since the entropy generated by 800 kW of isothermal heating at 77 K is 10.4 kW/K, this is one measure of the additional refrigeration capacity required for the helium pumping when compared with LN_2 cooling.

4.5.7 End-Cell Anchor and Plug Coil Support Structure

The best means of supporting the end-cell yin-yang coil sets was studied. Principal concerns were the nearness of the coils to one another and the need for access to the heating and drift pumping systems and to the internal nuclear shielding. The possibility of configuring the coil sets so as to reduce the size of an in-vault crane was considered, since a new crane will be required for MFTF-α+T, and its size has an impact on the modifications needed for the vault.

The first design studied was an adaptation of the MFTF-B yin-yang structural concept, in which the coils support each other against the minor lobe opening forces with an intercoil structure, and the major lobe opening forces are restrained by a deep beam case structure around the coil case (Fig. 4.55). However, for the MFTF-α+T loading, the case structure would cause interference between neighboring coils.

In the second concept studied, the six C coils at each end of the device were supported in yin-yin and yang-yang pairs (Fig. 4.56). The major lobe opening forces are balanced by structurally tying the two back-to-back coils together. Toward the center the structure would be in tension, and toward the sides it would be in compression, due to the tendency of the coils to go flat and of the major lobes to spread (Fig. 4.57). The minor lobe forces are carried by spanning beams, located over the major lobes of the two adjacent coils, to two outer ring beams (Fig. 4.58). In a limited structural analysis to size the ring and spanning beams, it was found that the ring beams could not be tapered enough to prevent interference at their minor-lobe ends because of the close-fitting winding geometry.

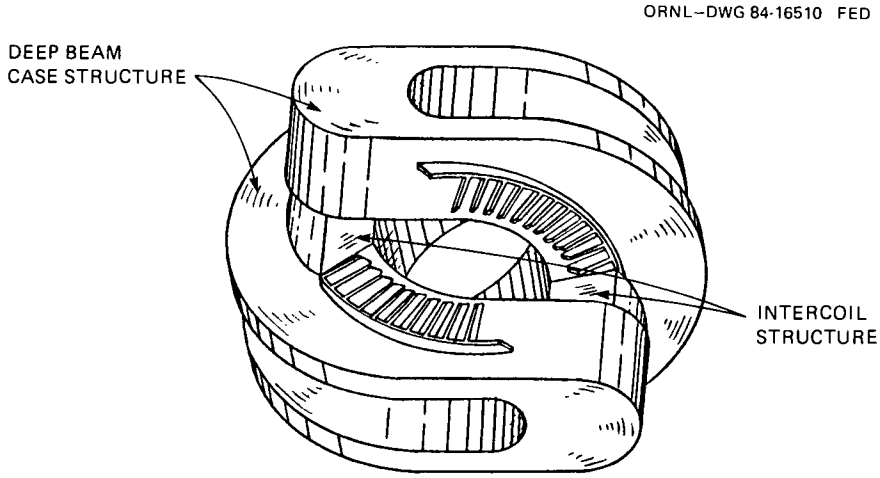

Fig. 4.55. MFTF-B yin-yang coil with a deep beam case structure supporting the major lobe opening forces.

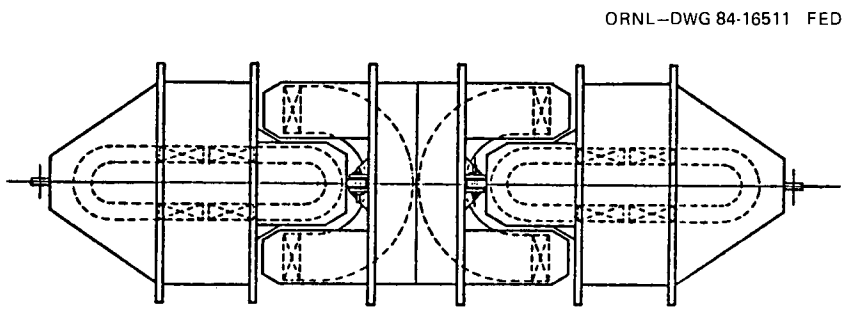

Fig. 4.56. Support of C coils in yin-yin and yang-yang pairs.

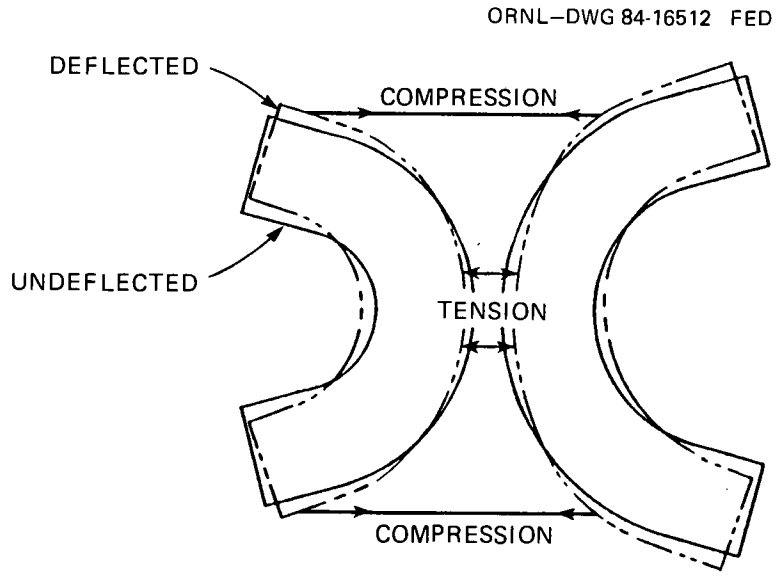

Fig. 4.57. Forces on back-to-back coils.

ORNL-DWG 84-16513 FED

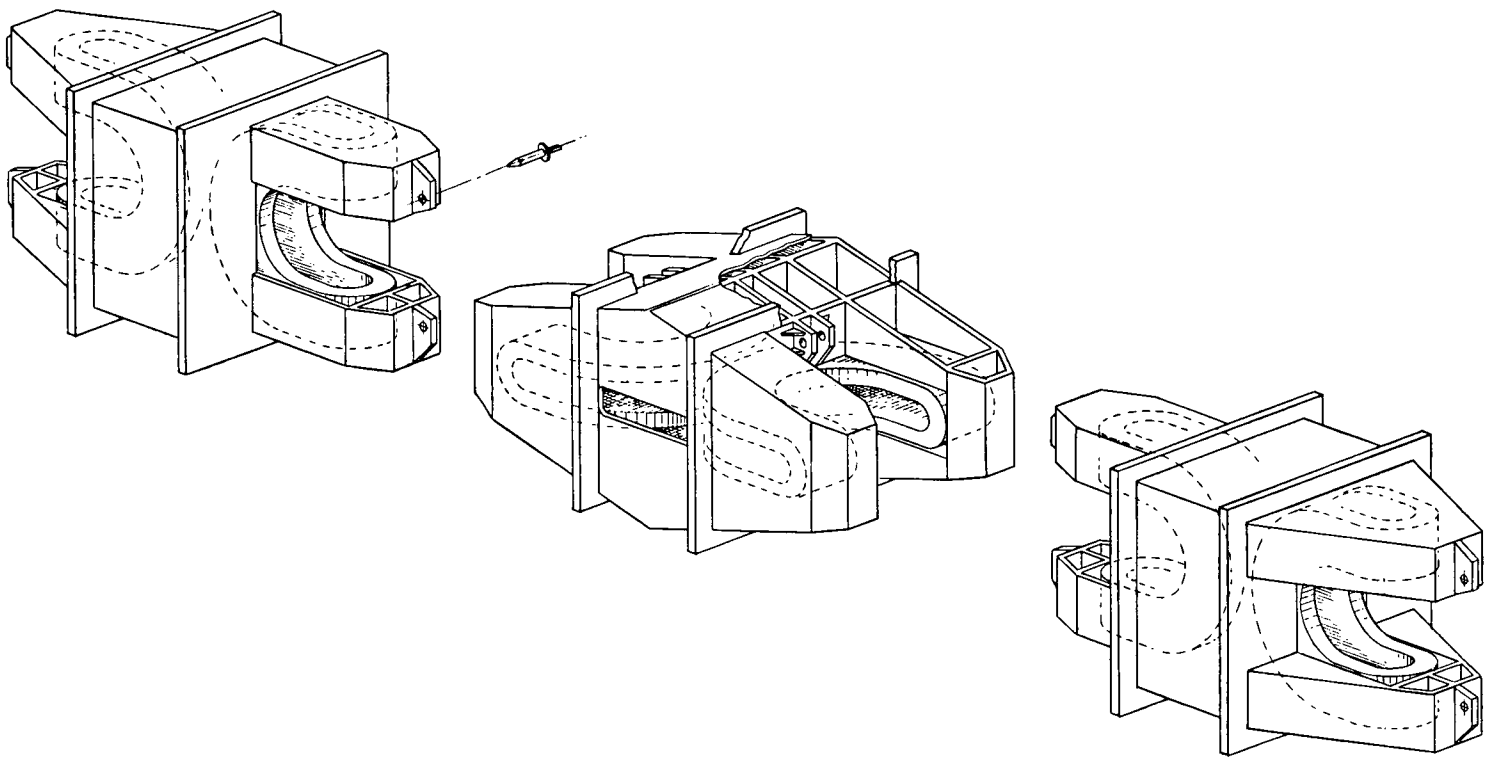

Fig. 4.58. Outer-ring beams and spanning beams.

As part of this study, the concept was varied to investigate the possibility of dismantling the support structure in place so that parts of the structure and each of the coils could be removed individually, thus reducing the size of the crane. Strongbacks on each side of a pair of coils would support the minor lobe opening forces (Fig. 4.59). The strongbacks would be joined at the four corners by tension struts (Fig. 4.60). The two coils are linked together axially and the coil cases are stiff enough so that each case supports the coil's major lobe opening forces. A set of wedge plates on the upper surface of the coils is tightened to preload the corner struts. Wedge plates on the lower surface would ensure a tight fit to the lower strongback. The coil set would have a double set of attachment points to its lower gravity support structure. A special lifting fixture would lift the coil set and rotate it 45°. After rotation, the remotely activated attachment pins

ORNL–DWG 84-16514 FED

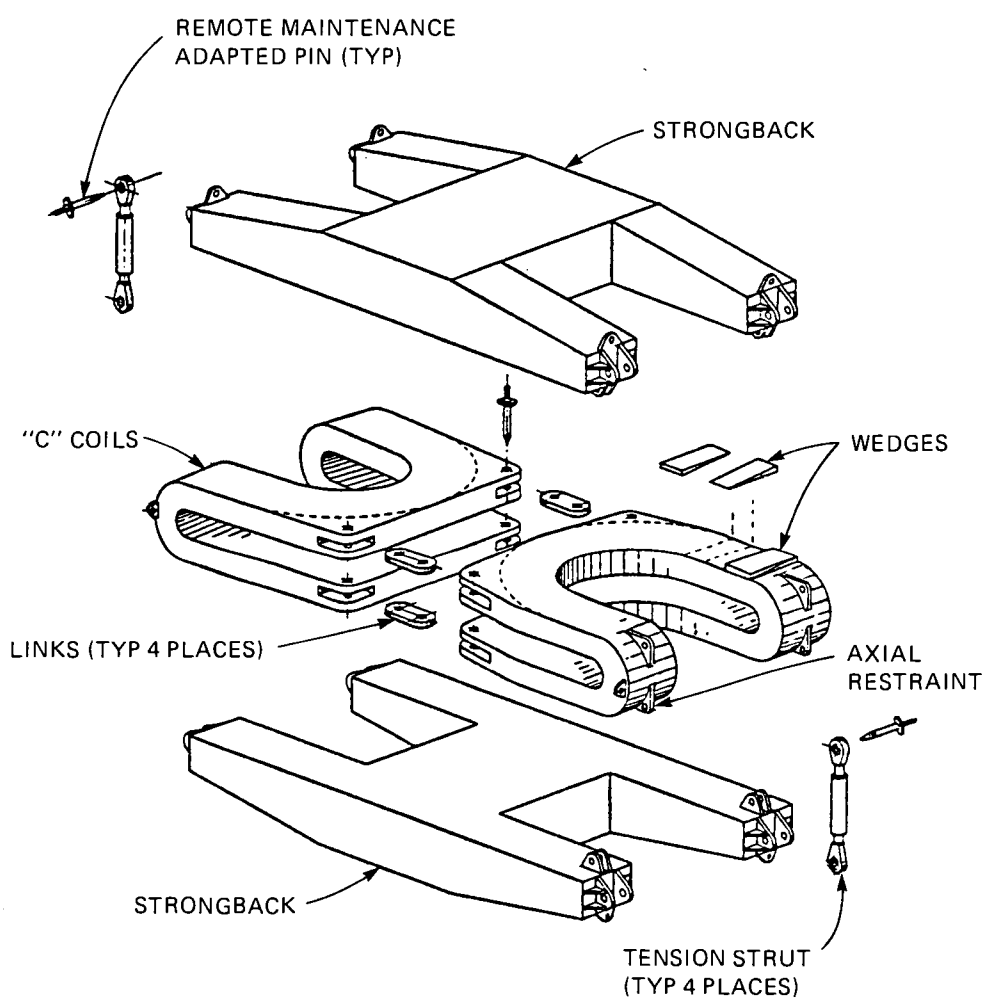

Fig. 4.59. View of C coil support structure that can be disassembled in place.

ORNL–DWG 84-16515 FED

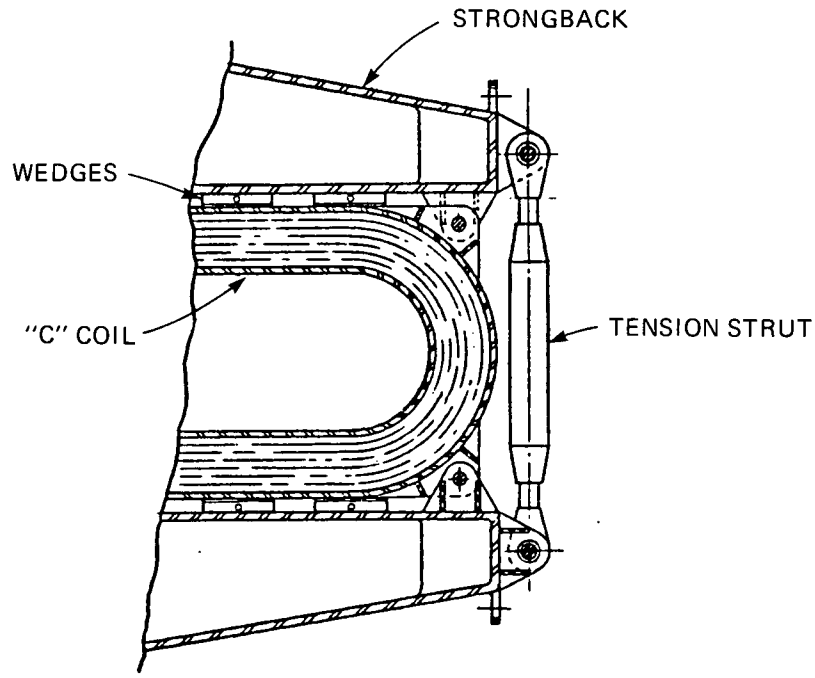

Fig. 4.60. Tension struts joining strongback corners of C coil support structure.

would be secured to hold the coil set during disassembly. This procedure makes it unnecessary to move one coil off the other at a 45° angle. When the structure was sized as for the first concept, interferences occurred at the four corner points because of the closeness of the windings.

The third concept has been described in Sect. 4.3.7 of this report. Each coil case supports the major lobe opening forces of its coil, and the minor lobe opening forces are supported by the companion coil's case and by the four collar structures (Fig. 4.30). This design, developed independently at the Fusion Engineering Design Center, is similar to one for a tandem mirror reactor (TMR) presented in ref. 21. Significant differences include a lower magnetic loading and smaller coil and case dimensions for MFTF-α+T. The geometry and magnetic loading for the two designs are compared in Table 4.39. In addition, the design collar plate over the major lobe of the coils is thicker in the MFTF-α+T design. This plate carries a significant portion of the load from the companion coil in bending around the coil's major arc.

Both designs include a heavy angle beam between the companion coils that is integral with the collar structure and intercoil stiffeners (Fig. 4.61). However, there is no minor radius reinforcement (Fig. 4.62) in the MFTF-α+T coils because of the access requirements for the neutral beams and the proximity of the neighboring coils.

The MFTF-α+T design requires a relatively thin outer cap in the major radius area, where the coil is close to its neighbor. A box ring structure was added to this area of the

Table 4.39. Comparison of coil parameters for MFTF-α+T and TMR

Parameter	TMR	MFTF-α+T
Major arc radius, m	2.7	1.3
Minor arc radius, m	1.18	0.5
Conductor cross section, m	2.1 × 0.36[a]	0.869 × 0.298
Coil section current density, A/cm^2	2330–2500[b]	2162
Maximum conductor field, T	9.04	5.8
Lobe spreading force, N	360 × 10^6	52.5 × 10^6
Mirror length, m	4.9	3.8
Vacuum center field, T	4	2.13
Mirror ratio	1.5	2.25
Conductor weight (both coils), kg	201,000	22,500

[a]Increased to 2.1 × 0.44 at the center of the minor radius.
[b]2330 for inner coil, 2500 for outer coil.

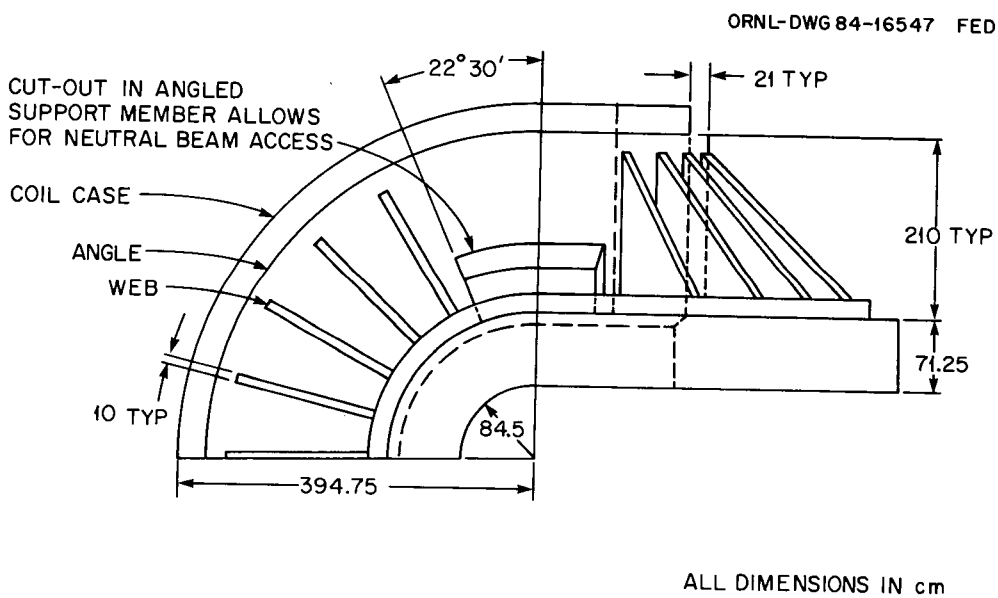

Fig. 4.61. TMR support concept.

ORNL–DWG 84-16548 FED

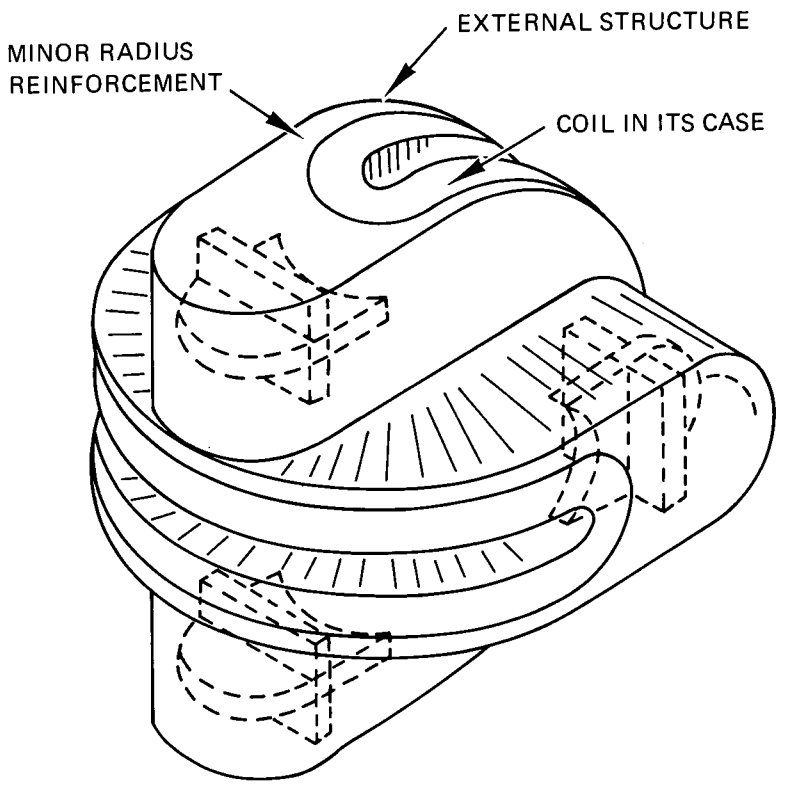

Fig. 4.62. Minor radius reinforcement for TMR coils.

collar structure (Fig. 4.37). This structure tapers around the collar, with a maximum height at the major arc center. The small space for structural material between neighboring coils is the primary design concern.

A comparison of the structural thicknesses and properties of the MFTF-α+T design with the TMR design shows that the MFTF-α+T design is generally feasible. A structural analysis of the MFTF-α+T design is required to establish its feasibility and to develop the design details. Analysis of the required magnitude awaits final resolution of the magnet geometry, which is affected by the shield thickness near the neutral beams and by details of the beam geometry. Although it may be possible to build the selected concept for disassembly in place (to minimize crane size), a welded design, which is more straightforward, is presented here. The structural design of the in-place disassembly concept will be investigated later.

REFERENCES

1. R. D. Pillsbury et al., *MFTF-B+T Magnetostatic and Circuit Fault Induced Forces*, PFC/RR-83-21, Plasma Fusion Center, Massachusetts Inst. Technol., Cambridge, 1983.

2. M. S. Walker et al., "Nb_3Sn Conductors for 12 Tesla Toroidal Field Coils," *IEEE Trans. Magn.* **MAG-17**, 670 (1981).

3. R. E. Schwall and G. M. Ozeryansky, "Fabrication of 12 Tesla Conductor Using External Bronze Process MF Nb_3Sn," *IEEE Trans. Magn.* **MAG-19**, 920 (1983).

4. L. R. Turner, "Safety of Superconducting Magnets for Fusion: Thermal Analysis of Large Cryostable Magnets," *IEEE Trans. Magn.* **MAG-17**, 463 (1981).

5. *Part I Final Report, 12-Tesla Toroidal Field Coils Engineering Test Facility (ETF)*, General Electric Co., Schenectady, N.Y., 1979, p. 2-66.

6. R. E. Schwall et al., "Properties and Performance of High Current Density Sn-Core Process MF Nb_3Sn," *IEEE Trans. Magn.* **MAG-19** (1983).

7. J. H. Schultz and D. B. Montgomery, *Design of the Alcator DCT Tokamak at M.I.T.*, PFC/JA-83-15, Plasma Fusion Center, Massachusetts Inst. Technol., Cambridge, 1983.

8. R. W. Baldi et al., "Development of a 12-Tesla Multifilamentary Nb_3Sn Magnet for MFTF-B," *Adv. Cryog. Eng.*

9. M. Suenaga, Brookhaven National Laboratory, personal communication, 1983.

10. J. W. Ekin, "J-B-T-ϵ Interaction and Strain Limits in A15, B1, and C15 Crystal Structure Superconductors," *IEEE Trans. Magn.* MAG-**19** (1983).

11. M. M. Steeves, M. O. Hoenig, and C. J. Cyders, "Effects of Incoloy 903 and Tantalum Conduits on Critical Current in Nb_3Sn Cable-in-Conduit Conductors," presented at the IEEE Magnet Technology Conference, Grenoble, France, September 1983.

12. *Final Design Review for the A-Cell, Transition, and Solenoid Coils for MFTF-B*, GDC-MFTF-B-81-014, General Dynamics Corp., San Diego, 1982.

13. D. P. Brown, "Design of 24.8 kW, 3.8 K Cryogenic System for Isabelle," *Adv. Cryog. Eng.* (1981).

14. J. H. Van Sant, "Thermal Performance of the MFTF Magnets," *Adv. Cryog. Eng.* (1983).

15. J. H. Van Sant, *Cryogenic System for the Mirror Fusion Test Facility*, UCRL-83590, Univ. California, Lawrence Livermore Lab., Livermore, Calif., 1980.

16. D. N. Cornish, *Superconductivity and Cryogenics for Mirror Fusion*, UCRL-83916, Univ. California, Lawrence Livermore Lab., May 1980.

17. W. H. Sterbentz and R. L. Nelson, *Cryogenic Aspects of the Mirror Fusion Test Facility*, UCRL-82913, Univ. California, Lawrence Livermore Lab., November 1979.

18. J. H. Schultz, "Design Practice and Operational Experience of Highly Irradiated, High Performance Normal Magnets," *J. Fusion Energy* (1983).

19. J. Booth et al., "The Manufacture of the Toroidal Field Coils of the Joint European Torus," *Proceedings of the 6th International Conference on Magnet Technology*, Bratislava, Czechoslovakia.

20. L. Bromberg, D. Cohn, et al., "LITE: A Long-Pulse Ignition Test Experiment," pp. 1013–1018 in *Proceedings of the American Nuclear Society Topical Conference on Fusion Energy*, Knoxville, Tenn., August 1983.

21. I. V. Ojalvo and J. L. Erickson, *Structural Support Conceptual Studies for a Yin-Yang Magnet of a Tandem Mirror Reactor*, UCRL-15291, Univ. California, Lawrence Livermore Lab.,

5. HEATING, FUELING, AND DRIFT PUMPING

D. H. Metzler

General Electric Company/Fusion Engineering Design Center

CONTENTS

5.1 INTRODUCTION 5-3
5.2 SUMMARY OF STUDY RESULTS 5-3
5.3 SYSTEM REQUIREMENTS 5-4
5.3.1 Central-Cell Neutral Beam Injection 5-6
5.3.2 Anchor-Cell Ion Heating 5-6
5.3.3 Sloshing-Ion Beam Injection 5-8
5.3.4 Plug Barrier Electron Heating 5-8
5.3.5 Drift Pumping 5-9
5.3.6 Deuterium Gas Injectors 5-10
5.4 DESIGN DESCRIPTIONS 5-11
5.4.1 Axicell Neutral Beam Injectors 5-11
5.4.2 Anchor-Cell Ion Heating 5-15
5.4.3 Sloshing-Ion Beam Injectors 5-18
5.4.4 Plug Barrier Electron Heating 5-21
5.4.5 Drift Pumping 5-28
5.4.6 Deuterium Gas Injectors 5-32
5.5 PERFORMANCE ANALYSES 5-37
5.5.1 Axicell Neutral Beam Injectors 5-37
5.5.2 Anchor-Cell Ion Heating 5-40
5.5.3 Sloshing-Ion Beam Injectors 5-40
5.5.4 Plug Barrier Electron Heating 5-44
5.5.5 Drift Pumping 5-47
5.6 TRADE STUDIES 5-60
5.6.1 Shielding for Axicell Neutral Beam Lines 5-60
5.6.2 Sloshing-Ion Neutral Beam Injectors 5-64
5.6.3 ECRH Transmission System 5-71
5.6.4 Drift Pumping Alternatives 5-75
5.6.5 Fueling 5-85
REFERENCES 5-86

5. HEATING, FUELING, AND DRIFT PUMPING

5.1 INTRODUCTION

In this chapter, the heating, fueling, and drift pumping systems required for MFTF-α+T are described. Six systems are needed:

1. axicell or central-cell neutral beam injectors for plasma heating and fueling,
2. anchor-cell ion heating systems to maintain beta in the anchor cells,
3. plug-cell sloshing-ion neutral beam injectors to establish a potential well that separates hot electrons in the plug from cold electrons in the central cell,
4. plug-cell electron heating systems to create potential and thermal barriers,
5. anchor-cell and plug-cell drift pumping systems to enhance radial drift, and
6. central-cell and end-cell gas injectors to establish initial pressure before startup.

Only the drift pumping and sloshing-ion neutral beam injection systems are new; the other systems are equipment from the Mirror Fusion Test Facility (MFTF-B). The emphasis in this chapter is on describing the new systems and the modifications required for existing systems.

The baseline configuration evolved during the design effort is summarized in Sect. 5.2. The system requirements are given in Sect. 5.3. Section 5.4 contains a design description of each system, and Sect. 5.5 gives estimates of system performance. The trade studies that led to the baseline configuration are described in Sect. 5.6.

5.2. SUMMARY OF STUDY RESULTS

Two neutral beam injectors like those developed for the Technology Demonstration Facility (TDF) are used to meet the heating and fueling requirements in the central cell. The positive-ion sources in these injectors (one with tritium, the other with deuterium) are scaled down to meet the requirement for 240 A at 80 keV.

The anchor-cell ion cyclotron resonance heating (ICRH) is supplied by one MFTF-B transmitter scaled up to 50 MHz to provide 700 kW and two additional units converted to 25 MHz to provide 1600 kW. These transmitters require 4.27 MW of prime power for an overall efficiency of 54%. The sloshing-ion neutral beams are produced by self-extracting negative-ion sources designed by Lawrence Berkeley Laboratory (LBL). The sources supply 4.2 A per plug at 200 keV with an overall efficiency of 41%. A transverse field-focusing (TFF) beam transporter makes it possible to place these sources out of the direct path of streaming neutrons.

For electron heating in the plug cell, all eight MFTF-B channels are used, along with six modified channels to supply a total of 2.4 MW. The efficiency of the 35-GHz systems is 32%; of the 56-GHz systems, 22%.

Each of the drift pumping systems (one for the anchor cell at ~70 kHz, one for the plug cell at 600 kHz) uses 12 narrow-bandwidth channels. For the anchor cell, the 40% bandwidth spectrum is only approximated by these channels, but for the plug cell, the 14% bandwidth spectrum is completely covered. The anchor-cell system efficiency is ~30%; the plug-cell system efficiency, ~35%.

Two deuterium gas injectors will be installed in the central cell, and one will be located between the anchor cell and the plug cell at each end. The gas is >99% D_2, and the maximum flow is 180 g/h.

For ease in maintenance, each launcher/injector is accessible through a shield plug. Matching networks for the drift pumping and ICRH systems are located on the outside of the device biological shield near the launcher plug, which makes it possible to use low-loss transmission lines between the transmitter vault and the device. Each system has its own monitor and control equipment. Methods for real-time control of power, frequency weighting (for drift pumping), and beam energy are being developed.

The baseline system characteristics are summarized in Table 5.1. The results of the trade studies performed for these systems are given in Table 5.2. Briefly, passive rather than active magnetic shielding techniques were selected for the axicell neutral beam injectors because the stray field is <2 kG and passive techniques are the most practical.

Negative-ion-based beams were selected for the sloshing-ion beam injectors because of their higher (3:1) efficiency, and the conventional (rather than TFF) accelerator was chosen as a more mature and reliable technology. The magnetic ion separator was selected for the positive-ion source because a stable stray field is available and insulation requirements are lower than with electrostatic separators. Ion transport with a TFF system is preferred because of reduced neutron flux on the source. The gas neutralizer was the only practical choice, given the proposed MFTF-α+T program schedule.

For the drift pumping system, the narrow-bandwidth approach was preferred for the anchor cell because it has been proven, whereas the wide-bandwidth case required development. For the plug cell, 12 channels covered the entire spectrum. A single coil was recommended to reduce interface complexity and space requirements. The two-transformer matching approach lowers the required transmission line impedance to a practical value. The conventional rf power chain offers lower risks than the chopper approach (although the latter should be studied further). For the anchor cell's narrow-bandwidth channels, the discrete tone was the easiest modulation form; for the plug cell, all forms were acceptable. The overmoded waveguide was selected for electron cyclotron resonance heating (ECRH) transmission because of limited access between the plug coils.

5.3 SYSTEM REQUIREMENTS

The geometry of MFTF-α+T is shown in Fig. 5.1. In Cartesian coordinates, the z-direction is along the machine axis, and x and y are rotated 45° from the horizontal and vertical axes, respectively. In polar coordinates, ϕ is taken with respect to z and θ with respect to x.

The injection points for the heating, fueling, and drift pumping systems are given in terms of this geometry. Injection angles are taken as the angle formed by the reference direction and the beam center. For the neutral beam and ECRH systems, which have narrow beams, this definition is clear; for the ICRH and drift pumping coils, it is easier to think in terms of a perpendicular to a radiating surface.

Because MFTF-α+T will operate in two modes (see Chap. 2), there are two sets of requirements for some system parameters. In all cases, systems are designed to meet the most stringent requirement. Interface considerations, which include geometric constraints and environmental concerns, are also addressed in the descriptions that follow.

Table 5.1. Heating, fueling, and drift pumping system characteristics

System	Cell incident power, kW	Cell prime power, kW	Overall efficiency, %	Frequency or energy	Number of sources	Number of injectors or launchers
Axicell heating and fueling	14,400	28,000	50	80 keV	4 per injector	1 deuterium, 1 tritium
Sloshing ion	840	2,049	41	200 keV, D^-	4 per injector	1 per cell
Anchor cell						
Ion heating	800	1,489	53.7	25 MHz	2 per cell	2 per cell
Ion heating	348	647	53.8	50 MHz	1 per cell	2 per cell
Drift pumping	300	982	30.6	70–80 kHz (±20%)	12 per cell	2 per cell
Plug cell						
Electron heating	120	540	22.2	56 GHz	1 per cell	1 per cell
Electron heating	600	1,892	31.7	35 GHz	3 per cell	3 per cell
Electron heating	480	2,162	22.2	56 GHz	3 per cell	3 per cell
Drift pumping	48	134	35.7	600 KHz (±7%)	12 per cell	2 per cell

Table 5.2. Summary of trade study results
Selected options are shown in bold type

System	Options
Magnetic shield for axicell neutral beam injectors	**Passive**, active
Sloshing-ion neutral beam injection	
Source	Positive ion, **negative ion**
Accelerator	**Conventional**, TFF
Ion separator	**Magnetic**, electrostatic
Ion transport	**TFF**, straight line
neutralizer	**Gas**, photodetachment, plasma
Drift pumping	
Coil tuning	
Anchor	Wide band with recovery, **narrow band**
Plug	**Wide band**, narrow band
Number of coils	**Single**, multiple
Matching networks	1 transformer, **2 transformers**
Transmitter	Inverter, **rf power chain**
Modulation	
Anchor	**Noise, tone**; sweep, all
Plug	Noise, tone; **sweep, all**
ECRH transmission	Quasi-optical, **waveguide**

ORNL-DWG 83-3790A FED

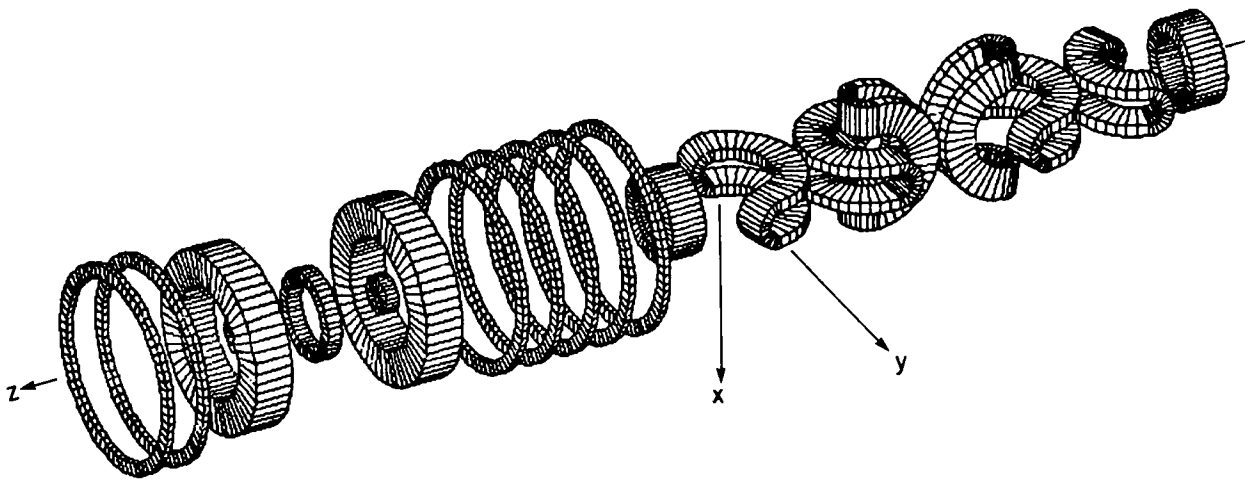

Fig. 5.1. Standard coordinate set.

5.3.1 Central-Cell Neutral Beam Injection

The neutral beam injectors provide heating and fueling for the central cell. Because of the fueling requirement, half the injected current is tritium and half is deuterium. The system requirements are summarized in Table 5.3. The specified power levels assume a neutral power fraction that yields an average of 60 keV, based on an ion source with a species mix of 80:15:5 and the specified full energy of 80 keV. The injection angle is 80°, set to keep the particle velocity in the parallel direction to the required level. In the orthogonal plane, the injection angle was offset to allow injection from both sides with clearance for beam dumps. Power and energy-level controls are needed for the startup sequence; values of power and energy are related because the source current density varies as $E^{3/2}$. Startup time is from 1 to 2 s, so beam control time (after neutral beam injector conditioning) is a few tenths of seconds.

For the high-Γ mode, the design-point tritium and deuterium injection currents are 120 A. For the high-Q mode, these currents are only 23 A. For fueling, therefore, each source must have an injection current of 30 A and operate over a wide range. To reduce the operating range, only two sources are used for the high-Q mode. The neutral beam control requirements are detailed in Chap. 10, Electrical Systems.

5.3.2 Anchor-Cell Ion Heating

Ion heating is required in the anchor cells to maintain the plasma beta. System requirements are listed in Table 5.4. Both the fundamental and the second harmonic of the cyclotron frequency for deuterium are used. For the high-Γ mode, 800 kW at 25 MHz and 340 kW at 50 MHz are injected at Z = 14.5 m. The estimated trapping fraction is 50%. The axis of the radiator's E field is parallel to the large dimension of the elliptical plasma. This makes an injection angle of 90° in both ϕ and θ. Only the power level is controllable, with a response time that is small compared to the startup time.

Table 5.3. Axicell neutral beam injection system requirements

	Mode-specific requirements		
	High-Q mode	High-Γ mode	Overall requirements
Trapped power, MW	1.86	11.4	
Trapped current, A	31	190	
Average beam energy, keV			60
Fuel species, %			
Deuterium			50
Tritium			50
Injection point			
z-axis, m			0.85
x-y plane (θ), deg			80
x-z or y-z plane (ϕ), deg			42, 137
Beam voltage, keV			80
Species mix			80:15:5
Beam trapping fraction			0.75:0.80:0.80
Incident power, MW	2.4	14.76	
Incident current, A	40.15	246	
Redundancy, %			25
Maximum magnetic field at source, G			2
Maximum magnetic field at neutralizer, G			10
Control			
Power, %			100–50
Energy, %			100–50
Response time, s			A few tenths

Table 5.4. Anchor-cell ion heating requirements

	Mode-specific requirements		
	High-Q mode	High-Γ mode	Overall requirements
Power per anchor, kW			
25-GHz system			
Incident	700	800	
Trapped	350	400	
50-GHz system			
Incident	130	340	
Trapped	67	170	
Injection point			
z-axis, m			14.5
x-y plane (θ), deg			90
x-z or y-z plane (ϕ), deg			90
Pulse length, s			~1–continuous
Control			
Power, %			10–100
Response time, s			~0.1

5.3.3 Sloshing-Ion Beam Injection

The sloshing-ion beam injection system provides warm plasma confinement. System requirements are listed in Table 5.5. Only 4.2 A of deuterium is required for the high-Γ mode. Because of the high purity required for the full-energy component, the full and average energies are the same to within 1 or 2%. A small plasma target restricts the beam divergence; at the axis, the beam spot is ±25 cm axially and ±7.5 cm in the crossplane. Injection perpendicular to the axis is required. The beam is passed through the large dimension of the elliptical plasma to achieve the best trapping fraction (~20%).

Table 5.5. Sloshing-ion beam injection requirements

Fuel	Deuterium
Power per end cell, kW	
High-Q mode	
Injected	840
Trapped	125
High-Γ mode	
Injected	440
Trapped	85
Energy, keV	
Full	200
Average	~200
Pulse length, s	~1–continuous
Injection point	
z-axis, m	±18.6
x-y plane (θ), deg	0, 90
x-z or y-z plane (ϕ), deg	~90
Plasma target, cm	50 (axial) × 50 (radial)
Control	
Power, %	100–50
Energy, %	100–50
Response time, s	A few tenths

5.3.4 Plug Barrier Electron Heating

The plug-cell electron heating systems provide thermal and potential barriers in the end plug. System requirements are listed in Table 5.6. Power is injected at Z = 20.2 m (point a), where the electrons are classified as warm (~110 keV), and at Z = 18.6 m (point b), where there is a population of energetic (~700-keV) electrons. Two frequencies, 35 and 56 GHz, have been selected based on plasma conditions. Taking into account the beta, relativistic mass effect, and Doppler effects, the electron cyclotron frequency of the warm electrons is $0.81\omega_{ce}$, and that of the energetic electrons is about $0.6\omega_{ce}$, where ω_{ce} is the electron cyclotron frequency. Plasma analyses, including ray tracing studies, on devices similar to MFTF-α+T yield trapping frequencies of ~85%. The trapped and incident powers for this system are based on these analyses. The X mode is believed to provide the best absorption. Injection angles must be optimized for this device, but based

Table 5.6. Plug-cell barrier electron heating requirements

		Point *b*		
	Point *a*	System 1	System 2	Overall system
Frequency, GHz	56	35	56	
Power per plug, kW				
High-Q mode				
Incident	72	384	360	
Trapped	60	320	300	
High-Γ mode				
Incident	120	600	480	
Trapped	100	500	400	
Mode	X	X	X	
Injection point				
z-axis, m	± 20.2	± 18.6	± 18.6	
x-y plane (θ), deg	0, 90	± 45	± 45	
x-z or y-z plane (ϕ), deg	~ 80	~ 45	~ 45	
Pulse length, s				$\sim$1–continuous
Control				
Power, %				TBD[a]
Response time, s				$\sim$0.2

[a]To be determined.

on previous studies, the injection point is through the small-radius opening of the plug coil at point *b* and through the large-radius opening at point *a*. At point *a*, the beam center forms an angle of $\sim 45°$ to the plane of the coil and is about 10° off normal. At point *b*, injection is 45° off normal. It is expected that control of the power level will be required during startup.

5.3.5 Drift Pumping

The drift pumping systems enhance radial drift by degrading the geodesic curvature in a controlled manner. The field in the plug and anchor regions is perturbed at a frequency corresponding to the ion particle transit frequency (70 to 80 kHz for the anchor and 600 kHz for the plug). Because there is a large spread in particle transit times, the drift pumping frequency has a spread of $\pm 20\%$ at 70–80 kHz and $\pm 7\%$ at 600 kHz. System requirements are listed in Table 5.7.

Plasma engineering analyses and simulations indicate that for operation in the high-Γ mode, 6 kA·turns is required to perturb the field in each cell. This is divided between two coils modeled after those in the Mirror Advanced Reactor Study (MARS) straddling the plasma. (The reactive power listed in Table 5.7 is an estimate for one 3-kA coil.)

Injection is broadside to the large radius of the elliptical plasma. At least three approaches are acceptable for frequency modulation: band-limited noise, swept frequency, and discrete tones. With the swept approach, the time required to change frequency across

Table 5.7. Drift pumping requirements

	Anchor	Plug
Power per coil		
Reactive,[a] MVA		
High-Q mode	6.6	0.2
High-Γ mode	30	0.2
Plasma, kW		
High-Q mode	50	24
High-Γ mode	150	24
Current per coil, kA	3	0.4
Frequency		
Center, kHz		
High-Q mode	80	600
High-Γ mode	70	600
Deviation, kHz	± 14	± 42
Sweep time, s	~0.07	0.1
Number of discrete frequencies		
High-Q mode	12	$\geqslant 60$
High-Γ mode	10	$\geqslant 60$
Injection point		
z-axis, m	± 13.8	± 17.4
x-y plane (θ), deg	0, 90	90, 0
x-z or y-z plane (ϕ), deg	90	90
Coil to plasma, cm	TBD[b]	TBD[b]
Control		
Power, %	20–100	20–100
Frequency, %	TBD	TBD
Bandwidth, %	TBD	TBD
Response time, s	50.2	$\geqslant 0.2$

[a]Not a requirement.
[b]To be determined.

the band must be 0.1 s. For the discrete frequency approach, it is assumed that the frequencies are equally spaced across the band. The power at each of these tones is the total power divided by the number of frequencies (coil current divided by the square root of the number of tones). Control requirements depend on the startup requirements. Control of power level and possibly of frequency and frequency deviation may be necessary.

5.3.6 Deuterium Gas Injectors

Deuterium gas injectors, also known as gas puffers, are needed to backfill the vacuum vessel to establish the initial pressure at startup. These injectors will be installed at four locations: two in the central cell and one between each anchor and plug cell. During the glow discharge and during startup, all gas injectors will be in operation. Both pulsed-flow and modulated-flow modes are provided. System requirements are listed in Table 5.8.

Table 5.8. Deuterium gas injection requirements

Number of central-cell injectors	2
Number of end-cell injectors	2
Maximum gas flow per central-cell injector, g/h	180[a]
Maximum gas flow per end-cell injector, g/h	180
Gas composition	>99% D_2

[a]Design-point neutral-beam injection current rate is 240 A (=18 g/h of D_2) in high-Γ mode.

5.4 DESIGN DESCRIPTION

5.4.1 Axicell Neutral Beam Injectors

The axicell neutral beam system is based largely on existing technology, but there are three aspects of MFTF-α+T that complicate the design of the system: the requirement for steady-state operation, the environmental difficulties presented by the neutrons and the magnetic fields, and the need for tritium. These issues were addressed in the TDF study,[1] and the design of the MFTF-α+T axicell neutral beams is based on that for the TDF central-cell beams.

The total beam current injected into the plasma (246 A) can be achieved with two beam lines configured in one of two ways: (1) two TDF beam lines, each with four sources (three operating, one redundant), and lower source currents than in TDF, or (2) two beam lines, each with three sources (five operating and one redundant), at the TDF 70-A current level, which reduces beam line size. The first option was chosen because the lower current (60 A) relaxes issues associated with steady-state operation of the accelerator grids and because a redundant source is required for both the tritium and the deuterium species. Because the neutral beam sources will probably require the most frequent maintenance of all reactor components, 33% redundancy seemed a reasonable level.

The two axicell beam lines are located on opposite sides of the device; their beams intersect the plasma axis at an angle of 80°. The beam lines are angled 2° downward from horizontal so that their internal components can be withdrawn into a hot cell on the first floor. Figures 5.2 and 5.3 show the locations of the beams in the central cell.

The beam dump for each beam is located in a chamber opposite the beam line and attached to the vacuum vessel. This provides area for pumping and allows maintenance by simple vertical removal of the modular hardware. The grouping of four sources in a single vacuum vessel allows them to share cryopanels, drift ducts, reflecting magnets, shields, and shinethrough beam dumps, thus reducing engineering, fabrication, maintenance, and cost. The arrangement of the beam line components is shown schematically in Figs. 5.4 and 5.5. The concepts are standard except for the total power level in the beam line. The sources use the Oak Ridge National Laboratory (ORNL) long-pulse design.[2,3] Using fewer grids for the lower MFTF-α+T energy, the sources should extract 60 A at 80 keV in a steady-state mode.

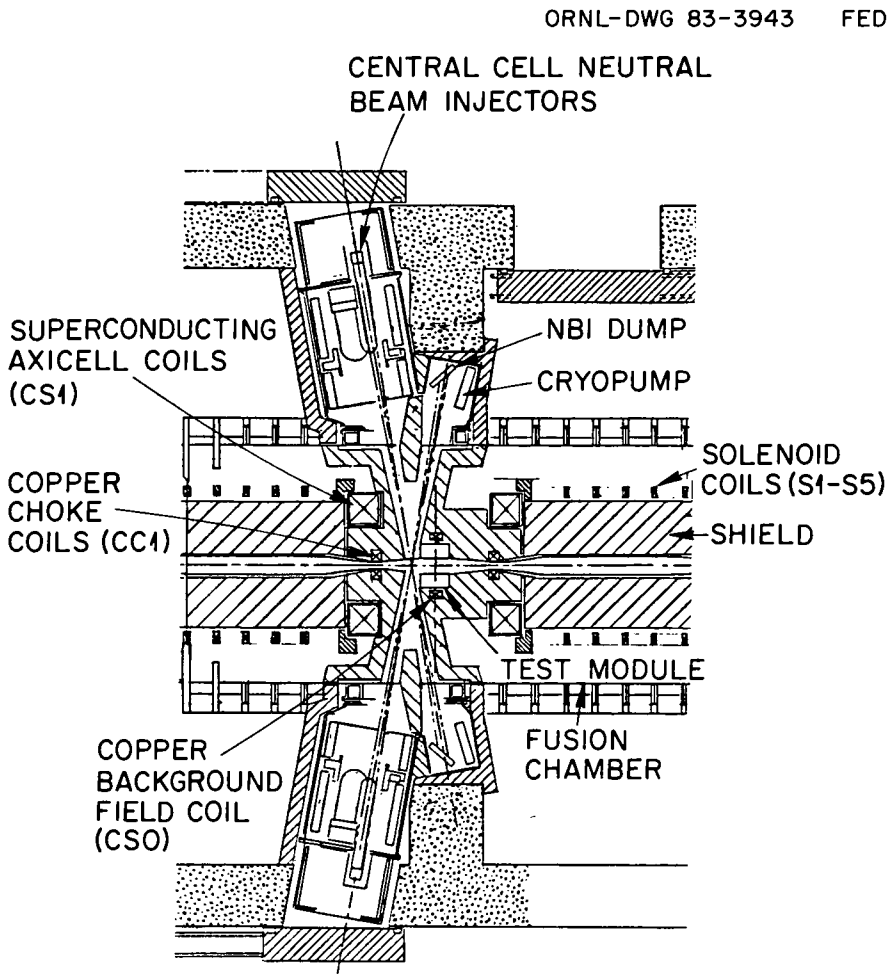

Fig. 5.2. The D-T axicell insert, showing the neutral beam lines.

Grids with a circular aperture are used because spatial and neutronic constraints on the duct design required the smallest possible divergence in the x- and y-directions and because of the small plasma radius in the axicell. Replacement sources can be aligned with the grids, which are suspended from gimbals and controlled by a step motor.

The neutralizer is a low-conductance, water-cooled, tapered rectangular duct with little clearance between the beam and the duct walls. A high target density can be maintained with a low gas load into the beam line cryopanels. The neutralizer length provides optimum target thickness (95% of equilibrium neutralization).

The reflector magnet that separates the neutral particles and the ions is based on the Doublet III (DIII) beam line magnet.[4] Beam loss due to background gas is minimized. The copper magnet and adjacent baffle separate the beam line vessel into two sections: a short high-pressure section and a low-pressure transition section between the magnet and the beam duct. The magnet strengths are 0.128 T for deuterium and 0.157 T for tritium.

The drift duct (through which the neutralized beam is injected into the plasma) is long, narrow, and tapered to meet shielding and neutronic constraints. In TDF, a detailed

ORNL-DWG 83-4028 FED

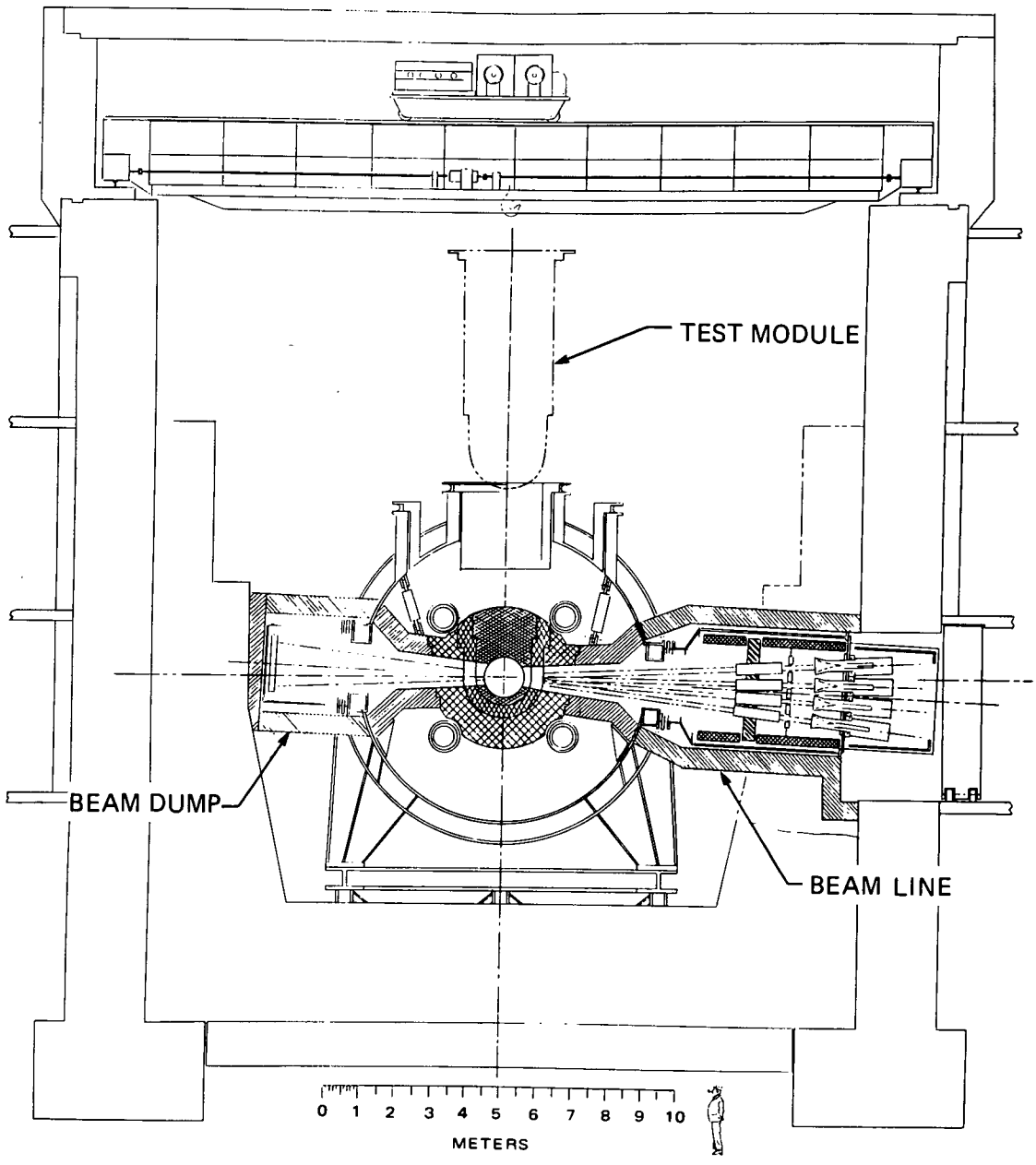

Fig. 5.3. Elevation through center cell, showing a neutral beam line.

analysis was performed to determine the beam loss, the density distribution in the duct, and the duct conductance.[1] The duct cross section was chosen as the best compromise between a narrow, low-conductance duct that limits neutron flux but has high beam losses and a wide duct.

ORNL–DWG 84-16493 FED

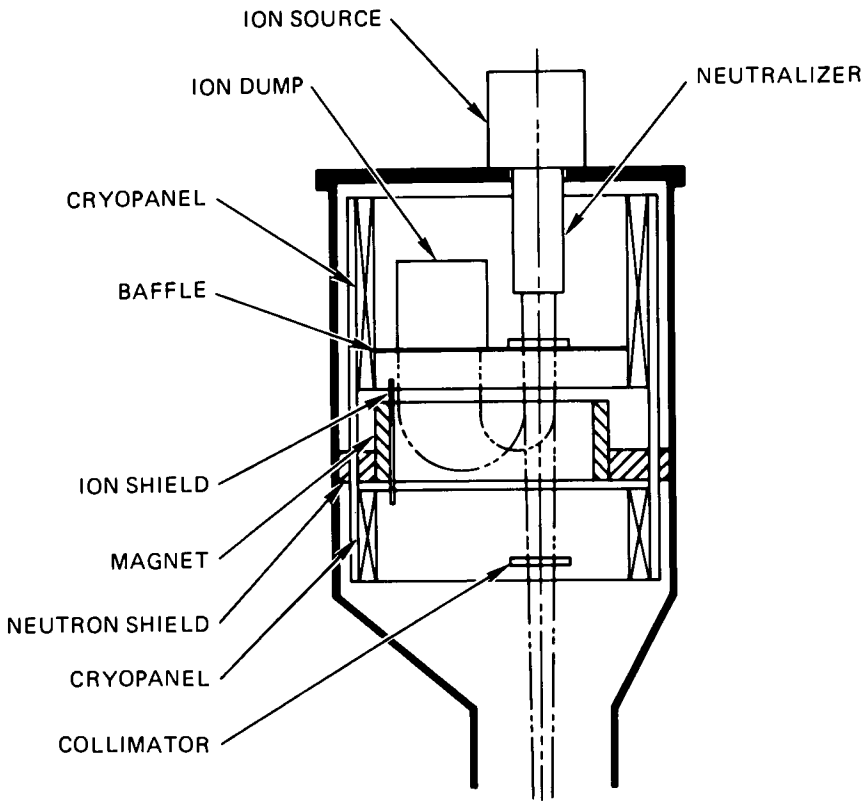

Fig. 5.4. Arrangement of beam line components.

ORNL–DWG 84-16494 FED

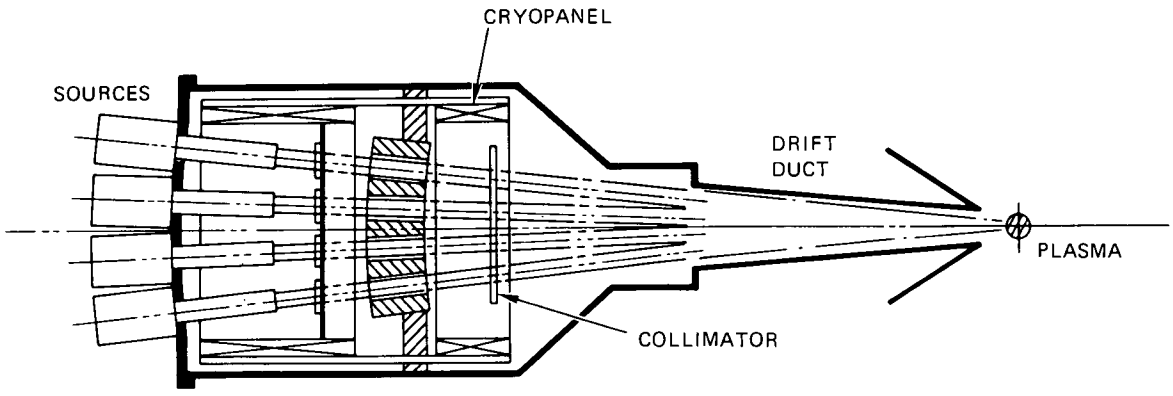

Fig. 5.5. Beam line layout.

Analysis and description of the rest of the beam line (i.e., ion dumps, vacuum system, cooling requirements, collimator placement, instrumentation, controls, data acquisition, and servicing procedure) are documented extensively in ref. 1. The shielding for the beam line is described in Sect. 5.6.1. The system performance is discussed in Sect. 5.5.1.

5.4.2 Anchor-Cell Ion Heating

System overview

Figure 5.6 shows the ICRH launchers interfacing with MFTF-α+T. There are two sets of launchers (see Fig. 5.7), one for fundamental heating at 25 MHz and one for second harmonic heating at 50 MHz. Each launcher is supplied with power from a transmitter via a pressurized 3.125-in. coaxial cable. Common signal sources provide the excitation for the high-power amplifiers. Instrumentation and control interfaces with major components are effected with fiber optics. The power chains are modified versions of those used on MFTF-B. The main difference between the two units is the center frequency, so only one of them is described in detail.

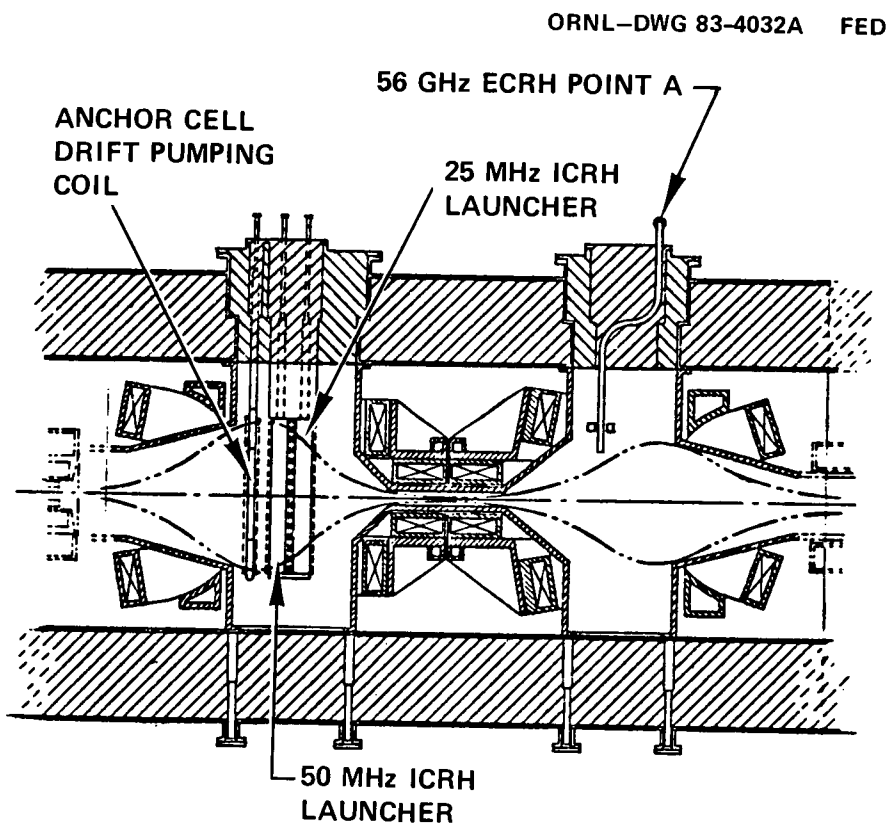

Fig. 5.6. Anchor-cell ICRH system.

ORNL–DWG 84-16489 FED

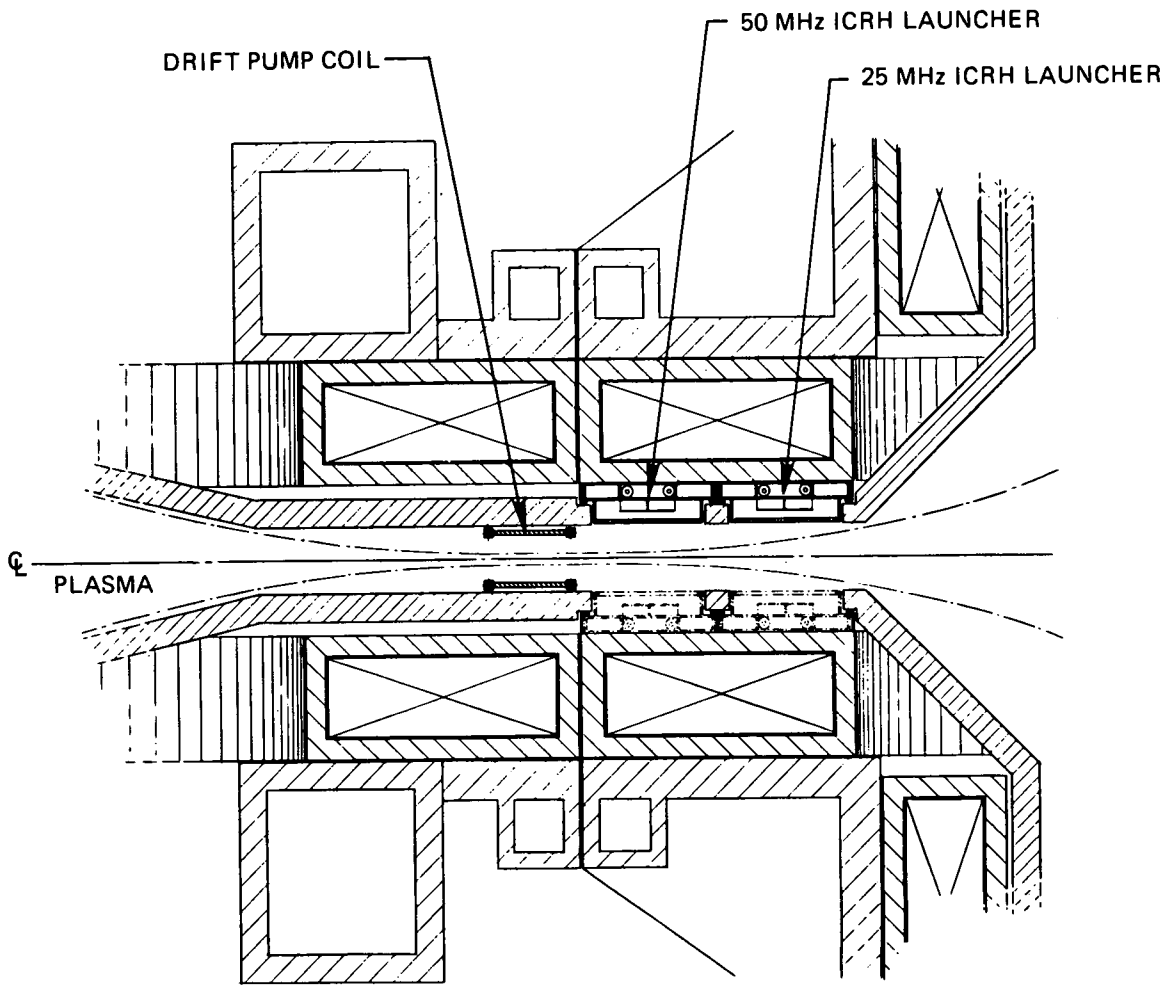

Fig. 5.7. ICRH launcher.

Antenna/launcher

The center-fed loop antenna (Fig. 5.8) is about 3 m long. At 50 MHz, this is a half-wave dipole and therefore presents a resistive load to the line; at 25 MHz, it is a quarter-wave dipole and requires significant matching. A cooled Faraday shield protects the loop conductor from particle flux and polarizes the radiation. Two 1.675-in. coaxial cables that feed the loops are routed under the ground plane to a convenient connection point on the end of the launcher assembly. A box beam on each side of the cables stiffens the assembly; access is through a plug in the nuclear shield (Fig. 5.8). An impedance-matching network is used on each cable to tune out the reactive component of the impedance. These networks are supplied by a hybrid power splitter, which in turn is fed by the 3.125-in. cable from the transmitter.

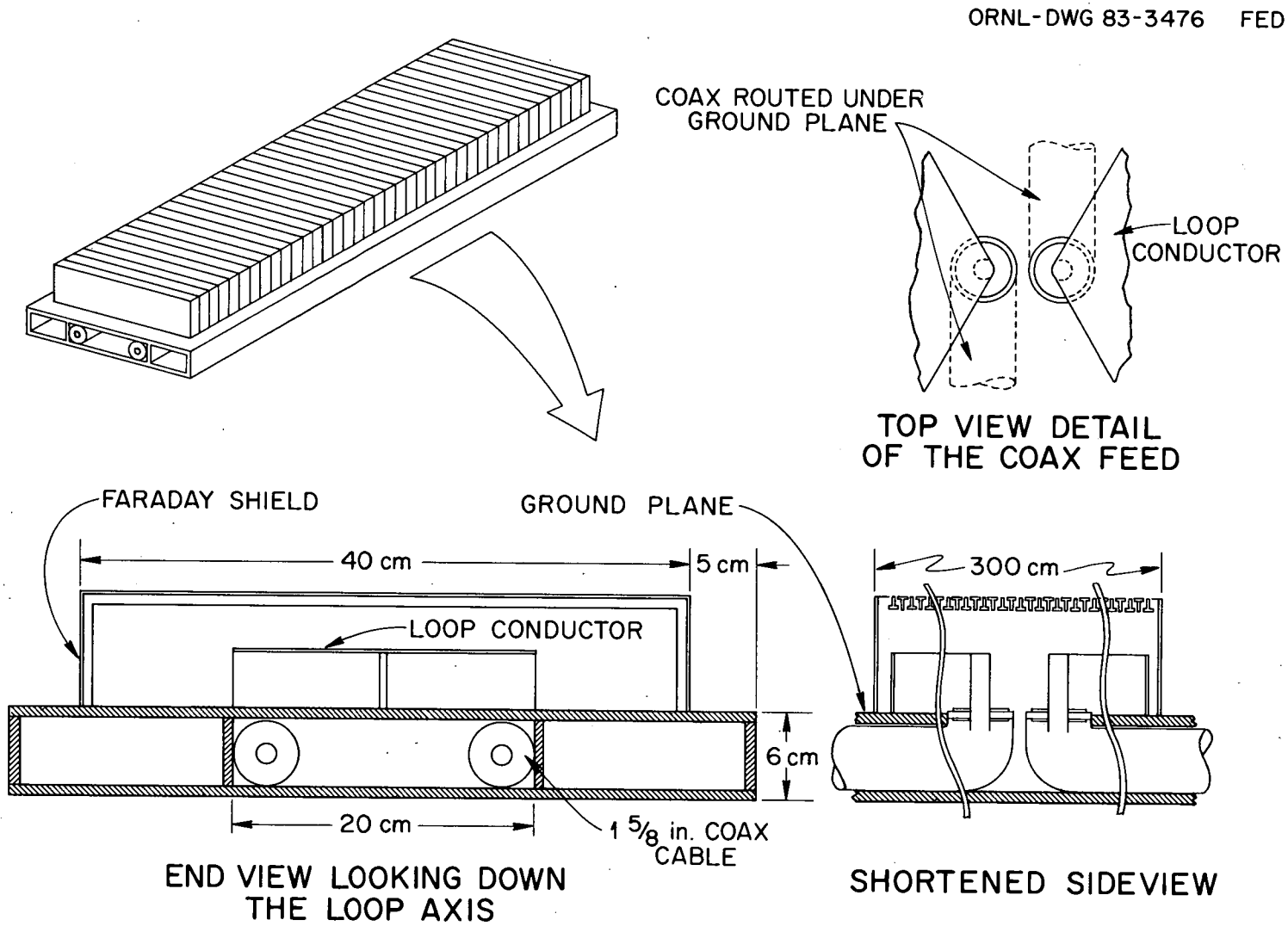

Fig. 5.8. Antenna structure.

Transmitter

An ICRH system used for central-cell heating on MFTF-B, which provides 900 kW (at the tube flange) in the range from 12 to 20 MHz, will be upgraded to operate at 25 MHz with two outputs for pulses of 30 s. New resonators will replace the old 12- to 20-MHz circuits. A 3-dB hybrid will be fitted to the output to supply 400 kW to each antenna. For redundancy, a transmitter feeds one loop in each anchor cell. A second modified MFTF-B transmitter will supply the second set of loops on the other side of the plasma (see Fig. 5.9).

These transmitters should operate in a steady state with few or no modifications. The planned high-power amplifier tubes (Eimac 2159) should be able to operate at 50 MHz. The requirement for 340 kW per cell is met by the 400-kW capability of each output port. The modified power chains have been fitted with digital attenuators and provisions for bias control to allow control of the power output.

5.4.3 Sloshing-Ion Neutral Beam Injectors

The sloshing-ion neutral beam injectors perform the function, essential in tandem mirror reactors, of aiding in the formation of thermal barriers by maintaining the sloshing ions. The neutral beams, aimed slightly off the midplane of the end plugs, generate high-energy ions that are trapped by the magnetic well formed by the end-plug magnets. These ions, sloshing back and forth, help form a potential minimum at the center of the magnetic well.[5] This potential separates the cold electrons in the central cell from the hot electrons in the end plugs and collects low-energy ions that fill out the low-energy end of the ion distribution in velocity space. These ions dampen out the oscillations that cause microinstabilities. To be effective, the potential minimum must be great enough to hold back the hot electrons while sustaining an adequate density of low-energy ions. In MFTF-α+T, with a moderate mirror ratio of three to four, this requires a 200-keV beam of several amperes.

The negative-ion-based neutral beam injector used to generate sloshing ions has four LBL self-extracting, 200-keV, negative-ion sources, similar to the 80-keV source[6] shown in Fig. 5.10. Each source can deliver 3.4 A of D^- ions; three sources are active and one is a spare.

Negative ions are formed at a pressure of roughly 10^{-3} torr by positive ion bombardment of the cesium-coated, negative-ion-forming electrode.[7] Because the electrode is curved and biased at about -150 V with respect to the discharge plasma and is surrounded by a positive sheath that aims the newly formed negative ions at the ion exit aperture, it accelerates the ions to 150 V.

The negative ions emitted from each source are formed into a 3- by 56-cm ribbon beam and then accelerated to 200 keV by a sequence of grids. The beam travels to the neutralizer via a pair of electrostatic TFF electrodes,[8] as shown in Fig. 5.11. The injector, including the four ion sources, is enclosed in a magnetic shield extending from the sources to the far end of the neutralizer. The sources, accelerators, and ion transports are mounted side by side within a radiation-shielded chamber equipped with a neutron trap.[9] Two sources are located above the neutralizer, and two are below.

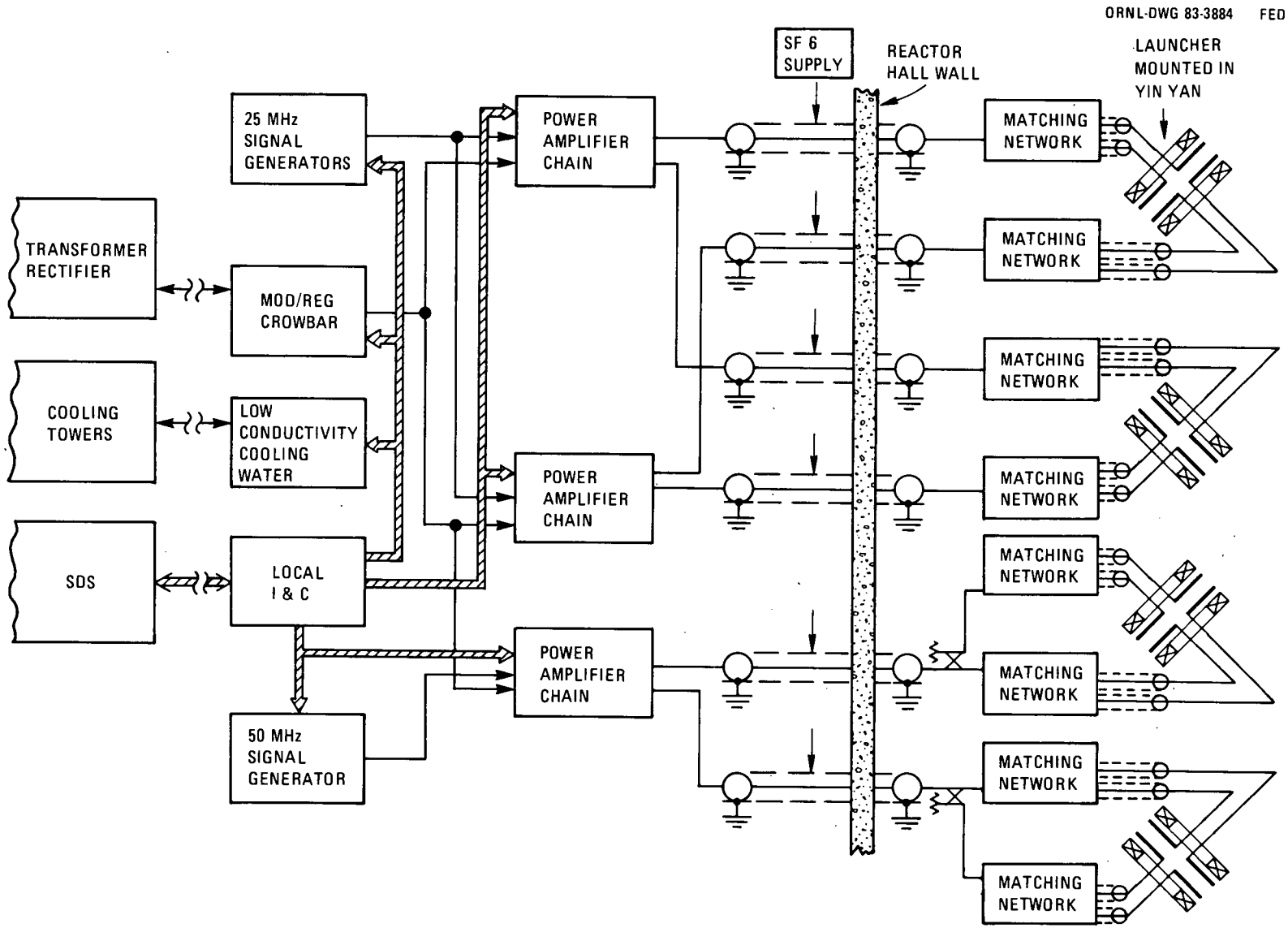

Fig. 5.9. ICRH transmitter setup.

ORNL-DWG 83-3900 FED

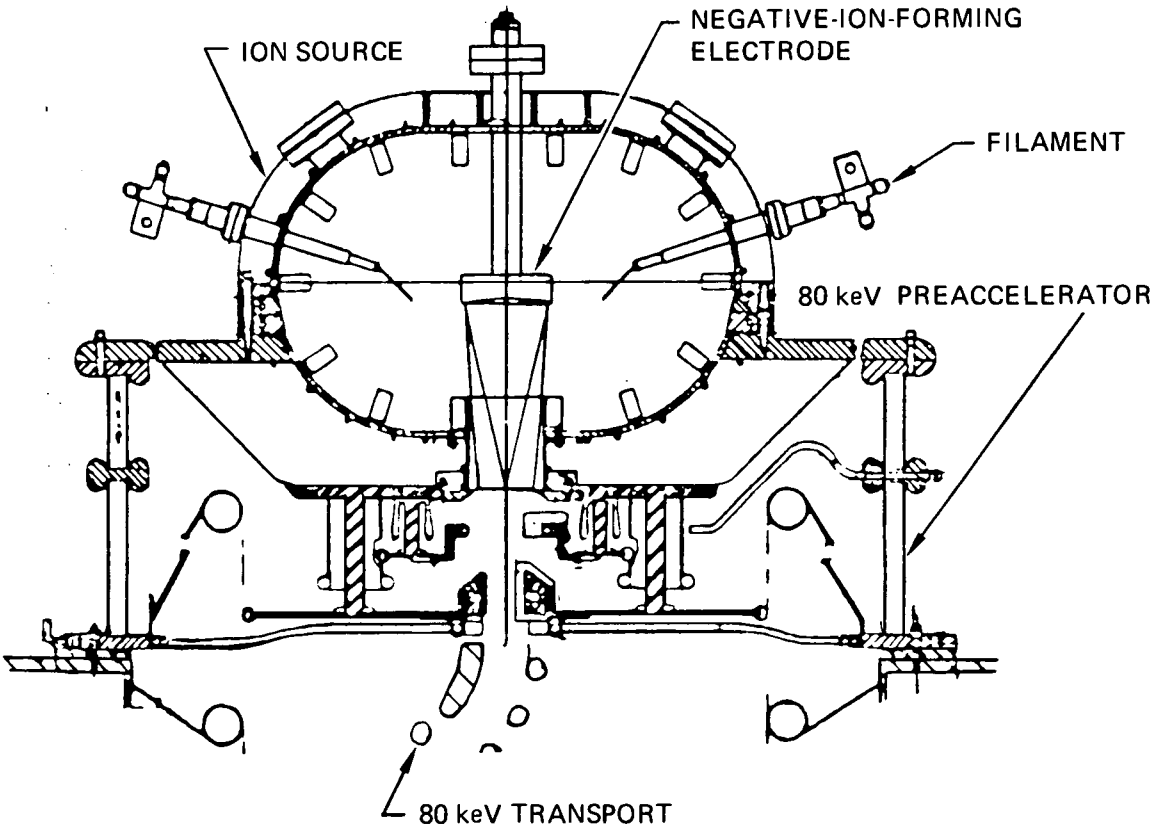

Fig. 5.10. Self-extracting negative-ion source.

To minimize the loss of negative ions that results from collisions with the background gas, the pressure in the shielded chamber must be 5×10^{-5} torr or less. A set of continuously recycling cryopumps[10] removes the gas coming out of both the ion sources and the neutralizer.

To obtain the maximum fraction of neutrals in the beam, the neutralizer must be at an optimum thickness, that is, a specific average gas density multiplied by the neutralizer length.[11] This is accomplished by feeding gas into the center of the neutralizer and letting it flow out both ends. The desired thickness is maintained by adjusting the inlet pressure and matching it to the flow of gas through the neutralizer.

The gas that flows into the shielded chamber from the neutralizer is pumped away by cryopumps. At the other end of the neutralizer, gas flows into the end-plug chamber and is ionized by the halo of ions and electrons surrounding the target plasma,[12] after which it is pumped away, with the rest of the halo,[13] by cryopumps at the end wall of the end-plug chamber.

At the output of the neutralizer, where the magnetic shielding stops, the unneutralized ions traveling with the beam encounter the magnetic field of the end-plug magnets. This ~0.2-T field is parallel to the wide dimension of the ribbon beam, so that the positive and

ORNL–DWG 83-4016A3 FED

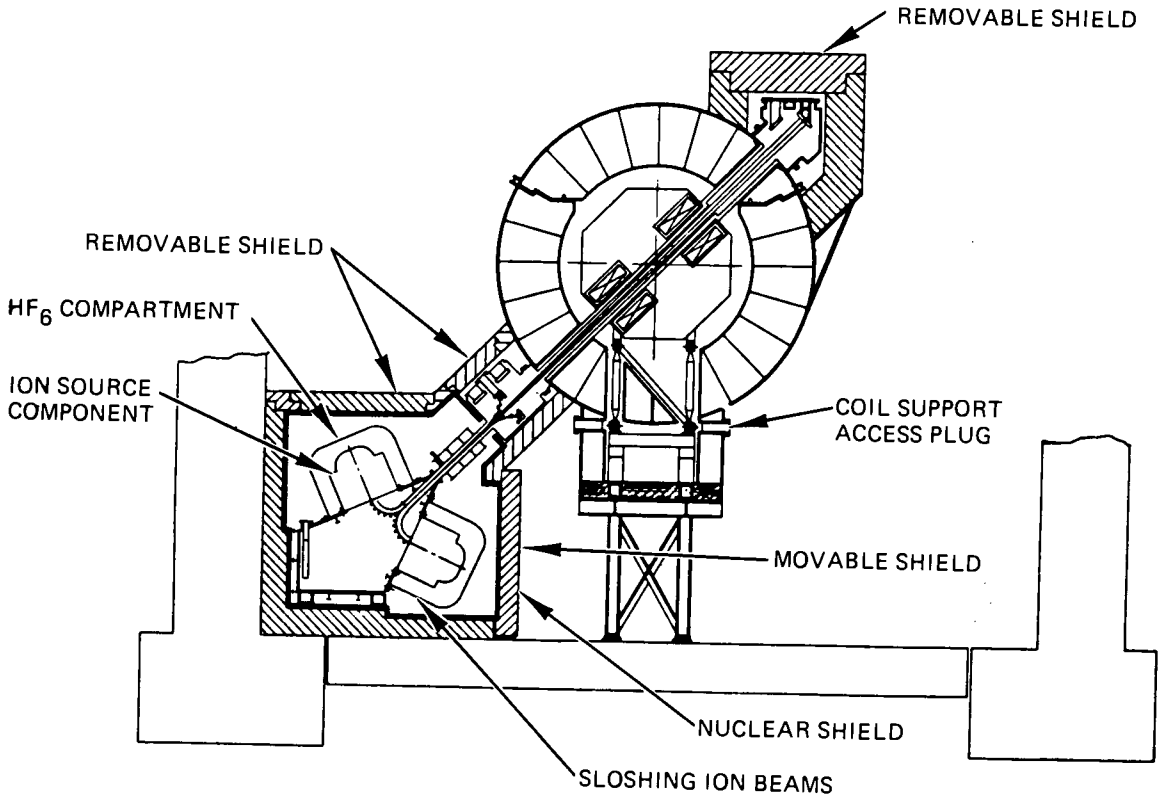

Fig. 5.11. Sloshing-ion neutral beam arrangement.

negative ions are deflected in opposite directions across the narrow dimension of the beam and are collected in their respective ion dumps. Additional cryopumps in this region limit the amount of gas flowing into the reactor.

While traveling toward the plasma target, a small fraction of the high-energy neutral beam is subject to ionization from impact with the background gas. At the plasma target, meanwhile, the majority of the 4.2-A beam of neutrals is ionized. To collect the neutrals that pass through the plasma target unperturbed, a beam dump is mounted on the far wall of the end-plug chamber.

5.4.4 Plug Barrier Electron Heating

System overview

Electron cyclotron resonance heating is applied at two points, designated point *a* ($Z = \pm 20.2$ m) and point *b* ($Z = \pm 18.6$ m) in the plug cell. Figure 5.12 shows the six 2.5-in.-diam circular waveguides that provide power to point *a*, and Fig. 5.13 shows the seventh that provides power to point *b*. The supply system for these waveguides, shown in Fig. 5.14, is composed of modified equipment from MFTF-B and new equipment built to

ORNL–DWG 83-4031A FED

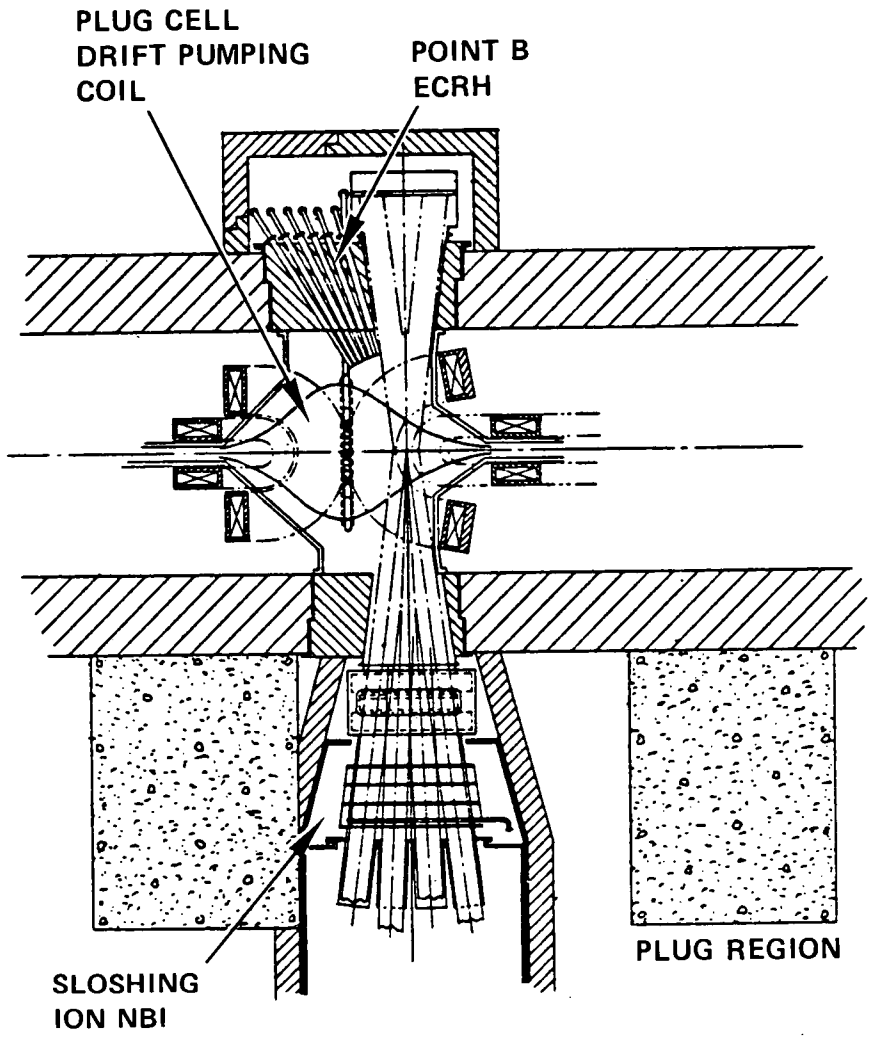

Fig. 5.12. Point *a* ECRH injection interface.

the same design. The 28-GHz gyrotron and most of its transmission system from MFTF-B will be replaced with 35-GHz components. The new gyrotron will operate at 320 kW, compared to 200 kW in the existing tubes. (Justification for the assumption of the higher tube power is discussed in Sect. 5.5.4.) Given an efficiency from gyrotron to launcher[14] of ~70% *for the desired mode*, these two converted units plus one MFTF-B unit supply the needed 600 kW to the west plug cell (launchers 1bW, 2bW, and 3bW). The other launchers at this point (4bW, 5bW, and 6bW) are supplied by 56-GHz equipment from MFTF-B, and the 56-GHz power at launcher 1aW is supplied by the fourth MFTF-B 56-GHz channel.

The east plug cell will have new equipment except for one 35-GHz channel from MFTF-B. The low-conductivity cooling equipment can be duplicated and used without

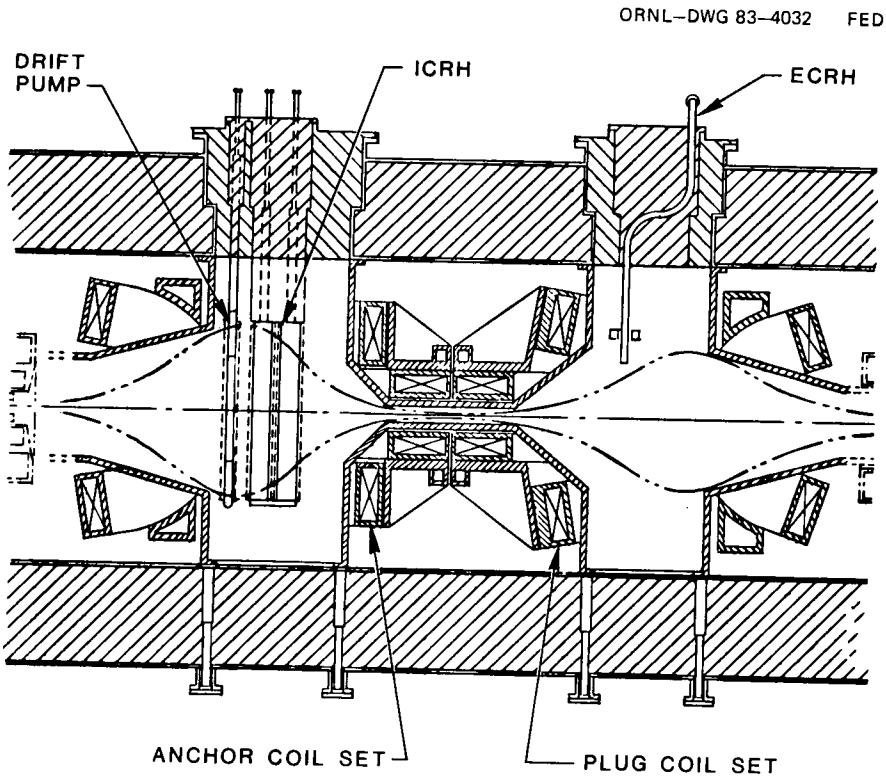

Fig. 5.13. Point *b* ECRH injection interface.

modification. Some modifications to the instrumentation and control (I&C) equipment will be needed so that 14 channels can be monitored. Although the detail of the mode control components is different because of the different modes and mode mixes, each channel has the same arrangement of components, so only one equipment description follows.

Launcher and interface

In 1983, the MFTF-B transmission system was changed from a conventional waveguide to a quasi-optical system. The advantages of each system were examined for MFTF-α+T in a trade study (see Sect. 5.6.3). Mainly because of access constraints, the conventional approach was selected. Figure 5.15 shows the details of the interface. The launcher consists of an open-ended waveguide fitted with a cooled, double-disk rf window. A corrugated circular waveguide is used for the HE mode, producing a Gaussian radiation pattern.[15] Behind the window, the waveguide is pressurized to about 15 psi. The assembly is designed for easy remote maintenance. To replace the window, for example, the external waveguide is disconnected and the ECRH receptacle mounting is loosened and removed. In the device vault or in the hot cell, the launcher is loosened and slid out of the receptacle, which exposes the window assembly.

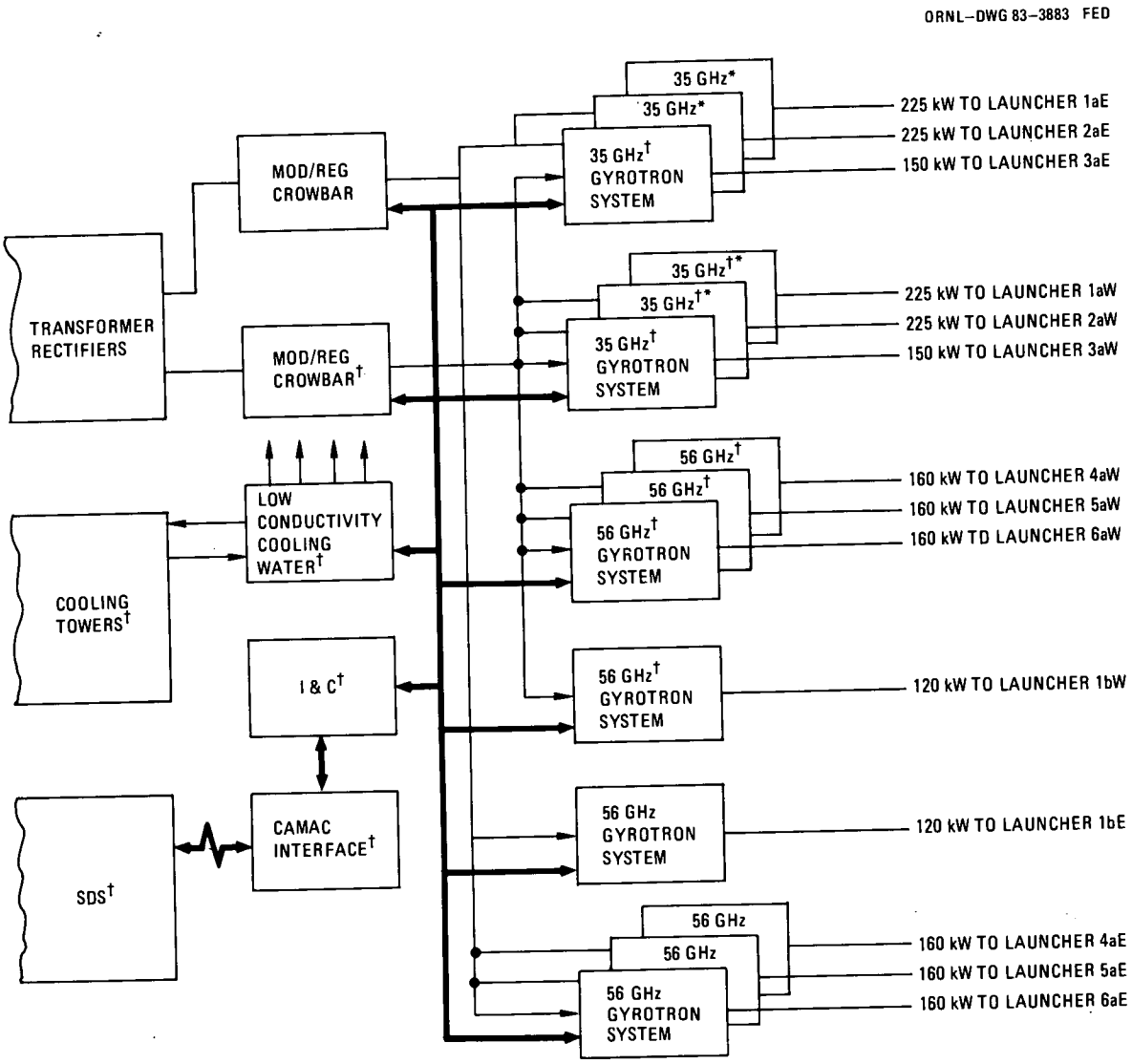

Fig. 5.14. ECRH gyrotron system. (* = New 300-kW gyrotron. † = MFTF-B equipment.)

Transmitter and transmission system modification

Figure 5.16 is a block diagram of the MFTF-B ECRH system as of November 1982.[16] Note the overlap with Fig. 5.14. In the diagram, a separate modulator/regulator is shown for each gyrotron. More recent input[17] indicates that there will probably be a common modulator/regulator for all eight gyrotrons. Control will be via gun anode modulators, a technique successfully used on the Poloidal Divertor Experiment (PDX) and DIII. For MFTF-α+T, the number of channels will be increased to 14. The existing MFTF-B system uses a power supply system capable of 80 A at −90 kV, so a second unit will have to be added to meet the requirement for 160 A at −90 kV. It is expected that this load can be accommodated for long pulses (approaching steady state). An additional modulator/regulator will probably be needed because the load current is doubled.

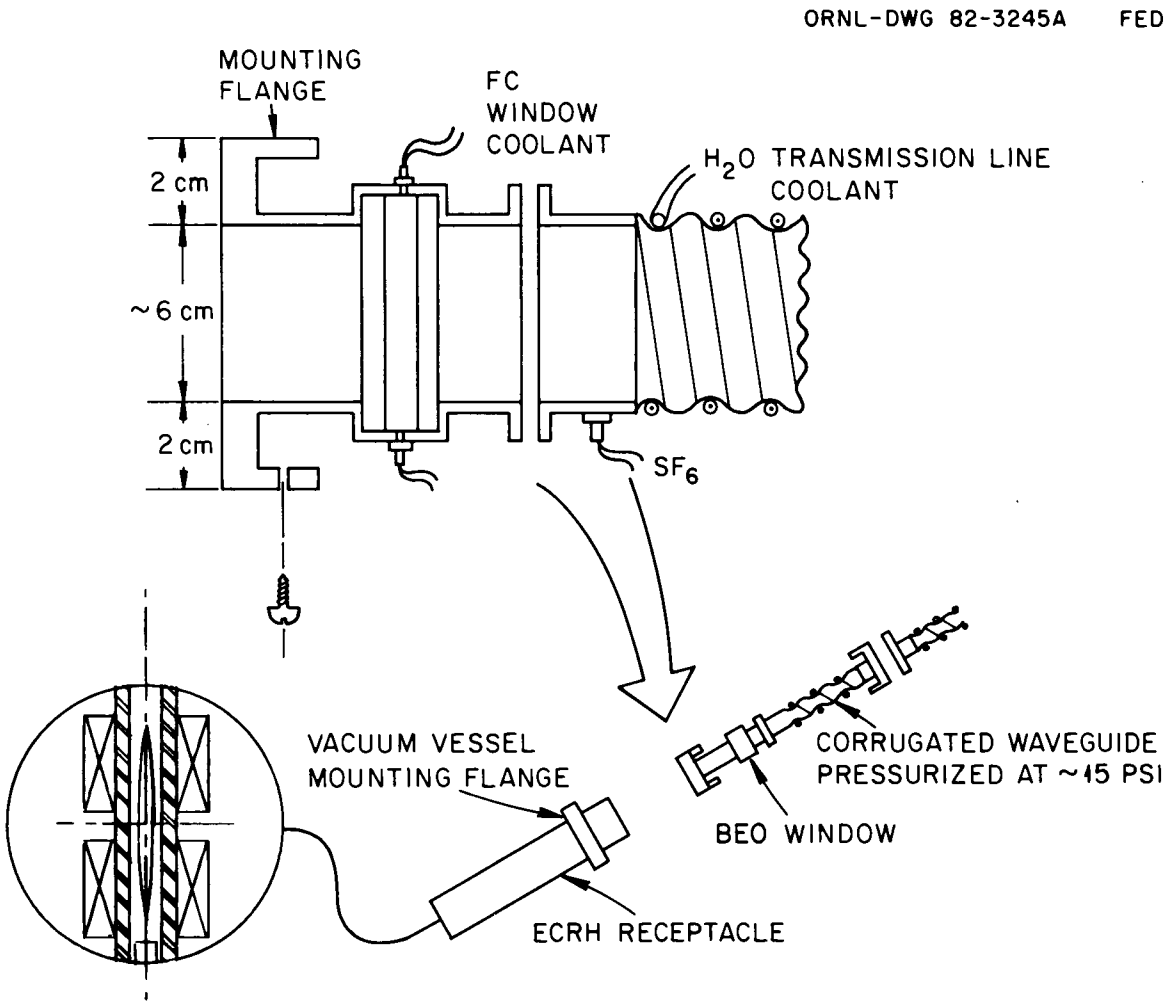

Fig. 5.15. Launcher interface design.

The most recent arrangement planned for MFTF-B and the modifications for MFTF-α+T are shown in Fig. 5.17. The system is the same up to the mode converter. A new mode converter with an HE_{11}-predominant mode output will be installed on MFTF-α+T to drive the corrugated waveguide that supplies the launcher. An arrangement developed for PDX[15] with a 60-GHz pulsed gyrotron employed a cascade of mode convertors from TE_{02} to TE_{01} to TM_{11} and finally to HE_{11}. If this arrangement is adopted for MFTF-α+T, the MFTF-B mode conversion to TE_{01} could be used. At this point, the mode mixes for 35 and 56 GHz for a continuous wave (cw) tube are not known, so the exact detail of the mode converter is speculative.

ORNL–DWG 83-3869 FED

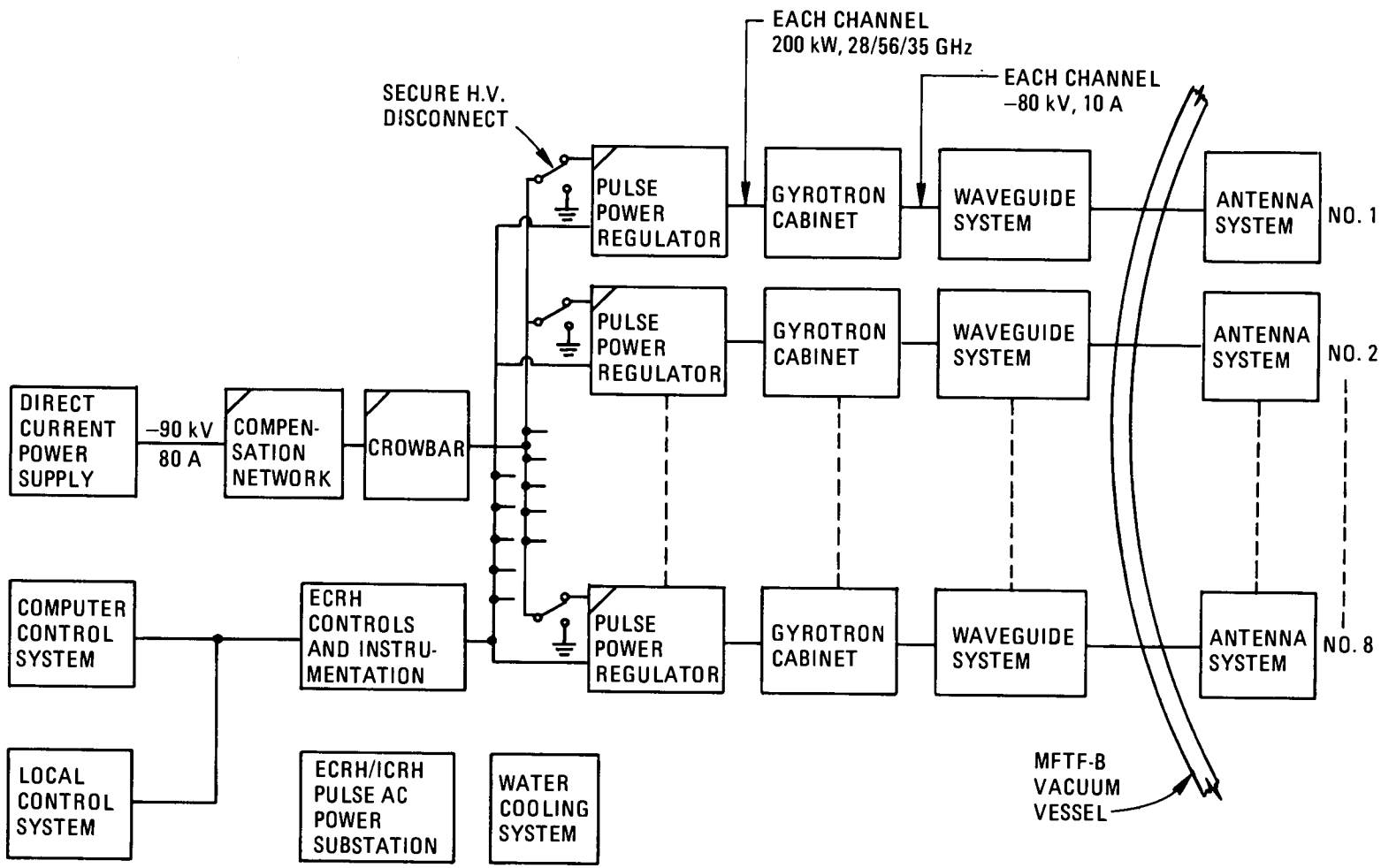

Fig. 5.16. MFTF-B ECRH system (November 1982).

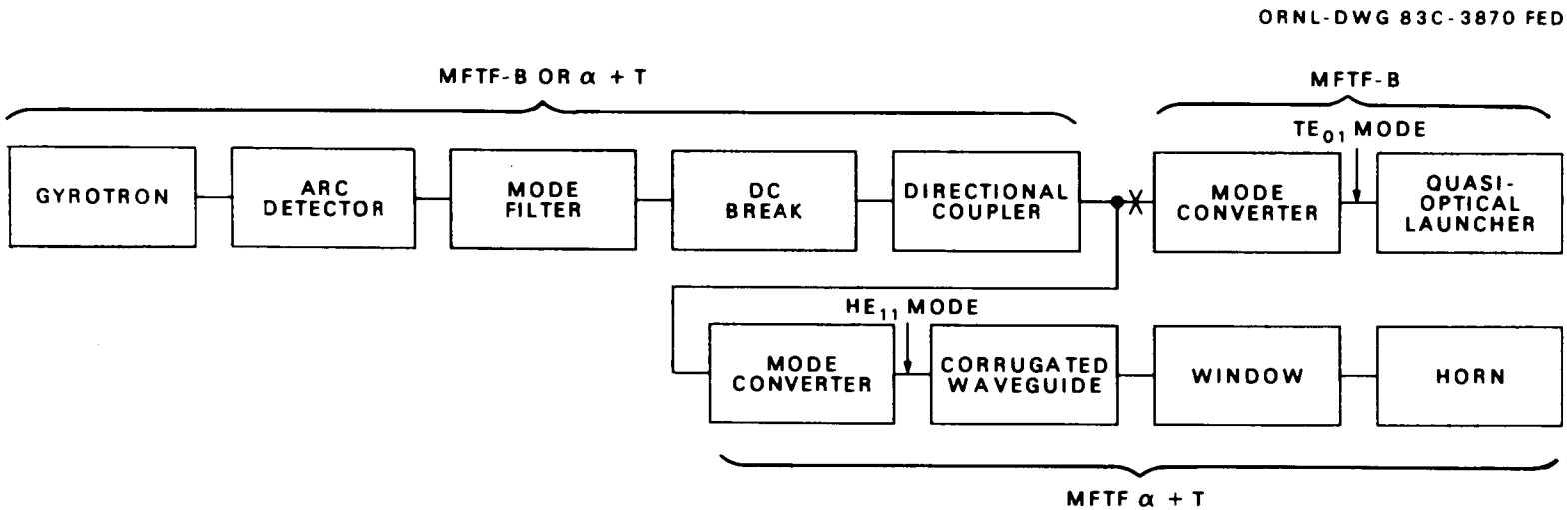

Fig. 5.17. Transmission systems for MFTF-B and MFTF-α+T.

5.4.5 Drift Pumping

Figure 5.18 shows the 70-kHz system for the anchor cells and the 600-kHz system for the plug cells. Both systems use multiple channels to cover the wide-bandwidth spectrum required for drift pumping. The rationale for multiple channels is discussed in Sects. 5.5.6 and 5.6.4. Briefly, it is based on the fact that the drift pumping coil has a high loaded quality factor Q (50–100), corresponding to a 1-dB bandwidth of 1% or 2%. The value of Q can be lowered by increasing the loading, but this wastes power. Expending many megawatts is not practical unless this power can be recovered (this alternative approach is proposed in Sect. 5.6.4).

Two approaches to the multichannel configuration were considered: one in which each channel drives a separate drift pumping coil and one in which a single coil is driven by multiple channels. The second technique is favored at present.

The drift pumping coils themselves use the design developed in the MARS study, which is taken as a "given" for this application. The anchor and plug systems are fairly similar, so that descriptions of the plug system draw on the more detailed descriptions of the anchor system.

System overview

The anchor drift pumping system is shown in the upper part of Fig. 5.18. The anchor signal starts at the spectrum generator, where a choice of spectra, each centered around 70 or 80 kHz, is available. A sweep (linear frequency modulation), band-limited noise, or discrete tones can be transmitted. This excitation drives 12 power amplifier channels combined with tuning channels to drive the set of 2 drift pumping coils connected in series. Each power chain provides about 25 kW to the coils over a channel bandwidth of about 200 Hz. Power is transmitted via 50-Ω pressurized coaxial lines through the reactor vault wall to the matching network units on MFTF-α+T. One drift pumping coil is located on each side of the elliptical plasma (see Fig. 5.19). Details of the matching network layout are shown in Fig. 5.20.

The plug drift pumping system is shown in the center of Fig. 5.18. It has the same basic configuration but a 600-kHz center frequency for both modes. Each channel has a 3-dB bandwidth of ~6.5 kHz and a power output to the coil pair of about 5 kW. Details of the plug matching transformers are shown in Fig. 5.21.

All major components are monitored and controlled by the local data system (LDS) modules. The system may be operated locally for test purposes using the LDS modules. During normal operation, the power and/or frequency scenario is microscheduled from the LDS modules based on macroschedules transmitted via CAMAC from the supervisory control and data system (SCDS). Fiber-optic links are used to communicate with sensors and controllers on the major components and to communicate through the reactor vault wall to monitor power and coolant quantities (temperature, flow and pressure), which are formatted (analog to digital) and buffered before transmission to the LDS modules.

Figure 5.18 also shows inputs from the transformer rectifiers and cooling towers. Modulator/regulators provide the high-voltage plate and screen supplies. A dual loop cooling system provides low-conductivity water to the power chain and drift pumping coils. Forced air cooled by a chiller is also used.

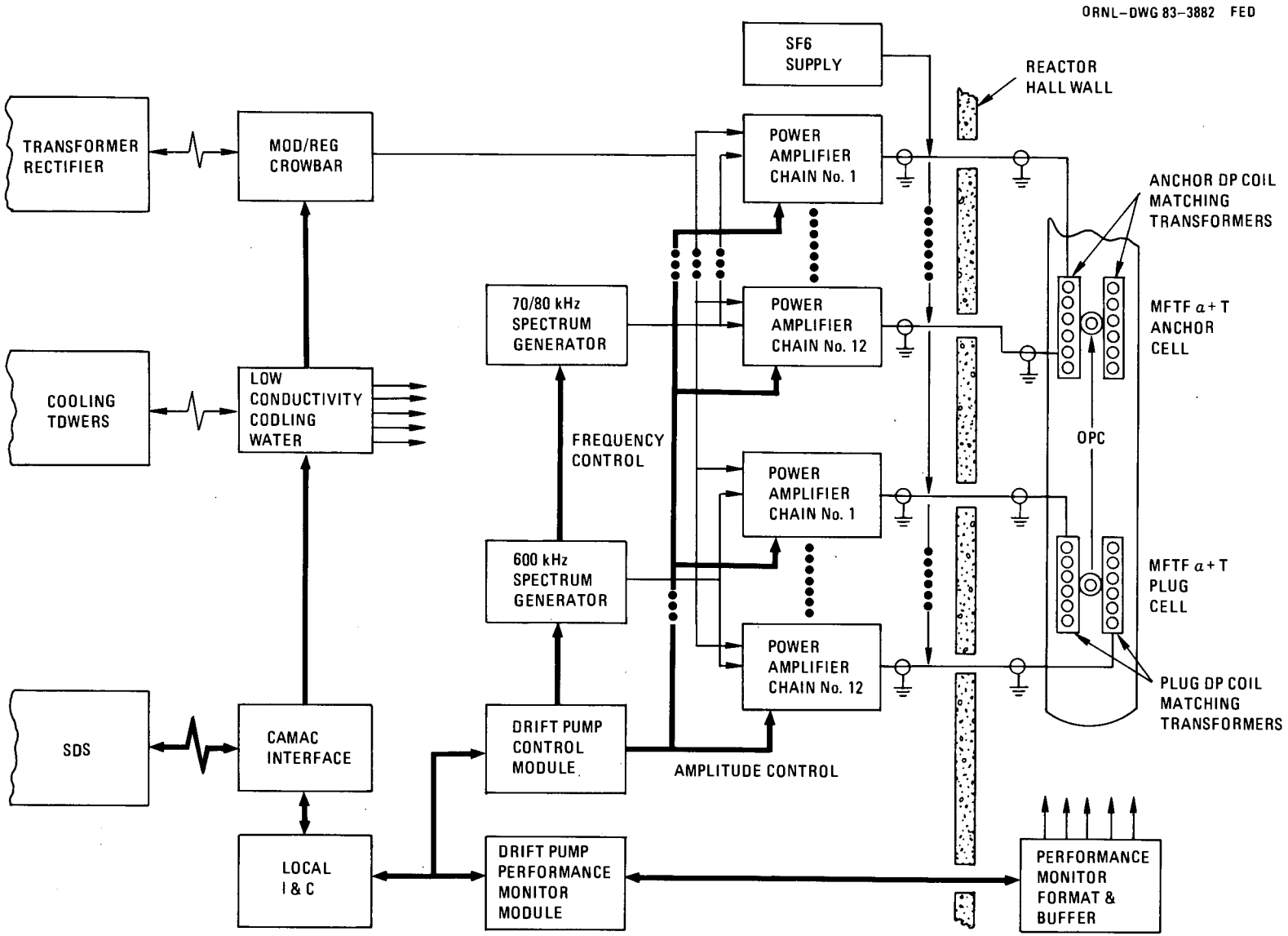

Fig. 5.18. Anchor- and plug-cell drift pumping systems.

ORNL-DWG 83-4005 FED

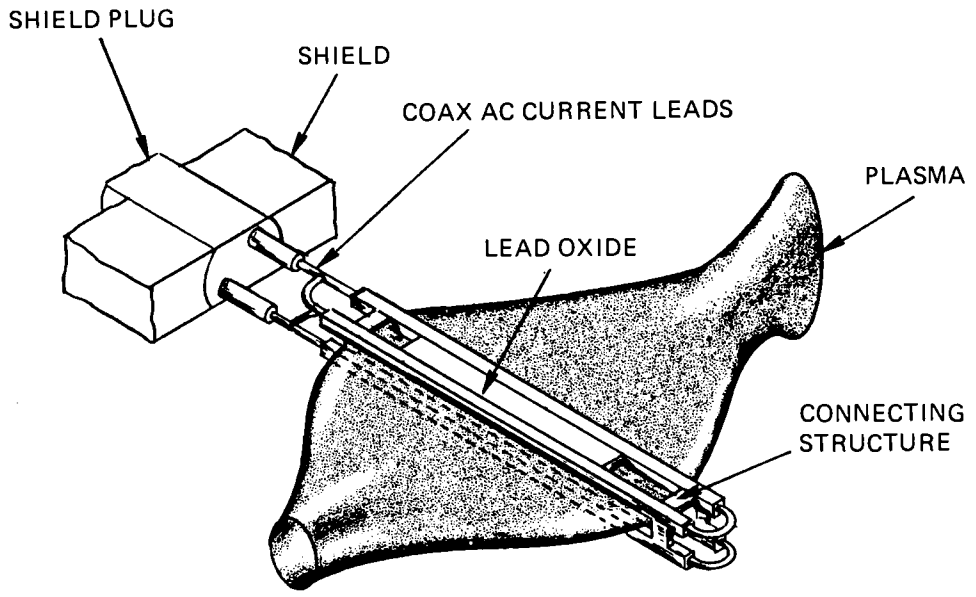

Fig. 5.19. Drift pump antenna arrangement.

Anchor-cell drift pumping transmitter

Figure 5.22 is a detailed block diagram of the anchor-cell drift pumping transmitter. There are 12 channels, each with 3 modulation inputs to choose from. Discrete-tone excitation is provided by a crystal oscillator; band-limited noise, by a random noise generator; and the swept cw drive, by a voltage-controlled oscillator driven by a sawtooth generator. Because the Q of the drift pumping coil is high, its bandwidth is small compared to that required to cover the 40% bandwidth with only 12 channels. Therefore, the anchor drift pumping spectrum is approximated by the 12 narrow-band channels (see Fig. 5.23). This arrangement is used for both the high-Q and high-Γ modes.

The high-power amplifier (HPA) has a power gain of only about 10 to 20 dB when operating in class C, so an intermediate power amplifier (IPA) is used. These amplifiers provide about 4 kW. Operation will be in class AB. Most of the time, the drive requirements are much lower. Since the HPA is operated in this linear class, power output can be controlled via a digital attenuator in its drive circuit. The details of the HPA plate circuit and transmission system are shown in Fig. 5.24. This power chain has an overall efficiency (prime power to plasma power) of about 30%.

Plug-cell drift pumping transmitter

Because of similarities in the anchor-cell and plug-cell drift pumping transmitters, the block diagram of the anchor-cell system (Fig. 5.22) is applicable to the plug-cell system. However, the plug-cell HPA output circuit and transmission system are different; they are shown in Fig. 5.25. The total bandwidth, (600 ± 42) kHz, is covered by 12 channels,

ORNL-DWG 83C-3881 FED

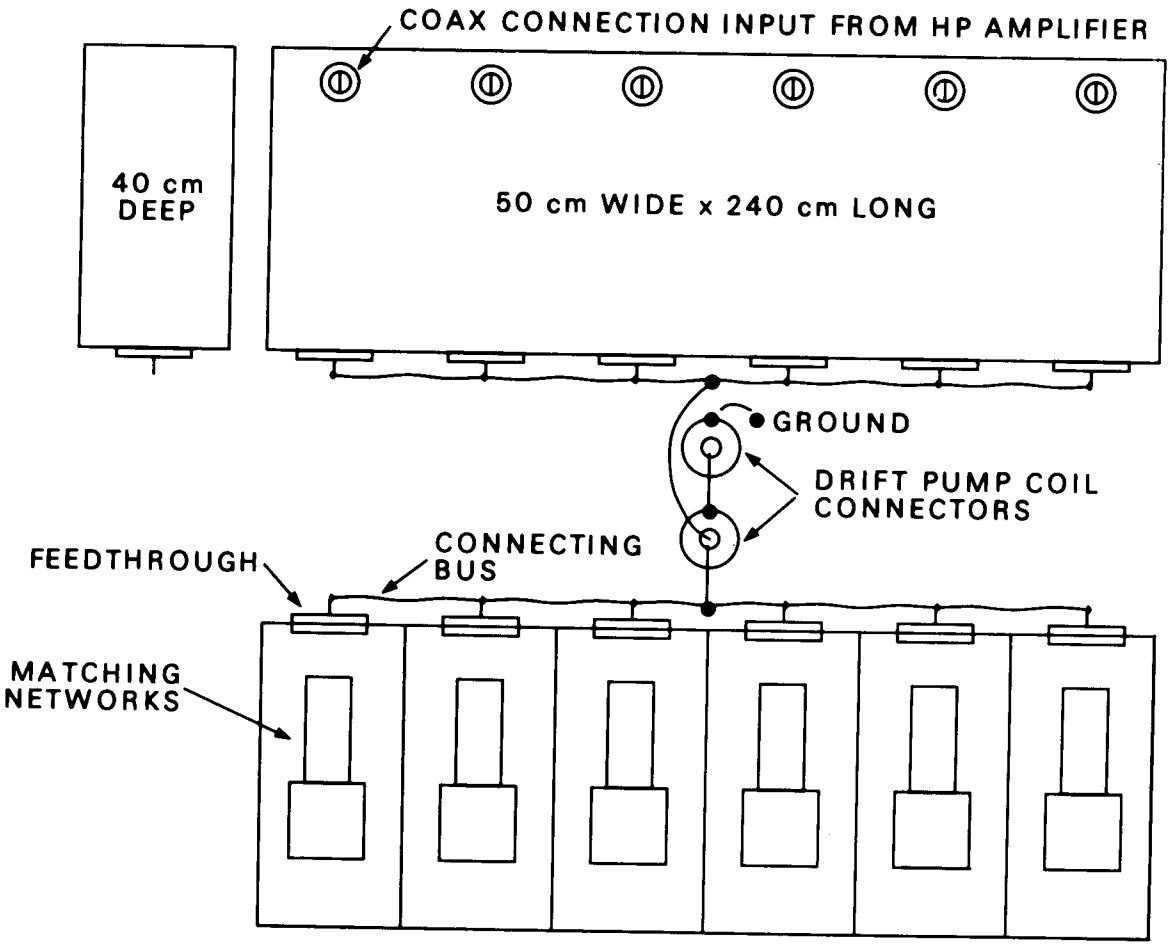

Fig. 5.20. Details of anchor matching network units.

each with a −3-dB bandwidth of ~6.5 kHz (see Fig. 5.26). With a noise generator or a swept cw input, a block spectrum is achieved with only a slight amplitude ripple (less than 0.5 dB). With discrete tones, the frequencies can be set anywhere within the required band.

Each channel (Fig. 5.25) provides about 5 kW to the drift pumping coil circuit. The overall efficiency (prime power to plasma power) is about 35%. As in the anchor-cell system, an IPA is used to provide about 0.5 kW more than the HPA input circuit. The digital attenuators in the input circuit are expected to have a switching time of a few microseconds and could therefore be used to program the power in real time. They can also be used to shape the transmission spectrum by controlling the relative gain between channels.

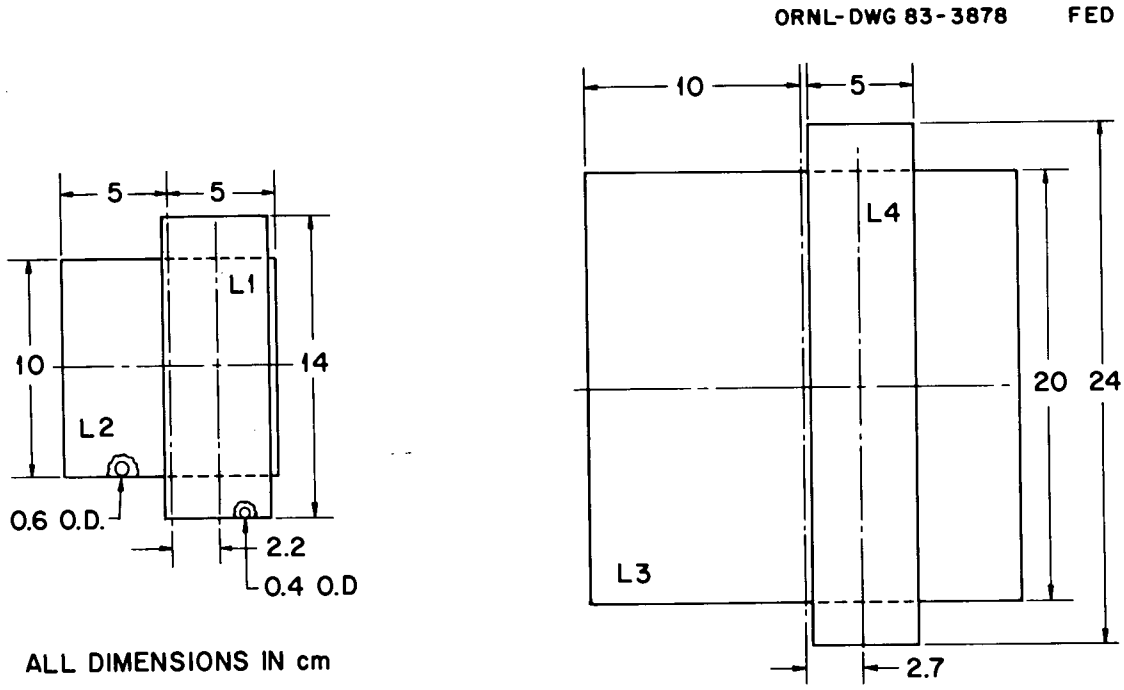

Fig. 5.21. Details of plug matching transformers.

5.4.6 Deuterium Gas Injectors

Figure 5.27 is a diagram of the flow system for the deuterium gas injectors and the axicell neutral beam injectors. The system consists of three kinds of equipment: gas supply, control valves and injectors, and I&C. Some of the fuel recovery and reprocessing equipment is shown as well.

For the pulsed-flow control mode, the pressure regulators and flow control valves are preset and the pulse selector valves are opened and closed by a programmable sequence controller to produce the desired background gas pressure (BGP). For the modulated-flow control mode, the pressure regulators are preset, the desired pulse selector valves are opened, and the flow valve controllers are modulated to produced the desired BGP.

The gas flow rate for both end-cell and central-cell injectors is 180 g/h. This is ten times the design-point neutral beam injection current rate for the high-Γ mode (240 A = 18 g/h of D_2).

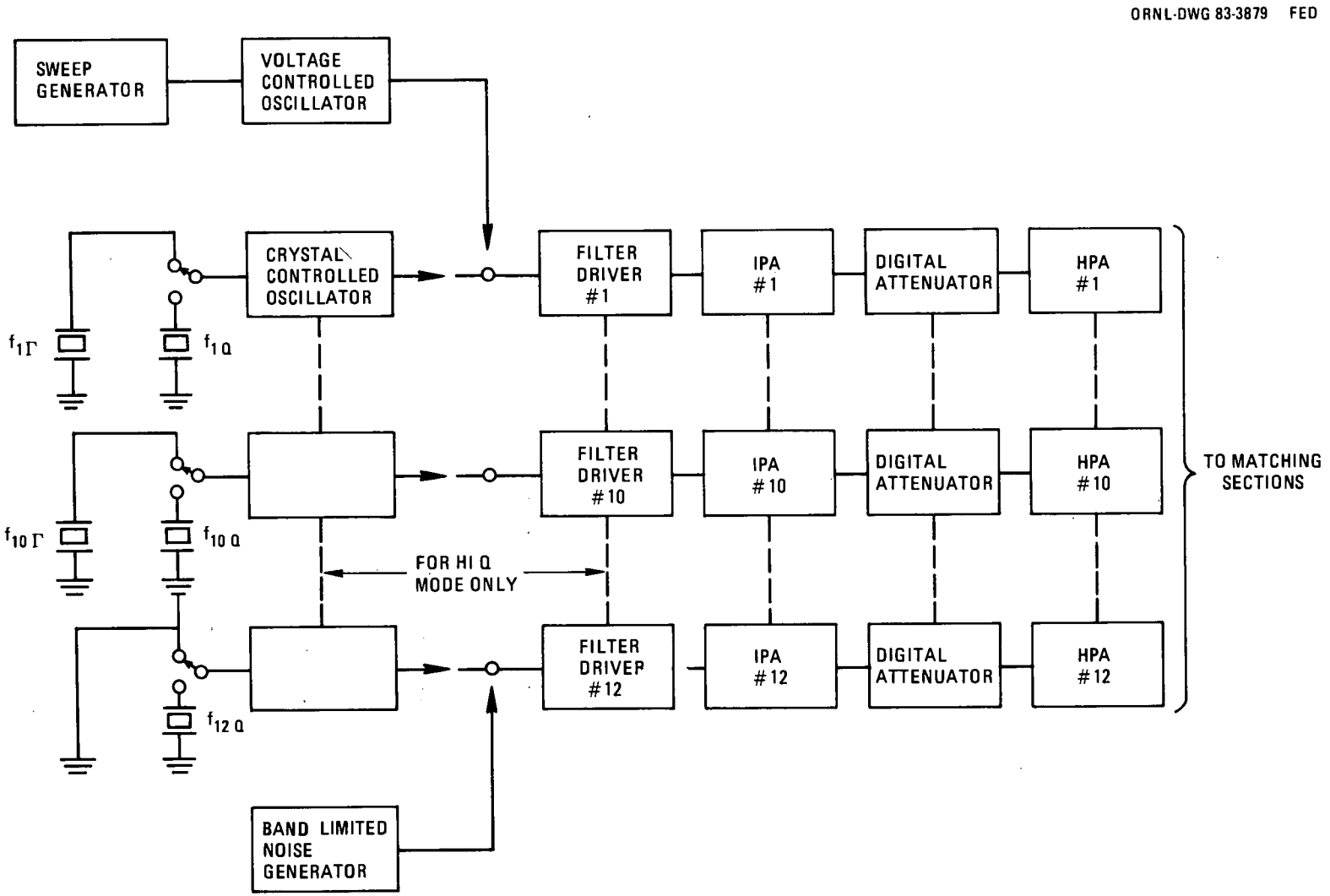

Fig. 5.22. Anchor-cell drift pumping transmitter.

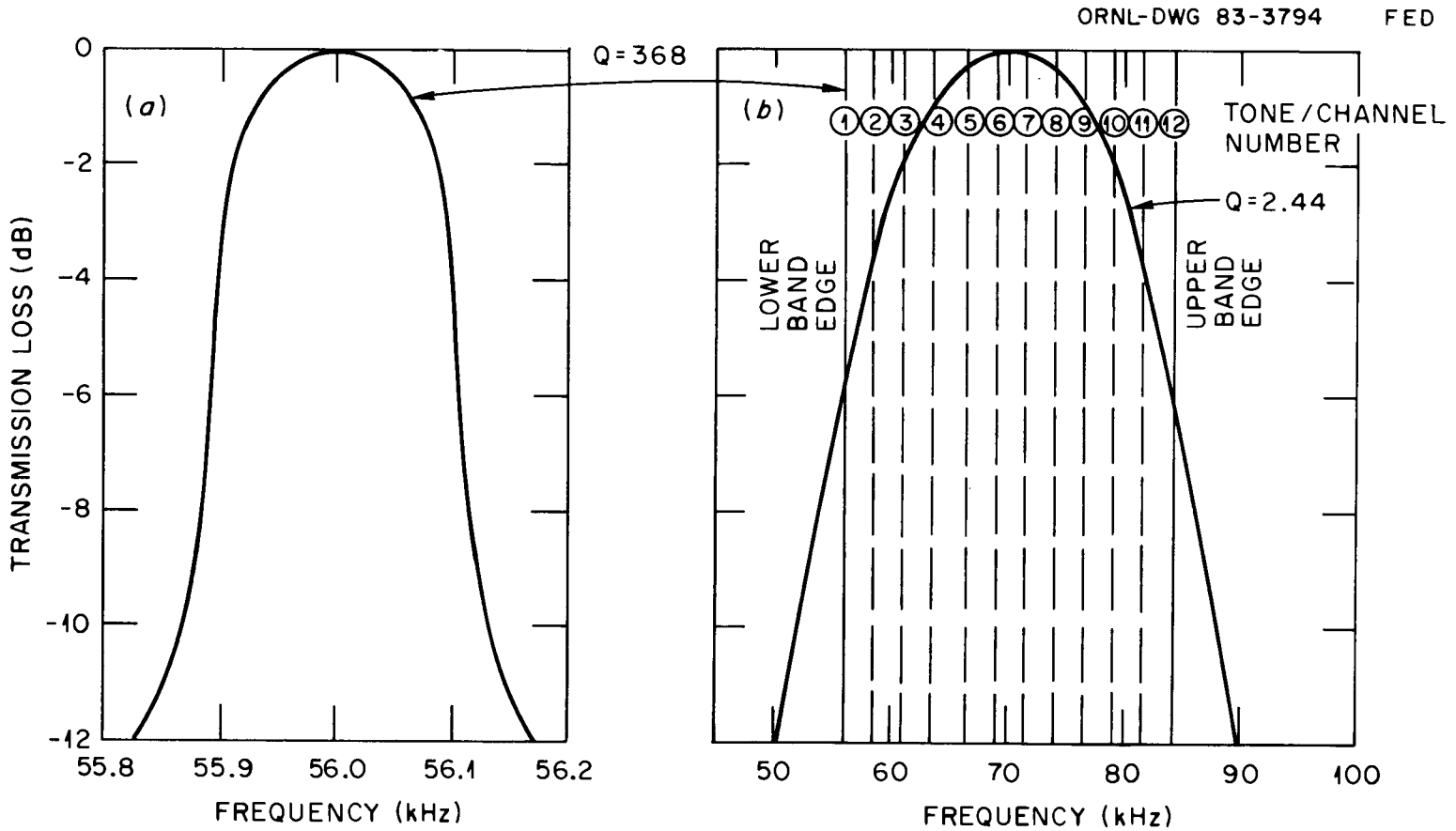

Fig. 5.23. (a) Anchor-cell drift pumping coil circuit response. (b) Response of 12 channels to the anchor-cell spectrum.

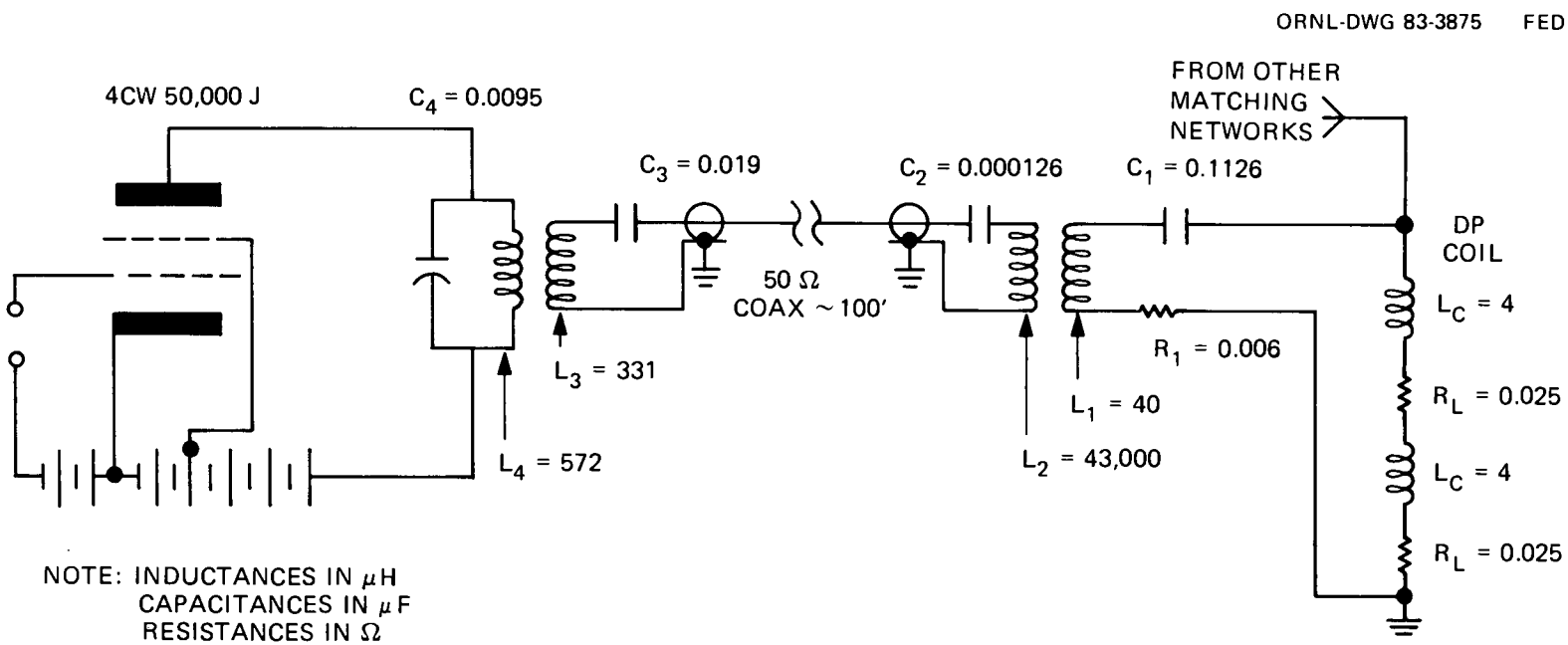

Fig. 5.24. Details of the anchor-cell HPA plate circuit and transmission system.

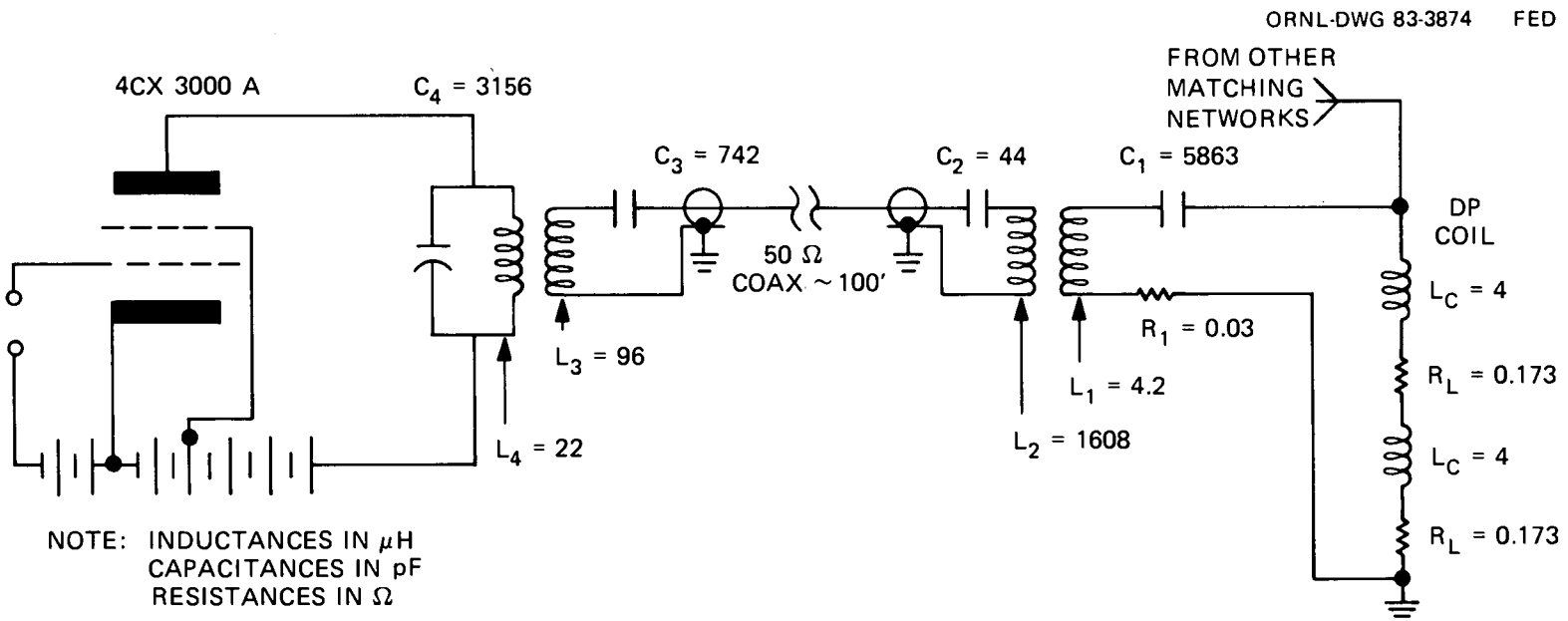

Fig. 5.25. Details of plug-cell HPA plate circuit and transmission system.

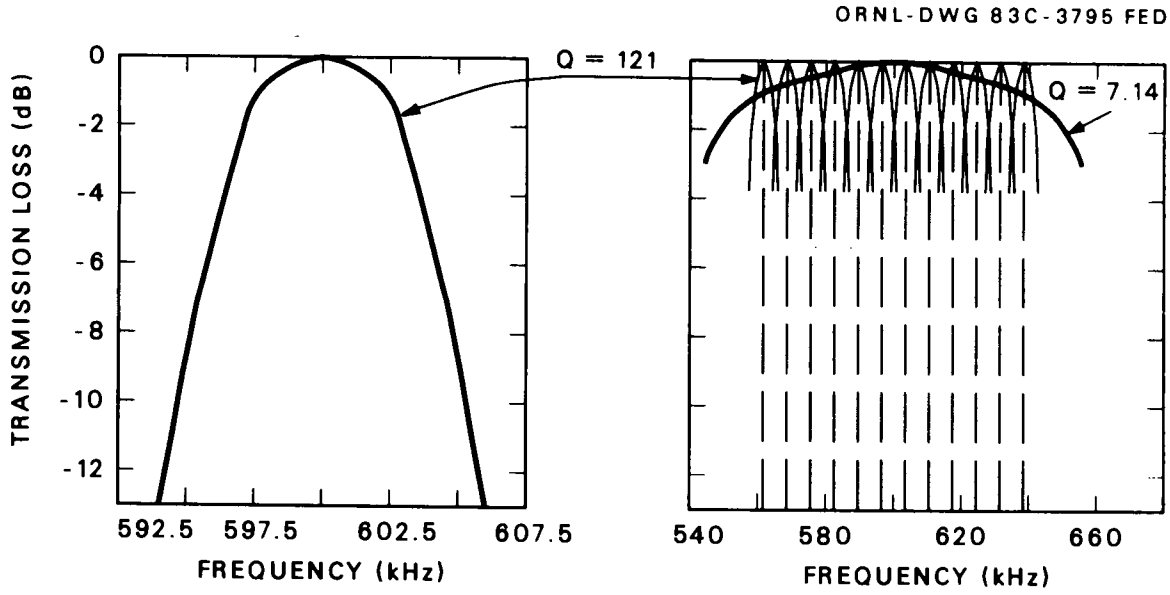

Fig. 5.26. Plug-cell drift pumping coil circuit response and response of 12 channels to the plug-cell spectrum.

5.5 PERFORMANCE ANALYSES

5.5.1 Axicell Neutral Beam Injectors

Each axicell neutral beam line delivers 7.4 MW to the plasma at an average energy of 60 keV, with ~5.6 MW in the 80-keV full-energy species. The system characteristics and key design parameters are summarized in Table 5.9. With the injector efficiency (ratio of delivered power to line power) of 51%, the total high-voltage dc power required for the system is 28.7 MW. General beam line losses include reionization losses in the beam line (2.5%) and unexplained losses (10%) that are observed in experiments but are not yet fully understood. The source focal length and beam line optics dictate an 8.3- by 8.3-cm beam footprint.

The 60-A source current was obtained by taking into account trapping and neutralizer efficiencies for each species and all beam losses. The beam divergences listed are conservative, since the theoretical minimum value is 0.4° by 0.4° and the experimentally achieved value is 0.42° by 0.42°.

The two collimators clip 70 kW (2.5%) of the beam power, and 635 kW (7.5%) is dissipated in the drift duct, which accounts for the remaining beam losses. The low-voltage dc power requirement is the supply for the bending magnets, 35 kW for the deuterium beam line and 43 kW for the tritium beam line. The cryopanel parameters in Table 5.9 are given for the pumping regions described in Sect. 5.4.1 and shown in Figs. 5.2 and 5.3.

ORNL–DWG 82-3162A FED

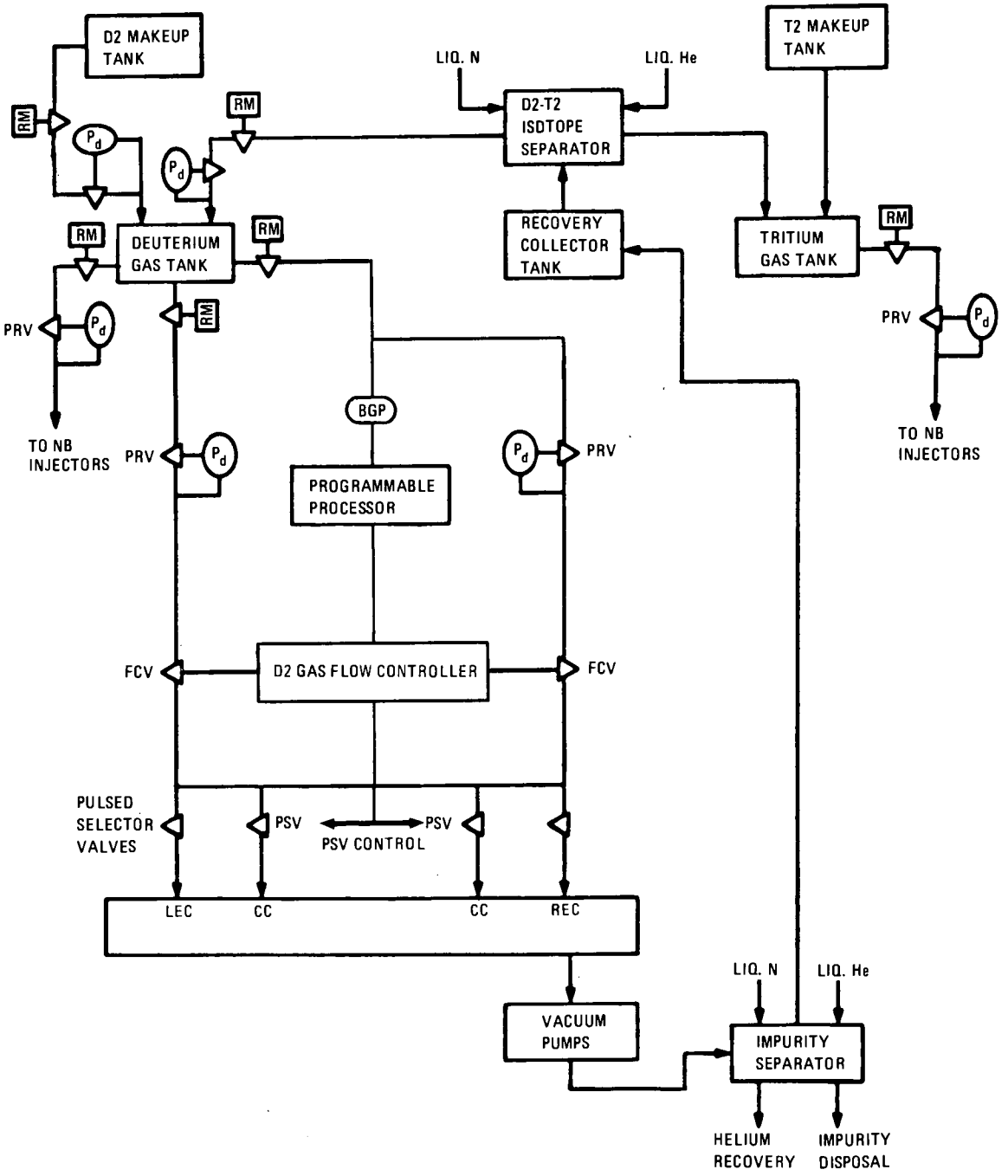

Fig. 5.27. Deuterium gas injector flow system. (CC = central cell, LEC = left end cell, REC = right end cell. FCV = flow valve controller, Pd = pressure regulator, PRV = pressure regulator valve, PSV = pulse selector valve, RM = remote shutoff valve.)

Table 5.9. Axicell neutral beam injection system characteristics and design parameters

Beam line	
Beam energy, keV	80
Delivered power, MW	
Full energy	11.1
Half energy	2.7
Third energy	1.0
Total	14.8
High-voltage dc power requirement, MW	28.6
Injector efficiency, %	41
Number of beam lines	
Deuterium	1
Tritium	1
Diameter, m	~3.25
Length, m	11.5
Number of sources per beam line	4[a]
Angular separation of beams, deg	3.31
Reionization losses, %	2.5
Unexplained losses, %	10
Beam footprint on plasma, cm	8.3 × 8.3
Source	
Current, A	59.7
Cross section $2x_0 \times 2y_0$, cm	16 × 40
Beam divergence, deg	0.5 × 0.5
Focal length, m	9.50
Gas pressure, torr	5×10^{-3}
Grid transparency	0.45
Neutralizer	
Length, m	1.5
Cross section, cm^2	
$a_1 \times b_1$	16 × 44
$a_2 \times b_2$	16 × 35
Target thickness (95% of equilibrium neutralization), cm^2	7.68×10^{15}
Optical transmission factor	0.99661
Dissipated power, kW	16.3
Ion dumps	
Ion power per source, MW	2
Tritium leakage to coolant, g/full-power year	2.9
Bending magnet	
Field strength, T	
Deuterium	0.128
Tritium	0.157
Magnet power requirement, kW	
Deuterium	35
Tritium	43
Collimators	
Transmission factor	
Front	0.977
Rear	0.995
Power deposition, kW	
Front	35
Rear	25
Drift duct	
Length, m	2.25
Cross section, cm	
$a_1 \times b_1$	60 × 35
$a_2 \times b_2$	35 × 19
Transmission factor	0.925
Dissipated power, kW	635
Cryogenic system	
Neutron and thermal heat loads per beam line, kW	
LN_2	1.6
LHe	112
Flow rates per beam line, mL/s	
LN_2	10
LHe	43
Gas load, torr·L/s	
Region 1	5.3
Region 2	1.5
Region 3	1.0
Pump surface, m^2	
Region 1	8.3
Region 2	3.3
Region 3	8.3
Pressure, torr	
Region 1	6×10^{-5}
Region 2	2.5×10^{-5}
Region 3	5×10^{-6}

[a]Three operating; one redundant.

To obtain a reasonable dump lifetime (~100 full-power days), the beam magnet defocuses the ion beam to keep power densities below 2 kW/cm^2. Because the shinethrough dump is on the outside of the MFTF-α+T vacuum vessel, the impinging power density is much less than that on the TDF dump, which increases the dump lifetime. Tritium leakage into the dump is also lower because of the lower beam currents. In the tritium beam line, 4.1 mg/day diffuses into the shinethrough coolant, and about twice that much leaks into the ion dump cooling system. This corresponds to a tritium holdup of 1.4 g per full-power year in the shinethrough coolant and 2.9 g per full-power year in the ion dump coolant.

Radiation flux and neutron heating in the beam line components were addressed in the TDF study.[1] Both the cryopanel heating and the expected lifetime of the source insulators were within design requirements. The wall loading in the MFTF-α+T axicell region is slightly higher than that in the TDF central cell, but the design requirements are still met.

5.5.2 Anchor-Cell Ion Heating

The ICRH equipment for MFTF-α+T will be modified MFTF-B components. At the time this study was undertaken, the MFTF-B equipment was under development, and its actual performance was unknown. Therefore, a typical system was modeled and estimates of power and efficiency were made. This equipment is well within the state of the art, and a system in use on the Princeton Large Torus (PLT) is similar in power level, frequency, and launcher design.

As noted in Sect. 5.4.2, two frequencies are required: 25 and 50 GHz. The amplifier tube under consideration for MFTF-B is the Eimac 2159, which has performed well at frequencies as high as 55 to 60 MHz. This should ensure operation at the MFTF-α+T frequencies. The tube can produce 2158 kW in class C and 1225 kW in class AB1 (rf linear amplifier). Only about 900 kW is required from the amplifier in MFTF-α+T.

The system block diagram in Fig. 5.9 was taken as a starting point, and components from the transformer rectifier input to the loop launcher at the plasma interface were detailed (see Fig. 5.28). The efficiency of each component was estimated for operation at both frequencies. For the final power amplifier, two classes of operation were considered: class C (82% efficiency) and class AB1 (70% efficiency). The efficiencies of the passive components are assumed to have ohmic and reflection losses; they are rounded to the nearest hundredth. For the 3-dB hybrids, the 2:1 power split factor is obviously not included in the transmission efficiency value. Table 5.10 summarizes performance at three points in the system. At 50 MHz, one amplifier drives both cells, so 409 kW $\times$ 2 = 818 kW is required from the amplifier. For the 25-MHz system, one amplifier provides half the power in each cell; the value of 922 kW in Table 5.10 is the total provided by two amplifiers. The total prime power is twice the value shown in the table or 3914 kW.

5.5.3 Sloshing-Ion Neutral Beam Injectors

The three negative-ion sources operating at an efficiency of 20 kW/A require an input power of 0.2 MW to deliver an emitted current of 10.1 A of D^- ions.[7] Each beam is assumed to have a total cross section of 3 by 56 cm, corresponding to 0.06 A/cm of

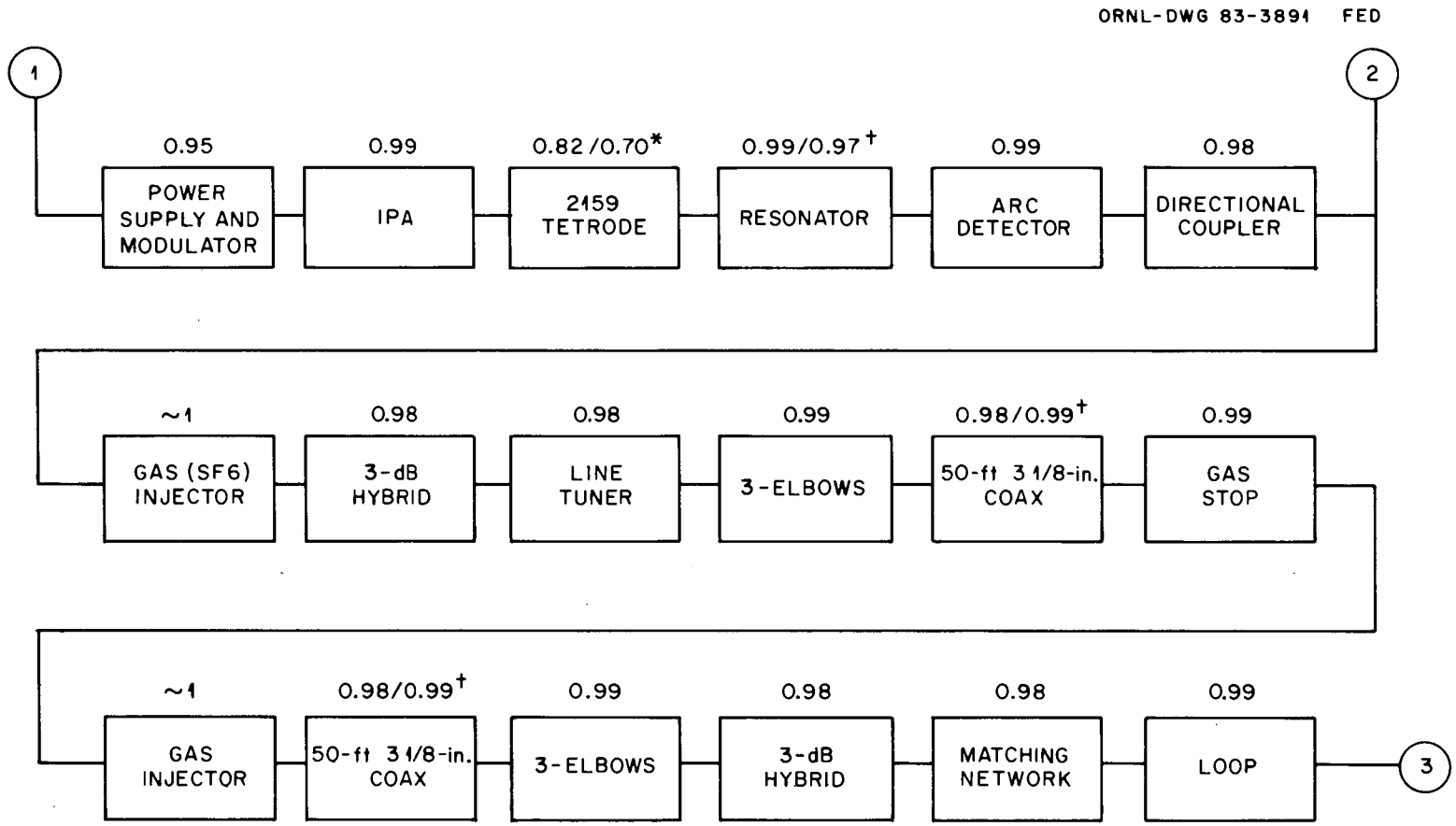

Fig. 5.28. Anchor-cell ICRH system components and efficiencies. (* = Class C operation/class AB1 operation. † = 50-MHz channel/25-MHz channel.)

Table 5.10. Anchor-cell ICRH system performance

	25-MHz system	50-MHz system
Prime power, kW		
Class C operation	1405	552
Class AB1 operation	1489	647
Efficiency through point 2,[a] %		
Class C operation	65.6	74.1
Class AB1 operation	61.9	63.2
HPA output power, kW	922	409
Efficiency through point 3,[a] %	86.8	85.1
Launcher power, kW	800	348

[a]See Fig. 5.28 for location.

source length. It is expected that the emitted current per unit length will probably be even larger, although only 0.04 A/cm has been achieved to date.[18] In the accelerator, it is expected that 15% of the extracted ions will be neutralized at less than the rated beam energy by impact with the background gas. The resulting low-energy ions and associated electrons create a grid loading equal to about 7.5% of the power in the accelerated ions (i.e., 0.13 MW). As a consequence, a total of 1.85 MW is required to accelerate the beam. An additional 10% of the emitted ions are lost due to optical aberrations.

The beams are transported from their accelerators to the entrances of their neutralizers by TFF electrodes.[8] These curved, strongly focusing electrodes guide the ribbon beams over circular paths. The centrifugal force on the ions is balanced by the electric field between adjacent electrodes.

For a field between the electrodes E (in volts per centimeter) and an ion beam energy V (in electron volts), the radius of curvature of the beam path is

$$R = 2V/E \tag{5.1}$$

(in centimeters). Space charge forces in the beam are negligible if the current density of the transported beam J is

$$J = 9qV^{3/2}/R^2 \ , \tag{5.2}$$

where $q = 3.85 \times 10^{-8}$ A/V$^{3/2}$, the perveance of a D^- planar beam.

For a narrow beam width a (in centimeters), the beam current per unit length carried by the TFF electrodes is

$$I/l = aJ \tag{5.3}$$

(in amperes per centimeter). At the ion source, $I/l = 0.06$ A/cm and $a = 3$ cm, so the

emitted current density is 0.02 A/cm^2. However, 15% of the ions are lost in the accelerator and another 10% are lost as a result of optics. Therefore, at the entrance to the TFF electrodes, $J = 0.015$ A/cm^2, and, for a 200-keV beam, $r = 45$ cm [from Eq. (5.2)]. From Eq. (5.1), E must be 8.9 kV/cm. The ion loss encountered while traveling at that radius over an angle of 135°, through a region in which the average pressure is 5×10^{-5} torr, is about 7%.

To maintain the gas pressure at 5×10^{-5} torr near the TFF electrodes, it is necessary to continuously pump both the gas flowing out of the ion source and that flowing out of the neutralizer. The gas flow out of the source is

$$Q_s = 0.1I^-(1/G - 1) \tag{5.4}$$

(in torr·L/s), where $I^- = 10.1$ A is the total current of the negative ions emitted by the sources and $G = 12\%$ is the gas efficiency of the source. Thus, $Q_s = 7.4$ torr·L/s. The gas flow out of the neutralizer Q_N depends on the pressure at which gas is introduced at the center of the neutralizer P_c, the conductance of half the length of the neutralizer C_h, and the optimum thickness of the neutralizer π_0. The pressure in the TFF chamber (5×10^{-5} torr) is at least an order of magnitude less than P_c, so

$$Q_N = C_h P_c \tag{5.5}$$

If the cross section of the beam coming out of one neutralizer is $a \times b$ (in square centimeters) and the cross section of the neutralizer for the four beams is, on the average, 5 cm larger, then the conductance of the neutralizer to the gas flowing in at the center and out at either end is

$$C = \frac{84.1(a + 5)^2(4b + 5)^2}{[(a + 4b + 10)L/2] + [8(a + 5)(4b + 5)/3]} \tag{5.6}$$

For $a = 3$ cm, $b = 56$ cm, and $L = 222$ cm, $C = 8.5 \times 10^3$ L/s.

The thickness of the neutralizer is such that

$$\pi = (10^{19}/T_G)(P_c/2)L \tag{5.7}$$

per square centimeter, where T_G is the temperature of the gas. The optimum thickness for a 200-keV deuterium beam is $\pi_0 = 3.1 \times 10^{15}$ cm^{-2}, with $T_G = 300$ K, $P_c = 8.3 \times 10^{-4}$ torr, and, from Eq. (5.5), $Q_N = 7.4$ torr·L/s.

In the TFF chamber, the continuously recycling cryopumps have a pumping speed of 6 L/s per square centimeter of pump area. At 5×10^{-5} torr, this corresponds to 3×10^{-4} torr·L/s of gas per square centimeter. To accommodate the 7.4 torr·L/s of gas coming out of the source and the 7.4 torr·L/s of gas coming out of the neutralizer,

the cryopump area must be 4.9×10^4 cm^2. Because the TFF chamber is deeper than the four neutralizers mounted side by side (224 cm), the length of cryopumps needed to maintain 5×10^{-5} torr is 220 cm, as shown in Fig. 5.7.

At the reactor side of the neutralizer, a quantity of gas equal to that flowing into the TFF chamber (i.e., 7.4 torr·L/s) must be pumped away. At a pressure of 5×10^{-5} torr, this corresponds to a pumping load of 1.48×10^5 L/s. Continuously recycling cryopumps can pump 6 L/s per square centimeter, so cryopump panels with an area of 2.47×10^4 cm^2 are needed. Approximately 15% of the beam leaves the neutralizer as negative ions; the other 85% becomes positive somewhere in the gas cell. About 64.5% of the beam remains neutral as it enters the end-plug chamber,[11] and the 20.5% that was neutral becomes positive from ionizing collisions.

Of the original 10.1 A of D^-, 15% is lost to charge exchange in the accelerator, 10% to poor optics, and 7% to charge exchange in the TFF chamber. Of the 7.2 A of D^- that enters the neutralizer, 1.1 A of D^- is collected at the negative ion dump, 1.5 A of D^+ is collected at the positive ion dump, and 4.6 A of neutrals proceeds toward the plasma target. En route to the target, another 9% of the beam is lost to ionizing collisions; then the required 4.2 A of 200-keV deuterium neutrals finally arrives at the plasma. Given the principal power requirements at the ion source (0.2 MW) and at the accelerator (1.85 MW), the beam line efficiency is approximately $(4.2 \times 200)/[(0.2 + 1.85) \times 10^6]$ or 41%.

Beam optics is another important consideration. At the source, a 3-cm-wide, 150-V beam is emitted through electrodes that physically constrict the beam half-angle to 0.42°, which corresponds to a 0.011-rad angle in the 3-cm-wide, 200-kV beam (which appears to be emitted from a virtual source) established by the TFF focusing system at the neutralizer entrance. For this beam to be fully intercepted by the 14.7-cm-wide plasma target with room to spare, the virtual source (i.e., the neutralizer entrance) must be no more than 670 cm from the center of the target. However, it is possible to clip the extreme edges of the ion beam at the ion source and tailor it to fit the target. A 3-cm-wide virtual source 900 cm from the target must deliver a 200-keV beam with a divergent angle of $\leq 8.2 \times 10^{-3}$ rad. At the source, where the ions have an energy of 150 V, the corresponding angle is $\theta_s = 0.30$ rad.

The transverse energy of the emitted negative ions will probably be on the order of 5 V. Thus, the most probable angle at the source is $\theta_e = 0.18$ rad. For a Gaussian ion distribution, the current per unit length is proportional to the error function of the ratio of θ_s/θ_e. For the values given here, the ratio is 1.63 and the error function is 0.979. The beam loss to scraping is less than 2.1%.

5.5.4 Plug Barrier Electron Heating

Channel sizing

The requirement of 600 kW at 35 GHz for ECRH at point *b* is met by one 35-GHz MFTF-B channel and two 28-GHz channels "retubed" to 35-GHz, high-power channels. For the 56 GHz at point *a*, one channel of the existing system is more than adequate.

Finally, the requirement for 56 GHz at point *b* can be met using existing equipment with a modest (10% to 15%) increase in power. Since the components to be used in the systems are to be developed or, at best, are under development, estimates have been made based on existing components at other frequencies or on pulsed systems. The estimated efficiency of the system from the prime power input to the gyrotron output is 32% to 45%; for the transmission system, the estimated efficiency is ~70%. These data and the system requirements were used to generate the values presented in Table 5.11. Taking into account the number of channels and the prime power for each type of channel, the total prime power for the ECRH system is estimated at 9166 kW.

Table 5.11. Plug-cell ECRH system performance

	Power, kW				Efficiency, %	
	35-GHz systems		56-GHz systems		35-GHz	56-GHz
	New	MFTF-B	Point *a*	Point *b*	systems	systems
Prime	703	470	725	538		
Through point 2[a]					45.5	31.8
Gyrotron	320	214	230	171		
Through point 3[a]					69.8	69.8
Launcher	225	150	160	120		
Overall					31.7	22.2

[a]See Fig. 5.30 for location.

The values for power given in Table 5.11 are reasonable based on recent developments. For the retubed channels, 320 kW cw at 35 GHz is needed; a Naval Research Laboratory gyrotron achieved values of 340 kW pulsed with an efficiency over 50% (ref. 19), and a Varian 28-GHz tube has been operated at 340 kW for 20 min and at >300 kW for 2 h (ref. 20). The requirement for a 230-kW gyrotron at 56 GHz is practical, given the development program for a 56-GHz tube (a scaled version of the 60-GHz tube) at Varian and the development of the 60-GHz pulsed tube and the nearly completed cw version at Varian and Hughes. Both of these contractors have tubes that produce well over 200 kW (some as high as 240 kW) of output power in the range from 53 to 60 GHz with about 35% efficiency.[21]

Transmission efficiencies

Transmission efficiencies for system components are shown graphically in Fig. 5.29. Transmission efficiencies will be different for each channel. However, because the mode mix for the gyrotrons is not known, a representative design configuration was used for all channels. Loss estimates represent the total of ohmic, reflection, and mode conversion losses. It is difficult to separate the contributions because these losses are small and because distinguishing modes is still a developing art. Many of these estimates are based on the 60-GHz development work done for DIII and PDX. The two sections of corrugated

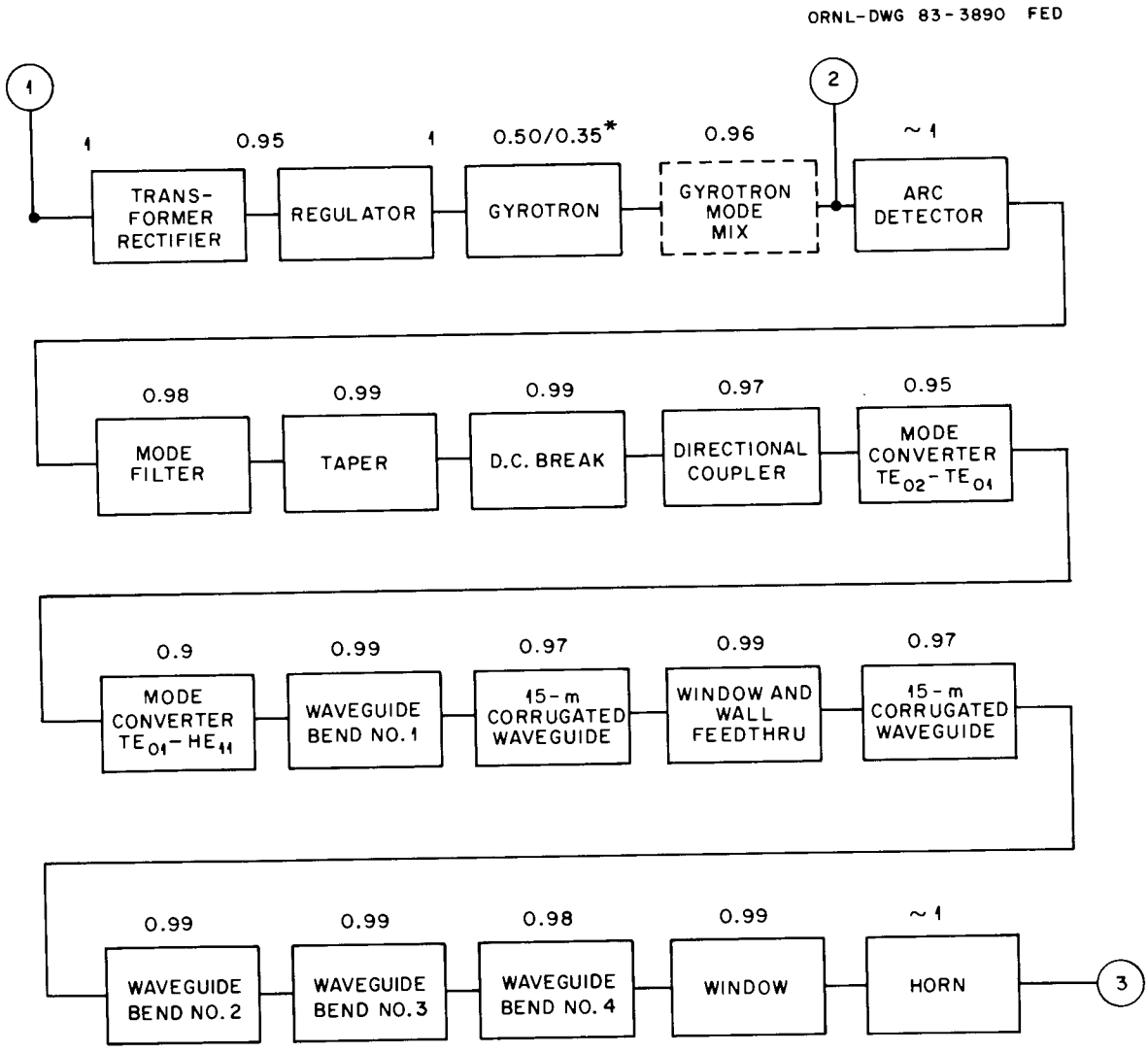

Fig. 5.29. Plug-cell ECRH system components and efficiencies. (* = 35-GHz system/56-GHz system.)

waveguide are expected to have mainly ohmic losses. The fourth bend, which is inside the nuclear shield, is assigned a lower efficiency because it will have a smaller radius. Mode conversion losses are expected to be the dominant form of loss in these bends and in the taper.

The mode mix for the Varian 60-GHz pulsed tube is estimated at 90% TE_{02}. (The cw tube had a mix of 20% TE_{01}, 10% TE_{02}, and 70% TE_{03}. Modifications to the output cavity are under way to alter this mix to meet specifications.) The 28-GHz gyrotron has mode mixes with the desired mode in the 90th percentile. Since the 60-GHz tube is still under development, it is reasonable to assume that its mode mix can be brought closer to that of the 28-GHz tube.

5.5.5 Drift Pumping

The MFTF-α+T drift pumping coil configuration is scaled from that in the MARS study. Because of the narrow bandwidth of the drift pumping coil system that establishes the system (power chain) bandwidth, the output spectrum for the anchor cell will be a 12-line discrete spectrum (200-Hz bandwidth) for any of the input modulations (band-limited noise, swept cw, or discrete tones). For the plug cell, a continuous or block spectrum can be obtained for the noise or swept cw input. The matching and transmission systems cover the total bandwidth required, and the band limiting (done by the drift pumping coil) requires multiple channels, the center frequencies of which are spaced equally across the band. A block diagram of the system is shown in Fig. 5.30.

This analysis begins with an investigation of the drift pumping coil and its geometry to determine losses and impedance. Performance analyses of the anchor and plug systems follow.

Drift pumping coil analysis

Figure 5.31 shows the drift pumping coil configuration and some of the models used in this analysis. The inductance is evaluated from a model of the coil as a two-wire transmission line with the radius of the conductor $r = 1$ cm, the conductor spacing $D = 30$ cm, the line length $l = 270$ cm, and the height above the surface $h = 15$ cm. From transmission line theory, the inductance is

$$L = \left[l + 4 \ln \frac{D - r}{r} \right] l \times 10^{-7} \text{ H} = 3.93 \ \mu\text{H} \ . \tag{5.8}$$

The flux density produced by this coil is estimated as

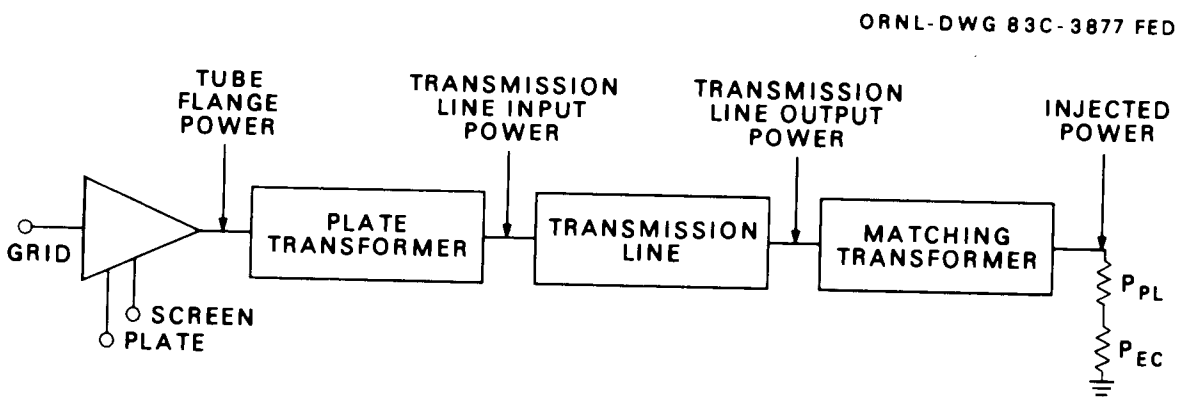

Fig. 5.30. Drift pumping coil circuit.

ORNL-DWG 83-3867 FED

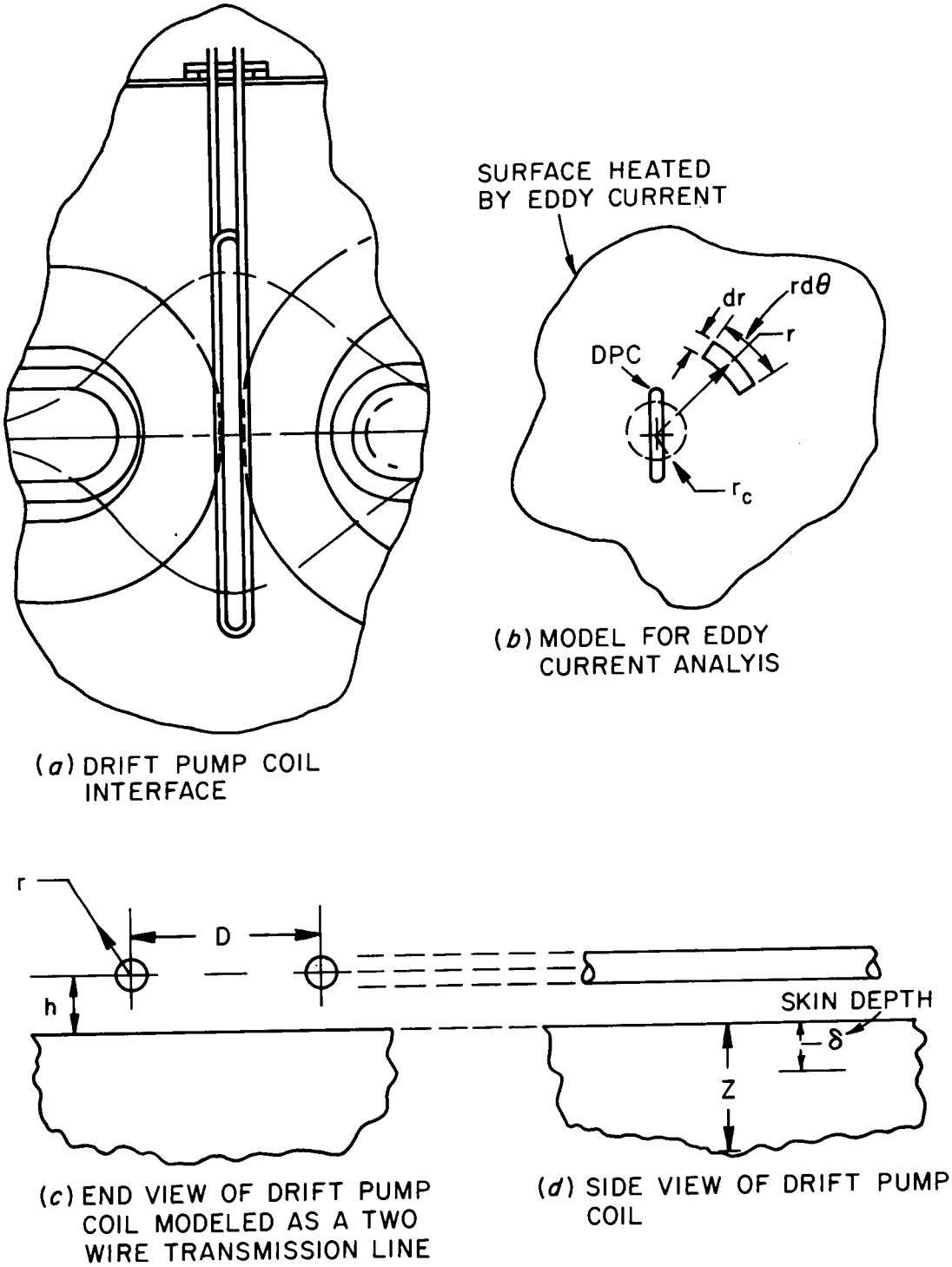

Fig. 5.31. Drift pumping coil configuration and models used in performance analyses.

$$B = \frac{\phi}{A} = \frac{LI}{NA} , \tag{5.9}$$

where I is the current (in amperes), N is the number of turns, and A is the area of the coil bore. The flux density for the anchor coils B_A is 1.46×10^{-2} Wb/m^2, or 146 G, and that for the plug coils B_p is 1.941×10^{-3} Wb/m^2, or 19.41 G. The capacitance of the line is given by

$$C = \frac{1}{3.6 \times 10^{10} \ln D/r\sqrt{1 + (D^2/4h^2)}} = 24.6\,\mu F . \tag{5.10}$$

For copper coils, the skin depth δ [$= (2/\omega\mu\sigma)^{1/2}$] is 2.49×10^{-4} m at 70 kHz and 9.18×10^{-5} m at 600 kHz. The coil resistance R is given by $(l_c/\sigma\delta 2\pi r)$ and is 6.7 mΩ at 70 kHz and 17.9 mΩ at 600 kHz. For the required current, the power dissipated by the coil $P_C = I^2R$ is 60.3 kW at 70 kHz and 2.86 kW at 600 kHz. The reactor power $MVA = I^2X_L$ is 15.84 MVA at 70 kHz and 2.4 MVA at 600 kHz. The coil voltage developed, $V = P/I$, is 5.27 kV for the anchor and 6.0 kV for the plug.

To calculate the eddy current losses, the coil is modeled as shown in Fig. 5.31 (b and d). For convenience, the paper-clip shape is replaced by an equivalent circle with radius $r_c = l_c/2\pi = 1$ m. The power loss under the coil center is

$$P_{EC}(r = 0) = \frac{\pi\delta f B_m}{6 \times 10^{16}} \tag{5.11}$$

(in watts per cubic centimeter). For stainless steel surfaces, where $\rho = 7.2 \times 10^{-5}$ Ω/cm and $\delta = 1.6 \times 10^{-1}$ cm at 70 kHz and 5.4×10^{-2} cm at 600 kHz, the value of Eq. (5.11) is 6.11 W/cm^3 at 70 kHz and 0.9 W/cm^3 at 600 kHz. For a flux density that falls off as

$$\frac{B(r)}{B(0)} = \frac{1}{1 + (r/r_c)^2} \tag{5.12}$$

and eddy currents distributed proportionally in z as

$$\frac{I^2(z)}{I^2(\text{surface})} = E \exp(-2z/\delta) , \tag{5.13}$$

the total eddy current loss is

$$P_{\mathrm{TEC}} = P_{\mathrm{EC}}(r = 0) \int_0^{\infty} \int_0^{2\pi} \int_0^{R \to \infty} \frac{rE \exp(-2z/\delta)}{1 + (r/r_c)^2} \, dz \, d\theta \, dr \ , \tag{5.14}$$

and integrating yields

$$P_{\mathrm{TEC}} = \frac{P_{\mathrm{EC}}(r = 0) r_c^2 \pi \delta}{2} \ , \tag{5.15}$$

which is 15.36 kW for 70 kHz and 0.848 W for 600 kHz. Other heat sources (in addition to P_C) were estimated as follows: nuclear heating, 10 W; plasma charge exchange, 20 W; and sloshing ion beam flux, negligible.

The mutual coupling between the drift pumping coils was investigated by modeling the two coils as loops separated by 25 cm and calculating the inductance of a two-turn coil. The mutual coupling was found to be about 0.54, assuming no plasma between the coils. The parameters assumed and calculated for this rough estimate are given in Table 5.12.

Table 5.12. Drift pumping coil analysis results

	70-kHz anchor coil	600-kHz plug coil
Inductance L, μH	4	4
Frequency ω, rad/s	0.43×10^6	3.76×10^6
$\Delta\omega$, rad/s	1.76×10^5	5.27×10^5
Current I, kA	3	0.4
Plasma power P, kW	150	24
σ, mho·m	5.8×10^7	5.8×10^7
Skin depth δ, m	2.47×10^{-4}	9.18×10^{-5}
R_c, mΩ	6.7	17.9
Power loss under coil center P_{EC}, kW	15.4	0.848
R_{EC}, mΩ	1.5	4.8
R_{PL}, Ω	1.5×10^{-1}	1.5×10^{-1}
Q_c'	68.8	86
Q_c	25.7	842
R_L, Ω	0.025	0.173
P_L, kW	229	27.7

Anchor-cell analysis

The band edge frequencies for the anchor cell are 56 kHz and 84 kHz. The corresponding mean and edge frequencies are

$$\omega_m = 2\pi\sqrt{f_{\text{high}} \times f_{\text{low}}} \times 10^3$$

$$= 4.3 \times 10^5 \text{ rad/s} \tag{5.16}$$

and

$$\Delta\omega = 2\pi(f_{\text{high}} - f_{\text{low}}) \times 10^3$$

$$= 1.76 \times 10^5 \text{ rad/s} \ , \tag{5.17}$$

respectively;

$$\frac{\Delta\omega}{\omega_m} = 0.41 \ , \quad \left(\frac{\Delta\omega}{\omega_m}\right)^2 = 0.167 \ . \tag{5.18}$$

For the parallel-series matching network shown in Fig. 5.32,

$$C_3 = \frac{\Delta\omega}{\omega_m^2 z_0} = 0.019 \ \mu\text{F} \ , \tag{5.19}$$

$$L_3 = \left[1 + \left(\frac{\Delta\omega}{\omega_m}\right)^2\right] \frac{z_o}{\Delta\omega} = 331.5 \ \mu\text{H} \ , \tag{5.20}$$

$$Q_3 = \frac{1}{\omega C_3 z_0} = 2.44 \ . \tag{5.21}$$

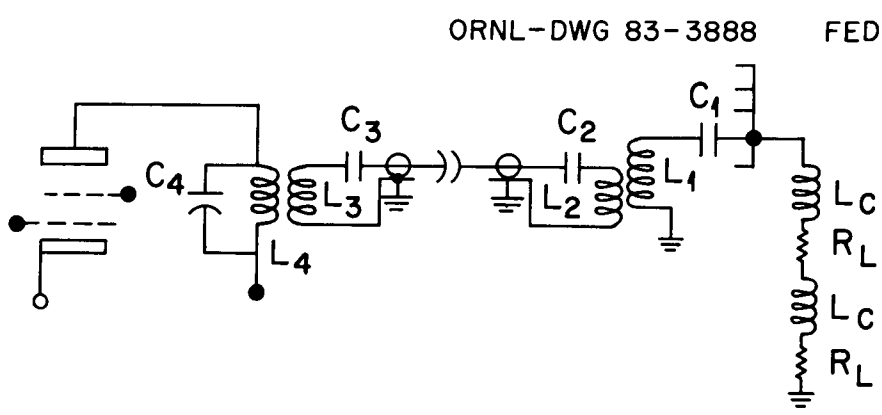

Fig. 5.32. Drift pump matching network.

For the primary side, $Q_4 = Q_3 = \omega C_4 2r_p$, and solving for C_4 with $2r_p = 600\ \Omega$,

$$C_4 = \frac{2.44}{\omega 2r_p} = 9458\ \text{pF} . \tag{5.22}$$

For resonance,

$$L_4 = \frac{1}{\omega^2 C^4} = 572\ \mu\text{H} , \tag{5.23}$$

$$K_{34} = \frac{\Delta\omega/\omega}{[1 + (\Delta\omega/\omega^2)]^{1/2}} = \frac{1}{Q}\frac{1}{[1 + (\Delta\omega/\omega^2)]^{1/2}}$$

$$= 0.38 , \tag{5.24}$$

$$M_{34} = K_{34}\sqrt{L_4 L_3}$$

$$= 165\ \mu\text{H} . \tag{5.25}$$

The drift pumping coil matching network is also a series-parallel tuned transformer. The two drift pumping coils are connected in series and retain the same loaded Q (68.8). Adding the transformer winding inductance L_1 (with its inherent resistance R_1) gives

$$Q_1 = 68.8\ \frac{1 + L_1/2L_c}{1 + R_1/2R_c} , \tag{5.26}$$

$$\eta_1 = 68.8\ \frac{1}{1 + R_1/2R_L} . \tag{5.27}$$

Assuming that $L_1 = 5(2L_c)$ and $R_1 \approx 6\ \text{m}\Omega$, then $Q_1 = 368$ and the efficiency $\eta = 59.6\%$. For resonance, $C_1 = 1/\omega^2(L_1 + L_c) = 0.1126\ \mu\text{F}$. The Q in the series-tuned primary is indicative of the bandwidth,

$$\frac{\Delta\omega}{\omega} = \frac{1}{Q} = 2.7 \times 10^{-3} , \tag{5.28}$$

$$\Delta\omega = 1161\ \text{Hz} . \tag{5.29}$$

Using the expressions for the series-tuned circuit,

$$C_2 = \frac{\Delta\omega}{\omega_m^2 z_0} = 126 \text{ pF} , \tag{5.30}$$

$$L_2 = \left(1 + \frac{\Delta\omega}{\omega^2}\right) \frac{z_0}{\Delta\omega} = 43 \text{ mH} . \tag{5.31}$$

This inductance can be met with a coil consisting of two 100-turn layers, each 25 cm in diameter and 25 cm long. For a 2-mm-diam conductor, the coil resistance is about 2 Ω, which is small compared to the "coupled" resistance of 50 Ω. The coupling coefficient K_{12} is approximately $1/Q_1 = 1/Q_2 = 0.00272$, and the mutual inductance is

$$M_{12} = K\sqrt{L_1 L_2} = 3.57 \text{ mH} . \tag{5.32}$$

The transmission loss vs frequency is shown in Fig. 5.23. The $Q = 2.44$ response is shown centered at midband. However, in each channel it will be centered on the center frequency of the drift pumping coil response.

The power transmission and losses can now be evaluated. The additional power used in the L_1 coil is

$$P_{L_1} = \frac{2P_{PL}}{N}\left(\frac{1}{\eta_1} - \frac{1}{\eta_c}\right) = 4.52 \text{ kW} , \tag{5.33}$$

and the power transmitted to the drift pumping coil matching transformer secondary is

$$P_1 = \frac{2P_{PL}}{N} = \frac{1}{0.596} = 41.95 \text{ kW} . \tag{5.34}$$

The power loss in this transformer's primary is

$$P_2 = \frac{R_2 P_1}{R_2 + z_0} = 1.61 \text{ kW} \tag{5.35}$$

for the transmission line power ($P_{TX} = 43.63$ kW) and current ($I_{TX} = 29.5$ A). For a 0.875-in. coaxial cable, the loss over 100 ft is 0.004 dB, for an efficiency η of 0.999. The L_2 coil resistance is about 0.05 Ω, which corresponds to 43 W of dissipated power. The plate circuit power is then ~43.7 kW, which is easily handled by an Eimac 4CW50000V tube. The tube element powers are plate, 79.0 kW; screen, 1.5 kW; and drive, 0.3 kW; for a total of 80.8 kW. Efficiencies are summarized in Fig. 5.33.

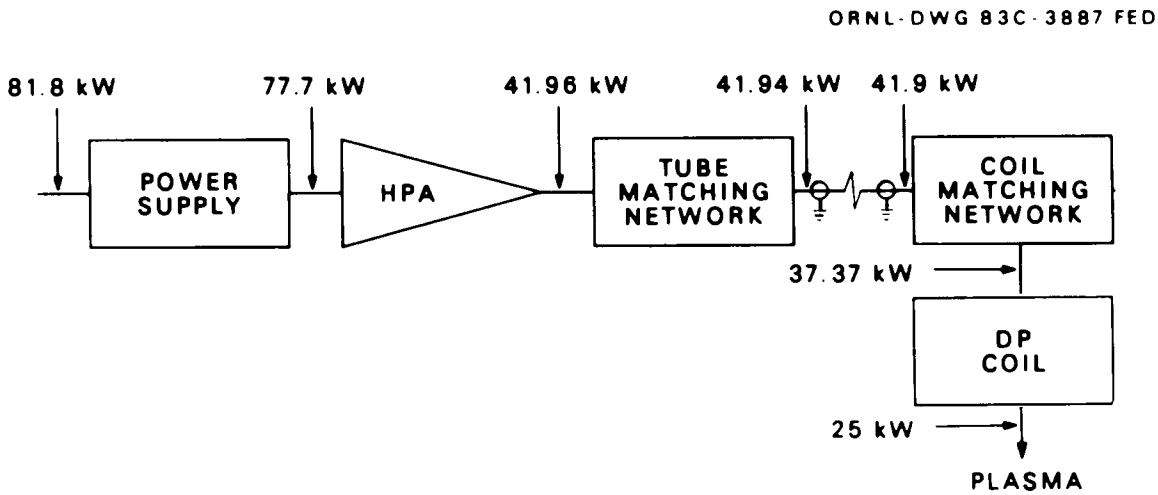

Fig. 5.33. Anchor-cell drift pumping system efficiencies. Power supply: 95%; HPA: 54%; tube matching network: 99.5%; transmission line: 99.5%; coil matching network, 89.2%; drift pumping coil: 66.9%. Overall efficiency: 30.2%. Power input: 81.8 kW/channel.

Plug cell analysis

The tube matching circuit (see Fig. 5.32) must match a 600-Ω plate resistance to a 50-Ω coaxial cable. The capacitance is

$$C_3 = \frac{\Delta\omega}{\omega_m^2 z_0} = 742 \text{ pF} ;$$

$$L_3 = \left[1 + \left(\frac{\Delta\omega}{\omega_m}\right)^2\right] \frac{z_0}{\omega_m} = 96.7 \ \mu\text{H} ;$$

$$Q_3 = \frac{1}{\omega C_3 z_0} = 7.14 .$$

The values of Q in the primary and secondary are equal, $Q_3 = Q_4 = \omega C_4 2 r_p$. Then

$$C_4 = 3.156 \times 10^{-3} \ \mu\text{F} .$$

For resonance,

$$L_4 = \frac{1}{\omega^2 C_4} = 22.3 \ \mu\text{H} .$$

The coupling coefficient is

$$K = \frac{1}{Q} \frac{1}{[1 + (\Delta\omega/\omega)^2]^{1/2}} = 0.139 \ ,$$

and the mutual inductance is

$$M = K\sqrt{L_4 L_3} = 6.42 \ \mu\text{H} \ .$$

The loaded Q of the drift pumping coil is 85.9, and the 1-dB bandwidth is

$$\frac{\Delta f}{f} = \frac{1}{Q} = 0.0116 \ .$$

The number of channels needed to meet the requirement of $\Delta\omega/\omega_m = 0.14$ (i.e., responses overlapping at the 3-dB point) is $N = 8.5$. If the two coils straddling the plasma are connected in series, then

$$Q_c' = \frac{\omega 2L_c}{2R_L}\left(\frac{1 + L_1/2L_c}{1 + R_1/2R_L}\right) = 85.9\left(\frac{1 + L_1/8}{1 + R_1/346}\right) \ ,$$

and

$$\eta_1 = \frac{2R_{PL}}{2R_L(1 + R_1/2R_L)} = \frac{0.0867}{1 + R_1/346} \ .$$

For 12 channels, the Q_1' of the L_1 circuit is evaluated from

$$\frac{0.14}{\sqrt{2} \times 12} = \frac{1}{Q_1'} \ ;$$

$Q_1' = 121.2$. Then, using this value to solve for $(1 + R_1/346)$, and the expression for η_1, it is possible to obtain

$$L_1 = 8\left(\frac{1.22}{\eta_1} - 1\right) \mu\text{H}$$

for $\eta_1 < 0.867$. For $\eta = 0.8$ and $L_1 = 4.2$ (from Fig. 5.34),

$$R_1 = \left(\frac{0.867}{\eta} - 1\right)346 = 29.97 \ \text{m}\Omega \ .$$

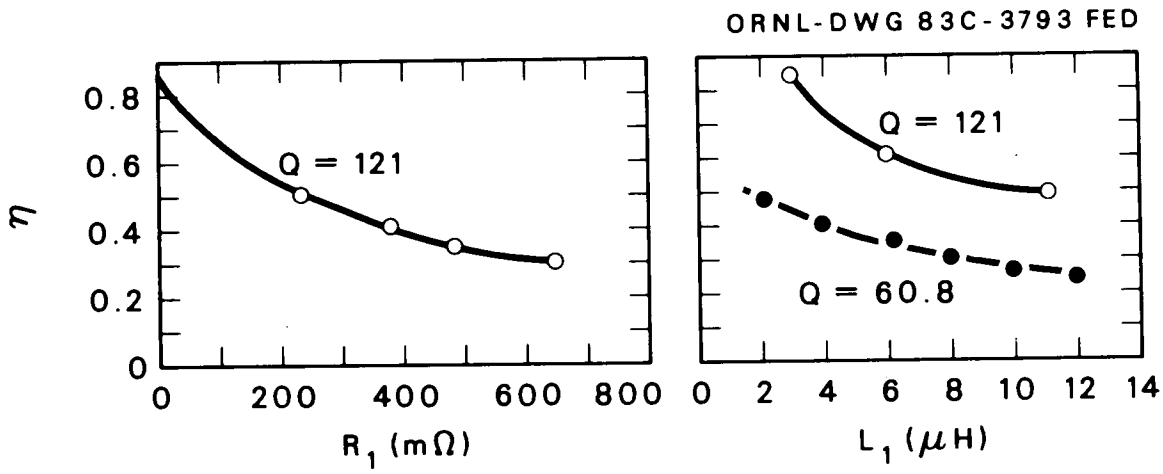

Fig. 5.34. Resistance and inductance as functions of efficiency η.

These values for resistance and inductance can be met with a 14-cm-diam, 5-cm-long coil with two turns.

The resonance capacitance is

$$C_1 + \frac{1}{\omega^2(2L_c + L_1)} = 5863 \text{ pF} .$$

The series-tuned L_2–C_2 circuit is designed for the same Q, $Q_1 = Q_2 = 121$, and $Q_2 = (\omega_m/\Delta\omega)$; $\Delta\omega = 3.22 \times 10^4$ rad/s, so

$$C_2 = \frac{\Delta\omega}{\omega_m^2 z_0} = 43.77 \text{ pF} ,$$

$$L_2 = \left[1 + \left(\frac{\Delta\omega}{\omega_m^2}\right)^2\right] \frac{z_0}{\Delta\omega} = 1608 \ \mu\text{H} .$$

This inductance can be met by a 10-cm-diam, 10-cm-long coil with 60 turns of a 0.3-cm-diam conductor. The coil resistance is about 0.40 Ω. The coefficient of coupling is

$$K = \frac{1}{Q} \frac{1}{[1 + (\Delta\omega/\omega)^2]^{1/2}} = 8.18 \times 10^{-3} ,$$

and the mutual inductance is

$$M_{12} = K\sqrt{L_1 L_2} = 0.57 \ \mu\text{H} .$$

Now the power transmission and loss can be calculated. The power to the plasma from each channel is

$$P = \frac{2P_{PL}}{N} = 4 \text{ kW} ;$$

to the pair of drift pumping coils,

$$P_c = \frac{P}{\eta_c} = 4.61 \text{ kW} ;$$

to the drift pumping coil transformer secondary,

$$P_1 = P_c + P\left(\frac{1}{0.8} - \frac{1}{0.867}\right) = 5 \text{ kW} .$$

The primary power is

$$P_2 = P_1 + I_2^2 R$$

$$\approx 5\left(1 + \frac{R_2}{z_0}\right)$$

$$= 5.04 \text{ kW} .$$

For a 100-ft-long, 0.875-in.-diam coaxial cable with an efficiency of 0.999, P_{TX} = 5.05 kW. In the secondary of the tube matching network,

$$P_3 = P_{TX} = \left(1 + \frac{R_3}{z_0}\right) \approx 5.05 \text{ kW} .$$

Finally, the HPA tube plate circuit power output is

$$P_4 = P_3\left(1 + \frac{R_4}{2r_p}\right) \approx 5.05 \text{ kW} .$$

Power levels and efficiencies are shown in Fig. 5.35, and design details are given in Fig. 5.36 and Table 5.13. The formulas used are as follows:

$$F = g(x_2/x_1) \ ,$$

$$K = f(2a/l) \ ,$$

$$L = \frac{0.254a^2N^2K^2}{l}$$

$$M_{12} = \frac{FN_1N_2(a_1a_2)^{1/2}}{2.54} \ ,$$

$$R = \frac{l}{\sigma a} \ .$$

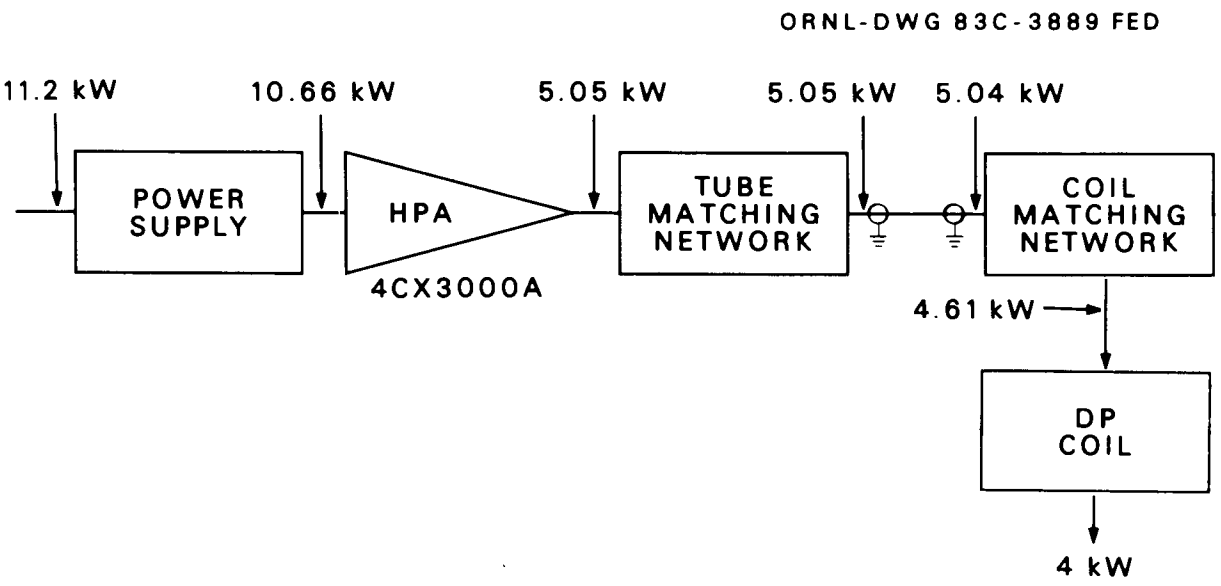

Fig. 5.35. Plug-cell drift pumping system efficiencies. Power supply: 95%; HPA: 47.4%; tube matching network: ~100%; transmission line: 99.5%, coil matching network: 92.2%; drift pumping coil: 86.7%. Overall efficiency: 35.3%. Power input: 11.2 kW.

ORNL-DWG 83-3880 FED

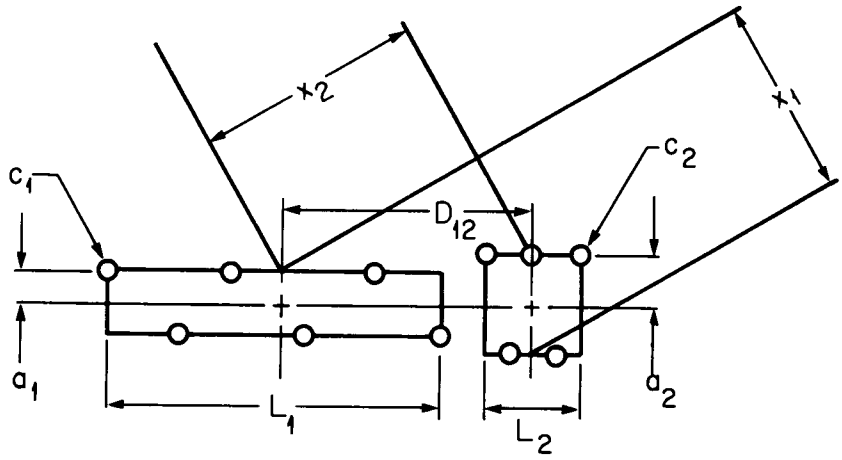

Fig. 5.36. Drift pumping coil system geometry.

Table 5.13. Summary of matching network coil data

Coil number	Inductance L, mH	Radius cm	Length, cn	Number of turns	Conductor diameter, mm	Center-to-center, cm	Resistance R, mΩ
			Anchor-cell coil design				
L1	40	10	10	30	14		6.4
L2	4300	12.5	25	200	2		2000
M12	3.57					41.35	
3	332	8	32	29	10		19.1
4	572	10	40	33	6		89.3
3/4	165					0.92	
			Plug-cell coil design				
L1	4.2	7	5	2	2		30
L2	1608	5	10	60	3		0.4
M12	0.6					2.2	
L3	96.7	10	20	10	14		31
L4	22.3	12	5	3	14		9.3
M34	6.4					2.7	

5.6 TRADE STUDIES

5.6.1 Shielding for Axicell Neutral Beam Lines

For the neutral beam lines to operate properly, the area between the point of ion generation (i.e., the discharge) and the point of separating the neutral particles from the residual ions (i.e., the reflection magnet) must be practically free from external magnetic fields. In the arc chamber, a magnetic field would primarily influence electron orbits; this could result in unwanted discharge characteristics and nonuniform plasma densities and could also affect the ion velocity distribution function at the extraction point. In the neutralizer, where the ion trajectory must be maintained before neutralization, perpendicular magnetic fields could result in beam defocusing and an increased beam divergence. In the space between the neutralizer and the reflection magnet, the beam consists of an equilibrium mixture of ions and neutrals; deflection of the ions in this space could result in beam loss due to ionization of neutrals and in uncontrolled modification of the ion distribution at the ion dumps. For these reasons, the maximum field allowed in the arc chamber is 2 G; the maximum at the entrance of the reflection magnet, 10 G. The main source of magnetic fields near the beam line is the stray field from the central-cell and axicell coils.

For the TDF study,[1] a multilayered, superconducting, magnetic shield concept developed at Lawrence Livermore National Laboratory (LLNL) was adopted because the field parallel to the beam axis could not be shielded with passive ferromagnetic shields of a reasonable size. The locations of the beam line and the magnets created fields that were essentially parallel to the beam axis, which complicated the shielding problem.

The situation in MFTF-α+T is quite different. The fields near the beam line are plotted in Fig. 5.37; they correspond to the configuration shown in Fig. 5.2. The field can be decomposed into components parallel and perpendicular to the beam axis. In the x-z plane (i.e., $y = 0$), the beam line axis is given by $Z = 0.75$ m $+ d \sin \theta$ and $x = d \cos \theta$, where d is the distance from the plasma axis and θ is the angle between the surface normal to the plasma axis and the beam line axis. The parallel and perpendicular components are shown in Fig. 5.38.

Comparison of Figs. 5.37 and 5.38 shows that the magnetic fields at the last grid of the source/accelerator are $B_{\perp 1} = 236$ G and $B_{\parallel 1} = 256$ G; those at the entrance to the bending magnets are $B_{\perp 2} = 1200$ G and $B_{\parallel 2} = 336$ G. Not only are the stray fields smaller, but also they are more nearly perpendicular to the beam axis than those in TDF. For these reasons, the magnetic shielding has been reevaluated for MFTF-α+T.

Analyses were performed for the source region at $d = 10$ m (point 1) and for the entrance to the bending magnet at $d = 8$ m (point 2). Field components and required shielding factors are given in Table 5.14. The shielding factors that dominate the analysis—those that determine the shield thickness—are those in the source region, but the high fields at the bending magnet do have an impact, since the shielding must be thick enough to keep the field in the shield below saturation levels.

Three single-shell shields, described in Table 5.15, and two double-shell shields, described in Table 5.16, were studied. The shielding factors $S_\perp$ and $S_\parallel$ are approximations based on a uniform external magnetic field.[22,23] As in TDF, cast iron (the material usually selected based on cost and availability) does not have a high enough permeability,

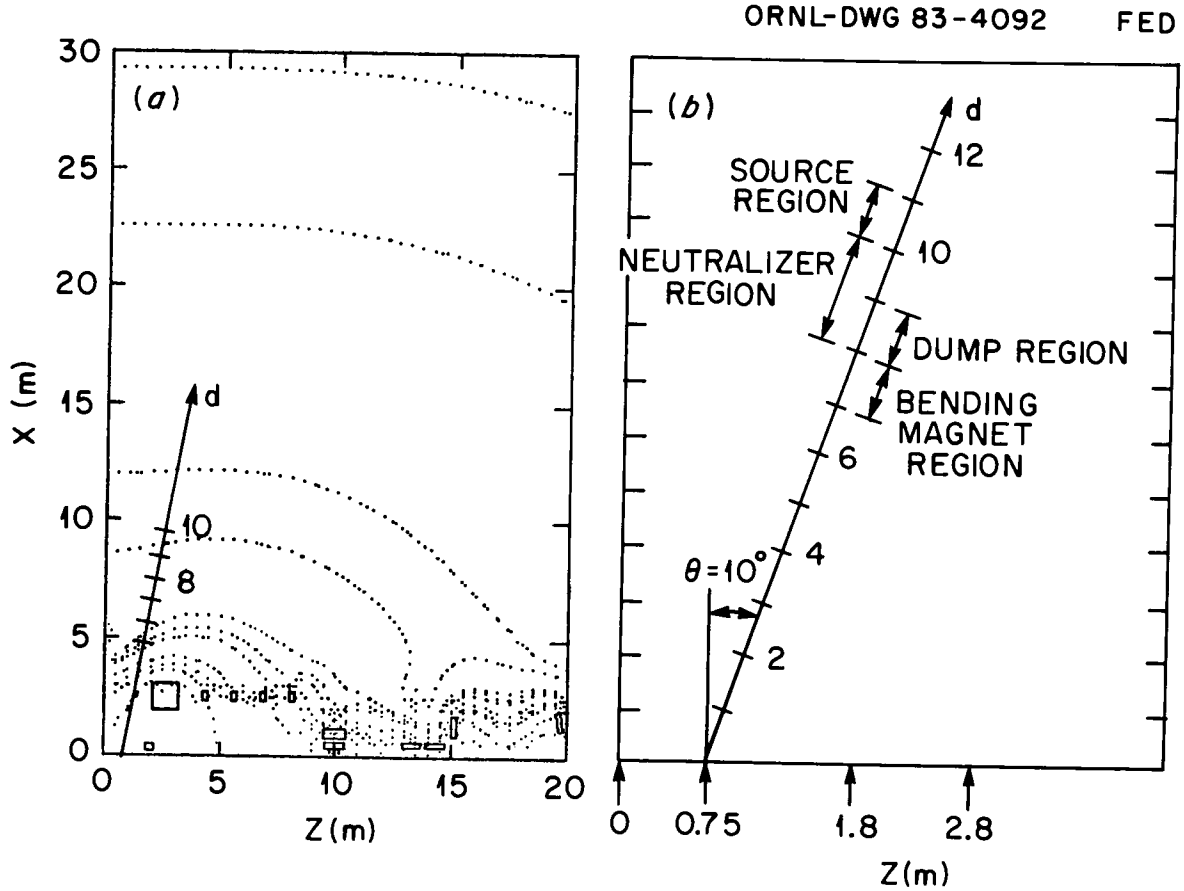

Fig. 5.37. Magnetic field in axicell bending region.

even for multiple shields. However, there are several materials that can provide adequate shielding at reasonable thickness. Materials with much higher permeability could be used, but at the high fields in MFTF-α+T the saturation limit would force the shield to be thicker than required (hence, the shield would be overdesigned). The cases in Tables 5.15 and 5.16 contain materials with permeabilities and required thicknesses that just satisfy the shielding requirements.

In all cases, a tapered section on a partial cap at the front end of the beam line is required to provide adequate shielding of the parallel components, as shown in Fig. 5.39. A backplate is assumed for all shields. The double-shell shields provide shielding at lower material weight and cost and are recommended over single-shell shields.

The superconducting shield is described in detail in refs. 24 and 25. Although superconducting shields require less material and structure and are much lighter than ferromagnetic shields, they are more complex operationally. Neutron shielding is required for both passive and superconducting shields. However, the weight of ferromagnetic shields can be offset by a decrease in the concrete shielding, since the magnetic shield also acts as a neutron shield; in contrast, the superconducting magnetic shield will itself need to be shielded from neutrons.

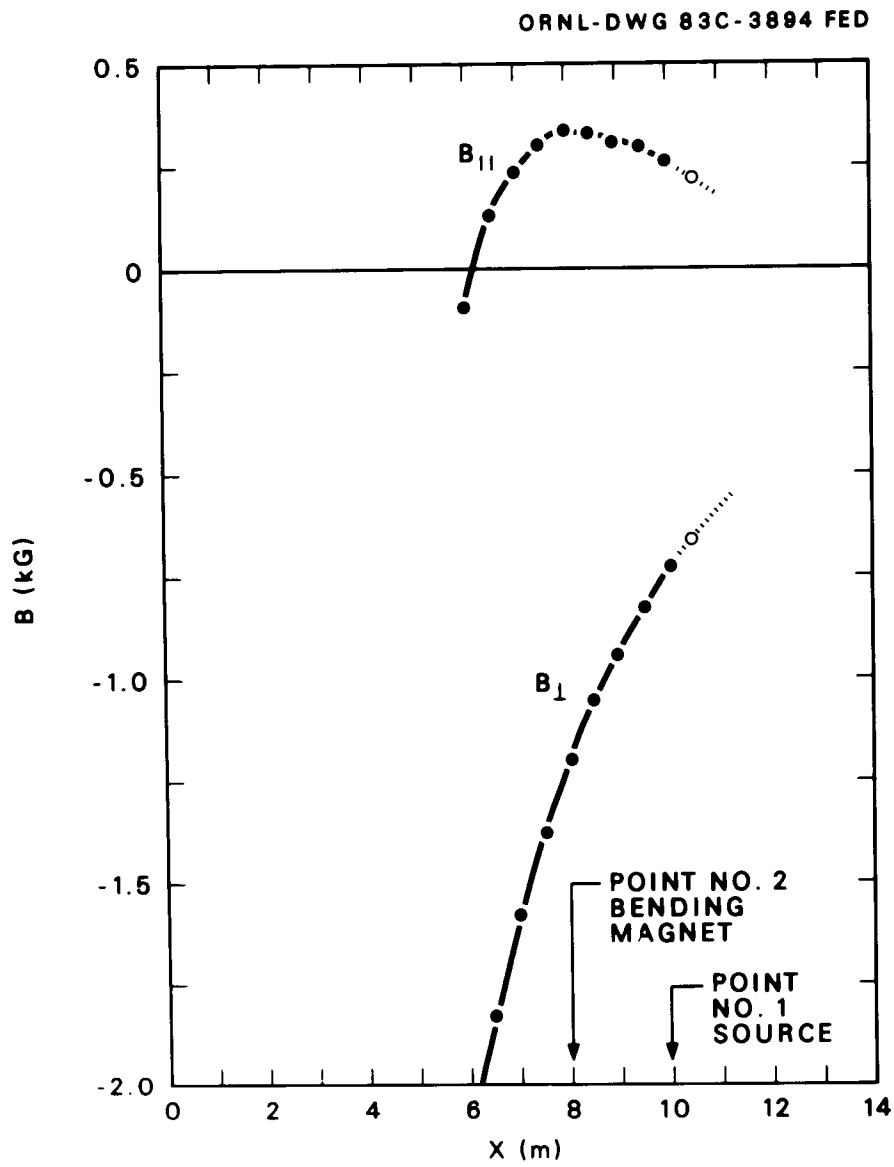

Fig. 5.38. Magnetic field components parallel and perpendicular to the beam line axis.

Table 5.14. Field components and required shielding factors

	Source region, point 1	Bending magnet, point 2
Parallel field component		
$B_{\parallel}$, kG	0.26	0.34
Required shielding factor $S_{\parallel}$	1.30	34
Perpendicular field component		
$B_{\perp}$, kG	0.75	1.2
Required shielding factor $S_{\perp}$	375	120

Table 5.15. Single-shell passive shields with high-permeability materials

Material	Outside diameter D_o, m	Inside diameter d, cm	μ at 1.25 kG	$S_\perp$	$S_\parallel$	μ at 800 G	$S_\perp$	$S_\parallel$	B_s, kG	Mass, tonnes
Cast iron	∞	∞	210	51	43	150	39	35		∞
M-14 (4.5% Si)	4.15	45	4,600	316	23+	3900	377	168	~18	343
Supermendur	3.75	25	10,500	408	22+	7500	460	186		182

Table 5.16. Double-shell passive shields with high-permeability materials

Material	Outside diameter, m			Inside diameter, cm		μ at 1.25 kG	$S_\perp$	$S_\parallel$	μ at 800 G	$S_\perp$	$S_\parallel$	B_s, kG	Mass, tonnes
	D_{o1}	D_{i2}	D_{o2}	d_1	d_2								
Hot-rolled carbon sheet steel	3.55	3.89	4.25	15	18	1435	416	125	1050	380	93.5+	21	250
M-27 (2.75% Si)	3.47	3.70	3.95	11	12.5	2500	478	138	1700	423	97.5+	19.5	180

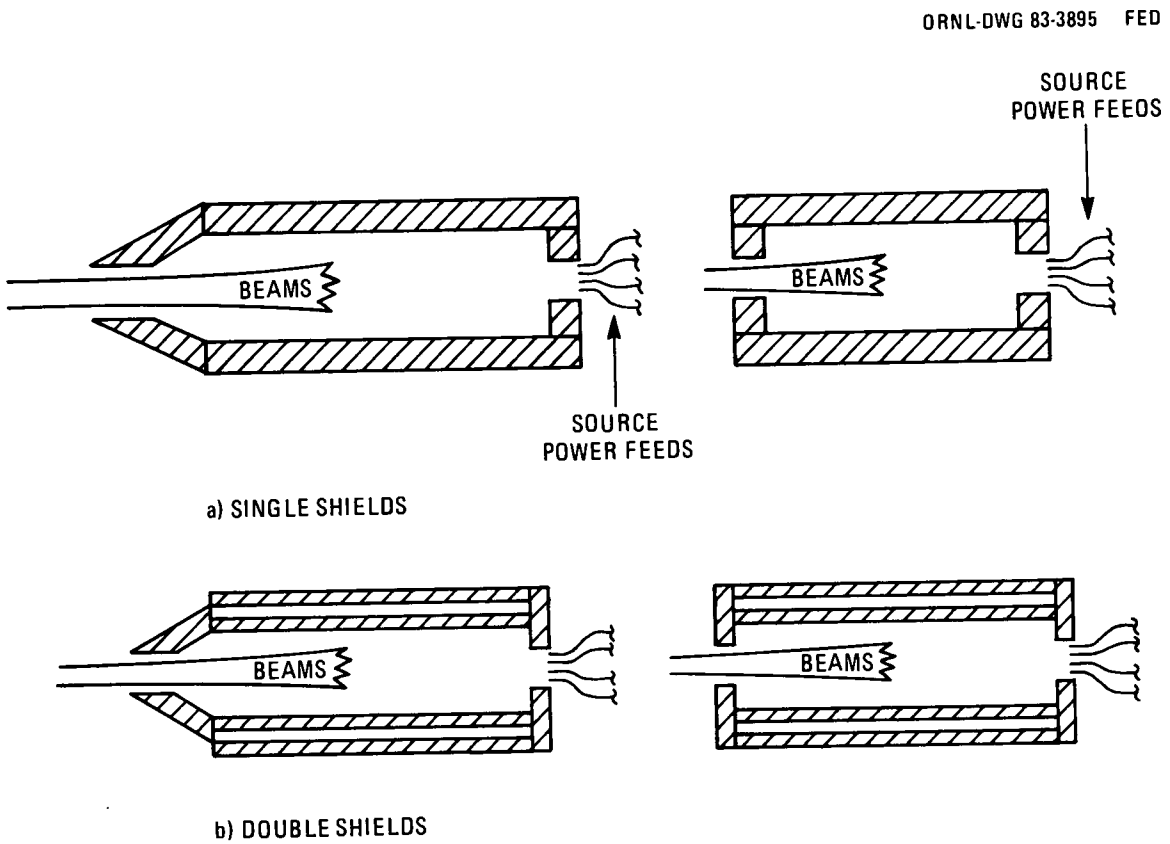

Fig. 5.39. Passive shield configurations.

5.6.2 Sloshing-Ion Neutral Beam Injectors

Because of the limited time available for development, only three relatively simple beam lines were analyzed for the sloshing-ion beams. Their performances are compared in Table 5.17. The first beam line (Fig. 5.40) is based on a positive-ion source closely coupled to a gas neutralizer. The second (Fig. 5.41) uses a negative-ion source, also closely coupled to a gas neutralizer. The third (Fig. 5.42) uses a negative-ion source with a TFF ion transport system to guide the ions from the source to the gas neutralizer. With this arrangement, the sources can be mounted out of the path of the neutrons that stream directly out of the reactor.

Given the time limit, the preferred approach would normally be that requiring the least development—in this case, the positive-ion beam line. However, despite the maturity of the positive ion technology, there is little difference in the amount of effort needed to make a positive- or a negative-ion-based system satisfy the MFTF-α+T requirements. Both need new 200-keV accelerators, power supplies, controls, diagnostics, and related facilities; both must be made to operate reliably for many hours; and both must be designed to use gas neutralizers.

Table 5.17. Performance comparison of three beam lines

	Positive-ion-based beam line	Negative-ion-based beam line	Negative-ion-based beam line with TFF
	Beam line		
Type of ions	Positive	Negative	Negative
Special features	Magnetic separation	None	TFF
Neutralizer	Gas	Gas	Gas
Efficiency, %	13	44	41
	Ion source		
Emitted current, A	34.4	9.4	10.1
Gas efficiency, %	40	12	12
Input power per ampere, kW/A	2.0	20.0	20.0
Input power, MW	0.07	0.19	0.2
	Accelerator		
Grid dimensions, cm	5×57	3×52^a	3×56^a
Grid transparency, %	60	100	100
Current density, A/cm^2	0.2		
Current/length, A/cm		0.06	0.06
Ion loss, %	8	15	15
Aberration loss, %	10	10	10
Input power, MW	6.58	1.782	1.85
	Magnetic separator		
Molecular ions, %	10		
	Ion transporter (TFF)		
Radius, cm			45
Transverse field, kV/cm			9
Pressure, torr			5×10^{-5}
Cryopump load, torr·L/s			14.8^b
Cryopump length, cm			220
Charge-exchange loss, %			7
	Neutralizer		
Neutral fraction, %	18.0	64.5	64.5
Thickness, cm^{-2}	22.6×10^{15}	3.1×10^{15}	3.1×10^{15}
Length, cm	350	225	225
Average cross section, cm^2	11×63	11×217^c	8×229^c
Gas flow, torr·L/s	5.7	6.9	7.4
	Drift region		
Ionization loss, %	9	9	9

Table 5.17 (continued)

	Positive-ion-based beam line	Negative-ion-based beam line	Negative-ion-based beam line with TFF
	Target plasma		
Plasma width, cm	14.7	14.7	14.7
Beam current, A	4.2	4.2	4.2
Beam power, MW	0.84	0.84	0.84

[a]One of four sources.

[b]7.4 torr·L/s from ion source, 7.4 torr·L/s from neutralizer.

[c]Four beams side by side.

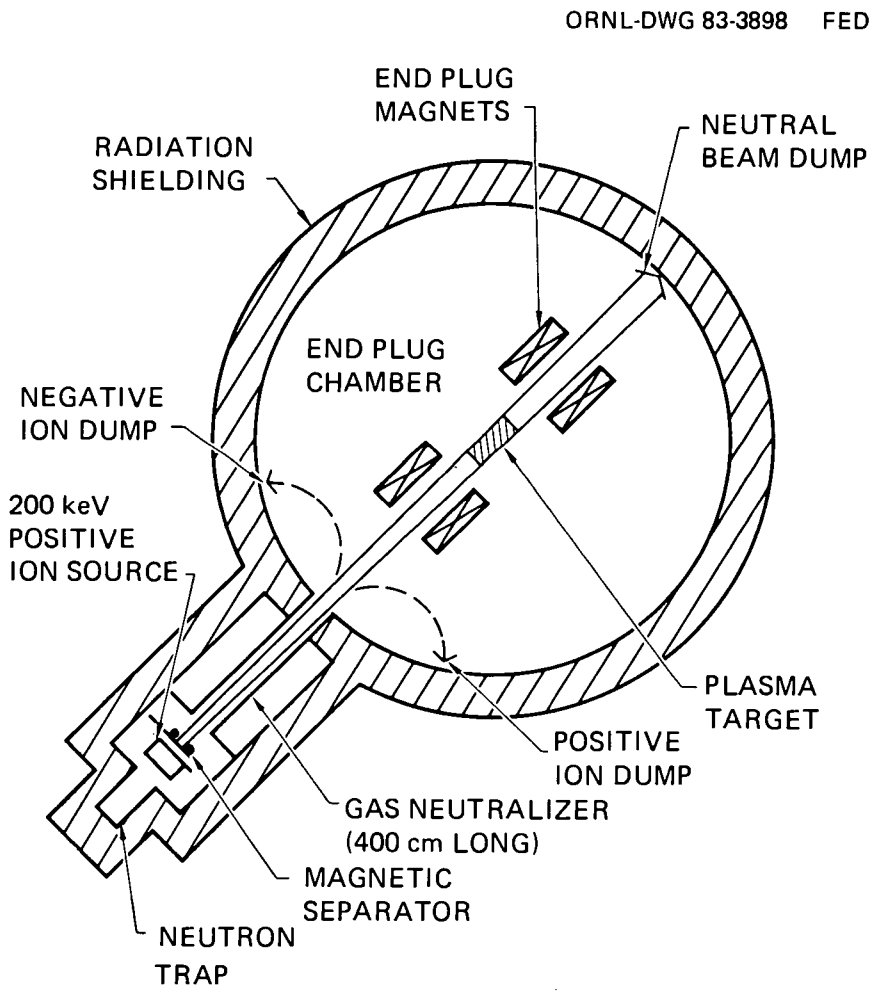

Fig. 5.40. Positive-ion-based beam line.

ORNL-DWG 83-3897 FED

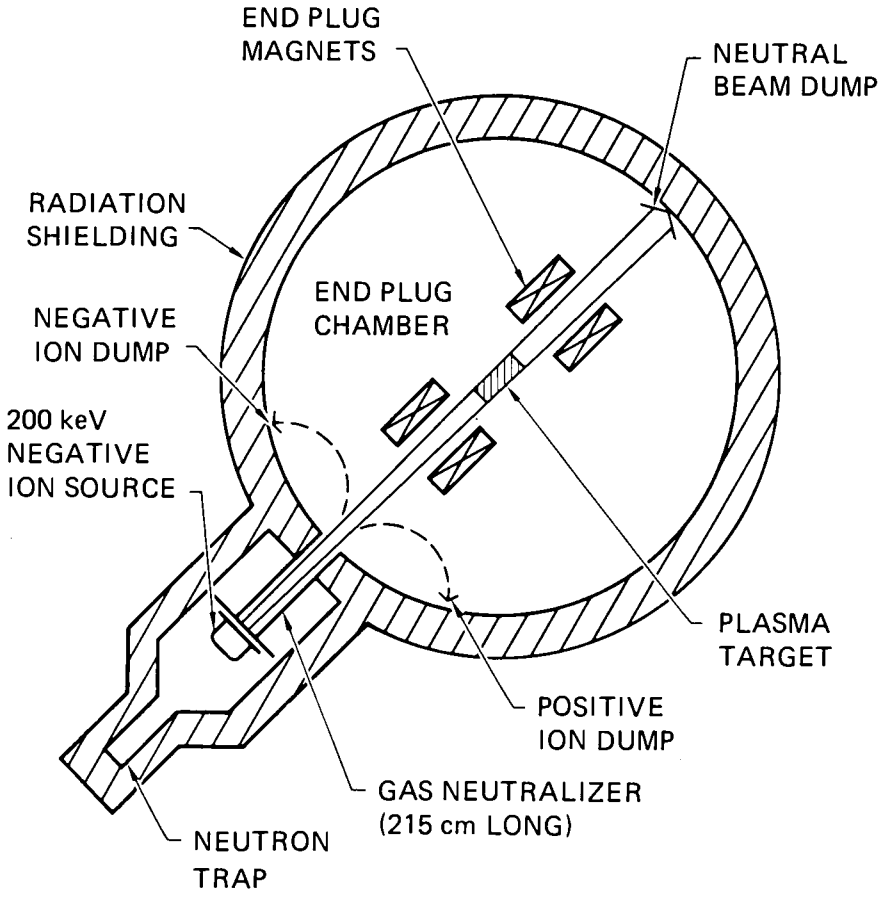

Fig. 5.41. Negative-ion-based beam line with conventional gas neutralizer.

In the long run, negative-ion beams are preferable because they are more efficient—44% vs 13% for positive-ion systems. They require smaller power supplies (3.5 times) and are therefore less expensive. In addition, the gas neutralizer in the negative ion beam line is shorter (225 cm vs 350 cm).

There is one additional factor that makes the negative-ion-based beam line with TFF preferable to the one without it. Because one of the major objectives of MFTF-α+T is to demonstrate the performance of components under reactorlike conditions, it is desirable to pursue an ion source that is housed (as it would be in a reactor) in a region of low neutron flux, where the induced radiation will not exceed acceptable levels. Thus, the third beam line appears to be the best choice, even though it involves a small loss of efficiency (41% instead of 44%), the introduction of cryopumps (roughly 220 cm by 224 cm), and the development of a completely new ion transport system (the TFF transporter).

The considerations that went into the choices of the components for the beam lines are presented in this section.

ORNL-DWG 83-3899 FED

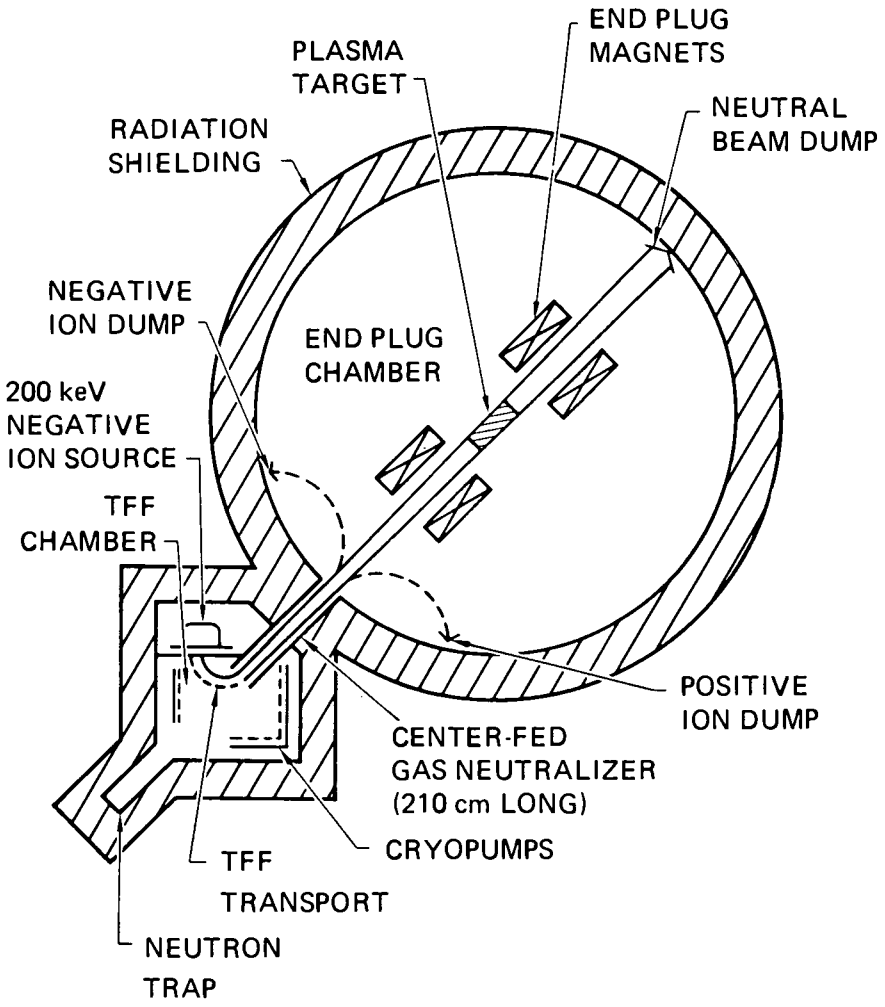

Fig. 5.42. Negative-ion-based beam line with TFF ion transport system.

Ion sources

The positive-ion source described in Table 5.17 is assumed to be an extrapolation of the 120-keV source for the Tokamak Fusion Test Reactor (TFTR)[26] with a 30-s pulse length. It is obvious that considerable effort must be expended to make this unit operate reliably for 100 h. The filaments and discharge that generate the plasma in existing sources would probably be replaced with some form of electrodeless rf heating. In addition, it would be necessary to find a means of offsetting the degradation of the beam that results from grid sputtering. With the fine grid structures used in positive-ion sources today, this would be particularly difficult.

The negative-ion sources used in the negative-ion-based beam lines proposed here are the LBL self-extracting type. Although it is not of great importance at this time, it is assumed that the output of these sources would be increased from the present 0.04 A of

D^- per centimeter of source length to 0.06 A. Just as with positive-ion sources, considerable effort is required to ensure reliable operation for 100 h.

200-keV accelerator

Although the power supplies and associated equipment for positive- and negative-ion sources will be very similar, the accelerators will be different, because the grid polarities alter the trajectories of the background electrons and ions. These particles are formed by ionization of the background gas, charge exchange of the positive ions with the neutral gas molecules, stripping of electrons from the negative ions, and secondary electron emission from electrodes caused by radiation or ion bombardment. These processes are well understood, and computer codes are available to determine the particle trajectories. Hence, the electrode contours that intercept the fewest particles of either polarity, and as a consequence incur the lowest power loading, can be established.

Meanwhile, to minimize the probability of electrical breakdown in an accelerator, the field between adjacent grids should be limited. At reasonable current densities, a 200-keV accelerator of conventional design can be made to operate reliably. At higher voltages the field becomes excessive, making it necessary to accelerate beams of lower current density and to use more elaborate accelerators.

A ribbon beam of negative ions can be transported and accelerated with a series of curved electrodes mounted in pairs on either side of the ion beam. The ions are accelerated in steps by modest electrostatic fields between adjacent pairs of electrodes along the beam path. In this way, it is possible to design a conservative high-voltage accelerator. However, the ion path through the accelerator is much longer than it would otherwise be, and the ion loss at a given background gas pressure is much greater. To minimize this loss, the background pressure must be as low as possible, which necessitates pumping along the beam line. Conventional grids will be adequate for this application, since the accelerating voltage is only 200 kV and the impact of the required pumping for a TFF accelerator would be an added complication.

Magnetic separator

The positive-ion-based neutral beam line would require development of a magnetic separator (shown in Fig. 5.43). This component removes the molecular ions, D_2^+ and D_3^+, and impurity ions from the positive atomic D^+ ion beam. Although impurity ions are a problem in negative-ion beams, there are, for all practical purposes, no molecular negative ions. Therefore, if the negative-ion impurities can be eliminated in some other manner, no magnetic separator would be required for the two negative-ion-based beam lines proposed for MFTF-α+T. It is assumed that impurities can be reduced to acceptable levels in negative-ion beams by careful selection of the ion source material and by adequate conditioning of the sources before operation.

Ion transport

The curved TFF ion transport places the ion source in a region where the neutron flux density is low. However, further analysis is needed to determine whether the neutron trap

ORNL-DWG 83-3896 FED

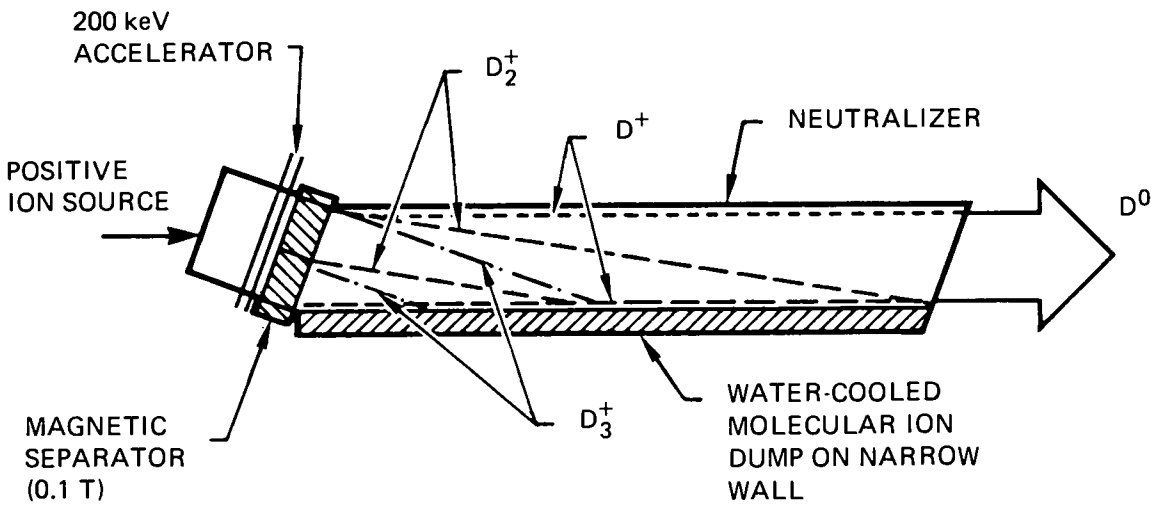

Fig. 5.43. Molecular-ion magnetic separator for a positive-ion-based beam line.

and the single TFF loop shown in Fig. 5.7 are adequate in this application. If not, additional loops of ion transport may be required.

If the ion transport must be elongated, the pumping capacity in the vicinity of the TFF will have to be increased as well. A critical consideration in the TFF design is the need to keep ion losses minimal, thereby limiting the power dissipation at the electrodes. To facilitate gas flow out of the ion beam path, the larger TFF electrode, as shown in Fig. 5.7, has an open structure.

An important feature of TFF transport is the strong focusing it provides. It forms a virtual ion source, as seen from the plasma target, just in front of the entrance to the neutralizer. This is critical in this application because the plasma target is so narrow (14.7 cm). If the ion source were located too far from the target, only a small fraction of the beam would be used. With this design, apertures at the ion source limit the beam divergence and clip the wings of the otherwise Gaussian-like spatial distribution of the ion beam.

Studies were made of the effects of trimming the beam even more. However, results showed a marked decrease in the available ion current per unit length and an increase in the power required by the source per ampere of emitted ion.

Neutralizer

The gas neutralizers used in all three beam lines under consideration were chosen because they required the least development. Other alternatives, including plasma neutralizers and photoneutralizers, offer the prospect of higher neutral fractions, but it is unlikely that they will be developed during the time available to the point at which they could be used for this application.

The pumpless systems described for the positive-ion-based and the ordinary negative-ion-based beam lines are very tricky. Gas inlets would probably have to be included in the neutralizers to supplement the gas flowing out of the ion sources. This would permit operation of the sources at maximum ion input, regardless of their actual operating gas efficiency.

The design for the neutralizer of the negative-ion-based beam line with TFF is not straightforward either. The clearance between the beam and the neutralizer walls is slightly less than that in the other beam lines. This lowers the conductance and thus limits the gas flowing into the end-plug chamber. In addition, the neutralizer was increased to maintain its thickness, so gas flow is reduced to a quantity that might be removed by the plasma halo.

Physical constraints make it desirable to have a virtual source located 900 cm from the center of the target. However, this limits the beam clearance and incurs beam scraping at the source, which introduces a loss of about 2%. Questions concerning the gas flow about the magnet coils in the reactor and the pumping capacity of the halo make it desirable to reintroduce cryopumping about the beam line as it leaves the neutralizer. Further studies must determine the details of the gas flow and the need for cryopumps, and additional work is needed to explore ways to reduce the beam line length.

5.6.3 ECRH Transmission System

Experimental ECRH transmission systems have consisted of pressurized, overmoded waveguides with a number of mode control components.[27–30] These systems are relatively inefficient (<70%) and would be quite cumbersome when scaled to larger tandem mirror devices. In studies for three such devices,[31–33] the high-power transmission systems used quasi-optical transmission. A trade study was conducted to examine the possibility of using quasi-optical transmission on MFTF-α+T and the desirability of doing so.

The configuration for TASKA,[32] as shown in Fig. 5.44, consists of a number of dual-mode conical horn reflectors/offset Cassegrainian systems arranged in a circular array. Each launcher is designed to inject ~4 MW. For simplicity, the MARS design[33] has evolved to use arrays of single paraboloid reflector beam launchers.[34] Because of the longer horn geometry, the single launcher still provides the ability to shield the gyrotrons from streaming neutrons. Each thermal barrier launcher delivers 48 MW to the plasma. The MFTF-α+T requirements for 500 kW at 35 GHz and 500 kW at 56 GHz are modest compared to those for an advanced tandem mirror reactor (TMR) and could be met with existing waveguide systems.

The design of the plug magnets and their structure (Chap. 4) has an impact on the area available for beam injection, and the vacuum vessel diameter (Chap. 8) defines the minimum beam path (i.e., the distance between the launcher and the plasma). The end-cell magnet set was designed to produce the required plasma fields with minimum magnet size, conductor weight, and cost; the neutron shielding and structure further restrict the area for beam access. Quasi-optical beams would have to be injected in the 15-cm gap in the minor radius region of the coils, as shown in Fig. 5.45, since the access in the major radius gap is even more restricted (only 10 cm).

ORNL–DWG 84-16495 FED

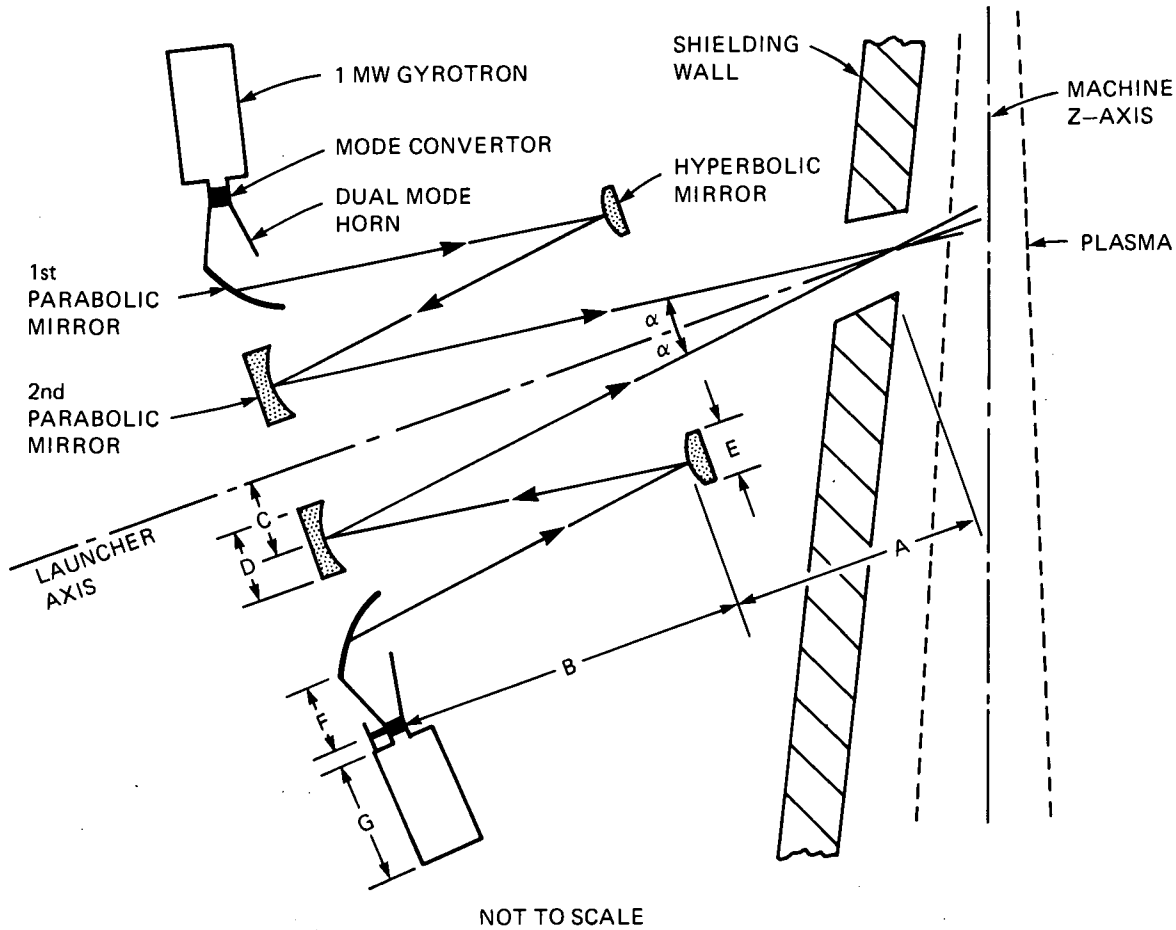

Fig. 5.44. Cross section of the TASKA quasi-optical launching system.

The phase corrections required to form a beam waveguide may be accomplished by either reflectors or lenses; lenses are not considered for high-power applications because of their high losses from reflection and absorption. Multiple reflectors are also eliminated because they are bulky and add complexity to the problem of alignment while offering few advantages, given the divergence and beam diameter.

The single-reflector beam launcher shown in Fig. 5.46 was considered.[35] The apex of the horn coincides with the focus of the paraboloid, and the axis of the horn is perpendicular to the axis of the reflector. The paraboloid acts as a combined right-angle reflector and phase corrector for the diverging spherical wave, so that the Gaussian wave coming out of the reflector has a plane wave with beam diameter $4f'\tan\alpha_0$.

A Gaussian beam has a divergence angle $\theta = \tan^{-1}(19.1/D_0 f)$ with D_0 in centimeters; for frequencies f = 35–60 GHz, the divergence angles can be quite large. The beam width along the propagation path is approximated by $D(X) = D_0 + 2X\tan\theta$ (quantities are defined in Fig. 5.47a). Since $\theta = fn(D_0)$, for a given frequency and distance

ORNL–DWG 83-4021A FED

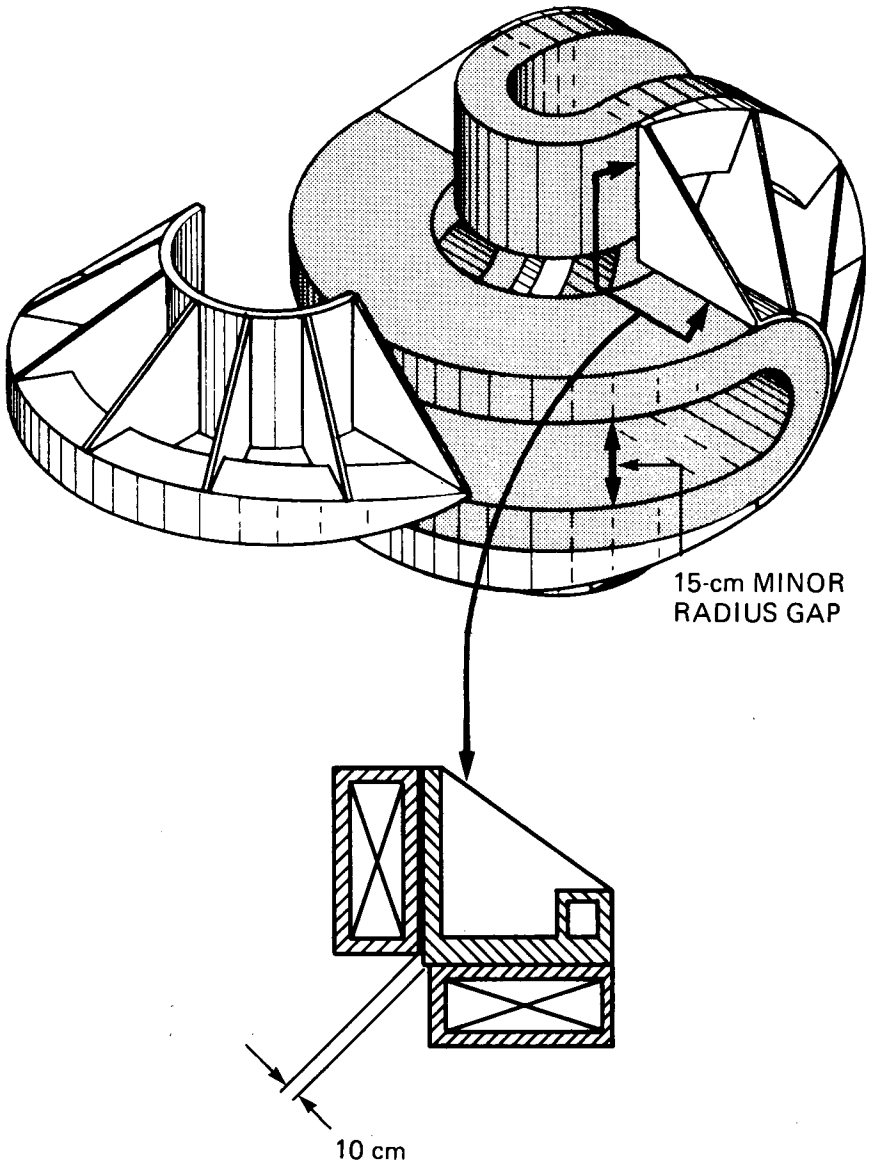

Fig. 5.45. Beam injection point.

along the path there is an optimum D_0 that minimizes $D(X)$, $D_0 = [(2X \cdot 19.1)/f]^{1/2}$.

For $f = 35$ GHz and $X = 500$ cm (where X is the distance between the vacuum vessel and the farther magnet edge along the beam path), $D(X)$ is 47 cm; the beam would be far too large for the 15-cm magnet gap. To keep the beam diameter less than 15 cm, the last reflector of a multiple-reflector system would lie in the gap. For 56 GHz, the beam diameter decreases, but not enough to allow access.

ORNL-DWG 83-3865 FED

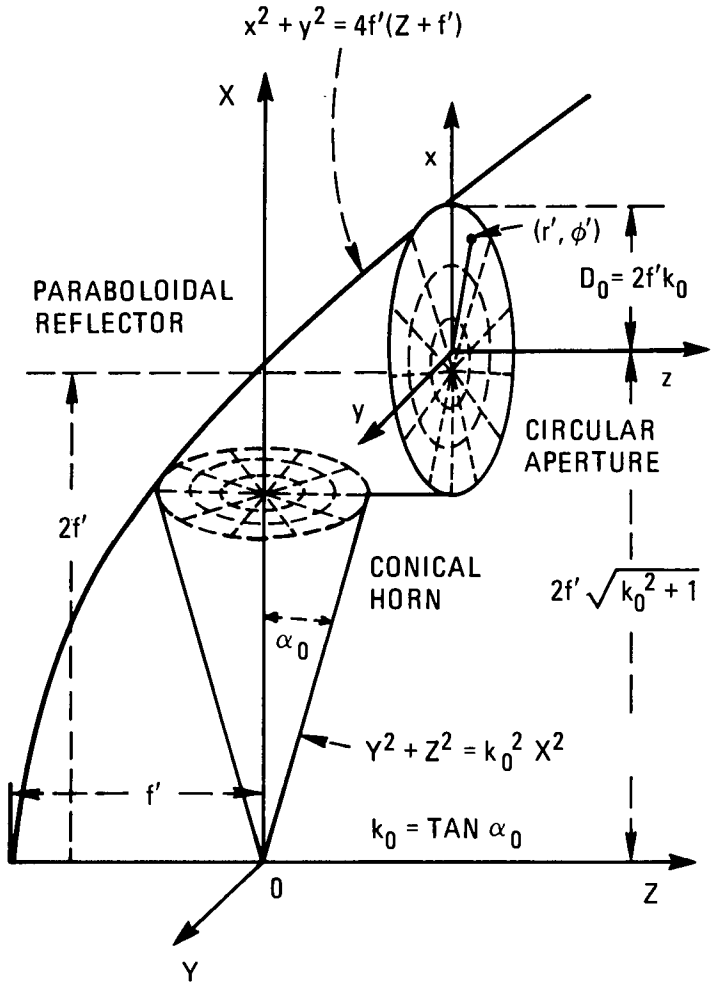

Fig. 5.46. Geometry of the conical horn/reflector antenna.

If the reflector is pulled away from the horn along the paraboloid axis, so that the apex no longer coincides with the focal length, then the beam is focused. The geometry of the beam is similar to that of a neutral beam and is shown in Fig. 5.47b. The beam width is approximated by $D(X) \approx (D_0/X_0)(X_0 - X) + 2X \tan^{-1}(19.1/D_0 f)$, where $\tan \theta_1 = [(D_0/2)/X_0]$, $a_0 \approx b_0 \approx [X^2 + (D_0^2/4)]^{1/2} \approx X$, and $\theta \ll 1$, so that $[2 \times (1 - \cos \theta)]^{1/2} \approx \theta$ has been used. Note that $D(X)$ is approximately constant with X within the accuracy of the $a \approx b$ approximation. Hence, the focusing of the beam provides an improvement of a factor of 2 in the beam width through the magnet gap, but the beam is still too large.

Quasi-optical systems cannot be used for the frequencies, magnet set, and vacuum vessel established for MFTF-α+T because of restricted access and large beam divergences. The technical advantage of quasi-optical systems at the MFTF-α+T power levels is not

ORNL-DWG 83-3866 FED

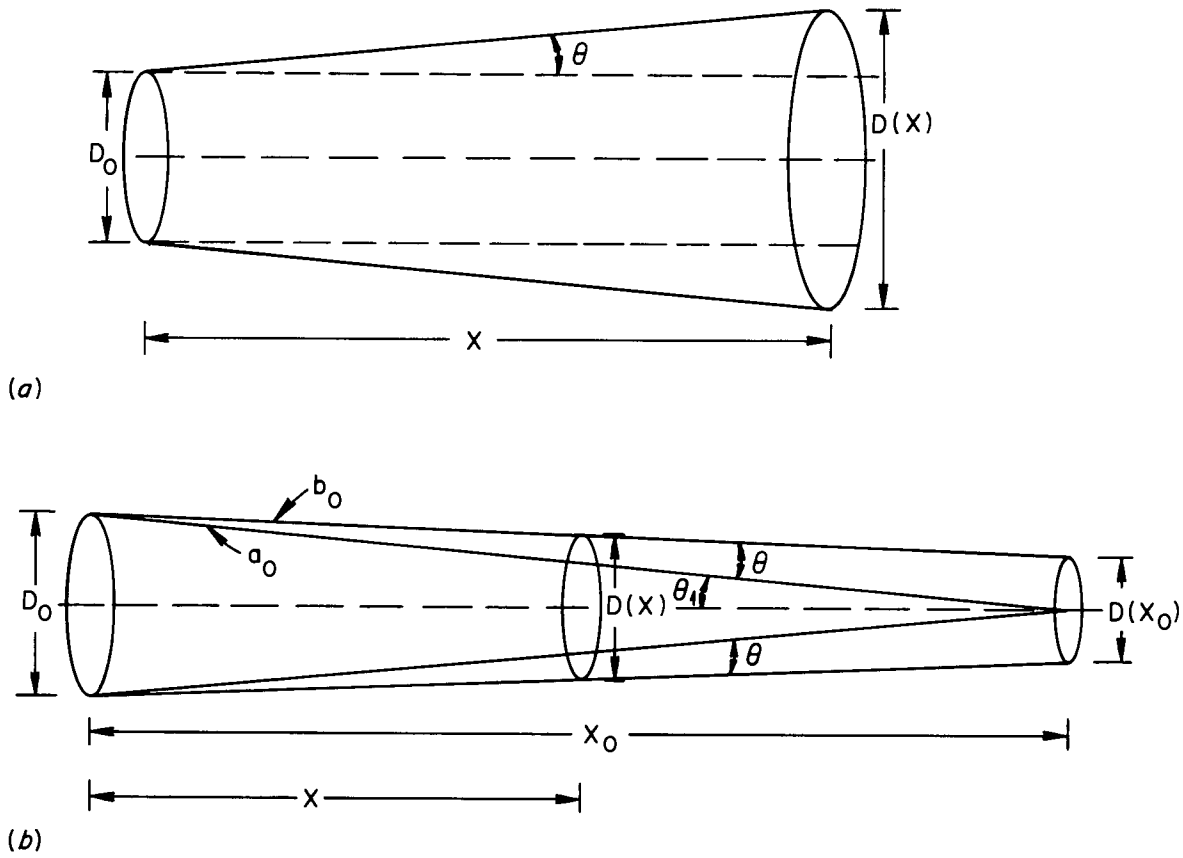

Fig. 5.47. Beam geometry for (a) parallel beam and (b) focused beam.

large enough to justify a larger magnet set. Even if quasi-optical systems were used, their higher efficiency (~15%) is not significant at the low powers, and the difference in cost between the two systems is not significant because of the high gyrotron and power supply costs. The only incentive for requiring quasi-optical transmission in MFTF-α+T would be the desire to have reactor-relevant systems.

5.6.4 Drift Pumping Alternatives

Anchor-cell drift pumping coil tuning and matching

Achieving block or continuous spectrum. From the performance analysis of the drift pumping coil (Sect. 5.5.5), the intrinsic Q is 256 and the loaded Q is 68.8. The effective loading is shown schematically in Fig. 5.48, which also shows possible methods for tuning and feeding the coil. The parallel-tuned circuit has a reasonable impedance to drive but has a narrow band and is fixed tuned. The series-tuned circuit can be tuned by feeding it from separate generators through a capacitor that resonates at the generator frequency,

ORNL–DWG 83-3892 FED

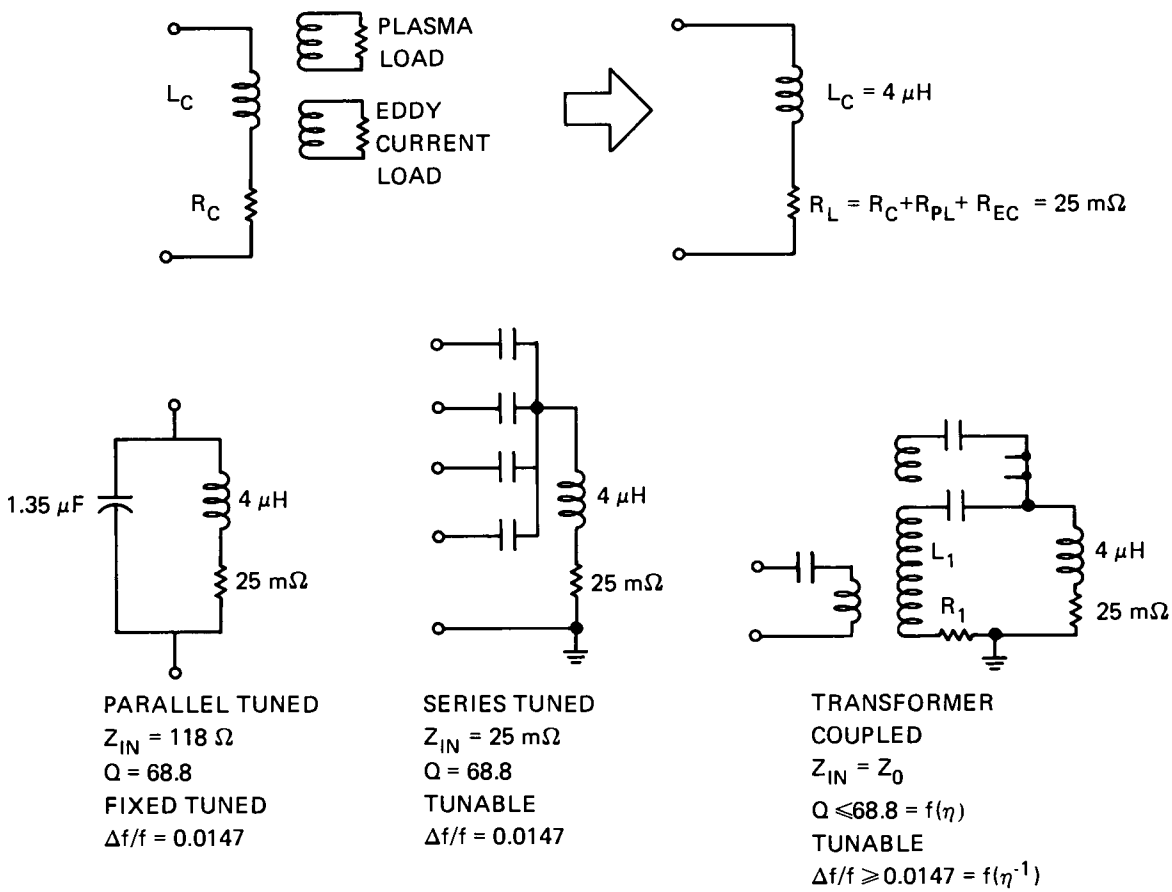

Fig. 5.48. Anchor-cell drift pumping coil tuning and matching schemes.

but this has an unacceptably low input impedance. The transformer-coupled circuit is the preferred arrangement. The primary side is matched to the transmission line impedance, and the secondary side resonates with the drift pumping coil. Some number of secondary circuits will be required, however, to sample or fill the desired spectrum width.

The secondary circuit has a Q of

$$Q = \frac{\omega L_C(1 + L_1/L_C)}{R_C(1 + R_1/R_C)} = \frac{f}{\Delta f} = 68.8\ \frac{1 + L_1/4}{1 + R_1/25}$$

and an efficiency η of

$$\eta = \frac{R_{RL}}{R_L(1 + R_1/R_L)} = \frac{0.668}{1 + R_1/25}\ .$$

To provide a block spectrum, it is necessary to maximize η and make $Q \leqslant f/\Delta f = 2.44$. Hence,

$$2.44 = 68.8 \left[\frac{1 + L_1/4}{1 + R_1/25}\right] ;$$

by solving for $1 + R_1/25$,

$$1 + R_1/25 = \frac{68.8(1 + L_1/4)}{2.44} ,$$

and substituting into the expression for η, we obtain

$$\eta = \frac{0.668}{68.8(1 + L_1/L_C)} 2.44 = \frac{2.37\%}{1 + L_1/L_C} .$$

For the best case ($L_1 = 0, \eta = 0.0237$) a generated power $P_{gen} = P_{PL}/0.0237 = 6.329$ MW is required, exclusive of other losses (which can be held to a negligible amount). Even so, generating 6.329 MW to obtain an output of 150 kW is unacceptable. From the expression for η, the coil resistance dissipating this power is $R_1 = 25[(0.668/\eta) - 1]$ (in milliohms), which is 0.68 Ω.

Discrete tone approach. To obtain discrete tones, Q is left at 68.8 and the continuous spectrum is sampled by some number N of equally spaced narrow-bandwidth spectra. (This is the approach proposed for use in MARS.) The power available in this case is the sum of the power of each tone.

If the drift pumping coil is supplied by enough circuits to cover the entire band by spectra interfacing at the -3-dB (half-power) points, then $N = 19$, and the power per channel is $P_{chan} = (P_{PL}/\eta_{max}N) = 11.8$ kW. The requirements (see Sect. 5.3.5) allow a minimum of 10 or 12 channels, depending on the operating mode. For the drift pumping coil's intrinsic Q, the percentage of the spectrum filled is about 45%. Figure 5.49 shows an arrangement of 12 channels with $Q = 47$ interfacing at the -3.5-dB points.

If the two drift pumping coils straddling the plasma are connected in series, the value of Q remains the same. For the L_1 matching circuit, $Q = \Delta f/f = 68.8[1 + (L_1/8)/(1 + R_1/50)]$, where L_1 is in microhenries, R_1 is in milliohms, and the efficiency is $\eta = 0.688/(1 + R_1/50)$. Letting $Q = 47$ and substituting into the expressions for Q and η gives $(1 + R_1/50) = (68.8/47)(1 + L_1/8)$ and

$$\eta = \frac{(47 \times 0.688)}{[68.8(1 + L_1/8)]} = \frac{45.64\%}{(1 + L_1/8)} .$$

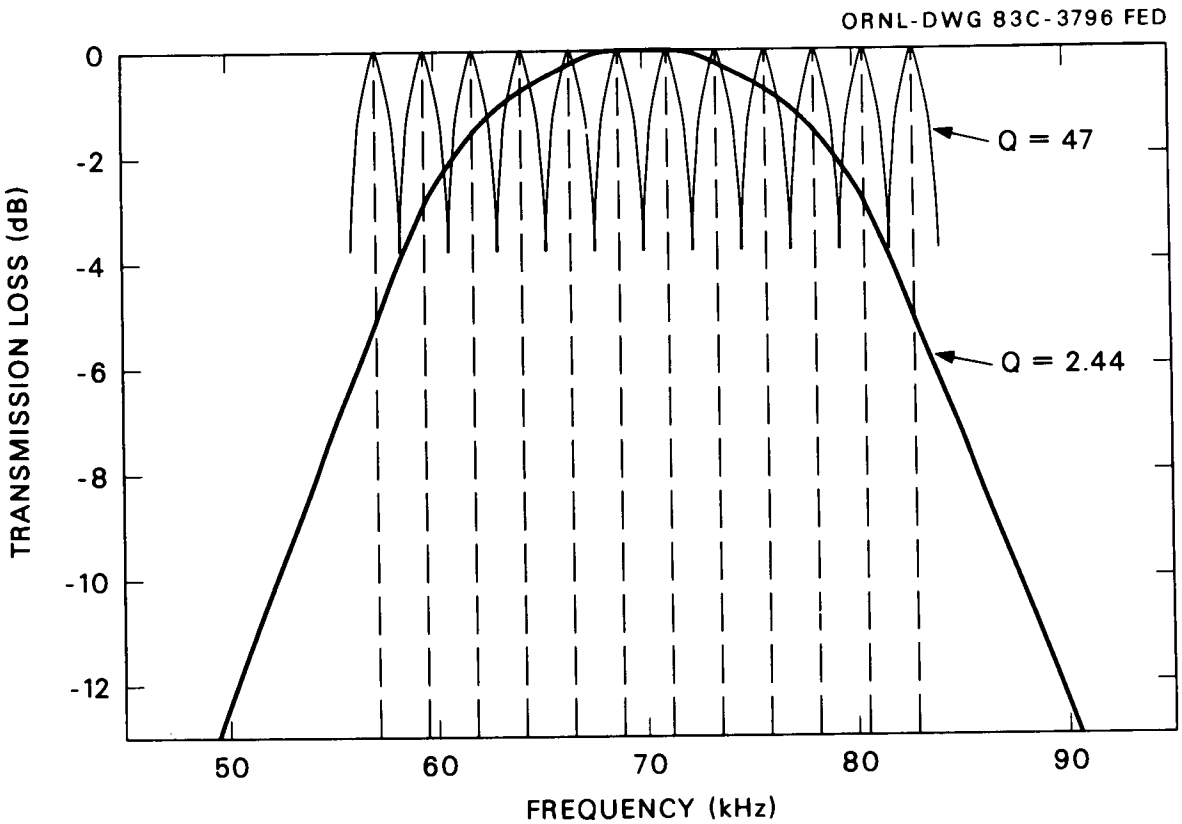

Fig. 5.49. Arrangement of 12 channels with Q = 47 interfacing at the −3-dB points.

Thus, there is a trade-off of η and L_1 (see Fig. 5.50). For η = 30% and L = 4.17 μH, R_1 = 61.4 mΩ. The added power consumed by this L_1 circuit is $P_{R_1} = (2P_{PL}/N) \times [(1/0.3) - (1/0.668)] = 45.9$ kW. Because a coil having only a few microhenries of inductance would have only a few milliohms of resistance, some added dissipative element would be needed. This is not very attractive unless this power can be recovered, as in the circuit shown in Fig. 5.51.

If Q in the matching circuit is increased, as it can be if discrete tones only are used, then L_1 can be arbitrarily large. For the MARS study, an L_1/L_C factor of 5 was used; hence, $Q = 68.8[(1+5)/(1+R_1/50)] = 412.8/(1 + R_1/50)$. For a 40-$\mu$H coil, the coil resistance is estimated to be about 6 mΩ, so Q = 368. Substituting into the expression for efficiency yields $\eta = 0.668/(1 + 6/50) = 0.596$. The power dissipated in this coil is then $(2P_{PL}/N)[(1/0.5969 - (1/0.668)] = 4.5$ kW. The surface area of the 40-μH coil is estimated to be 1500 cm^2, making the power density dissipated about 2.7 W/cm^2. The −3-dB bandwidth of this circuit is 190 Hz. Figure 5.23 shows this response and the spread of discrete tones. This is the baseline system arrangement.

Plug-cell drift pumping coil tuning and matching

The plug-cell drift pumping coil tuning and matching system is easier to design than the anchor-cell system, because the bandwidth and power requirements are lower and the

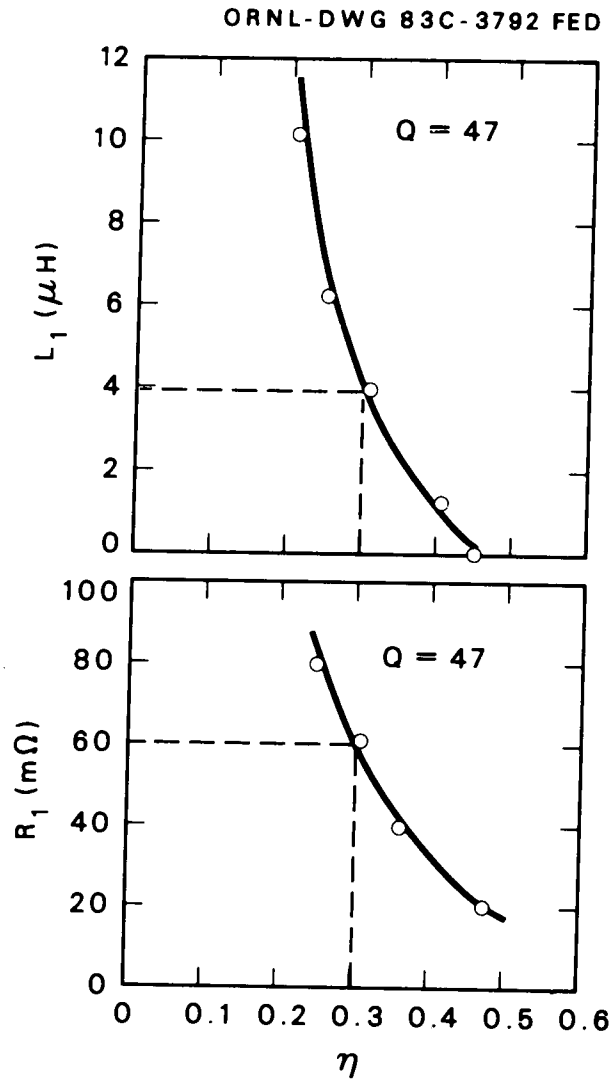

Fig. 5.50. Trade-off of L_1 and R_1 vs η.

center frequency is higher. The same trade-offs apply in the areas of feeding and matching. In this system the continuous spectrum was both practical and desirable for its flexibility. Thus, it was chosen for the baseline configuration. The efficiency is about 35% for a drift pumping coil circuit Q of 121.

Single vs multiple drift pumping coils

The baseline approach is to use multiple narrow-band transmitter channels to supply the two drift pumping coils of each cell in series. Two other approaches were considered: using multiple sets of coils in a cell, each covering a different portion of the desired band, and driving each of the two coils in a set at different frequency bands. These approaches seemed reasonable, since the high Q of the drift pumping coils limits the channel

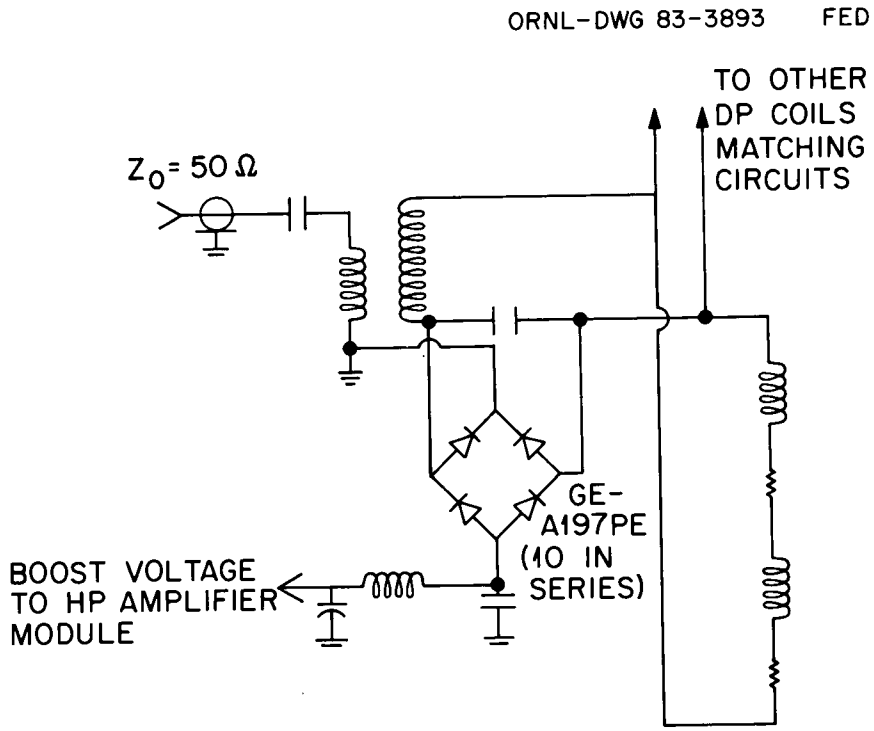

Fig. 5.51. Anchor-cell drift pumping coil matching network.

bandwidth. For a single coil, there was concern about the tuning interaction between multiple transmitters feeding a common drift pumping coil. This interaction is dependent on the coupling, which in turn depends on the band pass overlap of the two channels. This is illustrated for a 10-channel arrangement for the anchor-cell system in Fig. 5.52.

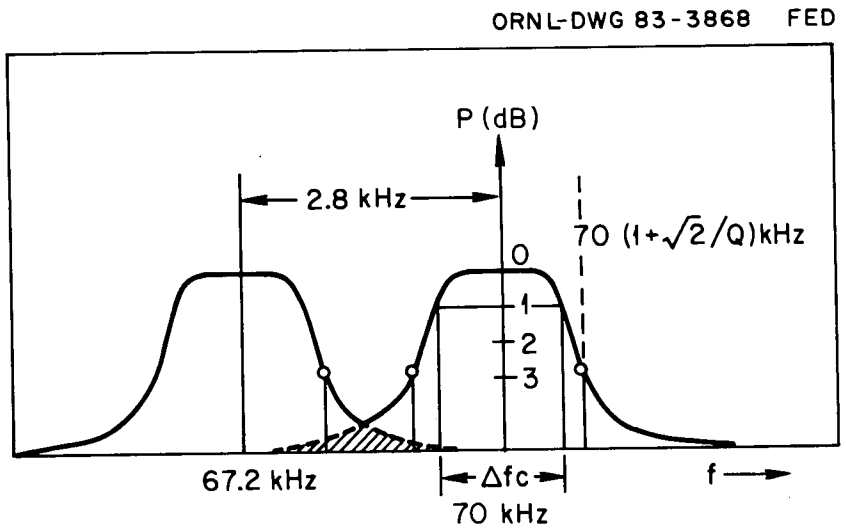

Fig. 5.52. Tuning interaction between channels. Shaded area indicates coupling.

Two qualitative analyses of this coupling were carried out. One used approximations, the other exact expressions. A model using two transmitter channels driving a single drift pumping coil was assumed, and superposition was used (see Fig. 5.53). With one transmitter channel assumed to be at zero power, the load impedance of the other channel was investigated. In both analyses, the impedance was calculated at $A - A1$, $B - B1$, and $C - C1$, as

$$A_{zz'} = R_{P_1} + \frac{1}{[1/(R + j\omega L_1)] + (1/Z_B)} ,$$

$$Z_B = \frac{1}{j\omega C_1} + \frac{1}{[1/(R_C + j\omega L_2)] + (1/Z_C)} ,$$

$$Z_C = \frac{1}{j\omega C_2} + \frac{1}{[1/(R_2 + j\omega L_2)] + (1/R_{P_2})} .$$

When Q is large (10 to 100), $R_1 \approx R_2 \approx R_C \approx 0.1\ \Omega$, there are 10 channels so that $|f_i - f_{i+1}| = 0.4 f_m$, $Q_{\text{series}} = \omega CR$, $Q_{\text{parallel}} = \omega L/R$, and $\omega = 1/\sqrt{LC}$, then for the resonance condition $(C_1 L_1)^{1/2} = \omega^{-1}$

$$Z_A \approx R_{\text{PL}} + Q_1^2 \frac{R_1}{1 + R_2/R_1} .$$

There are no reactive components in this impedance. For the resonance condition $[(L_1 + L_C)C_1]^{1/2} = \omega^{-1}$

ORNL-DWG 83C-3876 FED

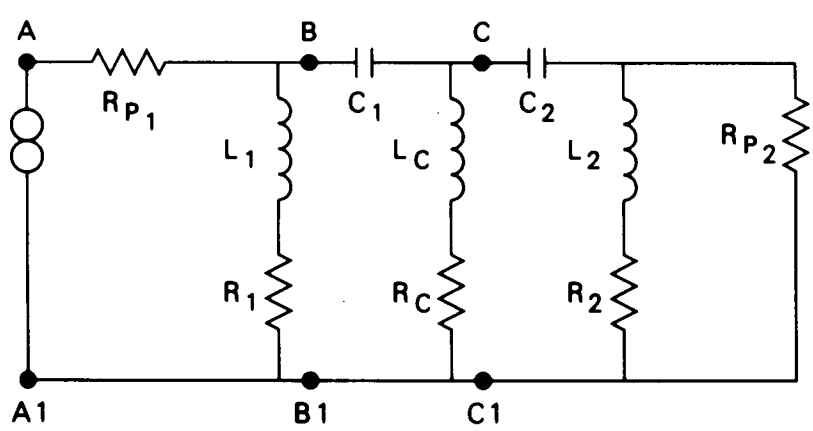

Fig. 5.53. Model of two transmitters driving a single coil.

$$Z_A \approx R_{\mathrm{PL}} + \frac{jQ_1R_1}{L_C/(L_1 + L_C) + j(1/Q)(1 + R_2/R_1)[L_1/(L_1 + L_C)]} .$$

There are only negligible reactive components in the impedance. Without the assumptions for the values of Q, R, etc., the expression for Z_A is

$$Z_{AA} = R_{\mathrm{PL}} + \mathrm{Re}\{Z_{AA}\} + j\,\mathrm{Im}\{Z_{AA}\} ,$$

where the two components are

$$\mathrm{Re}\{Z_{AA'}\} = \frac{(L_1 + \omega_1 L_1 C_1 \,\mathrm{Im}\{Z_{CC'}\})C_1 \,\mathrm{Re}\{Z_{CC'}\}}{|Z_D^2|}$$

$$+ \frac{\omega L_1 C_1 \,\mathrm{Re}\{Z_{CC'}\}(\omega_1^{-1} + C_1 \,\mathrm{Im}\{Z_{CC'}\} - \omega_1 C_1 L_1)}{|Z_D^2|}$$

with $|Z_D|^2 = Z_D Z_D^*$ and

$$\mathrm{Im}\{Z_{AA'}\} = 0 \text{ (for resonance)}$$

$$= \frac{C_1^2 \,\mathrm{Re}\{Z_{CC'}\}\omega_1 L_1}{|Z_D|^2}$$

$$+ \frac{(L_1 + \omega_1 L_1 C_1 \,\mathrm{Im}\{Z_{CC'}\})(\omega_1 L_1 C_1 - \omega_1^{-1} - C_1 \,\mathrm{Im}\{Z_{CC'}\}}{|Z_D|^2} .$$

In addition,

$$Z_{CC'} = \frac{R_C + R_{P_2} - R_C\omega_1^2 R_{P_2} L_2 C_2 - \omega_1^2 L_C L_2}{D}$$

$$+ j\frac{R_c\omega_1 L_2 + R_P^2\omega_1 L_C - \omega_1^3 L_C R_{P_2} L_2 C_2}{D} ,$$

and finally

$$D = [R_{P_2} - \omega_1^2(R_{P_2}L_C C_2 + R_C L_2 C_2 + R_{P_2}L_2 C_2)]$$

$$+ \; j(R_{P_2}R_C\omega_1 C_2 - \omega_1^3 L_2 C_2 L_C + \omega_1 L_2) \; .$$

After this exercise it was concluded that a computerized network analyzer would be appropriate for an exact analysis of the interaction. However, based on the approximate analysis, interaction does not appear to be a problem.

Other aspects considered in determining the number of drift pumping coils were cost, complexity, and reliability. Because the multiple low-power channels do not enjoy an economy of scale, this approach is expected to cost more. Although it is more complex, it should offer high reliability, even though this factor is somewhat devalued because of the relatively low duty factor (1% to 10%) of the MFTF-α+T system.

Matching and transmission networks

Two approaches to matching and transmitting the high-power tube output to the drift pumping coil are shown in Fig. 5.54. The two-transformer approach (Fig. 5.54a) was adopted for the baseline. The one-transformer approach has the advantages of simplicity and possibly of lower cost, but in the course of the study it was found that multiple lower power channels were needed to drive the drift pumping coil. The lower power tetrodes have resonant plate load resistances of 500 to 1000 Ω, rather than 100 to 200 Ω as in high-power tetrodes. Because the design of the coaxial transmission line becomes increasingly difficult for characteristic impedances greater than about 200 Ω, the two-transformer approach was selected. The series-tuned circuit that drives and terminates the coaxial cable provides the possibility of low Q (broad band) and high efficiency.

Transmitters

The possibility of using a dc-to-ac chopper to provide ac power at 70 kHz was briefly considered early in the design study. Transistorized inverters have been used for motor control at variable voltages and frequencies for several years. Devices such as the GE D77FP/GP Power Darlington can handle 500 V and 100 A or 50 kW at switching times of 10 μs (total), comparable to a 100-kHz frequency. However, a minimum of 30 transistors in parallel will be required to switch the 3 kA required by the coil. Since the coil voltage is about 500 V rms, about 20 transistors in series would be needed for each of the 30 parallel branches, for a total of about 600 transistors per coil. A unit containing these transistors could be mounted on the device to drift the coil directly; the drive signal could be band-limited noise or a swept cw signal. This approach requires further study.

ORNL–DWG 83-3872 FED

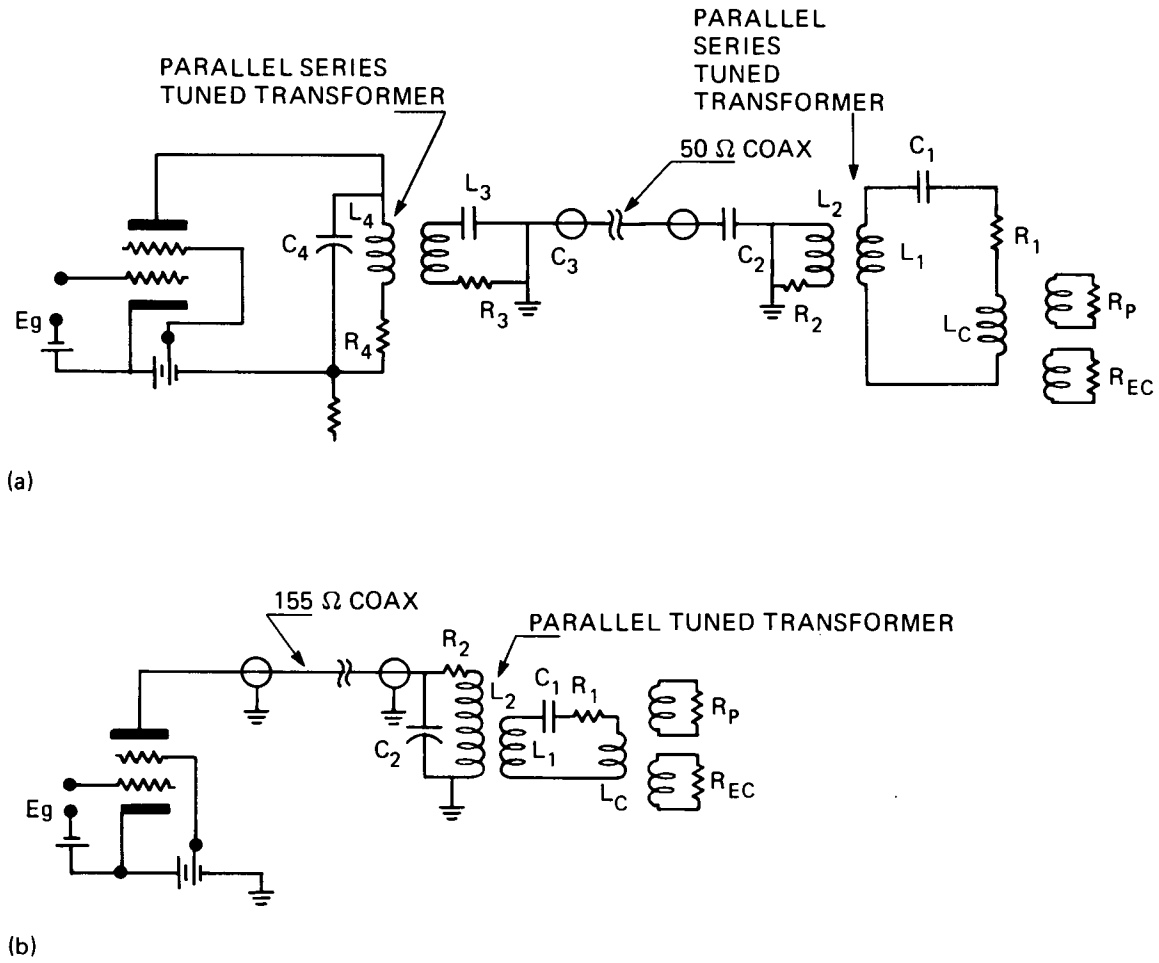

Fig. 5.54. (a) Two-transformer matching system. (b) One-transformer matching system.

Modulation

The system requirements (Sect. 5.3.5) allow three forms of frequency modulation. From a physics standpoint, band-limited noise is probably preferable, since the particle transit time is random; from an engineering viewpoint, however, it is the least attractive approach. A sinusoidal signal is easier to estimate, measure, and control, and the required spectrum can be filled to the extent desired with multiple narrow-bandwidth channels. For the baseline approach, the fill factor for the 600-kHz plug-cell drift pump is 100%; for the 70-kHz anchor-cell drift pump, 10%. Any of the three modulation approaches can be used to drive these channels, but neither noise nor swept cw excitation through 200-Hz channels has any advantage over discrete tones.

Because the spectrum is produced by 12 channels, amplitude weighting of these channels can affect frequency weighting. This is accomplished by controlling the power level

with digital attenuators in the drive circuit of the HPA. The response time of the attenuators will be on the order of a few milliseconds, so they can be programmed in real time. The spectrum width could be changed along with the power level during startup. A cosine weighting could be applied to attenuate the band edge power and accentuate the center band.

For the discrete tone excitation, the plug-cell system allows any spread or bunching of the tone frequencies. This can be controlled in real time by selecting different crystal oscillators. For the anchor-cell drift pump, the flexibility is limited by the 12 narrow-bandwidth channels and their selected bandwidth.

5.6.5 Fueling

Gas injection components and systems have been developed for use on existing machines. Because of the low availability needed for MFTF-α+T and the accumulated experience with gas puffing systems, only limited redundancy is proposed. Two independent systems can be provided if a need for higher availability is determined.

High-energy fueling will be necessary on MFTF-α+T because of the physics requirements. However, several difficulties are associated with the use of pellet injectors. These include (1) insufficient pellet penetration into the plasma, (2) the need for small pellets and a high pellet injection rate, and (3) the need for ICRH heating to raise the fuel to the desired temperature. In the relatively small MFTF-α+T, high-energy fueling can be accomplished with neutral beam injectors. If pellet injectors were used, they would probably be restricted to low-energy ion flow stabilization, as proposed for TDF.

REFERENCES

1. *A Tandem Mirror Technology Demonstration Facility*, UCID-19328, Univ. California, Lawrence Livermore Natl. Lab., Livermore, Calif., October 1983.

2. E. F. Marguerat et al., "Advanced Design of Positive Ion Sources for Neutral Beam Applications," in *Proceedings of the 8th Symposium on Engineering Problems of Fusion Research*, Institute Electrical and Electronics Engineers, New York, 1980.

3. C. C. Tsai et al., "Long-Pulse Ion Source for Neutral Beam Applications," *Rev. Sci. Instrum.* **53**, 417 (1982).

4. R. A. Dewitt, "Coil Design Considerations and Analysis for Neutral Beam Magnets," in *Proceedings of the 7th Symposium on Engineering Problems of Fusion Research*, Institute Electrical and Electronics Engineers, New York, 1977.

5. K. I. Thomassen and J. N. Doggett, *Options to Upgrade the Mirror Fusion Test Facility,* UCID-19743, Univ. California, Lawrence Livermore Natl. Lab., Livermore, Calif., 1983.

6. R. G. Kerr, "Multi-Megawatt Neutral Beams for MFTF-B," in *Proceedings of the 7th Conference on the Application of Accelerators in Research and Industry,* 1982.

7. K. W. Ehlers, "Negative Ion Sources for Neutral Beam Systems," *J. Vac. Sci. Technol. A* **1**, 974 (1983).

8. O. A. Anderson et al., "A Transverse Field Focusing (TFF) Accelerator for Intense Ribbon Beams," in *Proceedings of the 1983 Particle Accelerator Conference, Santa Fe, 1983.*

9. L. Ruby and X. DeSeynes, "Shielding of Future Neutral Beam Injectors," submitted to *Trans. Am. Nucl. Soc.*

10. T. H. Batzer and W. R. Call, "A Continuous Cryopump for Steady State Mirror Fusion Reactors," *J. Vac. Sci. Technol. A* **1**, 1315 (1983).

11. K. H. Berkner, R. V. Pyle, and J. W. Stearns, "Intense Mixed Energy Hydrogen Beams for CTR Injection," *Nucl. Fusion* **15**, 249 (1975).

12. W. L. Barr, Lawrence Livermore National Laboratory, private communication, May 1983.

13. W. L. Pickles et al., "Dynamic Gas Flow During Plasma Operation in TMX-U," *J. Vac. Sci. Technol. A* **1**, 1288 (1983).

14. C. Moeller, "Design of the 60 GHz System," presented at the ECRH Transmission System Workshop, June 16, 1983.

15. J. L. Doane, "ECRH Transmission System for PDX, PLT, TFTR, and Upgrades," presented at the ECRH Transmission System Workshop, June 16, 1983.

16. Overview of the MFTF-B Electrical System, presented at the Department of Energy Semi-Annual Review, November 17–18, 1982.

17. K. Kraus, Lawrence Livermore National Laboratory, personal communication with D. H. Metzler, Oak Ridge National Laboratory, August 25, 1983.

18. W. S. Cooper, "Summary of the Status of Negative-Ion Based Neutral Beams," *Nucl. Technol./Fusion* **4**(2), 632–41 (1983).

19. J. Levine, "ECH Current Drive on the ISX-B Tokamak," presented at the Gyrotron User/Developer Meeting, June 15, 1983.

20. H. Jory et al., "Gyrotron Oscillators in Fusion Heating," in *Heating in Toroidal Plasmas*, ed. C. Gormezano, G. G. Leotta, and M. Sindoni, Commission European Communities, Brussels, 1982.

21. H. Jory, "Varian Gyrotron in Plasma Experiments," presented at the Gyrotron User/Developer Meeting, June 15, 1983.

22. A. J. Mager, "Magnetic Shields," *IEEE Trans. Magn.* **MAG-6**, 67 (1970).

23. W. G. Gustafson, "Magnetic Shielding of Transformers at Audio Frequencies," *Bell Syst. Tech. J.* **17**, 416 (1983).

24. C. Henning et al., *Engineering the Baseball Magnet System*, UCRL-73067, Univ. California, Lawrence Livermore Laboratory, Livermore, Calif., 1971.

25. A. K. Chargin and C. J. Anderson, *Solving Problems of Neutral Beam Injectors at LLL*, UCRL-75023, Univ. California, Lawrence Livermore Laboratory, Livermore, Calif., 1973.

26. K. H. Berkner et al., "Long-Pulse Neutral Injector Development at the Lawrence Berkeley Laboratory," in *Heating in Toroidal Plasmas*, ed. C. Gormezano, G. G. Leotta, and M. Sindoni, Commission European Communities, Brussels, 1982.

27. C. P. Moeller, "Electron Cyclotron Resonance Heating on the JFT-2 Tokamak," paper D1 in *Proceedings of the 4th Topical Conference on RF Plasma Heating*, Univ. Texas, Austin, 1981.

28. J. S. Levine et al., "Electron Cyclotron Resonance Heating of the VERSATOR-II Tokamak," paper D6 in *Proceedings of the 4th Topical Conference on RF Plasma Heating*, Univ. Texas, Austin, 1981.

29. C. Moeller et al., "60 GHz Transmission System for DOUBLET-III Electron Cyclotron Heating Experiment," in *Proceedings of the 5th Topical Conference on RF Plasma Heating*, Madison, Wisconsin, Feb. 1983.

30. K. H. Krause, "Waveguide Transmission System for TMX-U," p. 1 in *Proceedings of the ECRH Transmission System Workshop*, CONF-830653, Natl. Tech. Inf. Serv., Springfield, Va., 1983.

31. B. Badger et al., *WITAMIR-I, A University of Wisconsin Tandem Mirror Reactor Design*, UWFDM-400, Univ. Wisconsin, Madison, 1980.

32. B. Badger et al., *TASKA, A Tandem Mirror Fusion Engineering Facility*, UWFDM-500, Univ. Wisconsin, Madison, 1982.

33. *Mirror Advanced Reactor Study Interim Design Report*, UCRL-53333, Univ. California, Lawrence Livermore Natl. Lab., Livermore, Calif., April 1983.

34. L. J. Perkins et al., "Engineering Design of the Quasi-Optical ECRH Injection System for the Mirror Advanced Reactor (MARS)," *Nucl. Technol./Fusion* **4**(2), 1407 (1983).

35. J. N. Hines et al., "The Electrical Characteristics of the Conical Horn-Reflector Antenna," *Bell Syst. Tech. J.* **17**, 1187 (1983).

6. HALO SCRAPER, DIRECT CONVERTER, AND VACUUM PUMPING SYSTEM

P. T. Spampinato

Fusion Engineering Design Center/McDonnell Douglas Astronautics Company

B. A. Cramer

McDonnell Douglas Astronautics Company

J. D. Galambos

Fusion Engineering Design Center/Oak Ridge National Laboratory

G. E. Gorker

Fusion Engineering Design Center/General Electric Company

J. G. Murray

Princeton Plasma Physics Laboratory

CONTENTS

6.1 INTRODUCTION 6-3
6.2 HALO SCRAPER 6-5
6.2.1 Radial Heat Load Profiles 6-5
6.2.2 Design Description 6-10
6.2.3 Thermodynamic Performance 6-12
6.2.4 Erosion Life 6-16
6.3 DIRECT CONVERTER 6-22
6.3.1 Requirements 6-23
6.3.2 Design Description 6-26
6.3.3 Scope of Future Work 6-29
6.4 VACUUM PUMPING SYSTEM 6-32
6.4.1 Baseline Design 6-32
6.4.2 System Performance 6-32
6.4.3 Choice of Pumps 6-35
REFERENCES 6-36

6. HALO SCRAPER, DIRECT CONVERTER, AND VACUUM PUMPING SYSTEM

6.1 INTRODUCTION

The MFTF-α+T device will be the first device to feature a halo scraper for impurity removal. It will also have a direct converter, which in a tandem mirror reactor (TMR) would provide a means of recovering energy lost through the ends of the plasma. The direct converter in MFTF-α+T is not required to demonstrate useful power output and is used to provide radial and axial potential control. The locations of the halo scraper and the direct converter are sketched in Fig. 6.1 and shown schematically in Fig. 6.2. Separate hatches are provided for component removal.

Following the method used in the Mirror Advanced Reactor Study (MARS) design, the end-cell region is divided into three regions that correspond to different plasma loss mechanisms (see Fig. 6.3). In the center is the electron direct converter region, which is subject to the axial electron and ion losses. The next radial region, designated the inner halo plate, absorbs the drift-pumped ion heat flux. The outer radial location, the outer halo plate, collects the radial ion heat loss and some trapped injection power heat loss.

The requirements for handling the energy in the end cell of a tandem mirror device are not clearly defined. The definition of particle flux distribution for MFTF-α+T has

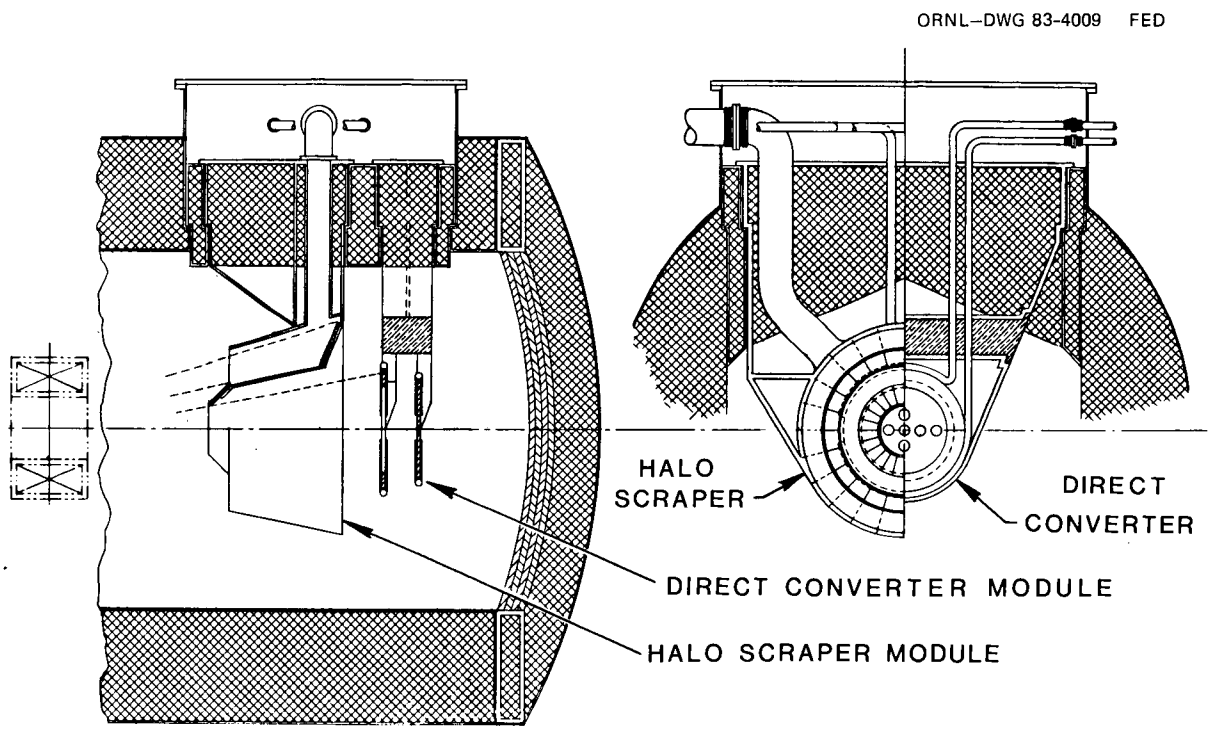

Fig. 6.1. Halo scraper and direct converter.

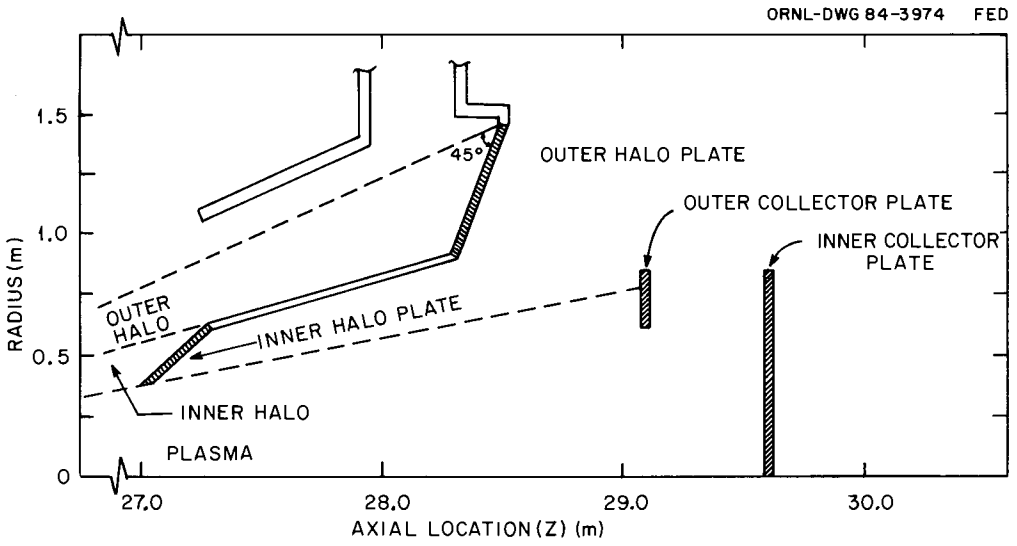

Fig. 6.2. Schematic of halo scraper and direct converter components.

changed during the course of this study. The preliminary designs presented here therefore represent the nature of the design solutions that will be needed and the expected performance of the components.

The design of the halo scraper is presented in Sect. 6.2, and the direct converter is described in Sect. 6.3. Section 6.4 contains a description of the vacuum pumping system for the region in which these components are located.

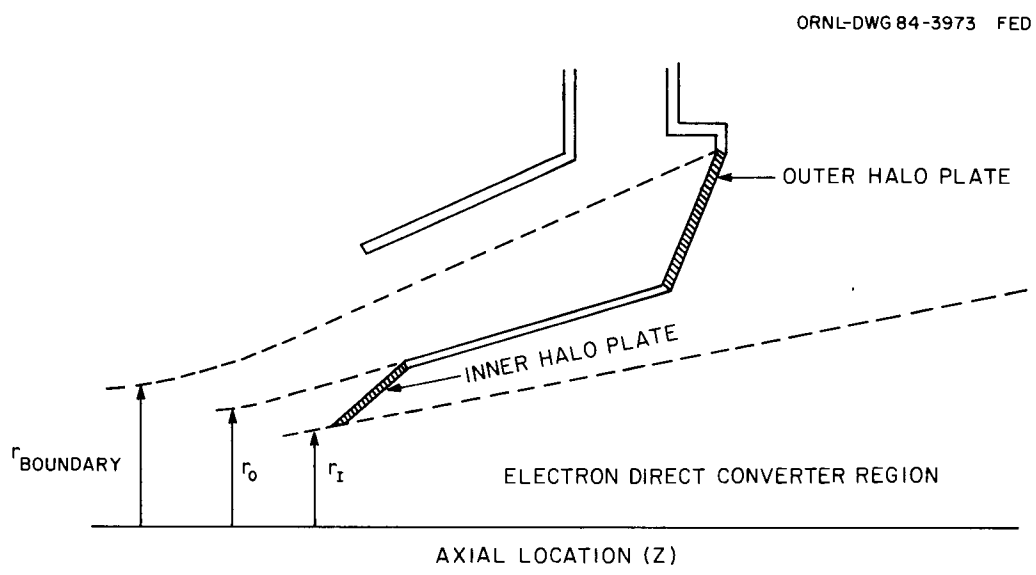

Fig. 6.3. Schematic of radial regions of the plasma.

6.2 HALO SCRAPER

The halo scraper must be constructed to handle the heat loads in the inner and outer halo regions, must have a reasonable lifetime (preferably equal to the device lifetime), and must not interfere with normal device operation. The radial heat load profiles are analyzed in Sect. 6.2.1. The design description is presented in Sect. 6.2.2. Thermodynamic performance is assessed in Sect. 6.2.3, and component lifetime is addressed in Sect. 6.2.4.

6.2.1 Radial Heat Load Profiles

Inner halo region

In the inner halo region (see Fig. 6.3), the drift-pumped ions exit the end of the device. This region lies between the direct converter and outer halo radial regions and is a sloshing-ion gyrolength wide.[1] In this analysis to determine the drift-pumped ion heat load, which follows the method of Barr,[2] the radial profile of the pumped ion current I_{ih} is taken to have a Maxwellian shape,

$$I_{ih}(r) = B\left(\frac{4}{\pi}\right)^{1/2}\left[\frac{E(r)}{T^{3/2}}\right]^{1/2} \exp[-E(r)/T]_b \ , \tag{6.1}$$

where B is a normalization constant, $T = 15$ keV, and $E(r)$ is the radial energy profile corresponding to the confining potential, which varies from 30 keV at the inner halo radius r_i to 0 at the outer halo radius r_o,

$$E(r) = 30\,\text{keV} \times 1 - \left(\frac{r - r_i}{r_o - r_i}\right) \ . \tag{6.2}$$

The normalization constant B can be found through the relation

$$\int_{r_i}^{r_o} 2\pi r I_{ih}(r)\, dr = 48.5 \ \text{A} \ , \tag{6.3}$$

where it is assumed that half of the 97 A of drift-pumped ions goes to each end of the device. Letting $X = 1 - (r - r_i)/(r_o - r_i)$, Eq. (6.1) may be rewritten as

$$4\left(\frac{2\pi}{15}\right)^{1/2} B(r_o - r_i)\int_0^1 [r_o X^{1/2} - X^{3/2}(r_o - r_i)]\exp(-2X)\, dX = 48.5 \ \text{A} \tag{6.4}$$

or

$$0.668(r_o - r_i)\left[\frac{r_o}{2^{3/2}}\gamma(3/2,2) - \frac{r_o - r_i}{2^{5/2}}\gamma(5/2,2)\right] = 48.5 \ \text{A} \ , \tag{6.5}$$

where $\gamma(a,b)$ is the incomplete gamma function. The reasoning for using the inner halo radius is that, ideally, the sloshing ions will thermalize rapidly if their orbits intersect the cold area halo plasma (hence, the confining potential is 0 at r_o) and those sloshing ions located greater than one gyrolength in from the outer halo will remain unaffected, since the radial temperature profile is assumed to be constant in the MFTF-α+T main plasma (hence, the confining potential has its maximum value of 30 keV at r_i). The sloshing-ion gyrolength is evaluated here at $Z = 19.3$ m, where the magnetic field is a minimum and the gyrolength is a maximum. At this location, the plasma is 18 by 28 cm and the sloshing-ion gyrolength is $\approx$3 cm. Here the inner halo is taken to lie between $r = 15$ cm and $r = 18$ cm. Judging from the expansion of the outer halo flux lines, it is estimated[3] that at $Z \approx 27$ m (the axial inner halo collector location) $r_i/r_o \approx 3/4$. Using the minor axis to define the inner halo location gives an upper limit on the width of the inner halo plasma. Using this ratio for r_i/r_o, solving for B, and substituting back into Eq. (6.4),

$$I_{ih}(r) = \frac{2.36 \times 10^{20}}{(r_o - r_i)r_o} X^{1/2} \exp(-2X) \ , \tag{6.6}$$

where r_o and r_i are in meters. The heat load is

$$P_{ih}(r) = I_{ih}(r)E(r) = \frac{1.08X^{3/2}\exp(-2X)}{(r_o - r_i)r_o} \tag{6.7}$$

(in megawatts per square meter). The maximum heat load is located one-fourth of the distance across the inner halo plasma and is sensitive to the axial location due to the expansion of the flux lines, as shown in Fig. 6.4. These values are for normal incidence and are mitigated somewhat by angling the plate with the field lines. It should be noted that there is some uncertainty in the results presented here, stemming from assumptions made in the analysis. For instance, use of a less conservative temperature profile, with a more gradual falloff than the step function profile assumed here, leads to a potential that declines over a greater distance than one sloshing-ion gyrolength. This will tend to smear out the power load over a larger area and reduce the peak value somewhat. Thus, some of the pumped ion heat load may be incident on the regions surrounding the inner halo scraper (i.e., the direct converter and the outer halo scraper). Also, radial tailoring of the potential with a segmented direct converter biased at different potentials could produce a more gradual falloff of the potential in the radial divertor. This would tend to spread the pumped ion heat flux over a larger radial cross section than that predicted here.

The inner halo plate has a circular cross section with the leading edge at a radius of 36 cm at $Z = 27$ m, as shown in Fig. 6.2. This corresponds to the location of the minor axis of the elliptical innermost flux surface of the inner halo. The inner halo scraper extends to $Z = 27.3$ m, where its radius is 62.2 cm, corresponding to the major axis of the outermost flux surface of the inner halo at $Z = 27.3$ cm. For this inclination of the inner halo plate (41° to the z-axis), the angle of incidence of the field lines on the plate is $\approx$26°. This choice of dimensions for the circular inner halo plate encompasses the entire

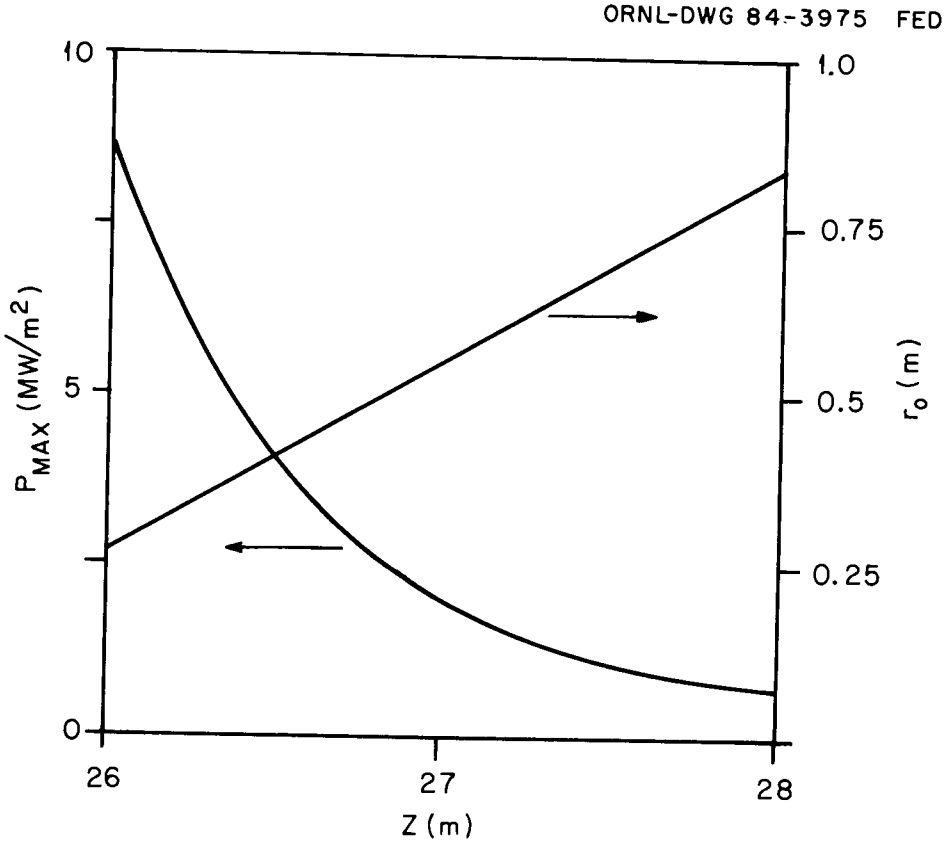

Fig. 6.4. Maximum heat load (normal) and halo radius of inner halo.

elliptical inner halo plasma, as shown in Fig. 6.5. Although it is possible to use an elliptical scraper, uncertainties in the exact inner halo plasma boundaries make this approach unwarranted, since only a small portion of the present inner halo scraper plate is not intercepted by the inner halo plasma.

The calculated particle flux and heat loads are assumed to be circularly symmetric and distributed over the range between the minor and major radii of the ellipse; they are normalized as though they were spread over a circular cross section with the minor radius. This tends to overestimate the value of the major axis part (by $\approx$25%), since the loads are actually spread over a larger surface area at the major axis side.

An additional component P_2 to the heat load on the inner halo scraper comes from the axial leakage of ions and electrons because the inner halo scraper extends into the main plasma region. With r_o = 53.5 m (at Z = 27.0 m), $I_2 = 2.05 \times 10^{20} \times [1 - (r/r_o)^4]$ s^{-1} · m^{-2}, and $P_2 = 3.25 \times 1 - (r/r_o)^4$ MW/m^2.

The pumped ion fluxes and the corresponding heat loads are shown in Fig. 6.6. The maximum heat load is $\approx$3 MW/m^2 and is primarily from the axial leakage component.

ORNL-DWG 84-3976 FED

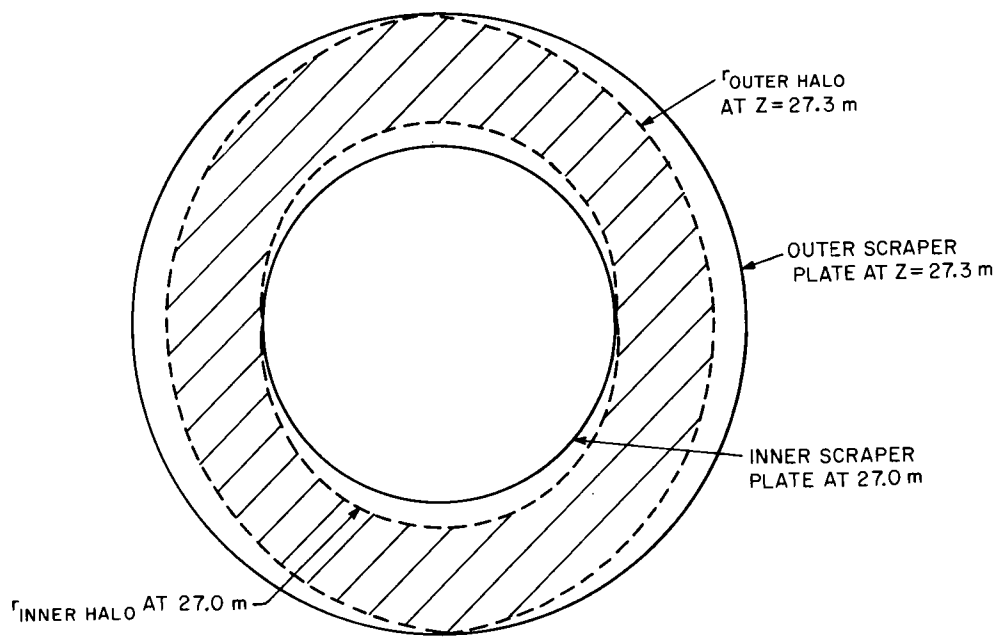

Fig. 6.5. Footprint of inner halo plasma on circular inner scraper plate.

Outer halo region

The outer halo channel extends inside the scraper housing from $Z = 27.3$ m ($r = 0.63$ m) to $Z = 28.3$ m ($r = 0.9$ m), as shown in Fig. 6.2. This channel length ensures that neutrals from the plasma flow onto the outer scraper plate. The outer scraper plate, on which the outer halo field lines are incident, extends from $Z = 28.3$ m ($r = 0.9$ m) to $Z = 28.5$ m ($r = 1.43$ m). The angle of incidence of the field lines on the plate is 45°. The total heat deposited on the outer scraper is ≈0.5 MW per end, from radial ion losses, neutral beam trapping, and fusion product trapping.

The power loading on the outer halo P_{oh} is

$$P_{oh} = \frac{0.5}{\pi(1.4^2 - 0.9^2)} \sin 45° = 0.1 \ \mathrm{MW/m^2} \ .$$

For a plasma density of 10^{13} cm^{-3}, the ion flux, Γ_{oh}, is $\approx 10^{19}$ cm$^{-2}\cdot$s^{-1} and the plasma temperature is ≤ 5 eV. These quantities are shown in Fig. 6.6.

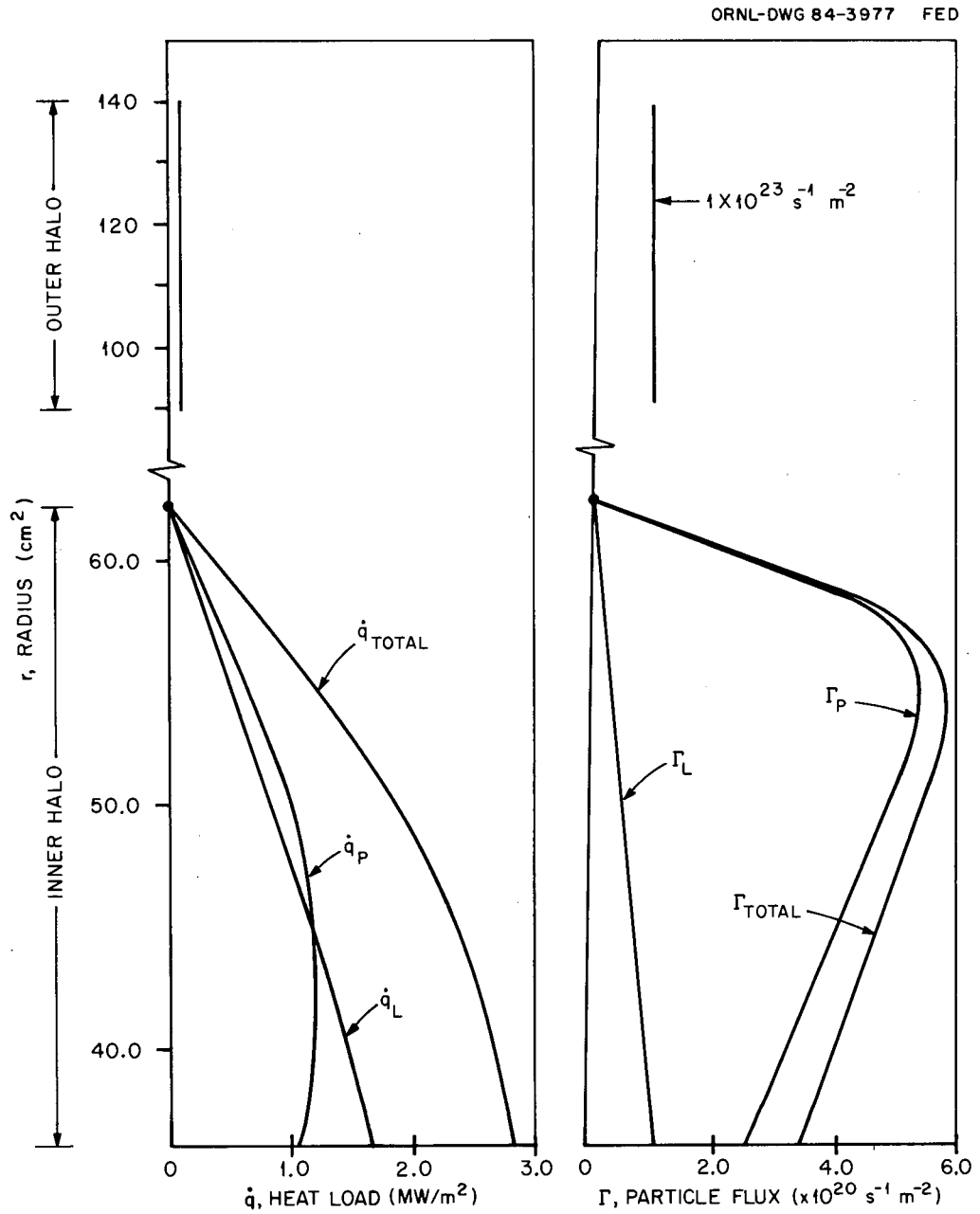

Fig. 6.6. Heat loads and particle fluxes.

6.2.2 Design Description

The halo scraper consists of an inner halo plate, an outer halo plate, a scraper housing, pump ducts, and a support frame, as shown in Fig. 6.7. The inner and outer plates, which accept the major heat and particle loads, may have a limited lifetime or may interact unacceptably with the plasma, so they are designed for easy separation from the scraper housing. The scraper housing to which the plates are attached also provides a collection chamber for particles. Particles are pumped from the scraper housing through two pump ducts that connect the housing to 5000-L/s turbomolecular pumps outside the vacuum vessel. The housing is supported from the vacuum vessel by a support frame. Scraper components are removed as a unit through the top of the vacuum vessel.

The leading edge of the inner halo plate is located at $Z = 27$ m for the baseline study on the basis of the heat load profile shown in Fig. 6.4. The corresponding radial location is 0.36 m, as shown in Fig. 6.3. At $Z < 27$ m, the heat loads increase rapidly; at $Z >$ 27 m, the reduction in heat loads is not as significant. In addition, greater axial distance increases the inner radius and, therefore, the size of the components, as well as increasing the overall length of the vacuum chamber.

No studies have been conducted to define the optimum location from an overall system cost standpoint. However, in the Technology Development Facility (TDF) studies, a trade study of end-cell size showed that minimizing the length of the end cell minimized cost, even though the cost for the end heat dump increased with decreasing length. Therefore, the axial location of 27 m is considered to be very close to optimum for MFTF-α+T.

The inner halo plate slopes outward from the leading edge at an angle of approximately 30° to impinging particles. This results in the heat and particle flux distributions shown in Fig. 6.6. The peak heat flux of approximately 2.8 MW/m^2 occurs at the leading edge. Sputtering erosion calculations indicate that minimum erosion is obtained with beryllium as the inner halo plate surface material.

The outer halo plate is located at $Z \simeq 28.3$ m, as shown in Fig. 6.2. This plate is located inside the scraper housing and is oriented at an angle of approximately 45° to the impinging particles, which should deflect particles toward the pump duct and provide some reduction in heat loads from normal incidence. Neither of these effects is considered to be a strong requirement. Heat loads defined in Fig. 6.6 for the outer scraper plate are very low. However, these heat loads are subject to great uncertainty. Therefore, for design purposes, a surface heat load of approximately 0.5 MW/m^2 is considered appropriate.

The scraper housing is supported from a hatch on top of the device. The support frame transfers seismic and deadweight loads to the vacuum vessel. Two 0.5-m-diam pump ducts are provided from the scraper housing through the hatch to flanges at which the pumps can be connected. Connections to inlet and outlet cooling lines are also provided outside the hatch. Cooling is provided for all the scraper components. Components have joints to allow for thermal expansion and detachment of components from one another.

A rigorous material selection study has not been performed for the scraper components. Surface materials are chosen primarily for desirable sputtering and thermophysical properties; structural materials, for desirable mechanical and thermophysical properties. Major issues include (1) safety requirements for beryllium, (2) sputtering, and (3) fabrication and bonding of coatings and refractory materials.

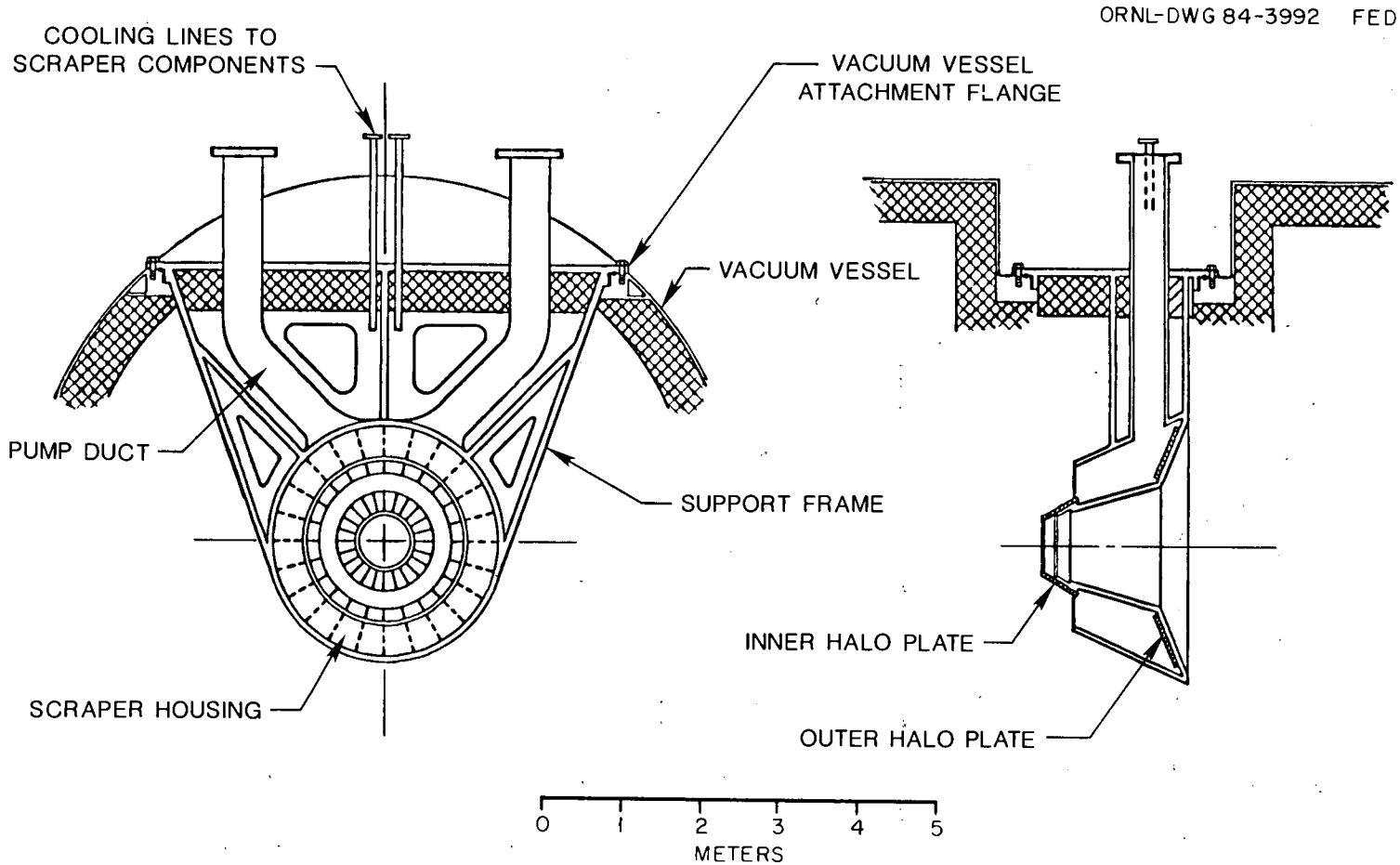

Fig. 6.7. Halo scraper components.

Procedures for safely handling beryllium are well established, and no safety issues are expected. However, safety requirements may increase maintenance time.

Sputtering erosion calculations (Sect. 6.2.4) show that high-Z materials provide the lowest erosion rates in the region of the outer scraper, and beryllium provides the lowest erosion rate on the inner scraper. Combining these rates with allowable thicknesses shows that the inner disk may need replacement during the life of the device. The outer disk is less likely to need replacement. However, provisions have been made for its replacement since the actual environmental conditions are uncertain. A summary of scraper material and design considerations is shown in Table 6.1.

Table 6.1. Halo scraper materials

Component	Candidate materials	Design considerations
Inner disk	Ta-10W, copper alloys, beryllium	Sputtering erosion, surface heating, cost
Outer disk	Ta-10W, copper alloys	Sputtering erosion, surface heating, cost
Scraper housing	Stainless steel, copper alloys	Surface heating, nuclear heating, cost
Support frame	Stainless steel	Surface heating, nuclear heating, cost

The tantalum alloy Ta-10W is proposed as a refractory material for application to both the inner and outer disks. This does not preclude the use of other refractory materials. Fabrication of refractory metals is considered more difficult than fabrication of more standard alloys (e.g., copper alloys), and the industrial base for refractory metal technology is small; bonding and coating techniques will require considerable development. Copper alloys (e.g., AMZIRC, AMAX-MZC) are also candidates for these components.

The most likely material for the scraper housing and support frame is stainless steel. Cooling tubes are attached to these components as required. Design heat loads to the housing have not been defined but include stray surface heat loads from particles, radiation from heated components (scraper disks, direct convertor), and nuclear heating. These heat loads are anticipated to be low, but they do place a cooling requirement on the housing and probably on the support frames.

6.2.3 Thermodynamic Performance

The thermodynamic performance of the inner and outer disks was evaluated for three surface materials: beryllium, a copper alloy (AMAX-MZC), and a tantalum alloy (Ta-10W). A thick layer of material is critical because the lifetimes of these components may be limited by sputtering erosion. Table 6.2 lists the temperature limits and the values for calculating the thermal conductivity used in steady-state temperature calculations.

For disks with double-wall ribbed panels and coolant flowing between the walls, the coolant flow conditions needed to prevent subcooled boiling of water are listed in Table 6.3. The lower heat fluxes on the outer disk (0.5 MW/m^2 vs 3.0 MW/m^2 for the inner disk) mean that coolant performance requirements are lower. Although the pressure

Table 6.2. Temperature limits and thermal conductivities for halo scraper plate materials

	Beryllium	AMAX-MZC	Ta-10W
Maximum permissible temperature for vaporization limit of 1 mm/year, °C	860	900	2300
Temperature causing reduction in tensile strength to ≈40% of value at 20°C, °C	550	500	1500
Maximum permissible temperature difference[a] through heated surface, °C	130	200	800
Values for calculating thermal conductivity $[(A + B)T]$,[b] W/m·K			
A	233	345	82
B	−0.15	−0.0728	−0.015

[a]Based on thermal stress limit.
[b]T in kelvin.

Table 6.3. Coolant flow performance parameters for halo scraper plates

	Inner halo plate	Outer halo plate	Overall
Inlet temperature, °C	60	60	60
Outlet temperature, °C	70	100	72
Mass flow rate, kg/s	58	3	61
Average flow velocity, m/s	10	1.6	
Heat transfer coefficient, kW/m²·°C	44	11	
Pressure drop through panels, MPa	0.29	0.15	0.29
Pumping power, kW	17	0.9	17.9

drop in the outer disk is only 0.15 kPa, a single coolant system will probably be used for both scraper disks, so orifice plates will be needed in the outer disk system to match the 0.29-MPa drop in the inner disk.

Maximum temperatures and temperature differences for the three candidate materials are shown in Fig. 6.8 for the inner halo plate and in Fig. 6.9 for the outer halo plate. For tantalum, the maximum permissible temperature difference, $(T_1 - T_2)_{max} = 800°C$, gives an allowable thickness for the inner disk $t_i = 19$ mm and for the outer disk $t_o = 132$ mm. For AMAX-MZC, $(T_1 - T_2)_{max} = 200°C$, so $t_i = 20$ mm and $t_o = 122$ mm, although the outer disk would be designed to be much thinner (e.g., 20 mm) so that it could operate at lower temperatures and would not be a lifetime-limited component. For beryllium, $(T_1 - T_2)_{max} = 130°C$, so $t_i \leq 7.5$ mm and $t_o = 42$ mm, although again the outer disk would be designed for a thickness on the order of 20 mm.

Results of these surface material studies are summarized in Table 6.4. The thicknesses listed were used along with the erosion rates specified in Sect. 6.2.4 to determine the expected erosion lifetimes of the inner and outer disks.

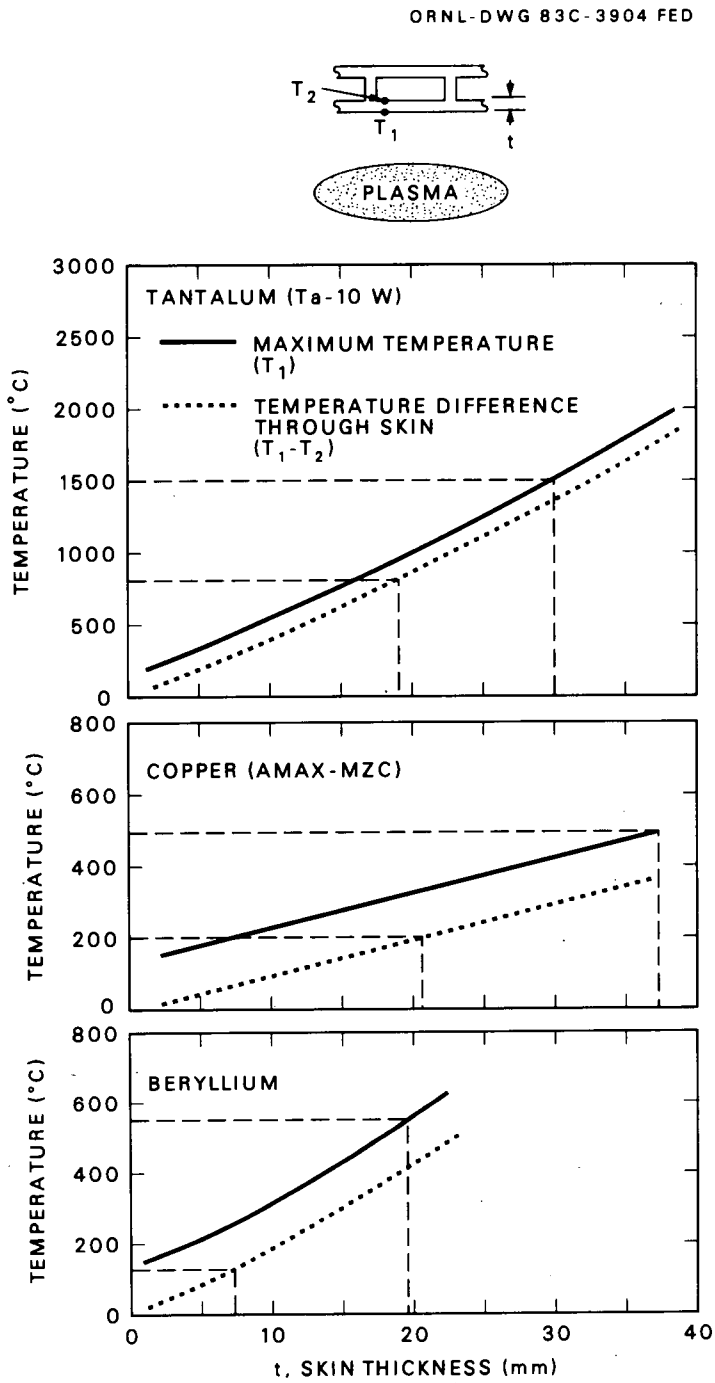

Fig. 6.8. Maximum temperature and difference through skin for inner halo plate (heat flux = 3.0 MW/m^2).

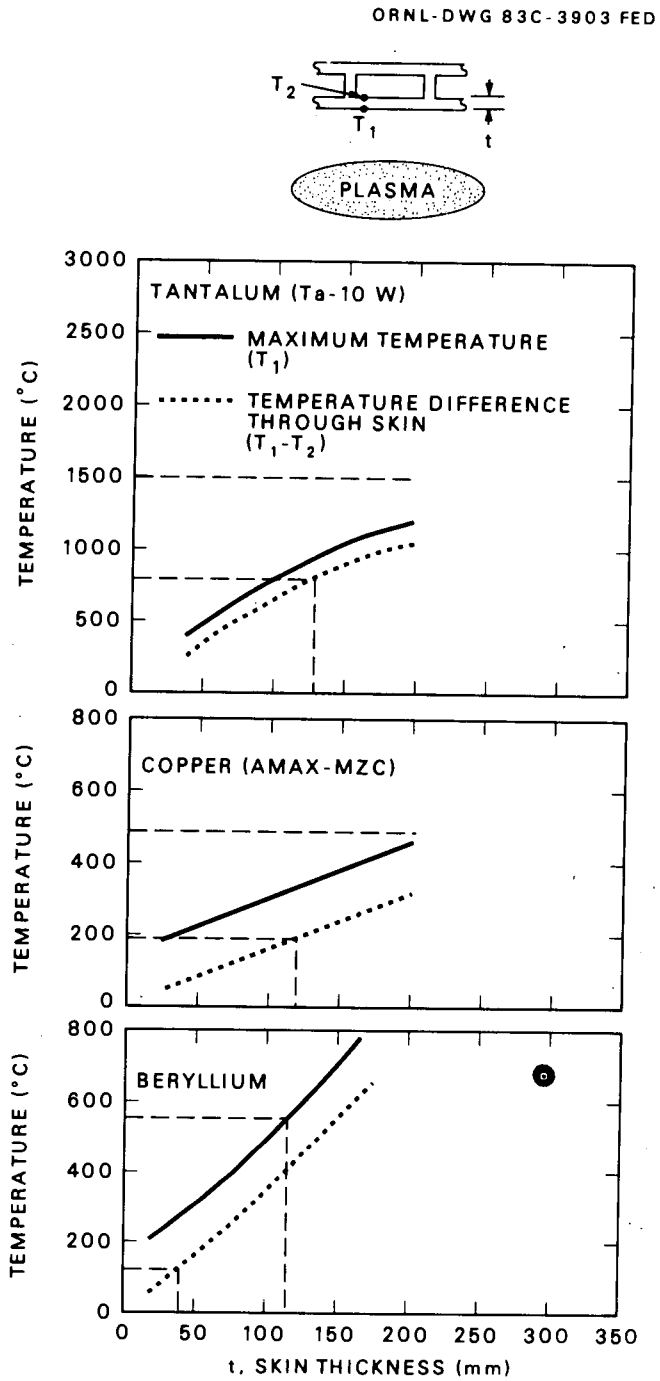

Fig. 6.9. Maximum temperature and difference through skin for outer halo plate (heat flux = 0.5 MW/m^2).

Table 6.4. Results of surface material sizing studies

	Thickness available for erosion,[a] mm	
	Inner halo plate	Outer halo plate
Ta-10W	17	130
AMAX-MZC	18	120
Beryllium	5.5	40

[a]Assumes 2-mm thickness remaining at end of lifetime.

6.2.4 Erosion Life

Calculations of erosion due to sputtering were made for three materials: beryllium, representing a low-Z coating, and nickel and tungsten, representing respectively medium- and high-Z coatings or structural materials. Because of uncertainties in the physics parameters of the halo edge region, a range of edge temperatures was used in the computations. Sputtering calculations were made for the inner and outer halo plates. The erosion phenomena expected in inner and outer plates differ substantially.

Sputtering erosion rates

Sputtering erosion of the inner halo plate was computed for a range of design cases. Because the inner halo plasma density is so low, the plasma is essentially transparent to sputtered neutral atoms. As a result, there is virtually no ionization of sputtered neutrals in the inner region and hence no redeposition. There is also no self-sputtering. The net erosion rate is therefore equal to the gross sputtering rate. Erosion was computed based on the particle fluxes specified in Sects. 6.2.2 and 6.2.3 for the pumped deuterium-tritium (D-T) ions and the D-T ions resulting from axial leakage from the main plasma. These are given respectively by

$$\Gamma^{P}_{D\text{-}T} = (3.7 \times 10^{21}) X^{1/2} \exp(-2X) \cos \alpha \ ,$$

$$\Gamma^{L}_{D\text{-}T} = (2.0 \times 10^{20}) X \cos \alpha \ ,$$

where α is the angle between the inner plate and the surface normal to the field line (i.e., $\alpha = 0°$ denotes normal incidence) and X is the normalized distance perpendicular to the field lines. The energy of the pumped and leakage particles was taken to be monoenergetic at any point X, as given by

$$U^{P}_{D\text{-}T} = 30X \ ,$$

$$U^{L}_{D\text{-}T} = 54 + (84 - 54)X \ .$$

In addition, a flux of pumped helium equal to 5% of the pumped D-T flux was used in the calculations. The sputtered flux was computed as

$$\Gamma^{s}_{z} = \Gamma^{P}_{D\text{-}T} Y^{P}_{D\text{-}T}(U^{P}_{D\text{-}T}, \alpha) + \Gamma^{L}_{D\text{-}T}(U^{L}_{D\text{-}T}, \alpha) + \Gamma^{P}_{\alpha} Y^{P}_{\alpha}(U^{P}_{\alpha}, \alpha) \ ,$$

where Y is the sputtering coefficient for pumping (Y^{P}_{α}) or leakage (Y^{L}_{α}). These coefficients depend strongly on energy and the angle α. They were computed using the DSPUT code,[4] and the estimates are believed to be reasonable, although they are clearly uncertain due to a lack of experimental data.

Figure 6.10 shows the erosion rate along the inner plate for the three different surface materials. The erosion rate is computed in each case using the theoretical density for steady-state operation. A value of $\alpha = 60°$, corresponding to the nominal reference design case, was used. The erosion is due mostly to the pumped D-T flux. In general, the erosion profile tends to follow the spatial variation of the pumped D-T flux, with some difference due to the sputtering coefficient energy dependence. As shown, the erosion rates are much higher for tungsten and nickel than for beryllium. The peak erosion rate for tungsten is about ten times higher than that for beryllium. With beryllium, the incident particle energies are much higher than the energy for peak sputtering. This is not true for the higher Z materials.

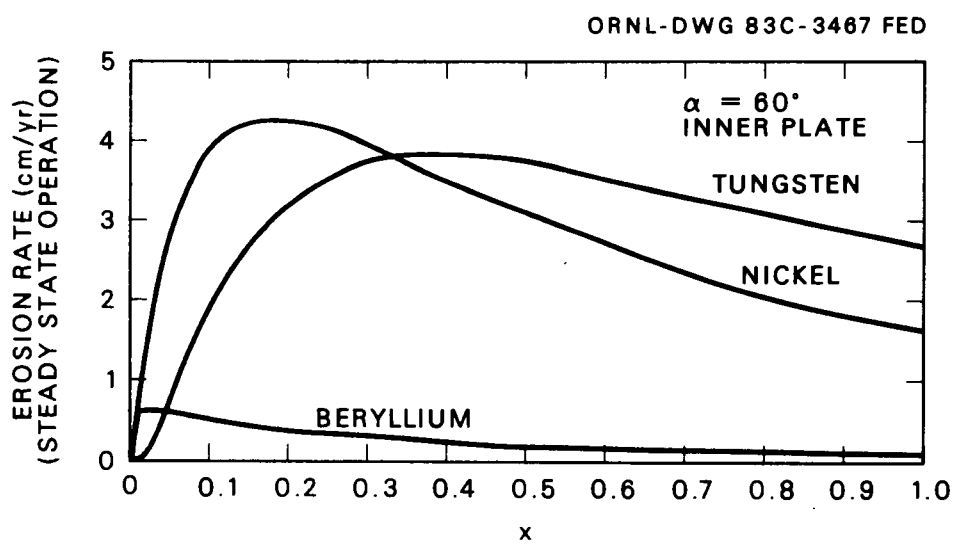

Fig. 6.10. Net erosion rates on inner halo plate for $\alpha = 60°$.

The erosion rates shown are for steady-state (i.e., continuous) operation. The actual erosion rates would be the rates shown times the MFTF-α+T availability factor, so yearly rates would be much lower.

Erosion rates for different inclination angles were computed. The peak rate vs α is shown in Fig. 6.11. Generally, the erosion profiles are similar to the $\alpha = 60°$ case. The inclination angle has two offsetting effects: as α increases, (1) the particle flux decreases since there is more plate surface area and (2) the sputtering coefficients increase.

For beryllium, these effects tend to cancel, and the peak erosion is nearly constant with inclination angle. A high value of α could then be chosen to minimize heat flux. For tungsten, erosion increases with angle, since the sputtering coefficients increase rapidly. For nickel, erosion increases up to $\alpha = 60°$ and is fairly constant thereafter. For high-Z materials, therefore, there is a trade-off between heat flux, which scales as cos α, and erosion. Another option is to use a plate with variable curvature.

Erosion of the outer plate depends heavily on redeposition, whereby sputtered atoms are ionized by the relatively high-density plasma, collide with incoming D-T ions, and return to the surface. Redeposited ions are then accelerated through the sheath potential and cause self-sputtering. Calculations were made for the outer plate using the REDEP

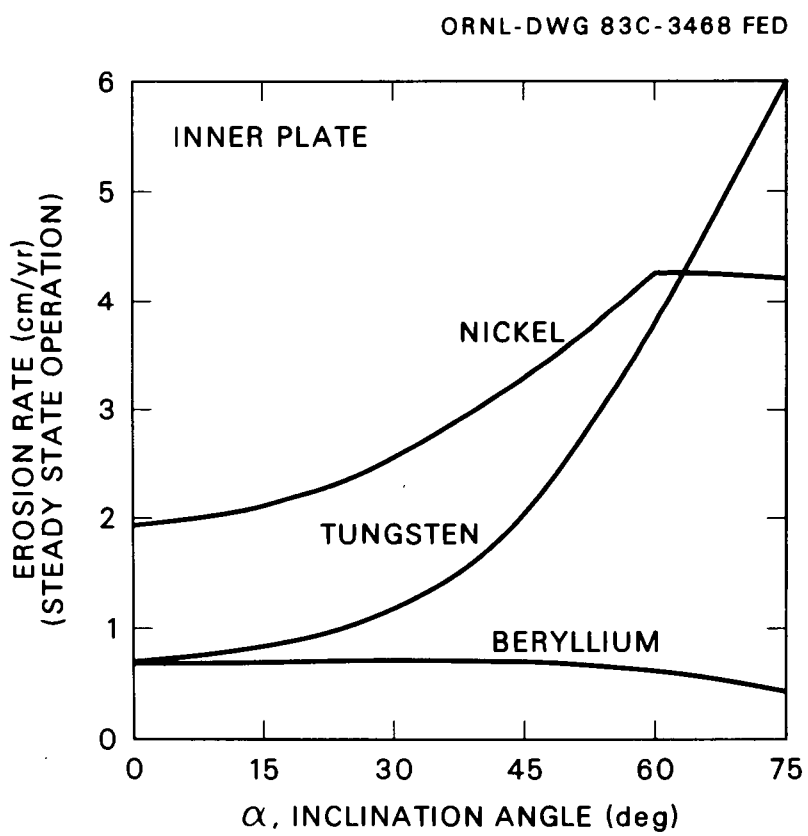

Fig. 6.11. Peak net erosion rates on inner halo plate as a function of α.

code.[5] Constant fluxes and plasma parameters across the outer plasma halo were used, and average erosion rates were computed. Because the halo parameters are uncertain, a range of plasma temperatures from 5 to 50 eV was used.

The D-T flux to the plate was scaled with temperature to give a constant heat flux

$$\Gamma_{\text{D-T}} = \frac{q \cos\theta}{2(1+\alpha)kT} ,$$

where $q = 0.14\ \text{MW/m}^2$, $\gamma = 3$ is the sheath heat transmission factor, and $\theta = 45°$. A helium flux equal to 5% of the D-T flux was assumed. Edge density was also scaled with edge temperature as $N_e \sim T^{-1.5}$. A sheath potential of $e\phi = 3kT$ was used in the calculations. The resulting gross erosion rates are shown in Fig. 6.12.

The net erosion rate is the difference between the gross rate and the redeposition rate. For all cases in which the self-sputtering coefficients are less than unity, redeposition is predicted to be very intense, essentially equal to the gross erosion. Thus, no net erosion is predicted. However, the gross erosion rate for beryllium is clearly of some concern until the uncertainties of the redeposited material properties (e.g., adhesion, flaking) are clarified. Nickel has lower gross erosion at low temperatures but starts to blow up due to a self-sputtering cascade at about 35 eV. In contrast, tungsten has a very low gross sputter rate up to 50 eV. Thus, tungsten or the nearly identical tantalum or tantalum-tungsten alloys seem to be superior materials for the outer plate. However, if the edge temperature

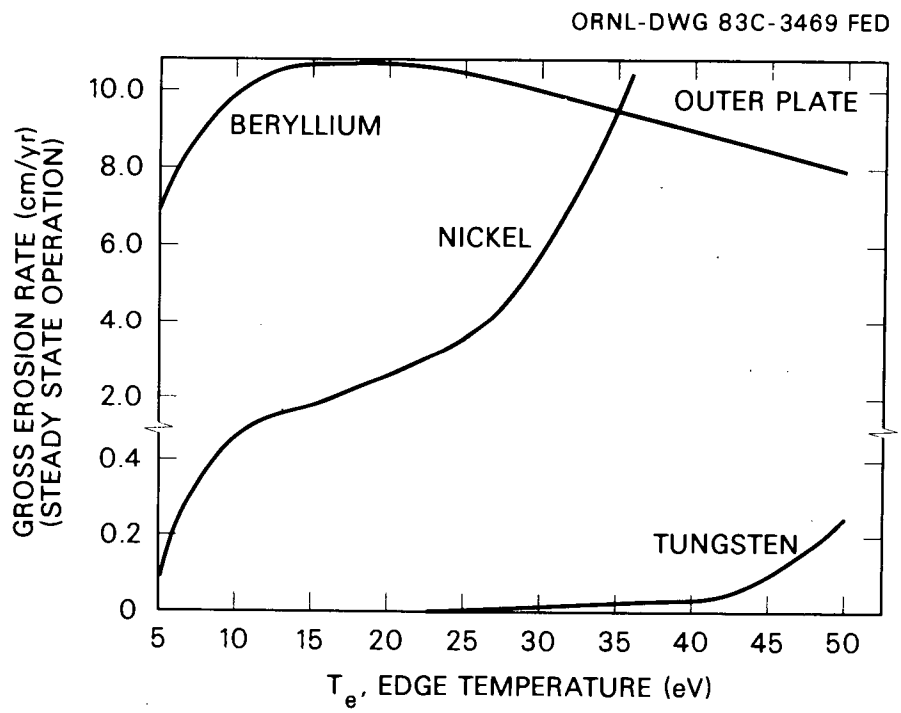

Fig. 6.12. Gross erosion rates on outer halo plate as a function of the plasma edge temperature.

exceeds 50 eV, then a low-Z material will be required, and if even small rates of tungsten transport to the main plasma are unacceptable, then a low-Z material will be preferable.

Another source of erosion of the outer halo plate is the transfer of material from the inner plate. Based on the plate geometry, most of the sputtered atoms from the inner plate will be ionized in the outer halo region. They will then undergo momentum transfer with the incoming D-T ions and tend to flow to the outer plate. The resulting sputtering of the outer plate can be fairly high. An initial analysis of this problem used the CHARGE code[6] to compute the energy and charge states of the transferred impurities and the REDEP code to compute the erosion/redeposition. (The CHARGE code solves kinetic and rate equations for impurities flowing in a D-T plasma.) A number of simplifying assumptions were also used to determine the general scope of the transfer problem.

From these calculations it was assumed that (1) all sputtered atoms from the inner plate are ionized immediately on entering the outer halo; (2) the distance between the newly ionized impurities and the outer halo plate is 1 m; and (3) the plasma density, temperature, and flow velocity are constant in the outer halo region. In addition, a number of other simplifying assumptions, involving rate coefficients, were employed.

From the transfer analysis, the following results were noted: (1) ions sputtered from the inner plate and arriving at the outer plate will be flowing at nearly the D-T sound speed; (2) charge states will be ~2–3 for beryllium and 4–5 for tungsten; (3) ions will diffuse a distance of ~2.5 cm based on a transit time of ~60 μs and a Bohm diffusion coefficient of ~10 m^2/s; and (4) based on a 2:1 expansion of the field lines, the ions will impinge on the outer plate over a distance of ~5 cm. The resulting gross erosion rate due to the transfer of material from the inner plate to the first 5 cm of the outer plate is shown in Fig. 6.13 for $\alpha = 60°$. These calculations are for similar outer and inner plate materials (i.e., tungsten-tungsten, beryllium-beryllium, etc.).

Since almost all of the sputtered material should be redeposited, the *net* erosion rate should still be low. However, the rates for nickel and tungsten are high enough to be of some concern. This is particularly true because the start of the halo region may have transition effects not modeled in this analysis. For different values of α, the transfer-caused erosion on the outer plate scales approximately as the peak erosion rates shown in Fig. 6.11.

A calculation was also made for an inner plate of beryllium and an outer plate of tungsten. In this case the sputtering due to transfer of beryllium to the tungsten surface was negligible. Beryllium would then merely deposit itself on the tungsten surface, where it would presumably migrate due to tungsten as well as hydrogen sputtering. This subject requires further analysis.

Based on these results, there are a number of interesting options and trade-offs for the halo scraper material. A beryllium coating would result in a very long-lasting inner plate. For the outer plates all materials are predicted to last indefinitely, subject to uncertainties in the redeposition process and the redeposited material characteristics. The use of tungsten virtually eliminates sputtering of the outer plate by D-T ions if the plasma temperature is low. However, a tungsten inner plate would result in a nontrivial gross sputter rate on the first ~5 cm of the outer plate, due to the transfer of sputtered inner plate material. A beryllium inner plate and a tungsten outer plate may be a good combination.

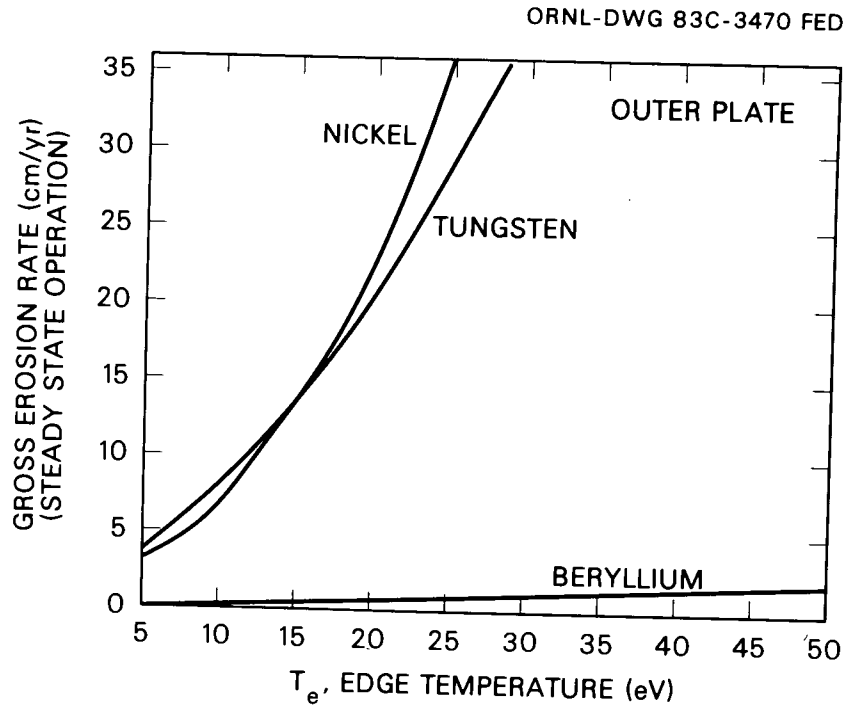

Fig. 6.13. Gross erosion rates on the first 50 cm of outer halo plate due to sputtering by material from inner plate.

The trends found here are similar to those found for the MARS design, which is not surprising because essentially the same physics assumptions are used. A wide range of halo materials and shapes could profitably be used on MFTF-α+T to help resolve questions about a mirror reactor.

Lifetime evaluation

The erosion rates just specified were combined with the material sizing studies presented in Sect. 6.2.3 to predict the erosion lifetimes of the inner and outer plates for three candidate plate materials, beryllium, copper, and Ta-10W. Erosion rate predictions for nickel were assumed to be representative of a medium-Z material and were used to evaluate copper. Erosion rate predictions for tungsten were used for Ta-10W, since sputtering yield coefficients for these two high-Z materials are approximately equal.

Erosion lifetime predictions are summarized in Table 6.5. An inner plate constructed of beryllium will have an erosion lifetime of 0.9 full-power year. This is slightly less than the device lifetime of 1 full-power year. Lifetimes of the other candidate materials are about a factor of 2 shorter. Since there are large uncertainties in the input parameters used for the erosion lifetime calculation, the actual lifetimes may be significantly longer or shorter than those predicted. Therefore, provision for replacement of the inner plate is a highly desirable design feature.

Table 6.5. Summary of erosion lifetime predictions

	Beryllium	Copper	Ta-10W
Thickness available for erosion,[a] mm			
Inner plate	5.5	18	17
Outer plate	130	120	40
Erosion rate, mm/year			
Inner plate	6.0	42	38
Outer plate[b]	70	0.9	0
Erosion lifetime, full-power years			
Inner plate	0.9	0.4	0.5
Outer plate	1.9	130	∞

[a]Assumes 2-mm thickness remaining at end of lifetime.
[b]Edge temperature assumed to be 5 eV.

An outer plate constructed of any of the three candidate materials is predicted to last the entire device lifetime. High-Z surface materials such as Ta-10W are recommended because the particle energies in this region are likely to be below the sputtering threshold for these materials.

6.3 DIRECT CONVERTER

In a working mirror reactor, direct converters at each end of the device will provide a means of energy recovery for useful power output. Dish-shaped collectors will operate at the maximum temperature across the surface to obtain high-grade heating of the coolant fluid.

To maintain a minimum-cost system for MFTF-α+T, the conversion of energy in a useful form is not required. However, the direct converter will be used for control of the axial and radial potential, and engineering test information on erosion, tritium penetration at high temperatures, and neutron damage can be obtained by adding a small test module.

The MFTF-α+T direct converter will be a low-cost, flat plate configuration. Cooling will be provided by deionized water, and several 6-in.-diam holes in the converter plates will be provided for diagnostics (primarily ion spectrometers).

The radial potential will be controlled using an outer collector plate between the halo scraper and the inner direct converter plate (see Fig. 6.2). The outer plate will have a radial length greater than a sloshing-ion gyroradius and will intercept the flux lines on the periphery of the inner plate. If the radial potential gradient across the plasma is too steep, which leads to poor confinement, the outer collector plate voltage can be set at an intermediate level between that of the halo scraper and that of the inner collector plate.

Both collector plates are negative and are used to control the axial potential so as to plug the mirror ends as follows. Electrons escape from both ends of the machine, maintaining plasma neutrality. Ions also leak out the ends, but drift pumping (Chap. 5) provides a preferred radial path for impurity, helium, and D-T ions. As the ions migrate radially outward, they reach a position at which they are no longer confined by the potential

and move to the halo scraper. Here the radial potential is controlled by the halo scraper and collector plate potentials.

Neutrals produced by collisions of particles with the end collectors and halo scraper, as well as those outgassing from the structure surface, are to a large degree ionized as they attempt to pass through the halo region; they join the radial drift ions at the halo scraper and are evacuated by a vacuum pumping system (Sect. 6.4). Neutrals produced at the direct converter plate can migrate to the halo by traveling through the end of the active area where the flux lines are directed to the converter, or they can travel around the back of the converter and into the halo region.

Previous designs for mirror converters included grid wires or tubes to keep cold electrons from returning to the plasma. These grids were expected to be difficult to design and maintain. With the adaptation of the MARS end-cell design for MFTF-α+T, there is a dip in the axial potential at the outer edge of the end plugs that eliminates the need for these grids. In addition, the latest designs are for circular end collectors, which result in a smaller vacuum structure around the collector.

6.3.1 Requirements

Axial potential control

The direct converter on each end of the machine consists of two concentric collectors, the inner plate and the outer plate or washer. Each collector will be connected to ground through variable resistors that control the voltages. To provide a low-cost system, the plates must operate in both the high-Q and high-Γ modes.

In the high-Q mode, the total neutral beam injection current is 53 A with a collector voltage of -75 kV. In the high-Γ mode, the total neutral beam injection current is 250 A with a collector voltage of about -40 kV. With radial drift pumping, most of the ions leaving the system move into the halo and are collected at the grounded halo scraper. Most of the electrons escape axially to the insulated direct converter collectors.

The potential bias of the system is shown in Fig. 6.14 for the high-Q mode and in Fig. 6.15 for the high-Γ mode. To maintain the desired plate voltage, the load resistor is automatically adjusted. Its reference input will be a programmable control that can be set to a constant value or adjusted as a function of time or as a function of the input neutral beam current (see Fig. 6.16). The figure also shows the main features of the water control system used to cool the plate, washer, and associated resistors.

Both the collectors and the resistors operate at voltages up to 75 kV, and a cooling system will be required. The coolant, which must be a nonconducting fluid, is deionized water for the base design. The flow demand is compared with the measured flow, and the control valves are modulated to provide the proper flow. Nearly any desired relationship between flow and temperature can be maintained with the programmable control. If the cooling flow falls below a minimum safe value for a period of time, operation is terminated. Alternatives to the base design are insulating coolant, shunt power control tubes, and load converters.

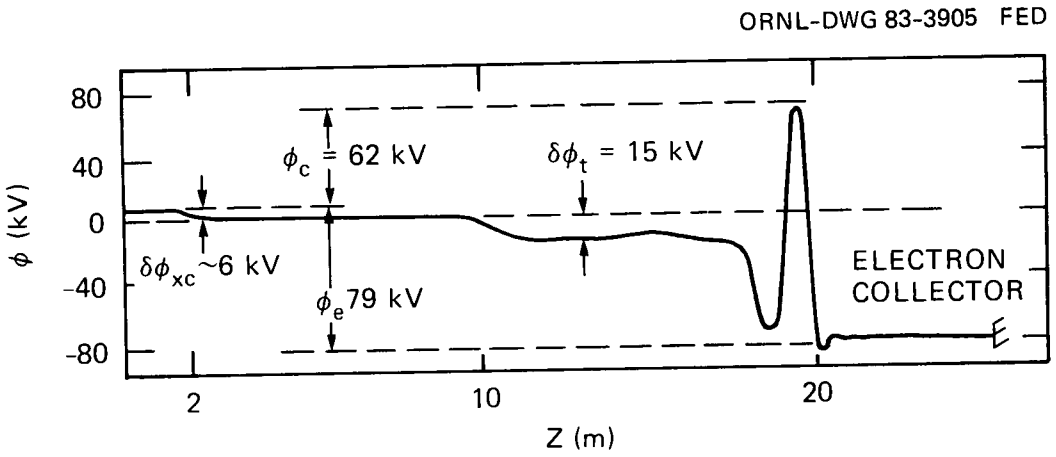

Fig. 6.14. Axial potential bias in high-Q mode.

Radial potential control

The collector washer is electrically isolated from both the inner collector plates and the halo dump, which is at ground potential. The washer can be operated at the same potential as the collector plate, or its voltage can be set at some intermediate potential between the collector plate and the halo scraper to provide a radial potental bias. The magnitude of the voltage bias on the washer may be determined by the need to improve confinement (providing a more gradual radial potential gradient) or by the desire to limit the erosion of the halo scraper plates by providing a reduced radial gradient. The base design provides for a continuously tapped load resistor on the plate, so that the washer bias voltage is regulated by the collector plate controller. An alternative is to provide an independent voltage controller similar to that provided for the plate voltage.

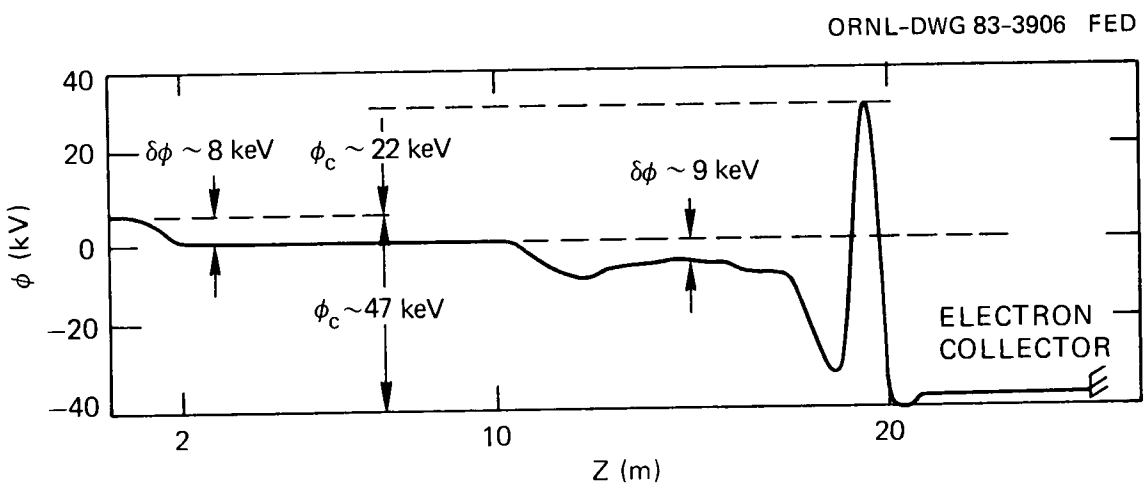

Fig. 6.15. Axial potential bias in high-Γ mode.

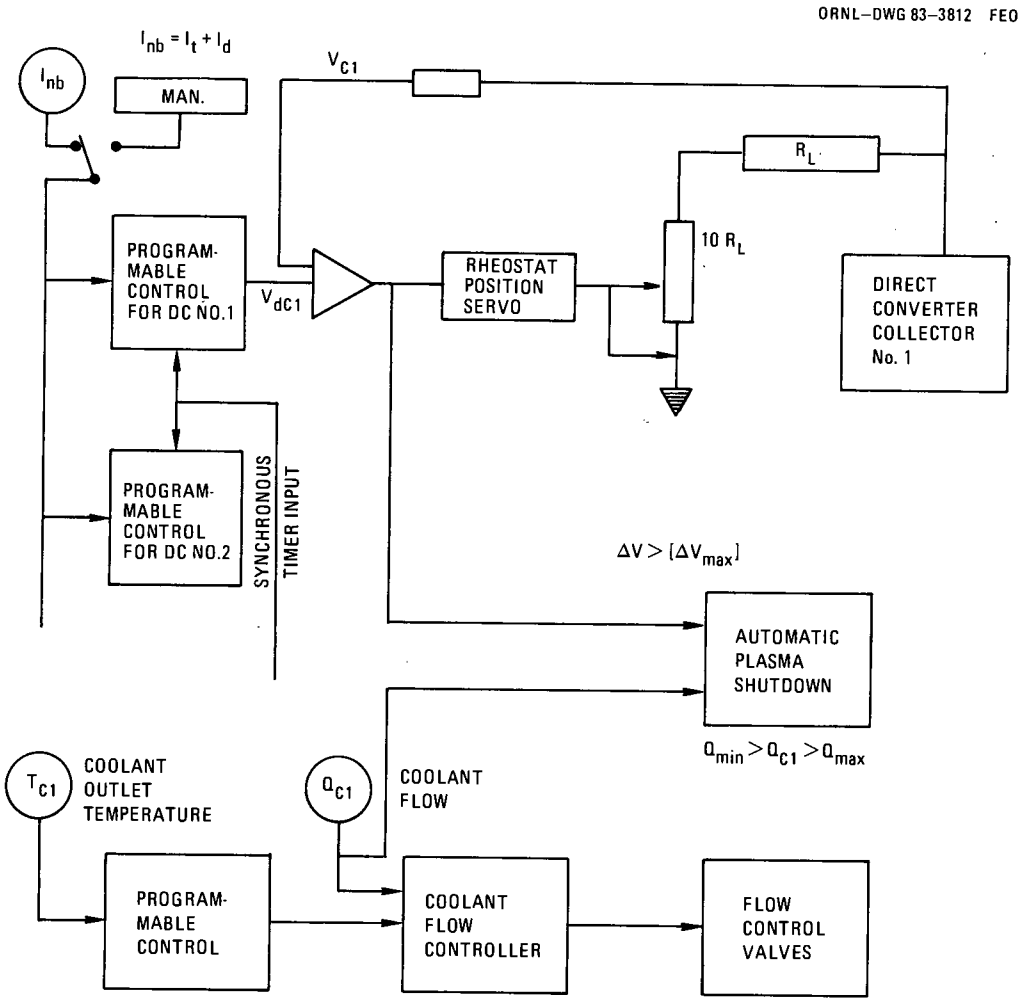

Fig. 6.16. Direct converter control system.

There is also a need to ensure that arcing will not occur between the plate and the washer or between the washer and the halo pump structures. To accomplish this, the gradient can be modified by the bias voltage of the washers, and special devices can be provided to shape the field lines connecting the halo scraper edge and the washer and those between the inner edge of the washer and the plate. Antiarcing devices such as those provided for MARS may be required.

Instrumentation for collector measurements

The following measurements will be provided for each collector: (1) collector voltage, (2) collector current, (3) ion current/electron current, (4) coolant inlet and outlet temperature, (5) coolant inlet and outlet flow, and (6) maximum potential of the plug cell. In addition, there will be a number of water quality measurements to ensure that the water is deionized. Because tritium is a beta emitter, its presence in water influences water conductivity. Therefore, radiation monitors and measurements of water pH and conductivity are needed. Some general requirements follow.

- Instrumentation for each cooling path must be sufficient to determine the presence of contamination in the water and to perform a heat balance analysis.
- Pressure measurements must be sufficient to determine the status of all components (filters, valves, pumps, regulators, and heat exchangers).
- Response time of flow measurements should be ≤1 s (for safety reasons).
- Response time for measurements of collector currents and voltages used in feedback control should be ≤0.1 s.
- Five 6-in.-diam penetrations through each collector are required. Penetrations will be on the machine axis and at several radial positions to determine the radial potential profile of the plug cell using ion spectrometers.
- One additional 6-in.-diam penetration through each collector is needed to accommodate a diagnostic for measuring ion current and electron current separately.

6.3.2 Design Description

The components of the direct converter are shown in Fig. 6.17. It is located ≃1.5 m from the scraper housing and can be removed from the vacuum vessel through its own hatch. The outer collector (washer) and the inner collector plate are attached to fittings, which in turn are attached to a support frame. The mounting fittings are electrically insulated from the support frame, as are the coolant tubes. The insulation allows appropriate electrical potentials to be established on each component.

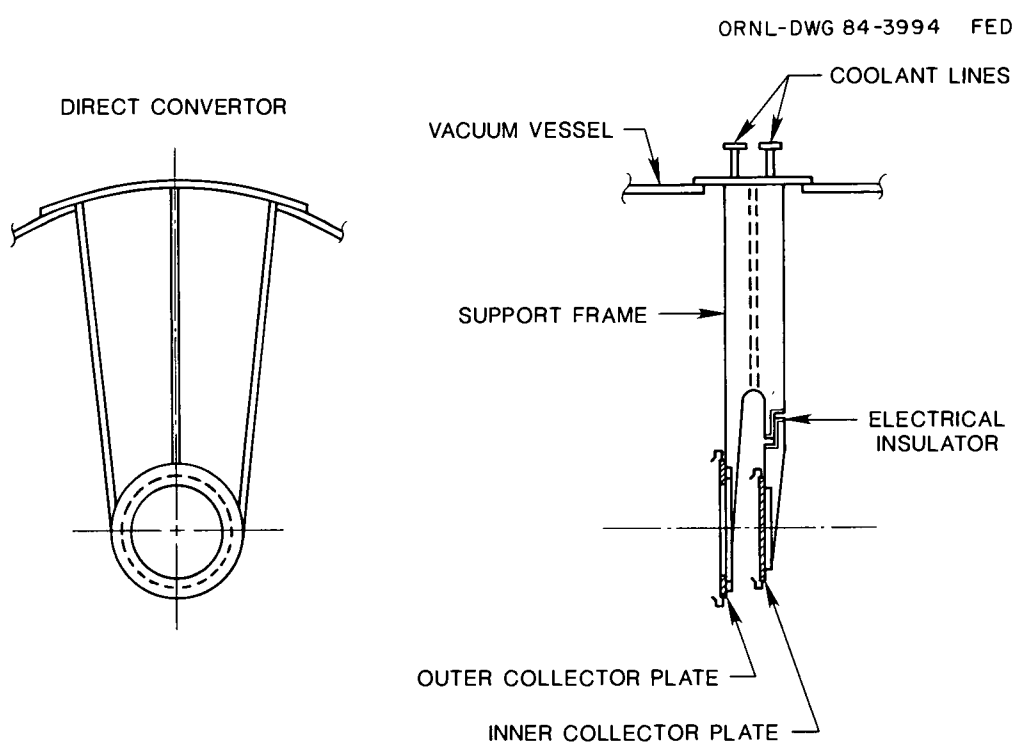

Fig. 6.17. Direct converter components.

The direct converter is divided into two radial segments so that the field lines can be biased to provide a gradual falloff of the potential between the grounded halo plasma and the −70-kV (in the high-Q mode) electron collector potential. Because the radial electric field gradient in the end cell is not yet well quantified, only two segments are provided in the baseline design; however, the concept can be generalized to more segments, as discussed in Sect. 6.3.3.

Details of the collector plates have not been defined. Copper alloys are the initial choice for material. The heat loads on these components do not represent technology challenges. However, the uncertainties associated with the heating and particle energies dictate conservative design approaches.

The direct converter inner collector plate is shown in Fig. 6.18, which indicates the complexity resulting from the requirement for instrumentation access. The six 15-cm-diam holes required are shown, as is an area designated for a test module. Specific tests have not been defined, but it is assumed that an easily replaceable test module would be desirable to measure the effects of particle impingement.

Thermodynamic performance

Thermodynamic analyses of the inner and outer collector plates were performed to determine the maximum permissible surface material thickness and to establish coolant flow performance requirements. The thickness of the surface material is a key design feature, since sputtering erosion may limit the lifetime of these components.

The design heat flux for the inner and outer collector plates is 1.0 MW/m^2. Material candidates are a copper alloy (AMAX-MZC) and a tantalum alloy (Ta-10W). The total area integrated heat loads are 1.7 MW to the inner plate and 0.5 MW to the outer plate.

Coolant flow performance parameters are listed in Table 6.6 for the plate configuration shown in Fig. 6.17. A total water flow rate of 13 kg/s provides adequate cooling of the collector plates.

Maximum thicknesses, based on maximum temperature and temperature difference cutoffs listed in Table 6.2, are presented in Table 6.7. Copper plates could be designed to be 64 mm thick without exceeding the temperature limits. The maximum thickness for tantalum plates is 61 mm.

Instrumentation

Each collector and dump resistor must be force cooled with a coolant that has low conductivity at high voltage (100 kV). Water may be used if the water treatment system removes impurities so that the water stays deionized. Figure 6.19 shows a small part of the cooling system and the associated instrumentation. For a single dump resistor on each collector and each washer, there would be a total of eight main coolant circuits, and the collectors, washers, and resistors may have two or more cooling channels. Each channel must be monitored for flow, temperature, and radiation; if there are 32 cooling channels, then 96 measurements are required. Pressure, temperature, and flow measurements are needed for all major components: pumps, heat exchangers, pressure regulators, filters, and the water treatment system. Critical factors that require redundant measurements are the

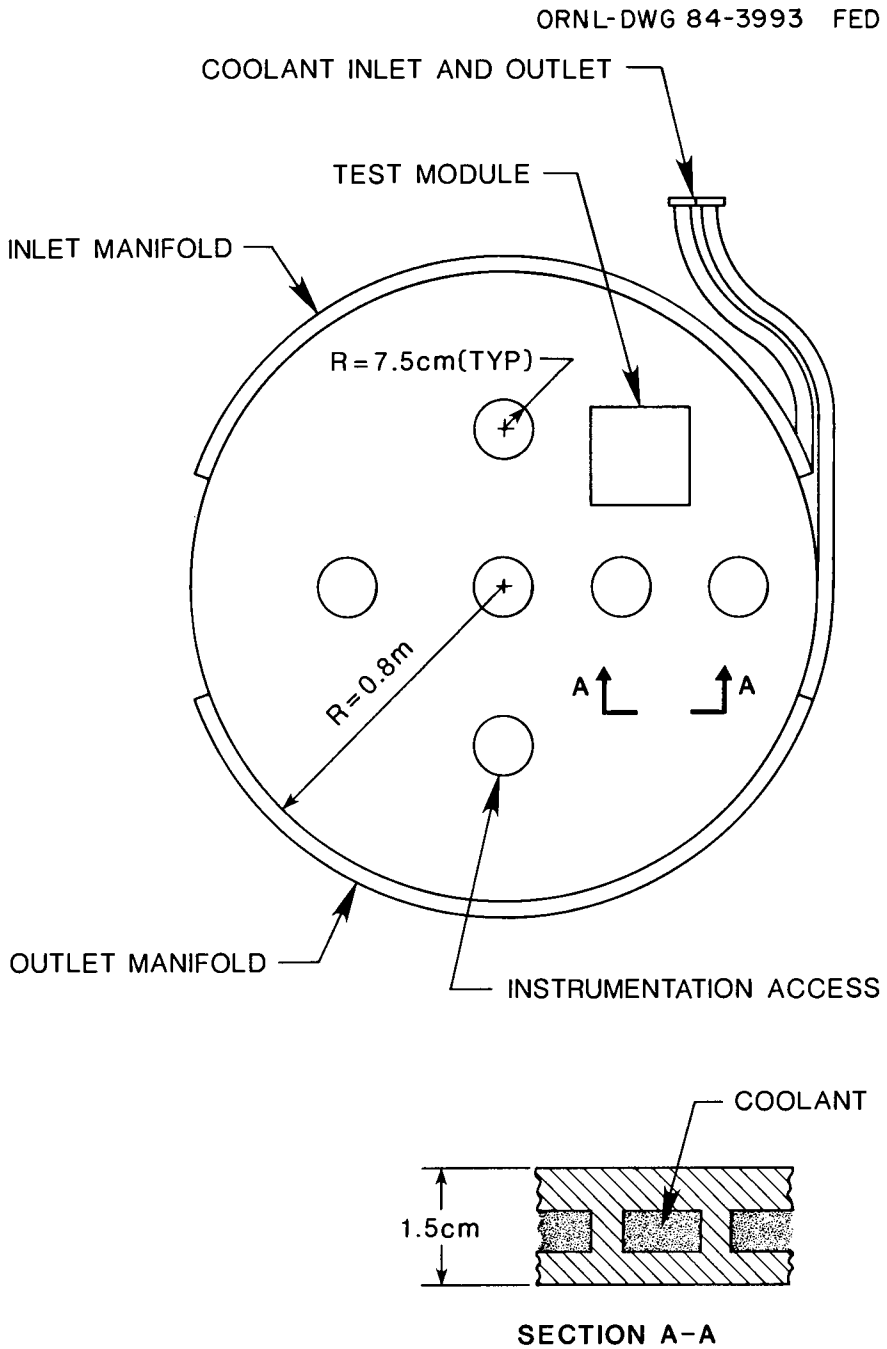

Fig. 6.18. Direct converter inner collector plate.

Table 6.6. Coolant flow performance parameters for direct converter plates

	Inner plate	Outer plate	Overall
Inlet temperature, °C	60	60	60
Outlet temperature, °C	100	100	100
Mass flow rate, kg/s	10	3	13
Average flow velocity, m/s	1.4	2.7	
Heat transfer coefficient, $kW/m^2 \cdot °C$	12	21	
Pressure drop through panels, MPa	0.013	0.14	0.14
Pumping power, kW	1.5	0.5	2.0

Table 6.7. Maximum thicknesses for direct convecter collector plates

	Inner plate, mm	Outer plate, mm
Copper alloy (AMAX-MZC)	64	64
Tantalum alloy (Ta-10W)	61	61

storage tank water level, the pH of the water, and its electrical conductivity. The water treatment system will require instrumentation (not shown in Fig. 6.19) for measuring pH and electrical conductivity. In addition, redundancy will probably be required for the collector electrical measurements used for control. Thermocouples and strain gages can be added at critical locations. The direct converters and their support systems will probably reqiure more than 180 sensors.

6.3.3 Scope of Future Work

Physics

As noted in Sect. 6.3.2, the direct converter is divided into two radial sections so that a gradual falloff in the potential can be provided. Because the radial electric field gradient in the end cell is not yet well quantified, the choice of only two segments was made for the baseline design. The concept described here can be extended to additional segments if this becomes necessary.

The outer collector plate extends from $r = 1.0$ m, the flux surface at the inner halo scraper ($Z = 30$ m) to $r = 0.75$ m; the inner collector plate has a radius $r = 0.84$ m at $Z = 30.5$ m. The radial width of the outer plate (or washer) at $Z = 30$ m corresponds to a sloshing-ion gyroradius, so that the inner collector plate is isolated from the halo plasma. In calculations of the heat loads on the electron collector, it is assumed that both collectors are at the same potential, since the actual variation is not known. For this calculation, the high-Γ case is considered because it represents the worst case.

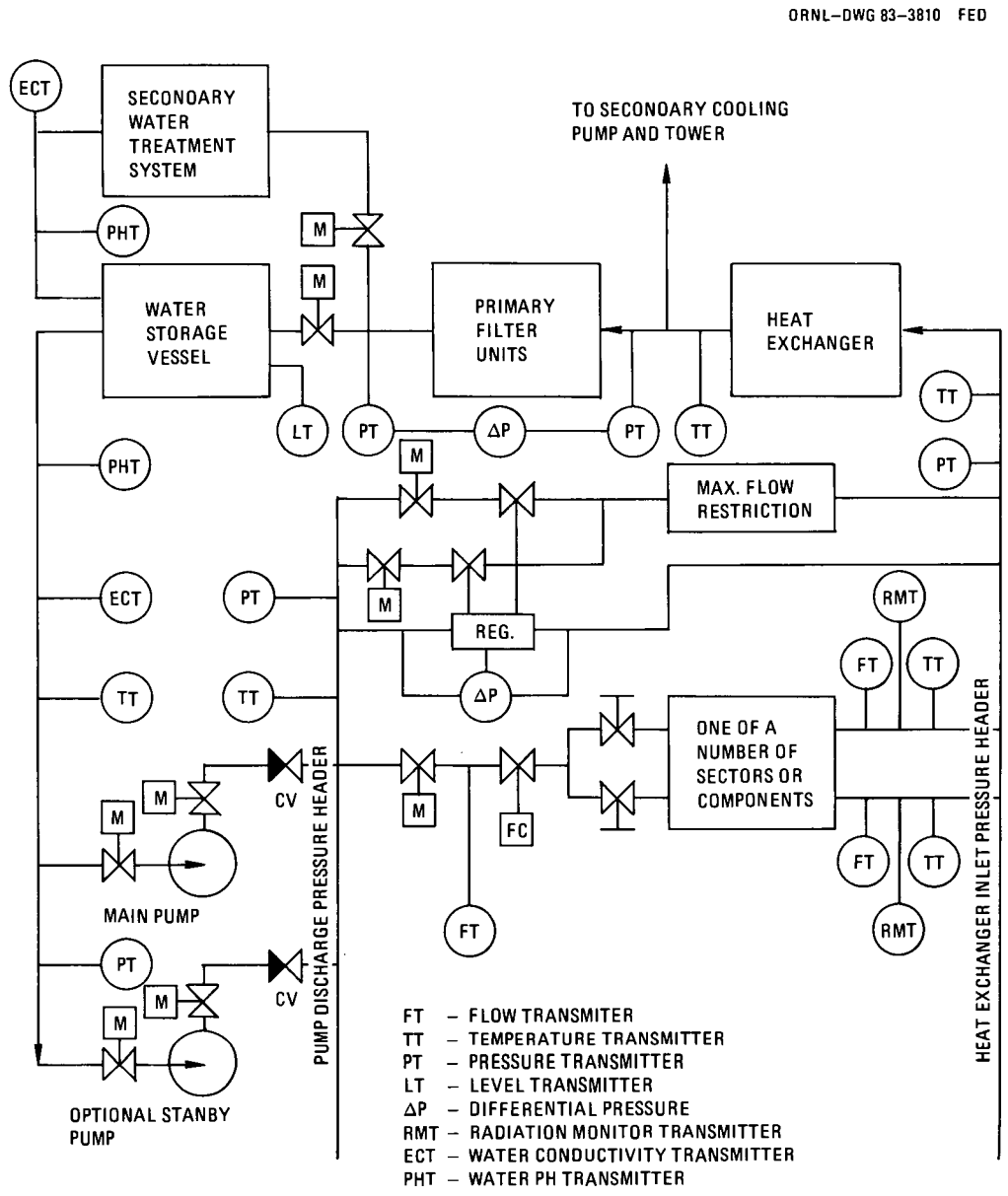

Fig. 6.19. Direct converter cooling system and instrumentation.

The axial ion and electron losses are taken to be proportional to the radial quartic density profile (Chap. 2). The total ion power loss (per end cell) is 45 A for $(\phi_e + \phi_c) + T_i = 84$ keV/ion, and the total electron loss (per end cell) is 80 A for $T_e = 54$ keV/electron. The current profile in the direct converter region $I_{DC}(r)$ is

$$I_{DC}(r) = C[1 - (r/r_o)]^4 \ ,$$

where C is a normalization constant (particles per second), r is the plasma radius (in meters), and r_0 is the outer halo radius (also in meters). Integrating from $r = 0$ to $r = r_0$, we find

$$C = 45\ \mathrm{A} \times (3/2\pi r_0^2)$$

for the ions, so the radial distribution of the ion current on the direct converter is

$$(I_{DC})_i(r) = \frac{1.34 \times 10^{20}}{r_0^2}[1 - (r/r_0)^4] \ .$$

Similarly, the radial distribution of the electron current is

$$(I_{DC})_e(r) = \frac{2.38 \times 10^{20}}{r_0^2}[1 - (r/r_0)^4] \ .$$

The total heat load on the direct converter is thus

$$P_{DC}(r) = \frac{2.12}{r_0^2}[1 - (r/r_0)^4]$$

(in megawatts per square meter). The heat loads are fairly uniform across the collectors since the outermost radius is only 75% of r_0. For the outer collector plate, the heat load is $\approx 1\ \mathrm{MW/m^2}$ and the particle flux is $\approx 1.1 \times 10^{20}\ \mathrm{cm^{-2} \cdot s^{-1}}$; for the inner collector plate, the heat load is $\approx 0.8\ \mathrm{MW/m^2}$ and the particle flux is $\approx 9 \times 10^{19}\ \mathrm{cm^{-2} \cdot s^{-1}}$.

A general observation on the end region heat loads for MFTF-α+T is that most of the power is deposited on the direct converters and the inner halo scraper. This is because most of the power is lost axially, rather than radially, and relatively little power is transported to the outer halo plasma.

The lack of accurate knowledge of the radial temperature profile introduces uncertainty into the exit location of the pumped particles and the power profile of the axial leakage component. Another area of uncertainty is the ability of the halo plasma to shield the main plasma from neutrals impinging perpendicular to the halo axis. The halo "scoop" at the scraper plate will prevent the return to the plasma of neutrals originating from the halo plasma flow onto the plate. However, the path length to the main plasma for neutrals originating on the chamber wall is the halo thickness, which is less than the "scoop" length, and the halo shielding ability for these neutrals is much less certain. These uncertainties must be addressed as the design progresses.

Engineering

Iteration of the direct converter design is needed to confirm the electrical, thermal, and electrical power requirements of the plate and the collector. Better quantification of the radial potential is needed to determine whether additional segments will be needed and to determine the radial dimensions of the segments.

To determine the need for antiarcing fields or components, the potential and magnetic gradients must be plotted for various protection systems and the effectiveness of the systems evaluated.

The selection of deionized water as the insulating coolant should be studied. A detailed coolant system should be configured to include the instrumentation for the system and its protection.

The use of a variable resistor to regulate the collector voltage should be studied, and the possibility of using a shunt power tube or an inverter should be investigated.

6.4 VACUUM PUMPING SYSTEM

6.4.1 Baseline Design

The baseline vacuum pumping system configuration is shown in Fig. 6.20. The halo scraper and direct converter regions are combined into a single vacuum pumping system. During device operation, particles entering the halo scraper region will be neutralized after striking either the inner or the outer disk and will then be pumped through one of the two 0.5-m-diam vacuum pumping ducts. Both ducts are connected to turbomolecular pumps with speeds of 5 m^3/s.

Ions striking the direct converter plates will be neutralized and then allowed to pass either through or around the cutouts in the halo scraper support frame (see Fig. 6.20). These neutral gas particles are entrained and pumped by the halo plasma flowing to the halo scraper. Thus, particles leaving the plasma either radially (to the halo) or axially (to the direct converter plates) are eventually pumped by the halo scraper vacuum pumps.

A set of cryopanels with a 3-m^2 total exposed surface is provided between the halo scraper and the choke coils at each end to remove any particles that are not pumped in the halo scraper.

6.4.2 System Performance

The vacuum pumping system performance was evaluated to determine its adequacy for particle removal/impurity control during device operation and its effectiveness during initial pumpdown. Conditions assumed for these phases of operation are listed in Table 6.8.

Ion losses to the direct converter and halo scraper were taken to be 90 A and 111 A, respectively.[7] These ion currents result in a gas load of 16 torr·L/s to the direct converter and 20 torr·L/s to the halo scraper. Particles neutralized on the direct converter will migrate into the halo scraper region (see Fig. 6.20) and will then be pumped by the halo plasma. Therefore, the halo scraper pumps must be capable of handling the entire

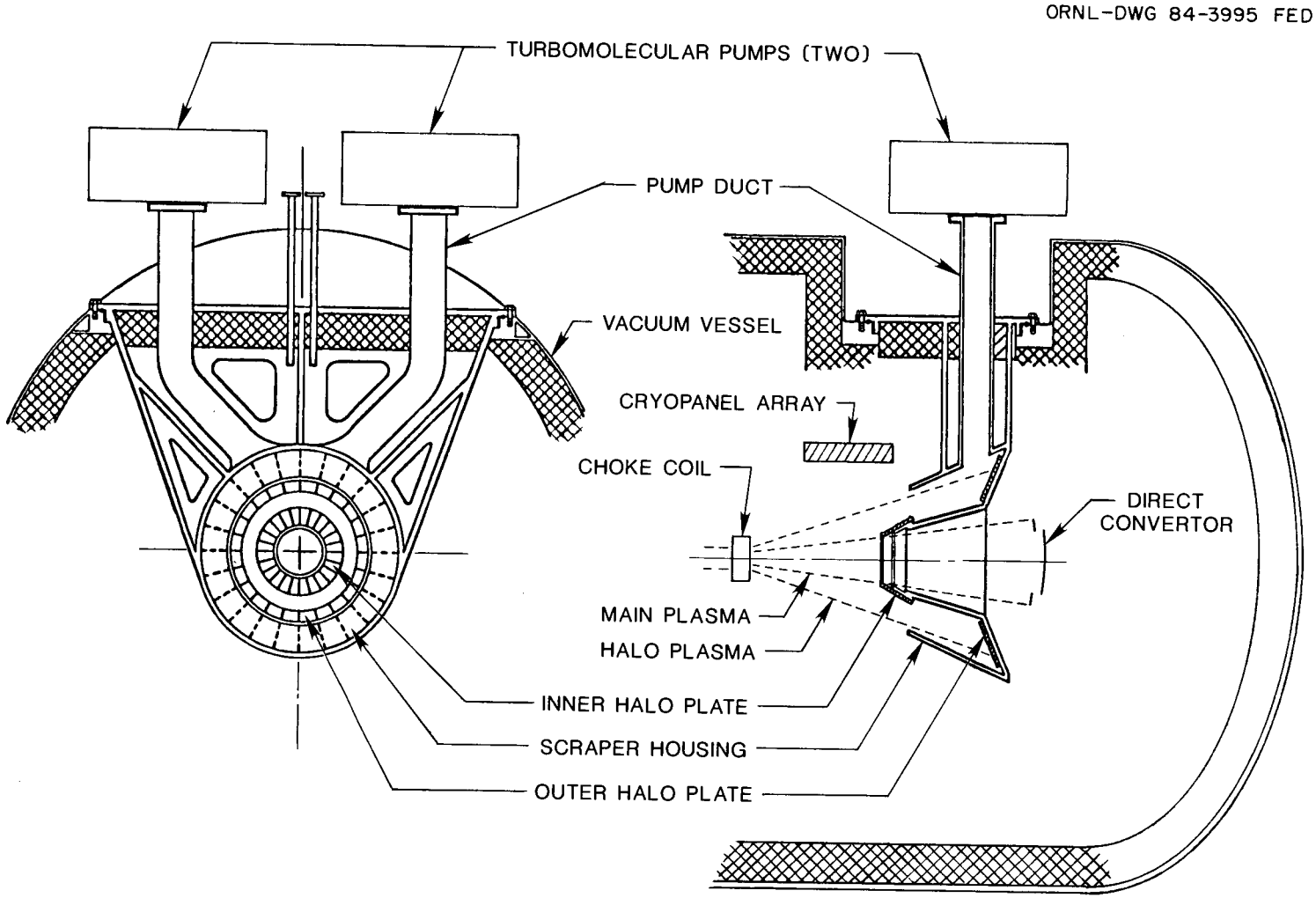

Fig. 6.20. Vacuum pumping system configuration.

Table 6.8. Assumptions and conditions for evaluation of vacuum pumping system performance

Particle removal/impurity control	
Gas load to end dump, torr·L/s	16
Gas load to halo scraper, torr·L/s	20
Gas leakage to region between halo scraper and choke coil, %	1
Pressure in halo scraper chamber, torr	$<10^{-2}$
Initial pumpdown	
Ultimate pressure, torr	$<5 \times 10^{-6}$
Outgassing rate (stainless steel surfaces), torr·L/s·m^2	5×10^{-5}
Exposed stainless steel surface area, m^2	1000

36-torr·L/s gas load. The cryopanels located in the region between the halo scraper and the choke coils are sized (3 m^2 per end) to handle 5% of the total gas load (1.8 torr·L/s) when operating at a pressure of 5×10^{-6} torr.

Conductances for the components of the halo scraper vacuum pumping system are listed in Table 6.9. For the conductances of all components and the 5-m^3/s pump speed, the effective pump speed was determined to be 2.5 m^3/s for each pump/duct assembly. The net pump speed of all four pump assemblies (two per end) is, therefore, 10 m^3/s. The resulting neutral gas pressure close to the neutralizer plate of the halo scraper is 3.6×10^{-3} torr, which is judged acceptable for operation of the impurity control system.

If only one of the two pumps at an end is operating, the pressure is 7.2×10^{-3} torr at that end, which still meets the 0.01-torr guideline. Therefore, the device can be operated with only one pump operating at each end.

During initial pumpdown of the device, outgassing of the stainless steel surfaces inside the vacuum boundary is assumed to be the major gas load (i.e., the device is leaktight). An outgassing rate of 5.0×10^{-5} torr·L/s·cm^2 is assumed for the stainless steel surfaces.[8] This corresponds to the degassing rate of polished and vapor-degreased stainless steel after 10 h of vacuum pumping. The area exposed to the plasma is estimated to be 500 m^2. For purposes of outgassing, a total stainless steel surface area of 1000 m^2 was used to account for convolutions in the surfaces. Achieving a pressure of 5×10^{-6} torr was established as a guideline for initial pumpdown.

Table 6.9. Conductances of components of the halo scraper pumping system

	Conductance, m^3/s
Halo scraper chamber to pump duct entrance	34
Aperture to pump duct	62
Pump duct	10.3
0.50-m-diam plate valve	20

Taking into accout only the turbomolecular pumps and cryopanels located in the halo scraper/end-cell region, the ultimate pressure in the central cell was estimated to be 2×10^{-5} torr. However, including the cryopanel arrays present in the two central-cell neutral beam lines and beam dump modules, an ultimate pressure of about 4×10^{-6} torr is reached. Therefore, the total vacuum pumping system is marginally acceptable for initial pumpdown purposes. Significant improvement in the pumpdown performance is possible by adding more pumps and ducts near the central cell or by baking the exposed surfaces to elevated temperatures (>150°C). Pumping provided by exposed cryogenic surfaces surrounding the magnets was not accounted for in this analysis.

6.4.3 Choice of Pumps

The choice of pumps to be used for providing high vacuum in the plasma chamber is constrained by the presence of tritium in the vacuum system and by the requirement for a relatively high pumping speed. Turbomolecular pumps and compound cryopumps were the main alternatives considered for the high-vacuum stage of the halo scraper vacuum pumping system. Mercury diffusion pumps were not considered seriously because of concern about mercury contamination of the plasma chamber.

Compound cryopumps, which remove most gases by cryocondensation and contain a sorption stage to remove helium, can easily be made with high enough pumping speed and are readily scalable to larger sizes. Pumps of this type are being tested in the Tritium Systems Test Assembly (TSTA).[9] While some development would be required before cryopumps could be used on MFTF-α+T, their feasibility has been amply demonstrated. An important drawback of the cryopumps is the tritium inventory that accumulates within them between regenerations. This characteristic raises safety concerns and may require the provision of containment structures to prevent a release of tritium.

Two compound cryopumps with speeds of 10 m^3/s would be located at each of the four halo scraper pumping stations (Fig. 6.20). During long-pulse operation, one pump would operate while the other is undergoing regenerations. Time between regenerations is 1 h, and the total tritium inventory in the pumps is 20 g (2×10^5 Ci). Details of the remainder of the halo scraper pumping system (ducts, valves, etc.) are assumed to be the same for both design options.

Turbomolecular pumps are limited to lower pump speeds than cryopumps, but this is not a limitation for MFTF-α+T. The largest commercially available pump has a speed of 5 m^3/s for air and 6.2 m^3/s for hydrogen and helium and was selected as the reference turbomolecular pump design. Manufacturers of turbomolecular pumps see no difficulty in producing pumps with higher speeds, such as 20 m^3/s (ref. 10). The size of commercially available turbomolecular pumps seems to be limited by the lack of a market for larger pumps.

Turbomolecular pumps were selected for the Tokamak Fusion Test Reactor (TFTR). A commercial pump design was modified to allow it to be used with tritium. One concern associated with the use of turbomolecular pumps is contamination of the pump's bearing

lubrication oil with tritium. Such contamination can be eliminated by using a fluorocarbon oil, as long as the oil does not lead to any fluoride corrosion of the pumps. It also appears feasible to use a mineral oil and replace the oil fairly frequently as it becomes contaminated with tritium; this procedure will be used on TFTR.[11]

A simple cost study was performed to compare the difference in the cost of cryopumps and turbomolecular pumps. Only those features that differed for the two options were considered (ducts, valves, etc., not included). Using compound cryopumps results in a slightly lower cost (savings of less than $0.2 million) for the vacuum pumping system. Since the cost difference is negligible, cost was not a significant factor in the pump selection.

Turbomolecular pumps were selected over compound cryopumps primarily to reduce the tritium inventory available for potential release into the reactor building in the event of an accident.

REFERENCES

1. W. L. Barr, Lawrence Livermore National Laboratory, personal communication, July 1982.

2. W. L. Barr, Lawrence Livermore National Laboratory, personal communication, June 1982.

3. J. A. O'Toole, Fusion Engineering Design Center, Oak Ridge, Tenn., personal communication, August 1983.

4. D. L. Smith et al., *DSPUT: A Physical Sputtering Code for Fusion Applications,* ANL/FPP/TM-157, Argonne Natl. Lab., Argonne, Ill., 1982.

5. J. N. Brooks et al., "Modeling and Analyses of Erosion and Redeposition for Limiter and Divertor Impurity Control Systems," *Nucl. Technol./Fusion* **4,** 33 (1983).

6. C. D. Boley et al., *Charge State of Sputtered Impurity Ions Near a Limiter or Divertor in a Tokamak,* ANL/FPP/TM-171, Argonne Natl. Lab., Argonne, Ill., 1983.

7. K. E. Thomassen and J. N. Doggett, *Options to Upgrade the Mirror Fusion Test Facility,* UCID-19743, Univ. California, Lawrence Livermore Natl. Lab., Livermore, Calif., March 1983.

8. L. O. Mullen, "High and Ultrahigh Vacuum by Pumping with Cryocooled Surfaces," in *Vacuum Technology at Low Temperatures, AIChE Symp. Ser.* **68** (125), 24–30 (1972).

9. D. O. Coffin and C. R. Walthers, "Vacuum Pumping of Tritium in Power Reactors," p. 513 in *Proceedings of the 8th Symposium on Engineering Problems,* Institute Electrical and Electronics Engineers, New York, 1979.

10. J. A. Freeman, Balzers Corporation, personal communication.

11. B. D. Abel, "TFTR Vacuum Systems," *J. Vac. Sci. Technol.* **15,** 726 (1978).

7. TRITIUM PROCESSING

P. A. Finn

Argonne National Laboratory

CONTENTS

7.1 INTRODUCTION 7-3
7.2 KEY PARAMETERS 7-3
7.3 SELECTION OF DISPOSAL METHOD 7-4
7.4 SYSTEM DESCRIPTIONS 7-7
7.4.1 Fuel Processing Systems 7-8
7.4.2 Atmospheric Detritiation Systems 7-9
7.4.3 Coolant Systems and Tritium Migration 7-19
7.4.4 Test Module Systems 7-20
7.5 ACCIDENT SCENARIOS 7-20
7.6 OPERATING CONDITIONS 7-22
7.6.1 Assessment of Tritium Sources 7-22
7.6.2 Tritium Needs of an FPD 7-23
7.7 KEY ISSUES 7-27
REFERENCES 7-28

7. TRITIUM PROCESSING

7.1 INTRODUCTION

The MFTF-α+T device, an upgrade of the Mirror Fusion Test Facility (MFTF-B) at Lawrence Livermore National Laboratory (LLNL), is designed to provide a relatively high fractional burn (0.02), 20 MW of fusion power, and a high wall loading in the central cell. Tritium systems are needed to process the tritium (T) and deuterium (D) fuel of the plasma, the water coolant, and the atmosphere in tritium areas and to provide tritium control throughout the facility. The units of the system, especially the atmospheric processing units, are designed to function during normal operation, maintenance, and accidents.

A complete fuel cycle is provided. This includes not only the components needed to process and store the fuel (fuel cleanup unit, isotope separation unit, storage beds, receiving glovebox), but also the units required for (1) secondary containment (glovebox detritiation system), (2) waste processing (tritium waste treatment for gases, tritiated water recovery unit for water, and tritiated waste processing system for solids), (3) tritium analysis (for the detection and solution of problems in the fuel cycle and for maintenance of accountability records), (4) tritium monitoring (for safety), and (5) process control with an associated data acquisition system. Specifications for many of these units are found in ref. 1.

The tritium systems are located in a leaktight, earthquake-proof building separate from the reactor (see Chap. 3). Earthquake valves are located on lines and between units to minimize possible releases. An atmospheric processing system in the tritium processing building handles any tritium releases in the area. The atmospheric processing units for the reactor vault and the hot cells are also in this building. The size of these units determines the size of the tritium processing building; its estimated volume is $\sim 3 \times 10^4$ m^3.

In sizing the tritium systems for MFTF-α+T, several areas were addressed: (1) the tritium inventories, tritium mass flow rates, and tritium fuel costs for 10- and 100-h burns; (2) the tritium systems needed for 10- and 100-h burns; and (3) the space requirements for these systems. Key parameters used in the assessments are given in Sect. 7.2. The choice between on-site and off-site processing is examined in Sect. 7.3. The tritium systems needed for MFTF-α+T under the current set of assumptions are described in Sect. 7.4. Section 7.5 presents accident scenarios, and Sect. 7.6 presents operating considerations. Key issues are summarized in Sect. 7.7.

7.2 KEY PARAMETERS

The following key parameters and assumptions were used to assess the tritium systems needed for MFTF-α+T.

1. The reactor produces 20 MW of fusion power and has a burn fraction of 0.02.
2. The burn time is 10 to 100 h, corresponding to an availability between 1% and 10%.
3. The tritium and deuterium in the fuel cycle are processed at LLNL. (At present there is no capability to isotopically separate D and T on site.[2])

4. The regenerable cryopanels close perfectly, and one-sixth of the cryopanel area is processed every 10 min.
5. Positive-ion neutral beams supply 120 A of tritium and 120 A of deuterium to the central cell at total gas efficiencies between 20% and 30%.
6. Negative-ion neutral beams supply <20 A of deuterium at total gas efficiencies between 7% and 11%.
7. The tritium fueling rate is 21 to 31 g/h. The deuterium fueling rate is 14 to 21 g/h for the central cell and 3 to 5 g/h for the end cells.
8. The vault volume is 3×10^4 m^3.
9. A leak rate of <1 vol %/h in the vault will be provided either with grouting and sealing or with an internal wall of steel or aluminum.

7.3 SELECTION OF DISPOSAL METHOD

The tritium inventories resulting from on-site and off-site processing of the tritium in MFTF-α+T are summarized in Table 7.1. If the gas is not processed on site, then 208 to

Table 7.1. Summary of tritium inventories (in grams) for MFTF-α+T

	10-h burn	100-h burn
At end of run with no on-site processing		
T_2 on getters	208–312	2080–3120
D_2 on getters	170–260	1700–2600
Total	380–570	3800–5700
At steady state with on-site processing		
Neutral beams[a,b]	4–10	4–10
End cells[b]	5	5
Beam dumps[b]	1	1
Surge tank	3–5	3–5
Structure[c]	<1	~20
Tritium in vault	14–22	~33–41
Fuel cleanup	≤50	≤50
Isotope separation[d]	120–250	120–250
Storage[e]	21–31	81–121
Tritium in processing area	191–331	251–421
Total	205–353	284–461

[a]Efficiency of neutral beams: positive-ion-based, 20% to 30%; negative-ion-based, 7% to 11%.

[b]Regenerable cryopanels are used; one-sixth of them are processed very 10 min.

[c]Amount is dependent on structure temperature and cleanliness, coolant used, and D-T flux impinging on the structure.

[d]Amount is a function of design, purity requirements, and gas composition.

[e]For 10-h runs, 1 h; for 100-h runs, 4 h.

312 g of tritium is collected on getters located either inside or outside the vault after 10 h of continuous operation, and an additional 10 to 16 g, which is considered vulnerable, accumulates within the vault in the neutral beams, the end cells, and the beam dumps. The safety hazard associated with off-site processing was evaluated.

Unless isotopic separation/purification facilities are constructed at LLNL,[2] the tritium waste generated during a run must be removed from the site and replaced with new tritium. It was assumed that the tritium would be supplied as tritium gas and removed as waste deuterium-tritium (D-T) gas. Removal would be in LP-50 containers, each holding ~2 moles of gas at STP or 12 g of tritium (whichever is less), transported by truck.

The probability of the occurrence of an accident per vehicle mile was evaluated in ref. 3 and is shown in Table 7.2. The probability of an accident is the product of the probability of occurrence per vehicle mile times the vehicle miles per year. Table 7.3 shows accident probabilities evaluated for one-way trips of 1600 and 3200 km (1000 and

Table 7.2. Accident probability for trucks

Severity	Vehicle speed, mph	Fire duration, h	Probability per vehicle mile
Minor	0–30	<0.5	6×10^{-9}
	0–30	0	4×10^{-7}
	30–50	0	9×10^{-7}
			Total: 1.3×10^{-6}
Moderate	0–30	0.5–1	5×10^{-11}
	30–50	<0.5	1×10^{-8}
	50–70	<0.5	5×10^{-9}
	50–70	0	3×10^{-7}
			Total: 3×10^{-7}
Severe	0–30	>1	5×10^{-12}
	30–50	>1	1×10^{-11}
	30–50	0.5–1	1×10^{-10}
	50–70	0.5–1	6×10^{-12}
	>70	<0.5	1×10^{-10}
	>70	0	8×10^{-9}
			Total: 8×10^{-9}
Extra severe	50–70	>1	6×10^{-13}
	>70	0.5–1	2×10^{-13}
			Total: 8×10^{-13}[a]
Extreme	>70	>1	2×10^{-14}[b]

[a]For comparison, probability is 1.3×10^{-11} for rail transport.

[b]For comparison, probability is 1.2×10^{-13} for rail transport.

Source: Environmental Survey of Transportation of Radioactive Materials to and from Nuclear Power Plants, WASH-1238, U.S. Government Printing Office, December 1972.

Table 7.3. Probability of truck accidents in one, five, or ten years of tritium operation

	Distance from tritium source, km	Distance traveled per year, km	Accident probability								
			1 year			5 year			10 year		
			Minor	Moderate	Severe	Minor	Moderate	Severe	Minor	Moderate	Severe
Case 1 (~500 g of T gas in, 820 g of D-T gas out)	1600	1.92×10^5	0.16	0.036	9.6×10^{-4}	0.8	0.18	4.8×10^{-3}	1.6	0.36	9.6×10^{-3}
	3200	3.84×10^5	0.32	0.072	1.2×10^{-3}	1.6	0.36	9.6×10^{-3}	3.2	0.72	1.9×10^{-2}
Case 2 (700 g of T gas in, 1150 g of D-T gas out)	1600	2.88×10^5	0.23	0.054	1.4×10^{-3}	1.1	0.27	6.0×10^{-3}	2.3	0.54	1.4×10^{-2}
	3200	5.76×10^5	0.46	0.11	2.8×10^{-3}	2.2	0.54	1.4×10^{-2}	4.6	1.1	2.8×10^{-2}
Case 3 (1076 g of T gas in, 1752 g of D-T gas out)	1600	4.32×10^5	0.35	0.081	2.2×10^{-3}	1.8	0.40	1.1×10^{-2}			
	3200	8.64×10^5	0.70	0.16	4.4×10^{-3}	3.6	0.80	2.2×10^{-2}			
Case 4 (1528 g of T gas in, 2492 g of D-T gas out)	1600	6.24×10^5	0.51	0.12	3.1×10^{-3}	2.5	0.60	1.6×10^{-2}			
	3200	1.25×10^6	1.0	0.24	6.2×10^{-3}	5.0	1.1	3.2×10^{-2}			

2000 miles) as needed to transport the following quantities of tritium (produced with 10-h burns) per year:

1. ~500 g of T gas in, 820 g of D-T gas out,
2. ~700 g of T gas in, 1150 g of D-T gas out,
3. ~1076 g of T gas in, 1752 g of D-T gas out,
4. ~1528 g of T gas in, 2492 g of D-T gas out.

The probability of a moderate accident is 1.1 in five or ten years of operation with off-site processing. With on-site processing, this probability is <0.036 in ten years of operation. The desirability of on-site processing is even more obvious when the burn time is increased to 100 h and the tritium in the D-T waste increases from 0.3 kg to 3 kg. The cost of tritium for 10- and 100-h burns with and without processing is given in Table 7.4.

Table 7.4. Cost of tritium fuel

	Operating time, s	
	2×10^5	2×10^6
Without processing		
Fueling needs, kg	≤1.7	≤17
Decay, g/year	≤95	≤950
Burn, g	~6	~62
Cost for 10 years of operation, millions of dollars[a,b]	13–17	130–170
With processing		
Fueling needs, kg	≤0.35	≤0.46
Decay, g/year	~20	~26
Burn, g	~6	~62
Cost for 10 years of operation, millions of dollars[a]	5.3	7.5

[a]Computed at $1/Ci.

[b]~25% cost recovery assumed if waste tritium is processed off-site. This accounts for range.

An on-site processing system does not increase the amount of tritium present at a given time, and it provides greater flexibility of operation, since reprocessing allows compensation for any reduced efficiency in the operation of the neutral beams. If gas is processed at a rate equal to the fueling rate, then the total tritium inventory is 205 to 353 g. (If the processing rate is slower than the fueling rate, then a larger tritium inventory is required.) On-site processing of tritium is assumed for MFTF-α+T.

7.4 SYSTEM DESCRIPTIONS

The location of major amounts of tritium in MFTF-α+T at steady state for 10- and 100-h runs is shown in Table 7.1. The major difference is the increased reserve storage for

the 100-h run (4 h vs 1 h). As the device availability and the burn time increase, the amount of tritium in the reactor increases slightly. The mass flow rates shown in Fig. 7.1 are the same for both 10- and 100-h runs. Gas flow paths are shown in Fig. 7.2.

The tritium systems needed for 10-h and 100-h runs are summarized in Table 7.5, and the estimated sizes of the major components are given in Table 7.6. A preliminary layout for the MFTF-B tritium systems is shown in Figs. 7.3 and 7.4.

7.4.1 Fuel Processing Systems

As shown in Table 7.5, the components of the fuel processing systems are based on existing systems. The characteristics of three working isotope separation systems are shown in Table 7.7. The cryogenic distillation system best meets the needs of a D-T fusion plant because it is the most efficient in removing gaseous tritium from gaseous waste protium. In addition, its capacity (>400 g/year) matches that needed for MFTF-α+T. Therefore, it was selected for the reference tritium processing system.

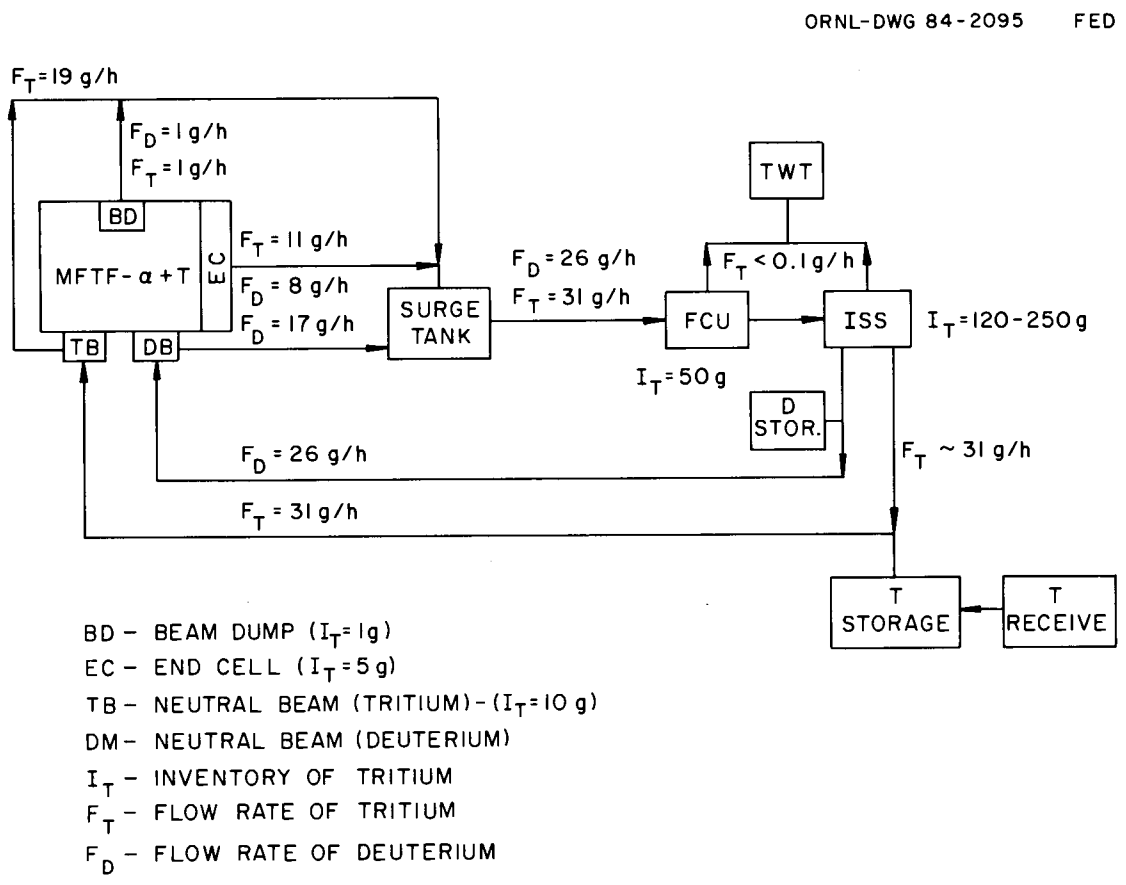

Fig. 7.1. Tritium mass flow rates for MFTF-α+T. (See Table 7.6 for other acronyms.)

ORNL-DWG 84-2086 FED

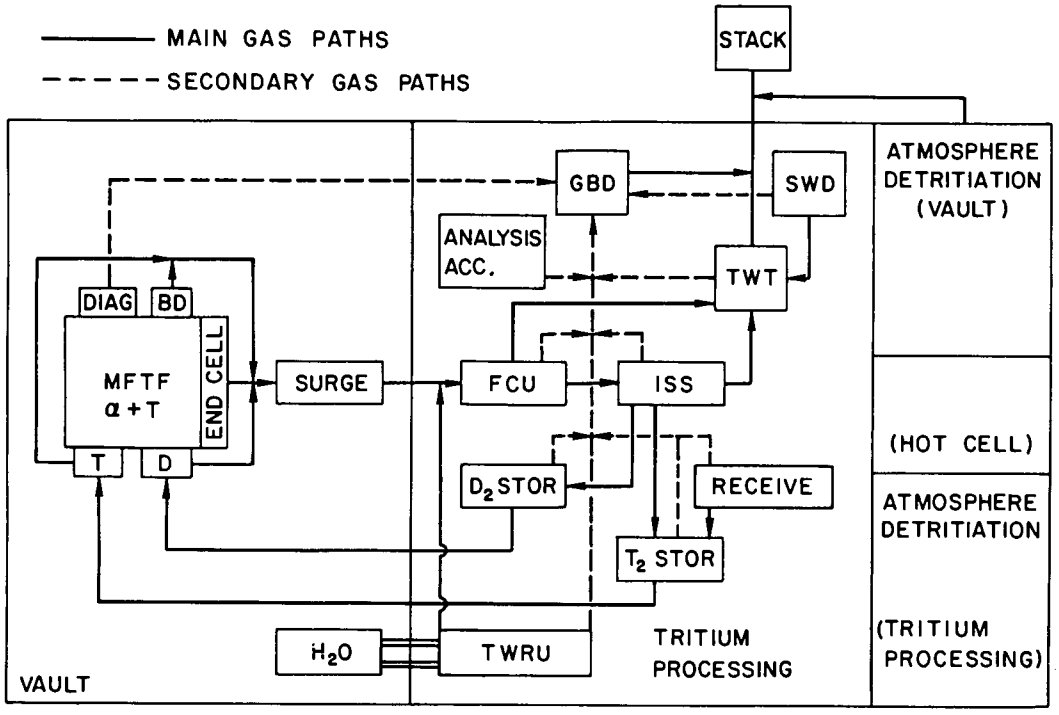

Fig. 7.2. Tritium flow paths in MFTF-α+T tritium processing units. (See Table 7.6 for other acronyms.)

7.4.2 Atmospheric Detritiation Systems

The atmospheric detritiation units remove from atmosphere any tritium released from primary or secondary containment in areas in which tritium is routinely handled. Units must operate during normal conditions, maintenance, and accidents and thus must be sized to handle all three conditions. When installed, the units are coupled directly to the ventilation and venting systems. As part of the safety systems, the units must be redundant if a single unit is used or able to supply the capacity needed even if one of several small units fails.

Size of units

The size of the atmospheric detritiation units depends on the required processing rate to be achieved, which is calculated as the total time needed to attain cleanup of the atmosphere to desired levels. The processing rate selected should not lower the availability needed in a given area.

Three levels of tritium in the atmosphere (5, 50, and 500 $\mu Ci/m^3$) were considered.[4] A level of 50 $\mu Ci/m^3$ was chosen based on atmospheric tritium recovery system cost,

Table 7.5. MFTF-α+T tritium systems

Description	Basis[a]	Quantity	Cost,[b] millions of dollars
Fuel processing systems			
Receiving glovebox for tritium, upgraded for ~ 100 g/month of T_2	TSTA, TFTR	1	0.2
Uranium beds for D and T storage, capacity ~ 100 g/bed	TSTA, Mound	8 or 9[c]	2.0–2.3[c]
Fuel cleanup unit with helium removal, 600–2000 g/day of D-T	TSTA	1	1.5
Isotope separation unit with storage beds for accident control, 600–2000 g/day of D-T	TSTA	1	2.9
Glovebox detritiation system, flow rate of 0.3 m^3/min, ~10^{-2} g/day	TFTR, TSDCS	1	1.6
Tritiated water recovery unit, flow rate of 100 L/day (no dedicated isotope separation column)	CECE at Mound	1[d]	3.0[d]
Tritium waste treatment unit, flow rate of 1.5 m^3/min, ~10 g/day of T_2	TSTA	1	1.2
Tritiated waste processing unit, capacity of ~1 kg/day (individual units for atmospheric processing area)	TSTA	>1	~1.3
Tritium analysis system (accountability)	Mound, TFTR,TSTA	1	1.6
Monitors for gaseous tritium (4 areas)	TSTA	4	2.0
Data acquisition system	TSTA, Mound	1	5.0[e]
			22.3–22.6
Atmospheric detritiation systems			
Tritium processing area system, 140 m^3/min or a flow rate of ~1 vol%/min		1	4[f]
Vault system, 140 m^3/min or a flow rate of ~0.5 vol %/min		1	4[f]
Hot cell system, 140 m^3/min or flow rate of ~0.5 vol %/min		1	4[f]
			12
	Grand total		34.3–34.6

[a]Mound = Mound Laboratories, Miamisburg, Ohio
TFTR = Tokamak Fusion Test Reactor
TSTA = Tritium Systems Test Assembly.

[b]Transfer pumps are included in each unit's cost; design, engineering, and installation costs are not included.

[c]Lower number for 10-h case, higher number for 100-h case.

[d]May increase if worst-case estimate for permeation rate is accurate.

[e]No software cost included.

Table 7.6. Dimensions of tritium system components

Component	Abbreviation	Dimensions, m	Volume, m^3
Atmospheric tritium recovery unit[a]	ATR	12 × 21 × 5	1260[b]
Isotope separation system	ISS	3 × 3 × 12	108
Fuel cleanup unit	FCU	6 × 2 × 2	24
Tritium waste treatment	TWT	5 × 5 × 5	125
Solid waste disposal	SWD	5 × 5 × 4	100
Transfer pump unit	TPU	4 × 1 × 2	8
Tritium storage		8 × 2 × 2	32
Tritiated water recovery units	TWRU	6 × 9 × 3	162
		3 × 4× 3	36
Glove box detritiation unit	GBD	5 × 5 × 5	125
Heating, ventilation	HVAC	8 × 6 × 5	240
Gas storage	He/N_2	1 × 1 × 1	1
Receiving glove box	RGB	4 × 1 × 2	8
Tool room			100
Chemistry analysis			100
Radiation monitor laboratory			100

[a]This unit is also referred to as the atmospheric detritiation unit and as the atmospheric tritium cleanup unit (ATCU).

[b]Compressor, 350 m^3. Other units (catalytic bed, cooler, dryer, molecular sieve beds, storage tanks), 910 m^3.

worker exposure levels, availability, and environmental release considerations. The release associated with venting a building volume of 10^5 m^3 is <10 Ci.

In selecting an adequate processing time, it is necessary to consider (1) the tightness of the building (i.e., the leak rate to the environment if negative pressure is not maintained), (2) the generation and/or adsorption of HTO on surfaces in the area, (3) the efficiency of the total system, and (4) the imperfect mixing present in any large area. It is assumed that leakage from the building is ≤1 vol %/h. If the leak rate is higher than this, then a greater burden is placed on the atmospheric detritiation systems because a more rapid processing rate is required to minimize environmental impact. This results in increased capital costs.

The effect of generation and/or adsorption of HTO on surfaces in a given area is shown in Fig. 7.5 for a 10-g release of either HT or HTO. In this figure, the cleanup time was calculated[5] assuming a process flow rate of 0.2 vol %/min for a building volume of 7.1×10^4 m^3. A sensitivity study was done in which the rate of net release of HTO was

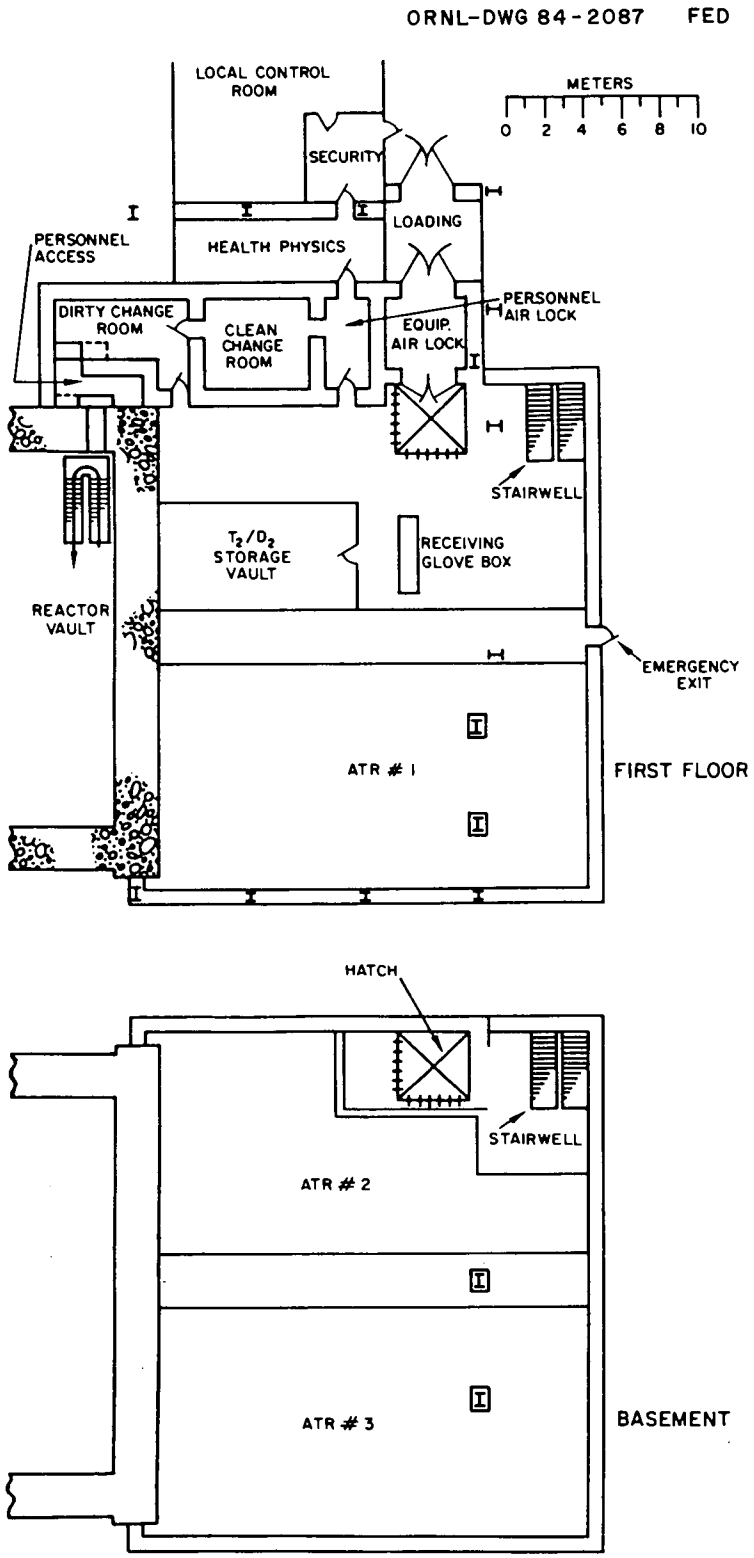

Fig. 7.3. Basement and first floor of tritium processing building.

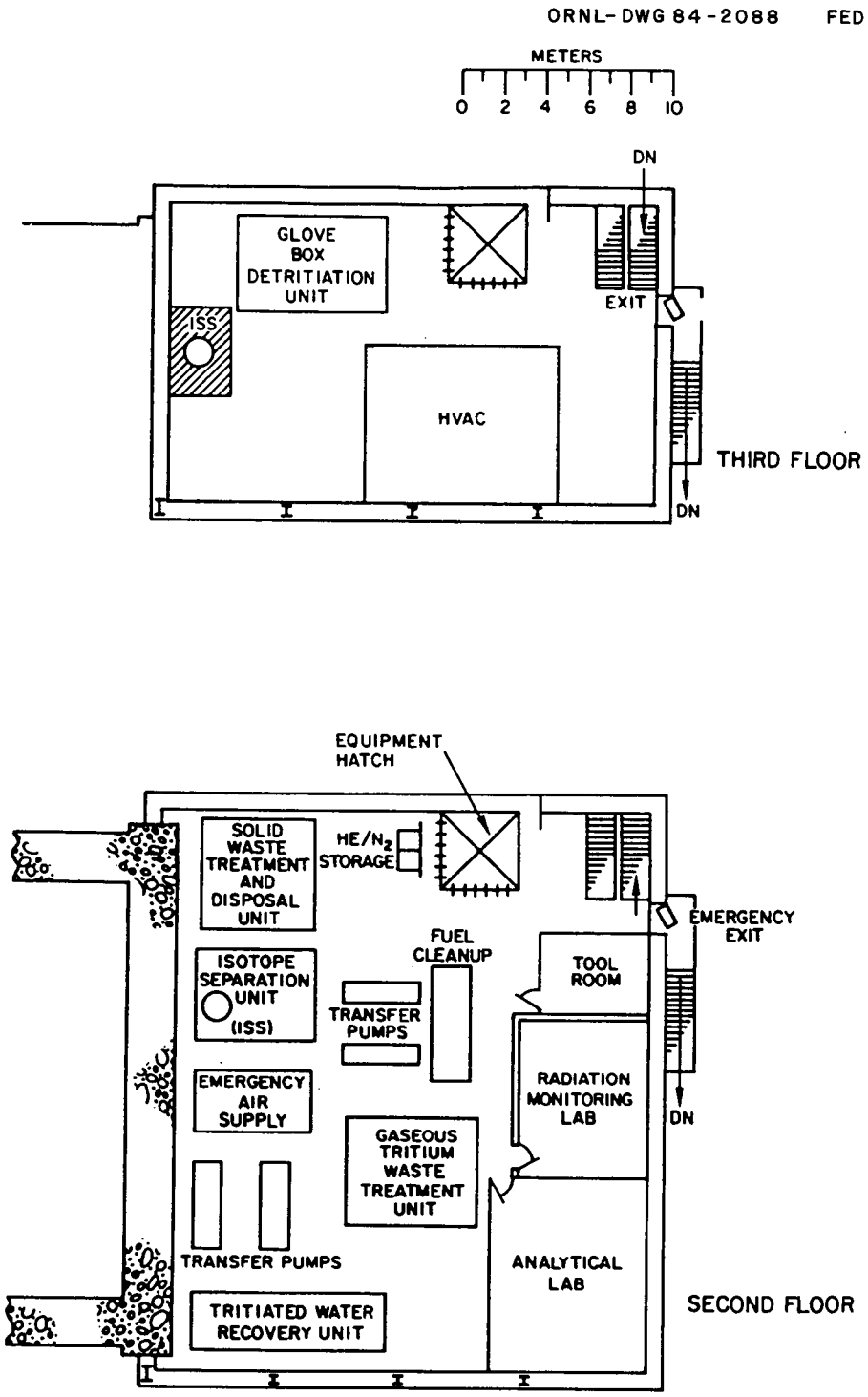

Fig. 7.4. Second and third floors of tritium processing building.

Table 7.7. Characteristics of working isotope separation systems

System	Processing capacity, g/year	T in protium	H or T in tritium, %
Cryogenic distillation	≥400[a]	10^{-6}–10^{-8} mol. fraction	~99
Thermal diffusion[a]	≤400	~0.1%	≥99.9
Palladium gas chromatography[a]	≤400	~0.1%	≥99.9

[a]Information provided by M. Rogers, Mound Laboratories, Miamisburg, Ohio.

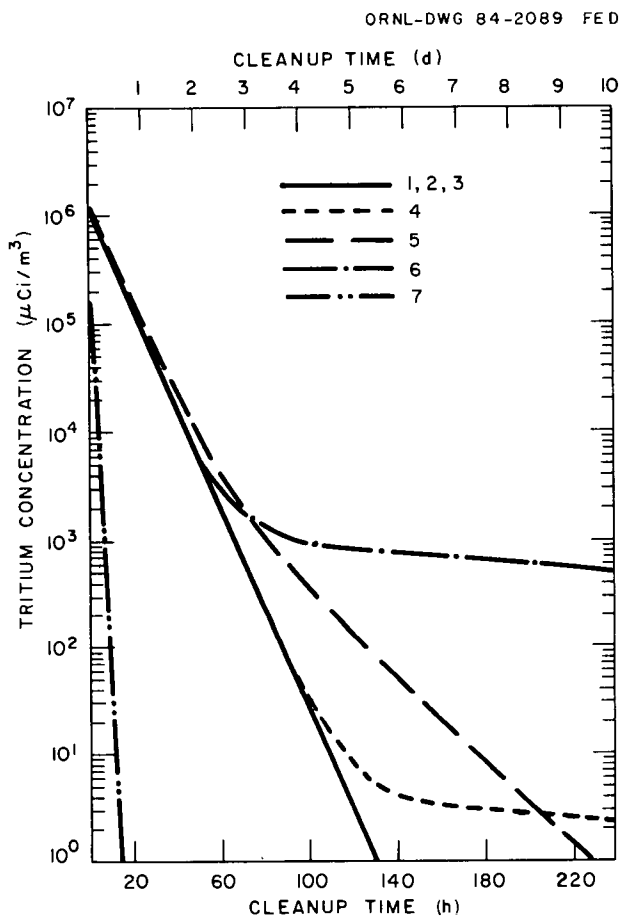

Fig. 7.5. Cleanup time required to reduce the atmospheric tritium concentration after a 10-g release. Flow rate = 0.2 vol %/min (144 m^3/min); building volume = 7.1 × 10^4 m^3; assumed surface area = 1 × 10^4 m^2. Case 1: 90% efficiency, HTO release; ratio of net release to adsorption = 100. Case 2: 90% efficiency, HT release with reaction rate of 10^{-13} m/μCi·s to form HTO, ratio of net release of HTO to adsorption = 100. Case 3: 90% efficiency, HT release with reaction rate of 10^{-13} m/μCi·s to form HTO, ratio of net release of HTO to adsorption = 10. Case 4: 90% efficiency, HT release with reaction rate of 10^{-13} m/μCi·s to form HTO, ratio of net release of HTO to adsorption = 1. Case 5: 90% efficiency, HTO release, ratio of net release to adsorption = 10. Case 6: 90% efficiency, HTO release, ratio of net release to adsorption = 1. Case 7: 100% efficiency, HT release with reaction rate of 10^{-13} m/μCi·s to form HTO, ratio of net release to adsorption = 100.

100 times, 10 times, or the same as the rate of adsorption. Limited laboratory experiments indicate that even with stainless steel walls, HTO is adsorbed on the walls and is not easily removed.[6] The main results are as follows.

- The minimum time to achieve 50 $\mu Ci/m^3$ is about four days. This requires that building or equipment surfaces release the tritiated water formed during cleanup of HT at a rate 1 to 100 times faster than it is adsorbed. To achieve cleanup of HTO in four days, the release rate must be 100 times faster than the adsorption rate.
- The minimum time to achieve 50 $\mu Ci/m^3$ during cleanup of HTO increases to six days if the release rate is only ten times faster than the adsorption rate.
- If the adsorption rate is equal to the release rate for cleanup of HTO, tritium concentrations level off at $\sim$400 $\mu Ci/m^3$ after ten days of detritiation.
- To achieve cleanup in less than 10 days to levels of 50 $\mu Ci/m^3$ with a process flow rate of 0.2 vol %/min, surfaces must be designed so that the HTO release rate is 10 to 100 times the adsorption rate.

The model does not account for elemental tritium, which diffuses at a low rate into some materials (e.g., stainless steel and aluminum) and at a high rate into others (e.g., plastics and concrete). Tritium lost because of diffusion must be accounted for and may be a problem when a plant is decommissioned. The amount that would diffuse when HT is released will increase as the processing rate decreases. In addition, the effect of cracks in surface coatings has not been addressed.

The effect of the system efficiency on cleanup time is also shown in Fig. 7.5. Cases 2 and 7 are identical except that the efficiency is 100% in case 7 and 90% in case 2, which is the realistic case. Lower efficiencies would mean that cleanup would be impossible to achieve or would take excessive amounts of time (>20 days).

The effect of an increased process flow rate is shown in Fig. 7.6 for a building with a volume of 7.1×10^4 m^3. The process flow rate is 0.4 vol %/min for cases 1 and 2; 0.2 vol %/min for cases 3 and 4. At the higher rate, cleanup of HT to 50 $\mu Ci/m^3$ is achieved in about two days. With optimistic surface conditions, cleanup in less than one day would require a process flow rate of $\geqslant$0.5 vol %/min.

Imperfect mixing in a large area is a problem in building design. Surfaces in unventilated areas may adsorb appreciable amounts of tritium. Thus, even with average atmospheric tritium levels below 50 $\mu Ci/m^3$, pockets of higher concentration could be present.

The processing rate also depends on the total volume to be processed. As the volume increases, the size or number of units needed to achieve a given processing rate increases rapidly. It would be cost-effective either to reduce the total building volume or to compartmentalize different sections so that the total building volume need not be processed at one time. If compartmentalization is used, the area must be designed so that access is available for normal maintenance and for construction and removal operations.

The effect of the amount of tritium released on the cleanup time may be approximated by decreasing the ordinate in Fig. 7.5 by a factor of 10 as the tritium release decreases by a factor of 10. Thus, for a 1-g release, the tritium concentration after two days of cleanup is $\sim$300 $\mu Ci/m^3$, whereas for a 10-g release it is $\sim$3000 $\mu Ci/m^3$. In determining the required processing flow rate, the units are sized not for the worst-case

ORNL-DWG 84-2090 FED

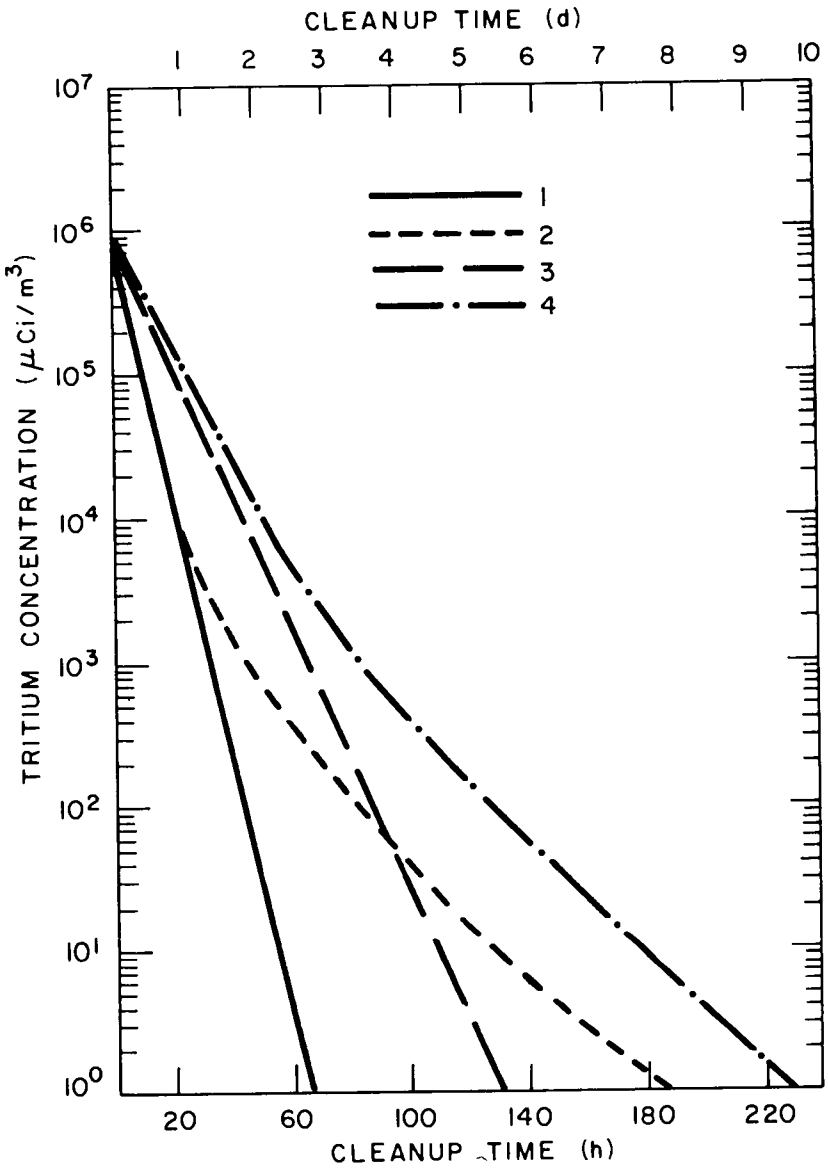

Fig. 7.6. Cleanup time required to reduce the atmospheric tritium concentration after a 10-g release for flow rates of 0.4 vol %/min (288 m^3/min) and 0.2 vol %/min (144 m^3/min) for a building volume = 7.1 × 10^4 m^3 and an assumed surface area = 1 × 10^4 m^2. Case 1: flow rate = 0.4 vol %/min, HT release with reaction rate of 10^{-13} m/μCi·s to form HTO, ratio of net release to adsorption = 10. Case 1: flow rate = 0.4 vol %/min, HT release with reaction rate of 10^{-13} m/μCi·s to form HTO, ratio of net release to adsorption = 10. Case 2: 0.4 vol %/min, HTO release, ratio of net release to adsorption = 10. Case 3: 0.2 vol %/min, other parameters same as case 1. Case 4: 0.2 vol %/min, other parameters same as case 2.

release but for the most probable release. This value may be minimized by good design practices for all tritium systems, as well as by minimizing the tritium content of all systems.

The plant availability is an important factor in determining the process flow rate. In the tritium processing building, the desired availability would be high (>50%). Therefore, the process flow rate required would be ≥0.5 vol %/min. In a reactor building with 1% availability for reactor operation and <20% availability for all other operations, a process flow rate of 0.2 vol %/min should be adequate, though this would not be the case for higher availability (i.e., ≥10% availability for reactor operation).

Location of units

The location of the atmospheric detritiation units depends on several important considerations. First, the main tritium processing area is designed to be free of gamma radiation, so the units in this area must prevent the entry of gamma-activated dust from the reactor or the hot cell. Second, atmospheric detritiation units must be located so that required maintenance can be performed while the units are operating. This is important for slow processing rates and units that are in operation for several days at a time and is extremely important for high-availability devices with units that may be in operation every day.[7] Third, units should be located so that they will not be disabled by fire. Fourth, if the connecting ducts are very narrow, extremely long, or tortuous, double or triple the speed at the building source may be required at the compressor, so it seems advantageous to locate compressors near the source. (The other units, dryers, storage tanks, etc., may be sited in other areas.) Last, the atmospheric detritiation units should be located so that they can be used during decommissioning, when all surfaces are to be decontaminated.

System requirements

Operating conditions within the plant were analyzed to determine the atmospheric detritiation requirements. The following assumptions were made.

- Building volumes (uncorrected for occupied space): reactor, 3×10^4 m^3; hot cell, $<1 \times 10^4$ m^3; tritium facility, 1×10^4 m^3.
- Availability (for a given area, includes maintenance, accidents, and reactor operation): usually 100%.
- Reactor operation with tritium: ≤10% availability.
- Tritium present in reactor building (Table 7.1): for reactor operation, <40 g (as T_2 and DT) total, <10 g in vulnerable components; for other purposes (beam dump maintenance, coolant maintenance, neutral beams), <20 g (as HT, DT, and HTO).
- Tritium present in hot cell: for beam dump maintenance and neutral beam sources, <20 g at steady state (as HT and DT).
- Tritium present in tritium facility: for tritium operation, <300 g (as T_2, DT, HT, and small amounts of HTO).
- Cleanup rates: at levels that will compensate for imperfect mixing; achieve adequate cleanup in the different buildings, each of which has a different function; account for adsorption/desorption on all surfaces (this becomes dominant as

the cleanup rate decreases); account for cleanup during maintenance or accident conditions; and achieve 50 $\mu Ci/m^3$ to minimize environmental tritium losses.

- Operating capability: either designed with redundant units or designed so that even with partial failure the system will be adequate (necessary because atmospheric tritium removal units are safety systems).

The maintenance and accident scenarios described in Table 7.8 were analyzed based on these assumptions and on a cleanup time of less than ten days for the reactor building and hot cell and of about one day for the tritium facility (where daily access is required).

Table 7.8. Tritium release scenarios used in analyzing atmospheric detritiation requirements

	Possible release	Amount
	Maintenance	
Reactor building	Coolant leaks	1–100 Ci/d
	Beam dumps, neutral beam sources, or halo scraper modules	<10 Ci/d
	Removal of test modules	
Hot cell	Beam dump, neutral beam sources, or halo scraper modules	<10 Ci/d
	Other activated components	<1 Ci/d
	Test modules	
Tritium facility	From secondary containment	<0.1 Ci/d
	Accident	
Reactor building	Break in line during reactor operation	<1 g
	Failure of neutral beam or end-cell cryopanels	<10 g
Hot cell	Heating of beam dump or halo scraper modules	~20 g
	Test modules	
Tritium facility	Break in processing line	<10 g
	Failure of primary and secondary containment of isotope separation unit	<200 g
	Failure of primary and secondary containment plus heater failure of one tritium storage bed	<50 g
	Failure of surge tank	<5 g

Range represents dependence on magnitude of all leaks (10–100 L/d) and on coolant concentration (0.01–1 Ci/L).

Function of component material and afterheat temperature.

During cutting operations or tritium removal operations, most of the tritium dissolved could be released.

Reactor building. The worst case for the reactor building[7] is the maintenance scenario in which 100 Ci/d could be released from the coolant system. If it is assumed that tritium migration will be minimized, a unit capable of ~142 m^3/min (0.5 vol %/min) is required to provide cleanup during operation.

Hot cell. The worst case for the hot cell is the accident scenario in which <5 g of tritium is released from a beam dump. To achieve cleanup in less than five days, the required processing flow rate is 50 m^3/min (~0.5 vol %/min). A 142-m^3/min unit is provided to serve as a backup for the reactor building unit.

Tritium facility. The most probable accidents are the failure of a line and the failure of a surge tank, either of which would release <10 g. The release of ≤200 g requires two simultaneous failures; that of 50 g, three simultaneous failures. The tritium facility units are isolated from the other atmospheric detritiation units to prevent gamma contamination; therefore, since they are a safety system, redundancy is required. A total unit flow of 144 m^3/min is provided. This is well above the level required to achieve cleanup in one day of a 10-g release to 50 μCi/m^3, ~100 m^3/min (1.0 vol %/min).

Recommendations

Space for three atmospheric detritiation systems, each with a capacity of 144 m^3/min, is required. The units serving the reactor building and the hot cell are safety backups for each other. In the tritium facility, five 30-m^3/min units provide the necessary processing rate plus redundancy. The space for these five systems should be equivalent to or slightly larger than that required for one 144-m^3/min unit. The estimated cost of these systems (not including design or installation) is $12 million.

7.4.3 Coolant Systems and Tritium Migration

To evaluate the magnitude of tritium migration into the coolant (and thus its effect on tritium concentration in the coolant), it was assumed that the device produces <20 MW of fusion power and has an availability of ≤10%. Migration may be modeled using a case in which the first wall is the source. The temperature gradient in a wall of type 304 stainless steel is ~300°C with an upper temperature of 400°C. The wall was assumed to have a surface area of ~400 m^2 and to be >0.5 cm thick near the water coolant. Three cases were considered: a clean surface, with a permeation rate at steady state of 50 Ci/d; a semiclean surface, with a permeation rate at steady state of 500 Ci/d; and a dirty surface, with a permeation rate at steady state of 5000 Ci/d. The water coolant volume was assumed to be ~10^5 L. Tritium concentrations after ten years are listed in Table 7.9. For

Table 7.9. Tritium concentration in coolant after ten years of operation

	At 1% availability, Ci/L	At 10% availability, Ci/L
Clean surface	<0.01	<0.2
Semiclean surface	<0.2	<2
Dirty surface	<2	<20

a dirty surface at 1% availability, a tritiated water recovery unit (TWRU) may be required; for a dirty surface at 10% availability, a TWRU will definitely be required to reduce the <20-Ci/L level. The unit provided would reduce the level to <10 Ci/L. A large unit, with associated capital costs of about $15 million, would be needed to reduce this concentration to <1 Ci/L. For all but the case of a dirty surface at 10% availability, the $3 million unit appears adequate.

Since the water system is isolated from all other site water systems and from public systems, no public water supply contamination is seen for either 1% or 10% availability. However, at 10% availability, appreciable amounts of tritium may enter the water system, and worker protection will be required even if a water detritiation system is used.

An associated issue is the question of tritium retention in the structure. The amount retained depends on the number of traps; the trapping energy, which could range from 0.7 to 1.0 eV;[7] the availability, which determines actual operating time; and the surface conditions. After 10 years of operation at 1% availability (0.1 year, real time), the tritium content in the structure for the case considered here could range from ~1 g for a clean surface to 100 g for a dirty surface. After 10 years of operation at 10% availability (1 year, real time), the tritium content could range from ~20 g (clean surface) to 1000 g (dirty surface). For both levels of availability, the lowest estimate should approximate reactor conditions after ten years because the wall of the reactor could be annealed, which would remove the tritium traps.

7.4.4 Test Module Systems

Tritium control measures must be provided for the blanket test modules. The areas to be focused on during the design phase include

- removal of the module after irradiation;
- design of the module to prevent tritium permeation into the reactor vault or other reactor structures;
- design of the heat removal apparatus, including its location, the method of dismantling the apparatus, and the connections and leakage rates involved;
- design of the tritium recovery apparatus, including its location, the method of dismantling the apparatus, the connections and leakage rates involved, and techniques for demonstration of recovery.

Additional guidelines will be provided when the size, function, and scope of the test program are decided.

7.5 ACCIDENT SCENARIOS

The current radiation dose limits for acute and chronic exposure established by the Nuclear Regulatory Commission (NRC), the Department of Energy (DOE), and the Environmental Protection Agency (EPA) are shown in Table 7.10. The chronic dose resulting from a routine release of 5000 Ci of tritium per year is shown in Fig. 7.7, and the acute dose for a release of 100,000 Ci is shown in Fig. 7.8. The MFTF-α+T site has a radius of ~1 km for its public exclusion boundary and is equipped with a 100-m-high stack. Thus, for the conditions considered, any radiation dose that the public receives will be well below the guidelines listed in Table 7.10.

Table 7.10. Radiation dose limits

	Chronic exposure, rem/year		Acute exposure, rem/year	
	Public	Worker	Public	Worker
EPA	0.01,[a] 0.03[b]			
DOE	0.5	5	25	25
NRC	0.005[a]	0.5	25	25

[a]Whole body.
[b]Organ.

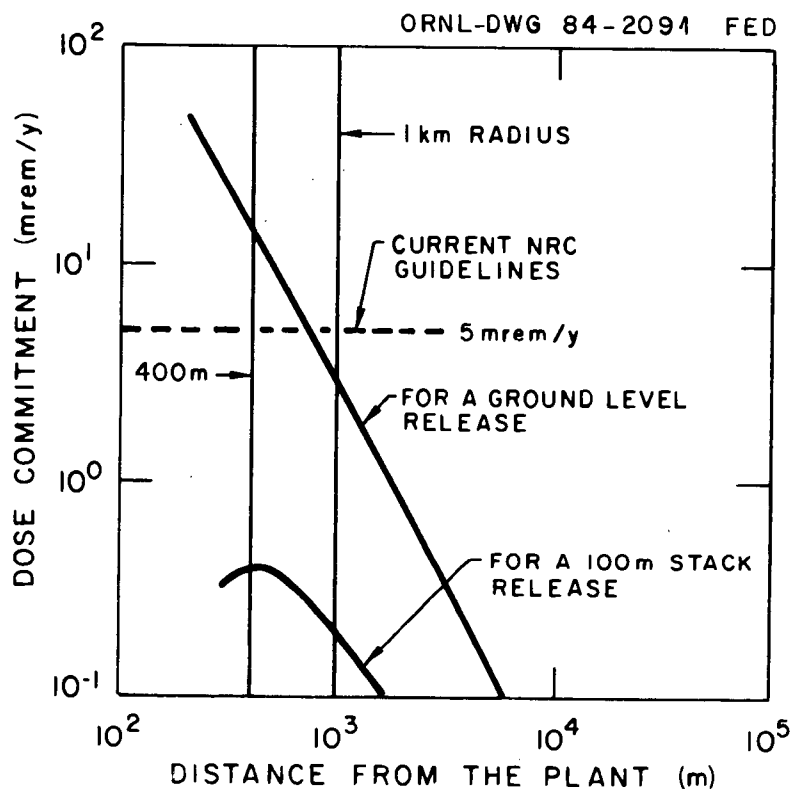

Fig. 7.7. Chronic dose received by the public from inhalation and skin exposures to a 5000-Ci/year routine release of tritium.

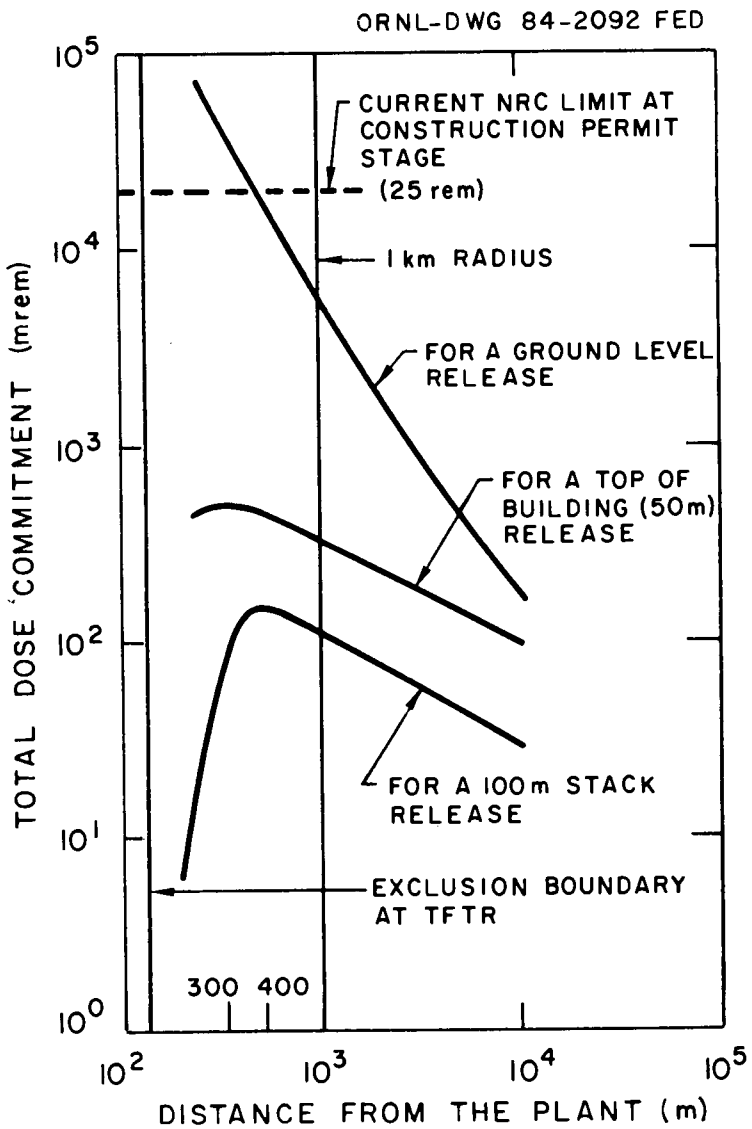

Fig. 7.8. Acute dose received by the public from inhalation and skin exposures to a 100,000-Ci (10-g) accidental release of HTO.

7.6 OPERATING CONSIDERATIONS

7.6.1 Assessment of Tritium Sources

The tritium needs of fusion reactors producing from 60 to 3600 MW at 10% to 50% availability were assessed. The amounts of tritium needed for a breeding ratio *BR* of 0, 0.6, 0.8, and 1.0 are shown in Table 7.11. The tritium needs for *BR* = 1.0 include the steady-state inventory (~3 kg for 600 MW, 10 kg for 1000 MW, and 10 kg for 3600 MW) and the associated decay losses. The assumed tritium production from

Table 7.11. Tritium needs of fusion reactors (in kilograms)

Availability, %	Power, MW 60	360	600	1000	3600
		***BR* = 0**			
50	1.8	10.5	18.0	27	105
20	0.7	4.2	7.3	10	42
10	0.4	2.1	3.7	5	21
		***BR* = 0.6**			
50	0.75	4.0	7.5	10	42
20	0.3	1.7	3.0	4	17
10	0.5	0.8	1.5	2	8
		***BR* = 0.8**			
50			3.6	5.2	21.0
20			1.4	2.0	8.4
10			0.7	1.0	4.2
		***BR* = 1.0[a]**			
≥50			5	12	12

[a]Includes the steady-state inventory of 3 kg, 10 kg, and 10 kg of tritium for 600 MW, 1000 MW, and 3600 MW, respectively.

CANDU plants is shown in Table 7.12. The reactor scenarios possible when tritium from the maximum number of heavy-water reactors becomes available, assuming reactor operation begins in 1995, are listed in Table 7.13. It may be seen that constructing a reactor with fusion power ≥360 MW requires a breeding blanket. The tritium production from the coolant in a heavy-water reactor is not sufficient to supply fueling needs, but it can cover decay and environmental losses.

7.6.2 Tritium Needs of an FPD

The tritium-related needs of a Fusion Power Demonstration (FPD) differ from those of MFTF-α+T in (1) the amount of tritium needed to maintain a burn at higher power and availability, (2) the tritium mass flow rates and inventories required within the plant for a base case, (3) the number of tritium systems required, and (4) the level of tritium control within the plant.

A nominal case of 400 MW of fusion power with a burn efficiency of 2% was evaluated. The amount of tritium burned in a 400-MW D-T reactor and its cost are shown in Fig. 7.9 as a function of availability. The amount of tritium needed for higher and lower fusion power can be determined by the equation

$$\frac{\text{desired power (MW)}}{400\ \text{MW}} \times \frac{\text{availability at desired power}}{\text{availability at 400 MW}} .$$

Table 7.12. Tritium production (in kilograms) from CANDU plants

	Year			
	1990	1995	2000	2005
Maximum number of plants; no decay since used immediately	2.9	10.5 (13.4)[a]	27.0 (40.4)	33.0 (73.4)
Minimum number of plants; no decay since used immediately	2.9	6.6 (9.5)	10.2 (19.7)	23.0 (42.7)
Maximum number of plants; decay included	2.3	(9.2)	(26.0)	(41.0)
Minimum number of plants; decay included	2.3	(6.3)	(12.0)	(25.0)

[a]Parentheses indcate cumulative totals.
Source: Ontario Hydro personnel.

Table 7.13. Reactor scenarios supported by tritium production levels

BR	Fusion power, MW	Availability, %
0	60	20–50
0	360	10–20
0.6	600	10–20
0.6	1000	10
0.8	600	20–50
0.8	1000	20
1.0	600–3500	>50

For a 100-MW reactor with 10% availability, the amount needed is 560 g/year. At \$1/Ci, the cost would be \$5.4 million.

The tritium and deuterium mass flow rates for a 400-MW D-T reactor are shown in Fig. 7.10. The reactor is assumed to have a blanket with $BR = 1.0$ that supplies the ~3 g/h of tritium burned. The tritium from the blanket is recovered in a blanket tritium recovery system (not yet specified) and purified in the fuel cleanup unit (FCU). If no blanket is used, then the ~3 g/h of tritium burned must be supplied from storage (~300 g for 100 h of operation, or a total of ~810 g in storage). The types of tritium systems needed are shown in Fig. 7.11. Storage needs are higher than for devices with lower availability (4 h vs 1 h of fuel). A larger TWRU may be needed (if water is the coolant) to handle the increased permeation resulting from the higher power and availability.

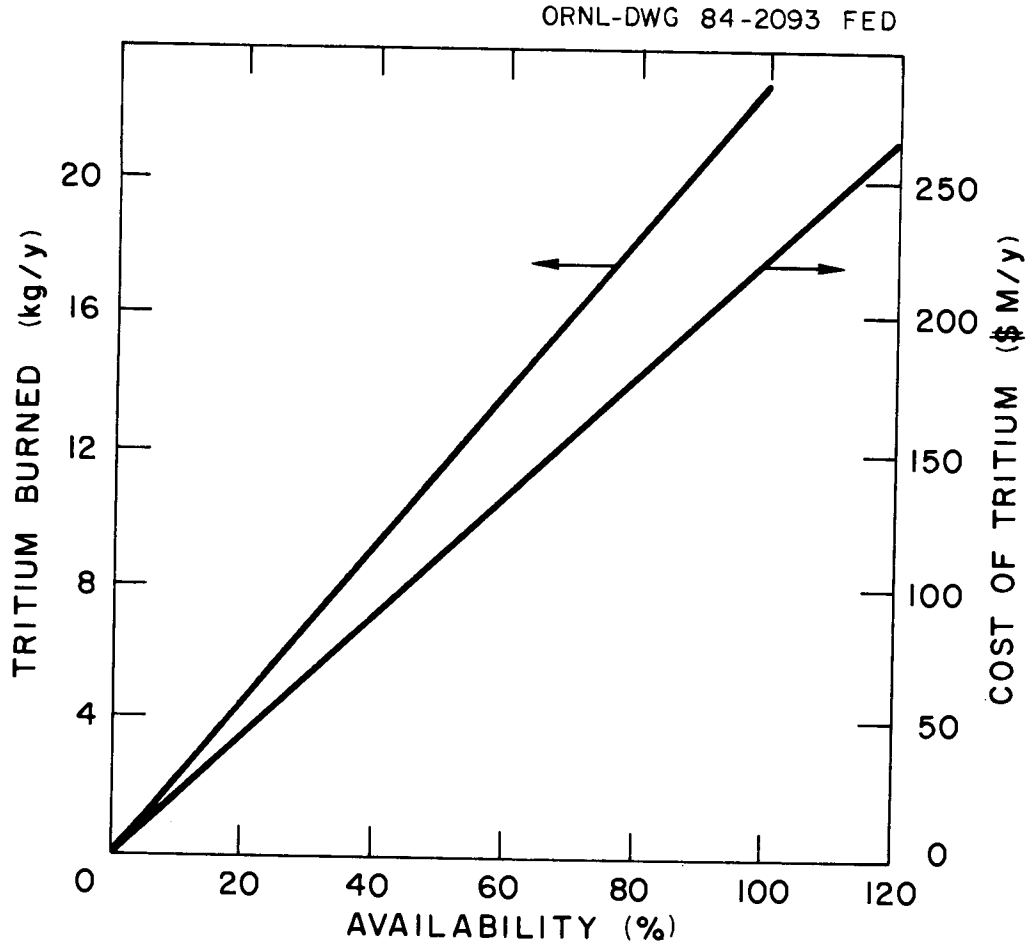

Fig. 7.9. Amount and cost of tritium burned in a 400-MW device as a function of availability.

Systems with major tritium inventories at steady state are shown in Table 7.14. Within the vault, there are three locations at which the inventory can only be estimated: the structure, the coolant, and the blanket. Estimates for the structure and the coolant have been derived, but the presence and function of the blanket must be more fully defined before further analysis can be done.

Tritium inventories in the vault increase from ~20 g for MFTF-α+T producing <20 MW at <10% availability to ~440 g for an FPD producing 400 MW at >10% availability. Within the processing area, inventories increase from ~420 g for MFTF-α+T to ~860 g for FPD because more storage is needed to ensure the higher availability at higher power.

As a consequence of the increased inventories, the atmospheric processing systems must be reevaluated. In the processing area, a rate of 1 vol %/min is required; in the vault, a rate of 0.5 vol %/min should be sufficient if the building is leaktight (<1 vol %/min). The rates are the same as those for MFTF-α+T, but because a

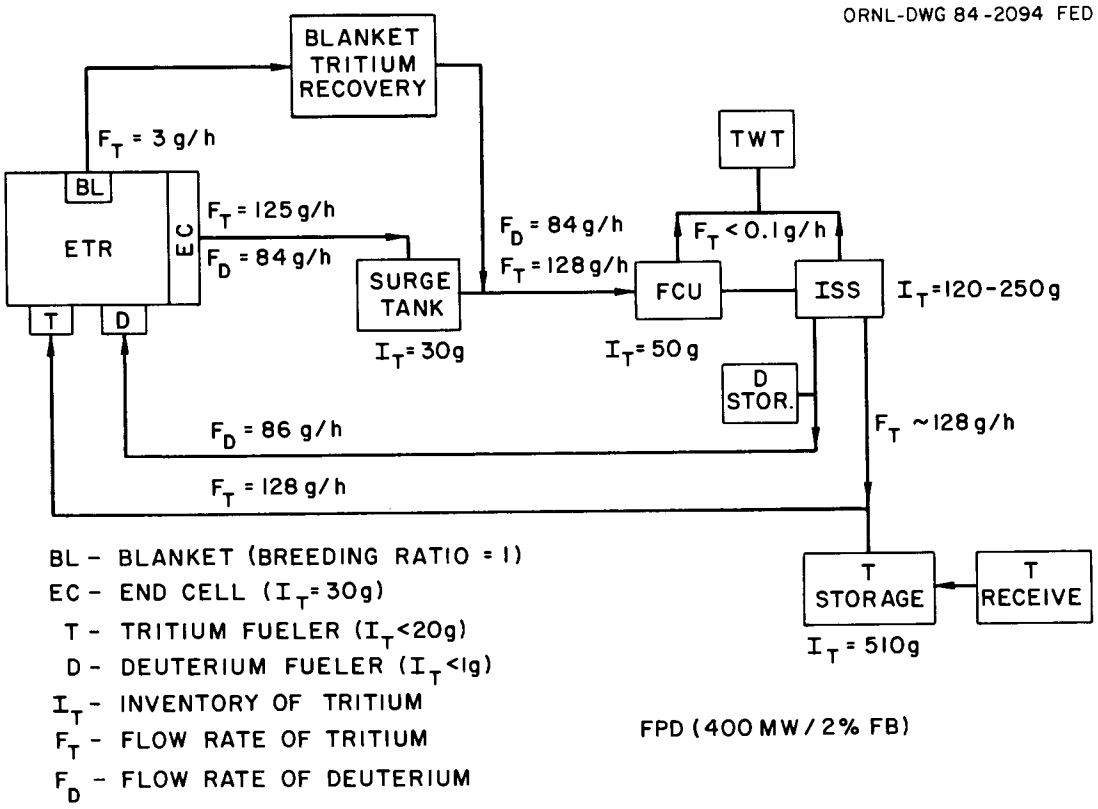

Fig. 7.10. Tritium mass flow rates for a 400-MW D-T mirror reactor.

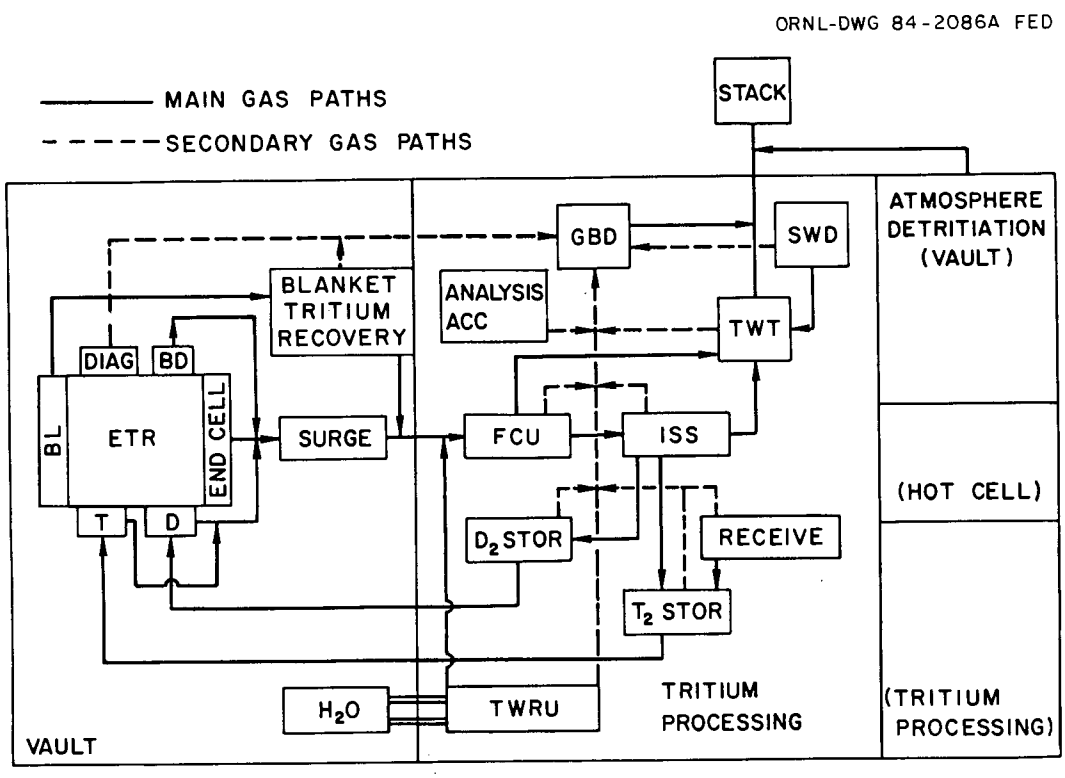

Fig. 7.11. Tritium flow paths for a 400-MW D-T mirror reactor.

Table 7.14. Summary of tritium inventories for a 400-MW FPD with a fractional burn of 0.02

Location	Amount, g
Vault	
Fuelers	20
End cells[a]	30
Surge tank	30
Structure[b]	5–350
Water coolant[b]	<10
Blanket	c
Total	95–400
Processing	
Fuel cleanup	50
Isotope separation	120–250
Storage for 4 h of fuel[d]	510
Blanket recovery	<50
Total	<730–860
Site total	<825–1300

[a]Regenerable cryopanels; one-sixth of area processed every 10 min.

[b]Dependent on temperature, material, and operating condition.

[c]Dependent on material, size, etc.

[d]Assumes a blanket.

400-MW FPD would probably occupy a larger volume, more units would be needed to maintain a given rate. If these units are located in the processing building, they increase the size of the building and also the number of units required for the processing area. A trade study is recommended to determine the minimum volume required, and the level of redundancy needed to achieve the desired availability should also be assessed.

7.7 KEY ISSUES

A continuous tritium processing system is proposed for MFTF-α+T with the goal of minimizing on-site tritium inventory. The atmospheric detritiation systems are designed for a flow rate of 0.5 vol %/min in the reactor and hot cell (10% availability) and 1.0 vol %/min in the tritium processing area. A tritiated water processing system is provided. The total tritium inventory is <400 g for 1% availability (10-h burns) and <500 g for 10% availability. The site boundary is at a 1-km radius. The total capital cost is $35 million, and the tritium cost for ten years of operation, assuming a cost of $1/Ci, is less than $8 million.

REFERENCES

1. J. Anderson et al., *Final Safety Analysis Report of the Tritium Systems Test Assembly*, SAR-82-1F, Los Alamos Natl. Lab., Los Alamos, N.Mex., 1982.

2. A. Sherwood, Lawrence Livermore National Laboratory, Livermore, Calif., personal communication.

3. *Environmental Survey of Transportation of Radioactive Materials to and from Nuclear Power Plants*, WASH-1238, U.S. Government Printing Office, December 1972.

4. P. A. Finn and M. L. Rogers, "The Effects of Tritium Contamination in the FED/INTOR Reactor Hall," presented at the 5th Topical Meeting on the Technology of Fusion Energy, Knoxville, Tenn., April 1983.

5. R. H. Land, V. A. Maroni, and M. Minkoff, *TSOAK-M1: A Computer Code to Determine Tritium Reaction/Adsorption/Release Parameters from Experimental Results of Air-Detritiation Tests*, ANL-79-82, Argonne Natl. Lab., Argonne, Ill., 1979.

6. P. A. Finn et al., "The Wall Tritium Concentration as a Factor in Fusion Reactor Hall Design," presented at the 5th Topical Meeting on the Technology of Fusion Energy, Knoxville, Tenn., April 1983.

7. M. Abdou et al., "Tritium and Blanket," Chap. VIII in FED-INTOR/TRIT-82-5, 1982.

8. VACUUM VESSEL, SUPPORT STRUCTURE, AND NUCLEAR SHIELDING

J. Kirchner

McDonnell Douglas Astronautics Company/Fusion Engineering Design Center

CONTENTS

8.1 INTRODUCTION 8-3
8.2 REQUIREMENTS AND GUIDELINES 8-3
8.2.1 Vacuum Vessel 8-3
8.2.2 Support Structure 8-3
8.2.3 Nuclear Shielding 8-4
8.3 DESIGN DESCRIPTION 8-4
8.3.1 Vacuum Vessel and Support Structure 8-4
8.3.2 Nuclear Shielding 8-18
8.4 STRUCTURAL ANALYSIS 8-28
8.4.1 End-Cell Double-Walled Vacuum Vessel 8-28
8.4.2 End-Cell Vacuum Vessel End Ring 8-28
8.4.3 End-Cell Magnet Shield Support 8-30
8.5 TRADE STUDIES 8-31
8.5.1 Vacuum Topology 8-31
8.5.2 Bulk Shield Location and Composition 8-38
8.5.3 Water Bulk Shield Location and Material Selection 8-44
8.5.4 Maintenance Considerations 8-46

8. VACUUM VESSEL, SUPPORT STRUCTURE, AND NUCLEAR SHIELDING

8.1 INTRODUCTION

The MFTF-α+T vacuum vessel provides the required vacuum integrity for the plasma and structural support for the nuclear shielding, magnets, test module, halo scraper, and direct converter. The vacuum vessel is the main load-carrying structure and transmits the loads through the support structure to the foundation. Hatches in the top of the vacuum vessel provide direct access to components for their replacement. The end-cell vacuum vessel is an integral part of the nuclear shielding system in this region of the machine.

8.2 REQUIREMENTS AND GUIDELINES

Four design requirements have been determined for the vacuum vessel, support structure, and nuclear shielding of MFTF-α+T. These systems must (1) maintain their structural integrity after a 0.5-g seismic event, (2) support the 13.43-MN magnetic centering load on the end-cell coil set, (3) provide sufficient nuclear shielding to achieve a dose rate of 0.5 mrem/h 24 h after shutdown, and (4) protect the internal components from nuclear-induced heating and damage. In addition to these requirements, design guidelines and functional requirements have been established for the vacuum vessel, the support structure, and the nuclear shielding.

8.2.1 Vacuum Vessel

The vacuum vessel must

- maintain base and operating vacuum,
- serve as a superconducting (SC) coil Dewar flask,
- support the magnet system, bulk shielding, test module, halo scraper, direct converter, and other related components,
- provide an interface for the central-cell beams and end-cell sloshing beams,
- provide an interface for the beam dumps,
- provide an interface for the rf heating components,
- provide an interface for diagnostic and control instrumentation, and
- maintain vacuum integrity after a 0.5-g lateral and vertical seismic acceleration.

8.2.2 Support Structure

The support structure must

- support the deadweight of the vacuum vessel, magnets, test module, bulk shield, halo scrapers, direct converters, and miscellaneous equipment and
- react the loads induced by seismic events.

8.2.3 Nuclear Shielding

The nuclear shielding must

- protect the SC coils from local heating, neutron fluence, insulation damage, and damage to the copper stabilizer (dpa);
- reduce total nuclear heating; and
- provide biological protection by limiting the shutdown dose rate to 0.5 mrem 24 h after shutdown to allow hands-on maintenance at the outside surface of the vacuum vessel.

8.3 DESIGN DESCRIPTION

8.3.1 Vacuum Vessel and Support Structure

The MFTF-α+T vacuum vessel and its support structure are shown in Fig. 8.1. The type 304L stainless steel vacuum vessel has an outside diameter of 8.3 m and is 65.0 m long at its axial centerline. The vacuum vessel is divided into three distinct regions: the central cell and the two end cells.

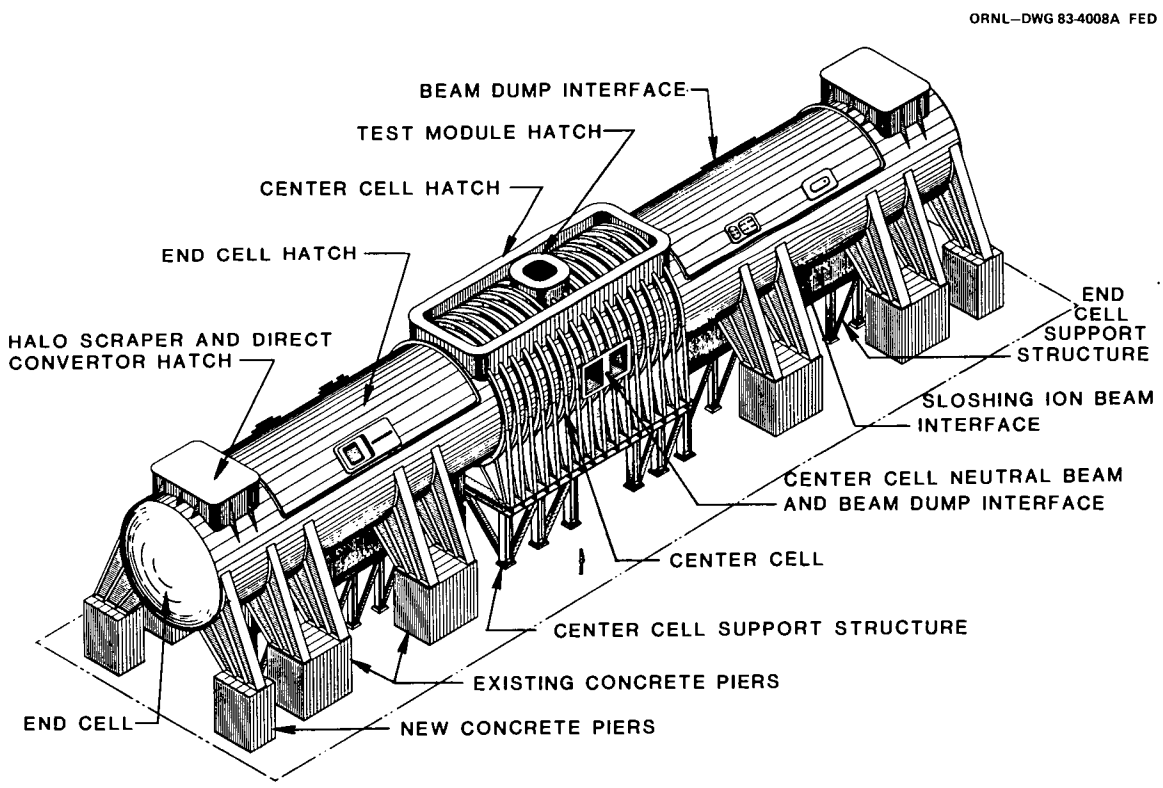

Fig. 8.1. MFTF-α+T vacuum vessel and support structure.

Central-cell vacuum vessel

The central-cell vacuum vessel (Fig. 8.2) is 18.0 m long and 8.3 m in diameter. This diameter is the same as that of the Mirror Fusion Test Facility (MFTF-B) and allows space for the MFTF-B solenoid coils (S1–S5) and their supports. Coincidentally, the end cells have the same diameter as the central cell.

A 5.6-m-wide access hatch extends over the top of the central-cell vacuum vessel from $Z = +8.9$ m to $Z = -8.9$ m, as shown in Fig. 8.3. The opening provides access to the axicell coils, eight of the ten solenoid coils, and the bulk shield in the solenoid area. Two of the solenoid coils (S5) require longitudinal translation before they can be removed from the vacuum vessel. Figure 8.4 shows the clearances needed for this hatch and for the adjacent end-cell access hatches. Because the 18-T coils are so close to the S5 coils, there

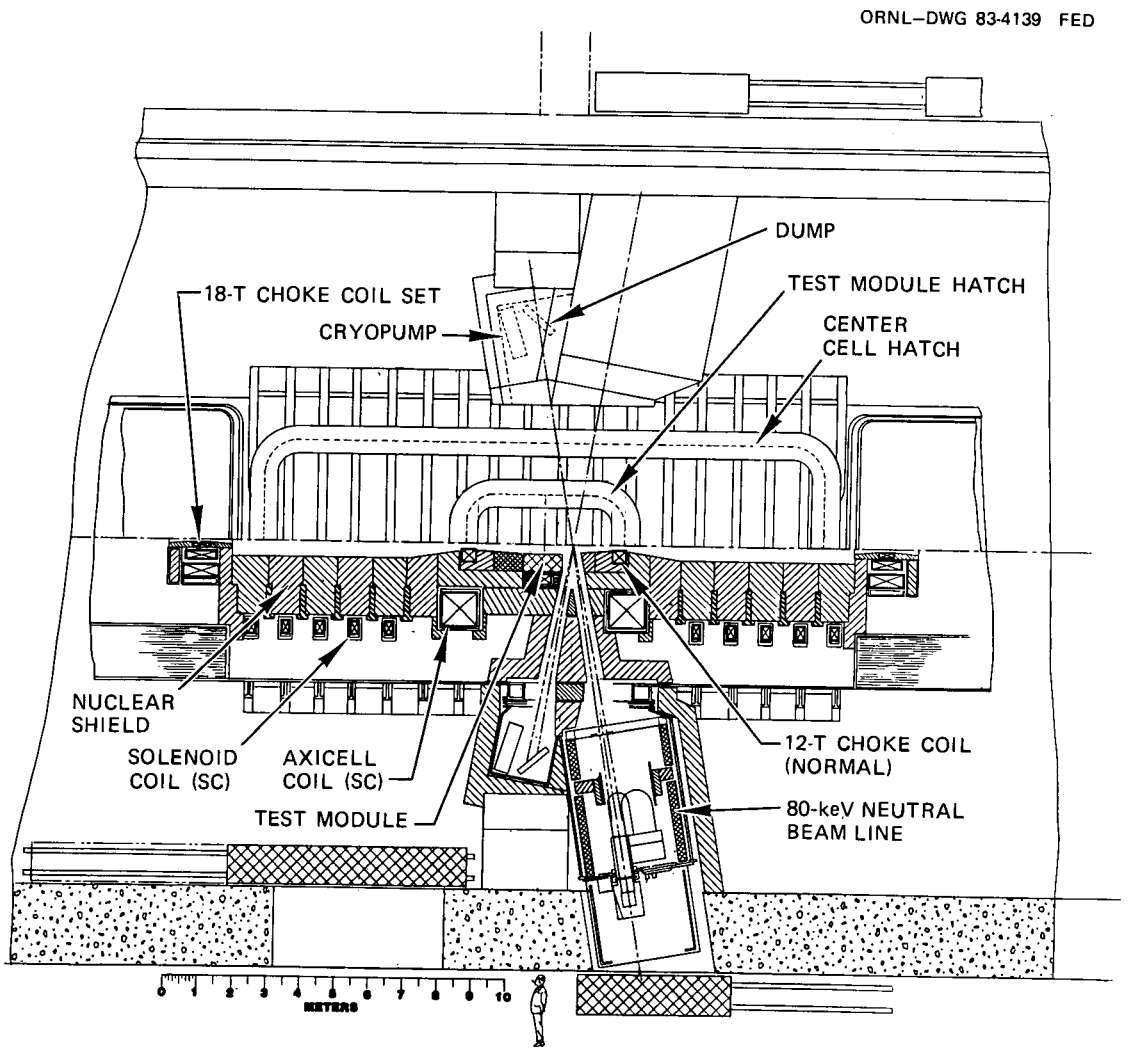

Fig. 8.2. Plan view of central-cell vacuum vessel.

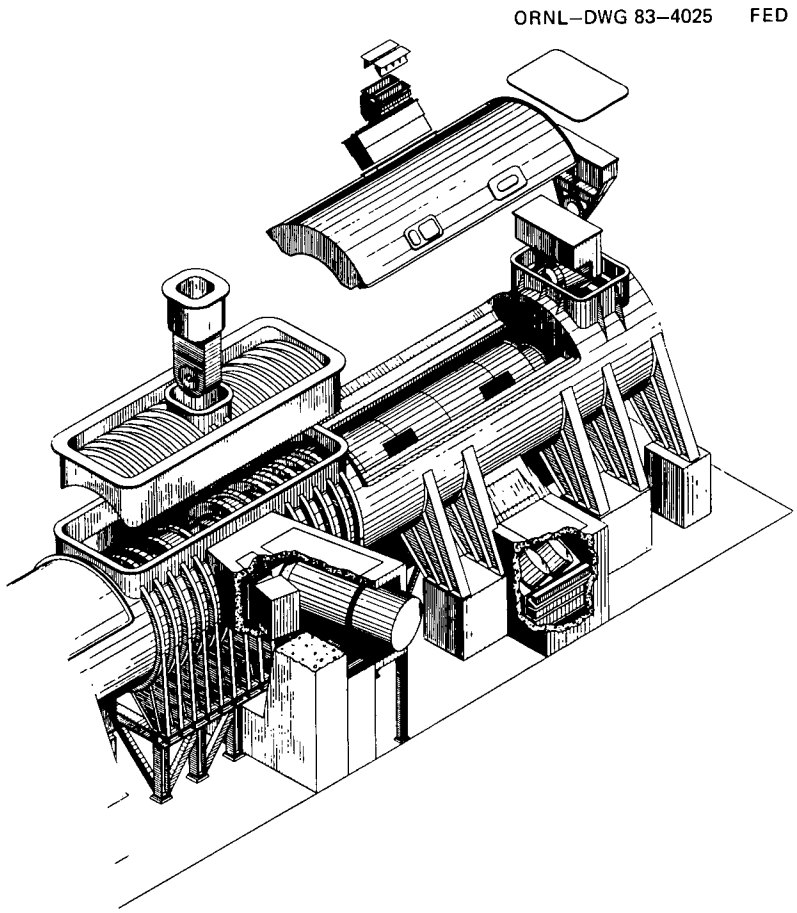

Fig. 8.3. End cell and central cell showing main access hatch.

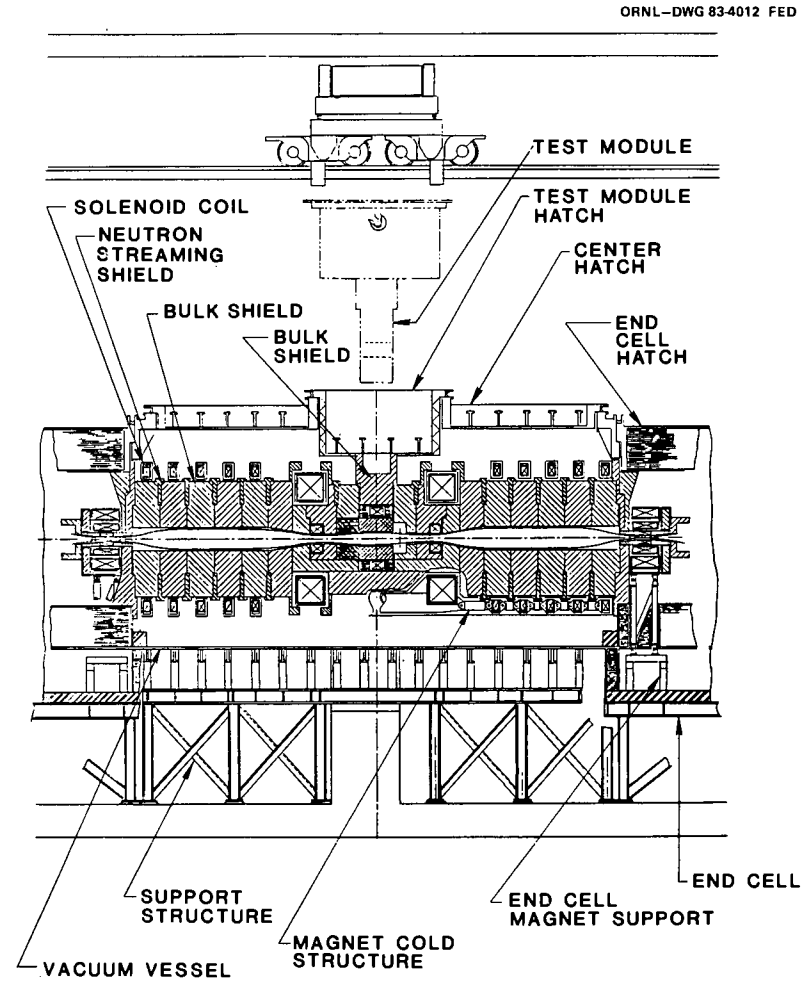

Fig. 8.4. Clearances needed for central-cell and end-cell access hatches.

is not enough room for two adjacent hatch seals. Because the S5 coils are considered lifetime components and the insert for the 18-T coil will probably require replacement, direct vertical lifting of the 18-T coil for maintenance was considered more important.

The vessel is supported against the side wall pressure loading not by the central-cell hatch but by the action of the cover sill beam and the circumferential stiffeners with their companion leg frames (Fig. 8.5). The pressure load is carried by the stiffeners up to the sill beam and down to the leg frames. The sill beam carries the load to the ends of the hatch opening, where it is balanced across the top of the vessel. The leg frames carry their load across the bottom of the vessel. The leg frames and their companion stiffeners also act as bending frames (Fig. 8.6). The locations of the stiffeners and leg frames correspond to the coil locations (Fig. 8.2). The stiffeners introduce the coil support strut loads to the vessel (Fig. 8.7), and secondary axial beams carry the nuclear shield support strut loads (which consist of the deadweight and vertical seismic loads) to the stiffeners. The nominal central-cell axial magnetic loads (Fig. 8.8) are balanced with a cold structure and thus are not carried by the vessel. The magnet fault loads, which are not yet defined, will be transmitted to the vacuum vessel by a set of axial load struts (Fig. 8.9). These struts will also support the axial seismic design load. A similar set of axial struts provides axial restraint for the deuterium-tritium (D-T) axicell and central-cell shield components during any seismic occurrence. The large hatch allows access to the interior of the central cell for initial assembly, final decommissioning, or replacement if these lifetime components should unexpectedly fail. The hatch cover is supported by the vessel sill beam,

ORNL-DWG 84-16508 FED

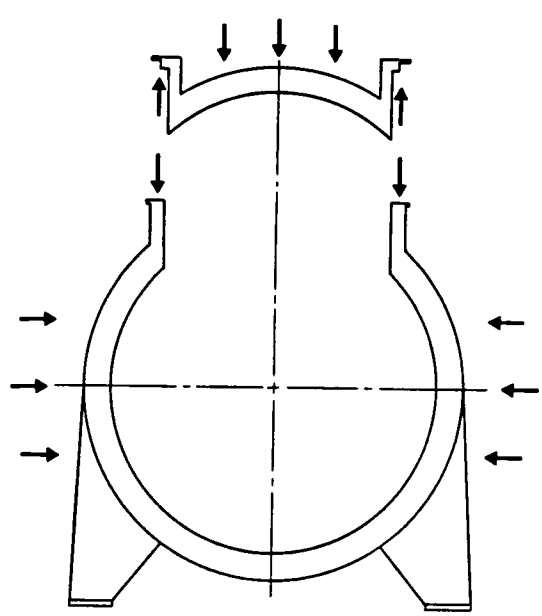

Fig. 8.5. Balance of pressure loads.

ORNL-DWG 84-18339 FED

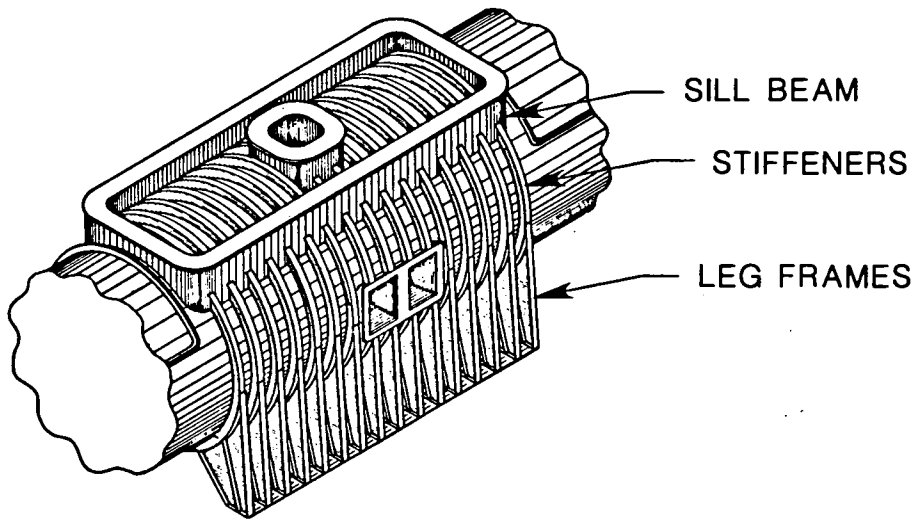

Fig. 8.6. Leg frames and stiffeners that carry pressure load from sill beam.

which circumscribes the opening. This beam supports the vertically downward-acting pressure load (Fig. 8.5) and the deadweight of the hatch cover, including any components mounted on it. Local deformation of the hatch cover is restrained by a set of curved beam stiffeners (the same size and spacing as the vessel stiffeners). A welded, single-convolute vacuum seal is used because of the large circumscribed length and because the components are expected to last for the machine lifetime. This seal can be cut and rewelded with a hands-on automatic welder/cutter, since it is outside the nuclear shielding.

A secondary access hatch (Figs. 8.2, 8.4, and 8.10) in the central portion of the main hatch cover allows replacement of the test module and the 12-T normal conducting choke coils. This hatch cover is similar to the main cover and provides a 2.7-m-wide by 4.6-m-long clear opening. The circumscribing sill beam provides a duct to raise the seal land above the surrounding main cover seals and provides a planar sealing surface. Because the test module must be removed once a year, and radiation levels in the seal area are very low, a bolted elastomer O-ring seal (Fig. 8.11) was judged to be more suitable than a welded bellows seal. The planar seal is designed for hands-on use of an automatic bolting machine. The test module, its plug shield, and the hatch cover are installed from a vertical position and are located by a guiderail support system built into the main hatch frame. The hatch structure supports the vertical and lateral loads on the test module, including those of its integral central coil. Axial loads are transmitted to the central shield module by a set of pins.

The vessel leg frames are supported by a frame structure of box beams, legs, and crossbracing (Figs. 8.4 and 8.7), which is secured to concrete footings. At the machine's

ORNL–DWG 83-4140 FED

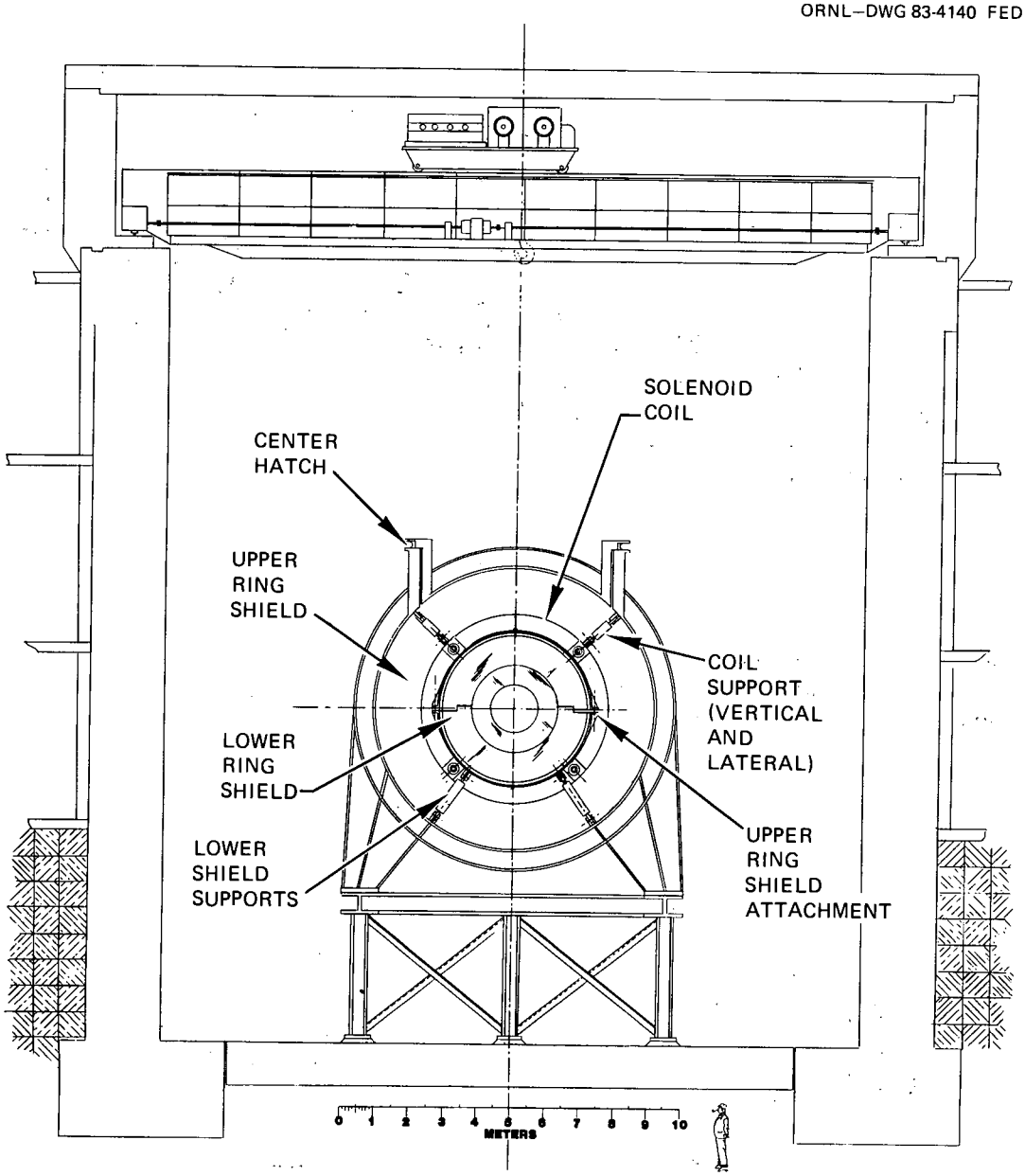

Fig. 8.7. Stiffeners that carry coil support strut loads to the vessel.

axial midpoint, a series of axial shear panels (Fig. 8.9) supports the machine against the overall axial loading that would be generated by a seismic event. The length and stiffness of the central-cell leg frames are tailored to accommodate the small axial deformation resulting from thermal strain and that caused by carrying the compression loading of the end-cell coil sets.

The interface of the vacuum vessel with one of the central-cell neutral beam lines and its associated beam dump is shown in Fig. 8.12. One beam line and one beam dump are

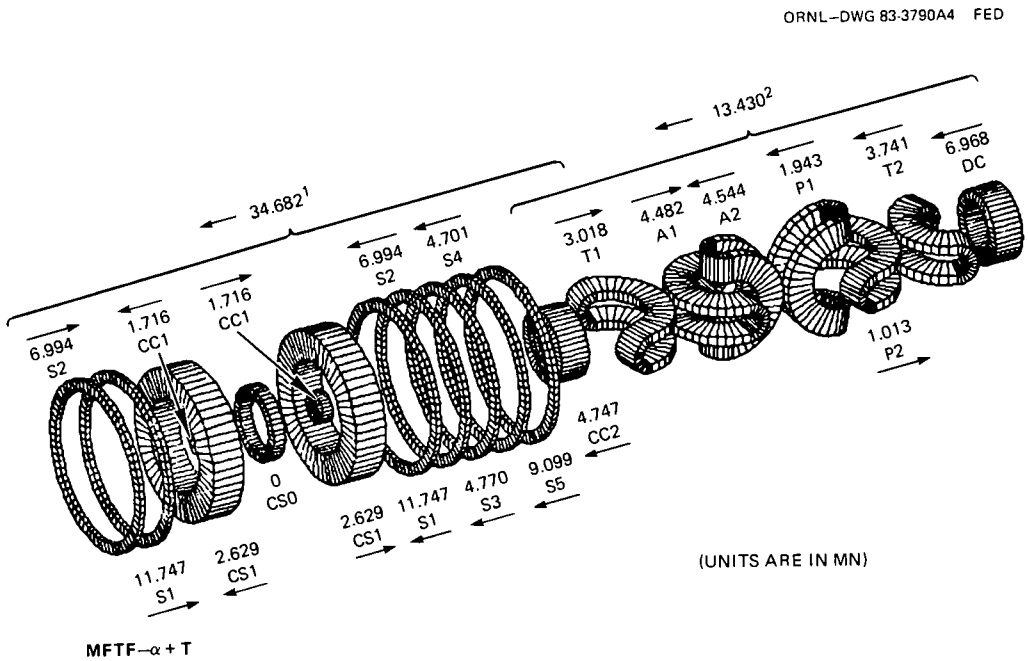

Fig. 8.8. Operating magnet loads. The total magnetic load taken in magnetic cold structure with the vacuum vessel reacting magnet fault loads is 34.682 MN; the load transmitted by two struts into the vacuum vessel structure and shell is 13.43 MN.

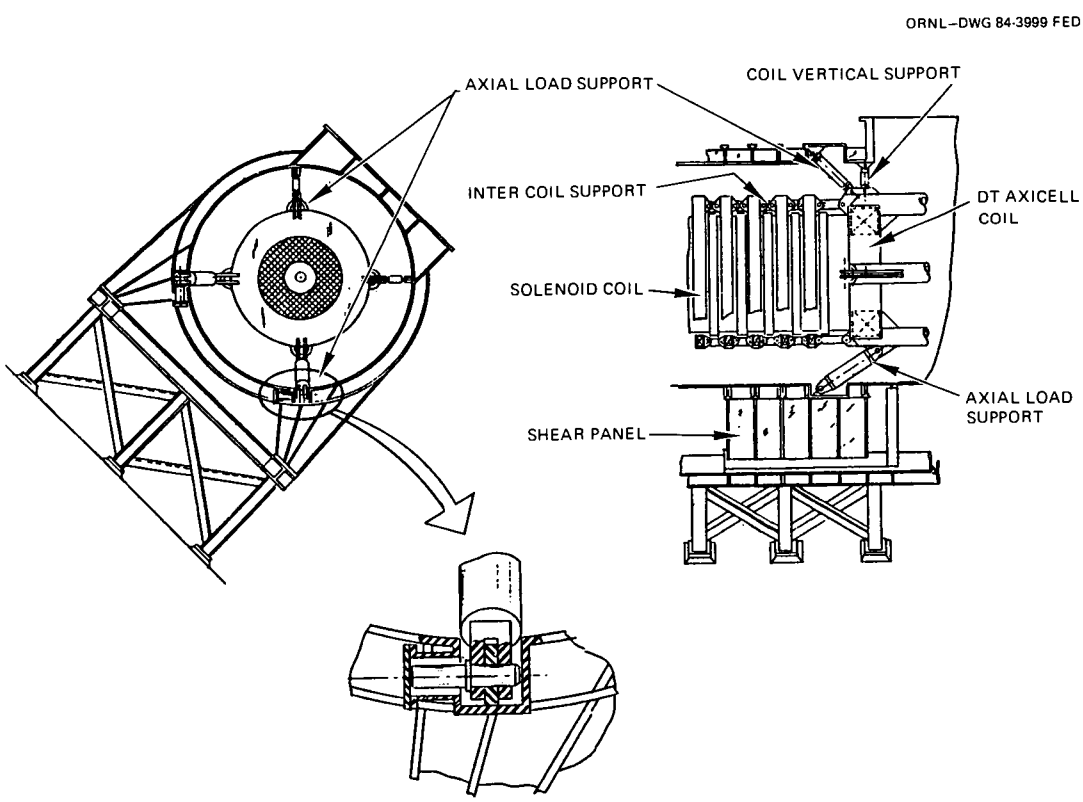

Fig. 8.9. Magnet set axial struts for center cell.

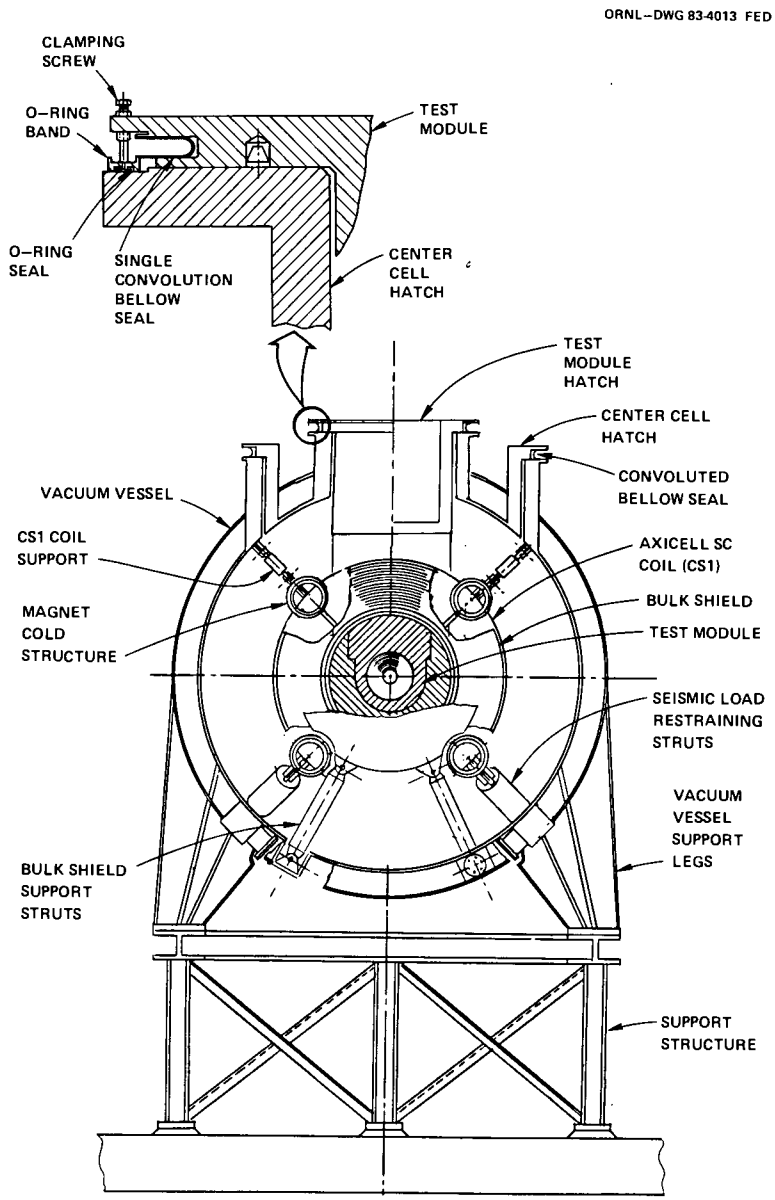

Fig. 8.10. Vacuum vessel showing replacement of test module.

located on each side of the vacuum vessel. A common flanged interface opening, framed by a box beam, is provided on each side of the vacuum vessel. The beam line and beam dump vacuum enclosures are attached to the flanges by bellows (Fig. 8.2) that accommodate manufacturing and installation tolerances. The bellows are also designed to limit the seismically induced interaction between the mass of the vessel, the dump, and (most important) the beam line to ensure vacuum integrity after a seismic event.

ORNL–DWG 84-3218 FED

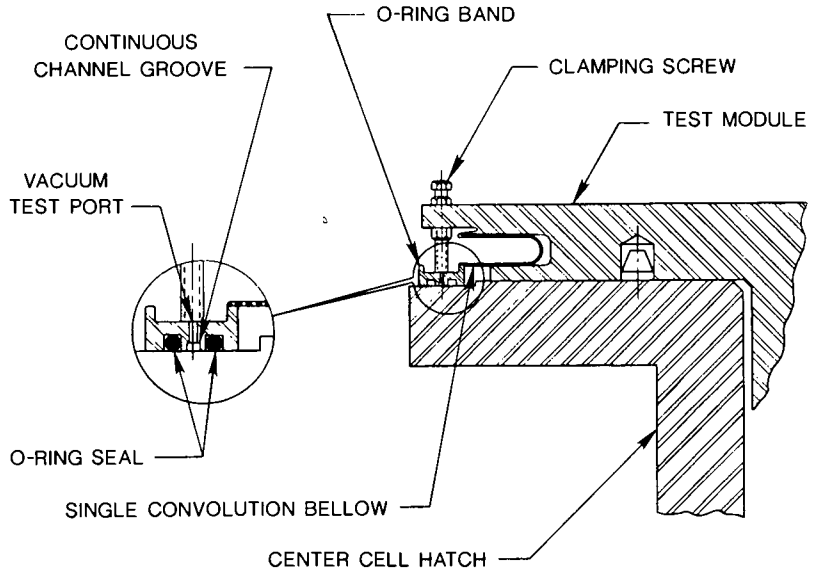

Fig. 8.11. Test module vacuum seal.

ORNL-DWG 83-4028 FED

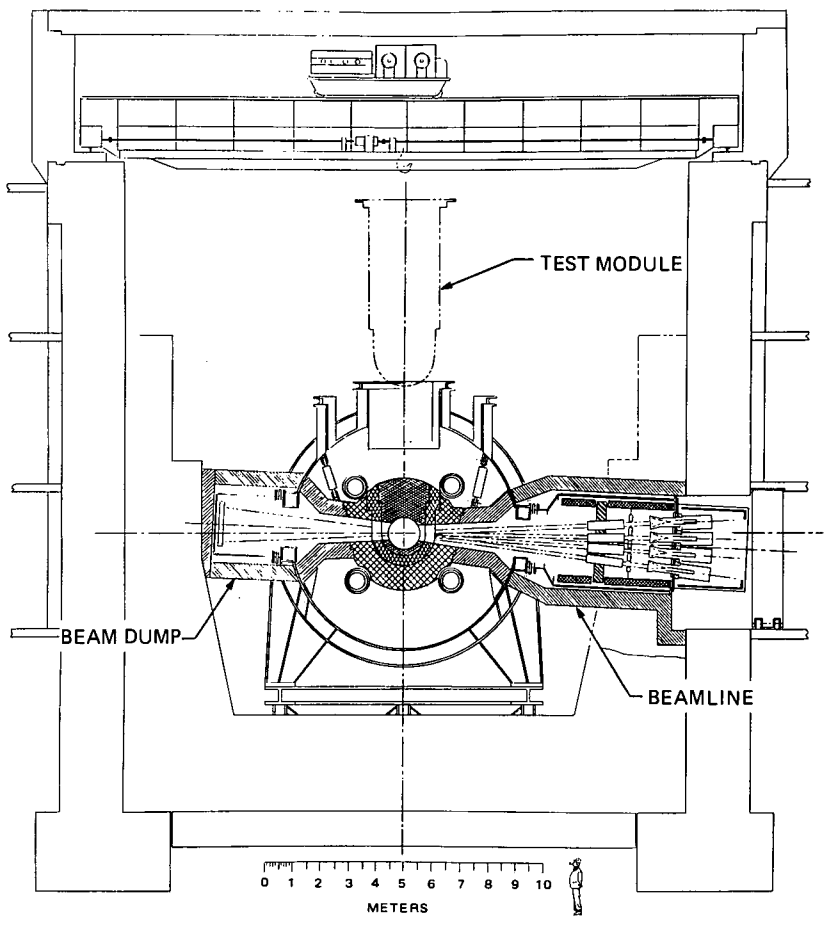

Fig. 8.12. Vacuum vessel, one neutral beam line, and its associated beam dump.

End-cell vacuum vessel

The only difference between the east and west end cells is in the orientation of their C coils. Plan and elevation views of the end cells are shown in Figs. 8.13 and 8.14, respectively.

Each end-cell vacuum vessel is a double-walled, internally framed design with an outer wall diameter of 8.3 m and an inner wall diameter of 5.0 m. The inner diameter leaves the minimum acceptable clearance between the vessel and the end-cell magnets with their cold wall. The space between the outer wall and the inner wall is sufficient to achieve the allowable biological dose rate using a water shield. The outer surface of the inner wall is lined with a layer of B_4C, and the outside of the outer wall is lined with a layer of B_4C followed by a layer of lead. The vacuum vessel consists of two concentric, cylindrical shells connected with 24 radial stiffeners located 15° apart (Fig. 8.15) that also serve as baffles for the shield water. The resulting cavities are connected by holes in the

ORNL–DWG 83-4007A3 FED

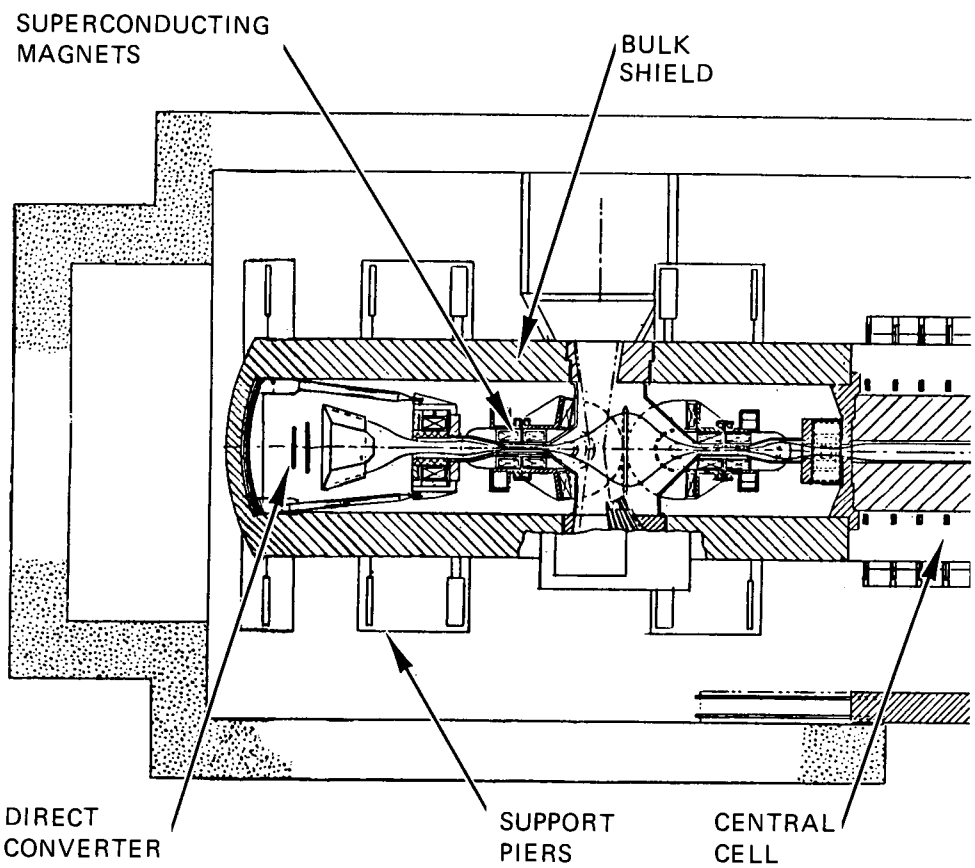

Fig. 8.13. Plan view of end cell identifying major components.

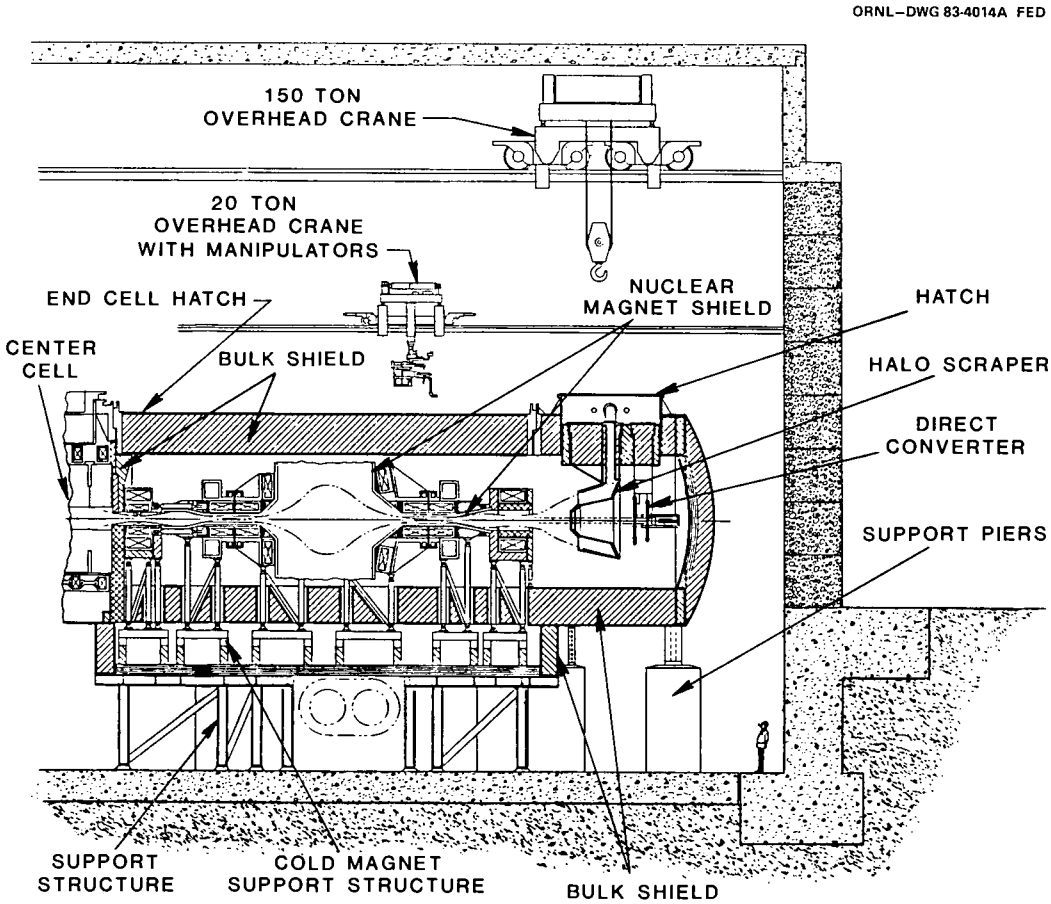

Fig. 8.14. Elevation view of end cell.

stiffeners that allow the water to be drained. Support legs at the same axial locations as on MFTF-B make it possible to use the existing concrete piers. An additional pair of legs and a pair of piers (Fig. 8.14) are added to each end of the vessel, which is slightly longer than the MFTF-B vessel and much heavier because of its shielding. In the area of the support legs, annular stiffener rings connect the inner and outer vessel walls and the radial stiffeners to provide a rigid load path. The vacuum vessel must support its own weight; the deadweight loads of the magnets, bulk shield, and other components; and dynamic loads, such as seismic and magnet fault loads. The intercoil magnetic forces are reacted by cold structures, but the resulting net load of 13.43 MN toward $Z = 0$ is reacted by a circular beam in the end cells (Fig. 8.14). The load is transmitted to the circular beam by two struts cooled with liquid nitrogen (LN_2). These two struts must also restrain the magnet system during longitudinal seismic acceleration. The loads are transmitted through the end-cell vacuum vessel to the central-cell vacuum vessel, where the magnetic loading portion is balanced by its complement and the seismic loading portion is reacted by the central-cell support structure, which consists of the axial shear panels and vessel support frame. The end-cell vacuum vessel is supported independently for vertical and lateral

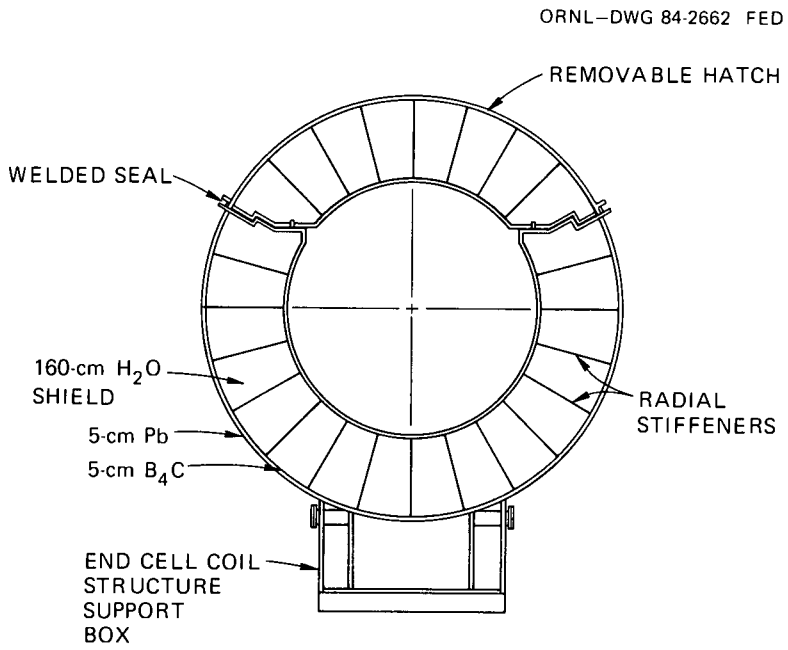

Fig. 8.15. Typical cross section of the end-cell vacuum vessel.

loads, but all longitudinal loads are transmitted to the central cell. The end-cell supports are designed to allow movement due to thermal growth.

The end domes of the vacuum vessel are also of double-walled design with water shielding; the inner steel wall is thicker than the side walls to provide the required shield design values. The lower portion of the vessel has a number of tubes through it to provide space for the coil support legs. A troughlike vacuum enclosure along the bottom of the vessel near the end-cell coil set houses the coil support structure (Fig. 8.16). The enclosure has double walls and internal framing; the space between the walls serves as a water shield. The floor of the trough is a double-walled, steel-filled nuclear shield. A pair of box beams runs along the bottom to support the coil legs, and a set of support frames carries the coil leg loads to the vault foundation. The support frames are positioned to leave a clear path for removal of the two lower sloshing-ion beam sources (Fig. 8.14). A set of ports with shield plugs in the trough side walls allows removal of the coil support leg attachment pins (Fig. 8.16).

There are two major hatches in the end-cell vacuum vessel. A large one in the top of the vessel (Fig. 8.17) provides access for replacement of any prematurely failing end-cell coils and will also be useful during assembly and decommissioning. The double-walled hatch cover provides a water shield, like that of the main vessel (Fig. 8.16). Water in the hatch cover would be drained before the cover was removed. The cover is supported on a set of pads on the main vessel, and a set of pins secures it against lateral motion. The pin connections are designed using a round hole with a set of slotted ones to prevent loading of the hatch cover by the main vessel. Thus, the cover carries only its own weight, possible

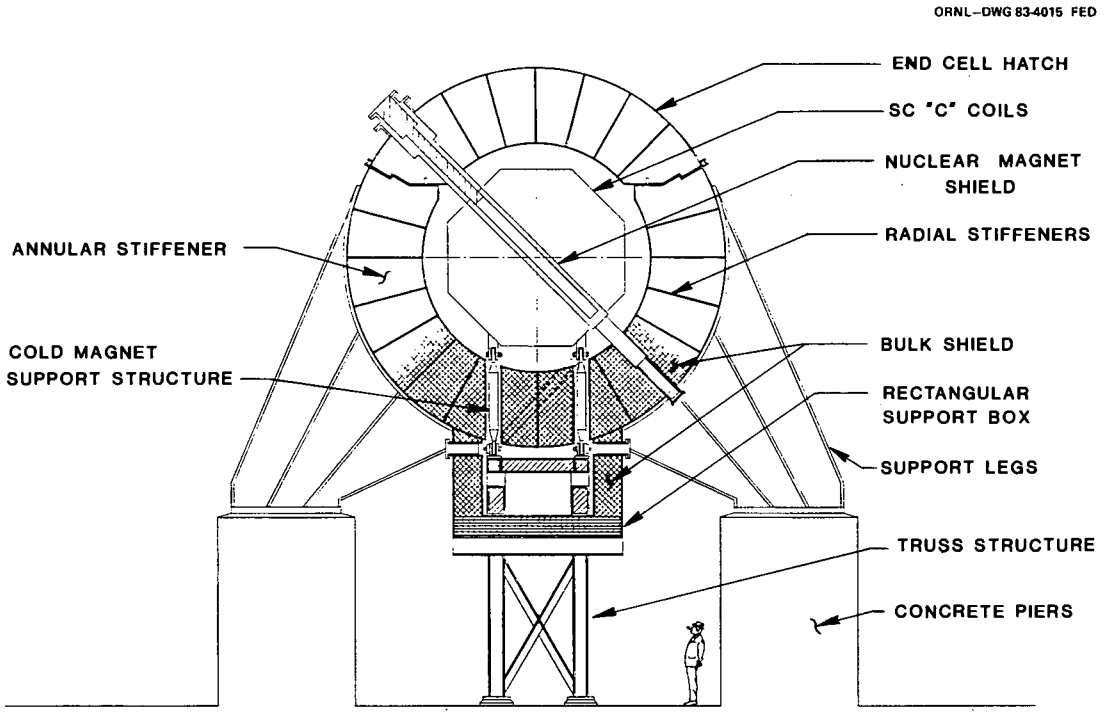

Fig. 8.16. Coil support structure in bottom of vacuum vessel.

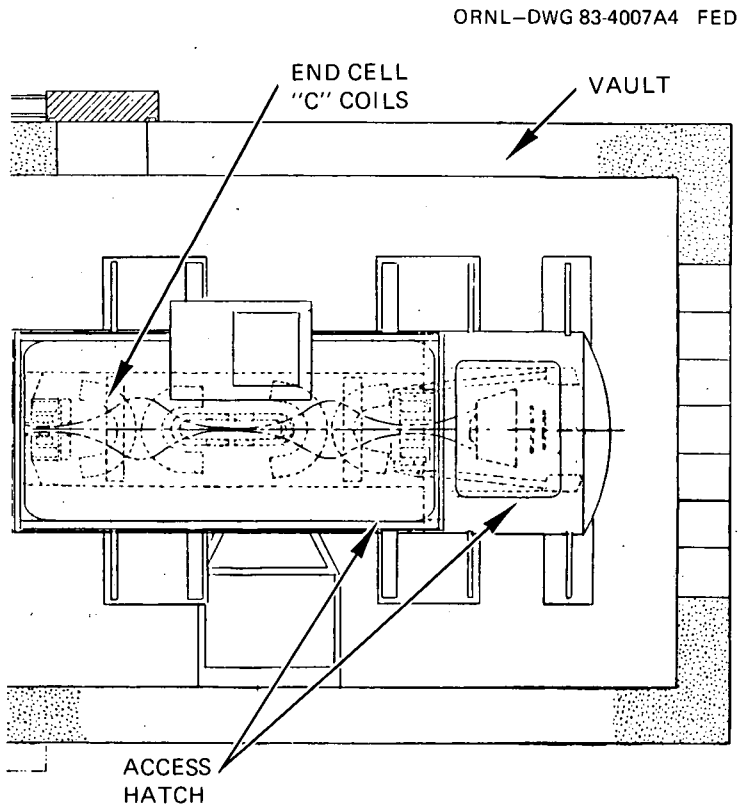

Fig. 8.17. Top of end-cell vacuum vessel showing main access hatch.

seismic loading, and the atmospheric load. A welded, single-convolute bellows vacuum seal is used around the hatch cover and could be removed and replaced with a hands-on automatic welder/cutter. A set of bolts in oversized holes restrains any induced upward motion.

A smaller hatch (Figs. 8.14 and 8.18) at the end of the vessel provides access for removal of the halo scraper and direct converter assemblies. The nuclear shield in this area is inside the hatch cover and is not attached to it to allow hands-on removal of the bolts that hold the hatch cover on the O-ring seal (which can be used because of low radiation levels) and disconnection of the utility connections.

Other ports provide access to the internal components of the device. These ports, at three locations along the length of the vessel, are at an angle of 45° to the horizontal midplane. There are three ports in the main hatch and one in the lower portion of the vessel, which provides access for the sloshing beam (Fig. 8.19). Each upper port provides access for removal of the nuclear shielding internal to the C coils in the area. A pair of ports (Fig. 8.17) provides access to the internal shield supports, as described in Sect. 8.3.2. All ports are provided with shield plugs that are integral parts of their covers. Built into these plugs are access ports for the various end-cell heating systems, as described in Chap. 5. Coil utilities will be provided through the main access hatch. Diagnostic access ports will also be provided through the main ports and in the end dome.

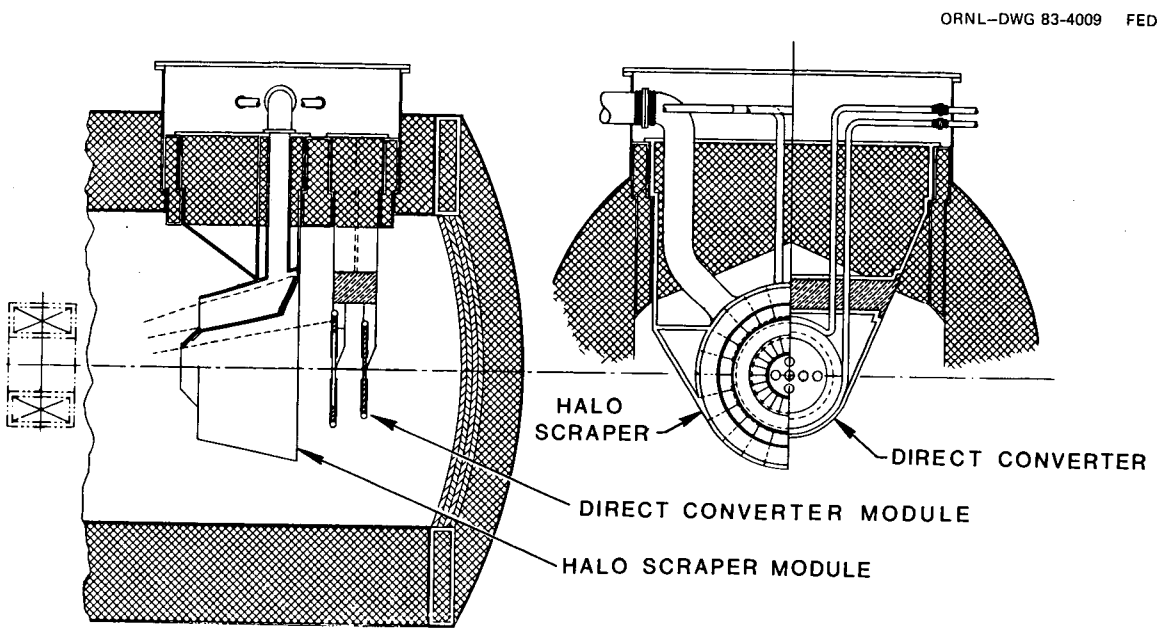

Fig. 8.18. Access hatch for halo scraper and direct converter.

ORNL–DWG 83-4016A FED

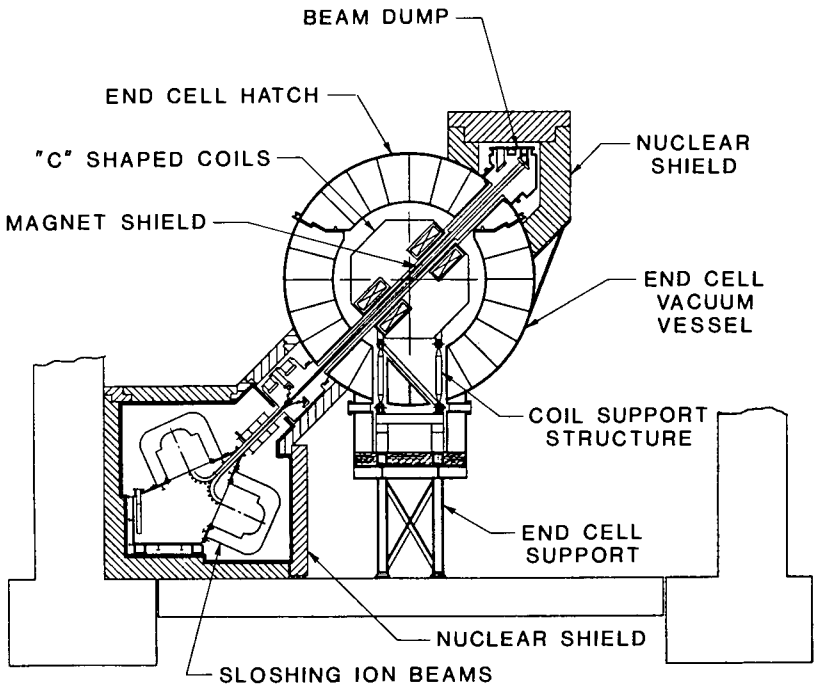

Fig. 8.19. End-cell section through sloshing-ion beam line.

8.3.2 Nuclear Shielding

The bulk shield requirements vary along the length of MFTF-α+T. The shielding thickness, composition, and location vary, depending on local requirements and neutron flux. For convenience, the bulk shield is separated into two major regions, the central cell and the end cells. In both regions, a shutdown dose rate of 0.5 mrem/h 24 h after shutdown at the outer surface of the shielding is required.

Central-cell nuclear shielding

For the purposes of engineering description, the central-cell nuclear shield can be divided into four areas: the central cell, the bore of the superconducting D-T axicell coils, the 12-T coil support shield area, and the central area of the D-T axicell. Shielding is also required for the blanket test module and the beam line ducts.

Central-cell shield. The shield in the central cell (Figs. 8.2 and 8.4) consists of a shield module centered on each solenoid coil and a pair of C-shaped shield segments with offsets at the midplane that prevent streaming at the interface between shield modules. The shield modules limit nuclear damage to the magnets, reduce the refrigeration load,

and provide biological shielding. The shielding provided to meet the rather low design criterion of 0.5 mrem/h 24 h after shutdown reduces the refrigeration load to a low level. It also provides good protection for the coils, even with the G-10 CR fiberglass insulation of the existing MFTF-B coils, which is more susceptible to damage than the polyimide used for the new MFTF-α+T coils.

The internal makeup of the central-cell shield modules is shown in Fig. 8.20. Closest to the plasma is an integral water-cooled layer of steel balls, followed by layers of concrete, B_4C, and lead, with a water shield outboard. The central-cell shield is considered a lifetime component.

Before installation of the shield module/coil assembly, the lower C-shaped shields are installed and supported by their struts. A pair of struts (Fig. 8.7) provides vertical and lateral support; additional struts provide axial support. These lower shields need not be removed if a coil or shield module must be replaced.

It is possible, with one exception, to replace any shield module/coil assembly without disturbing its neighbors. The exception, as noted in Sect. 8.3.1., is the S5 coil and shield module; to remove this assembly, the S4 shield module/coil assembly must be removed so that the S5 assembly can be translated toward $Z = 0$.

Each shield module and its companion coil are installed as follows. With both components suspended from a lifting fixture, the coil hangers are attached to the vessel and the

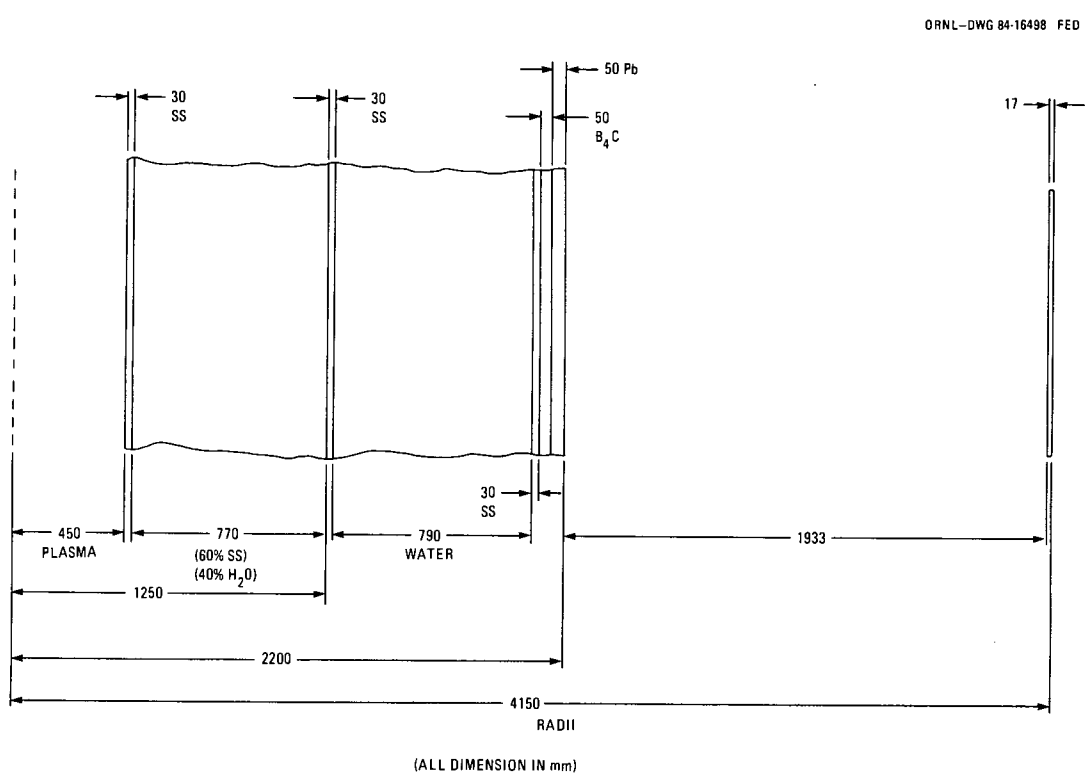

Fig. 8.20. Radial makeup of central-cell nuclear shield.

coil and shield are adjusted for correct position, then released from the lifting fixture. The weight of the shield module is supported by the two adjacent lower C-shaped shields and their support legs (Fig. 8.21). The last step is to position the upper C-shaped shields after two adjacent shield modules are installed. The central-cell shield modules are axially tied together by the C-shaped shields, which wedge the shield modules together (Fig. 8.21). The lower shield does this by means of the shield modules' weight as they are filled with water and by the action of the hoop side bolts. The upper shields are tightened down by a set of easily accessible bolts with oversize holes. After installation and bolting down of the upper shield, a set of hoop side bolts is tightened. These bolts allow the two upper shields to prevent upward motion of the shield module during a seismic event.

Shield in D-T axicell bore. The shield within the bore of the D-T axicell (Figs. 8.2 and 8.4) protects the coils and reduces the refrigeration load. The radial thickness of the

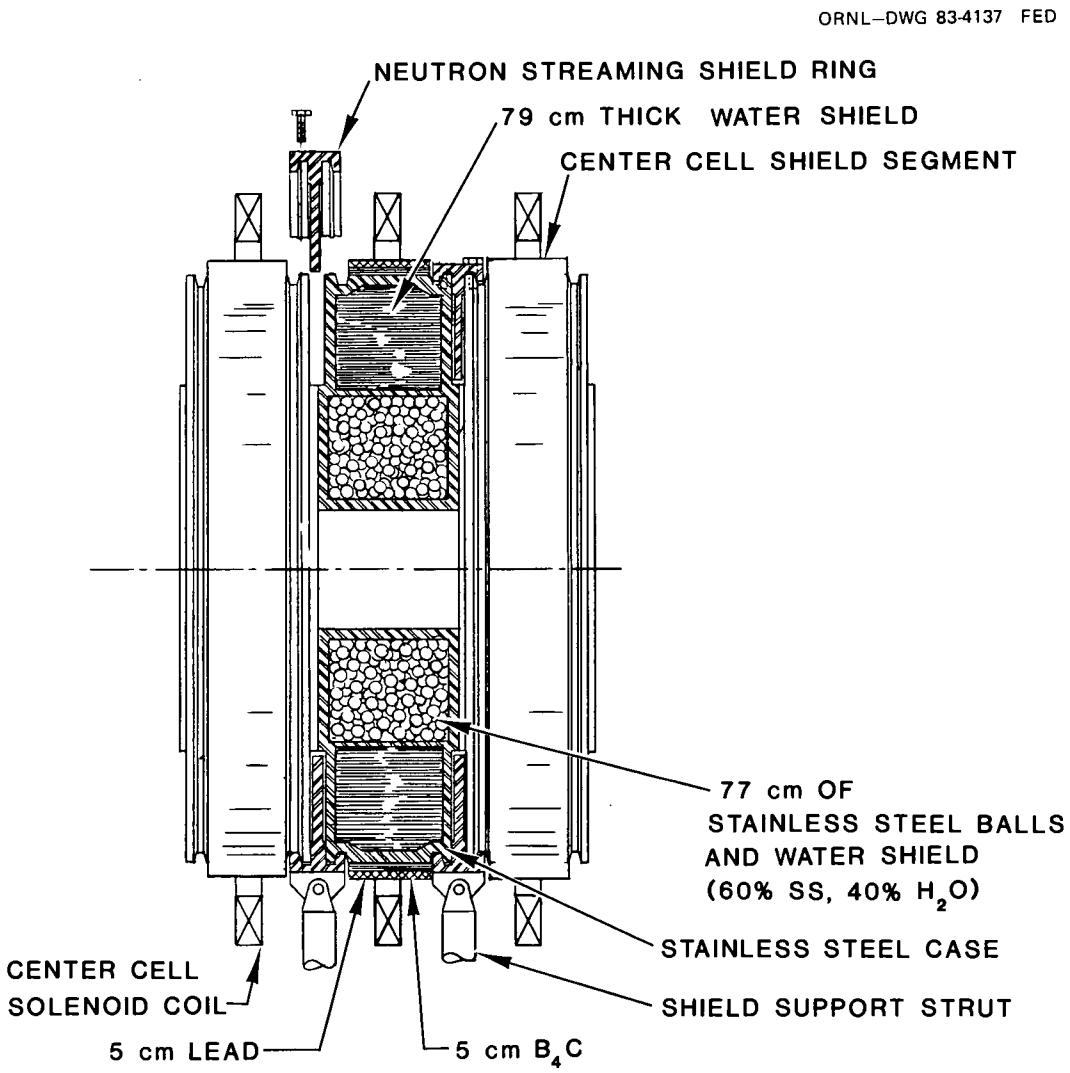

Fig. 8.21. Installation of shield modules.

shield was chosen to fill the space between the first wall and the bore of the magnet. This thickness, when combined with the effective shield thickness of the coil, provides more than adequate biological shielding. The water-cooled, stainless steel–ball shield has an integral water-cooled steel first wall and an outer layer of B_4C (Fig. 8.22). It is considered a lifetime component.

The shield module is supported by a set of shear pins and bolts that secure it to the end of the last central-cell shield module. The axicell shield module is positioned and bolted into place next to the 12-T coil/shield module using a lifting fixture. A set of adjustable pads on the side of the module next to the 12-T coil is adjusted to ensure correct positioning of the 12-T coils. Streaming shields like those for the central cell are installed (the wedging action needed in the central cell is not required here).

12-T coil support shield. In the area between the two large D-T axicell SC solenoid coils, the first shield module is especially made to support the 12-T coil (Figs. 8.2, 8.4, and 8.7). The shield is similar to a large washer with the coil attached to it. The coil's coolant piping is routed within the shield to the top of the machine, and the shield supports the coil's weight. The weight of the shield is supported by the central shield module on a pair of shoulder support structures. The 1.7-MN axial load that tries to move the coils toward the center of the machine is taken in compression by a set of wedging pads, which transfer the load so that it can be balanced through the central shield module in bulk compression. Adjustment of the wedging pads ensures a tight fit. Magnetic alignment is accomplished by adjusting the shoulder connections that attach the shield module/coil assembly to the central shield module. Axial alignment is ensured by adjusting the pads on the end of the shield section that is positioned inside the SC coil.

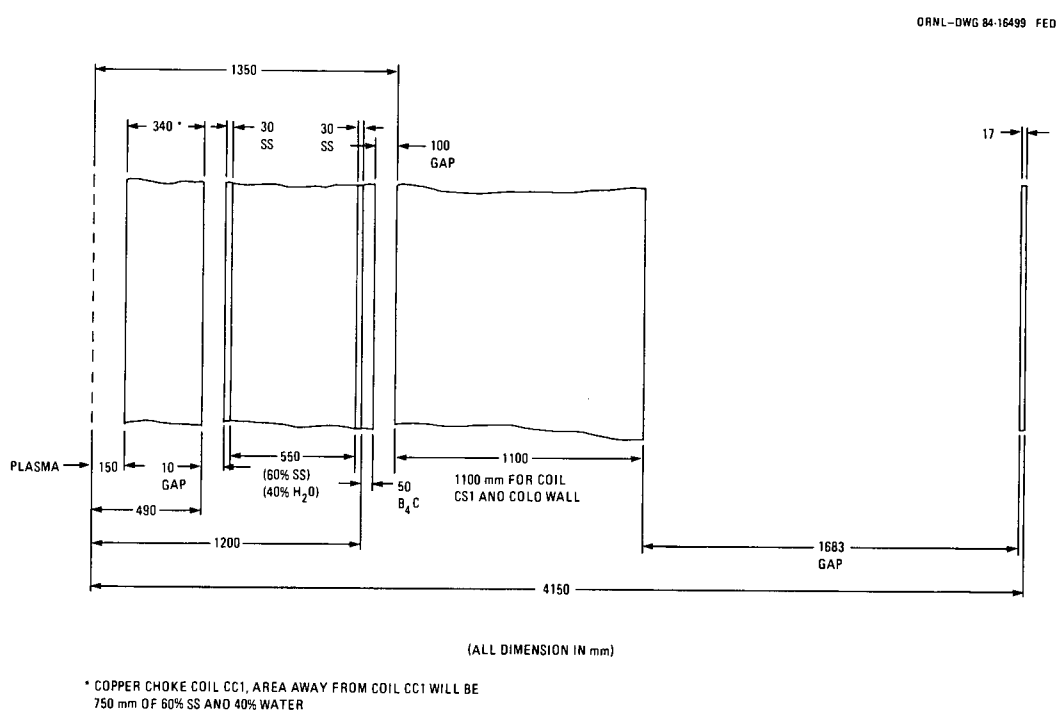

Fig. 8.22. Radial makeup of nuclear shield with the bore of the D-T axicell.

Central area of D-T axicell shield. The radial makeup of the center shield module is shown in Fig. 8.23. The center shield module has a special first wall, capable of handling high heat flux, that is attached to the inside of the water-cooled steel construction. It lines the inside of the shield module from the 12-T choke coil to the blanket test module and from the blanket test module to the neutral beam openings, then to the other 12-T coil. In studies of other devices, notably the Technology Demonstration Facility (TDF), heat loads in the regions near neutral beam dumps were relatively high (200 W/cm^2), while heat loads in the remainder of the region between the choke coils were relatively low (10–20 W/cm^2). Given the uncertainties associated with heat loads and particle energies in these regions, the design of a separable and removable first wall for the D-T axicell is a prudent step. The first wall units could be removed, if necessary, through the central access hatch when the test module with its shield plug, the two adjacent shield sections, and the 12-T coil/shield modules are removed. The first wall sections could then be repaired and replaced in the two 12-T coil support shield modules and the two shield sections.

Analysis of an array of cooling tubes for the lower heat loading shows that the first wall can be cooled with single-phase flow. The thickness of a stainless steel tubular design is 1.2 mm for a maximum wall temperature of 400°C. Copper is required in the region of higher heat flux around the beam dumps and may also be a desirable first wall material in

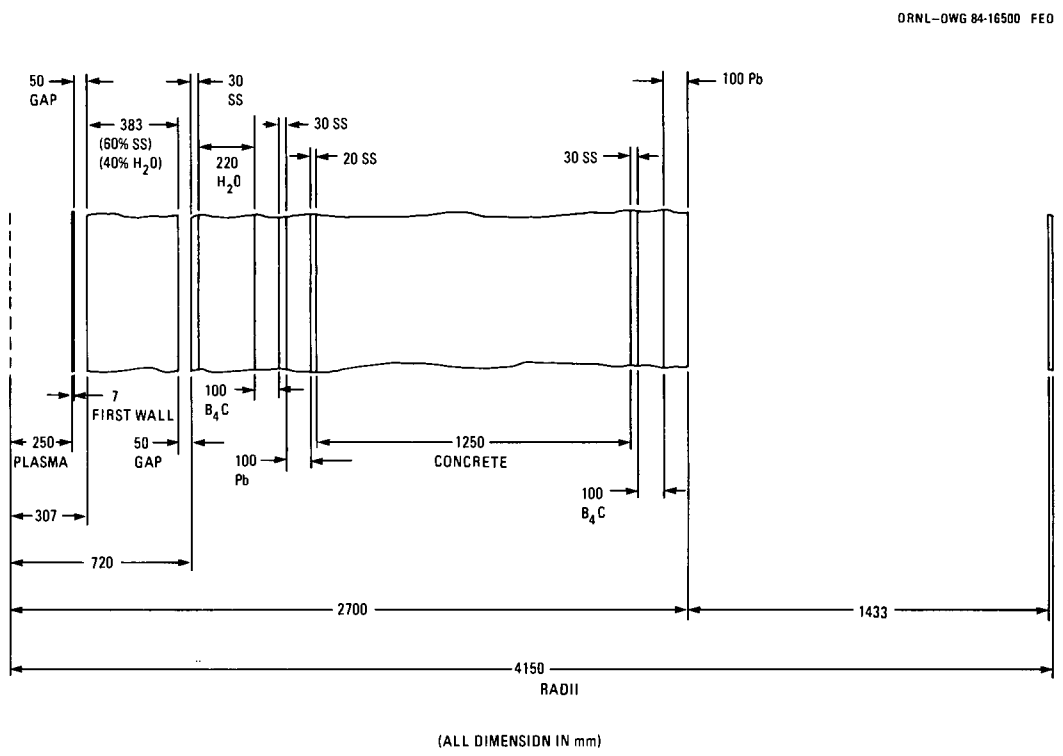

Fig. 8.23. Radial makeup of the central shield module.

regions of lower heat flux because the wall thickness can be increased, allowing for possible local erosion.

A study was conducted to determine a first wall geometry that would provide high neutron transparency for test modules. The resulting design, shown schematically in Fig. 8.24, is of water-cooled stainless steel. For a design surface heat of 50 W/cm^2, the attained neutron transparency is 0.90, and the pumping power is only 300 W. A first wall of this type could be used by the blanket test module and by any of the small nuclear test modules that might be required.

The central shield area (Figs. 8.2 and 8.4) is composed of a main shield module installed after the two lower coil support beams. The two upper beams are installed after the shield module. The shield is supported by four struts that restrain any seismically induced lateral or vertical motion. Two shield sections, one on each side of the test module, are inserted into the shield module, passing between the two upper beams. These two shield plugs are removed to permit the installation of a handling fixture for the 12-T coil when necessary. Axial seismic motion of the central cell and D-T axicell shield system is restrained by the action of the two central beam ducts that are attached to the central shield module and the vessel. A set of remotely installed and actuated wedges will be used to ensure a tight fit in the axial direction. Two shield sections, one on each side of the test

ORNL–DWG 82-4081A FED

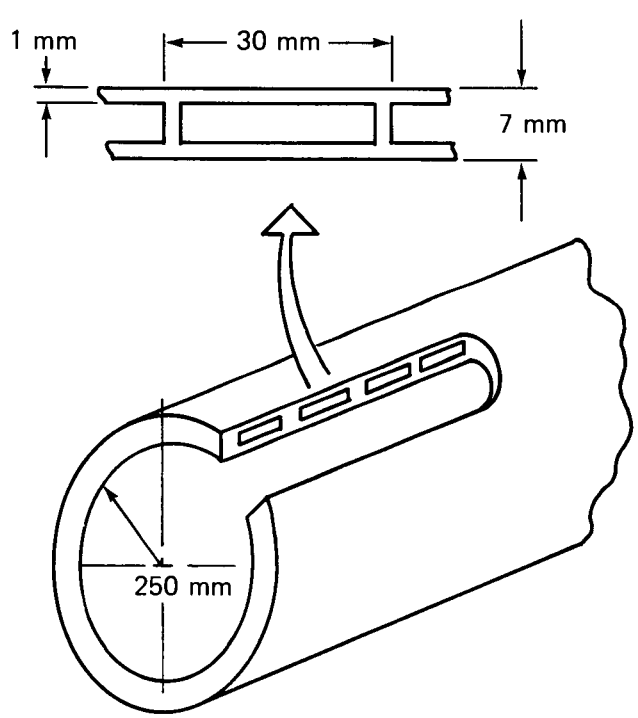

Fig. 8.24. First wall design for neutron transparency.

module, are inserted into the shield module, passing between the two upper beams. These two shield plugs are removed to permit the installation of a handling fixture for the 12-T coil, when necessary. The shield plugs are attached to the shield module by pins and bolts designed for remote removal and replacement. The central shield assembly has a pair of penetrations through which the central-cell beams pass. It also has an opening for the blanket test module and its plug shield. The area to the west of the blanket test module is reserved for blanket test module coolant piping and/or for small nuclear test modules, which would be installed when the blanket test module is replaced.

Test module shielding. The blanket test module (Figs. 8.2, 8.4, and 8.10), its companion coil, and its nuclear shield plug are installed through the vessel access hatch into the central shield module. The radial makeup of the nuclear shield and test module is shown in Fig. 8.25. The coolant lines and instrumentation cabling are preinstalled in the test module subassembly, which is supported by the central shield module against axial motion with a set of pins designed for remote installation of the subassembly. The blanket test module will be replaced every 12 to 18 months; it is expected that a new coil and shield plug will be provided with each new blanket test module.

Beam line duct shielding. The beam line ducts (Figs. 8.2 and 8.12) for the central cell consist of water-cooled steel first walls and water-cooled steel nuclear shielding. These ducts are installed before the installation of the central shield module. They are supported by a set of brackets mounted on the vessel side wall and by a set of struts that hang the ducts from the hatch sill beams.

The two central-cell beam lines are surrounded by a concrete nuclear shield with removable roof planks that provide access to the main beam line enclosure. A rolling

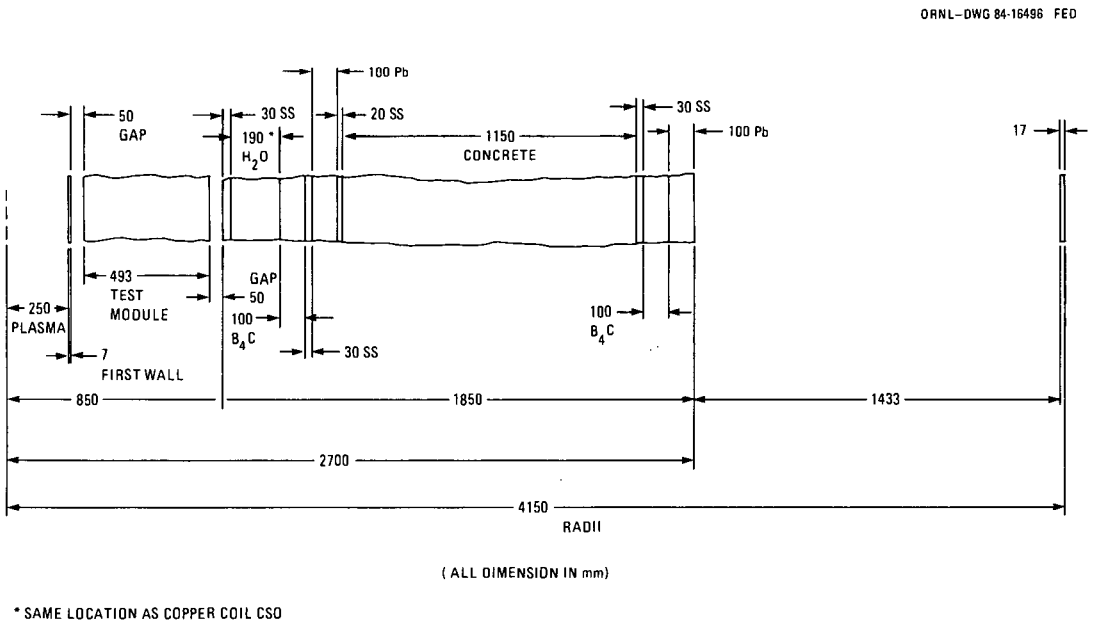

Fig. 8.25. Radial makeup of nuclear shield and test module.

shield door is used to close off the vault wall penetration. These two beam line internal component access vault doors have edge seals to limit the leakage of any tritium atmosphere into the hot cell from the vault.

The central-cell beam line dumps (Figs. 8.2 and 8.12) are positioned in vacuum enclosures outside the main vacuum vessel. The concrete nuclear shield around the dump enclosure has a removable roof with a shield plug over the dump and cryopump access ports.

End-cell nuclear shielding

The end-cell nuclear shielding consists of two distinct shields. One is the biological shield outside the coils, and the other is an internal shield that protects the coils. The biological shield (Fig. 8.16) consists of a water tank that is an integral part of the end-cell vacuum vessel and has layers of B_4C, lead, and steel, as shown in Fig. 8.26. The water will be circulated for control of temperature and water purity. The water circulating system consists of perforated tubes attached to the inner wall, which will allow uniform flow through the shield.

The support structures for the halo scraper and the direct converter collector assemblies are attached to dedicated shield plugs so that the preassembled modules can be lowered into their hatch (Fig. 8.18). The shield within the hatch is also designed to be removable if it becomes necessary to access this area of the end cell. This feature is used during initial assembly to gain access for the end-cell coil set drag struts and during

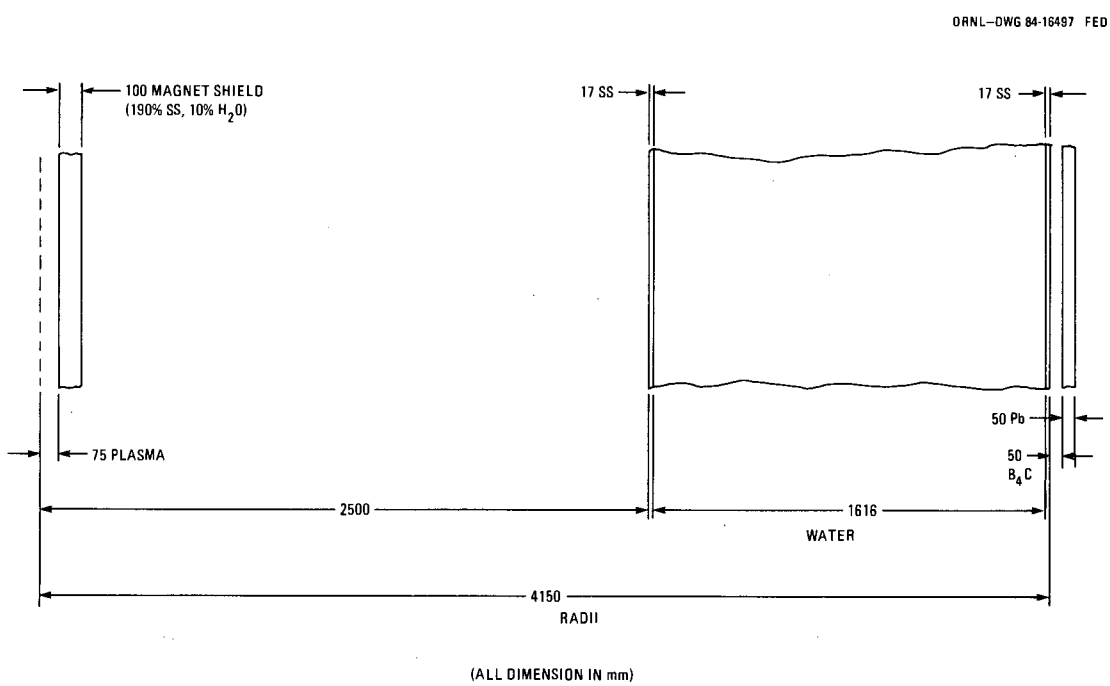

Fig. 8.26. Radial makeup of end-cell nuclear shield.

decommissioning. It would also be useful in replacement and repositioning of the halo scraper and/or direct converter modules, should this prove desirable.

The end dome nuclear shield (Fig. 8.14) consists of a water shield similar to that of the main vacuum vessel, except that the inner wall is thicker and serves as a water-cooled stainless steel shield.

The end-cell negative-ion neutral beam injector (NBI) is enclosed in a nuclear shield designed to provide the required biological shielding for workers inside the vault. Shield plugs allow access to the ion dumps, the cryopumps, and the two upper sources. The two lower sources are accessed through a rolling shield door (Fig. 8.19). The beam dump is positioned in a vacuum enclosure outside the main vessel. A concrete nuclear shield encloses the dump vessel, as well as the adjacent electron cyclotron resonance heating (ECRH) and drift pumping access port. Access plugs are provided to service the dump, its cryopump, and the ECRH and drift pumping equipment.

The ports provided for access to the end-cell internal components will be shielded by shield plugs. Plug designs will be specialized, according to the particular location and the equipment to which they interface. The details of these designs are presented in Chap. 5. As a general guideline, all components that penetrate the nuclear shielding (e.g., beam lines, beam dumps, instrumentation) will be shielded. The shield thickness, material, and composition will vary, depending on the level of protection required. The equipment shielding will meet the acceptable shutdown dose rate of 0.5 mrem/h 24 h after shutdown.

A nuclear shield is located within the end-cell coil set and surrounds the plasma (Fig. 8.27). This shield is designed to protect the coils from nuclear damage and to limit the refrigeration load. The shield extends from the end of the 18-T coil (Z = 10.9 m) to the end of the DC coil (Z = 25.5 m). The shield is 10 cm thick everywhere except within the bore of the DC coil, where it is 35 cm thick. The shield is made of water-cooled steel and is segmented so that it can be removed without disturbing the coil set. There are ten segments. Two of these are supported from the vessel by a pair of hanger struts in a manner similar to the center-cell shielding. They are lifted out vertically. Three other segments are supported by the vessel on their duct extensions (Fig. 8.16). Two of these are removed through ports in the vessel after the port covers and their integral shield plugs are removed. The lower end of each segment is supported by a pair of legs that extend through ports in the vessel. After removal of the port covers, extensions are attached to the legs, which then support the shield as it is withdrawn. The shield is detached from the legs after the legs appear at the upper port; then the legs may be withdrawn or attached to a repaired shield for replacement. The third segment would be handled in a similar fashion, except that the sloshing-ion beam line and its dump must be removed and the legs attached to the lower shield duct.

Two other segments are transition shields bolted to each other. These segments are unbolted and moved out through the area previously occupied by an adjacent segment using a counterbalanced lifting fixture.

The shield segment in the bore of the DC coil is supported on its T2 end by a pair of hanger struts from the vessel. It is supported at its other end by the DC coil end shield. This segment must be removed through the area occupied by an adjacent segment. Two transition segments will require a specialized lifting fixture designed to fit through the

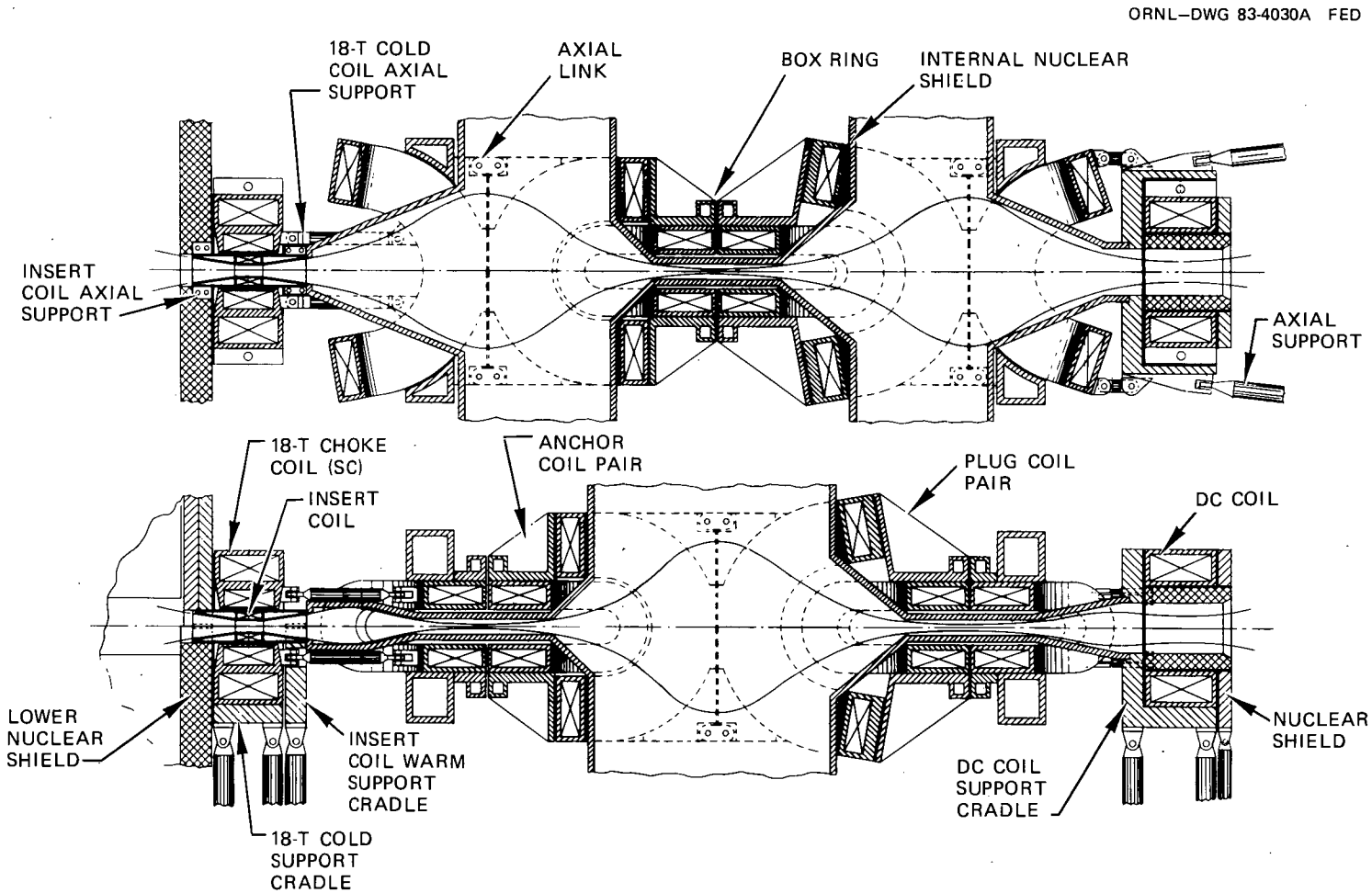

Fig. 8.27. End-cell coil structure and internal shield.

throat of the C coils and translate the segments axially before they are removed from within the coils.

In the area of the 18-T coil set, a transition from the internal shielding of the solenoid coils to the external shielding around the end-cell coils takes place. The lower half of this transition shielding is provided by the shielding within the warm structure of the cradle for the normal conducting coil of the 18-T coil set. The upper half of the shielding is designed to be removed before the 18-T coil is replaced. This shield is split at its axial midpoint (Fig. 8.14), and the section next to the 18-T coil is lifted out vertically. The other section is lifted by a lifting fixture designed to translate the section axially before the vertical lift.

In the area of the DC coil, the side of the magnet toward the center of the machine is protected by the nuclear shielding capability of the DC coil cradle. The other side of the coil is protected by a washer-shaped nuclear shield, which is supported by a set of struts attached to the vessel (Fig. 8.14). This shield is considered permanent but could be removed if damaged. This shield supports the end of the DC coil's internal shield.

8.4 STRUCTURAL ANALYSIS

A limited structural analysis was performed, and only areas critical to the feasibility of the configuration were analyzed. These areas were the end-cell double-walled vacuum vessel, the end-cell vacuum vessel end ring, and the end-cell magnet shield support.

8.4.1 End-Cell Double-Walled Vacuum Vessel

The double-walled vessel in the end cell is subjected to loads caused by various combinations of water static head, water pressure, and atmospheric pressure. A review of possible conditions indicated that when the tank is full of water and atmospheric pressure loads are applied (vacuum in vessel) critical hoop-compressive stresses occur in the outer wall. Comparison of applied hoop stresses with allowable stresses indicates a minimum required outer wall thickness of approximately 1.7 cm, as shown in Fig. 8.28, where both applied and allowable stresses are plotted as a function of thickness. The applied stress for the external atmospheric pressure load assumes that inner and outer walls are of equal thickness and also assumes 2.5-cm-thick radial stiffeners between the two walls.

The applied stress from the water is based on an analysis of bending in a water tank supported at the bottom. The compressive stress in the outer wall due to the bending moment is 65% of the total due to the water load and the atmospheric pressure. The allowable load shown in the figure is based on local instability of the skin between radial stiffeners.

8.4.2 End-Cell Vacuum Vessel End Ring

Figure 8.27 shows that the end-cell magnet system is restrained by a pair of struts. The struts and the end ring are shown schematically in Fig. 8.29a. The total axial load at each end is 22.2 MN (5.0×10^6 lb) directed toward the center of the device. This load is composed of the 13.43-MN normal magnetic axial load plus an allowance for a load induced by a seismic event. (Off-normal magnetic loads were not investigated.) The axial load applied to the ring is sheared into the vacuum vessel. The radial components of the

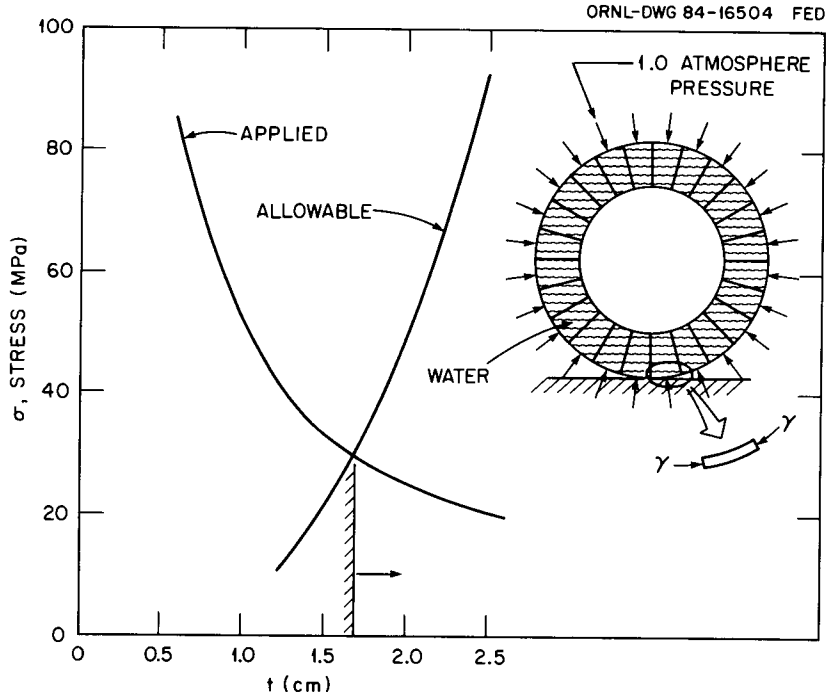

Fig. 8.28. Applied and allowable stress as a function of thickness.

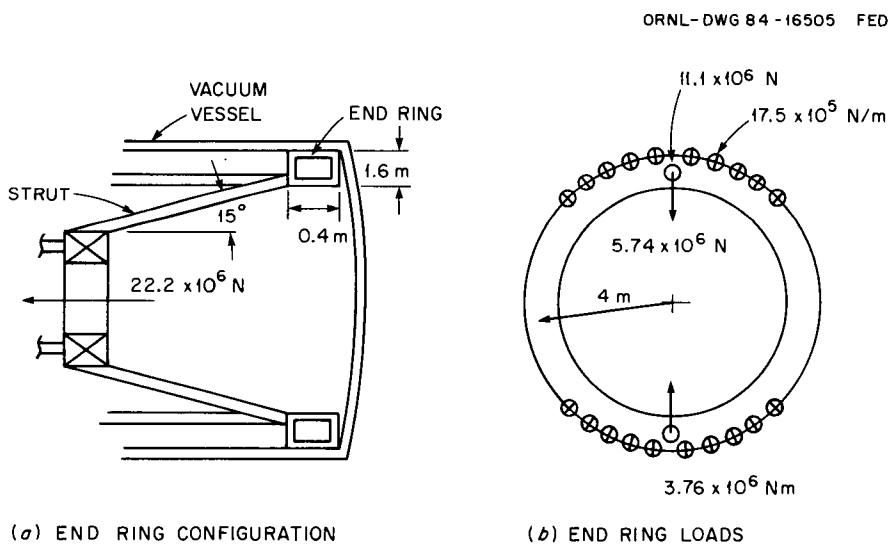

Fig. 8.29. End-cell ring (a) configuration and (b) loads.

load result in an in-plane bending load in the ring, as indicated in Fig. 8.29b. The radial components of the load act inward on opposite sides of the ring. The resulting maximum bending moment is given by $M = 0.52PR$, where P is the load and R is the ring radius. The resulting in-plane bending moment is 3.76 MN·m (33.2×10^6 in.·lb). This moment can be carried through the action of the built-in ring structure at the end of the vessel. The ring consists of the inner and outer walls of the vessel, which are 1.6 m apart, and the two annular frames that connect the two caps. For a wall thickness of 5 cm over the 40-cm axial length of the ring, a stress level of 111 MPa would result. This is acceptable, because the allowable bending stresses will be approximately 200 MPa. The ring will also be required to take other loads, such as some of the vessel and shield support, which have not been accounted for in this evaluation. The axial load can be eventually distributed into the vacuum vessel over two 90° arcs of the ring, as shown in Fig. 8.29b. This results in a running load of 1.75 MN/m, which corresponds to a stress of 69 MPa in a 2.5-cm-thick inner vacuum vessel wall.

8.4.3 End-Cell Magnet Shield Support

Stresses in a segment of the 10-cm-thick steel shield that protects the end-cell magnets were calculated for the support scheme shown in Fig. 8.30. The distributed loading shown results in bending in the shield plate. Stress in this plate under deadweight plus a 2.0-g seismic load is only 22.2 MPa.

The largest stresses are in the support legs. A cross section of 18 by 18 cm results in 138.0-MPa bending stresses. Bending stresses and torsional shear stresses in the side plate, shown balanced in Fig. 8.30, are 12.4 MPa and 27.6 MPa, respectively.

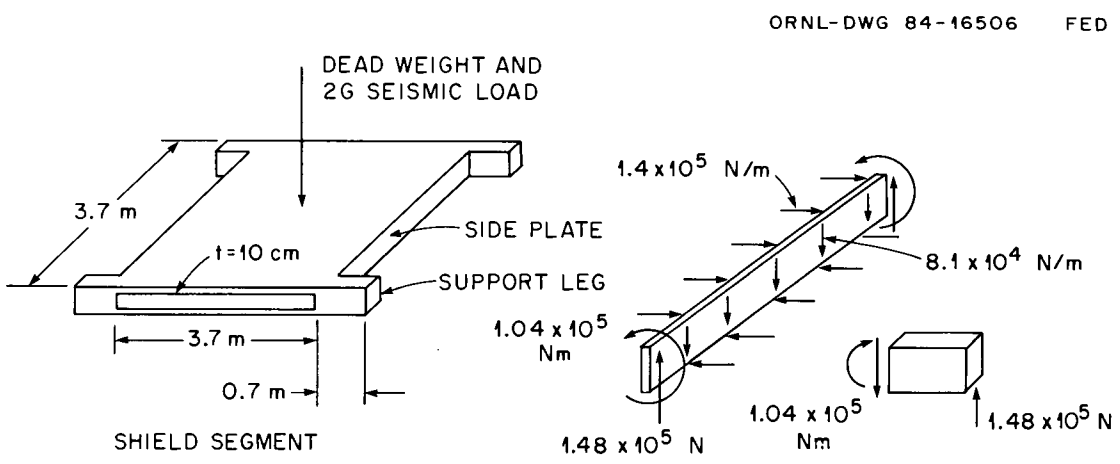

Fig. 8.30. End-cell internal shield support.

8.5 TRADE STUDIES

Three vacuum vessel and bulk shielding trade studies were performed. The vacuum topology study was conducted early in the program and is based on the MFTF-B magnet system with the addition of the D-T axicell. The MTFT-α+T magnet system was used for the other two trade studies. The selection process flow chart for the vacuum vessel and bulk shield is shown in Fig. 8.31.

8.5.1 Vacuum Topology

The objective of the vacuum topology trade study was to identify, evaluate, and select a viable vacuum boundary for the MFTF-B upgrade. Four configurations were studied. These configurations, with their advantages and disadvantages, are described.

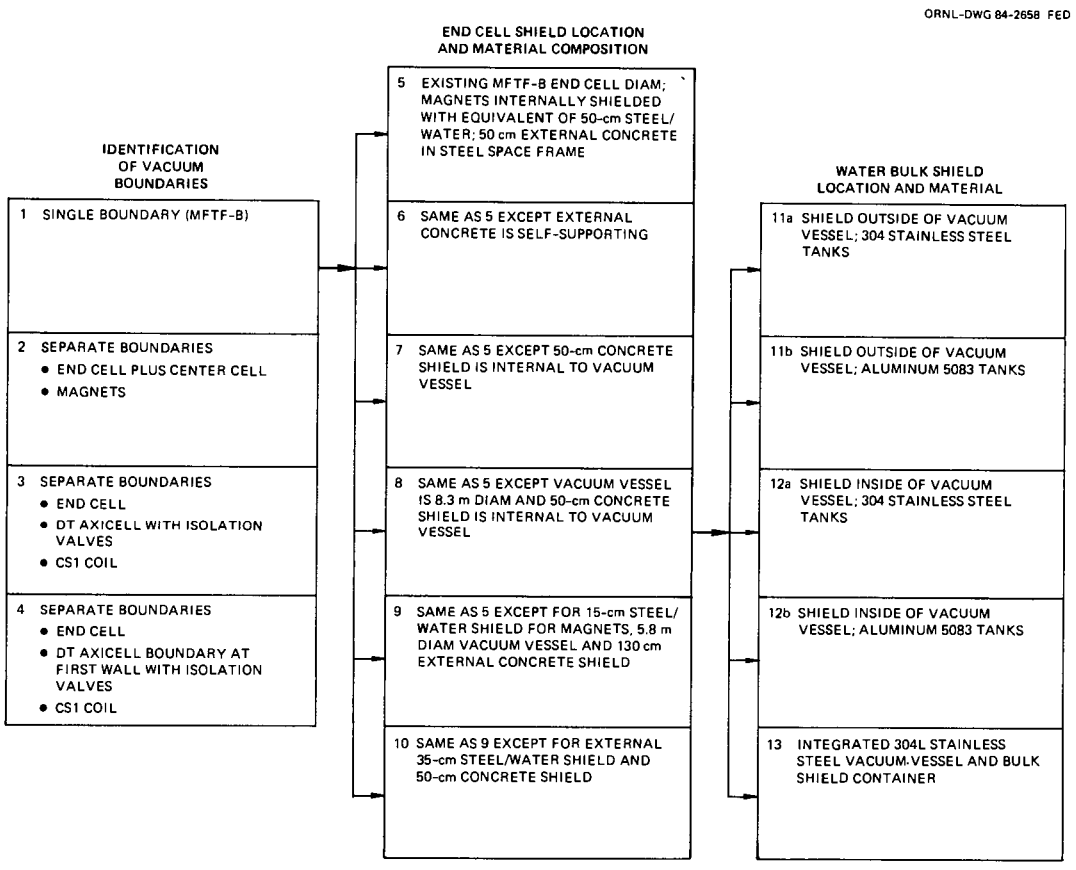

Fig. 8.31. Selection process flow chart for the vacuum vessel and bulk shield.

Configuration I

Configuration I uses the existing MFTF-B vacuum boundary, as shown in Fig. 8.32.

Advantages:

- Minimum reworking of existing components is needed.
- The test modules have a direct view of the plasma.
- The entire vacuum boundary is on the outside for ease in leak testing.
- Existing structural load paths are maintained.
- The (perceived) cost is low.
- Minimum time is required for upgrade modifications.

Disadvantages:

- The entire vacuum vessel must be opened to atmosphere for test module replacement.
- All SC magnets are brought to room temperature for module replacement.
- All cryopanels are brought to room temperature for module replacement.
- Tritium released from cryopanels must be processed.
- The entire vacuum chamber must be reconditioned (impurity removal) for subsequent operation.

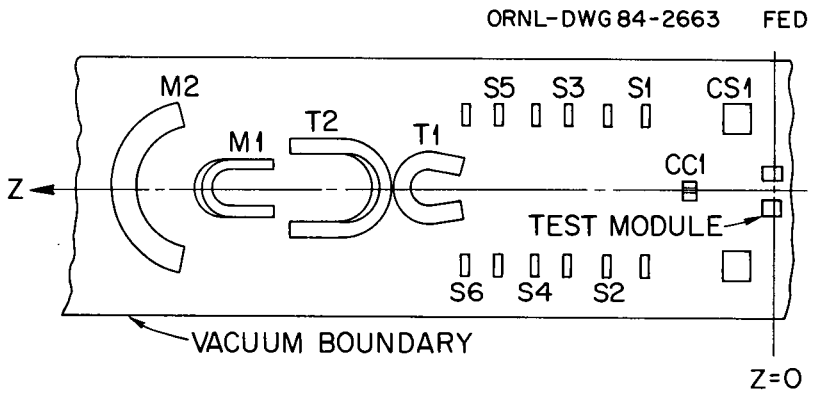

Fig. 8.32. Configuration I using MFTF-B vacuum boundary.

Configuration II

Configuration II uses the MFTF-B vacuum boundary and adds individual vacuum vessels around the new and existing SC coils, as shown in Fig. 8.33.

Advantages:

- SC magnets are kept cold during experiment changeover.
- Minimum reworking of the vacuum vessel is required.

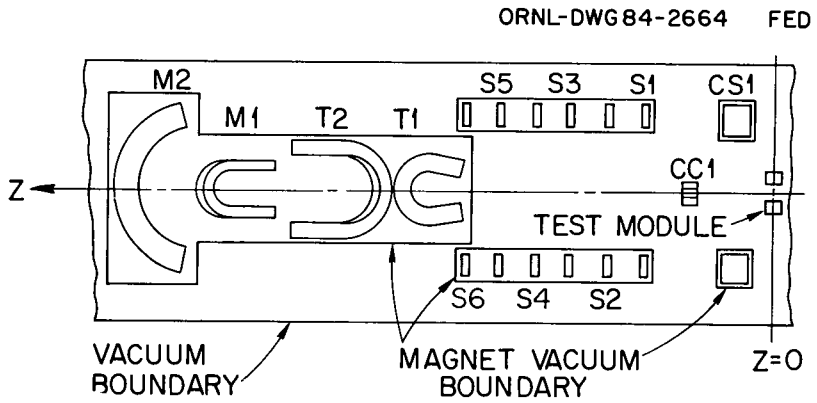

Fig. 8.33. Configuration II using MFTF-B vacuum boundary plus individual vacuum vessels around SC coils.

- The test modules have a direct view of the plasma.
- Existing structural load paths are used.

Disadvantages:

- The entire vacuum vessel must be opened to atmosphere for test module replacement.
- Separate vacuum vessels must be added to all SC magnets.
- Cryopanels are brought to room temperature for test module replacement.
- Tritium released from cryopanels must be processed.
- The entire vacuum chamber must be reconditioned before test operations are resumed.
- The cost is higher than that of configuration I.

Configuration III

Configuration III adds an isolation vacuum valve between the axicell and existing SC coils, as shown in Fig. 8.34.

Advantages:

- All SC magnets are kept cold during experiment changeover.
- All cryopanels are kept cold.
- Tritium processing needs are the same as for configuration I.
- Only the central-cell vacuum vessel must be reconditioned.
- Modest reworking of the existing vacuum vessel is required.
- The test modules have a direct view of the plasma.

Disadvantages:

- A vacuum valve must be added at both ends of the central cell.
- The central cell must be brought to atmosphere to replace test modules.

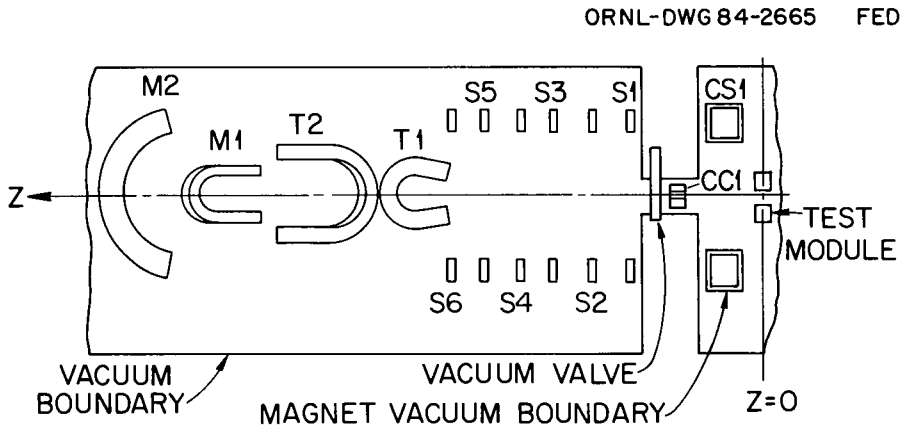

Fig. 8.34. Configuration III isolating SC coils from axicell with a vacuum valve.

- A separate vacuum vessel must be provided for the central-cell SC magnets.
- Access to the area around the choke coil is reduced.
- The cost is higher than that of configuration I.
- Vacuum valves must be developed.
- New structural load paths must be provided.

Configuration IV

Configuration IV is a first wall, vacuum vessel concept with an isolation vacuum valve between the test area and the remainder of the vacuum system (Fig. 8.35).

Advantages:

- All SC magnets are kept cold during experiment changeover.
- All cryopanels are kept cold.

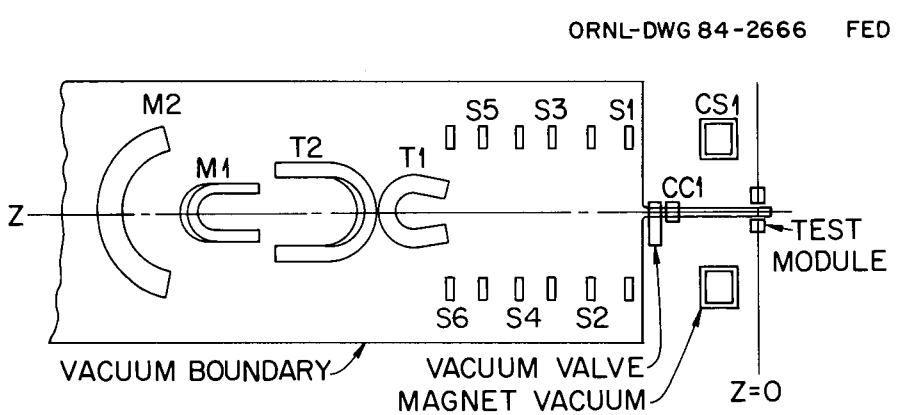

Fig. 8.35. Configuration IV isolating SC coils from axicell with a vacuum valve and using a combined first wall vacuum vessel concept for the test area.

- Tritium processing needs are the same as for configuration I.
- Moderate reworking of existing vacuum vessel is required.
- Rapid replacement of test modules is possible without opening the vacuum vessel.

Disadvantages:

- A separate vacuum vessel must be provided for the central-cell SC magnets.
- Neutron transparency at the test module is lower.
- Access for leak testing of the central-cell vacuum vessel is more difficult.
- The cost is higher than that of configuration I.
- Vacuum valves must be developed.
- New structural load paths must be provided.
- The test module will be in two or more segments.

Evaluation criteria

The four configuration options were evaluated on the basis of six criteria:

- feasibility of rework,
- experiment availability,
- test module performance,
- tritium control,
- cost, and
- schedule.

These criteria are defined as follows.

Feasibility of rework. Where the concept employs a vacuum boundary that is not dimensionally identical to MFTF-B, the feasibility of reworking the existing structure is assessed from the standpoint of new structural loads.

Experiment availability. The ability to change test modules with minimum effect on the rest of the system is desirable.

Test module performance. Test module performance was judged on the basis of exposure of the module components to high-energy (14-MeV) neutrons. High transparency to these neutrons is desirable.

Tritium control. Some surfaces, such as cryogenically cooled magnet surfaces, will cold-trap tritium. This is undesirable if, during a test module changeout, these components are warmed and give off their residual tritium.

Cost. Cost is qualitatively related to the amount of modification of MFTF-B and to the complexity of the concept (e.g., the use of longer vacuum isolation valves).

Schedule. Schedule is perceived to be qualitatively related to the amount of modification of MFTF-B and to the addition of new features.

Results

Three engineers responsible for conceptual definition of the vacuum vessel and shielding systems evaluated the configurations for four cases with the weighting factors shown in Table 8.1. In case 1 (Table 8.2), all the criteria were equally weighted; in case 2

Table 8.1. Weighting factors used to evaluate vacuum boundary configurations

Criterion	Case 1	2	3	4
Feasibility of rework	1	1	1	1
Experiment availability	1	2	1	2
Test module performance	1	1	1	1
Tritium control	1	1	1	1
Cost	1	1	2	2
Schedule	1	1	2	2

Table 8.2. Evaluation of vacuum boundary configurations, case 1 (all factors equally weighted)

	Configuration	Evaluation criteria: Feasibility of rework	Experiment availa-bility	Test module performance	Tritium control	Cost	Schedule	Total
I.	Single boundary (MFTF-B)	8.67	3.67	10.00	3.00	10.00	10.00	45.34
II.	Separate boundaries for end cells and center cell (MFTF-B) and for magnets	6.00	6.33	10.00	3.00	5.00	5.33	35.66
III.	Separate boundaries for end cells, for D-T axicell (with isolation valves), and for CS1 coil	5.33	7.00	10.00	7.00	5.33	5.67	40.33
IV.	Separate boundaries for end cell, for D-T axicell at first wall (with isolation valves), and for CS1 coil	3.67	10.00	4.33	10.00	5.33	4.33	37.66

(Table 8.3), the experimental availability was weighted with a factor of 2; in case 3 (Table 8.4), cost and schedule were weighted with factors of 2; and in case 4 (Table 8.5), experiment availability, cost, and schedule were all weighted with factors of 2. For case 1 (Table 8.2), configuration I was rated highest, five points better than the second-place configuration III. For case 2 (Table 8.3), configuration I was again rated highest, more than one point better than configuration IV. For case 3 (Table 8.4), configuration I is 14 points better than the second-place configuration III. For case 4 (Table 8.5), configuration I is better than configuration III by 11 points. Based on this evaluation, configuration I was chosen as the reference vacuum boundary concept.

Table 8.3. Evaluation of vacuum boundary configurations, case 2 (experiment availability weighted with a factor of 2)

	Configuration	Evaluation criteria						
		Feasibility of rework	Experiment availa-bility	Test module performance	Tritium control	Cost	Schedule	Total
I.	Single boundary (MFTF-B)	8.67	7.33	10.00	3.00	10.00	10.00	49.00
II.	Separate boundaries for end cells and center cell (MFTF-B) and for magnets	6.00	12.67	10.00	3.00	5.00	5.33	41.99
III.	Separate boundaries for end cells, for D-T axicell (with isolation valves), and for CS1 coil	5.33	14.00	10.00	7.00	5.33	5.67	47.33
IV.	Separate boundaries for end cell, for D-T axicell at first wall (with isolation valves), and for CS1 coil	3.67	20.00	4.33	10.00	5.33	4.33	47.66

Table 8.4. Evaluation of vacuum boundary configurations, case 3 (cost and schedule weighted with a factor of 2)

	Configuration	Evaluation criteria						
		Feasibility of rework	Experiment availa-bility	Test module performance	Tritium control	Cost	Schedule	Total
I.	Single boundary (MFTF-B)	8.67	3.67	10.00	3.00	20.00	20.00	65.34
II.	Separate boundaries for end cells and center cell (MFTF-B) and for magnets	6.00	6.33	10.00	3.00	10.00	10.67	41.00
III.	Separate boundaries for end cells, for D-T axicell (with isolation valves), and for CS1 coil	5.33	7.00	10.00	7.00	10.67	11.33	51.33
IV.	Separate boundaries for end cell, for D-T axicell at first wall (with isolation valves), and for CS1 coil	3.67	10.00	4.33	10.00	10.67	8.67	47.34

Table 8.5. Evaluation of vacuum boundary configurations, case 4 (experiment availability, cost, and schedule weighted with a factor of 2)

Configuration	Evaluation criteria						
	Feasibility of rework	Experiment availa-bility	Test module performance	Tritium control	Cost	Schedule	Total
I. Single boundary (MFTF-B)	8.67	7.33	10.00	3.00	20.00	20.00	69.00
II. Separate boundaries for end cells and center cell (MFTF-B) and for magnets	6.00	12.67	10.00	3.00	10.00	10.67	47.33
III. Separate boundaries for end cells, for D-T axicell (with isolation valves), and for CS1 coil	5.33	14.00	10.00	7.00	10.67	11.33	58.33
IV. Separate boundaries for end cell, for D-T axicell at first wall (with isolation valves), and for CS1 coil	3.67	20.00	4.33	10.00	10.67	8.67	57.34

8.5.2 Bulk Shield Location and Composition

The objective of the bulk shield location trade study was to establish whether the bulk shield should be inside or outside the vacuum boundary in the end-cell region. Six options for configuring the end-cell vacuum vessel and bulk shielding were identified and are summarized in Fig. 8.36. Three of these options retained the MFTF-B vacuum vessel with structural modifications, and three used new vacuum vessels for the end cell.

In general, the shield for the end cell is divided into two radial regions. Near the coils, there is a 50-cm-thick steel and water shield between the plasma and the vacuum vessel (35 cm of 90% steel, 10% water; 15 cm of 95% steel, 5% water). Where the magnet lies between the plasma and the vacuum vessel, a 15-cm-thick steel and water shield protects the magnet, and the magnet is assumed to provide the equivalent of 35 cm of steel and water shielding. The second radial region consists of 50 cm of concrete (plus steel rebar).

The first concept (Fig. 8.37) places the concrete shield outside the vacuum vessel. The concrete is in flat slabs supported by a steel frame. The slabs are removable, but the steel structure is semipermanent.

The second concept (Fig. 8.38) is very similar to the first, except that the concrete is monolithic and self-supporting. The top is removable, but access to the sides and ends would be through built-in apertures. The minimum wall thickness is 50 cm at the top, increasing to 150 cm at the bottom.

ORNL–DWG 84–2657 FED

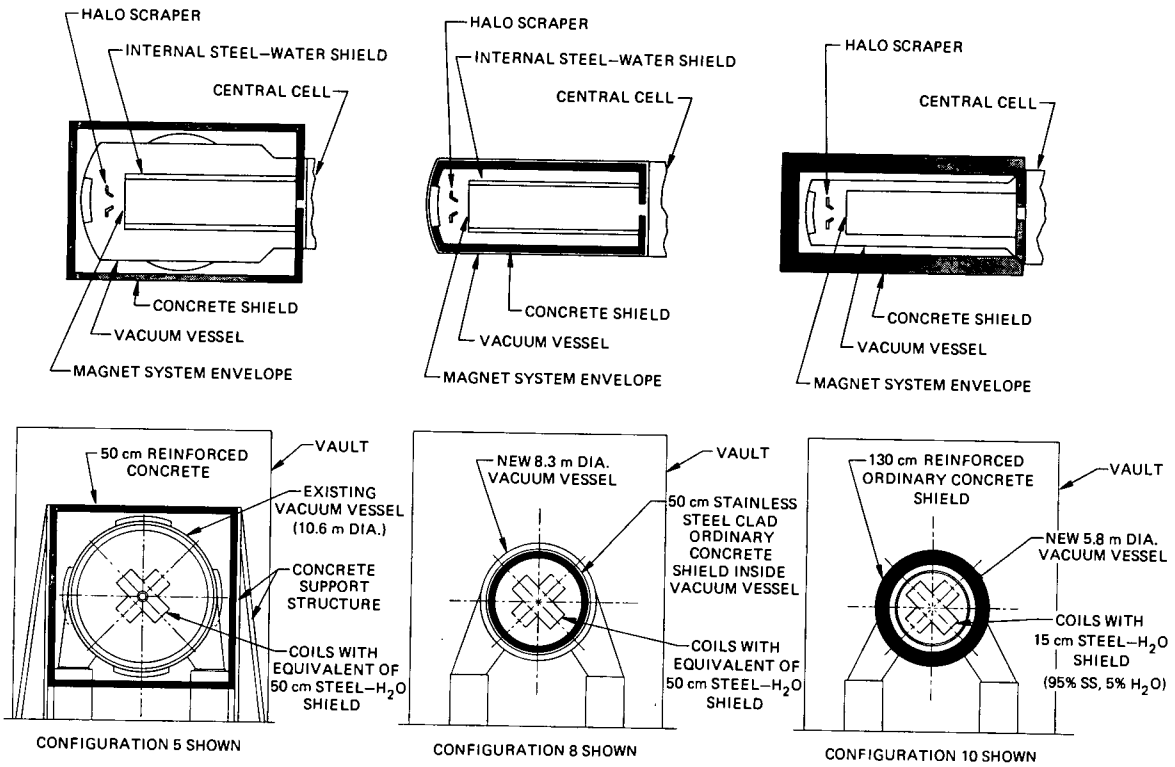

Fig. 8.36. End-cell concepts.

ORNL–DWG 84–2651 FED

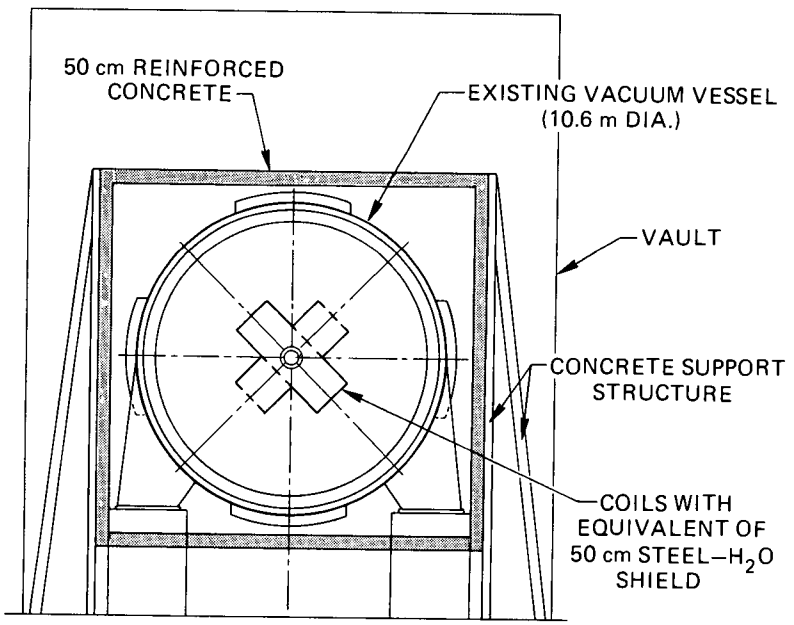

Fig. 8.37. Concept 1: reinforced concrete end-cell shield outside the vacuum vessel with structural supports.

ORNL–DWG 84–2652 FED

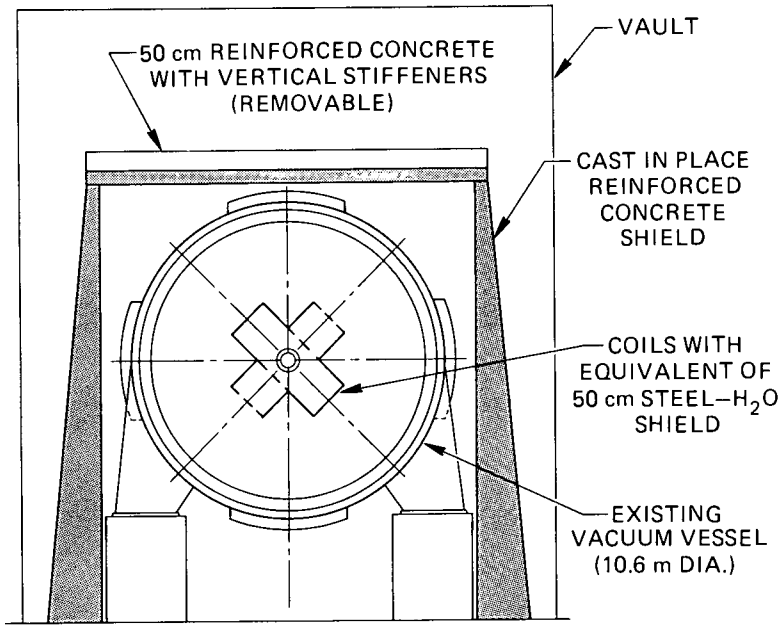

Fig. 8.38. Concept 2: reinforced concrete end-cell shield outside the vacuum vessel, self-supporting.

In concept 3 (Fig. 8.39), the shield is inside the vacuum vessel. The concrete is clad with steel, and shield units are attached to the vacuum vessel.

For concept 4 (Fig. 8.40), a new vacuum vessel is required. Its diameter is 8.3 m, and further reductions are possible if the 50-cm-thick steel and water internal shield is modified.

In concept 5 (Fig. 8.41), 35 cm of the 50-cm steel and water shield is moved outside the vacuum vessel, and there is also a 50-cm-thick concrete outside shield. The vacuum vessel diameter can be reduced to 5.8 m, but active cooling of the vacuum vessel is required because of nuclear heating.

In concept 6 (Fig. 8.42), the 35-cm-thick steel and water shield is changed to an ordinary concrete shield and combined with the 50-cm-thick concrete shield. The total shield thickness for the concrete is 130 cm.

Cost and weight summaries of the six concepts are shown in Table 8.6. The costs shown are for procurement of new items and some structural modifications (fittings, etc.) of the MFTF-B vacuum vessel; they do not include removing the existing vessel or relocating components before installing a new vessel. The cost analysis favors concepts 3, 4, and 6.

Since MFTF-α+T is located in an earthquake environment, a 0.5-g seismic acceleration was applied to the three favored concepts. This acceleration was double that used for

ORNL–DWG 84–2653 FED

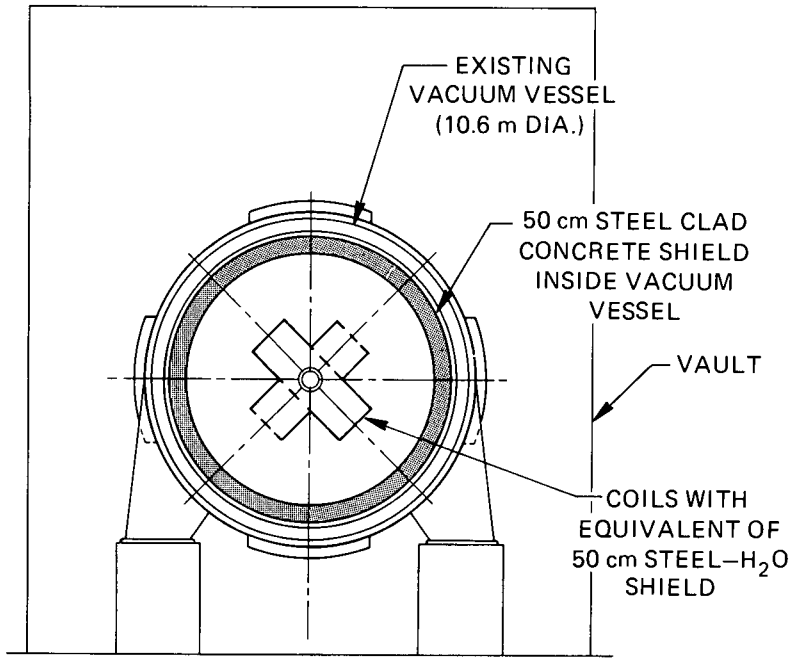

Fig. 8.39. Concept 3: steel-clad concrete end-cell shield inside the vacuum vessel.

ORNL–DWG 84–2654 FED

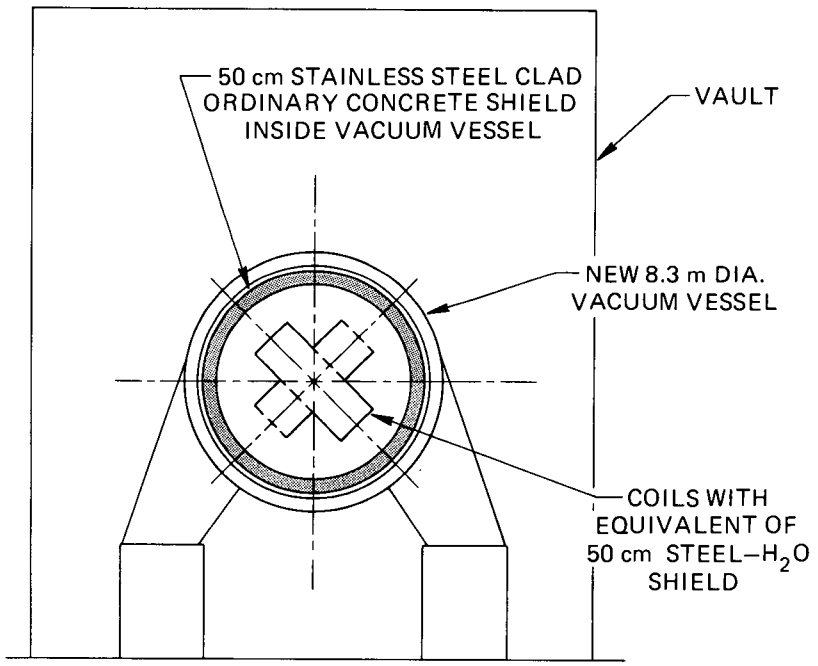

Fig. 8.40. Concept 4: concrete end-cell shield inside new 8.3-m-diam vacuum vessel.

ORNL–DWG 84–2655 FED

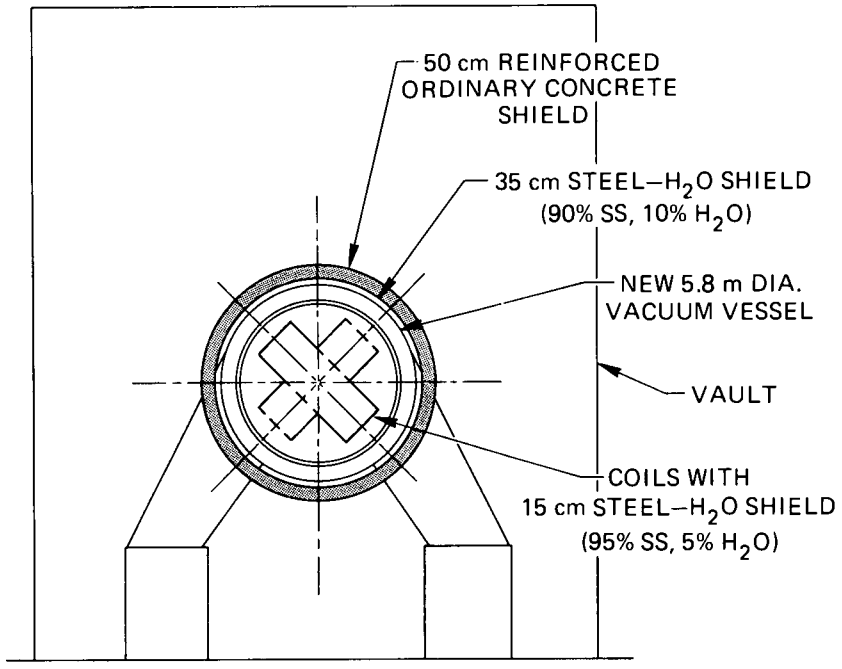

Fig. 8.41. Concept 5: concrete end-cell shield outside new 5.8-m-diam vacuum vessel.

ORNL–DWG 84–2656 FED

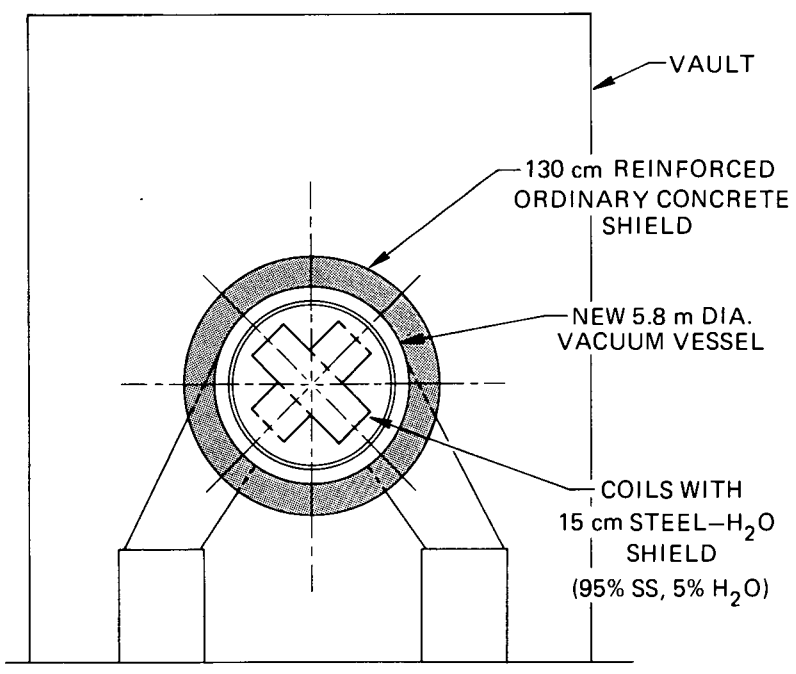

Fig. 8.42. Concept 6: concrete end-cell shield outside new 5.8-m-diam vacuum vessel, with equivalent of 35-cm-thick steel and water shield also outside the vacuum vessel.

Table 8.6. Summary of end-cell vacuum vessel and shielding concepts

	Concept					
	1	2	3	4	5	6
Vacuum vessel	Modified MFTF-B	Modified MFTF-B	Modified MFTF-B	New, 8.3 m in diameter	New, 5.8 m in diameter	New, 5.8 m in diameter
Vacuum vessel cost, millions of dollars	1.7	1.7	2.1	5.5	5.0	5.2
End-cell support cost, millions of dollars	0.2	0.2	0.7	0.5	0.5	1.3
Steel and water shield thickness and location	50 cm, all inside	50 cm, all inside	50 cm, all inside	50 cm, all inside	15 cm inside, 35 cm outside	15 cm inside
Concrete shield thickness and location	50 cm, outside, with rebar and supports	50 cm, outside, with rebar, self-supported	50 cm, inside, steel clad, supported by vacuum vessel	50 cm, inside, steel clad, supported by vacuum vessel	50 cm, outside, with rebar, supported by vacuum vessel	120 cm, outside, with rebar, supported by vacuum vessel
Concrete shield weight, Mg	2330.9	3536.3	835.5	653.5	638.2	1562.6
Concrete shield cost, millions of dollars	11.1	4.8	1.42	1.12	0.45	1.7
Removable parts of shield	Inside and outside	Inside and top of outside only	All	All	All	All
Cost of steel and water shield, millions of dollars	7.3	7.3	7.3	7.3	33.0	3.0
Total steel shield weight, Mg	278.1	278.1	278.1	278.1	1268.2	116.8
Total shield cost, millions of dollars	18.4	12.1	8.7	8.4	33.4	4.7
Total end-cell cost, millions of dollars	20.3	14.0	11.5	14.4	38.9	11.2

MFTF-B, and it was concluded that the vacuum vessel upgrade of concept 3 was not practical or cost-effective. Concept 4 was chosen over concept 6, even though concept 6 appeared to be less expensive (the total cost listed for concept 4 in Table 8.6 includes an estimate for the part of the cooling system integral to the vacuum vessel but does not include the cost of supporting utility subsystems that would be required). The question of vacuum vessel cooling and cooling system costs made the simplicity of concept 4 more attractive.

In summary, the concept selected for the end-cell shield yields an 8.3-m-OD vacuum vessel with a number of advantages, such as existing tooling (from the MFTF-B central cell), a good loading path for axial loads, access to the vacuum vessel from the outside, and no need for active cooling of the vacuum vessel. This concept was also estimated to have lower costs than several of the others considered.

8.5.3 Water Bulk Shield Location and Material Selection

After the vacuum vessel and bulk shield trade studies were completed, an alternative to the 35-cm-thick stainless steel shield and 50-cm-thick concrete shield was suggested. The basic concept is 165 cm of water with layers of boron carbide and lead. Originally, containers separate from the vacuum vessel, each 1.6 m deep and occupying one of 24 equally spaced radial sectors, were considered. Lengths were individually tailored to the requirements of penetrations in the vessel. The sides and ends of individual containers were stepped to prevent neutron streaming, and methods of water circulation were incorporated. Two basic locations were considered for the containers: (1) outside the vacuum vessel, as shown in Fig. 8.43, and (2) inside the vacuum vessel, as shown in Fig. 8.44. An integrated vacuum vessel/shield concept is shown in Fig. 8.16. The container materials considered were type 304L stainless steel and 5083-0 aluminum. Five options were considered:

1. Separate bulk shield water containers made of type 304 stainless steel, located on the outside of a new 8.3-m-diam vacuum vessel, with a total cost of $16.5 million for each end cell.
2. Similar to option 1, but with containers made of 5083-0 aluminum, for a total cost of $13.7 million for each end cell.
3. Separate bulk shield water containers made of type 304 stainless steel, located on the inside of an 8.3-m-diam vacuum vessel, with a total cost of $14.6 million for each end cell.
4. Similar to option 3, but with containers made of 5083-0 aluminum, for a total cost of $12.3 million for each end cell.
5. Integrated vacuum vessel and bulk shield of type 304 stainless steel and water, resulting in an 8.3-m-diam, double-walled vacuum vessel/bulk shield, at a total cost of $7.9 million.

The cost and weight comparisons in Table 8.7 show that the preferred option is option 5, on the basis of cost and system weight.

ORNL–DWG 84-2659 FED

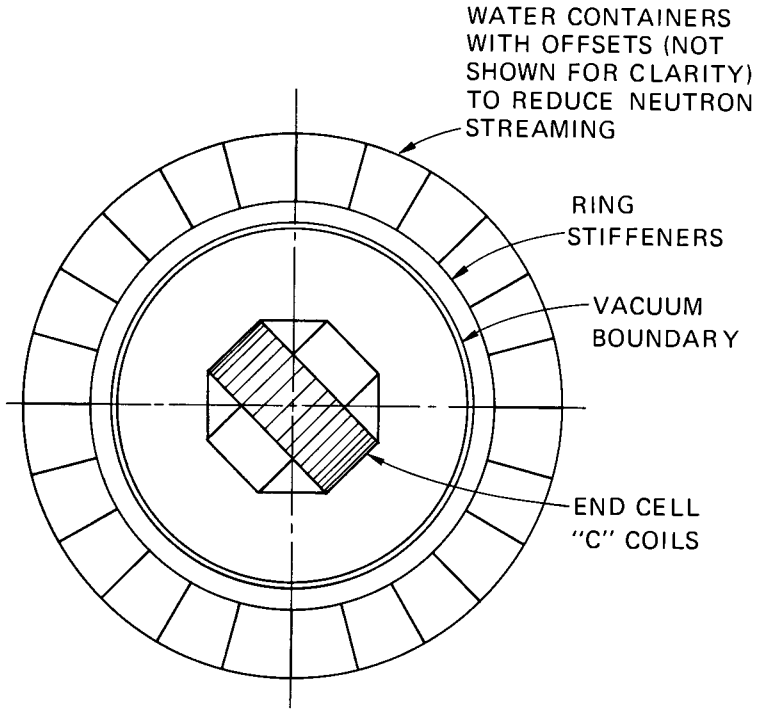

Fig. 8.43. Bulk shield water containers outside vacuum vessel.

ORNL–DWG 84-2660 FED

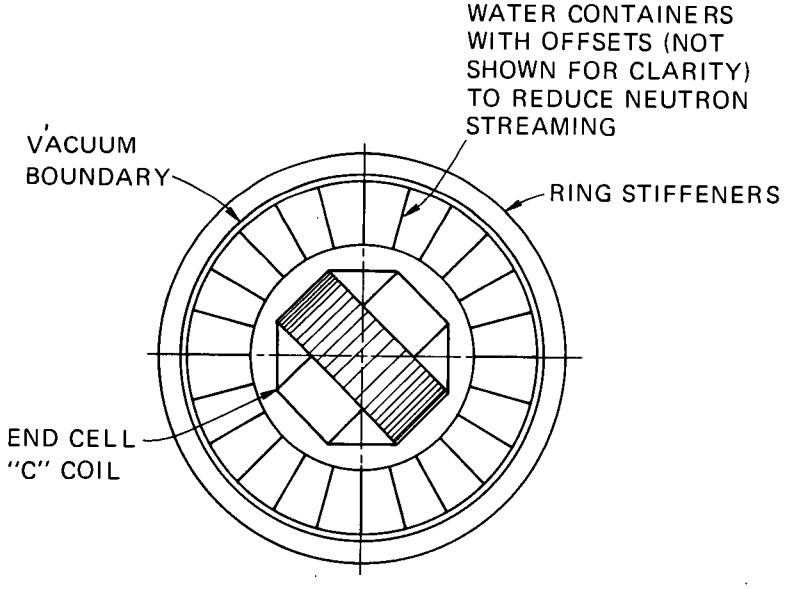

Fig. 8.44. Bulk shield water containers inside vacuum vessel.

Table 8.7. Summaries of cost and weight of water shielding for an 8.3-m-diam end cell

	Option				
	1	2	3	4	5
Weight of container, Mg	569.9	264.6	488.3	216.4	NA[a]
Weight of water, Mg	1013.4	1013.4	422.2	422.2	NA
Cost of container, millions of dollars	10.5	7.7	8.6	6.3	NA
Cost of vacuum vessel, millions of dollars	5.5	5.5	5.5	5.5	7.4
Cost of support structure, millions of dollars	0.5	0.5	0.5	0.5	0.5
Total shield weight, Mg	1583.3	1278.0	910.5	638.6	772.2
Total cost per end cell, millions of dollars	16.5	13.7	14.6	12.3	7.9

[a]NA = not applicable.

A final comparison of the options in Table 8.7 and the concepts presented in Table 8.6 results in the selection of option 5 as the reference vacuum vessel/shield design. The selection is based mainly on

- cost,
- bulk shield weight (higher weight results in higher costs for the support structure and foundation), and
- maintenance (water is drained from the shield before installation or removal).

After preliminary sizing of the structural requirements of option 5, the cost of the vacuum vessel was estimated to be $7.4 million per end cell, $4.9 million less than the cost per end cell of option 4. Incorporating the magnet support box structure and the access hatch discussed in Sect. 8.5.4 reduces the cost saving to $3.5 million per cell.

8.5.4 Maintenance Considerations

The objectives of the maintenance study were to identify a preferred approach to frequently scheduled maintenance activities and infrequently occurring major component failures and to study the effects of this approach on the design of the vacuum vessel and bulk shield.

Procedures for assembly, decommissioning, and maintenance of the MFTF-α+T magnet system, vacuum vessel, and shielding were studied. It was assumed that all major components have a high probability of lasting for the device lifetime and that if an unscheduled failure occurs the failed component will be replaced. If it is assumed that maintenance will be required, then decommissioning can be performed with the same techniques and equipment used for maintenance.

Three approaches to maintenance of MFTF-α+T were selected for evaluation:

1. Improvised techniques. Removal and installation of coils, shielding, and vacuum vessel will be performed with improvised techniques using available equipment.
2. Removal/installation through end cells. Coils and shielding will be removed and installed through the ends of the end cells using maintenance equipment designed for MFTF-α+T.
3. Vertical lifting. Coils, shielding, and vacuum vessel will be removed and installed with an overhead crane sized to lift the largest component.

Concept 1 will be the lowest-cost approach if component replacement is very infrequent, and it defers the cost of maintenance equipment to a later date. However, the feasibility of maintenance is unknown unless preplanning is done. For concept 1 to be attractive, extensive maintenance planning is needed; it must be possible to accomplish maintenance tasks with readily available equipment.

Concept 2 suffers from an inherent disadvantage: it may be necessary to remove many good components to reach a failed component (especially one in the central cell or axicell). The time needed for coil removal is not critical, due to the long lead time for acquiring new coils; however, the problem of disconnecting and requalifying satisfactory components will have a major impact on availability and operating cost. On the plus side, the capacity of the overhead crane provided for component removal need not exceed the weight of a single coil ($\sim 5.6 \times 10^4$ kg).

Concept 3, vertical lifting with an overhead crane, has the following impacts.

1. An overhead crane that can carry the heaviest component is needed.
2. The vault must include headroom for a large-capacity crane.
3. Hatches must be provided in the central cell and the end cells.
4. The vault walls must support the weight of the crane and the load.

An overhead crane with a 150-ton capacity can perform all the required functions. The weights of the major components are as follows.

Item	Weight, kg (tons)
Plug coils and structure	114,000 (125)
End-cell vacuum vessel hatch	91,000–109,000 (100–120)
Central-cell section with coils and shielding, ~2.3 m long	173,000 (>300)
D-T axicell	>273,000 (>300)

The D-T axicell can be designed in three sections, each weighing less than 150 tons.

Option 3, vertical lifting, is recommended because it requires removal of a minimum number of good components to reach a failed component and because it will improve the requalification of the total system with minimum effort and cost.

9. SHIELDING AND MATERIALS STUDIES

Y. Gohar
Argonne National Laboratory

B. Engholm
GA Technologies, Inc.

F. W. Wiffen
Oak Ridge National Laboratory

CONTENTS

9.1 INTRODUCTION 9-3
9.2 SHIELDING CRITERIA 9-3
9.2.1 Coil Shielding Criteria 9-3
9.2.2 Personnel Shielding Criteria 9-5
9.3 MATERIALS CONSIDERATIONS 9-6
9.3.1 Shielding System Materials 9-6
9.3.2 First Wall Materials 9-6
9.4 DESIGN ANALYSES AND TRADE-OFF STUDIES 9-8
9.4.1 D-T Axicell with Blanket Test Module 9-9
9.4.2 D-T Axicell Beyond Blanket Test Module 9-13
9.4.3 D-T Axicell 12-T Choke Coil 9-16
9.4.4 Central-Cell Shield and Coils 9-20
9.4.5 End-Cell Shield and Coils 9-23
9.5 ACTIVATION ANALYSES 9-27
9.5.1 Axicell and Central Cell 9-30
9.5.2 Choke Coils 9-37
9.5.3 End Cells 9-38
REFERENCES 9-40

9. SHIELDING AND MATERIALS STUDIES

9.1 INTRODUCTION

The shielding system has two major functions: (1) to protect the superconducting coils from radiation damage and excessive nuclear heating and (2) to provide biological protection by limiting the shutdown dose rate to 0.5 mrem/h after the machine has been shut down for 24 h. Design constraints require the superconducting coils to last for the device lifetime and require personnel access to the reactor vault 24 h after shutdown, which reduces both the reactor downtime and the capital cost of remote-maintenance equipment.[1]

Materials for the shielding system were selected based on trade studies and results from previous designs.[2–4] Cost, availability, and performance were considered. The reference shielding materials are water, concrete, and steel (Fe1422 or Nitronic 33). A small amount of boron carbide is used as a neutron absorber, and a thin layer of lead is used as a gamma-ray attenuator at the outermost shield surfaces.

The criteria and constraints adopted for the design, the reference shielding analyses and trade studies for each shielding component, and activation analyses for major components are presented in this chapter.

9.2 SHIELDING CRITERIA

9.2.1 Coil Shielding Criteria

In both normal and superconducting magnet coils, the critical material problems are irradiation-induced changes in the properties of the component materials. Degradation in the strength of insulators and changes in the resistivity of copper will be the changes of greatest significance. The neutron fluence in MFTF-α+T is not expected to affect the parameters of the superconductor materials. Nuclear heating of the coils is a consideration.

Radiation limits on electrical insulation

The most sensitive coil component is the insulation material, because radiation damage in this component is irreversible and limits the coil operating life.

The probable maximum radiation exposure that can be tolerated by the organic insulators used in superconducting magnets is reviewed in ref. 5. Irradiation studies at 4 K suggest that polyimide can be used at up to 1×10^{10} rad and retain 75% to 80% of its mechanical strength;[6,7] the epoxies G-10 and G-11 show serious degradation at 2×10^{9} rad. The limiting doses of 2×10^{8} rad for epoxies and 1×10^{9} rad for polyimides were judged in ref. 5 to be realistic. Further experimental data are needed to refine these limits.

The effects of irradiation temperature on the properties of organic insulators are not well known. Fatigue tests indicate that allowable doses at room temperature may be lower than those just stated; cyclic compression tests, however, indicate higher allowable doses.

Until both the required properties and the effects of irradiation are determined, the dose limits for organic insulators in cryogenic service should be used for service near room temperature.

Unshielded or lightly shielded normal coils may have to operate in much higher radiation fields than those stated for superconducting coils. If the lifetime exposure exceeds about 1×10^{10} rad [roughly equivalent to a neutron fluence near 1×10^{19} n/cm^2 (>0.1 MeV)], ceramic insulators should generally be specified. In the high-field coils of MFTF-α+T, the maximum calculated fluence is 2.6×10^{22} n/cm^2 (>0.1 MeV). Several candidate insulators have been irradiated to comparable fluences. At levels lower than 1×10^{20} n/cm^2, most ceramics show no change in structural properties.[8,9] From 1×10^{20} n/cm^2 to 1×10^{22} n/cm^2, ceramics show changes in properties, and swelling begins to affect stress levels in the coil pack. For irradiation of MgO and $MgAl_2O_4$ to 2.2×10^{22} n/cm^2 (>0.1 MeV) at 400°C and 540°C, densification of 0.4% or less results, and strength (measured in bend tests) increases by 20% to 90% above unirradiated values.[10] Even at about 5×10^{22} n/cm^2 the $MgAl_2O_4$ swelling is expected to be about 3 vol % (ref. 9), which can be accommodated in the design. In general, these ceramics will be unaffected by the magnet service environment.

Radiation limits on copper

The electrical resistivity ρ of the copper stabilizer in the superconducting coils is given by

$$\rho = \rho_0 + \Delta\rho_m + \Delta\rho_r \ , \qquad (9.1)$$

where ρ_0 is the initial resistivity, $\Delta\rho_m$ is the magnetoresistivity, and $\Delta\rho_r$ is the radiation-induced resistivity. The OFHC copper stabilizer in MFTF-α+T has a residual resistivity ratio of 180:240.[11] The resistivity of annealed OFHC copper of average purity at 4.5 K is $\sim 8 \times 10^{-9}$ Ω·cm. In general, $\Delta\rho_m$ is a function of ρ_0 and $\Delta\rho_r$ and of the magnetic field; also, $\Delta\rho_m$ and the magnetic field are space dependent, which complicates the evaluation of ρ. For unirradiated coils at 10 T, $\Delta\rho_m \sim 5 \times 10^{-8}$ Ω·cm; at a neutron fluence of 10^{18} n/m^2, $\Delta\rho_r \sim 7 \times 10^{8}$ Ω·cm (ref. 6).

This increase in resistivity can be accommodated in the design process

- by using more copper to reduce the resistance, which increases coil thickness and cost;
- by using a thicker shield to reduce the neutron fluence, which increases the coil size needed to produce a given field strength; or
- by warming the coil during shutdown periods to anneal the irradiation-induced resistivity.

Usually a combination of all three methods is used. If the heating limits on energy deposited in the magnet and the radiation limit on the organic insulator are met, neutron irradiation is not expected to significantly affect the stabilizer in the MFTF-α+T superconducting coils.

However, irradiation will produce potentially important property changes in the conductors of the high-field normal magnets. Perkins has considered effects on the insert coil for the MARS design,[12] and his results predict that with a conductor made of AMAX-MZC copper-base alloy (with 75% IACS conductivity), irradiation during service to a neutron wall loading $\Gamma_n = 2$ MW·year/m^2 will produce a maximum resistivity increase of ~24% and a volume-averaged resistivity increase for the coil of ~5.4%. Irradiation effects on dimensional stability and mechanical properties are of potential concern, but data for use in predicting these effects are not available. Probable results are swelling (of not more than 1% to 2%), increased tensile strength, and reduced elongation to fracture. Although ductility will be reduced by irradiation, ductile mode fracture with at least a few percent elongation is anticipated. Irradiation creep deformation during service can also be expected, but creep rates cannot be predicted until experimental data are available.

Radiation limits on superconductor materials

The superconductor materials to be used in MFTF-α+T are characterized by three parameters: critical current density J_c, critical temperature T_c, and upper critical field H_{c2}. Neutron irradiation of superconductor materials generally tends to lower J_c and T_c. At a neutron fluence of 4×10^{18} n/cm^2 ($E > 0.1$ MeV), J_c for NbTi is decreased by about 10% (refs. 13–15), and T_c and H_{c2} are unchanged.[16,17] However, T_c for Nb_3Sn significantly decreases at a fluence about 1×10^{18} n/cm^2 (ref. 17). Experiments on Nb_3Sn at low temperature[18,19] show that J_c increases, reaches a maximum, and decreases as the neutron fluence increases; this increase depends on the operating current and field.[20] The fluence in MFTFα+T [$<1 \times 10^{18}$ n/cm^2 ($E > 0.1$ MeV)] should produce no change in the basic parameters of the superconductor materials.

Nuclear heating

Nuclear heating of the coils must be minimized both to ensure cryogenic stability and to reduce refrigeration costs. About 500 W of electrical power is needed to remove 1 W of heat from the coils at 4 K. The design limit is a few milliwatts per cubic centimeter.

9.2.2 Personnel Shielding Criteria

Personnel access to the reactor vault 24 h after shutdown requires limiting occupational exposure to satisfactory levels. Federal regulations[21] limit the occupational dose to 5 rem/year (maximum 3 rem per quarter). Based on an 8-h work day and a 40-h work week, the maximum dose is 2.5 mrem/h. However, current practice is to keep radiation exposure to levels as low as reasonably achievable (ALARA); specifically, the Department of Energy (DOE) guidelines for new facilities state:

> Exposure rates in work areas should be reduced ALARA by proper facility design and equipment layout. Design factors to consider are: occupancy time, source terms, spacing, processes, equipment, and shielding. Onsite personnel exposure levels less than one-fifth of the permissible dose equivalent levels prescribed in this chapter should be used as a design objective.[22]

This policy limits the dose to on-site workers to less than 1 rem/year (i.e., 0.5 mrem/h). In fact, 90% of U.S. radiation workers are exposed to less than 0.2 rem/year (0.1 mrem/h).[23] The design goal for MFTF-α+T is 1 rem/year (0.5 mrem/h) in the reactor vault 24 h after shutdown.

9.3 MATERIALS CONSIDERATIONS

9.3.1 Shielding System Materials

All of the shielding materials have certain physical constraints that must be considered in the design process. Using low-temperature water as coolant largely eliminates compatibility problems, but careful design of the system (e.g., pipelines, pumps, bulk shield) is required to prevent the formation of gas pockets from radiolysis. Attention to pH values and corrosion products is also necessary.

To protect concrete from loss of water, temperature effects, radiation absorption, and stress, the following design recommendations[23] are made: (1) maximum heat deposition of 1 mW/cm^3, (2) maximum temperature gradient of 1°C/cm, (3) maximum internal temperature of 80°C, and (4) maximum ambient temperature of 71°C. Lining the concrete with a steel jacket and ventilating the shielding or cooling the jacket independently may be needed to meet the temperature limitations.

The use of Fe1422 and Nitronic 33 for the steel balls of the shielding material was motivated by their low nickel concentration. This factor reduces the production of long-lived isotopes, the biological dose after shutdown, and the cost.[24]

As noted in Sect. 9.1, a small amount of boron carbide (B_4C) is used as a neutron absorber to reduce the activation and nuclear heating of reactor components and structural materials. A density factor of 0.7 has been assumed for this material to avoid the fabrication cost of high-density material.

9.3.2 First Wall Materials

The selection of first wall materials depends on several requirements, including acceptable activation levels, resistance to radiation damage, and compatibility with coolant. Activation requirements for MFTF-α+T are not yet clearly defined; preliminary analyses are presented in Sect. 9.5. Neutron activation studies will determine the acceptable isotopes to minimize activation and storage of discharged reactor components. Radiation damage at the fluence levels expected in MFTF-α+T (peak $\Gamma_n \sim 2$ MW/m^2, with a lifetime integrated fluence of $\sim$2 MW·year/m^2) may be an important concern. With low-temperature water as the coolant, coolant compatibility is not expected to be a concern. A coating or cladding on the structural materal for impurity control will probably be unnecessary, since low sputtering is anticipated.

According to the design guidelines, the first wall material for MFTF-α+T can and should be selected from readily available and fabricable materials. Candidate materials evaluated include austenitic stainless steels (e.g., type 316), ferritic steels (e.g., HT-9), copper alloys, and aluminum alloys. The most likely choice is an austenitic stainless steel, followed by a ferritic steel. The use of copper or aluminum alloy was considered unlikely, so no analysis of the effects of irradiation on these systems has been done.

Austenitic stainless steels

The response of type 316 stainless steel to a first wall exposure of 2.0 MW·year/m^2 is shown in Table 9.1. The response of a ferritic/martensitic steel, the Sandvik alloy HT-9, is given for comparison. For the projected operating temperature range (100°C to 300°C), the following property changes are noted.

Table 9.1. Irradiation response of two steels to a first-wall integrated exposure of 2 MW·year/m^2

Alloy	Displacement damage, dpa	Helium production, appm	Hydrogen production, appm
Type 316	21	310	1100
HT-9	21	220	950

Displacement damage. The displacement damage will result in structural hardening and some loss of ductility. Gases produced by transmutation reactions should have little effect.

Swelling. Swelling caused by cavity formation is dependent on fluence and temperature. For cold-worked (CW) or solution-annealed (SA) type 316 stainless steel, swelling does not occur below about 380°C. The production of helium in the fusion reactor neutron spectrum may cause a population of tiny gas bubbles to develop, but this will make only insignificant contributions to swelling. For an MFTF-α+T first wall of type 316 stainless steel, swelling will range from zero to a few tenths of a percent.

Tensile properties. Irradiation of either CW or SA type 316 to fluence levels of 5 to 10 dpa at 100°C to 300°C affects the steel's tensile properties. Strength values increase, and both materials may approach similar limiting strength values. Irradiation to higher fluences produces no further significant changes in properties.

Elongation. In CW type 316, the strengthening produces a yield strength equal to the ultimate strength, and uniform elongation drops to the range 0.1% to 0.5%. Total elongation ranges from 3% to 10%, and reduction in area values exceeds 50%, indicating a ductile mode of fracture.

The ductility of SA type 316 in postirradiation tensile tests is much greater than that of CW type 316. Most experimental results show a uniform elongation above 15% and a total elongation above 20%. However, some lower values have been reported. Klueh found a uniform elongation of 0.2% for irradiation to 5 dpa at 250°C and 290°C, followed by tests at these temperatures.[25] Total elongation was >7%, indicating a ductile failure mode.

Austenitic stainless steel weldments exhibited an intermediate response. Samples containing weld material irradiated at 55°C and tested at 35°C and 300°C showed uniform elongation of ≥3%, and their yield and ultimate strengths were nearly the same as those of irradiated SA type 316. Thus, shielding for weldments will have the same requirements as that for the base metal.

Fatigue. The fatigue life of 20% CW type 316 was tested at 430°C following irradiation at this temperature to fluences that produced 9 and 15 dpa. Fatigue life in strain-controlled tests was reduced by a factor of 3 to 10. No data are available for lower irradiation temperatures.

Creep. Irradiation creep rates have not been measured at service temperatures of interest to MFTF-α+T. The phenomenon should be of little concern at the low stresses anticipated for this application.

Alternative first wall materials

Only two of the many alloy systems that can be considered as alternatives to the austenitic stainless steels appear to be serious contenders: the ferritic/martensitic steels and low-activation grades of steels.

Ferritic steels, such as the Sandvik alloy HT-9, have become of interest to fusion reactors because of their potentially greater resistance to swelling than the austenitic stainless steels. However, for the projected fluence limit of 21 dpa and service temperatures of 100°C to 300°C, swelling is not a concern. Body-centered-cubic steels, including the ferritic/martensitic class, are subject to a ductile-to-brittle transition temperature (DBTT) with brittle failure below this temperature. The DBTT is also shifted upward by irradiation, and for an alloy such as HT-9 it would probably be above the shutdown temperature for MFTF-α+T.

A further liability of HT-9 and similar alloys is the required postweld heat treatment during fabrication. This treatment, required to prevent cracking in all weld regions, involves holding the weld zone at a temperature of at least 700°C for times of 30 min or longer. This would include treatment of final assemblies of first wall/shield components.

New grades of steel are now under consideration to minimize the waste storage requirements of spent fusion reactor components. These steels will be new compositions, with alloy substitutions made to reduce the content of Ni, Mo, Cu, Nb, and N. These new steels can be expected to have properties similar to those of the "conventional" steels on which they are modeled. However, developing suppliers, fabrication technology, industrial experience, and an adequate database for these new alloys will require long-range programs. The risk of using these new compositions in a near-term project such as MFTF-α+T would not justify the potential advantages of waste disposal for a single reactor experiment, and use of such material should only be contemplated if it is judged to be a crucial step in gaining experience with the alloy system. This step can only be taken at the additional cost of using the unproven alloy.

9.4 DESIGN ANALYSES AND TRADE-OFF STUDIES

The reactor vessel was divided into five zones to account for the axial variation in neutron source, reactor geometry, and reactor components. A shielding analysis and trade-off study were performed for each zone to optimize the shield design and to satisfy the

design requirements and constraints. The five zones, shown in Fig. 9.1, may be characterized as follows.

- Zone 1: test blanket module and CS0 copper coil, with a D-T neutron source strength of 1.4×10^{16} n/cm^2·s (2-MW/m^2 neutron wall loading at the 25-cm first wall radius).
- Zone 2: similar to zone 1 except that it has steel-ball shielding instead of the test blanket module.
- Zone 3: CC1 and CS1 choke coils, which reduce D-T neutron source strength to 1.75×10^{15} n/cm^2·s.
- Zone 4: CC2 and S1 through S5 coils, with D-T neutron wall loading of 0.14 MW/m^2 at the 45-cm first wall radius.
- Zone 5: end cell (coils T1, A1, A2, P1, P2, T2, and DC).

Calculations were performed using the discrete-ordinate code ANISN[26] with an S_8 symmetric angular quadrature set and a P_3 Legendre expansion for the scattering cross sections. A 67-multigroup cross-section set (46 neutrons, 21 photons) collapsed from the CTR library[27] was used. The MACKLIB code[28] was used to calculate the nuclear response functions (nuclear heating, radiation damage, gas production, etc.), and the RACC code[29] was used to calculate gamma-ray sources after shutdown for dose equivalent analyses.

9.4.1 D-T Axicell with Blanket Test Module (Zone 1)

The 2-MW/m^2 D-T neutron wall loading at the first wall, the individual runs lasting 1 to 10 h, and the 10% availability provide an excellent environment for testing liquid metal blankets and some capacity for testing solid breeders. The parameters of the blanket test module and shield are given in Table 9.2. The dimensions and composition are based on the detailed analysis performed for the blanket comparison and selection study.[30] The blanket uses a lithium-lead breeder with 90% ^{6}Li enrichment; the breeder

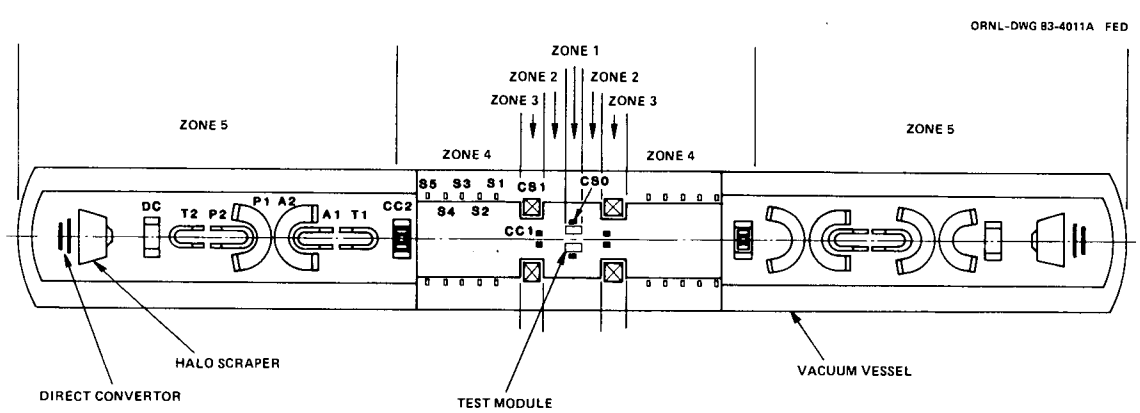

Fig. 9.1. Shielding analysis zones.

Table 9.2. Blanket and shield parameters for the D-T axicell with blanket test module

Region	Radial extent, cm		Thickness, cm	Composition by volume
	From	To		
Plasma	0	25	25	Vacuum (15-cm source radius)
First wall	25	26	1	50% $Li_{17}Pb_{83}$, 50% type 316 stainless steel
Breeder zone	26	65	39	80% $Li_{17}Pb_{83}$, 10% type 316 stainless steel, 10% vacuum
Reflector	65	85	20	10% $Li_{17}Pb_{83}$, 80% type 316 stainless steel, 10% vacuum
Water shield	85	110	25	90% H_2O, 10% Fe1422
Boron shield	110	120	10	80% B_4C, 10% H_2O, 10% Fe1422
Lead shield	120	130	10	100% Pb
Concrete shield	130	220	90	100% concrete
Boron shield	220	225	5	90% B_4C, 10% Fe1422
Lead shield	225	230	5	100% Pb

zone is 40 cm thick (including the 1-cm-thick first wall). The 20-cm-thick reflector zone uses lithium-lead as coolant. Type 316 stainless steel is used as the structural and reflector material. The reference design includes a water-concrete shield behind the blanket to satisfy the 0.5-mrem/h dose limit 24 h after shutdown.

The parameters (as defined from the magnetic analysis) of the blanket test module and shield with the CS0 copper coil inserted behind the blanket are given in Table 9.3. Table 9.4 lists the radiation response parameters in the lithium-lead blanket. The energy multiplication factor of this blanket is 1.18, with 1.28 tritons produced per D-T neutron in the blanket. With this neutron exposure, the type 316 stainless steel is subject to a maximum atomic displacement of 24.1 dpa and a neutron fluence ($E > 0.1$ MeV) of 3×10^{22} n/cm^2.

The radiation response of the CS0 copper coil is given in Table 9.5. The heat load is 11 W/cm of coil length in the axial direction, which can be removed without difficulty. However, the maximum radiation dose in the electrical insulator exceeds the radiation limits for polyimides. This high radiation dose can be accommodated by (1) replacing the lithium-lead breeder in front of the coil with shielding material, (2) using ceramic insulator with a dose limit of 10^{13} rad, or (3) increasing the inner radius of the coil by 28 cm to allow for adequate shielding for the coil.

Two options for test module shielding are considered. The first consists of steel (Fe1422 or Nitronic 33) as a basic shielding material, boron carbide as a neutron absorber, and lead at the outermost surface of the shield to attenuate the decay gamma

Table 9.3. Blanket and shield parameters for the D-T axicell with the blanket test module and the CS0 copper coil

Region	Radial extent, cm From	Radial extent, cm To	Thickness, cm	Composition by volume
Plasma	15	25	10	Vacuum (15-cm source radius)
First wall	25	26	1	50% $Li_{17}Pb_{83}$, 50% type 316 stainless steel
Breeder zone	26	65	39	80% $Li_{17}Pb_{83}$, 10% type 316 stainless steel, 10% vacuum
Reflector	65	85	20	10% $Li_{17}Pb_{83}$, 80% type 316 stainless steel, 10% vacuum
Coil case	85	87.5	2.5	100% type 304 stainless steel
Coil winding	87.5	117.5	30	60% Cu, 35% H_2O, 5% insulator
Coil case	117.5	120	2.5	100% type 304 stainless steel
Boron shield	120	125	5	80% B_4C, 10% H_2O, 10% Fe1422
Lead shield	125	130	5	100% Pb
Concrete shield[a]	130	220	90	100% concrete
Boron shield	220	225	5	90% B_4C, 10% Fe1422
Lead shield	225	230	5	100% Pb

[a]Concrete shield thickness was varied in the analysis.

Table 9.4. Radiation response parameters in the lithium-lead test blanket (based on 2-MW/m² D-T neutron wall loading and 2-MW·year/m² D-T neutron exposure at the first wall)

Nuclear heating in the first wall, W/cm³	
Neutron	6.04
Gamma	8.46
Total	15.50
Neutron fluence in the first wall, n/cm²	
$E > 0.1$ MeV	3.01×10^{22}
$E > 0.0$ MeV	3.41×10^{22}
Atomic displacement in the first wall, dpa	24.1
Maximum nuclear heating in the $Li_{17}Pb_{83}$ breeder, W/cm³	
Neutron	3.94
Gamma	11.50
Total	15.40
Total nuclear heating per fusion neutron in the blanket, MeV	
Neutron	8.46
Gamma	8.14
Total	16.60
Tritium production rate per fusion neutron in the blanket	1.28

Table 9.5. Radiation response parameters in the CS0 coil [based on 2-MW/m² neutron wall loading and 2-MW·year/m² D-T neutron exposure at the first wall (25-cm radius)]

Maximum neutron fluence in the winding pack, n/cm²	
$E > 0.1$ MeV	5.68×10^{20}
$E > 0.0$ MeV	1.24×10^{21}
Maximum nuclear heating in the coil case, W/cm³	
Neutron	2.09×10^{-2}
Gamma	4.18×10^{-1}
Total	4.39×10^{-1}
Maximum nuclear heating in the winding pack, W/cm³	
Neutron	1.41×10^{-1}
Gamma	5.23×10^{-1}
Total	6.64×10^{-1}
Total nuclear heating in the coil case, W/cm	7.07×10^{2}
Total nuclear heating in the winding pack, W/cm	3.88×10^{3}
Maximum radiation dose in the electrical insulator, rad	
Neutron	6.08×10^{11}
Gamma	2.65×10^{11}
Total	8.73×10^{11}

rays. The second option uses ordinary concrete instead of steel to reduce the cost and the radioactive inventory in the shield. The maximum nuclear heating in the concrete material is limited to 1 mW/cm³ (see Sect. 9.3.1). The use of concrete behind the lithium-lead test blanket results in a maximum heat load of ~0.4 W/cm³ in the concrete, which is unacceptable. To counteract this high heat load at the concrete surface, another shielding section was introduced behind the lithium-lead test blanket. The results show that a 45-cm-thick shield section reduces the maximum nuclear heating in the ordinary concrete to 0.2 mW/cm³.

These shield options were analyzed to determine the total shield thicknesses needed to achieve the 0.5-mrem/h dose equivalent one day after shutdown. Figure 9.2 shows the neutron flux at the outer surface of the shield as a function of the combined blanket and shield thickness. The CS0 copper coil at the back of the blanket reduces the combined blanket and shield thickness (including the CS0 coil) required to meet the dose criterion by 20 cm. Figure 9.3 shows the dose equivalent 24 h after shutdown as a function of the combined blanket and shield thickness. For the steel shield, a 148-cm combined blanket and shield thickness is needed to achieve the required dose level. The concrete shield with copper coil requires an additional 37 cm to get the same dose level. For the shield without the copper coil, the combined blanket and shield thickness is 205 cm, which is the reference shield thickness.

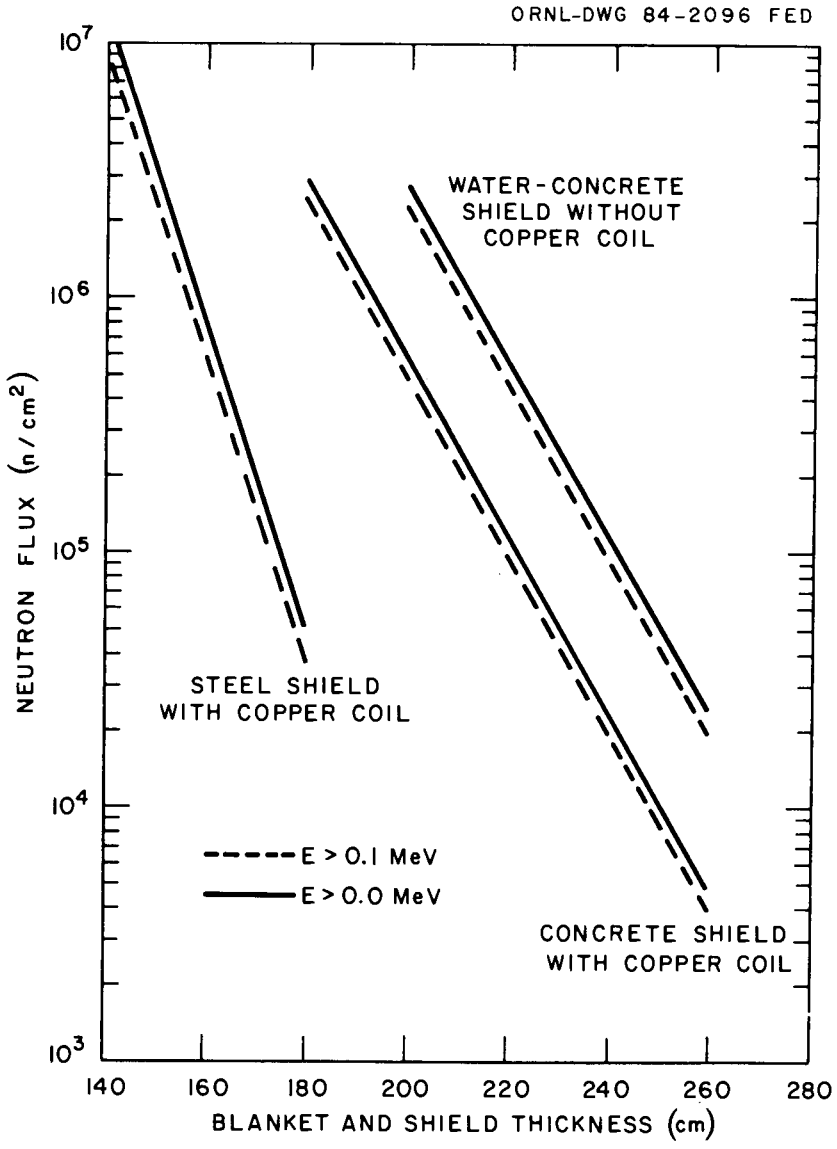

Fig. 9.2. Neutron flux at the outer shield surface as a function of the combined blanket and shield thickness (60-cm-thick blanket) based on a 2-MW/m² D-T neutron wall loading at the first wall.

9.4.2 D-T Axicell Beyond Blanket Test Module (Zone 2)

The section between the blanket test module and the D-T axicell 12-T choke coil is dedicated to capsule-type tests. Four options, described in Table 9.6, are considered for shielding this section.

The neutron flux as a function of shield thickness is shown for the steel shield and the water shield in Fig. 9.4. The thickness required to achieve a given neutron flux level with the steel shield is about two-thirds that required with the water shield.

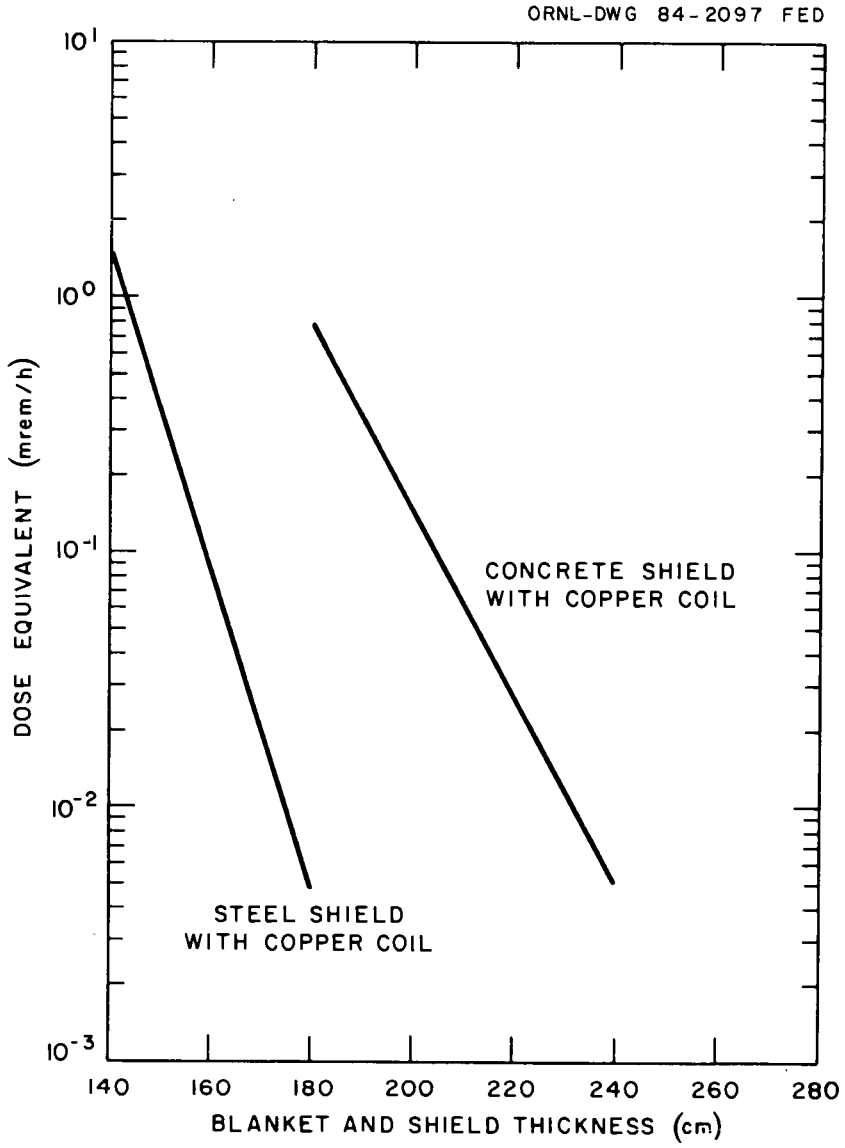

Fig. 9.3. Dose equivalent 24 h after shutdown as a function of the combined blanket and shield thickness.

The water-concrete shield includes a 59-cm-thick layer of 10% Fe1422, 90% H_2O that reduces the maximum nuclear heating in the concrete to <1 mW/cm^3. For a 240-cm-thick shield, the water shield reduces the total neutron flux an order of magnitude less than the water-concrete shield. However, the attenuation performance is reversed for neutrons with $E > 7$ MeV. For example, the 14-MeV neutron flux from the water shield is about a factor of 2 higher than that from the water-concrete shield. The difference in the attenuation of high-energy neutrons is a key factor in determining the required shield thickness, which is based on dose equivalent requirements and radioactivity levels in reactor components outside the shield. The dose analysis shows that either a water or a

Table 9.6. Shield composition for different options

Shield option	Composition	Layer thickness, cm
Steel shield	50% Fe1422, 50% H_2O	1
	90% Fe1422, 10% H_2O	Varied
	10% Fe1422, 90% B_4C	5
	100% Pb	5
Water shield	50% Fe1422, 50% H_2O	1
	10% Fe1422, 90% H_2O	Varied
	10% Fe1422, 90% B_4C	5
	100% Pb	5
Water-concrete shield	50% Fe1422, 50% H_2O	1
	10% Fe1422, 90% H_2O	59
	10% Fe1422, 10% H_2O, 80% B_4C	10
	100% Pb	10
	100% concrete	Varied
	10% Fe1422, 90% B_4C	5
	100% Pb	5
Steel ball–concrete shield	50% Fe1422, 50% H_2O	1
	60% Fe1422, 40% H_2O	59
	10% Fe1422, 90% H_2O	25
	10% Fe1422, 10% H_2O, 80% B_4C	10
	100% Pb	10
	100% concrete	Varied
	10% Fe1422, 90% B_4C	5
	100% Pb	5

water-concrete shield must be ~236 cm thick to meet the 0.5-mrem/h requirement; at this thickness, the neutron flux at the outer surface of the water shield is a factor of 4 lower than that of the water-concrete shield.

The large steel fraction of the steel ball–concrete shield reduces the shield thickness without adding to the cost by improving the attenuation characteristics. One layer (1 to 2 cm) of steel balls in a water tank yields a composition of ~60% Fe1422, 40% H_2O by volume, which is close to the optimum shield composition[31] of ~80% Fe1422, 20% H_2O. The steel balls are located in the front section of the shield to take advantage of the high inelastic cross section of the steel with the D-T neutrons and to keep the volume of the steel balls to a minimum. The steel ball–concrete shield has better attenuation characteristics than the water and the water-concrete shields, as shown in Fig. 9.5.

The thickness of the zone containing the steel balls is adjusted to achieve the 0.5-mrem/h dose equivalent 24 h after shutdown with the same outer shield thickness

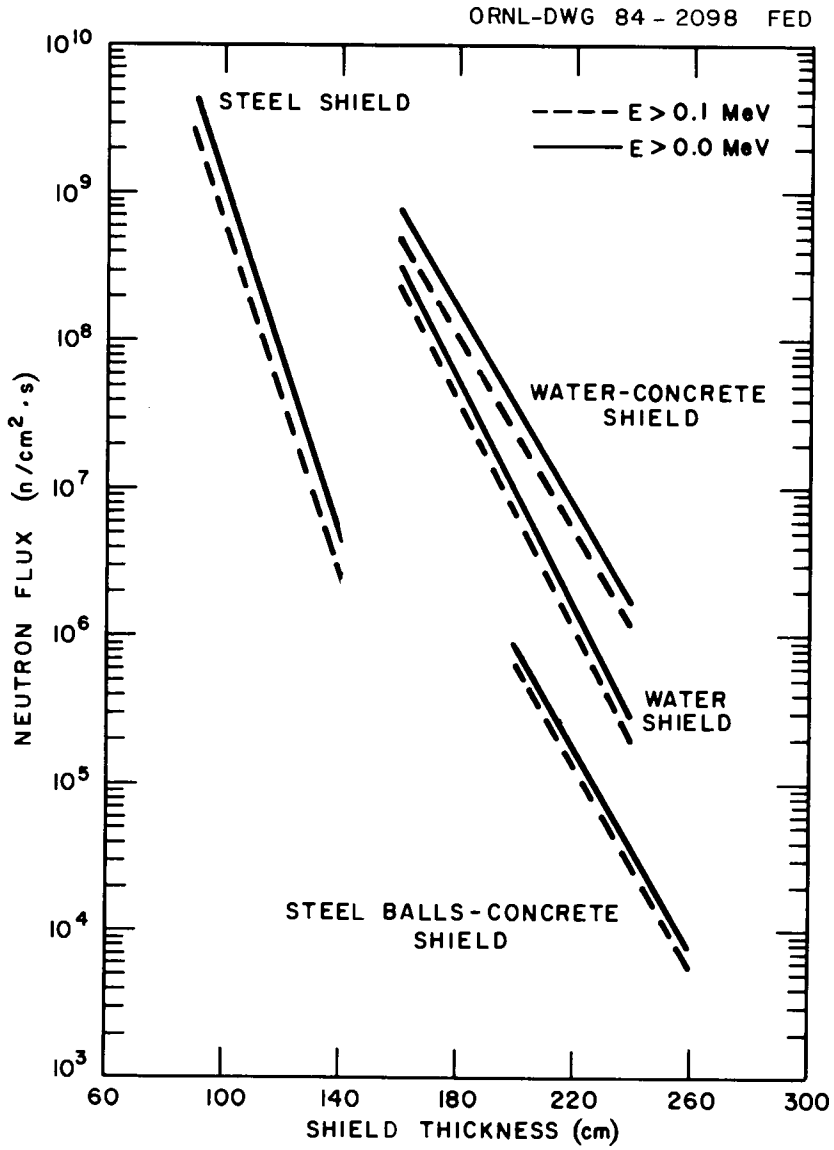

Fig. 9.4. Neutron flux at the outer shield surface as a function of shield thickness based on a 2-MW/m² D-T neutron wall loading at the first wall.

(230 cm) in both sections of the D-T axicell to facilitate the mechanical design of the shield system. The configuration given in Table 9.7 shows that a 60-cm-thick zone containing steel balls produces results similar to those given in Tables 9.2 and 9.3 for the D-T axicell with blanket test module.

9.4.3 D-T Axicell 12-T Choke Coil (Zone 3)

The choke coil for the D-T axicell consists of two coils designated CC1 and CS1. The CC1 coil is made of normal copper and has a 13-cm inner radius. Its radiation response

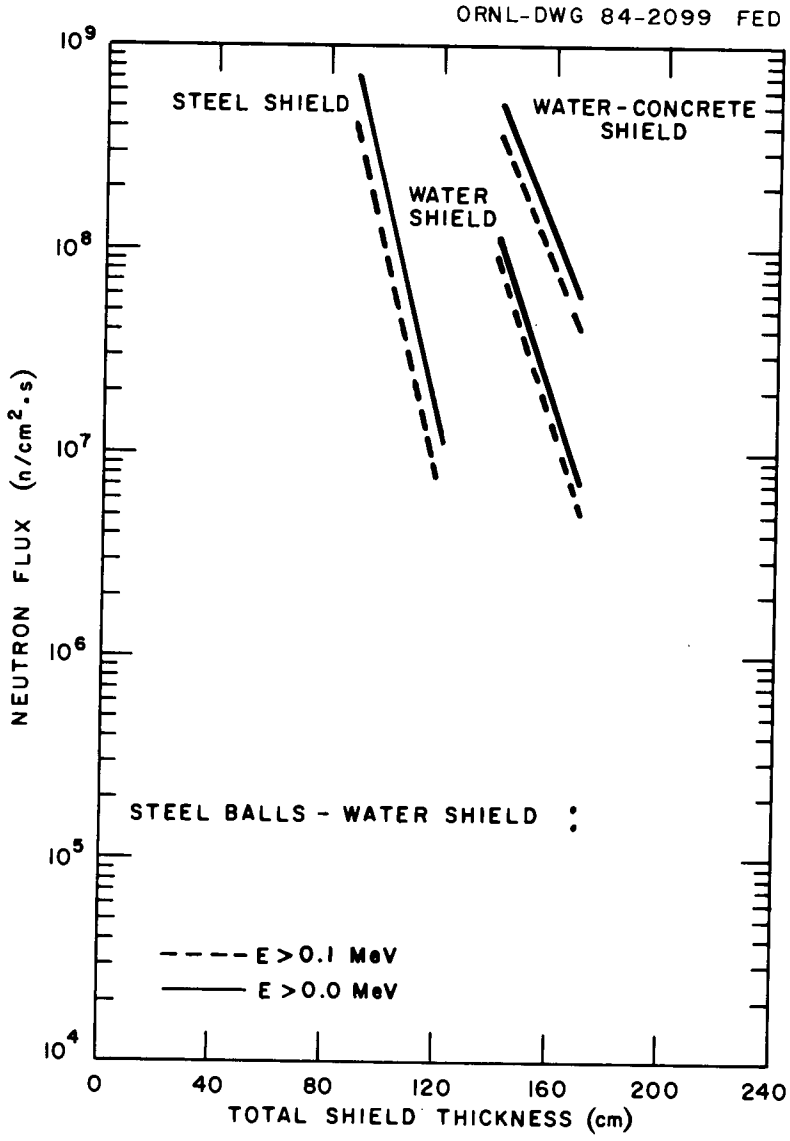

Fig. 9.5. Neutron flux at the outer shield surface as a function of shield thickness based on a 0.14-MW/m² D-T neutron wall loading at the first wall.

parameters are given in Table 9.8. The small radius of the coil increases the neutron wall loading by a factor of 25/13, which results in the high heat load shown in Table 9.8. The integrated heat load over the coil volume is 1.8 MW, assuming constant neutron wall loading. The maximum radiation dose in the insulator exceeds the dose limit for ceramic materials.

The CS1 superconducting coil is subjected to radiation leakage from the central-cell bulk shield at its inner surface and from the neutral-beam duct shield at its side surface, as shown in Fig. 9.1. Both radiation sources are treated in the shield analysis to define the

Table 9.7. Blanket and shield parameters for the D-T axicell beyond the blanket test module

Region	Radial extent, cm From	Radial extent, cm To	Thickness, cm	Composition by volume
Plasma	0	25	25	Vacuum (15-cm source radius)
First wall	25	26	1	50% H_2O, 50% type 316 stainless steel
Water-steel shield	26	85	59	40% H_2O, 60% Fe1422
Water shield	85	110	25	90% H_2O, 10% Fe1422
Boron shield	110	120	10	80% B_4C, 10% H_2O, 10% Fe1422
Lead shield	120	130	10	100% Pb
Concrete shield	130	220	90	100% concrete
Boron shield	220	225	5	90% B_4C, 10% Fe1422
Lead shield	225	230	5	100% Pb

Table 9.8. Radiation response of the CC1 coil (based on 2-MW/m² D-T neutron wall loading and 2-MW·year/m² D-T neutron exposure at the first wall)

Maximum neutron fluence in the copper material, n/cm²	
$E > 0.1$ MeV	1.66×10^{22}
$E > 0.0$ MeV	2.42×10^{22}
Maximum nuclear heating in the coil case, W/cm³	
Neutron	15.1
Gamma	29.9
Total	45.0
Maximum nuclear heating in the winding pack, W/cm³	
Neutron	12.3
Gamma	20.8
Total	33.1
Total nuclear heating in the coil case, W/cm	7.51×10^3
Total nuclear heating in the winding pack, W/cm	4.03×10^4
Maximum radiation dose in the electrical insulator, rad	
Neutron	5.61×10^{13}
Gamma	1.16×10^{13}
Total	6.77×10^{13}

coil's radiation response. The shield parameters are listed in Table 9.9. The configuration allows 80 cm of shielding between the first wall and the coil case. A steel ball shield was selected to reduce the cost and retain the attenuation characteristics of the steel shield. Table 9.10 gives the radiation response of the CS1 coil with different Fe1422 concentrations in the shield. Two concentrations are analyzed to represent the steel ball shield with one layer of steel balls and the optimum steel shield composition.[31] The change in the steel fraction from 60% to 80% increases the radiation response parameters by a factor of 2. However, the shield with 60% steel performs satisfactorily, as shown in Table 9.11.

Table 9.9. Shield parameters for the D-T axicell superconducting choke coil (CS1)

Region	Radial extent, cm		Thickness, cm	Composition by volume
	From	To		
Plasma	0	45	45	Vacuum (13-cm source radius)
First wall	45	46	1	50% H_2O, 50% Fe1422
Water-steel shield	46	120	74	40% H_2O, 60% Fe1422
Boron shield	120	125	5	10% H_2O, 80% B_4C, 10% Fe1422
Gap	125	135	10	Vacuum
Coil case	135	140	5	60% type 304 stainless steel, 40% vacuum
Coil winding	140	240	100	62% Cu, 18% insulator, 20% vacuum
Coil case	240	245	5	60% type 304 stainless steel, 40% vacuum

Table 9.10. Response of the CS1 coil with different Fe1422 concentrations to radiation leakage through the D-T axicell shield (based on 2-MW/m² D-T neutron wall loading and 2-MW·year/m² D-T neutron exposure at the first wall)

	Fe1422 concentration in the shield, %	
	60	80
Maximum nuclear heating in the coil case, W/cm³	1.18×10^{-3}	4.96×10^{-4}
Maximum nuclear heating in the winding pack, W/cm³	5.04×10^{-4}	2.17×10^{-4}
Total nuclear heating in the coil case, W/cm	2.38	1.0
Total nuclear heating in the winding pack, W/cm	4.47	2.0
Maximum neutron fluence ($E > 0.1$ MeV) in the winding pack, n/cm²	2.34×10^{17}	1.31×10^{17}
Maximum atomic displacement in the copper stabilizer, dpa	2.22×10^{-4}	9.67×10^{-5}
Maximum radiation dose in the electrical insulator, rad	7.72×10^{8}	3.43×10^{8}

Table 9.11. Response of the CS1 coil to radiation leakage through the D-T axicell shield (based on 2-MW/m² D-T neutron wall loading and 2-MW·year/m² D-T neutron exposure at the first wall)

Maximum neutron fluence in the superconductor, n/cm²	
$E > 0.1$ MeV	2.34×10^{17}
$E > 0.0$ MeV	3.51×10^{17}
Maximum atomic displacement in the copper stabilizer, dpa	2.22×10^{-4}
Maximum nuclear heating in the coil case, W/cm³	
Neutron	6.08×10^{-5}
Gamma	1.12×10^{-3}
Total	1.18×10^{-3}
Maximum nuclear heating in the winding pack, W/cm³	
Neutron	5.41×10^{-5}
Gamma	4.50×10^{-4}
Total	5.04×10^{-4}
Total nuclear heating in the coil case, W/cm	2.38
Total nuclear heating in the winding pack, W/cm	4.47
Maximum radiation dose in the electrical insulator, rad	
Neutron	5.22×10^{8}
Gamma	2.50×10^{8}
Total	7.72×10^{8}

Radiation streaming through the neutral-beam ducts is expected to have a significant impact on the performance of the CS1 coil. The current D-T axicell design allows 20 cm of shielding between the beam duct and the CS1 coil. The neutron source in the duct is calculated using an approximate approach,[32] and this source is used in one-dimensional (1-D) calculations to obtain the radiation response of the CS1 coil, which is shown in Table 9.12 for two shield thicknesses. The maximum radiation due to the duct streaming with a 20-cm-thick, 90% steel, 10% H_2O shield is two to three times that from radiation leakage through the D-T axicell shield (Table 9.11). Increasing the duct shield thickness to 25 cm reduces the radiation response parameters by a factor of 2. However, the 20-cm-thick shield provides sufficient protection to meet the design criteria for the CS1 coil, as shown in Table 9.13.

9.4.4 Central-Cell Shield and Coils (Zone 4)

The D-T neutron wall loading in the central cell is 0.14 MW/m² at the first wall (45 cm from the center). The outer shield radius is constrained to 220 cm so that the shield will fit inside the ten coils that will be taken from MFTF-B. The four shielding options described in Table 9.6 were considered for the central-cell shield. Figure 9.5 shows the neutron flux at the outer shield surface as a function of shield thickness for these options. A summary is presented in Table 9.14. For the water shield, the neutron

Table 9.12. Response of the CS1 coil to radiation leakage from the duct shield for two shield thicknesses (based on 2-MW/m² D-T neutron wall loading and 2-MW·year/m² D-T neutron exposure at the first wall)

Parameter	Shield thickness, cm	
	20	25
Maximum nuclear heating in the coil case, W/cm³	1.64×10^{-4}	9.12×10^{-4}
Maximum nuclear heating in the winding pack, W/cm³	8.85×10^{-4}	5.22×10^{-4}
Total nuclear heating in the coil case, W/cm	1.03	6.26×10^{-1}
Total nuclear heating in the winding pack, W/cm	4.06	2.31
Maximum neutron fluence ($E > 0.1$ MeV) in the winding pack, n/cm²	9.19×10^{17}	4.83×10^{17}
Maximum atomic displacement in the copper stabilizer, dpa	7.19×10^{-4}	3.52×10^{-4}
Maximum radiation dose in the insulator, rad	2.18×10^{9}	1.10×10^{9}

Table 9.13. Response of the CS1 coil to radiation leakage from the duct shield (based on 2-MW/m² D-T neutron wall loading and 2-MW·year/m² D-T neutron exposure at the first wall)

Maximum neutron fluence in the superconductor, n/cm²	
$E > 0.1$ MeV	4.83×10^{17}
$E > 0.0$ MeV	8.18×10^{17}
Maximum atomic displacement in the copper stabilizer, dpa	3.52×10^{-4}
Maximum nuclear heating in the coil case, W/cm³	
Neutron	8.88×10^{-5}
Gamma	8.23×10^{-4}
Total	9.12×10^{-4}
Maximum nuclear heating in the winding pack, W/cm³	
Neutron	7.58×10^{-5}
Gamma	4.46×10^{-4}
Total	5.22×10^{-4}
Total nuclear heating in the coil case, W/cm	6.26×10^{-1}
Total nuclear heating in the winding pack, W/cm	2.31
Maximum radiation dose in the electrical insulator, rad	
Neutron	8.65×10^{8}
Gamma	2.35×10^{8}
Total	1.10×10^{9}

Table 9.14. Neutron flux at the outer shield surface for different shield options (based on 0.14-MW/m² D-T neutron wall loading at the 45-cm-radius first wall)

Shield option	Thickness, cm	Total neutron flux ($E > 0.0$ MeV), n/cm²·s
Water	175	4.5×10^6
Water-concrete	175	3.7×10^7
Steel	120	1.1×10^6
Steel ball–water	175	1.8×10^5

flux with a 175-cm-thick shield (220-cm outer radius) is 150 times the desired value for the dose criterion. A 175-cm-thick water-concrete shield is also inadequate. A 117-cm-thick steel shield satisfies the dose criterion, but it is an expensive option. Therefore, the steel ball–concrete shield was selected to retain the attenuation characteristics of the steel shield at a lower cost. Table 9.15 gives the central-cell shield parameters. The 80-cm-thick steel ball zone gives a neutron flux of 1.8×10^5 n/cm²·s, which is about one-third the desired value for the dose criterion. The steel ball zone can be reduced to 50 cm with a 125-cm-thick water zone, lowering the cost of the shield and still satisfying the dose criterion.

The radiation responses of the S1 through S5 solenoid coils are given in Table 9.16 for the central-cell shield described in Table 9.15. The responses are about four orders of magnitude below the design criteria, because the levels of radiation leakage needed to meet the 0.5-mrem/h dose equivalent are much lower than those required to protect the coil components.

Table 9.15. Shield parameters for the central cell

Region	Radial extent, cm		Thickness, cm	Composition by volume
	From	To		
Plasma	0	45	45	Vacuum
First wall	45	46	1	50% H_2O, 50% Fe1422
Water-steel shield	46	125	79	40% H_2O, 60% Fe1422
Water shield	125	210	85	90% H_2O, 10% Fe1422
Boron shield	210	215	5	90% B_4C, 10% Fe1422
Lead shield	215	220	5	100% Pb

Table 9.16. Radiation response parameters in the S1 through S5 coils (based on 0.14-MW/m² D-T neutron wall loading and 0.14-MW·year/m² D-T neutron exposure at the 45-cm-radius first wall)

Maximum neutron fluence in the winding pack, n/cm²	
$E > 0.1$ MeV	3.38×10^{12}
$E > 0.0$ MeV	4.97×10^{12}
Maximum atomic displacement in the copper material, dpa	2.84×10^{-9}
Maximum nuclear heating in the coil case, W/cm³	
Neutron	6.33×10^{-10}
Gamma	5.14×10^{-8}
Total	5.20×10^{-8}
Maximum nuclear heating in the winding pack, W/cm³	
Neutron	6.47×10^{-10}
Gamma	2.13×10^{-8}
Total	2.19×10^{-8}
Total nuclear heating in the coil case, W/cm	2.15×10^{4}
Total nuclear heating in the winding pack, W/cm	1.85×10^{4}
Maximum radiation dose in the electrical insulator, rad	
Neutron	6.80×10^{3}
Gamma	1.23×10^{4}
Total	1.91×10^{4}

The 18-T central-cell choke coil has a hybrid design (both normal copper and superconductor) with an inner radius of 12 cm. The maximum neutron source strength along the coil axis is 10^{15} n/cm²·s. The coil geometry used in the analysis is given in Table 9.17. There is an 8-cm gap between the two sections of the coil for thermal insulation. Table 9.18 gives the radiation responses in both sections of the CC2 coil. The maximum dose in the insulator material of the copper section satisfies the design criterion for ceramic insulators, and the maximum nuclear heating in the coil case of the copper section can be removed without difficulty. In the superconducting section of the coil, the insulator dose and the neutron fluence exceed the design limit, and the maximum nuclear heating in the coil case (~46 mW/cm³) is considered excessive. To satisfy the design criteria for this section of the coil, the thickness of the copper section should be increased to 50 cm.

9.4.5 End-Cell Shield and Coils (Zone 5)

This end-cell analysis is based on simple 1-D transport calculations to obtain approximate definitions for the shield thicknesses and the nuclear responses in the coils. A detailed three-dimensional (3-D) analysis will be required later in the design process.

The maximum neutron source strength in the end cell is 5×10^{13} n/cm²·s, which corresponds to a neutron wall loading of 4.3×10^{-3} MW/m² based on the plasma geometry at this location. The end-cell configuration limits the shield thickness between

Table 9.17. 18-T choke coil geometry

Region	Radial extent, cm From	Radial extent, cm To	Thickness, cm	Composition by volume
Plasma	0.0	12.0	12.0	Vacuum
Steel case	12.0	14.5	2.5	100% type 304 stainless steel
Copper winding	14.5	39.5	25.0	60% Cu, 35% H_2O, 5% insulator
Steel case	39.5	42.0	2.5	100% type 304 stainless steel
Gap	42.0	50.0	8.0	Vacuum
Steel case	50.0	52.5	2.5	100% type 304 stainless steel
Superconductor winding	52.5	177.5	125.0	62% Cu, 18% insulator, 20% vacuum
Steel case	177.5	180.0	2.5	100% type 304 stainless steel

Table 9.18. Radiation response parameters in the CC2 coil (based on 10^{15} n/cm·s and 3.16×10^7 s of operation)

Maximum nuclear heating in the copper section, W/cm^3	
Coil case	3.38
Winding pack	2.32
Maximum nuclear heating in the superconductor section, W/cm^3	
Coil case	4.55×10^{-2}
Winding pack	2.67×10^{-2}
Maximum heat load in the copper section, W/cm	
Coil case	6.65×10^2
Winding pack	2.65×10^3
Maximum heat load in the superconductor section, W/cm	
Coil case	3.24×10^1
Winding pack	1.08×10^2
Maximum neutron fluence in the copper winding, n/cm^2	
$E > 0.1$ MeV	1.21×10^{21}
$E > 0.0$ MeV	1.77×10^{21}
Maximum neutron fluence in the superconductor winding, n/cm^2	
$E > 0.1$ MeV	1.77×10^{19}
$E > 0.0$ MeV	3.13×10^{19}
Maximum atomic displacement in the copper stabilizer, dpa	1.52×10^{-2}
Maximum insulator dose in the copper section, rad	4.71×10^{12}
Maximum insulator dose in the superconductor section, rad	4.86×10^{10}

the coils and the plasma to ~10 cm. Table 9.19 gives the maximum radiation response in the end-cell coils for a 90% Fe1422, 10% H_2O shield. With a 10-cm-thick shield, the maximum dose in the insulator is 10^{10} rad, and the maximum nuclear heating in the winding pack is 4 mW/cm^3. These responses satisfy the design criteria, but the neutron fluence in the superconductor exceeds the criteria by an order of magnitude. Increasing the shield thickness to 15 cm reduces the neutron fluence to 2.6×10^{18} n/cm^2·s. This analysis does not consider the radiation streaming from the D-T axicell or from the central cell; including the radiation streaming would probably increase the maximum responses shown in Table 9.19.

The biological shielding of the end cell has evolved from a strong desire to minimize the cost, the weight, and the radioactive inventory of the shield.[2] A water shield with boron carbide to absorb neutrons and lead to attenuate the gamma rays from the C coils was selected for this analysis; parameters are listed in Table 9.20. Figure 9.6 shows the flux at the outer shield surface as a function of shield thickness. The total shield thickness required to satisfy the dose criterion is 136 cm, excluding radiation streaming from the D-T axicell and the central cell and ignoring the reactor components outside the end-cell vessel. To account for these uncertainties, a 150-cm-thick shield is selected, which corresponds to lowering the neutron flux by a factor of 4 outside the vessel.

Table 9.19. Maximum radiation response parameters in the end-cell C coils (based on 4.3×10^{-3}-MW/m^2 D-T neutron wall loading and 4.3×10^{-3}-MW·year/m^2 D-T neutron exposure at the shield surface)

	Shield thickness, cm	
	10	15
Maximum neutron fluence in the winding pack, n/cm^2		
$E > 0.1$ MeV	9.74×10^{18}	2.58×10^{18}
$E > 0.0$ MeV	1.62×10^{19}	4.87×10^{18}
Maximum atomic displacement, dpa	3.16×10^{-3}	1.61×10^{-3}
Maximum nuclear heating in the coil case, W/cm^3		
Neutron	1.40×10^{-3}	5.72×10^{-4}
Gamma	8.29×10^{-3}	4.70×20^{-3}
Total	9.69×10^{-3}	5.27×10^{-3}
Maximum nuclear heating in the winding pack, W/cm^3		
Neutron	8.28×10^{-4}	4.26×10^{-4}
Gamma	3.31×10^{-3}	1.88×10^{-3}
Total	4.14×10^{-3}	2.31×10^{-3}
Maximum radiation dose in the electrical insulator, rad		
Neutron	7.88×10^{9}	4.06×10^{9}
Gamma	1.79×10^{9}	1.00×10^{9}
Total	9.67×10^{9}	5.06×10^{9}

Table 9.20. Shield parameters for the end cell

Region	Radial extent, cm From	Radial extent, cm To	Thickness, cm	Composition by volume
Plasma	0	10	10	Vacuum
Steel shield	10	20	10	90% steel, 10% H_2O
Gap	20	250	230	Vacuum
Water shield	250	380	130[a]	90% H_2O, 10% Fe1422
Boron shield	380	385	5	90% B_4C, 10% Fe1422
Lead shield	385	390	5	100% Pb

[a]Varied in analysis.

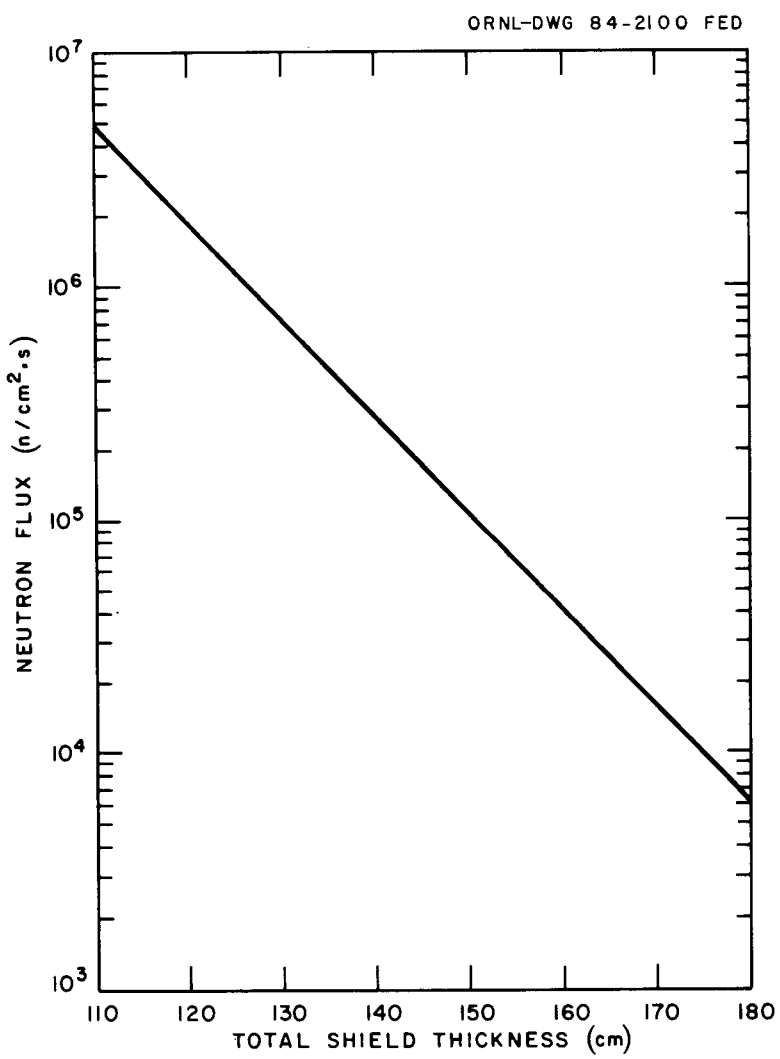

Fig. 9.6. Neutron flux at the outer shield surface as a function of shield thickness based on a 5 × 10^{13}-n/cm·s D-T neutron source in the end cell.

The direct converter (DC) coil at the end of the device is carried over from MFTF-B; the dose limit for its electrical insulator is 10^8 rad. Central-cell neutrons streaming into the end cell produce a dose rate of 2×10^9 rad to this coil, and the D-T neutron wall loading is 8.6×10^{-5} MW/m^2 on the coil surface perpendicular to the central-cell axis. A 20-cm-thick shadow shield is provided to reduce the radiation dose; parameters are given in Table 9.21. The dose to the electrical insulator is thus reduced to 10^7 rad, well within the dose limit.

Table 9.21. Maximum radiation response in the DC coil (based on 8.6×10^{-5}-MW/m^2 D-T neutron wall loading and 8.6×10^{-5}-MW·year/m^2 D-T neutron exposure at the shield surface)

Maximum neutron fluence in the winding pack, n/cm^2	
$E > 0.1$ MeV	4.42×10^{16}
$E > 0.0$ MeV	8.35×10^{17}
Maximum atomic displacement, dpa	2.76×10^{-5}
Maximum nuclear heating in the coil case, W/cm^3	
Neutron	7.21×10^{-6}
Gamma	5.92×10^{-5}
Total	6.64×10^{-5}
Maximum nuclear heating in the winding pack, W/cm^3	
Neutron	7.31×10^{-6}
Gamma	3.22×10^{-5}
Total	3.95×10^{-5}
Maximum radiation dose in the electrical insulator, rad	
Neutron	6.96×10^7
Gamma	1.72×10^7
Total	8.68×10^7

9.5 ACTIVATION ANALYSES

The accumulation of radionuclides in a fusion reactor during D-D or D-T operation has been widely discussed in the literature.[33,34] The amount, type, and location of radionuclides affect afterheat rates, shutdown dose rates, hot cell and remote handling requirements, radiation hazards, decommissioning plans, and waste disposal. These considerations are so important that an entire field of study is now directed toward developing low-activation fusion devices.[35]

Activation calculations have been performed for the axicell, central cell, and end cells of MFTF-α+T. The operating neutron fluxes were obtained using the method described in Table 9.22, and these fluxes were then used in the RACC radioactivity code,[29,36] as described in Table 9.23, to obtain curie inventories, biological hazard potential (BHP), afterheat, and shutdown gamma sources. It is important to note that only the first layers

Table 9.22. Neutron flux calculations

Method : 1-D ONEDANT discrete-ordinates code with Los Alamos National Laboratory 30-neutron-group cross sections

Geometry : Poloidal cylindrical, P_3S_8 approximation

Source terms : Axicell, 1.4×10^{16} n/cm·s D-T
Central cell, 1.75×10^{15} n/cm·s D-T
End cell, 2×10^{13} n/cm·s D-T

Region	Radial extent, cm From	To	Composition by volume
		Axicell	
Plasma	0	25	Vacuum (15-cm source radius)
Shield 1 or blanket	25	55	90% SS, 10% H_2O
Shield 2	55	90	90% H_2O, 10% SS
Shield 3	90	100	70% B_4C
Shield 4	100	110	100% Pb
		Central cell	
Plasma	0	50	Vacuum (15-cm source radius)
Shield 1	50	90	90% SS, 10% H_2O
Shield 2	90	95	70% B_4C
Shield 3	95	100	100% Pb
Shield 4	100	160[a]	100% concrete
		End cell	
Plasma	0	15	Vacuum (10-cm source radius)
Shield 1	15	25	90% SS, 10% H_2O
Cladding	25.0	25.15	100% SS
Shield 2	25.15	25.45	70% B_4C
Cladding	25.45	25.55	100% SS
Shield 3	25.55	41.35	100% H_2O
Cladding	41.35	41.5	100% SS
Shield 4	41.5	41.8	70% B_4C
Cladding	41.8	41.9	100% SS
Shield 5	41.9	42.4	100% Pb
Vault	100.0	160.0	100% concrete

[a]Arbitrary outer boundary albedo of 0.3 in all cases.

Table 9.23. Radioactivity calculations

Method : RACC code with RACCDLIB and modified RACCXLIB data libraries; ONEDANT fluxes converted to 46 groups for input to RACC

Geometry : 1-D cylindrical

Source terms : Normalized to 4-m-long axicell, 16-m-long central cell, or 6-m-long end cell

Materials : Axicell assumed to have shield blanket (90% Nitronic 33, 10% H_2O) instead of $Li_{17}Pb_{83}$; other axicell shielding is 10% Nitronic 33, 90% H_2O. Central-cell shield is 90% Nitronic 33, 10% water

Constituent JZA identification number	Atomic number density, atom/barn·cm
Nitronic 33	
70140	1.40×10^{-4}
249900	7.00×10^{-4}
240520	1.36×10^{-2}
240530	1.50×10^{-3}
240540	3.80×10^{-4}
250550	1.10×10^{-2}
260540	3.20×10^{-3}
260560	5.07×10^{-2}
260570	1.10×10^{-3}
260580	1.60×10^{-4}
260590	2.40×10^{-5}
280580	1.60×10^{-3}
280600	6.00×10^{-4}
280610	3.00×10^{-5}
280620	9.00×10^{-5}
280640	2.00×10^{-5}
Boron carbide	
50100	2.20×10^{-2}
50110	8.80×10^{-2}
Carbon	
60120	2.72×10^{-2}
60130	3.00×10^{-4}
Copper	
290630	5.88×10^{-2}
290650	2.61×10^{-2}
Water	
80160	3.35×10^{-2}
Liquid nitrogen	
70140	6.00×10^{-3}

of the shielding are included in these calculations because nearly all of the curie inventory will be located here. Also, the entire blanket in the axicell was assumed to be steel and water, rather than partly $Li_{17}Pb_{83}$ and partly steel and water. Detailed activation calculations for the breeding blanket can be made when its design is more fully defined.

The MFTF-α+T is likely to have a rather irregular operating history, but the available radioactivity code can treat only steady-state operation. Therefore, two cases were run: one for one month of operation at continuous full power and one for ten years of operation at continuous 13.7% power. Important results are summarized in Table 9.24.

Table 9.24. Important activation results for MFTF-α+T

Lifetime D-T operation of 100 h/month for 10 years

	Axicell	Central cell
Maximum afterheat level in shield after full-power operation, W/cm^3	4.5	3.2
Radioactivity immediately after full-power operation, curie	4×10^8	3.3×10^8
Radioactivity 10 years after end of life, curie	5×10^5	2.5×10^5
BHP in air immediately after full-power operation, km^3	2.3×10^7	1.2×10^7
BHP in air 10 years after end of life, km^3	5×10^5	1.6×10^5
^{60}Co inventory 10 years after end of life, curie	10^5	7×10^4

9.5.1 Axicell and Central Cell

Afterheat levels in the first two centimeters of the shield are shown in Fig. 9.7 for the axicell and in Fig. 9.8 for the central cell. Values are conservative because decay gammas were not transported from their points of birth but were assumed to deposit their energy in situ. A transport calculation would probably reduce these values by 30% to 50%.

Total afterheat levels are shown in Fig. 9.9 for the axicell and in Fig. 9.10 for the central cell. (The choke coils are not included.) The total heat load of ~20 kW in the axicell immediately after shutdown should present no problems.

Total curie inventories are shown in Fig. 9.11 for the axicell and in Fig. 9.12 for the central cell. (Again, the choke coils are not included.) The curves show a rapid dropoff beginning about three years after shutdown. The primary nuclide remaining at 300 years (10^{10} s) is ^{63}Ni.

Figures 9.13–9.16 show BHPs in air and water for the axicell and central cell. Inventories of ^{60}Co, ^{58}Co, and ^{56}Mn, which are of interest for shield design, shutdown dose rates, and maintenance procedures, are plotted in Figs. 9.17–9.20.

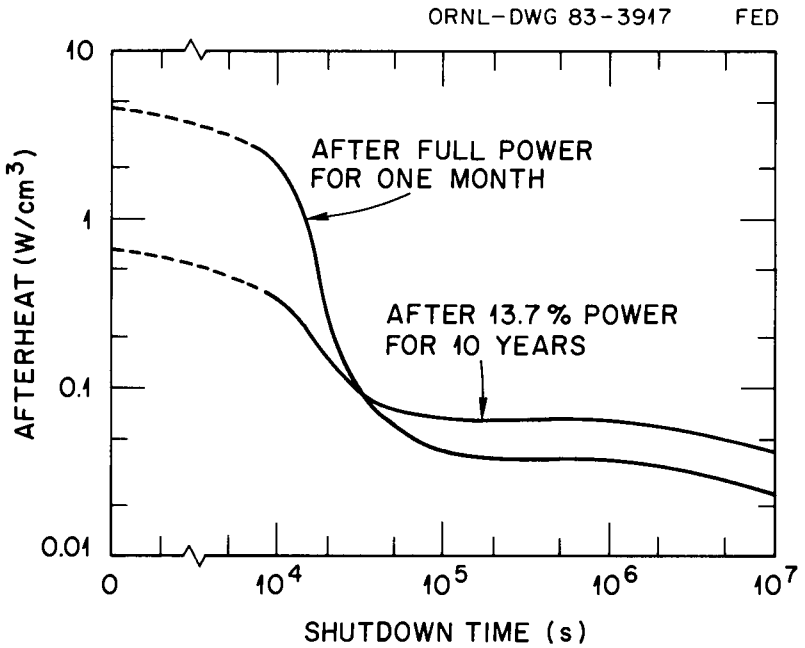

Fig. 9.7. Axicell afterheat in first 2 cm of Nitronic 33 shield.

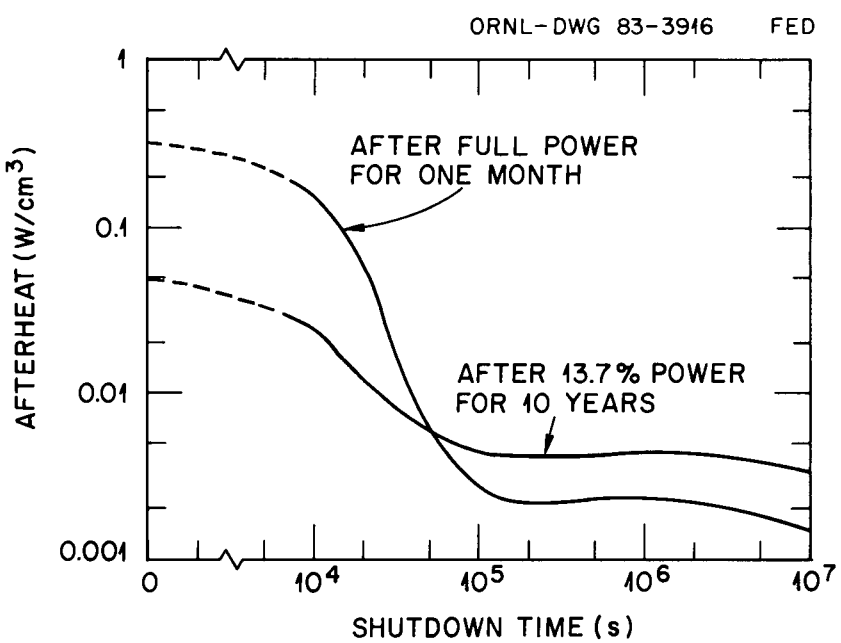

Fig. 9.8. Central-cell afterheat in first 2 cm of Nitronic 33 shield.

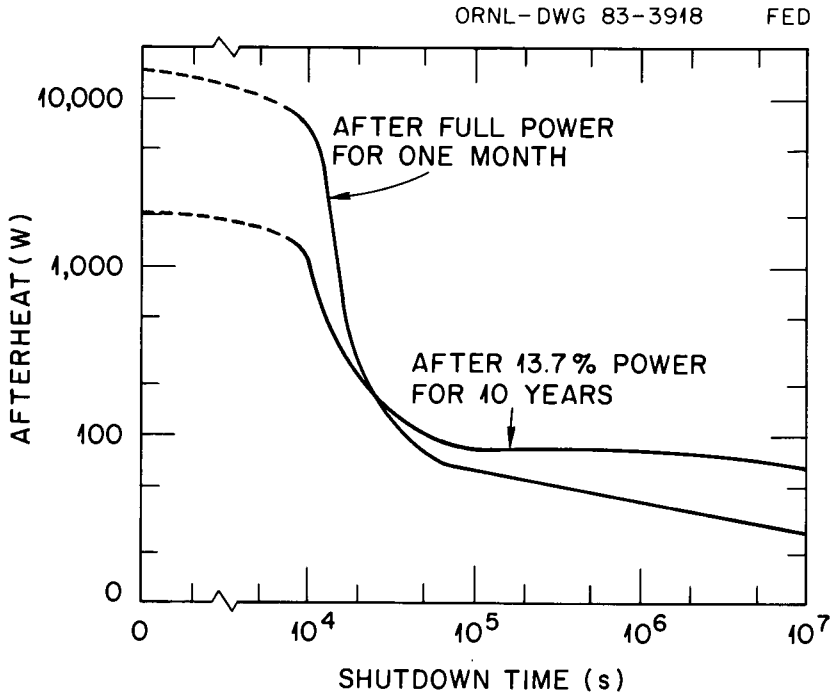

Fig. 9.9. Total afterheat in the axicell (excluding choke coils).

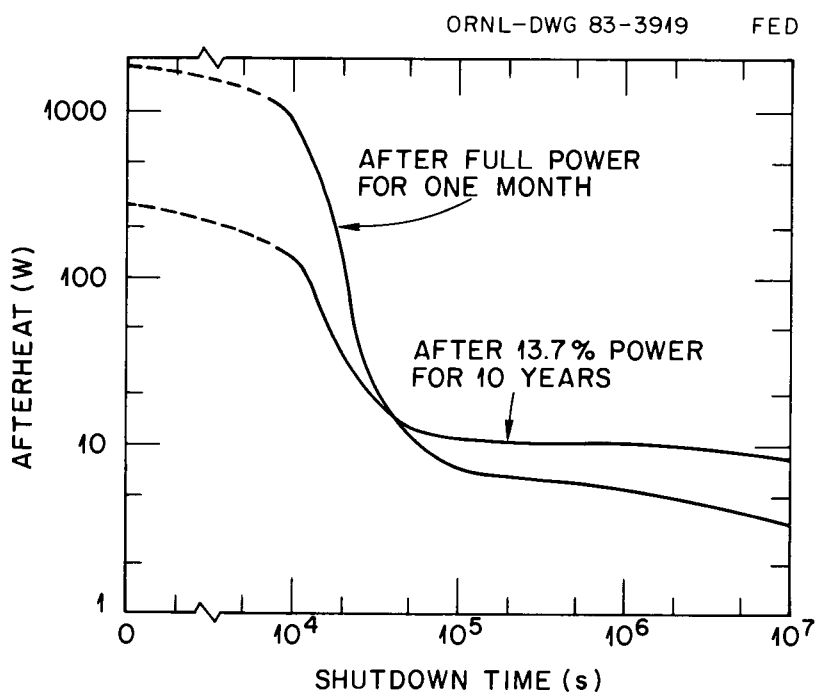

Fig. 9.10. Total afterheat in the central cell.

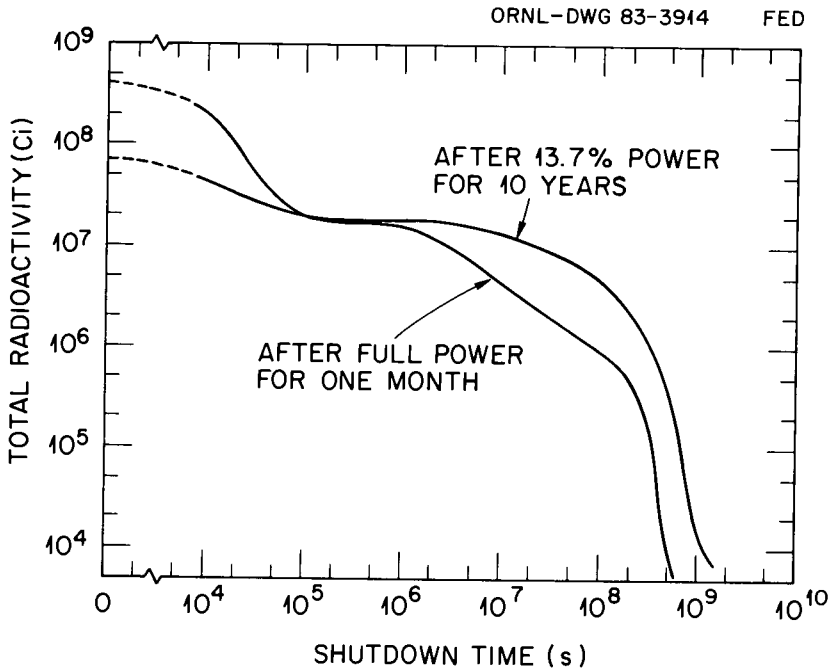

Fig. 9.11. Axicell radioactivity.

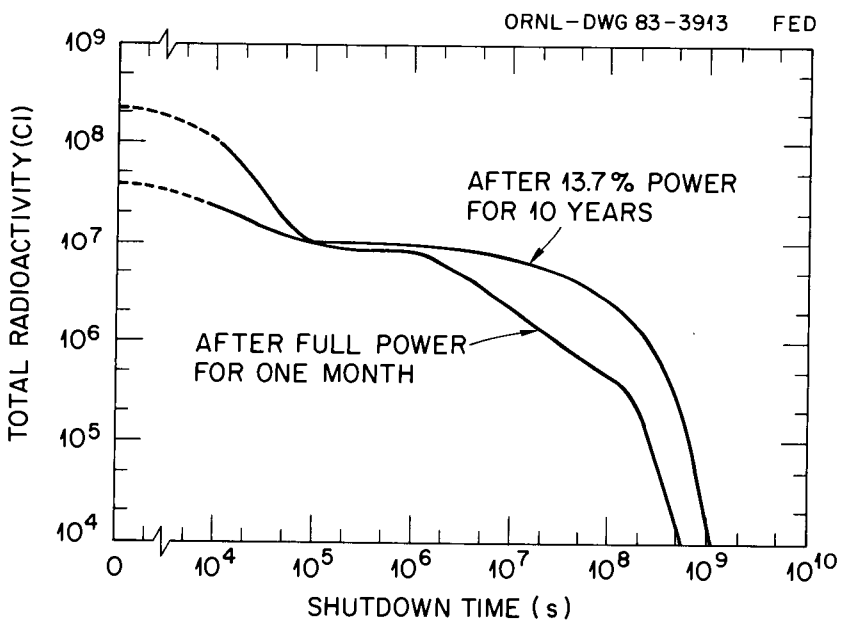

Fig. 9.12. Central-cell radioactivity.

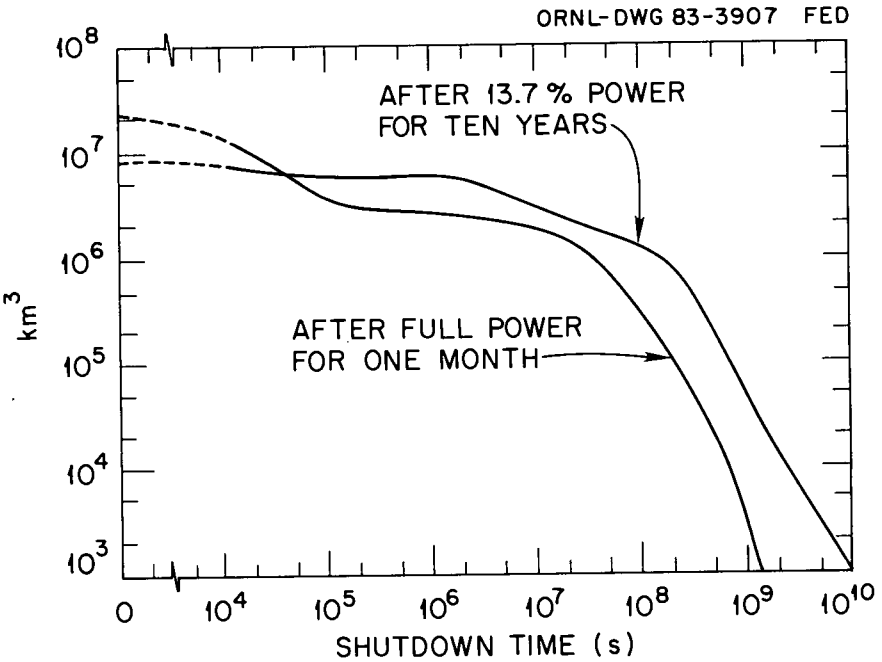

Fig. 9.13. Axicell air BHP (excluding choke coils).

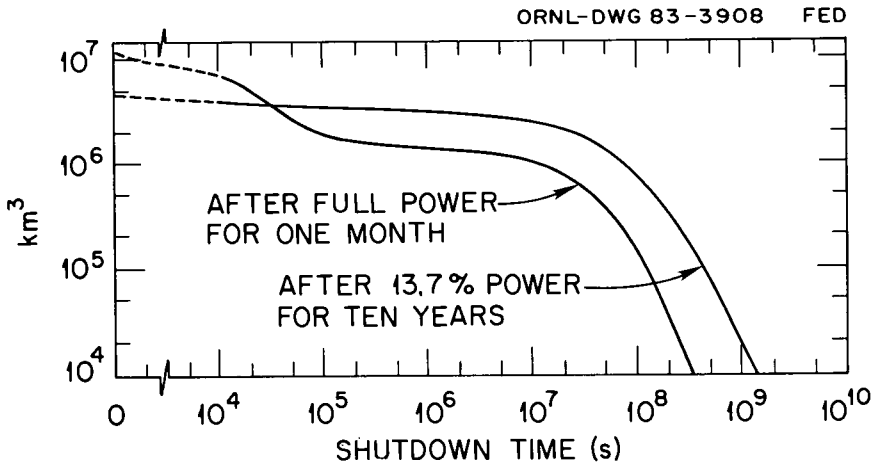

Fig. 9.14. Central-cell air BHP.

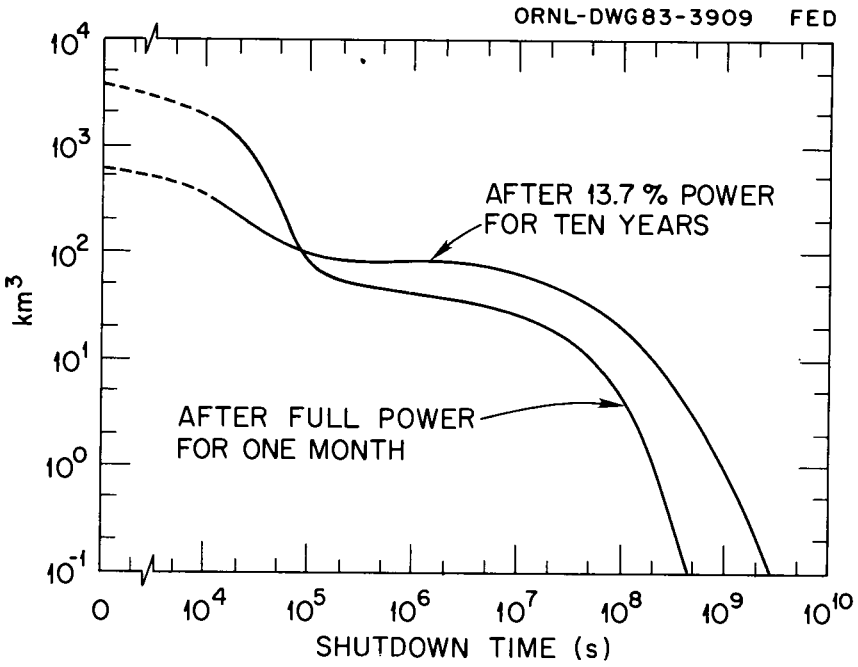

Fig. 9.15. Axicell water BHP (excluding choke coils).

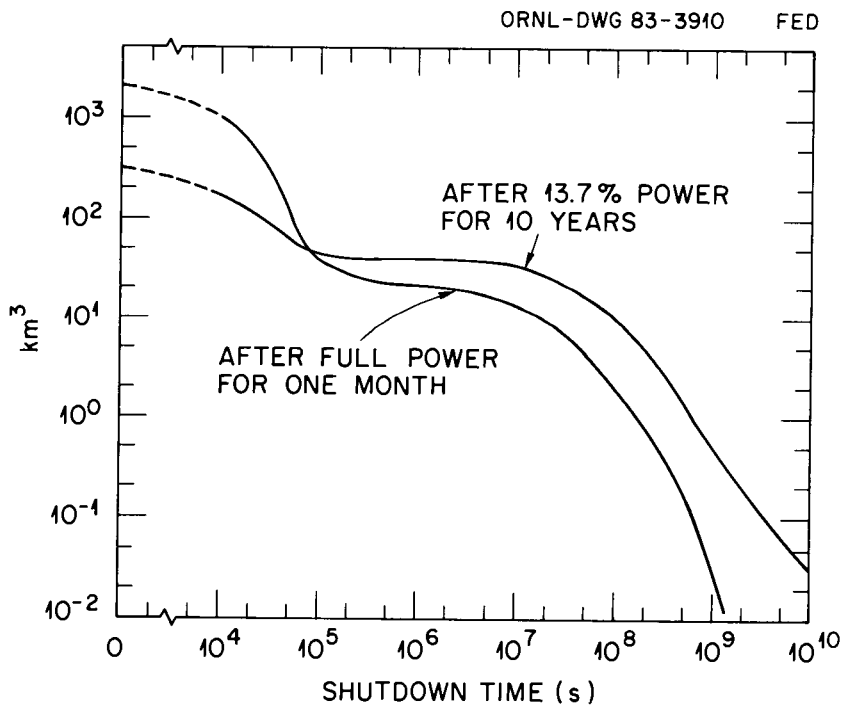

Fig. 9.16. Central-cell water BHP.

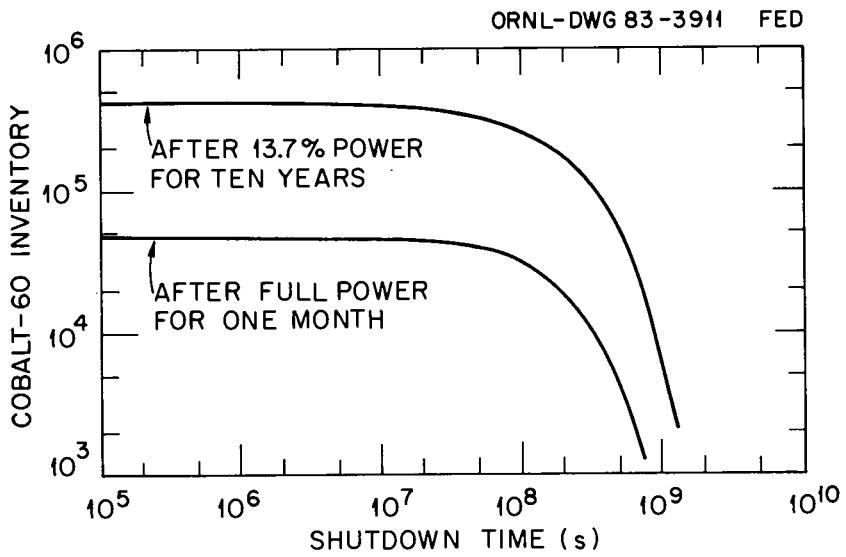

Fig. 9.17. Axicell ^{60}Co inventory (excluding choke coils).

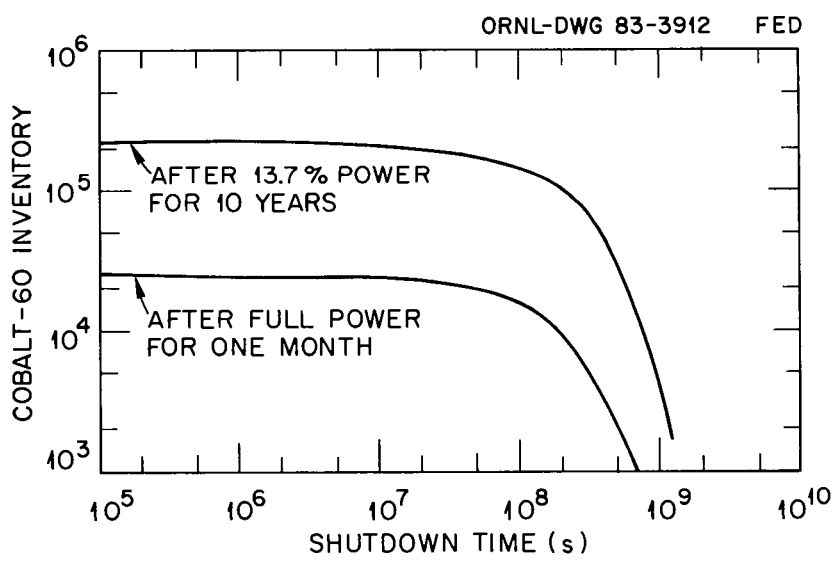

Fig. 9.18. Central-cell ^{60}Co inventory.

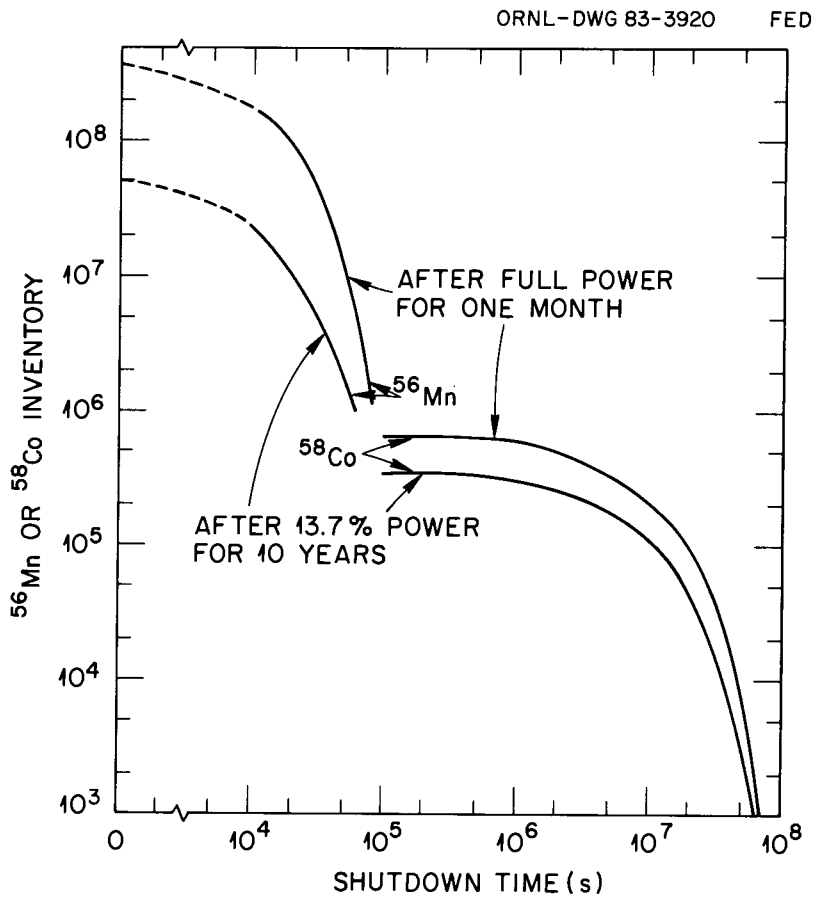

Fig. 9.19. Axicell ^{58}Co and ^{56}Mn inventories.

9.5.2 Choke Coils

A 1-D treatment of the choke coils is a rather gross approximation, but it was felt to be worthwhile in order to identify the major activation problems. Because of the limited geometry of the coils and the rapid variation of neutron source strength from one side to the other, a 3-D treatment should be undertaken during the next design phase.

For this analysis, the choke coil was represented in RACC by a 5-cm-thick annulus of solid copper with an inside radius of 15 cm and an outside radius of 20 cm. The 14-MeV flux at this location during full power is 5.5×10^{14} n/cm^2·s.

One very important activation product for afterheat in copper is ^{62}Cu, which is omitted from the RACC libraries. This nuclide is formed from the ^{63}Cu(n, 2n) reaction which has a cross section of about 0.6 barn at 14 MeV. Although ^{62}Cu has a short half-life (9.74 min), it decays by a strong positron emission with an average energy of 1.32 MeV. Hence, it can be a major contribution to the afterheat level in the choke coils immediately

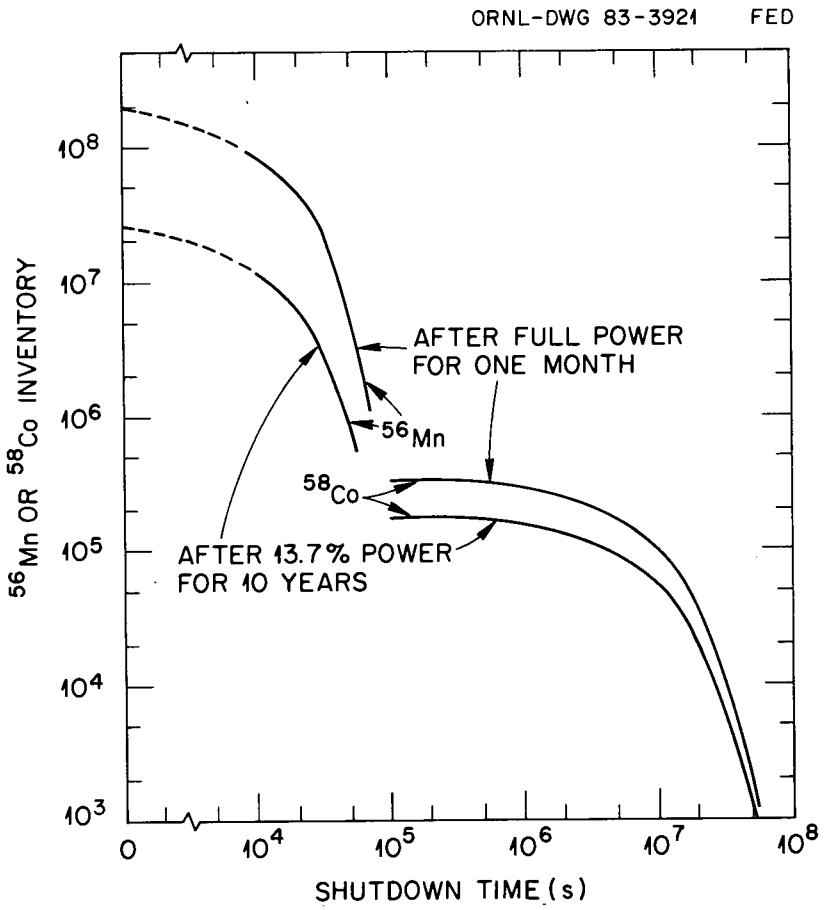

Fig. 9.20. Central-cell ^{58}Co and ^{56}Mn inventories.

after shutdown, particularly since all the positron afterheat is deposited in situ. Another unattractive feature of copper is the buildup of ^{63}Ni after a long 14-MeV neutron irradiation due to the ^{63}Cu(n, p) reaction, the cross section for which is ~0.1 barn.

Specific afterheat levels in the choke coils (the side facing the plasma) are plotted in Fig. 9.21. At shutdown two-thirds of the afterheat is contributed by ^{62}Cu.

Other specific activities for the choke coils are listed in Table 9.25. The cobalt concentration in the choke coil is considerably higher than that in the first two centimeters of the steel-water shield.

9.5.3 End Cells

The important activation issues associated with the MFTF-α+T end cells are:

- In which components, if any, will activation levels be low enough to permit hands-on handling and repair after components are removed from the end cells?
- What is the relationship between component composition and shutdown dose rate?

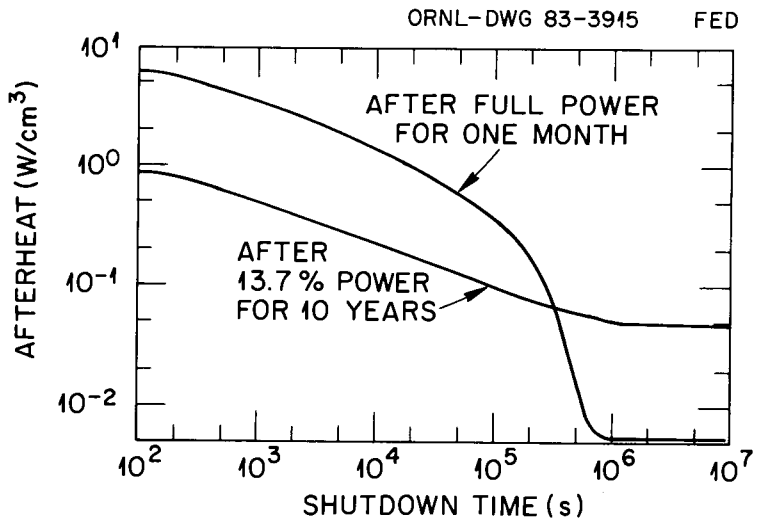

Fig. 9.21. Choke coil afterheat (side near plasma).

Table 9.25. Selected choke coil activities (side facing plasma)

Radioactivity immediately after full-power operation, Ci/cm^3	3.9×10^4
Radioactivity 10 years after end of life, Ci/cm^3	90
BHP in air immediately after full-power operations, km^3/cm^3	970
BHP in air 10 years after end of life, km^3/cm^3	9
^{60}Co concentration 10 years after end of life, Ci/cm^3	14

- Are activation rates of liquid nitrogen coolant excessive?
- Will the high sodium content in the vault concrete present an activation problem due to neutrons emitted from the end cell?

The answers to these questions must, in general, await the development of a 3-D neutronics model of the end cells, followed by Monte Carlo calculations of reaction rates in all the components in the cells.

A few preliminary activation calculations show that:

- The ^{14}C production rate is 0.1 μCi per gram of N_2 per 100-h run, if the liquid nitrogen is exposed to source radiation shielded by 15 cm of steel. The maximum permissible concentration (MPC) for ^{14}C in air is 10^{-4} μCi/cm^3.
- The dose rate in the space between the end cells and the vault wall due to sodium in the concrete is 10 mrem/h, which could be a problem 24 h after shutdown. This shutdown dose component could be larger than that coming from any other source.
- It is probably not worthwhile to specify low-cobalt type 304 stainless steel for the rebar or steel liner in the end-cell region.

REFERENCES

1. W. M. Stacey et al., *The U.S. Contribution to the International Tokamak Reactor Workshop*, Georgia Inst. Technology, Atlanta, November 1979.

2. Y. Gohar, "Low Cost Shield for Tokamak Fusion Reactors," *Nucl. Technol./Fusion* **4**, 373 (1983).

3. Y. Gohar and M. A. Abdou, "U.S. INTOR Radiation Shield Design," p. 12 in *Proceedings of the 6th International Conference on Radiation Shielding*, CONF-830538, Natl. Tech. Inf. Serv., Springfield, Va., 1983.

4. *A Tandem Mirror Technology Demonstration Facility*, UCID-19328, Lawrence Livermore Natl. Lab., Livermore, Calif., 1983.

5. P. H. Sager et al., *FED Baseline Engineering Studies Report*, ORNL/FEDC-82/2, Union Carbide Corp. Nuclear Div., Oak Ridge Natl. Lab., April 1983, pp. 5-19 to 5-25.

6. J. M. Williams et al., "The Effect of Irradiation on the Copper Normal Metal of a Composite Superconductor," *IEEE Trans. Magn.* **MAG-15**, 731 (1979).

7. T. Kato and S. Takamura, "Effect of Low Temperature Reactor Irradiation and Organic Superconductors in Superconducting Magnets (III)," *Cryog. Eng.* **15**, 173 (1980).

8. F. W. Clinard, Jr., and D. M. Parkin, "The Inorganic Insulator Program at LASL," in *Proceedings of the Meeting on Electrical Insulators for Fusion Magnets,* CONF-801237, Natl. Tech. Inf. Serv., Springfield, Va., 1981.

9. F. W. Clinard, Jr., and G. F. Hurley, "Ceramic and Organic Insulators for Fusion Applications," *J. Nucl. Mater.* **103 & 104**, 705 (1981).

10. F. W. Clinard, Jr., et al., "Structural Performance of Ceramics in a High-Fluence Fusion Environment," *J. Nucl. Mater.* **123 & 124**, 1386–92 (1984).

11. R. A. Van Konynenburg and M. W. Guinan, "Relative Radiation Sensitivity of Insulators, Stabilizers, and Superconductors," in *Proceedings of the Meeting on Electrical Insulators for Fusion Magnets*, CONF-801237, Natl. Tech. Inf. Serv., Springfield, Va., 1981.

12. L. J. Perkins, "Materials Considerations for Highly Irradiated Normal-Conducting Magnets in Fusion Reactor Applications," *J. Nucl. Mater.* **123 & 124**, 1371–75 (1984).

13. M. Söll et al., *IEEE Trans. Magn.* **MAG-11**, 178 (1975).

14. M. Söll, K. Böning, and H. Bauer, "Change of the Superconducting Critical Parameters of Nb_3Sn by Low Temperature Neutron Irradiation," p. 169 in *Proceedings of the 9th Symposium on Fusion Technology*, Pergamon Press, Oxford, 1976.

15. M. Söll, "The Influence of Low Temperature Neutron Irradiation on the Properties of Hard Superconductors," p. 965 in *Proceedings of the 8th Symposium on Fusion Technology*, Commission European Communities, Luxembourg, September 1974.

16. K. Schmelz and G. Ischenko, "Superconductivity of NbTi50 After Heavy Ion Irradiation at Low Temperature and High Fluences," *J. Nucl. Mater.* **67**, 109 (1977).

17. A. R. Sweedler, D. E. Cox, and S. Moehlecke, "Neutron Irradiation of Superconducting Compounds," *J. Nucl. Mater.* **72**, 50 (1978).

18. B. S. Brown and T. H. Blewitt, "Critical Current Density Changes in Irradiated Nb_3Sn," *J. Nucl. Mater.* **80**, 18 (1979).

19. B. S. Brown, "Radiation Effects in Superconducting Fusion Magnet Materials," *J. Nucl. Mater.* **97**, 1 (1981).

20. H. Ullmaier, "Radiation Damage in CTR Magnet Components," p. 403 in *Radiation Effects and Tritium Technology for Fusion Reactors*, vol. II, CONF-750989, Union Carbide Corp. Nuclear Div., Oak Ridge Natl. Lab., March 1976.

21. "Standard for Protection Against Radiation," Chap. 1, Pt. 20 in *U.S. NRC Rules and Regulations*, Title 10, U.S. Nuclear Regulatory Commission, 1977.

22. *Environmental Protection, Safety, and Health Protection Program*, DOE Executive Order 5480.1, May 5, 1980 (revised October 13, 1981).

23. A. E. Profio, *Radiation Shielding Dosimetry*, Wiley-Interscience, New York, 1979.

24. C. C. Baker et al., *STARFIRE—A Commercial Tokamak Fusion Power Plant Study*, ANL/FPP-80-1, Argonne Natl. Lab., Argonne, Ill., 1980.

25. R. L. Klueh, unpublished data, May 8, 1984.

26. W. W. Engle, Jr., *A User's Manual for ANISN, a One-Dimensional Discrete Ordinates Code with Anisotropic Scattering*, ORGDP-K-1963, Union Carbide Corp. Nuclear Div., Oak Ridge Gaseous Diffusion Plant, 1967.

27. R. W. Roussin et al., *VITAMIN-C: The CTR Processed Multigroup Cross Section Library for Neutronics Studies*, ORNL/RSIC-37, Union Carbide Corp. Nuclear Div., Oak Ridge Natl. Lab., July 1980.

28. Y. Gohar and M. A. Abdou, *MACKLIB-IV: A Library of Nuclear Response Functions Generated with MACK-IV Computer Program from ENDF/B-IV*, ANL/FPP/TM-106, Argonnne Natl. Lab., Argonne, Ill., 1978.

29. J. Jung, *Theory and Use of Radioactivity Code RACC*, ANL/FPP/TM-122, Argonnne Natl. Lab., Argonne, Ill., 1979.

30. M. A. Abdou et al., *Blanket Comparison and Selection Study*, ANL/FPP/TM-177, Argonnne Natl. Lab., Argonne, Ill., 1983.

31. Y. Gohar and M. A. Abdou, "INTOR Radiation Shielding for Personnel Access," p. 740 in *Proceedings of the 9th Symposium on Engineering Problems of Fusion Research*, Inst. Electrical Electronics Engineers, New York, 1981.

32. M. E. Sawan, C. W. Maynard, and L. A. El-Guebaly, "Buildup Factors for Magnet Shielding in Tandem Mirror Fusion Reactors," in *Proceedings of the 6th International Conference on Radiation Shielding*, CONF-830538, Natl. Tech. Inf. Serv., Springfield, Va., 1983.

33. Ref. 24, vol. II, Chap. 21.

34. L-P. Ku., *Nuclear Radiation Analysis for TFTR*, PPPL-1711, Princeton Plasma Physics Lab., Princeton, N.J., September 1980.

35. *Low Activation Materials Design Study Annual Report for FY 81*, GA-A16426, General Atomic Co., Inc., San Diego, September 1981.

36. B. A. Engholm, Fusion Engineering Design Center, Oak Ridge, Tenn., personal communication with G. M. Fuller, Aug. 3, 1983.

10. ELECTRICAL SYSTEMS

G. E. Gorker

Fusion Engineering Design Center/General Electric Company

CONTENTS

10.1 INTRODUCTION 10-3
10.2 AC POWER SYSTEM 10-3
10.2.1 Requirements 10-3
10.2.2 Design Description 10-5
10.2.3 Summary 10-8
10.3 POWER CONVERSION SYSTEM 10-13
10.3.1 Requirements 10-13
10.3.2 Design Description 10-15
10.3.3 Summary 10-22
10.4 PROCESS CONTROL AND DISPLAY SYSTEM 10-22
10.4.1 Requirements 10-25
10.4.2 Design Description 10-31
10.4.3 Key Issues 10-46
10.5 PLASMA CONTROL AND DISPLAY SYSTEM 10-49
10.5.1 Requirements 10-49
10.5.2 Design Description 10-51
10.5.3 Key Issues 10-55
10.6 PLASMA DIAGNOSTIC SYSTEM 10-56
10.6.1 Requirements 10-56
10.6.2 Design Description 10-59
10.6.3 Trade Studies and Key Issues 10-70
10.7 DATA ACQUISITION SYSTEM 10-76
10.7.1 Requirements 10-77
10.7.2 Design Description 10-79
10.7.3 Key Issues 10-82
REFERENCE 10-82

10. ELECTRICAL SYSTEMS

10.1 INTRODUCTION

Six types of electrical systems are required for MFTF-α+T:

- ac power systems,
- power conversion systems,
- process control and display systems,
- plasma control and display systems,
- plasma diagnostic systems, and
- data acquisition systems.

Requirements for and design descriptions of each system are presented, along with summaries of the results of trade studies and key issues for future work.

10.2 AC POWER SYSTEM

Two ac power substations were designed and built to provide power to the Mirror Fusion Test Facility (MFTF-B) at Lawrence Livermore National Laboratory (LLNL). A 230-kV/13.8-kV substation provides pulsed power to the neutral beam power supplies, and a 115-kV/13.8-kV/4.16-kV substation provides steady-state power to MFTF-B and other loads at LLNL. The substations and the neutral beam injector (NBI) power supplies must be upgraded as economically as possible to meet the ac power demands of MFTF-α+T.

10.2.1 Requirements

The ac power requirements and upgrades of the MFTF-B substations defined in this section are based on currently established design information. These general definitions may require revision as the design process continues.

Table 10.1 summarizes the ac power requirements for MFTF-α+T. All loads are essentially steady state to satisfy the 100-h burn time established as a mission requirement. The largest power demands are from the cryogen system, the neutral beam power supplies, and the resistive coil power supplies. Studies of the magnet system (see Chap. 4) indicate that nuclear heating of the magnets can be reduced so that cryogenic refrigeration requires about 20 MW of ac power, so this requirement is assigned to the 115-kV system. The ion cyclotron resonance heating (ICRH) and electron cyclotron resonance heating (ECRH) power loads are assigned to the 230-kV system to use the power supplies provided for the MFTF-B neutral beams. The power feeder cables from the 230-kV system to these power supplies were designed for 30-s pulsed operation and must be replaced with cables rated for continuous operation. Other additions are noted in Table 10.1.

Some essential backup power is provided for MFTF-B, but much more is needed for the fuel processing and tritium cleanup systems of MFTF-α+T. Diesel generators can be started and operated in a no-load condition when MFTF-α+T is operating. Both highly reliable, 4.16-kV marine diesel generators and less expensive, 480-V backup power diesel generators are commercially available. The less expensive 480-V, 1100-MW generators are selected to meet the essential power requirements of MFTF-α+T, listed in Table 10.2.

Table 10.1. MFTF-α+T ac power requirements

Load	Power, MW
230-kV substation	
Central-cell neutral beam injectors	30
Plug-cell neutral beam injectors	3
Anchor-cell ICRH[a]	5
Anchor-cell and plug-cell drift pumping[a]	2
Plug-cell ECRH	10
115-kV substation	
Resistive coil power[b]	25
Cryogenic system power[a]	20
Cooling and vacuum system power	3
Superconducting coil power	1
Fuel processing and tritium cleanup systems[a,c]	5
Total	104

[a]Three 5-kV circuit breakers and feeders must be added to the MFTF-B power system for the fuel processing system, the cryogenic system, and the ICRH and drift pumping power supplies.

[b]One 15-kV circuit breaker and feeder must be added to the MFTF-B power system for the resistive coil power supplies.

[c]Four 1100-kW diesel generators and power feeders must be added to the MFTF-B power system to provide backup power for the fuel processing system.

Table 10.2. Essential power requirements

	Power, kW
Emergency tritium cleanup system	3000
Fuel reprocessing system	500
Heating, ventilation, and air conditioning	200
Uninterruptible power supplies	25
Data system	50
Instrumentation and control	50
Lighting	50

10.2.2 Design Description

Figure 10.1 is a partial diagram of the 230-kV substation for the 30-s neutral beam power supplies of MFTF-B. There are 24 power supplies; each one has a separate 13.8-kV, 3-phase, 60-Hz feeder to its associated autotransformer. Only eight of these power supplies are needed for the positive-ion neutral beam injectors of MFTF-α+T. Some of these power supplies will be used to provide ECRH, ICRH, and drift pumping power.

Substation modifications for rf power generation

ECRH power generation. The substation voltage does not need to be modified for ECRH power generation because ECRH will use about the same voltage as the NBIs.

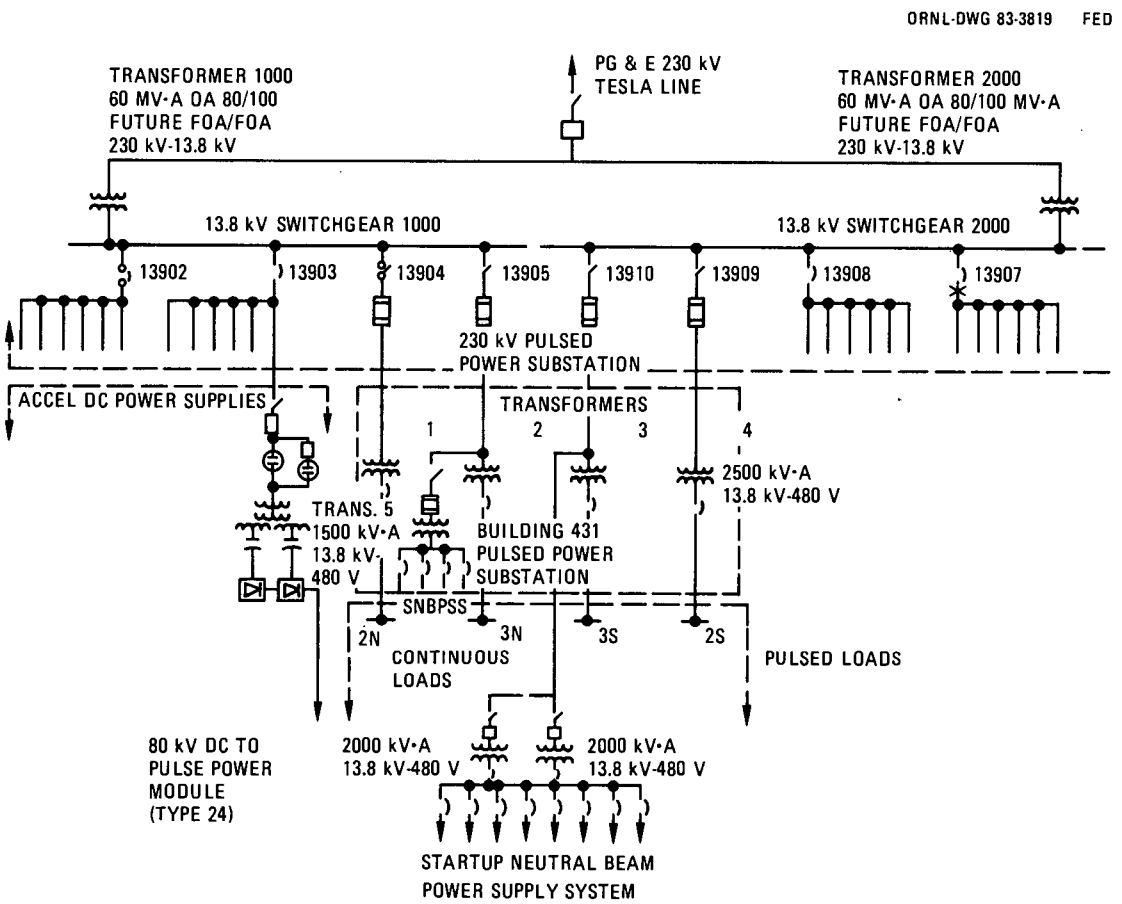

Fig. 10.1. The 230-kV substation for the MFTF-B neutral beam power supplies.

Larger 15-kV power cables will be needed to replace the existing pulsed power feeder cables to the two power supplies, one at each end of the device, that will be used for ECRH.

ICRH power generation. The ICRH power generation requires 20-kV dc power, rather than the 60- to 100-kV power used by the neutral beam injectors. If the input voltage to the autotransformers of the four power supplies used for ICRH is reduced from 13.8 kV to 4.16 kV, then these power supplies will be adequate. The voltage can be reduced by disconnecting circuit breaker 13907 from its neutral beam power supply feeders (see Fig. 10.1) and connecting it to the new 13.8-kV/4.16-kV transformer, as shown in Fig. 10.2. The 15-kV pulsed power feeder cables will be replaced with 5-kV power feeder cables for steady-state operation.

Drift pumping power generation. The anchor-cell drift pumping power generation requires 17.5-kV dc power, which will be provided by two neutral beam power supplies like those used for ICRH. The plug-cell drift pumping power generation requires 5-kV dc power and less than 200 kW. A 4.16-kV/480-V stepdown transformer will be provided, as shown in Fig. 10.2, and two new power supplies attached to it will supply drift pumping power to the east and west plug cells.

Substation modifications for accommodating additional loads

The additional power required for MFTF-α+T can be provided by modifying either the 230-kV substation (option 1) or the 115-kV substation (option 2). If option 1 is selected, the 230-kV substation (shown in Figs. 10.1 and 10.2) must be upgraded for steady-state operation. This entails increasing the cooling capacity of the transformers and contracting with Pacific Gas and Electric (PG&E) to operate in a steady-state mode. A new 15-kV feeder cable approximately 300 m long provides power to the power supplies of the resistive coils. A 4.16-kV breaker and 5-kV feeder provide power to the fuel processing and emergency tritium processing equipment.

Option 2 requires upgrading the existing 115-kV substation shown in Fig. 10.3. Additional power can be provided by replacing the T-4000 transformer with a 3-winding transformer, circuit breakers, and feeder cables as shown in Fig. 10.4. Three new circuit breakers are needed: a 5-kV breaker for the fuel processing system, a 15-kV breaker for the resistive coil power supplies, and a 15-kV breaker for the cryogen compressor motors. The feeder cable length is comparable to that for the 230-kV substation upgrade.

Essential backup power

Figure 10.5 is a diagram of the load center for the fuel processing building, where most of the essential power is needed. The 5-kV feeder from the substation provides the normal power to the load center and the four 480-V, 1100-kW diesel generators provide the essential backup power when normal power fails. Other essential loads, including the uninterruptible power supplies, are also connected to this 480-V load center.

An installation diagram of one candidate diesel generator is shown in Fig. 10.6. This 480-V, 1100-kW unit with its integral cooling system is skid-mounted for easy installation. It can be purchased with its own weatherproof housing or may be mounted inside a steel

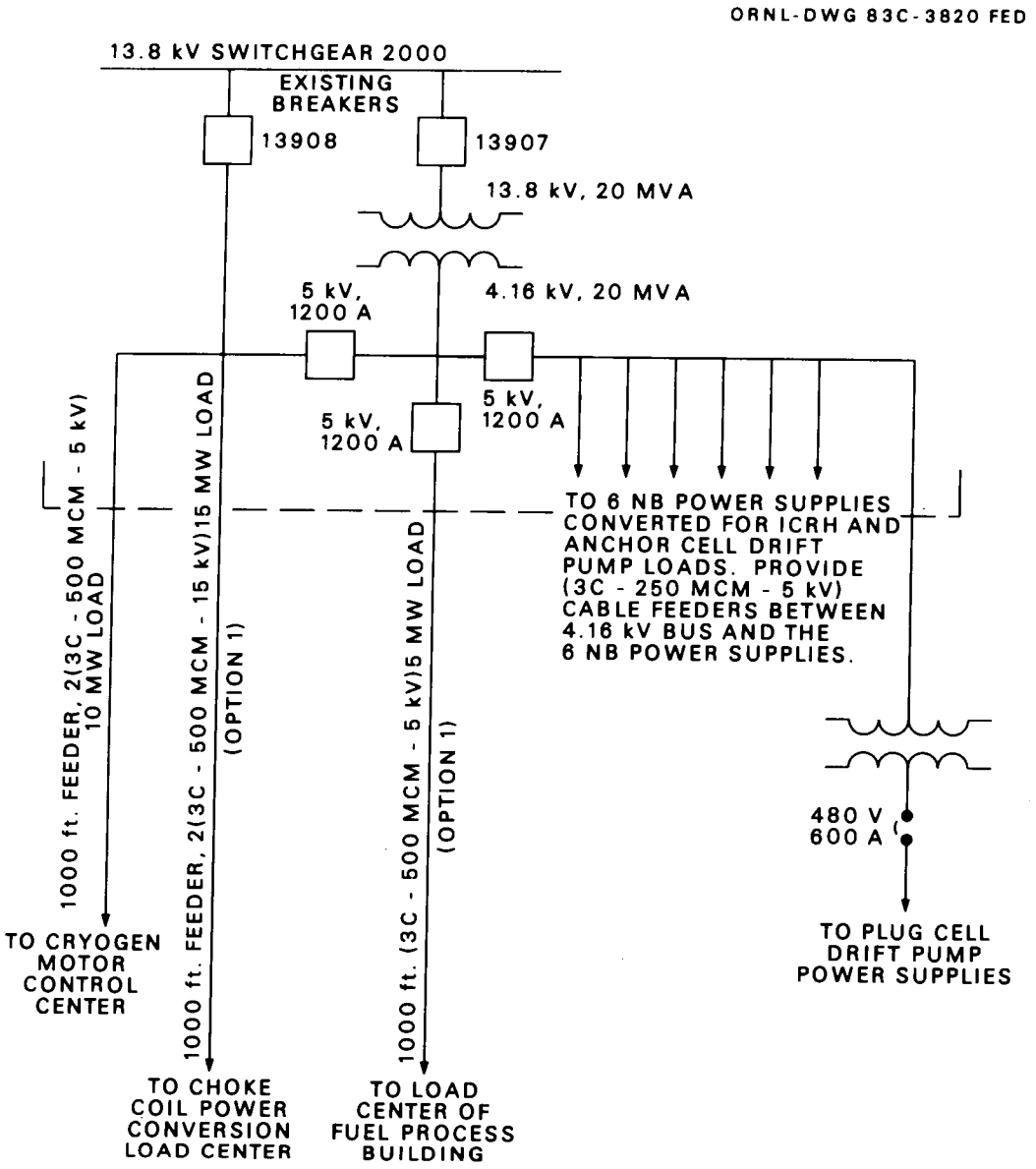

Fig. 10.2. Modification of 230-kV substation for MFTF-α+T.

building, as shown in Fig. 10.7. The latter is recommended for the four units proposed for MFTF-α+T. The steel building also shelters the local control cabinets, sketched in Fig. 10.8, that provide manual or automatic startup and parallel operation of the four diesel generators. A possible fuel storage and supply system is shown in Fig. 10.9. Storage tanks hold enough fuel to operate the diesel generators at full load for two days.

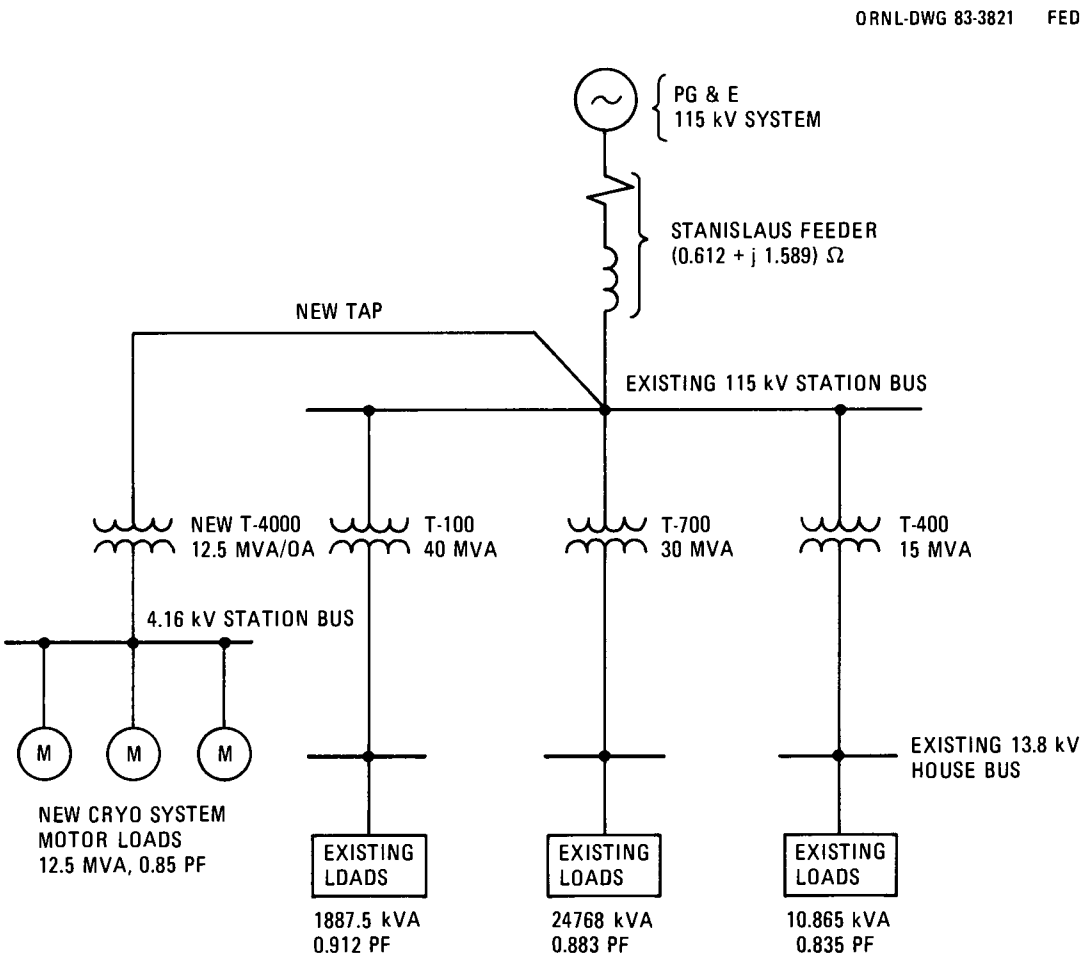

Fig. 10.3. Existing MFTF-B 115-kV substation.

10.2.3 Summary

The 230-kV substation can be upgraded to supply the neutral beam injection, ECRH, ICRH, and drift pumping power for MFTF-α+T. From the standpoint of capital cost, it would be more economical to supply the steady-state power for the cryogen compressors, resistive coil power supplies, and tritium processing facility from the 230-kV substation. From the standpoint of operations, the lower power rate makes it more economical to operate from the 115-kV substation. Further investigations of the substation options, including a joint study with the utility company, are needed.

Less reliable, low-voltage diesel generators will provide essential backup power and will run in a no-load state whenever MFTF-α+T is running. Because the operating time for MFTF-α+T is a small fraction of the machine lifetime, this more economical alternative appears to be the better design choice.

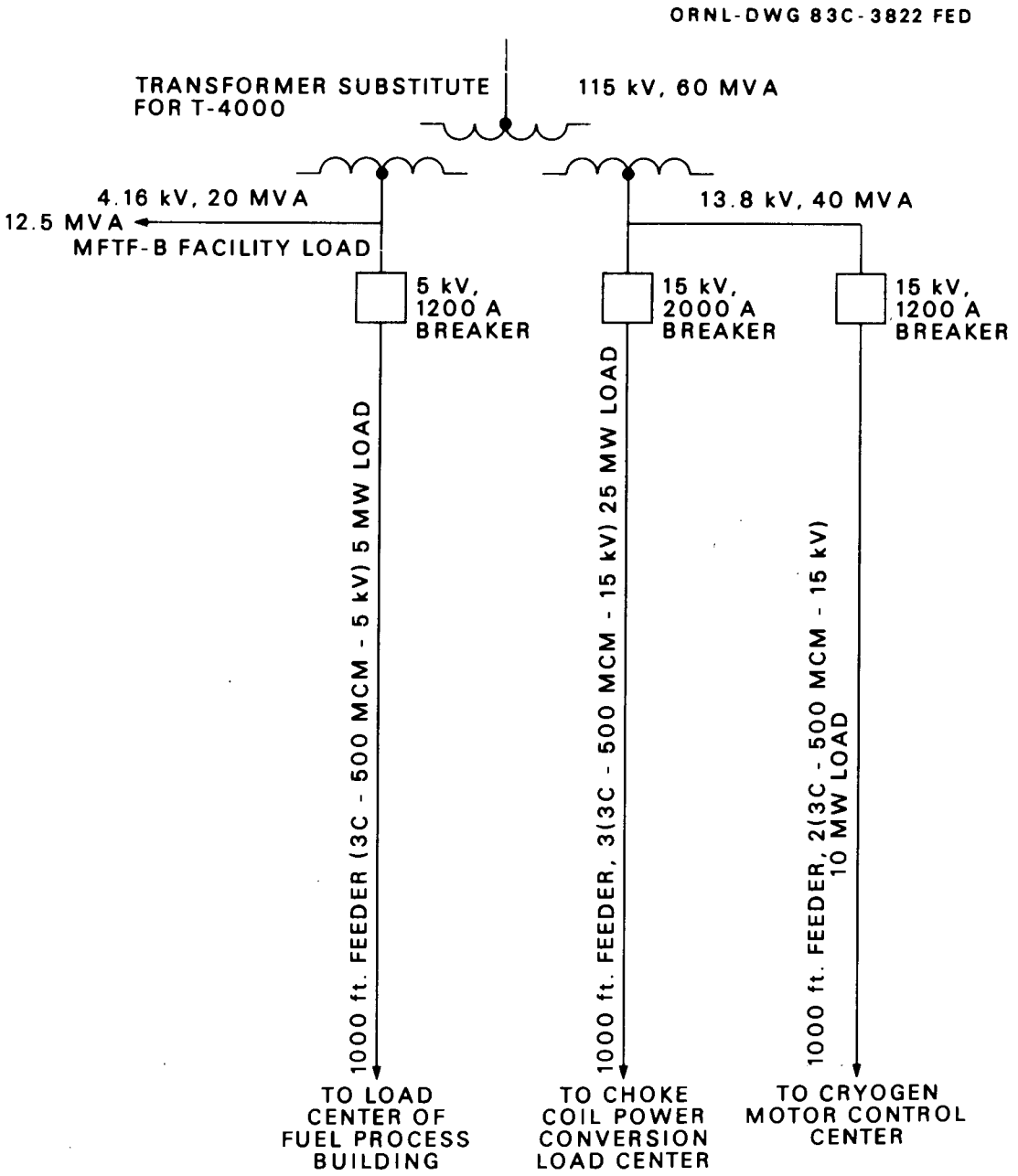

Fig. 10.4. Modification of 115-kV substation for MFTF-α+T.

ORNL–DWG 83-3823 FED

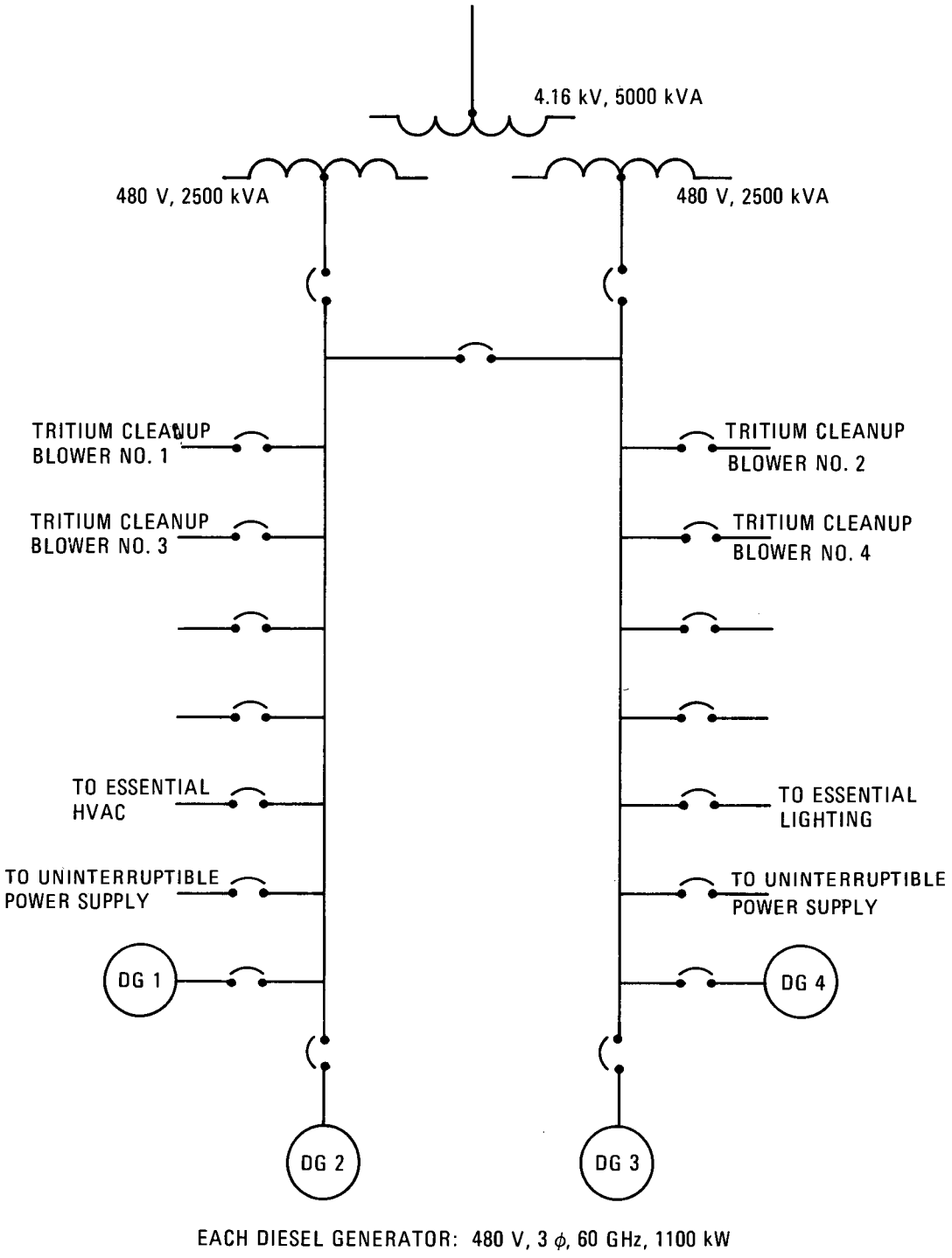

Fig. 10.5. Load center and backup power for the fuel processing system.

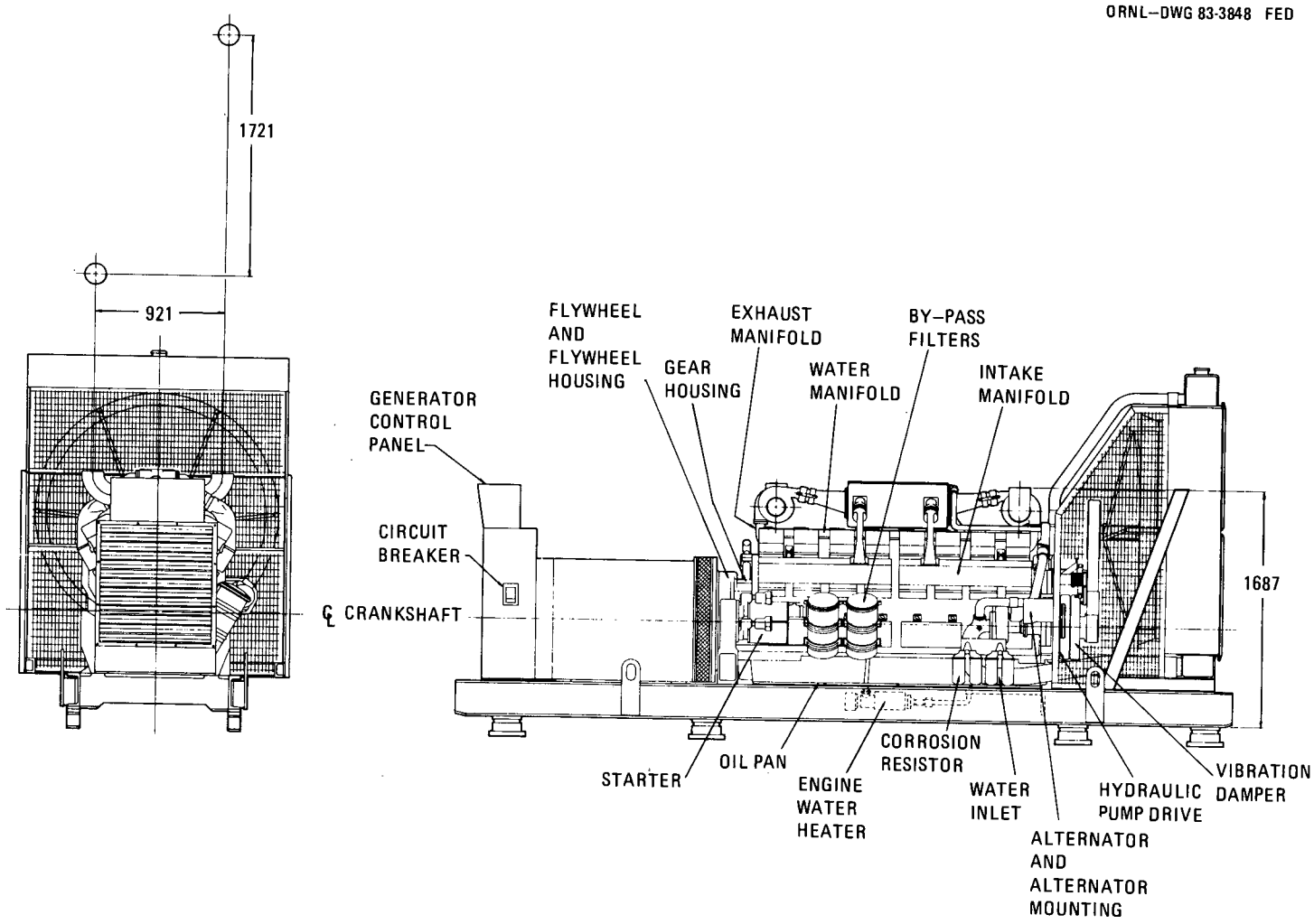

Fig. 10.6. Diesel generator installation diagram.

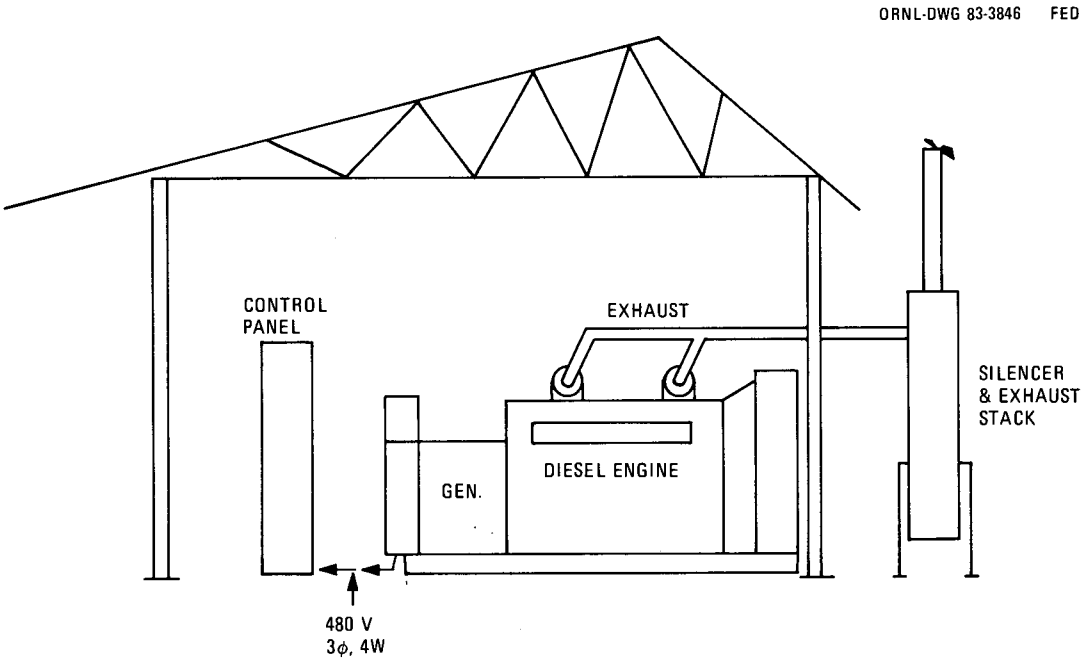

Fig. 10.7. Diesel generator installed in metal building.

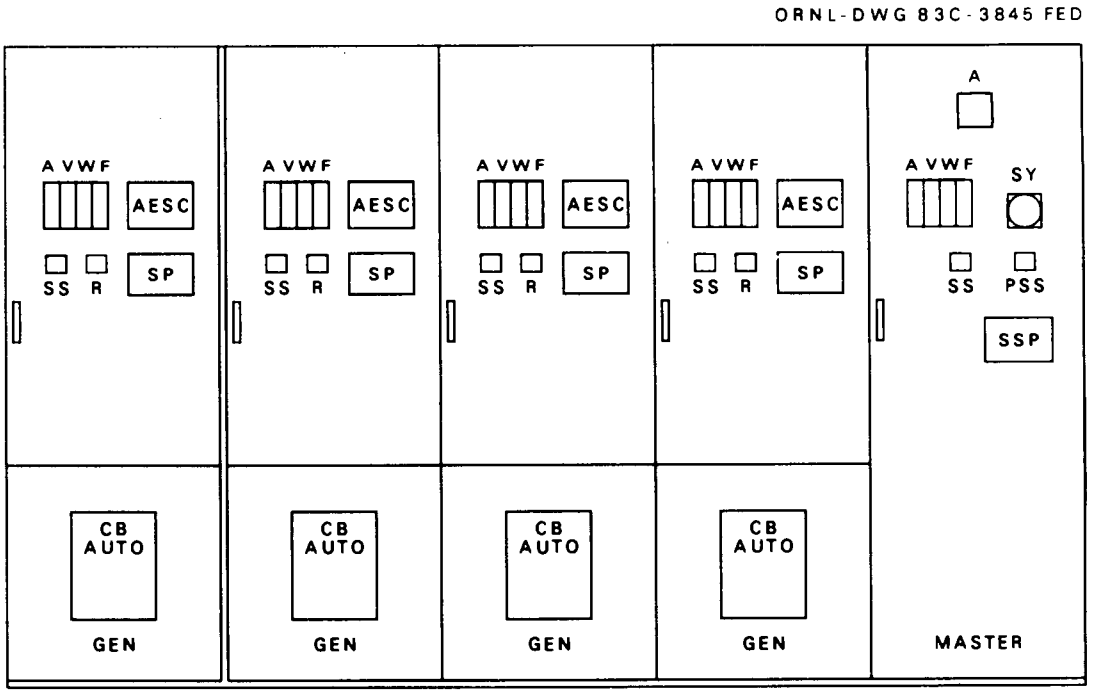

Fig. 10.8. Floor-mounted local control cabinets for backup power system.

ORNL-DWG 83C-3847 FED

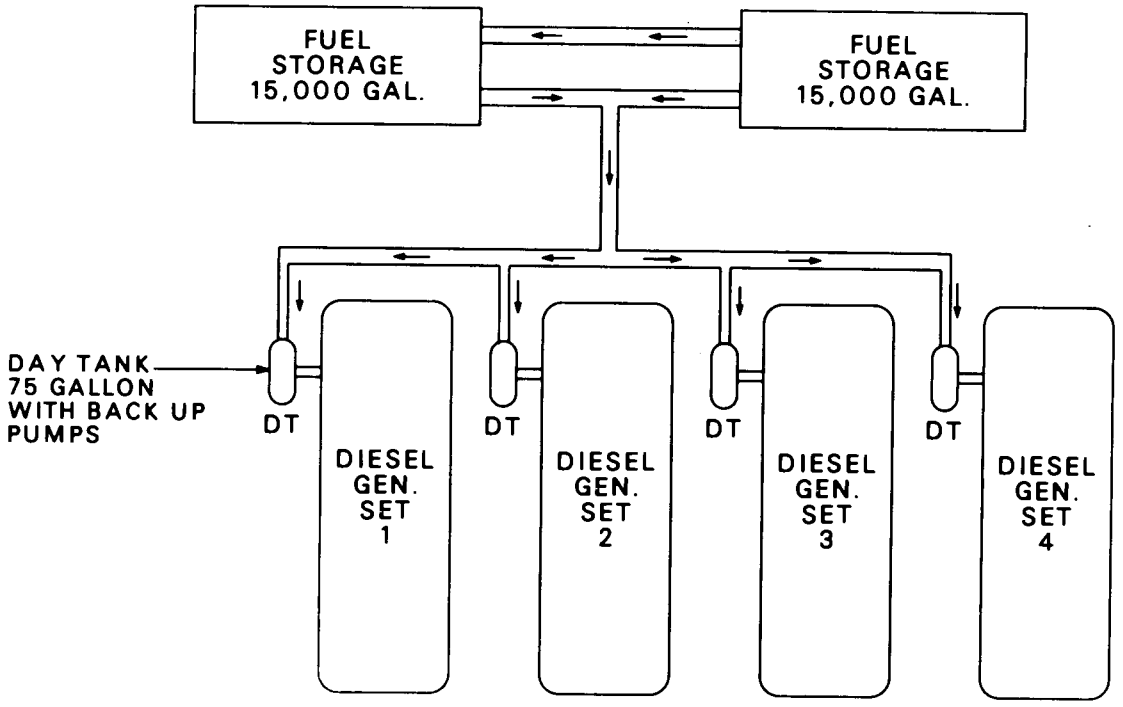

Fig. 10.9. Fuel storage and distribution system for diesel generators.

10.3 POWER CONVERSION SYSTEM

Five areas of MFTF-α+T require power conversion equipment: the magnets, the NBIs, the ECRH power generation system, the ICRH power generation system, and the drift pumping power generation system. As far as possible, existing equipment from MFTF-B will be used for these areas.

10.3.1 Requirements

Magnets

All of the magnets on MFTF-α+T are superconducting except for the copper insert portion of the choke coils and the central CS0 magnet. Low-voltage power supplies will be used to charge the magnets in about 4 h and to operate them in a steady state for up to 100 h. During a normal shutdown, the coils will be discharged in about 6 h through slow dump resistors. However, if the coil protection system detects an imminent quench, the coils will be discharged in less than 10 min. The fast discharge will transfer most of the energy in the magnets to dump resistors so that the maximum temperature of the coils is $\leq$200 K for faults, accidents, or operator errors. The coil protection system receives power from noninterruptible supplies to ensure operation when utility power fails and to prevent inadvertent fast shutdowns.

The power supply and coil protection requirements may be summarized as follows.

- Existing MFTF-B power supplies and protection equipment will be used as fully as possible.
- The peak temperature in the magnet coils during quench will not exceed 200 K.
- The magnet decay time constant will be <10 min during a fast dump to protect the coil leads.
- There will be no coil current peaking during a fast dump.
- The coil voltage to ground will not exceed 1 kV.
- The dc circuit breakers for fast dumps will be able to interrupt 300 kJ in a 750-V circuit.
- Normal charging or discharging will take about 4 h.
- The coil protection system will be supplied with noninterruptible power.
- New power supplies and coil protection equipment will be needed for several magnets, as described in Table 10.3.
- Power to the resistive coils will be interrupted when the cooling water flow drops below required levels.

The superconducting (SC) coil power supplies must supply the required design currents with enough voltage to overcome the bus, cable, and terminal voltage drops, and the L (di/dt) needed for startup. The resistive conductor (RC) coil power supplies must provide enough voltage to overcome the voltage drop across the coils during steady-state operation.

Neutral beam injectors

The central-cell NBIs will use eight MFTF-B power supplies, which may have to be refurbished for continuous 30-A operation. This may require upgrading the cooling systems of the rectifiers and their transformers and replacing MFTF-B ac and dc pulsed power cables with larger cables. It may be necessary to develop rf ion sources to achieve steady-state operation; if so, additional rf power generation and power supplies will be required.

Table 10.3. MFTF-α+T magnets requiring new power supplies and coil protection equipment

Coil	Power supply rating	
	Voltage, V	Current, kA
CC1 (12-T choke coils, east and west)	±40	135
CC2 (18-T choke coils, east and west)		
Inside (CC2I)	±20	65
Middle (CC2M)	±5	22
Outside (CC2O)	±6	25
CS0 (central coil)	±60	80
CS1 (east and west)	±12	18

The sloshing negative-ion neutral beam injection requires at least −200 kV, which is about twice the voltage available from an existing neutral beam power supply. One of these power supplies may be used as the base −100-kV power supply without modification. A second, isolated −110-kV, 10-A power supply that can operate 100 kV below ground potential is needed. When connected in series, these two power supplies provide the required voltage.

ECRH power generation

Two MFTF-B NBI power supplies will be used for the ECRH gyrotrons, one in the east plug cell and one in the west. The cooling system and power cables may have to be upgraded for continuous operation, unless four power supplies rather than two are used.

ICRH power generation

As described in Sect. 10.2, the 20 kV needed for ICRH power can be obtained from MFTF-B power supplies if the voltage to the autotransformers is reduced from 13.8 kV to 4.16 kV. Four power supplies are required, two in the east anchor cell and two in the west. The cooling system and power cables may have to be upgraded for continuous operation.

Drift pumping power generation

The anchor-cell drift pumping power generation requires 17.5 kV. Two MFTF-B NBI power supplies can be upgraded to meet this requirement. The plug-cell rf power generation requires <200 kW of 5-kV power, which will be provided with new power supplies using a 480-V, 3-phase, 60-Hz input.

10.3.2 Design Description

Magnets

Power supplies for the MFTF-B magnets have been reassigned to the MFTF-α+T magnets as listed in Table 10.4. The coil designations for both devices are identified in Figs. 10.10 and 10.11. Six additional power supplies are needed for MFTF-α+T—three for the SC coils CS1, CC2M, and CC2O, and three for the RC coils CC1, CC2I, and CS0.

The power system for the MFTF-α+T solenoid coils, shown in Fig. 10.12, is almost identical to that for MFTF-B, except that there are five coils on each side instead of six. The two remaining MFTF-B coils and their dump resistors will be retained as spares.

A separate 25-MW load control substation, shown in Fig. 10.13, will be provided for the three RC coil power supplies. Each power supply has a center ground that provides power to the east and west coils connected in series. A ground resistor between the coils equalizes the potential to ground and makes it possible to detect coil ground faults. Flywheel diodes provide coil voltage protection if a fault causes an open circuit.

Table 10.4. Assignment of coils to MFTF-B power supplies

Power supply[a]	DC rating		MFTF-B coils	MFTF-α+T coils
	Voltage, V	Current, kA		
1	40	3	ES1–ES6, WS1–WS6	S1–S5 (east, west)
2	10	0.6	WS5, WS6	S4, S5 (west)
3	10	0.6	ES5, ES6	S4, S5 (east)
4	10	0.6	WS3–WS6	S2–S5 (west)
5	10	0.6	ES3–ES6	S2–S5 (east)
6[b]	24	18		CS1 (east, west)
7[b]	10	22		CC2M (east, west)
8[b]	10	25		CC2O (east, west)
9[b]	80	135		CC1 (east, west)
10[b]	40	65		CC2I (east, west)
11[b]	120	80		CS0
12	10	5	EA1, WA1	DC (east, west)
13	12	6	EM1	A1, A2 (west)
14	12	6	EM2	A1, A2 (east)
15	10	5	WM1	P1, P2 (west)
16	10	5	WM2	P1, P2 (east)
17	10	6	ET1, WT1	T1 (east, west)
18	10	7	ET2, WT2	T2 (east, west)
19	10	0.6	ET1, WT1	T1 (east, west)
20	10	2	WA-2I	T1 (east, west)
21	10	0.6	ET2, WT2	CC2O (east, west)
22	10	0.6	EA1, WA1	DC (east, west)
23	10	2	EA-2I	CS1 (east, west)

[a]The 10-V, 5-kA and 10-V, 0.6-kA power supplies used on MFTF-B for coils EA20 and WA20 are not used for MFTF-α+T.

[b]New power supply for MFTF-α+T.

Figure 10.14 shows a generic power circuit diagram for all other SC coil pairs. The main power supply provides most of the current, and the trim power supply and associated circuit breakers make it possible to increase the current in one of the coils. This configuration is used for MFTF-B, so for MTFT-α+T it will only be necessary to substitute a new coil pair and its associated dump resistors for the MFTF-B coil pair. For new MFTF-α+T SC coils, power supplies like those used on MFTF-B (shown in Fig. 10.15) will be procured to maintain a standard line of equipment.

Data for coil and dump resistors needed for the coil protection sytem are listed in Table 10.5, which identifies the coils, their self-inductances, their equivalent stored energies, and their nominal design currents and includes the dump resistor sizes and fast discharge time constants, based on coil self-inductance and dump circuit resistance. Magnet control and coil protection are discussed further in Sect. 10.4.

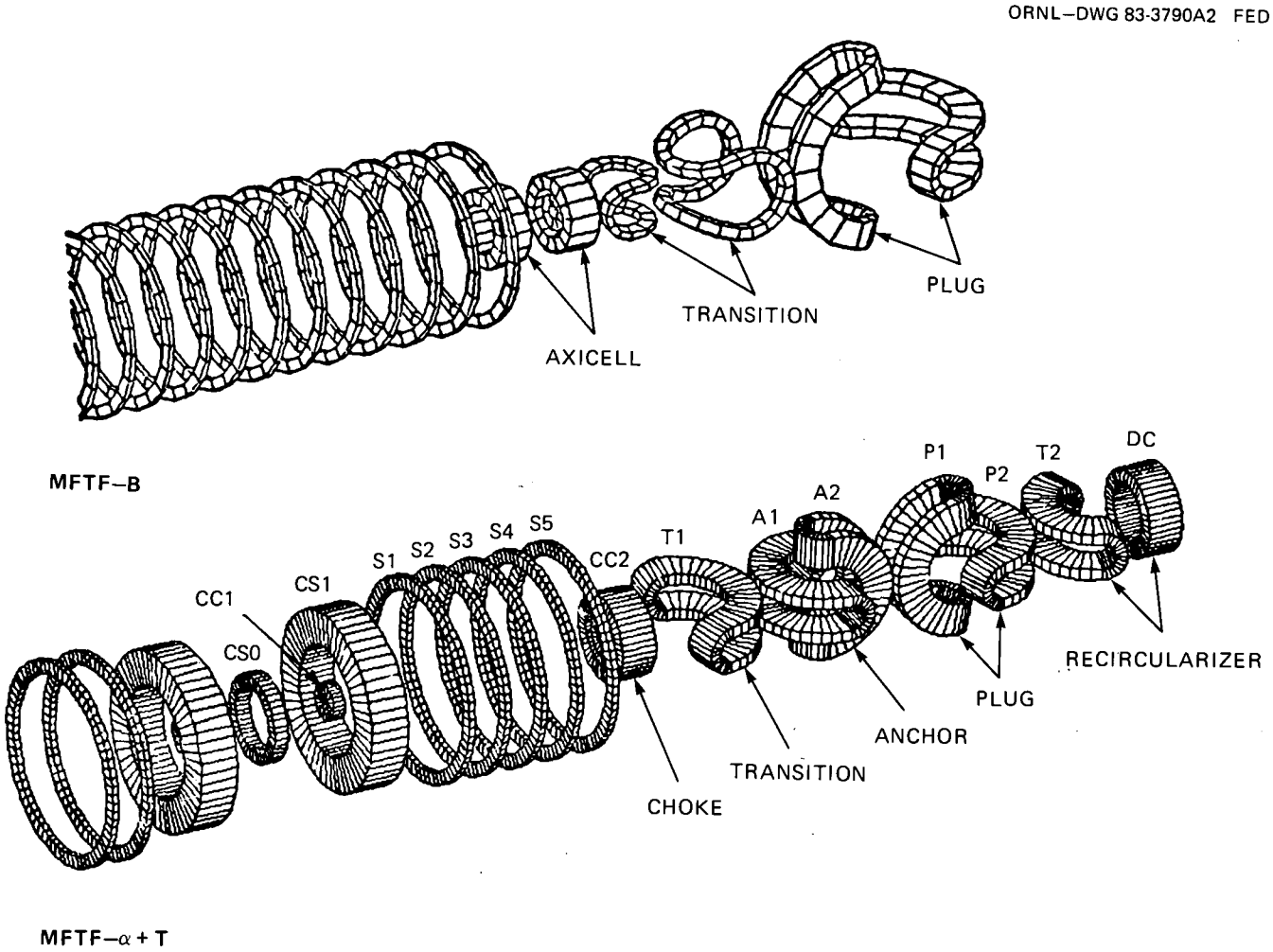

Fig. 10.10. Magnet configurations of MFTF-B and MFTF-α+T.

ORNL–DWG 83-4011 FED

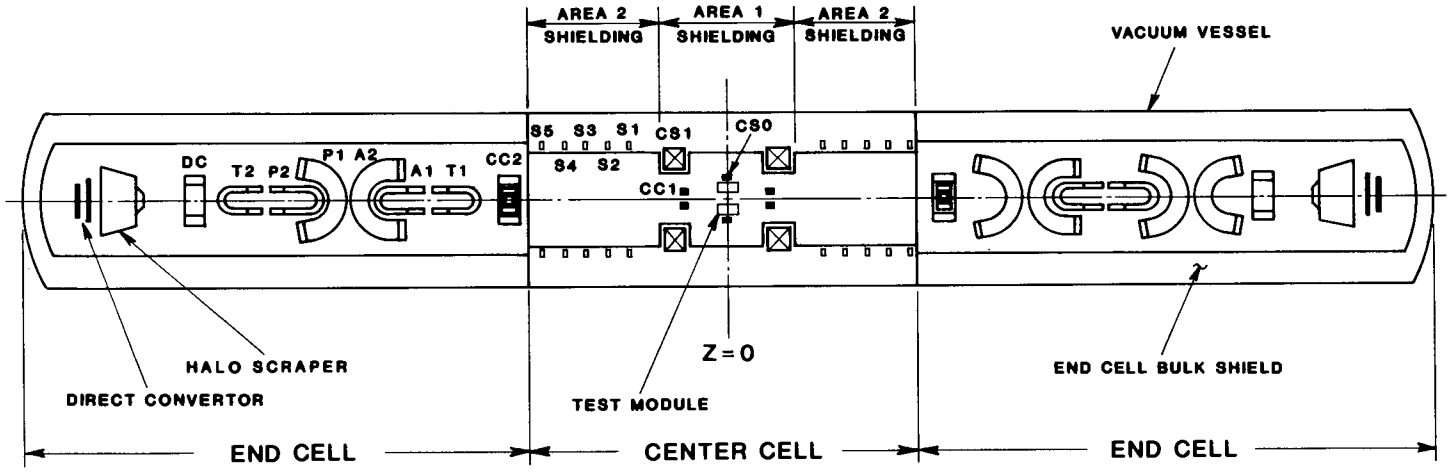

Fig. 10.11. MFTF-α+T magnet configuration.

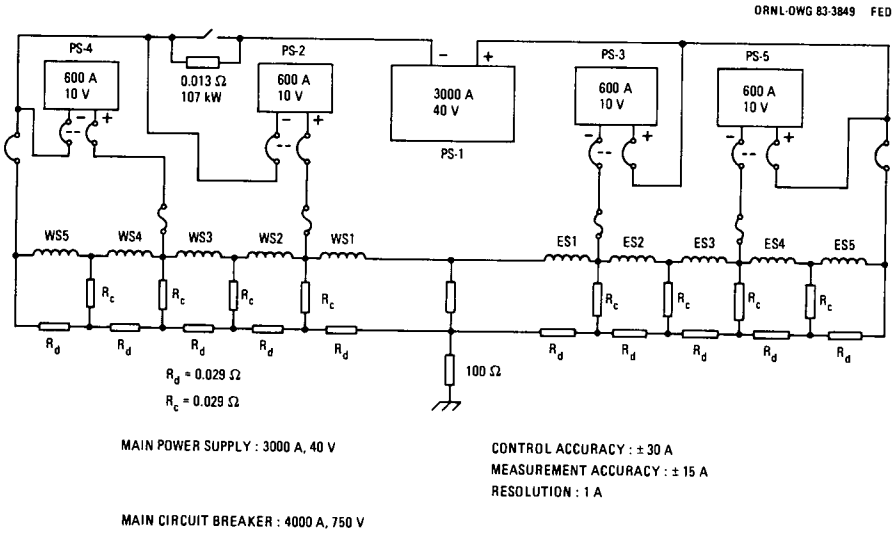

Fig. 10.12. Power system for solenoid coils (S1–S5).

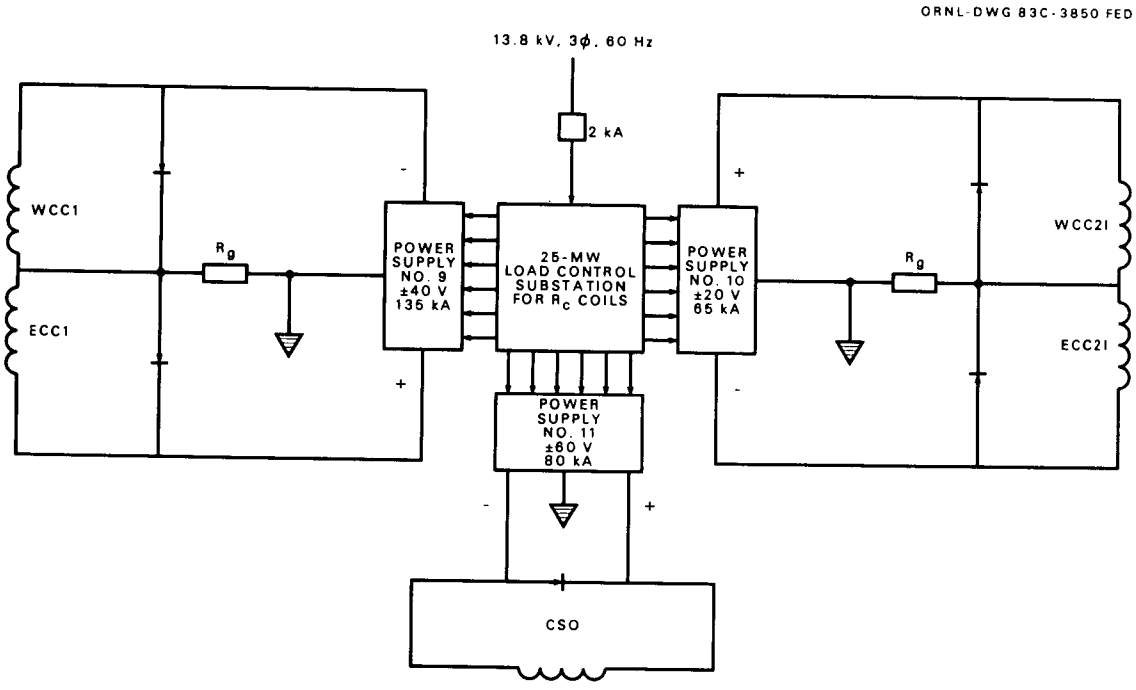

Fig. 10.13. Option 1 RC coil power conversion system (group 2).

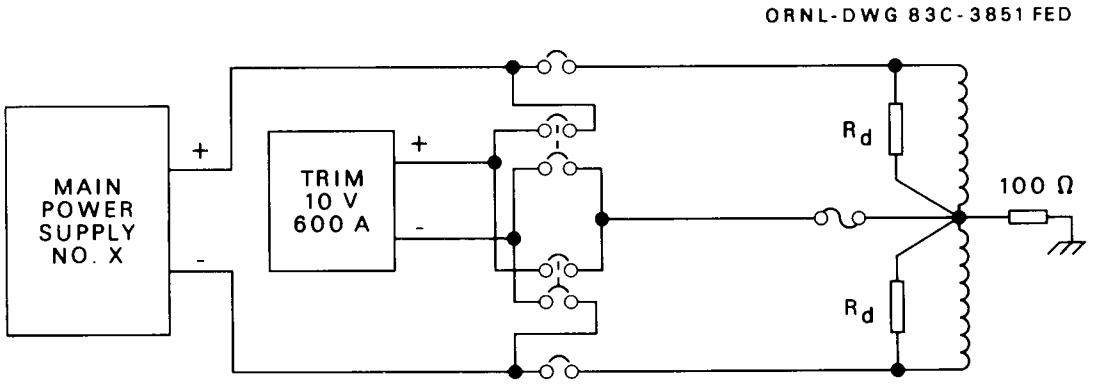

Fig. 10.14. Generic power circuit for pairs of SC coils.

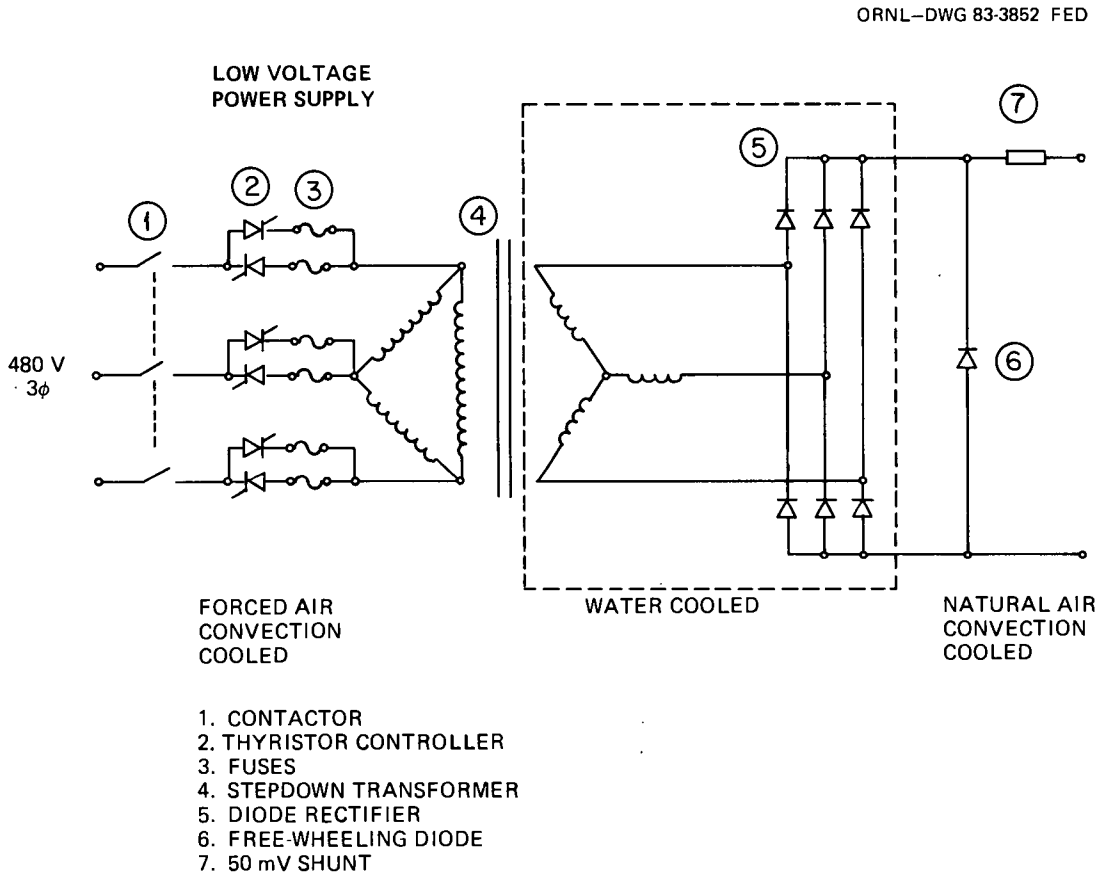

Fig. 10.15. Typical primary-controlled SC coil power supply.

Table 10.5. Coil protection data

Coil	Self-inductance L_{self}, H	Current I_{coil}, kA	Maximum energy, MJ	Number of dump resistors	Resistance, Ω	Equivalent time constant, s
CS0	0.00188	77.3	5.6	0		
CC1	0.00171	135	15.6	0		
CS1	8.6	16.5	130.2	4[a]	0.060	73
S1–S5	3.62	2.73	25.7	10	0.029	238
CC2I	0.00525	57.5	8.7	0		
CC2M	0.90	20.5	451	2[b]	0.024	90
CC2O	1.82	25.0	831	2[a]	0.020	133
T1	3.58	5.0	60.6	2	0.085	57
A1, A2	8.17	5.0	123	2	0.085	58
P1, P2	7.93	5.0	120	2	0.085	56
T2	2.93	5.0	45.2	2	0.085	43
DC	6.04	4.5	65.0	2	0.055	115

[a]All new dump resistors.
[a]One new, one old dump resistor.

Neutral beam injectors

Each of the eight neutral beam injection sources for the central cell requires an independent set of power supplies. Each set comprises six power supplies: one each for arc, filament, acceleration, deceleration, electron collector, and bending magnets. Existing MFTF-B power supplies will be upgraded as described in Sect. 10.3.1.

Power supplies for sloshing negative-ion neutral beam injection do not currently exist. The acceleration power supplies require only a small current (~10 A for all eight negative-ion sources). The MFTF-B power supplies used for the positive-ion sources may not be satisfactory for the negative-ion sources. It may be more economical to procure new power supplies than to refurbish the positive-ion power supplies, as described for the 210-keV acceleration supply described in Sect. 10.3.1. A detailed study of these two alternatives is needed before a final design selection is made.

ECRH power generation

The neutral beam power supply now being used for pulsed ECRH power generation on MFTF-B will be upgraded for continuous operation, as will another neutral beam power supply. This will provide one supply for each end of MFTF-α+T. Voltages for ECRH power are about the same as those for positive-ion neutral beam injection, so only cooling system modifications and larger power cables are needed.

ICRH power generation

About 400 kW of 20-kV dc power is being procured for MFTF-B. (Neutral beam power supplies are not available for ICRH power generation on MFTF-B.) About 2400 kW of ICRH power is needed for MFTF-α+T; this can be supplied by purchasing new power supplies or by reducing the ac input voltage of the two neutral beam power supplies dedicated to ICRH power generation from 13.8 kV to 4.16 kV. The latter option appears to be the most economical, but further investigation is needed before the associated ac power upgrade, described in Sect. 10.2, is undertaken.

Drift pumping power generation

The anchor cells require most of the drift pumping power (1.2 MW of 18-kV power). The options for supplying this power are the same as for ICRH power supplies. The plug-cell drift pumps require <200 kW of 5-kV power; new power supplies that operate from 480-V, 3-phase, 60-Hz power were selected for this design.

10.3.3 Summary

All but two of the MFTF-B magnet power supplies are reassigned to MFTF-α+T magnets. Three additional SC coil power supplies with currents between 17 and 25 kA and three RC coil power supplies with currents between 60 and 140 kA will be needed for MFTF-α+T.

Central-cell neutral beam injection sources on MFTF-α+T can use eight of the MFTF-B neutral beam power supplies. These sources require only 30 A from each 90-kV, 80-kA power supply. Upgrades to the cooling system and larger power cables will be required to accommodate continuous operation. The most economical way to supply the −210-kV negative-ion power may be to combine an existing −100-kV adjustable voltage neutral beam power supply with two isolated −110-kV, 6-A fixed voltage power supplies, so that each negative-ion NBI will have a separate source of power. However, the negative-ion NBIs are not well defined and may require an entirely new set of power supplies.

The existing neutral beam power supplies can probably be upgraded to provide dc power for ECRH, ICRH, and anchor-cell drift pumping power generation. Two smaller power supplies will be needed for drift pumping power generation in the plug cells.

10.4 PROCESS CONTROL AND DISPLAY SYSTEM

The general description given in this section is based on available information. It will require revision as the design, analyses, and startup scenarios for MFTF-α+T evolve. A list of acronyms, abbreviations, and symbols used in this section is given in Table 10.6.

Table 10.6. Process control system acronyms and abbreviations

AC	anchor cell or alternating current
ACCEL	acceleration
B_{ma}	maximum magnetic field in anchor cell
B_{mb}	maximum magnetic field in plug cell
B_{mc}	maximum magnetic field in central cell
B_{mx}	maximum magnetic field in axicell
BGP	background gas pressure, torr
CC	central cell
CONT	controller
CV	check valve
DC	direct converter or direct current
DENST	trim control output of CC plasma density controller
DG	diesel generator
DTF	drift
DS*X*	deuterium source power supply (*X* indicates number)
E	east
E_{ia}	energy of anchor cell ions
ECRH	electron cyclotron resonance heating
ECT	electrical conductivity transmitter
EMF	electromagnetic fluctuations
FC	flow control
FLUXT	trim control output of the axicell neutron flux controller
FT	flow transmitter
FW	first wall
GP	group
I_D	total deuterium NBI current, A
I_T	total tritium NBI current, A
I_{nb}	$I_D + I_T$, total NBI current, A
ICRH	ion cyclotron resonance heating
IDS*X*	current from deuterium source, A
INB*X*	current from negative neutral beam source, A
ITS*X*	current from tritium source, A
LCIS	local control and instrumentation system
LT	level transmitter
LTD	limited
MAG	magnet
MUX	data acquisition multiplexer
N_{ec}	Electron density in central cell
N_{ex}	electron density in plug cell
N_{ia}	ion density in the anchor cell
N_{ipa}	ion density at point *a* of the plug cell
N_{ipb}	ion density at point *b* of the plug cell
NBI	multiple-source neutral beam injector
NBS*X*	negative NBI source power supply
PC	programmable controller
P.S.	power supply
PHT	water pH transmitter
PT	pressure transmitter

Table 10.6 (continued)

Q_{cX}	controlled coolant flow of channel X
Q_{FX}	first wall coolant flow of channel X
Q_{max}	maximum coolant flow
Q_{min}	minimum coolant flow
RC	resistive conductor
REG	regulator
RMT	radiation monitor transmitter
RPS	resistive coil power supply
SC	superconducting
SCDS	supervisory control and data system
SCR	silicon controlled rectifier
SETPT	controller setpoint input
T_{ec}	electron temperature in central cell
T_{ic}	ion temperature in central cell
T_{FX}	first wall coolant outlet temperature of channel X
TEMPT	trim control output of the CC plasma temperature controller
TINBI	trim control input to the negative NBI of the plug cells
TPA56	trim input to 56-GHZ ECRH power control of point (a) of the plug cell
TPB35	trim input to 35-GHZ ECRH power control of point (b) of the plug cell
TPB56	trim input to 56-GHZ ECRH power control of point (b) of the plug cell
TP25M	trim input to 25-MHZ ICRH power control of the anchor cell
TP50M	trim input to 50-MHZ ICRH power control of the anchor cell
TPDP1	trim input to the drift pump RF power control of the plug cell
TPS	trim power supply of SC magnets
TSX	tritium source power supply
TT	temperature transmitter
V_{cX}	voltage of direct converter collector X
V_{dcX}	programmed demand voltage of collector X
ΔV	$V_{dcX} - V_{cX}$
ϕ_a	electrostatic potential at point a of plug cell
ϕ_b	electrostatic potential at point b of plug cell
ϕ_x	axicell neutron flux

Process control is required for the following systems on MFTF-α+T:

- magnets,
- neutral beam injection in the central cell,
- ICRH in the anchor cell,
- neutral beam injection in the plug cell,
- ECRH in the plug cell,
- rf drift pumping in the plug and anchor cells,
- direct converters,
- background gas pressure (BGP), and
- water cooling.

10.4.1 Requirements

Magnets

The magnetic confinement system includes 12 SC solenoid magnets, 5 RC choke-coil magnets, 12 SC C coils, and 2 SC recircularizing magnets. These magnets will be positioned and controlled to produce the magnetic field profiles shown in Figs. 10.16 and 10.17. In addition, 12 to 16 small field alignment coils will be needed if the main coils cannot be mechanically oriented to the required accuracy. Alignment diagnostics will make it possible to adjust currents in the alignment coils to compensate for misalignments in location and orientation of the large coils.

Most of the general requirements for the MFTF-B magnets also apply to the MFTF-α+T magnets. To meet the design objectives of MFTF-α+T, the following requirements apply.

- All SC coils can be charged slowly to their design-point currents in about 4 h.
- Coils are grouped and provided with main current and trim controls similar to those of MFTF-B.
- Coil charging will stop at the operator's command or when inhibited by automatic control.
- Coils can operate at currents less than the design point.
- Operating current regulators have a control accuracy of $\pm 1\%$ or better. Current measurements have an accuracy of $\pm 0.5\%$ or better.
- Normal discharge time is about 4 h, but if a fault condition that could result in a rapid quench occurs, then all coils can be discharged through dump resistors in ≤ 10 min.
- All fault protection requirements for the MFTF-B SC coils (listed in Table 10.7) apply to MFTF-α+T.
- New SC coils for MFTF-α+T are designed to use the programmable power supplies procured for MFTF-B.
- Computers and programmable controllers used on MFTF-B are used on MFTF-α+T to control the magnet power supplies and protect the coils. Additional controls are provided as needed.
- Power to RC coils is cut off in ≤ 0.1 s if a loss of coolant occurs. This may also require discharge of some SC coils.
- The magnet current controls can establish the field profiles shown in Figs. 10.16 and 10.17 and maintain them for up to 100 h.
- Alignment diagnostic measurements are provided to a computer that is programmed to calculate the currents needed in the alignment coils.
- The alignment computer may also be required to adjust the setpoints of the SCR controllers of the alignment coil power supplies.

ORNL–DWG 83-3490A FED

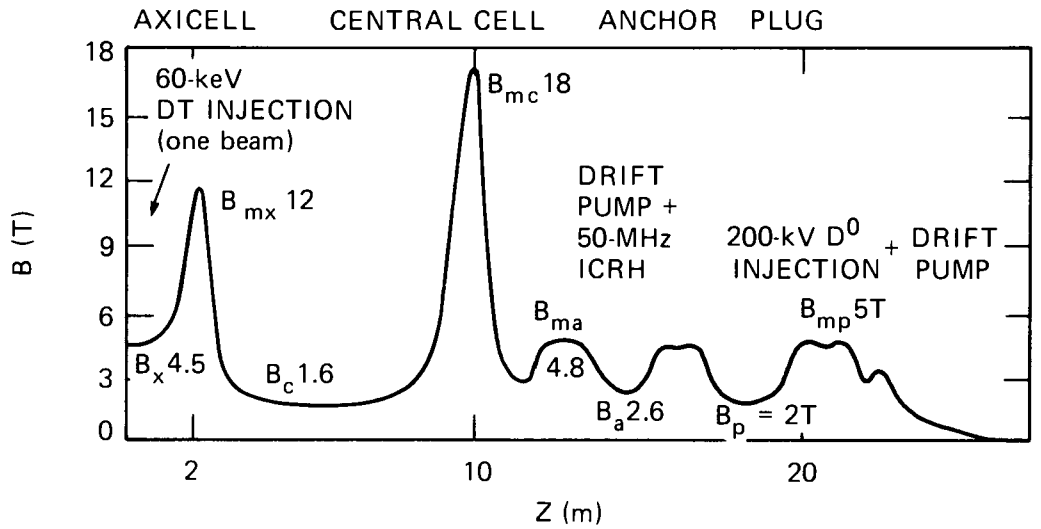

Fig. 10.16. Magnetic field profile in high-Q mode.

ORNL–DWG 83-3959A FED

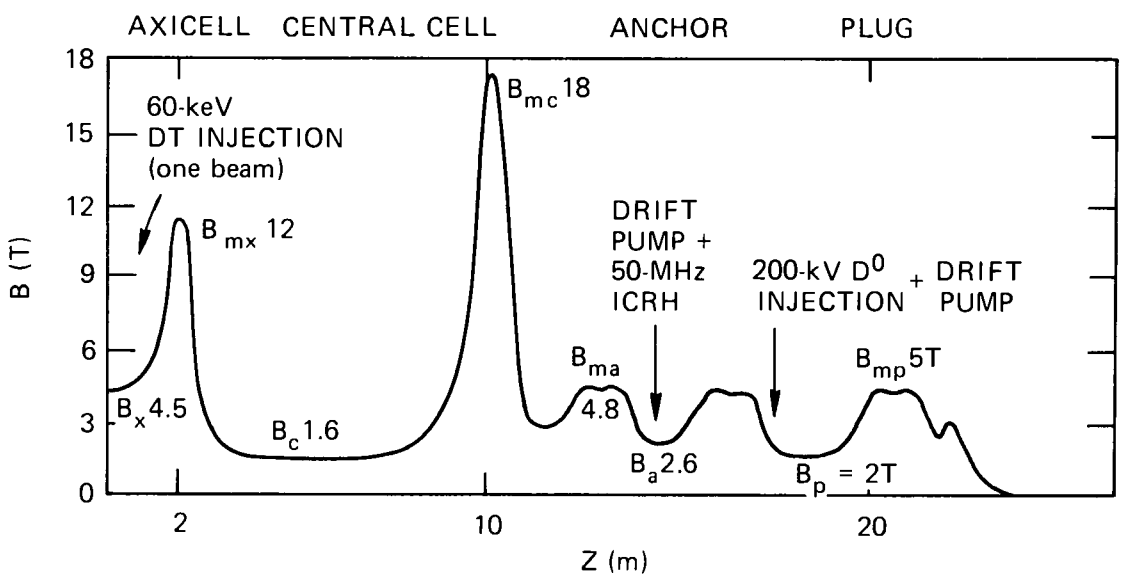

Fig. 10.17. Magnetic field profile in high-Γ mode.

Table 10.7. MFTF-B SC coil protection modes

Mode	Action	Possible causes
Hold	Maintain constant current	SCDS modview communications down SCDS exception
Slow dump	Turn power supplies off (maximum time to decay of 6 h)	Power supply failure Normal zone lower threshold exceeded Current lead lower threshold exceeded Control system failure Power failure Cryogenic system failure
Fast dump	Open dc circuit breakers (maximum time constant of 250 s)	Normal zone upper threshold exceeded Current lead upper threshold exceeded Magnet overcurrent (5% above maximum operating current)

Central-cell neutral beam injection

Two beam lines, one injecting deuterium (D) and the other tritium (T), provide the fueling and heating for the central cell. Each NBI has four sources that can provide up to 7.2 MW at 120 A. Based on a 1-s startup time, the following requirements apply.

- NBI currents are programmable over a range from 40% to 100%.
- NBI current regulation is accurate to $\pm 1\%$ or better. Current measurements are accurate to $\pm 0.5\%$ or better.
- Accel voltages are programmable fron 40% to 100% to produce the ion energies needed for startup and operation in the high-Q and high-Γ modes.
- Neutral beam injectors can operate with only two sources in the high-Q mode.
- The neutral beam response time is about 0.1 s.
- Loss of coolant to the NBI systems or loss of plasma will cut off power and terminate operation in ≤ 0.1 s.
- Neutral beam sources can be automatically restarted after an arc quench occurs so that long-term testing is not interrupted.
- The startup and operation control requirements for the 30-s NBI systems of MFTF-B apply to MFTF-α+T.

Anchor-cell ICRH

Each anchor cell uses two ICRH systems, one that generates 25-MHz power and one that generates 50-MHz power, to heat ions in the cell to about 400 keV. In the high-Q mode, the antenna power is about 700 kW at 25 MHz and about 130 kW at 50 MHz; in the high-Γ mode, the corresponding powers at these frequencies are about 800 kW and

340 kW. Control requirements depend to some extent on the startup scenario, which has not yet been defined, so the following requirements are based on a 1-s startup and a system with programmable ICRH power.

- Response time will be about 0.1 s.
- The power control range is from 10% to 100% (100% power is the design power in the high-Γ mode).
- Absolute power control accuracy will be within $\pm 5\%$ of setpoint.
- Loss of coolant to ICRH components will cut off power and terminate operation in ≤ 0.1 s.

Plug-cell neutral beam injection

Each plug cell contains a 200-keV negative-ion NBI with an incident power of 840 kW at 4.2 A in the high-Q mode and 440 kW at 2.2 A in the high-Γ mode. There are four 1.2-A sources in each beam line. The following requirements are based on a 1-s startup time and an NBI system with programmable currents and accel voltages.

- NBI currents are programmable over a range from 40% to 100%.
- NBI current regulation is accurate to $\pm 1\%$ or better. Current measurements are accurate to $\pm 0.5\%$ or better.
- Accel voltages are programmable fron 40% to 100% to produce the ion energies needed for startup and operation in the high-Q and high-Γ modes.
- The neutral beam response time is ≤ 0.1 s.
- Loss of coolant to the NBI systems or loss of plasma will cut off power and terminate operation in ≤ 0.1 s.
- Neutral beam sources can be automatically restarted after an arc quench occurs so that long-term testing is not interrupted.

Plug-cell ECRH

Each plug cell uses three ECRH systems, one generating 35-GHz power and the other two generating 56-GHz power, to heat electrons at two locations (points *a* and *b*). In the high-Q mode, the amounts of power incident on the plasma are 384 kW at 35 GHz, 360 kW at 56 GHz, and 72 kW at 56 GHz; the corresponding amounts of power at these frequencies for the high-Γ mode are 600 kW, 480 kW, and 120 kW. Control requirements depend to some extent on the startup scenario, which has not yet been defined, so the following requirements are based on a 1-s startup and a system with programmable ECRH power.

- Response time will be about 0.1 s.
- The power control range is from 10% to 100% (100% power is the design power in the high-Γ mode).
- Absolute power control accuracy will be within $\pm 5\%$ of setpoint.
- Loss of coolant to ECRH components will cut off power and terminate operation in ≤ 0.1 s.

RF drift pumps

Each anchor cell uses 12 rf drift pump frequencies ranging from 56 to 96 GHz or a single drift pump that can be frequency modulated (FM) over this range. The plug cell uses an FM drift pump that sweeps the range from 558 to 642 kHz every 0.1 s.

Drift pump control requirements depend to some extent on the startup scenarios, which have not yet been defined. Based on a 1-s startup time and programmable drift pumping power, the following requirements are established.

- The response time is about 0.1 s.
- The power control range is from 10% to 100% (100% power is the design power for all frequencies in the high-Γ mode).
- Absolute power control accuracy will be within $\pm 5\%$ of setpoint.
- Loss of coolant to drift pumping components will cut off power and terminate operation in $\leqslant 0.1$ s.

Direct converter

There are two direct converters, one at each end of the machine. Details of the design have not been established, but it is currently assumed that the collector of the direct converter will consist of two or more concentric sectors, each operating at a different potential and each with its own variable-resistance load. Controls are needed to adjust the load resistance in order to establish the desired potentials for operating the machine. The relationship between converter voltage and axicell neutral beam current will be established for each converter section, and this relationship will be enforced over the operating range. A manual control will be provided for off-design operation.

The following requirements are based on a grounded halo. Numerical values are taken from ref. 1.

- The dc voltage of the center section of the direct converter at the design point for high-Q mode operation will be about -75 kV when the axicell neutral beam current is 53 A.
- The dc load voltage of the center section of the direct converter at the design point for high-Γ mode operation will be about -40 kV when the axicell neutral beam current is 250 A.
- The direct converter load resistance for the high-Q mode will be about ten times that for the high-Γ mode.
- The total electric power on each converter will be <1200 kW in the high-Q mode and <3200 kW in the high-Γ mode.
- The voltage regulation of the direct converter will be accurate to within $\pm 2\%$ of the setpoint value in both modes. The measurement accuray will be within $\pm 1\%$ of the setpoint value.
- The response time of the voltage controller will be $\leqslant 1$ s.
- The coolant flow in the collectors, dump resistors, and tubes will be controlled so that the maximum outlet temperature is $\leqslant 60°C$ (maximum temperature rise is $\leqslant 40°C$).

- If the coolant flow falls below a minimum value or if the voltage regulator error exceeds a maximum value, the system is shut down in ≤ 0.1 s.
- The response time of the coolant flow controls is not critical and may therefore be as long as several seconds.

BGP system

Deuterium gas injectors will be used in conjunction with the vacuum pumping system to establish the desired BGP for startup and operation. The BGP system will be used during startup and possibly during operation for control of the temperature gradient in the plasma halo. Since the vacuum vessel is pumped down and backfilled before startup, the system response time can be on the order of minutes rather than seconds. The following requirements are established.

- BGP measurements are made along the entire length of the device. Selected BGP detectors in the central and end cells are used to control the pressure.
- Pulsed gas valves admit deuterium gas through injector nozzles as needed.
- There are two injectors in the central cell and one in each end cell.
- The BGP is established and maintained within $\pm 5\%$ of the setpoint.
- An intelligent processor reads the conditioned BGP signals, selects valid measurements, and sequentially pulses the gas valves to establish and maintain the desired BGP if it is above the design value.
- The MFTF-B BGP detectors, gas injector valves, and pressure regulators are used as fully as possible.

Water cooling systems

The first wall, shield, RC coils, NBIs, and beam dumps all require water cooling. Components subject to some tritium leakage (e.g., choke coils, first wall, tritium NBIs, beam dumps) must be connected to separate cooling systems; other components, less susceptible to tritium leakage into the water, may be connected to a common cooling system. The following requirements are defined.

- Separate controls are provided for each cooling system to monitor and control water flow and to control water treatment.
- Controls for pumps and valves provide enough water to all water-cooled components to keep material temperatures below design limits.
- Instrumentation is sufficient to permit detailed heat balance analyses.
- Radiation monitors are provided in each cooling path with surfaces exposed to the plasma, so that leak faults can be readily detected and located.
- The machine is rapidly shut down if loss of flow or low flow causing high water temperatures occurs. Instrumentation and control (I&C) is sufficient to permit automatic shutdown.
- Water filter units are monitored and replaced as needed for satisfactory performance.
- The water storage vessel is equipped with I&C to determine water quality and control the flow to the water treatment system.

- Manually adjustable equalization valves or orifices are provided so that satisfactory flow can be distributed to all coolant paths.
- The response time of the flow controls is not critical and may therefore be as long as several seconds.

10.4.2 Design Description

A preconceptual design for the process control and display system is described. There is some overlap with the plasma control and display system, which is more fully described in Sect. 10.5, because the two systems are so closely coupled.

Several options identified in this design need further evaluation. Considerable analysis, including computer simulation, is needed to define the plasma kinetics of the different regions of the device, their interaction with each other, and their interaction with the control systems. Additional options may be identified as the requirements are more fully defined. The control systems described in this section are for a neutral-beam-driven machine operating well below self-sustaining ignition conditions.

The proposed measurements and controlling inputs of major systems are identified in Table 10.8. The process measurements are used by the primary controls; the plasma diagnostics measurements are used by the secondary or trim controls. Figure 10.18 is a diagram of most of the process control systems. In general, the process variable demands are scheduled using the synchronous timer control. The process measurements and the demands are used as input to the primary controllers. The plasma variables are also scheduled and are used as input to the trim controls. The lower part of Fig. 10.18 identifies the controls on the plasma-confining magnetic field; the upper part identifies the controls on the heating and fueling systems, the direct converter, and the plasma-confining electrostatic field. Only one of the two end-cell regions is shown.

Magnets

The programmable power supplies for MFTF-B and MFTF-α+T are listed in Table 10.4. As indicated in the table, MFTF-α+T will require six new power supplies, three for RC coils and three for SC coils. Additional controllers and computer software will be needed for these power supplies.

Figure 10.19 is a diagram of the control system for the power supplies of the central-cell magnets, based on the power supply and coil arrangements described in Sect. 10.3. The data link from the associated supervisory control and data system (SCDS) console provides the setpoint data to the local control and instrumentation system (LCIS) and sends monitoring information to the SCDS. The local control computers and programmable controllers are part of the local current and voltage feedback control loops of each power supply. Similar control systems are provided for the end-cell magnet power supplies.

Figure 10.20 shows the general diagram of the SC coil protection system. The coil protection systems of MFTF-B (Table 10.7) are adapted to MFTF-α+T. Local control computers provide the signal processing and logical inputs to programmable controllers that operate the dump circuit breakers.

Table 10.8. Measurements and controlling inputs

Control	Process measure	Diagnostic measure
	Axicell and central cell	
D_2 and T_2 NBI power supply voltages	D_2 and T_2 NBI currents	Plasma ion temperature Plasma density Neutron flux
D_2 gas injector flow	BGP	
SC magnet power supply voltages	SC magnet currents	Magnetic field
RC magnet power supply voltages	RC magnet currents	Magnetic field
	Transition and anchor cells	
Drift pumping rf power gain	Low-frequency rf power	Electromagnetic fluctuations
ICRH power supply voltages	ICRH power	Ion energy Ion density
SC magnet power supply voltages	SC magnet currents	Magnetic field
D_2 gas injector flow	BGP	
	Plug cells and transition region	
Negative NBI power supply voltages	Deuterium NBI currents	Plasma density at point *a*
600-kHz drift pump power gain	RF power	Plasma density at point *b*
56-GHz ECRH power supply voltages	ECRH power	Plasma potential at point *a*
35- and 56-GHz ECRH power supply voltages	ECRH power	Plasma potential at point *b*
	Direct converter	
Direct converter load resistance	Collector voltages	Collector currents
Flow control valve position	Coolant outlet temperature and flow	

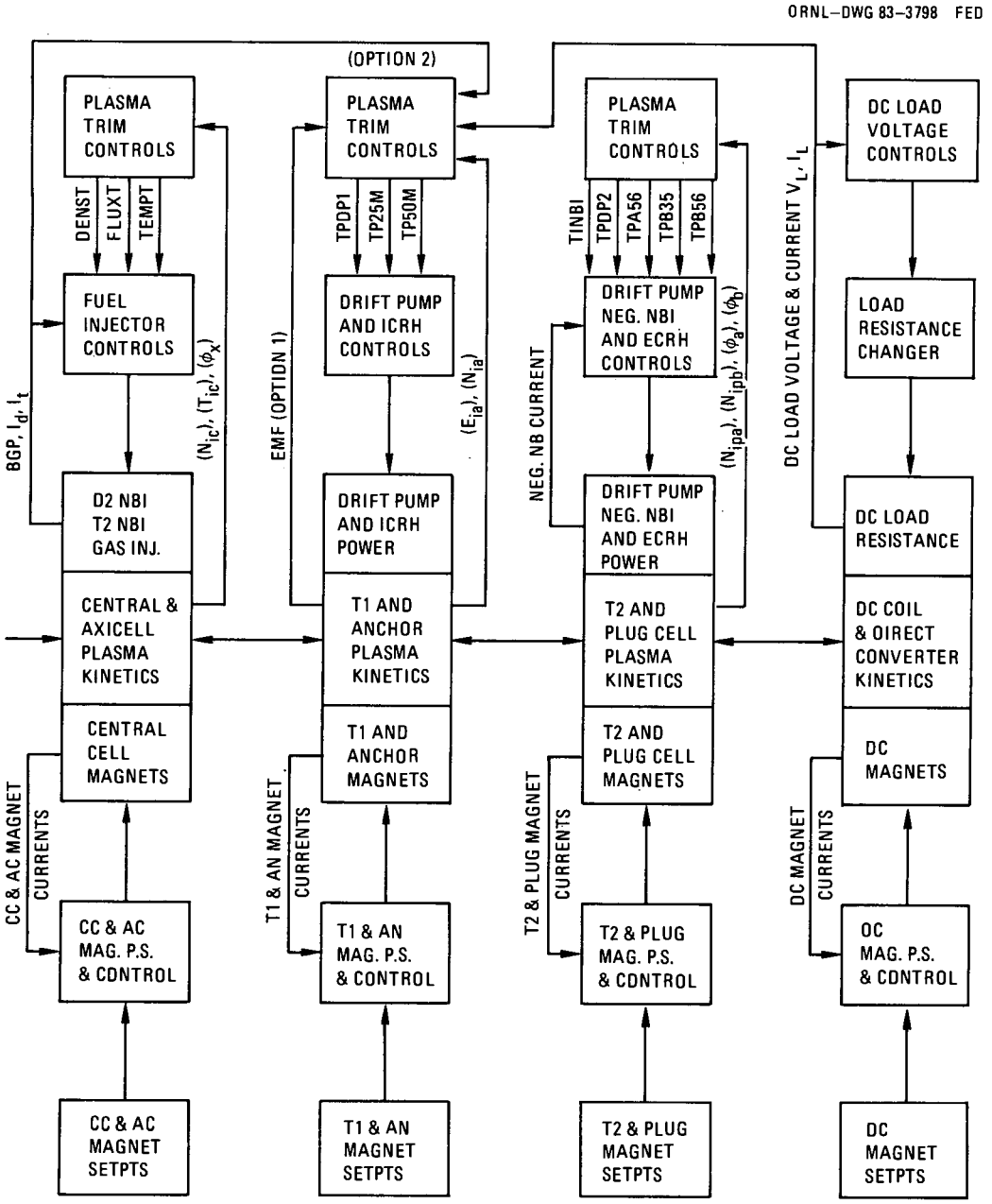

Fig. 10.18. Overall MFTF-α+T control system.

Figure 10.21 is a schematic diagram of the magnet LCIS for MFTF-B. This system includes local video displays. Additional programmable controllers may be required for the axicell, plug-cell, and transition magnets of MFTF-α+T, and existing programmable controllers and computers will require reprogramming. To align the heavy magnets of MFTF-α+T with each other and with the magnet axis, small alignment coils may be needed. Each alignment coil would need a small, two-quadrant programmable power supply. At least 8 alignment coils are needed for MFTF-B; MFTF-α+T may need as many

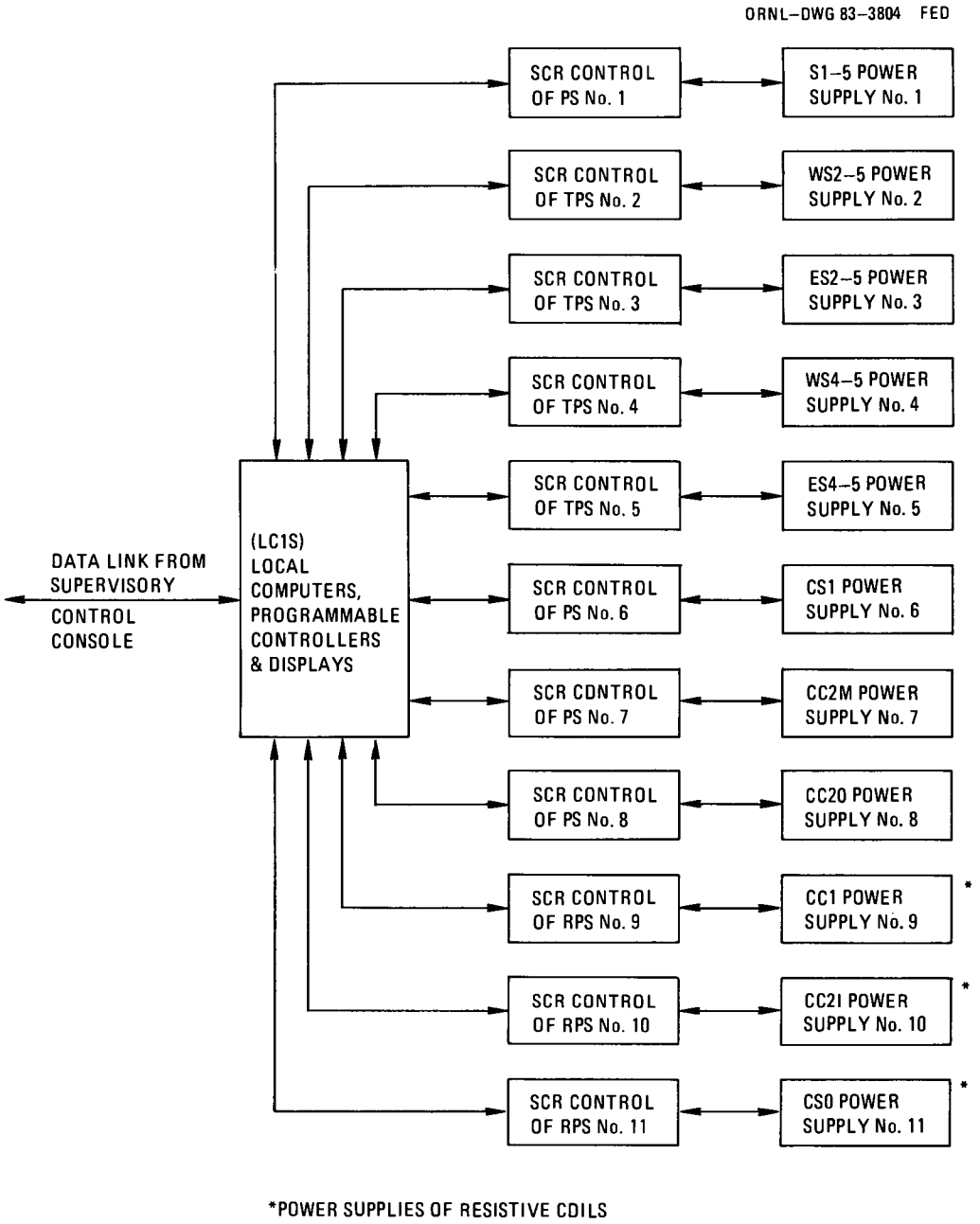

Fig. 10.19. Central-cell magnet control system.

as 16. The alignment coil power supply system is shown in Fig. 10.22. Alignment diagnostics provide input to the alignment computer, which generates setpoint data for the power supplies.

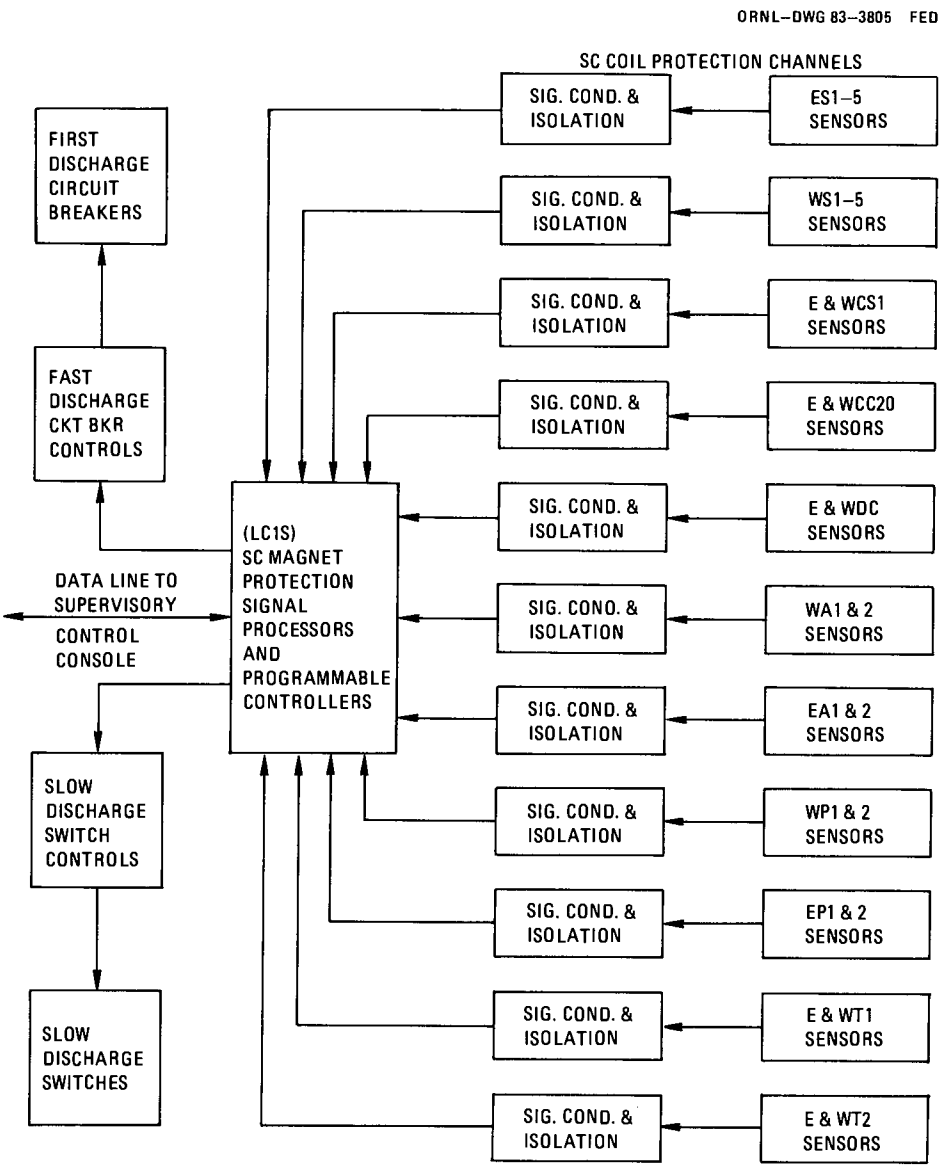

Fig. 10.20. SC magnet protection system.

Central-cell neutral beam injection

Two neutral beam lines, one tritium and one deuterium, provide fueling and heating in the central cell. Each beam line is equipped with four sources. The neutral beams are injected into the axicell, and leakage from the ends of the axicell heats and fuels the remainder of the central cell. Most of the neutrons are generated within the heavily shielded central cell.

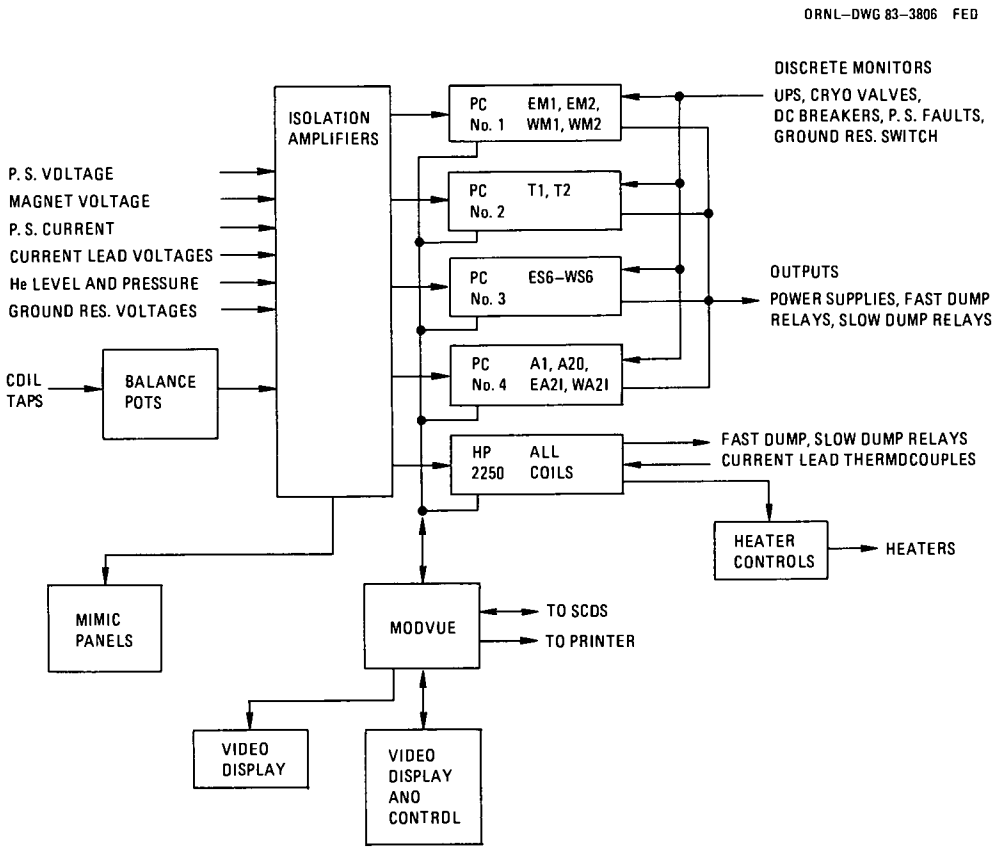

Fig. 10.21. MFTF-B magnet LCIS.

Figure 10.23 is a detailed diagram of the fuel injection control system. There are two injection schedules, one for the high-Q mode and one for the high-Γ mode. The total current demand is modulated by the plasma density control (DENST), as described in Sect. 10.5. A fuel ratio control then divides the total current demand into the deuterium and tritium current demands, which are the inputs to the deuterium and tritium current controllers shown in Fig. 10.23. The current demands are converted to arc and filament voltage setpoints using function tables; measured beam currents are summed and compared with current demand; and any error is used for trim control of the power supply setpoints.

The energy of the beam particles depends on the acceleration voltages applied to the unneutralized ions. The ion energy can be controlled over a substantial operating range by modulating the accel power supply voltage. During startup, the accel voltages increase with current until the operating range is reached. The plasma temperature secondary controller modulates the accel voltages, and the neutron flux secondary controller modulates the tritium-to-deuterium ratio.

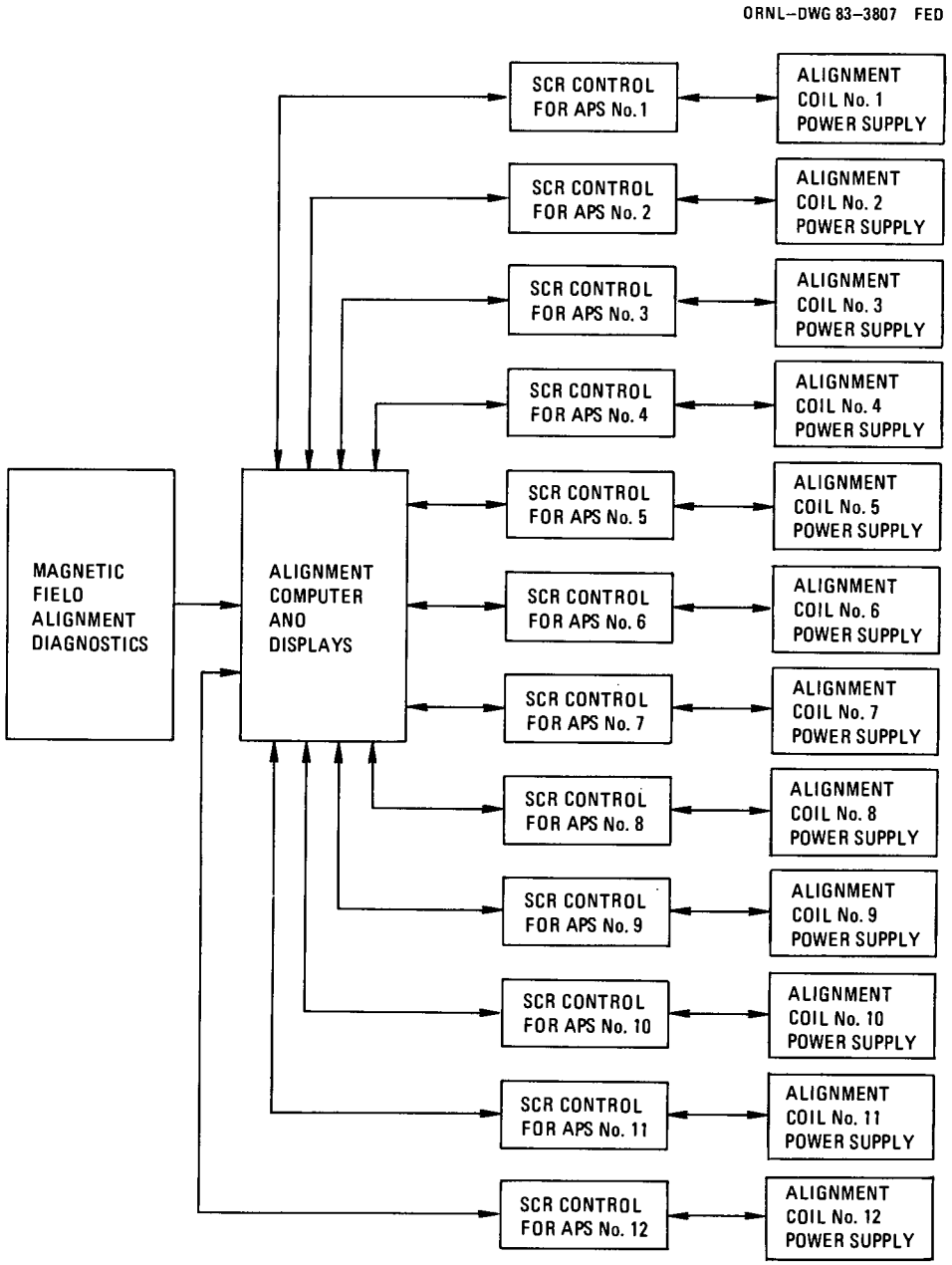

Fig. 10.22. Control system for alignment magnets.

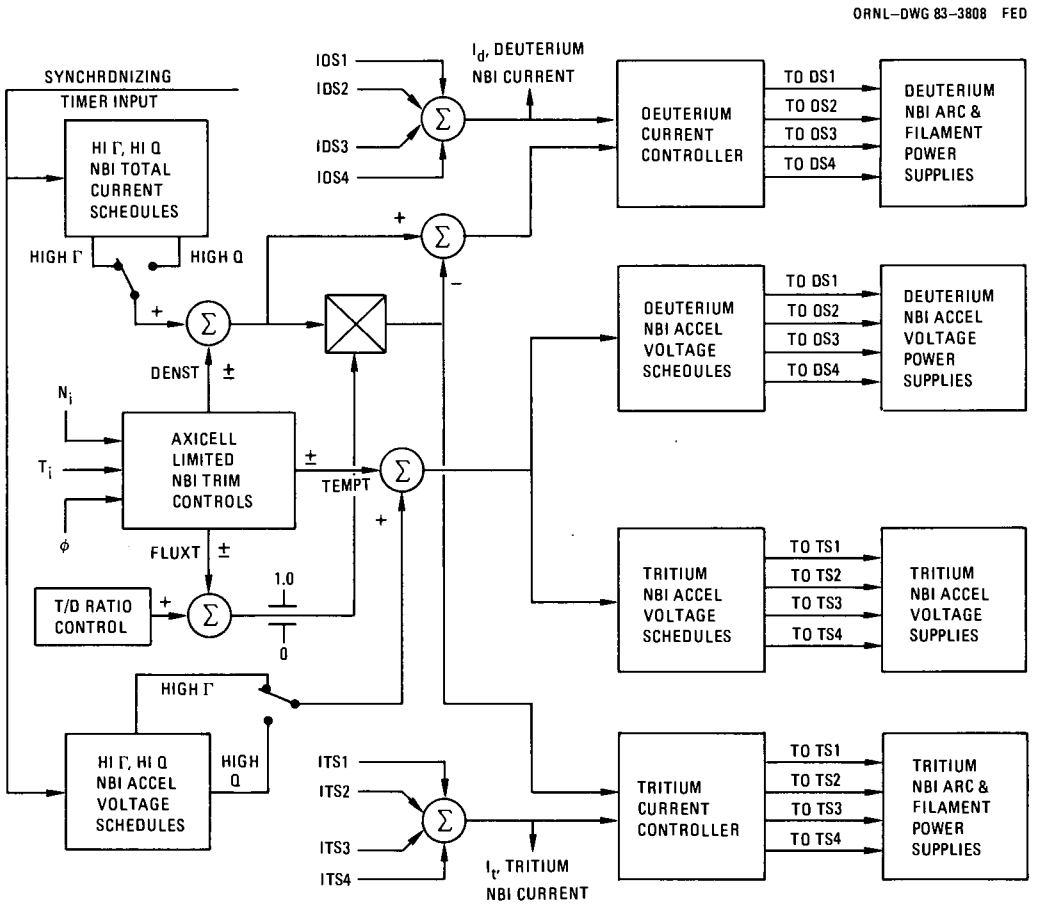

Fig. 10.23. Axicell NBI control system. (See Fig. 10.33 for details of trim controls.)

Anchor-cell ICRH

The proposed anchor-cell ICRH control system, shown in Fig. 10.24, schedules the power required for a particular mode of operation as a function of time. The power demand is converted to power supply voltage setpoints in the 25- and 50-MHz power controllers with function tables. The setpoints then control the firing angles of SCR power modules to provide the desired voltages. The power demand is corrected by trim controls so that the desired population of hot ions exists.

Plug-cell potential control (neutral beam injection, ECRH, and rf drift pumping)

The function of the plug cells is to create electrostatic potentials at points *a* and *b* as shown in Fig. 10.16 for the high-Q mode and in Fig. 10.17 for the high-Γ mode. Sloshing ions injected with high-energy, negative-ion NBIs, ECRH heating, and rf drift pumping are controlled to carry out this function. The proposed control system is shown in Fig. 10.25. Neutral beam current, ECRH power, and FM 600-kHz drift pumping power are scheduled as a function of time. There are separate schedules for high-Q and high-Γ operation because the potentials differ greatly for the two modes.

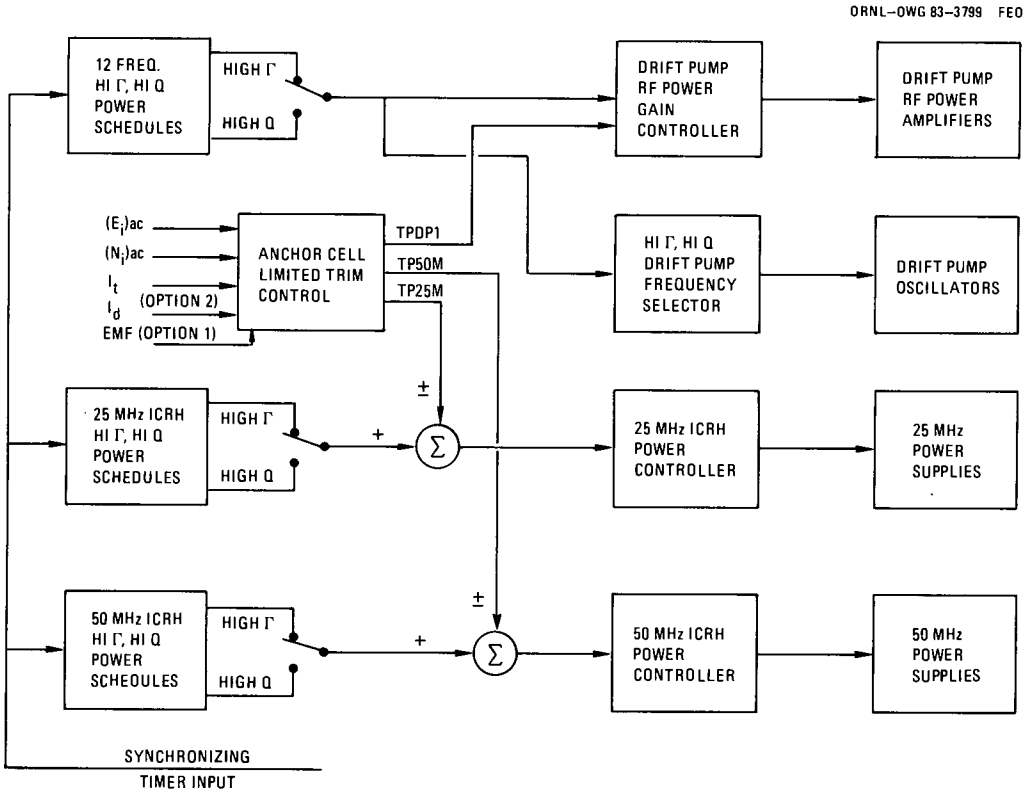

Fig. 10.24. Anchor-cell ICRH and drift pumping control system. (See Fig. 10.34 for details of trim controls.)

The neutral beam current demand is scheduled and corrected to provide the desired plasma density at point *a*. Arc and filament voltages of the neutral beam power supplies are adjusted so that the sum of the deuterium neutral beam currents meets the demand. Accel voltages are programmed as required for startup as a function of the current demand.

The ECRH power is also scheduled and corrected to provide the desired potentials at points *a* and *b*. There is one 56-GHz injector at each point. The power controllers for point *a* are shown in Fig. 10.26, which also shows the 600-kHz drift pumping power control; the power controllers for point *b* are shown in Fig. 10.25.

The drift pumping power is scheduled and controlled to help provide the desired plasma density at point *b*. The corrected power demand signal is converted to power supply voltages required to produce the desired drift pumping power.

Anchor-cell rf drift pumping

The anchor-cell rf drift pumping power is controlled by scheduling the power required for the selected mode of operation as a function of time. It is assumed that the power needed at each of the 12 frequencies will be programmable and that these frequencies may change depending on the mode of operation. The power demand is corrected by plasma diagnostic controls and used to set digital gain controls for the rf power amplifiers.

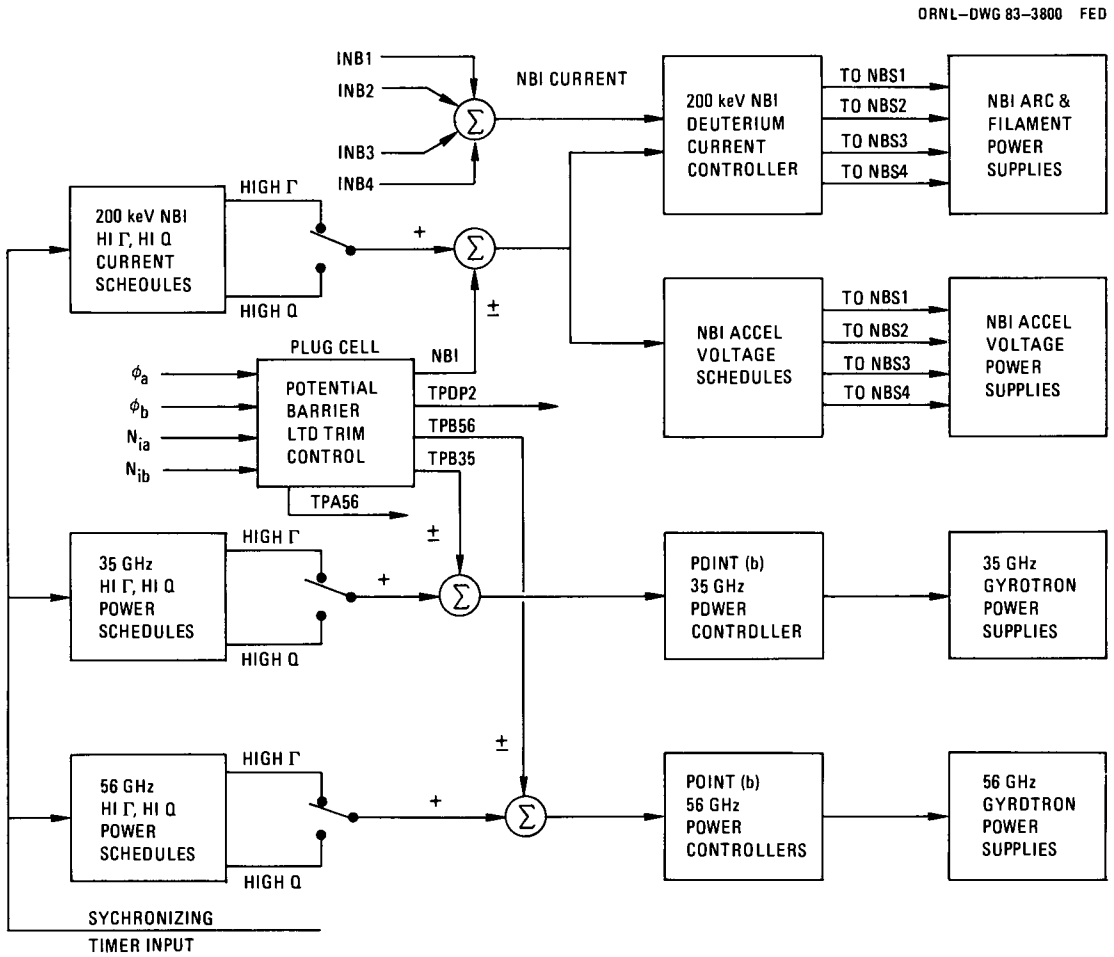

Fig. 10.25. Plug-cell potential control system (NBIs and point *b* ICRH). (See Fig. 10.35 for details of trim controls.)

Direct converter

The two major parts of the direct converter control system are the voltage controllers and the cooling system controllers. Each collector has at least two dump resistor load banks, and collector voltages are determined by the load resistance and the the total neutral beam injection current. The collectors and the dump resistors operate at high voltage and are assumed to be cooled by deionized water.

Two control systems are examined to meet the needs for direct converter control. Both use two banks of load resistors with resistances of R_L and $10R_L$. Alternative 1, shown in Fig. 10.27, uses a large motor-driven rheostat; the response of this electromechanical system is limited by the ratio of torque to inertia. Alternative 2, shown in Fig. 10.28, uses a fixed-resistance $10R_L$ resistor bank shunted by a power control tube. This system is inherently fast and free of mechanical maintenance but is more expensive than alternative 1. Selection of one alternative requires an evaluation of the requirements for high-Q and high-Γ mode operation.

ORNL–DWG 83–3801 FED

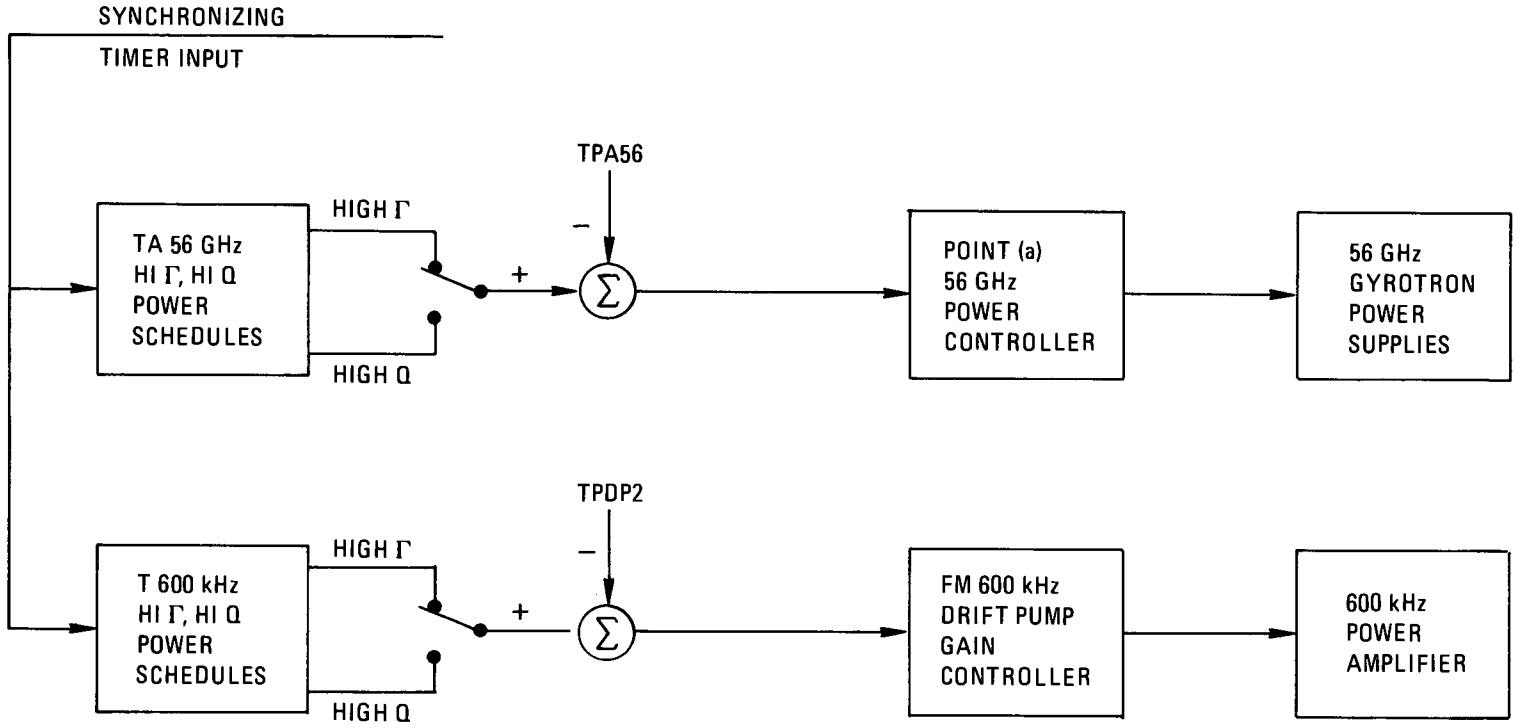

Fig. 10.26. Plug-cell potential control system (rf drift pumping and point *a* ECRH).

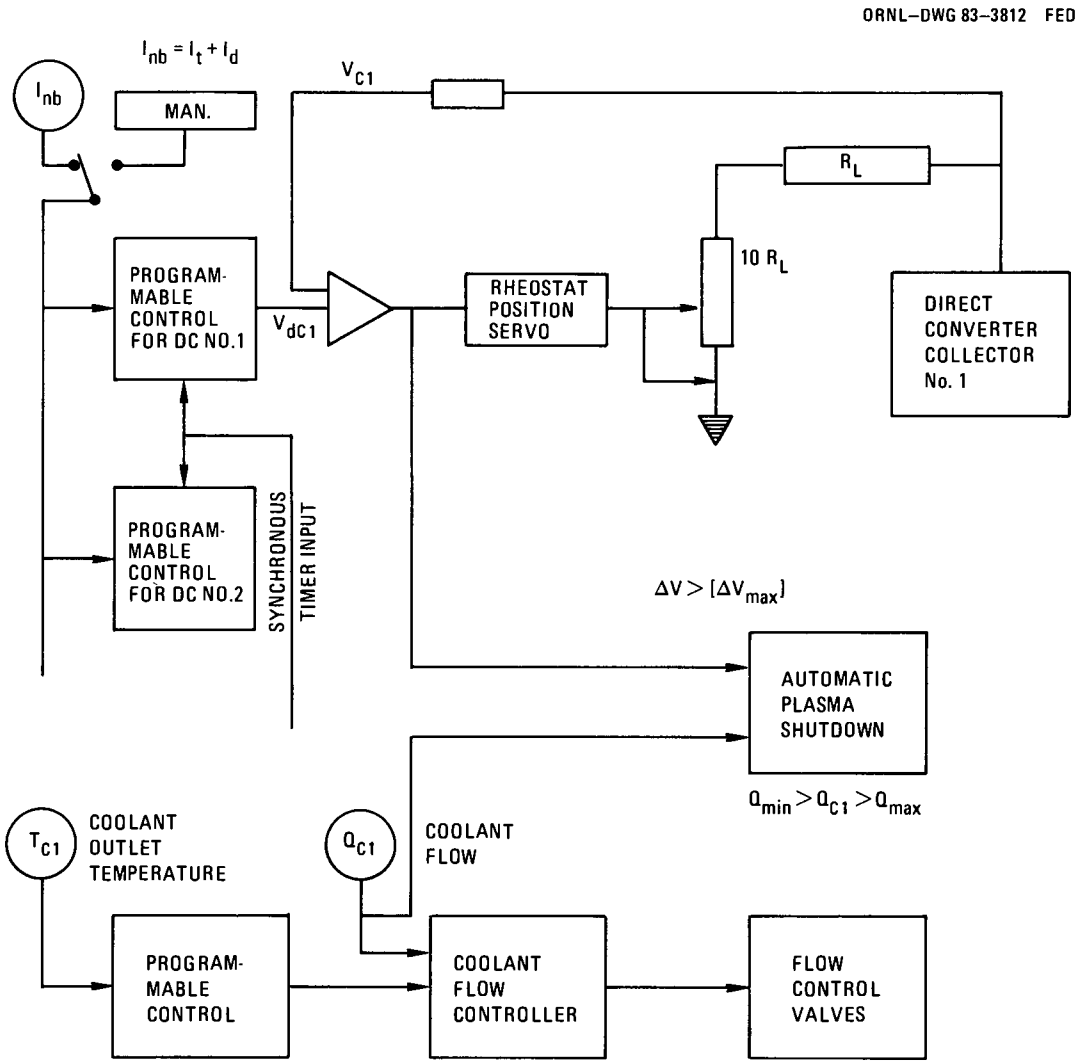

Fig. 10.27. Direct converter control system (alternative 1).

In the high-Q mode, the total neutral beam injection current is only 53 A at a collector voltage of about −75 kV. In the high-Γ mode, the total neutral beam injection current is 250 A at a collector voltage of about −40 kV. If radial pumping is effective, most of the plasma ions move into the halo and are collected at the plasma scraper, while most of the electrons escape axially to the insulated direct converter collectors. With ideal separation of the hydrogen-isotope ions and electrons, the neutral beam injection current would equal the total current to the direct converter collectors. Therefore, in the automatic mode of operation, the total neutral beam injection current I_{nb} is used as the input to the programmable function generators of both control systems (see Figs. 10.27 and 10.28). The programmable control can shape the transition between the two design points according to a prescribed schedule. A manual input to the programmable function generators is also provided for off-design operation.

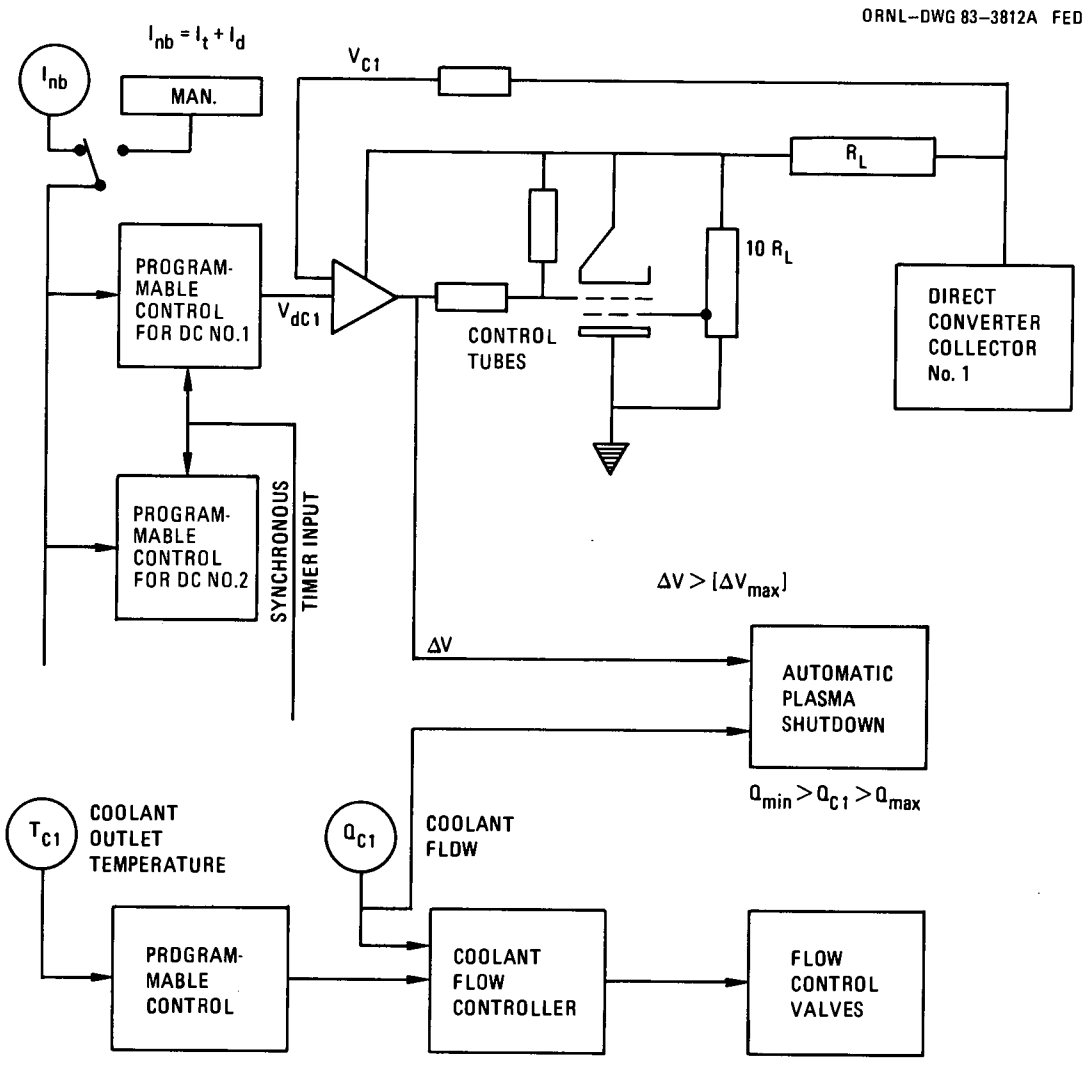

Fig. 10.28. Direct converter control system (alternative 2).

In both control systems, the programmed control generates the collector voltage demand based on the input value of I_{nb}. The voltage demand is compared to the measured voltage and used to vary the resistance of the load. In the high-Γ mode, nearly all the power is dissipated across the R_L resistance bank by setting the rheostat near zero for alternative 1 or by driving the power tube into high conduction for alternative 2. In the high-Q mode, nearly all the power is dissipated across the $10R_L$ resistance bank by setting the rheostat near $9R_L$ for alternative 1 or by driving the power tube near cutoff for alternative 2. The control tube requirements can be greatly reduced with the load resistor arrangement shown in Fig. 10.29 if the machine is operated only near the high-Q and high-Γ design points. With the switches open for operation in the high-Q mode, the tube plate-to-cathode voltage is ≤7.5 kV; with the switches closed for operation in the high-Γ mode, the tube voltage drop is ≤4 kV. However, the operating range is limited to within ±10% of the design point in both modes.

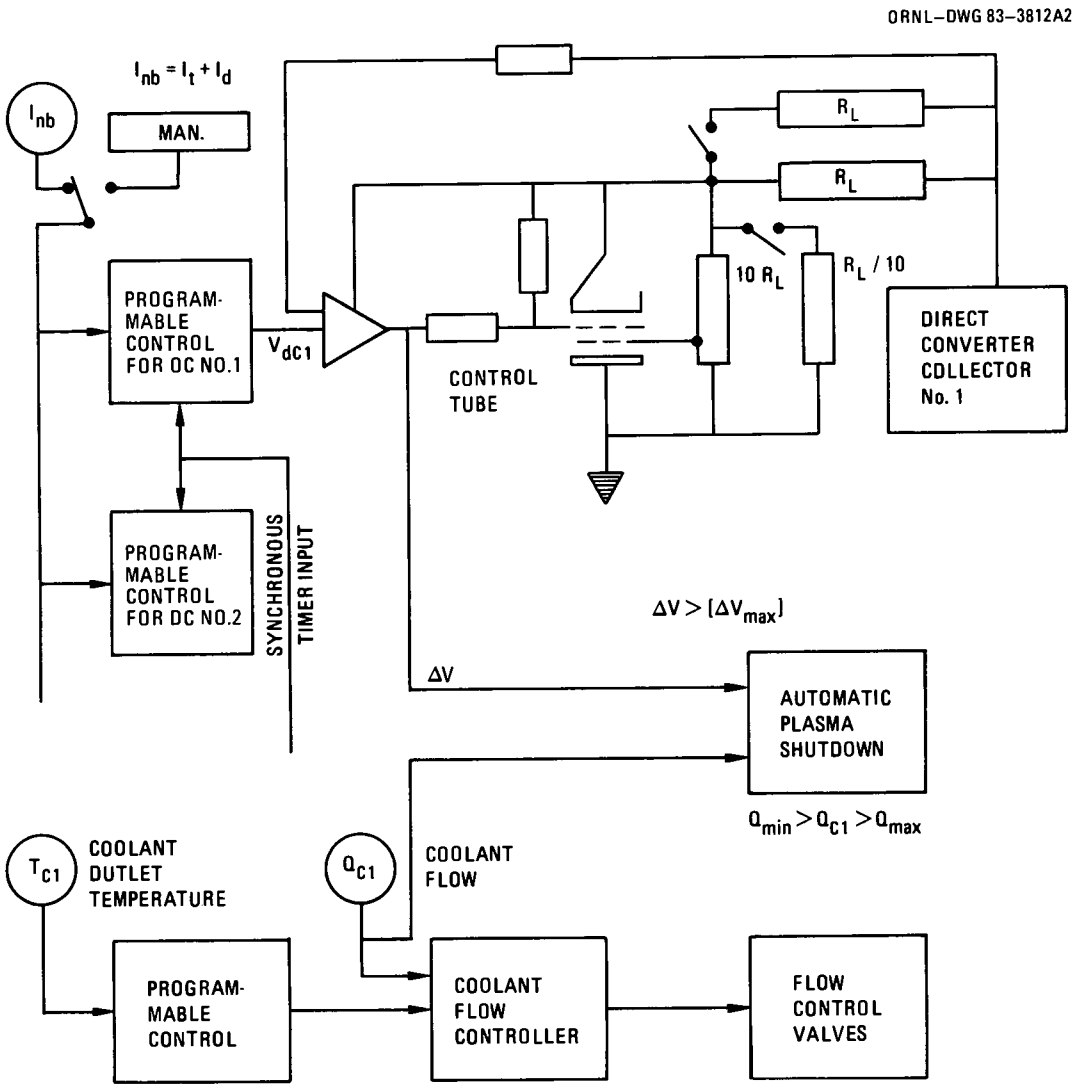

Fig. 10.29. Direct converter control system (alternative 3).

Cooling systems are identical for both alternatives. Controllers like that shown at the bottom of Figs. 4.27—4.29 are needed for each collector and each dump resistor bank; the minimum number per converter is six. The coolant outlet temperature is input to a programmable control that generates the desired flow demand. The flow demand is compared with the measured flow, and the control valves are modulated so that the measured flow is nearly equal to the demand. Nearly any desired relationship between flow and temperature can be obtained. As shown by the figures, if the cooling flow to the direct converters falls below a minimum safe flow or if the voltage control error exceeds a set maximum for more than a normal time, operation is terminated with an automatic plasma shutdown.

BGP

Figure 10.30 is a diagram of a possible BGP control system for MFTF-α+T. Selected BGP detectors provide input data to an intelligent controller, which rejects bad measurements and uses good measurements to control the four pulsed gas injector valves, two in the central cell and one in each end cell. The BGP error signal sequentially admits pulses of gas when the BGP is lower than the desired value. If MFTF-α+T can operate at the pressure produced by initial pumpdown, then the BGP control will be needed only during startup.

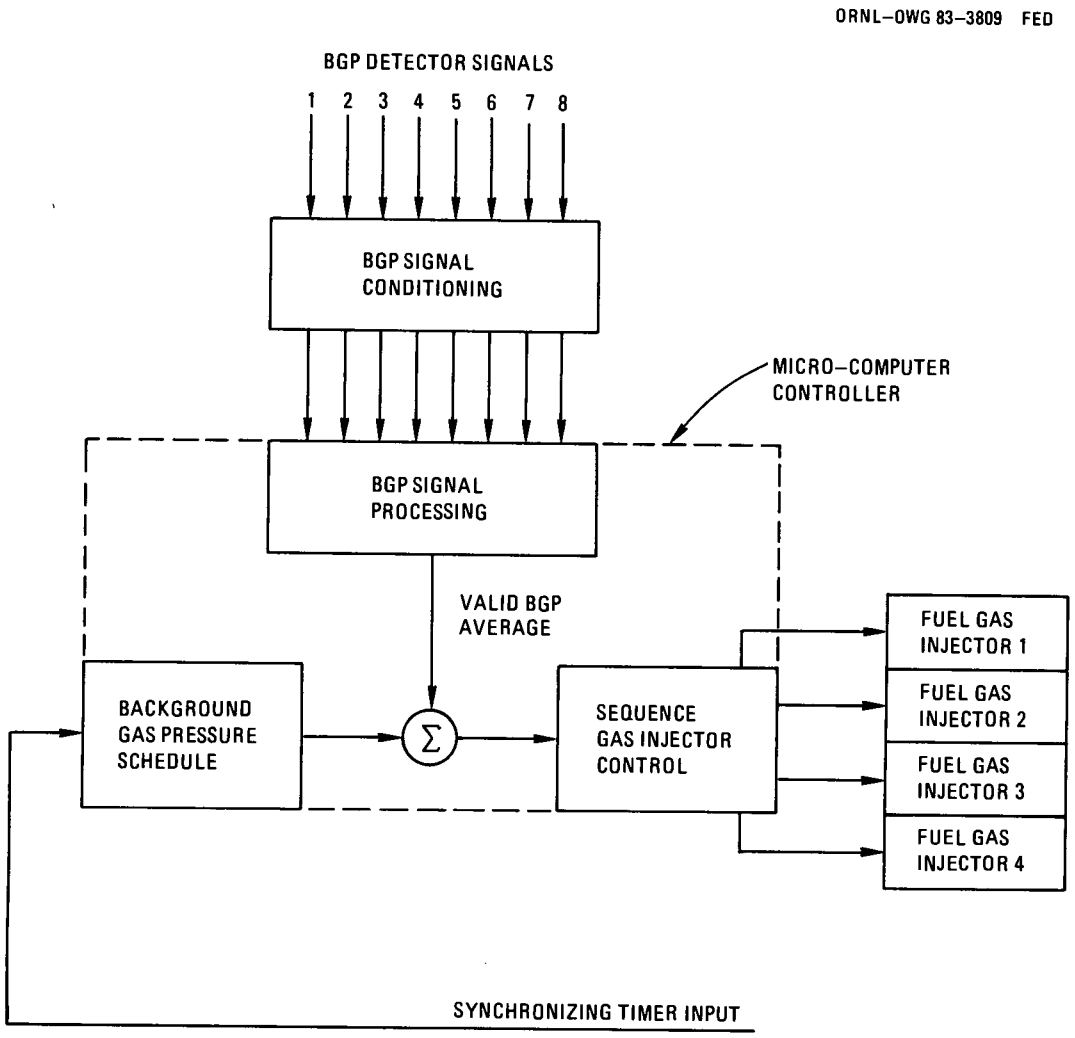

Fig. 10.30. BGP control system.

Water cooling

There are five major water cooling systems for MFTF-α+T components:

1. first wall cooling system,
2. shielding cooling system,
3. RC coil cooling system,
4. plasma heating equipment cooling system, and
5. direct converter cooling system.

Systems are independent of one another so that tritium, helium, and activation products can be easily located and isolated. Figure 10.31 shows a typical water cooling system and associated instrumentation. Only a few of the measurements are used for direct control; the majority are needed for monitoring, for measuring heat flow, and for analyzing water quality. The figure shows only one of the many components located between the pump and heat exchange headers. The shield and first wall consist of many sections, each requiring a separate flow control valve; only two are shown. Distribution valves or adjustable orifices divide the flow so that each coolant channel has approximately the same discharge water temperature. These valves are set manually and rarely adjusted. Radiation monitoring of each flow channel determines the origin of any small leaks.

Each system includes a main pump, a heat exchanger, filters, a water storage tank, and a water treatment unit, all of which require monitoring. Adjustable-speed pump systems are relatively expensive, so a constant-speed pump with pressure-controlled bypass flow is selected to reduce costs. A typical flow control system is shown in Fig. 10.32. Pressure between the pump discharge header and the heat exchange inlet header controls the bypass flow; the pressure difference can be scheduled so that flow to the sectors is nearly proportional to the valve port area. Each sector or component has independent flow control valves, and failure of flow through any sector will automatically shut down the machine. Flow through a sector is a programmable function of the average outlet temperature. The simplest program is an equalized maximum flow through each sector, independent of temperature, but this may not be desirable since more heat will be generated in some sectors than in others. This implies that providing sufficient flow for a high-power sector can cause a low-power sector to operate at lower temperature. A more desirable method is programmed flow to equalize the temperature increase of sectors or components.

10.4.3 Key Issues

The MFTF-B device is designed and constructed to operate with 30-s pulses in a deuterium environment. In contrast, MFTF-α+T requires up to 100 h of operation in a tritium environment. Plasma diagnostics are not sufficiently developed to be used for primary control of the machine; furthermore, it is desirable to use process controls similar to those used on MFTF-B.

There is no experience with NBIs that operate for long periods of time with either hydrogen or deuterium. Neutral beam injection with tritium will be even more difficult. Based on past experience with neutral beams, the MFTF-α+T beams will extinguish and require restarting frequently. Reliable controls for restarting the beams must be developed for tritium operation.

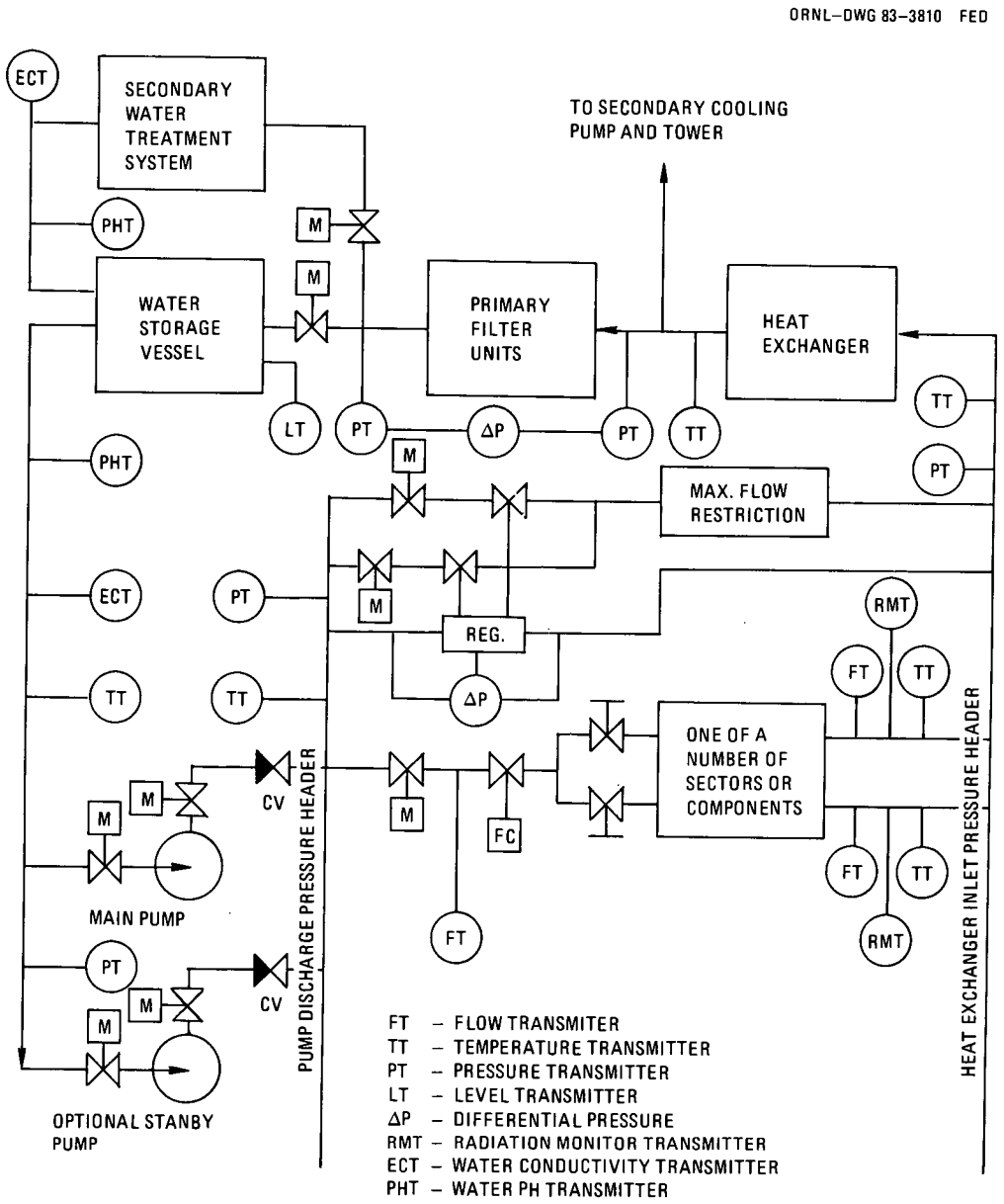

Fig. 10.31. Typical cooling system and instrumentation.

The physics of the anchor cells and the plug cells requires further study. To cope with the limited understanding in these areas, the primary control must be designed with considerable flexibility; that is, it must be programmable over a wide range to accommodate the physics experiments.

Correlation of the many ECRH, ICRH, neutral beam, and rf heating inputs with the performance parameters will require many experiments. Short pulsed operation will be required until the device behavior begins to be understood.

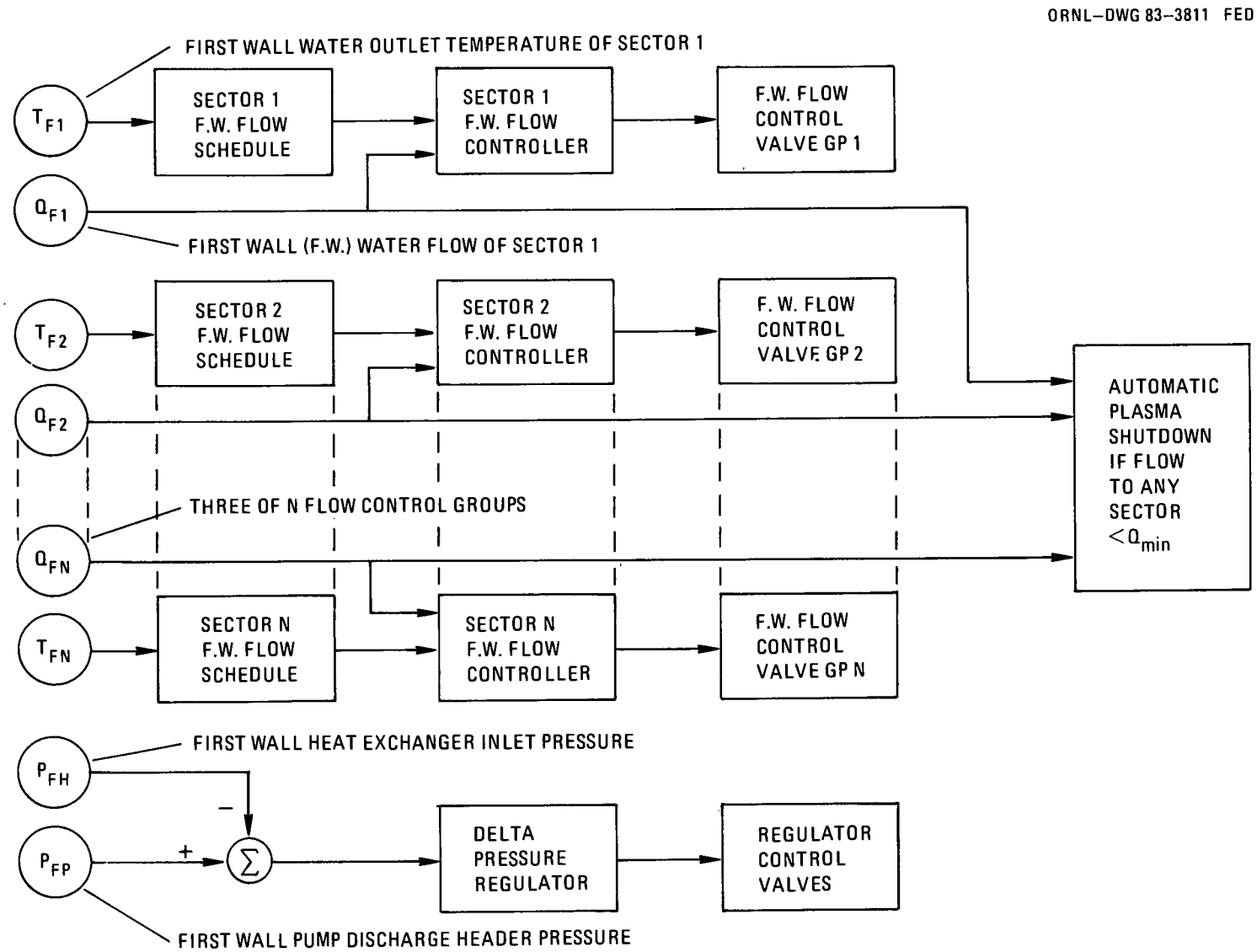

Fig. 10.32. First wall coolant flow control system.

A number of start/restart scenarios will be attempted and will require considerable use of programmable startup controls. Eventually, after the startup procedures and primary controls have been verified, the plasma trim control experiments described in Sect. 10.5 will begin.

10.5 PLASMA CONTROL AND DISPLAY SYSTEM

The general description given in this section is based on available information. It will require revision as the design, analyses, and startup scenarios for MFTF-α+T evolve.

The primary process controls described in Sect. 10.4 provide indirect controls that do not require real-time plasma measurements as input. Ultimately, it is the plasma parameters that we wish to control. To gain experience in real-time control of these parameters, we propose to provide secondary trim controls with limited control range that interface with the primary controls described in Sect. 10.4. These exploratory trim controls are required in the central cell, the anchor cells, and the plug cells.

10.5.1 Requirements

Central cell

Three types of injectors are available for real-time plasma control in the central cell: the gas injectors, the tritium NBIs, and the deuterium NBIs. The gas injectors can influence only the plasma halo and are not considered for core plasma control.

Three plasma parameters are of interest for core plasma control: plasma temperature, plasma density, and alpha particle or neutron flux generation. We propose to use the plasma temperature to control the energy of the neutral particles, the plasma density to control the total neutral beam current injected into the axicell I_{nb}, and the neutron flux to control the tritium-to-deuterium current ratio I_T/I_D. The neutron flux and plasma density controls are not independent, but the control can be made nearly noninteractive. Some general requirements have been established.

- Line-averaged plasma density and temperature measurements are provided on a real-time basis for D-D and D-T operation. If a sampling data system is used, the sampling rate will be at least 10 s^{-1}.
- Real-time neutron flux measurements are provided for trim control during the D-T operating phase only. If a sampling data system is used, the sampling rate will be at least 10 s^{-1}.
- The plasma diagnostic measurements have an absolute accuracy after calibration of within $\pm 5\%$.
- Programmable proportional gain controls are provided for all trim controllers. When the gain is set to zero, the controller provides no trim correction (i.e., it is completely decoupled from the primary control).
- Programmable limiters on all trim controllers limit the correction deviation to about $\pm 10\%$.
- Plasma density controls correct I_{nb} without significantly varying I_T/I_D.
- Neutron flux controls correct I_D/I_T without significantly varying I_{nb}.

- Plasma temperature controls adjust the neutral beam accel voltages to correct the injected particle energies without significantly varying I_{nb} or I_T/I_D.
- Displays are provided for each plasma measurement, for the difference between the measurement and the scheduled demand (error), and for the trim correction to the primary control (deviation).
- Displayed quantities are given in nondimensional units (percentages of design point).

Anchor cell

Three parameters are of interest for plasma control in the anchor cells: line-averaged hot ion energies resulting from ICRH heating, line-averaged plasma density, and electromagnetic fluctuation (EMF). The hot ion energy and the plasma density are used to correct the ICRH power; the EMF signal is minimized by controlling the drift pumping power. Some general requirements have been established.

- Line-averaged hot ion and plasma density measurements are provided on a real-time basis. If a sampling data system is used, the sampling rate will be at least 10 s^{-1}.
- Analog EMF measurements are provided with loop or pickup coil sensors in at least two orthogonal planes.
- EMF correlation, data processing, and filtering are provided to enhance the measurements for drift pumping control.
- The hot ion energy and plasma density measurements have an absolute accuracy after calibration of within $\pm 5\%$.
- A programmable proportional gain control is provided for the ICRH controller. When the gain is set to zero, the controller provides no trim correction (i.e., it is completely decoupled from the primary control).
- A programmable ratio control divides the deviation correction of the trim controller between the 25- and the 50-MHz power generators.
- A programmable limiter limits the total ICRH correction deviation to about $\pm 10\%$.
- Displays are provided for each plasma measurement, for the difference between the measurement and the scheduled demand (error), and for the trim correction to the primary control (deviation).
- Displayed quantities are given in nondimensional units (percentages of design point).

Plug cell

Four parameters are of interest for plasma control of the plug cells: the line-averaged plasma densities at points *a* and *b* and the electrostatic potentials on the *z*-axis at points *a* and *b*. The density at point *a* is used to correct the negative-ion neutral beam injection current; that at point *b*, to correct the 600-kHz drift pumping power. The electrostatic potentials at points *a* and *b* are used to correct the ECRH power injected at these points. Some general requirements have been established.

- Line-averaged plasma density measurements through points *a* and *b* are provided on a real-time basis. If a sampling data system is used, the sampling rate will be at least 10 s^{-1}.

- Electrostatic potential measurements at points *a* and *b* are provided on a real-time basis. If a sampling data system is used, the sampling rate will be at least 10 s^{-1}.
- The power measurements have an absolute accuracy after calibration of within $\pm 5\%$.
- Programmable proportional gain controls are provided for all trim controllers. When the gain is set to zero, the controller provides no trim correction (i.e., it is completely decoupled from the primary control).
- A programmable ratio control divides the total deviation correction between the 35- and the 56-GHz power generators for injection at point *b*.
- Programmable limiters for all trim controllers limit the correction deviation to about $\pm 10\%$.
- Displays are provided for all plasma measurements, for all trim control error measurements, and for all correction deviation measurements.
- Displayed quantities are given in nondimensional units (percentages of design point).

10.5.2 Design Description

There are five groups of secondary programmable controllers: one for the central cell, one for each anchor cell, and one for each plug cell.

Central cell

The central-cell trim controllers modulate the tritium and deuterium neutral beam injection currents and the NBI accel voltages to achieve the desired plasma density, plasma temperature, and neutron flux. The basic features of this group of controllers are shown in Fig. 10.33.

A desired schedule for the three parameters is programmed as a function of time for either the high-Q or the high-Γ mode. The scheduled demand is compared with the measured value, and the difference or error is amplified by the multipliers and then limited to provide a deviation correction signal to the NBI controllers. The total injection current and fuel ratio of the primary controls should be programmed so that the plasma parameter errors are relatively small. These errors should become negligible when stable trim controls are activated.

Initially, the proportional gain inputs of the multipliers are set to zero to decouple the secondary trim controls from the primary controls until plasma diagnostic measurements have been calibrated and proved sufficiently reliable. Once the plasma density measurement has been validated, its proportional gain is increased to provide feedback correction to I_{nb}. Similarly, when the neutron flux measurement has been validated, its proportional gain is increased to provide feedback correction to I_T/I_D without changing I_{nb}, and when the plasma temperature measurement is validated, its proportional gain is increased to provide feedback correction to the NBI accel voltages, which should increase or decrease the energy of the injected particles without appreciably changing the injection currents.

The central-cell trim controls are constructed from commercially available microcomputers that perform addition, multiplication, limiting, and function table operations. The three microcomputers operate on a real-time basis and are coordinated with the synchronous timer. These microcomputers also provide data to digital displays for the plasma

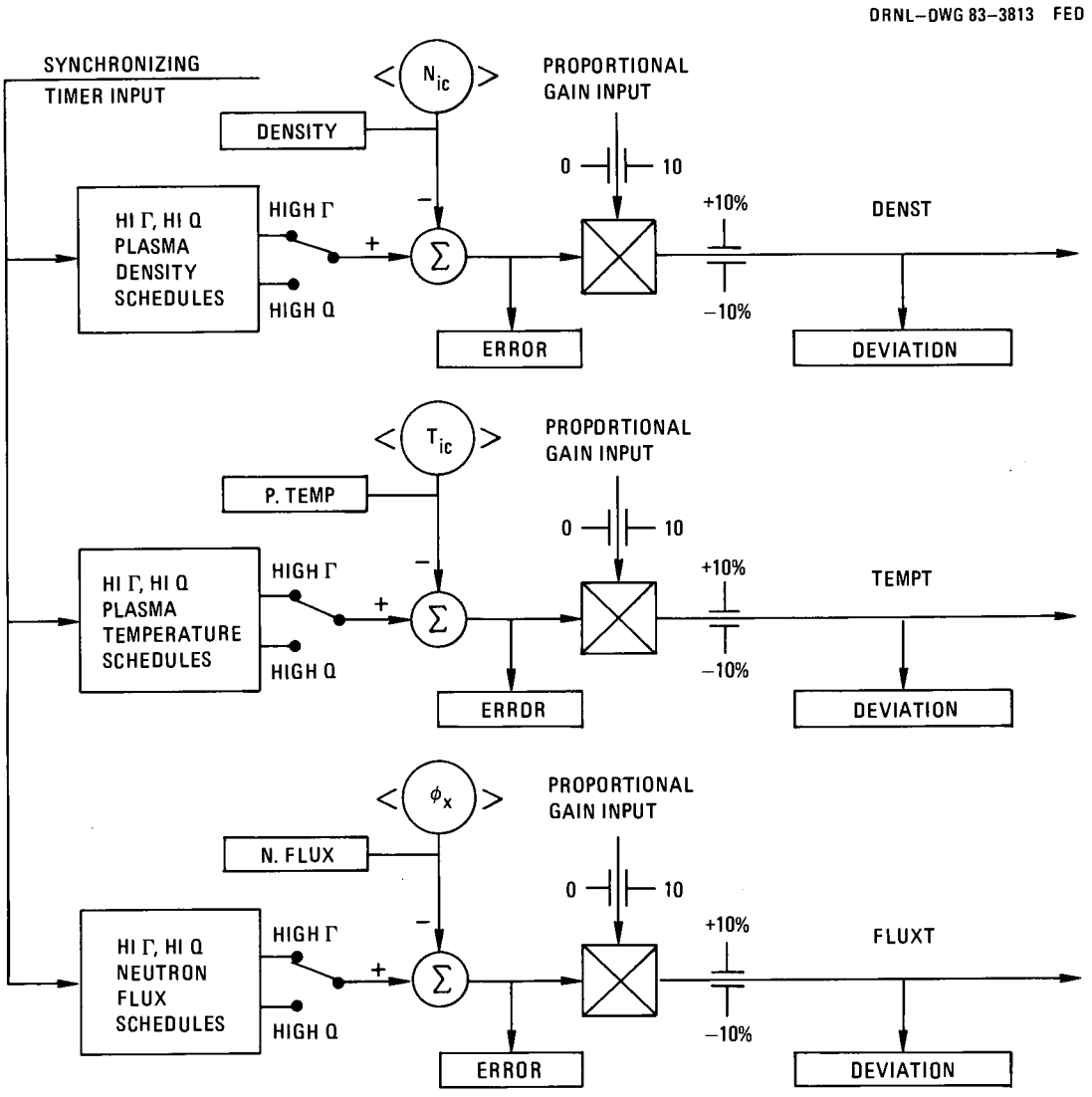

Fig. 10.33. Axicell plasma trim control system. (See also Fig. 10.23.)

diagnostic measurement, the error, and the deviation, meeting the requirements presented in Sect. 10.5.2.

Anchor cell

The anchor-cell trim controllers modulate the ICRH and the low-frequency drift pumping power to achieve the desired ion temperature and to optimize the radial pumping of the ions. The basic features of this group of controllers are shown in Fig. 10.34. The required hot ion energy is scheduled and compared with a measured value; the resulting error is multiplied by the plasma density in the anchor cell to convert the temperature error to power error. This value is multiplied by the proportional gain and used to correct

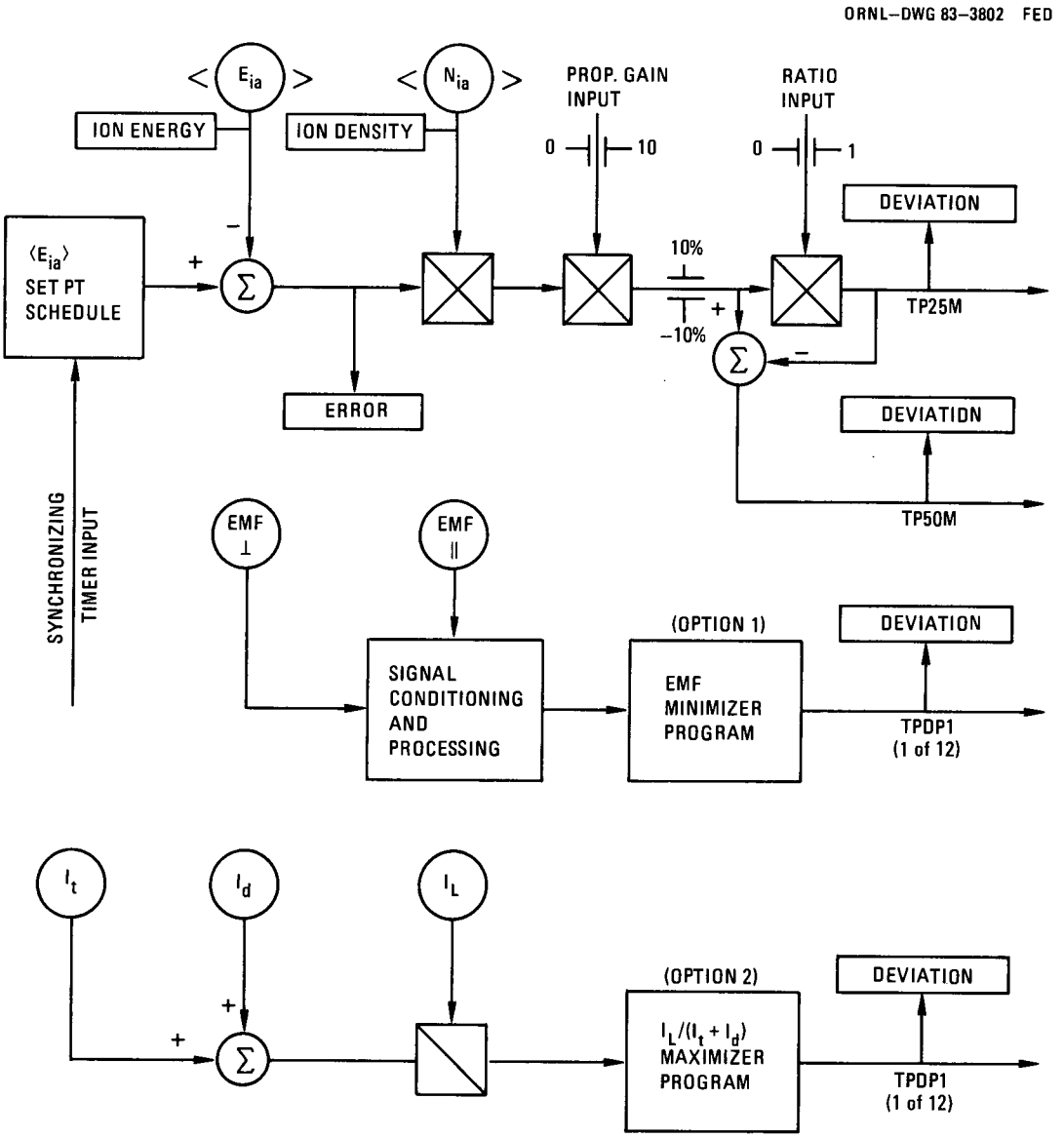

Fig. 10.34. Anchor-cell plasma trim control system. (See also Fig. 10.24.)

the ICRH power demand. Because there are two ICRH frequencies, a ratio control is provided to divide the power correction to any desired proportion. Values for the proportional gain and the ratio control may be programmed or input with digital thumbwheel selectors.

Two options for drift pumping control are shown in Fig. 10.34. Option 1 minimizes the plasma EMF under the assumption that maximum drift pumping performance occurs when the EMF measured in two orthogonal planes is minimized. Option 2 maximizes the ratio of the total collector current to I_{nb} under the assumption that maximum drift pumping performance occurs when the maximum separation of ions from electrons takes place.

There are 12 drift pumping oscillators with a frequency range from 56 to 96 kHz. All 12 are used in the high-Q mode, but only 10 are used in the high-Γ mode. The power at each frequency is controlled with a digital gain control (one for each frequency). If the power at each frequency were the same, there would be a flat power–discrete frequency distribution. However, it may be desirable to operate at something other than a flat rectangular distribution, so the power-frequency profile uses programmable gain controls. Either the option 1 minimizer or the option 2 maximizer can change the gains of each frequency over a limited range about the base programmable profile. During initial operation, the optimizer program will modify the gain settings within set limits. The changes in gain will indicate how the base profile should be changed. Later, after confidence in the optimizer program is established, the set limits can be extended. The optimizer could then begin with a rectangular power-frequency base profile and achieve the optimum power-frequency profile.

The anchor-cell trim controls are constructed from commercially available microcomputers that perform addition, multiplication, division, and optimization operations. The optimizing computer will require more memory than the others because of its more extensive program. The microcomputers provide data to digital displays and read inputs as required. Electromagnetic fluctuations may require extensive processing of high-frequency signals and a high-speed computer for real-time control. Option 2 (the maximizer) is preferred because the signals are large, are free from extraneous interference, and require less computation than those of option 1.

Plug cell

The plug-cell trim controllers modulate the ECRH power, the 600-kHz drift pumping power, and the neutral beam injection current to achieve the desired electrostatic potentials at points a and b in each plug cell and to assist the anchor cell in radial pumping of the ions. The basic features of this group of controllers are shown in Fig. 10.35.

The plasma density at point a is measured and compared to the scheduled demand value, the error signal is amplified, and the 200-keV injection current is modulated within limits to reduce the plasma density error. The plasma density at point b is similarly used to correct the FM 600-kHz drift pumping power to minimize the error.

End-cover $E_{\parallel}B$ ion spectrometers are used to determine the maximum potential both on and off the machine axis. The error in the maximum potential is amplified, and the deviation (TPA56) is used to modulate the 56-GHz power injected at point a. If the potential minimum at point b can be measured, it will be compared to the demand value and used to modulate the 35- and 56-GHz power injected at point b. Because there are two ECRH frequencies, a ratio control is provided to divide the power correction to any desired proportion. Values for the proportional gain and the ratio control may be programmed or input with digital thumbwheel selectors.

If it is not possible to measure the potential at point b, it may be possible to modulate the ECRH power at this point using the electron density measurement and to maximize the plasma density in the central cell by controlling the 600-kHz drift pumping power. Five control handles are available in the plug cell, but fewer reliable plug-cell diagnostic measurements are available for control. Simulation studies and operating experience are needed to guide the development of feedback controls, especially in the plug cells.

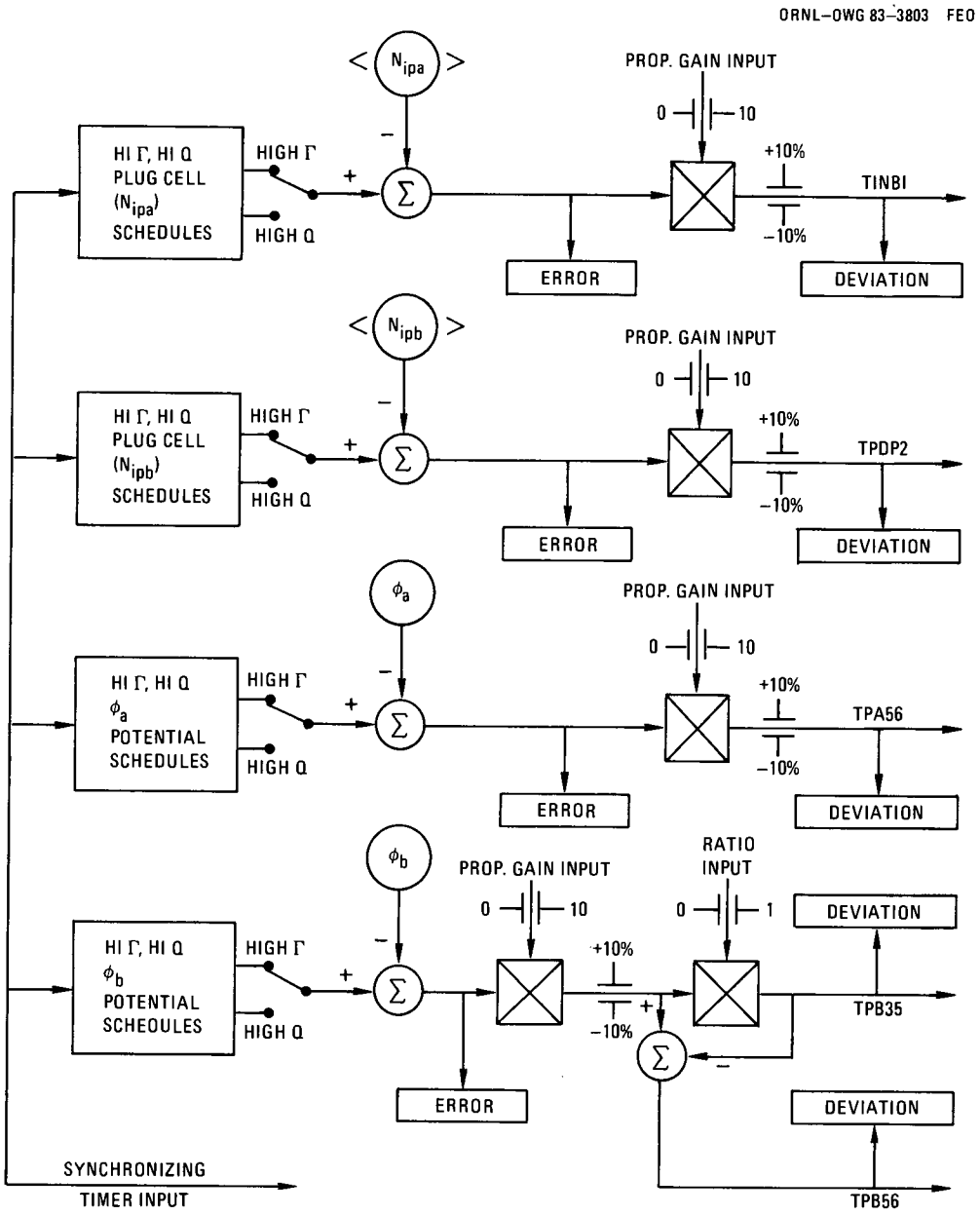

Fig. 10.35. Plug-cell plasma trim control system. (See also Figs. 10.25 and 10.26.)

10.5.3 Key Issues

Reliable real-time plasma measurements require the development and testing of key plasma diagnostics on fusion devices scheduled for operation prior to MFTF-α+T. Improved versions of some of these diagnostics may be installed on MFTF-α+T and used for trim control of the primary control system if the programmable trim controllers are provided on a timely basis. The measurements of principal interest for plasma control are plasma temperature, plasma density, plasma potential, and neutron flux. The diagnostics required for these measurements are described in Sect. 10.6.

10.6 PLASMA DIAGNOSTIC SYSTEM

The general description given in this section is based on the control requirements identified in Sects. 10.4 and 10.5. It is desirable to measure plasma profile parameters at many locations. Limiting factors include time schedules, cost, and environmental and diagnostic development considerations. The diagnostics developed for MFTF-B will be used as fully as possible. Plasma diagnostics selected to date are listed in Table 10.9.

10.6.1 Requirements

Axicell plasma

In the axicell, the NBIs, test modules, and magnets place severe limitations on the amount of space available for plasma diagnostics. The diagnostic instrumentation must be sufficient to make the following measurements during both D-D and D-T operation.

- BGP at two or more locations,
- neutron flux measurements at four or more locations,
- calorimetry of first wall heat load,
- integrated neutron flux, measured using foil or wire activation at selected neutron flux measurement locations,
- Doppler shift spectrometry of ion temperature (at least during the D-D phase).

If practical, it is desirable to make radial profile measurements of the plasma electron temperature and density before the test modules are installed.

Central cell

There is ample space in the central cell between the S1 and S5 solenoids to make both line-averaged and radial profile measurements. The diagnostic instrumentation must be sufficient to make the following measurements during both D-D and D-T operation.

- BGP at two or more locations,
- line-of-sight neutron flux profile measurements at five or more locations and neutron flux measurements at ten or more locations in the shield or reflector,
- calorimetry of first wall heat load,
- integrated neutron flux, measured using foil or wire activation at selected neutron flux measurement locations,
- plasma line density profile measurements across the plasma diameter at five or more locations, using a far-infrared (FIR) laser interferometer,
- EMF measurements at two or more locations, using loop antenna pickups in two or three orthogonal planes,
- electron cyclotron emission (ECE) measurements at two or more locations, using waveguide pickups in two or three orthogonal planes,
- X-ray spectrometry of plasma electron density and temperature across the plasma diameter at five or more locations,
- neutral flux spectrometry of particle energy at two locations,
- ultraviolet spectrometry of impurities, electron density, and electron temperature,

Table 10.9. Selected plasma diagnostics

Quantity measured	Type of measurement	Mnemonic	Type of penetration
Vacuum pressure	Ion gage	BGP	Offset
Neutron flux	Neutron counters: fission chambers, scintillation detectors	NCT	Shielded
Heat flow (power)	Calorimeter	CAL	LOS[a]
Integrated heat flow	Bolometer	BOL	LOS
Ion current	Charged particle flux	CPF	LOS
ϕ_{max} particle parallel energy	$E_{\parallel}B$ ion spectrometer	ISP	LOS
ϕ_c particle perpendicular energy	Neutral flux spectrometer	NFS	LOS
$\int n_e T_e \, dl$	Electron cyclotron emission	ECE	Offset waveguide
$\tilde{\phi}$, $\tilde{\mathbf{B}}$	Electromagnetic fluctuation	EMF	Offset coaxial line
$\int n_e T_e \, dl$ (low density)	Microwave interferometer	MIN	Offset waveguide
$\int n_e T_e \, dl$ (high density)	FIR laser interferometer	FLI	Offset mirrors
Ion temperature (D_2 phase)	Doppler shift spectrometer	DSS	Offset mirrors
Impurities, n_c, T_c	Ultraviolet spectroscopy	UVS	Offset mirrors
Color, impurities	Plasma image (television optics for startup only)	PIM	Offset mirrors
Neutron fluence	Neutron activation system	NAS	Offset pneumatic tubing
Ion temperature (T_2 phase)	Neutron energy spectrometer	NSP	LOS
n_c, T_c	X-ray energy spectrometer	XRS	LOS
$dn/d\theta$	Sloshing-ion sensors	SIS	LOS
$\int n_i T_i \, dV$, $\int n_e T_e \, dV$, B, I_p (startup)	Plasma current sensors, magnetic loops	PCS	Offset leads

[a]LOS = line of sight.

- plasma imaging of plasma boundary at two locations (for startup alignment),
- plasma current sensor (diamagnetic loop) measurements for startup.

Transition region and anchor cell

In the transition region and the anchor cell, the magnets, drift pumping coils, and ICRH launchers restrict the space available for plasma diagnostics. The neutron and

gamma radiation in these zones is about an order of magnitude lower than that in the central cell. The diagnostic instrumentation must be sufficient to make the following measurements during both D-D and D-T operation.

- BGP at six or more locations,
- neutron flux measurements at eight or more locations,
- integrated neutron flux, measured using foil or wire activation at selected neutron flux measurement locations,
- neutral flux spectrometry of particle energy at four or more locations,
- ECE measurements at two or more locations,
- EMF measurements at four or more locations,
- microwave interferometry of plasma line density at two or more locations,
- ultraviolet spectrometry of impurities, electron density, and electron temperature,
- X-ray spectrometry of plasma electron density and temperature,
- sloshing-ion sensor measurements of sloshing-ion angular distribution (at least two arrays of five or more detectors),
- plasma imaging of plasma boundary at two or more locations (for startup alignment),
- plasma current sensor (diamagnetic loop) measurements for startup.

Plug cell and direct converter

In the plug cell and near the direct converter, the drift pumping antennas, ECRH launchers, and negative-ion NBIs restrict the space available for diagnostics. The neutron and gamma radiation in these zones is about an order of magnitude lower than that in the central cell. The diagnostic instrumentation must be sufficient to make the following measurements during both D-D and D-T operation.

- BGP at six or more locations,
- neutron flux measurements at eight or more locations,
- integrated neutron flux, measured using foil or wire activation at selected neutron flux measurement locations,
- neutral flux spectrometry of particle energy at four or more locations,
- ECE measurements at two or more locations,
- microwave interferometry of plasma line density at two or more locations,
- ultraviolet spectrometry of impurities, electron density, and electron temperature in two or more locations,
- X-ray spectrometry of plasma electron density and temperature,
- plasma imaging of plasma boundary at two or more locations (for startup alignment),
- plasma current sensor measurements (four or more diamagnetic loops) for startup.

End wall

At the end wall the direct converter obstructs the view of any diagnostic unless penetrations through the converter are provided. The neutron and gamma radiation, which is much lower than in the central cell, is greatest on the z-axis and diminishes considerably in

the radial direction. The diagnostic instrumentation must be sufficient to make the following measurements during both D-D and D-T operation.

- BGP at six or more locations,
- neutron flux measurements at eight or more locations,
- calorimetric measurements at ten or more locations,
- ion spectroscopy at ten or more locations to determine the maximum potential in the plug cell at several radial positions,
- charged particle flux at ten or more locations,
- integrated neutron flux, measured using foil or wire activation at selected neutron flux measurement locations.

10.6.2 Design Description

In this section, the plasma diagnostic sensors, their general locations, and their interfaces with the vacuum vessel are described. Sensors may be grouped to reduce the number of penetrations and to provide better access for installation and maintenance. The electrostatic potential control is described in detail to provide an example of the electrical interfaces between diagnostics and the data acquisition system described in Sect. 10.7.

Locations of diagnostics

The magnets that provide the confinement field and their axial locations are identified in Fig. 10.36. Diagnostics are located with reference to the magnet positions. The axicell (or test cell) lies inside the two CS1 magnets, the two CC1 magnets and the CS0 magnet. The central cell includes the axicell and the east and west solenoid field zones, extending inside the magnets S1 through S5 to the choke coils (CC2). The anchor cells are inside the A1 and A2 magnets at either end, and the plug cells are inside the P1 and P2 magnets. In defining the zones of location for the diagnostic sensors, the T1 magnets are included with the anchor cells; the T2 magnets, with the plug cells.

Table 10.10 lists the plasma diagnostics proposed for each zone of MFTF-α+T, using the mnemonics defined in Table 10.9. It is assumed that the east and west ends of the

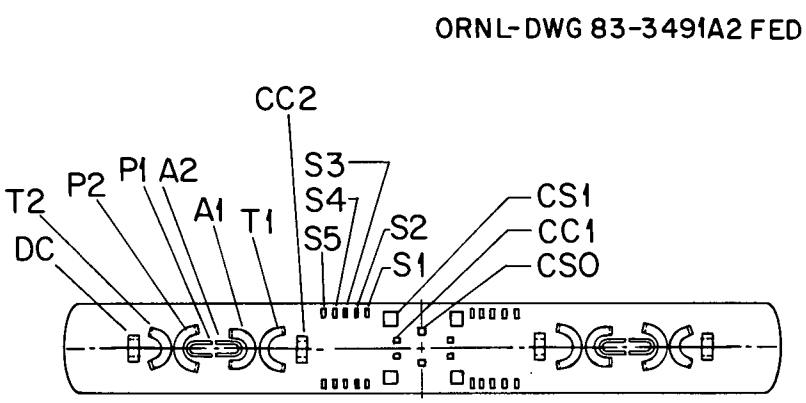

Fig. 10.36. Magnet locations.

Table 10.10. Number and locations of plasma diagnostics sensors

	MFTF-α+T									
	Location[a]									
Diagnostic	End wall	DC/T2	T2/P1	P1/A2	A2/T1	T1/CC2	CC2/S1	S1/CSO	Total	MFTF-B total
BGP	6	4	4	4	4	4	6	2	36	31
NCT	10	6	6	6	6	6	24	6	70	?
NAS	6	4	4	4	4	4	12	4	42	?
CPF	12	0	0	0	0	0	0	0	12	14
ISP	12	0	0	0	0	0	0	0	12	18
NFS	0	0	2	2	2	2	2	0	10	18
ECE	0	0	2	0	2	0	2[b]	0	6	3
EMF	0	0	0	2	2[b]	2	2[b]	0	8	10
FLI	0	0	0	0	0	0	2[b]	0	2	3
MIN	0	0	2	2	2	0	0	0	6	6
CAL (BOL)	12	0	0	0	0	0	2	2	16	100
NSP	0	0	0	0	0	0	0	0	0	3
DSS	0	0	0	0	0	0	0	1[c]	1	2
UVS	0	0	0	2	2	0	2	0	6	7
XRS	0	0	2	0	2	0	2[b]	0	6	5
SIS	0	0	0	0	2[b]	0	0	0	2	2
PCS	0	0	4	4	4	4	4	0	20	72
PIM	0	2	2	2	2	2	2	2	14	16

[a]Equally divided between east and west ends of machine, except as noted.
[b]Array of detectors for profile measurements across the plasma or at several angles to the plasma.
[c]West end only.

device will have equal numbers of sensors, although this probably will not be the case when the design becomes more firmly established. The number of diagnostics for MFTF-B is also shown, except for two cases in which considerable uncertainty exists. Except for neutron diagnostics, the number of diagnostics is comparable to or less than that for MFTF-B and is only slightly higher than the minimum needed to meet the requirements given in Sect. 10.6.1.

Grouping of diagnostics

Diagnostics can be grouped so that the number of penetrations is lower but their diameter is larger. This grouping provides a more rigid assembly that is easier to remove and replace. Large, vertically oriented assemblies are desirable because they can be installed and removed with an overhead crane; in addition, they are useful for making profile measurements across the plasma in the central cell, between the S1 and S5 coils, where the plasma is axially symmetric and more accessible.

Diagnostics are grouped according to the type of penetration they require. Optical diagnostics use mirrors to provide offset penetrations, thus reducing radiation streaming and damage to detectors. (Mirrors are much less prone to radiation damage than most diagnostic detectors.) Microwave diagnostics can use mitered bends, offset waveguides, and offset coaxial lines to reduce radiation streaming. Some detectors, such as BGP and neutron flux detectors, do not require direct viewing of the plasma. Others, such as ion spectrometers, calorimeters, and X-ray spectrometers, require direct line-of-sight penetrations. Table 10.11 lists five natural groups of diagnostics that can be integrated into single assemblies.

Table 10.11. Group integration of diagnostics

Group	Type	Diagnostics
Optical	Mirror offset penetrations	FLI DSS UVS PIM (startup)
Microwave	Offset waveguide penetrations	ECE EMF MIN
Neutron/X-ray	Line-of-sight penetrations	NSP XRS NCT (collimated) BOL (startup)
Hybrid 1	No line-of-sight penetrations	BGP NCT CAL
Hybrid 2	Line-of-sight penetrations	ISP CPF BOL CAL NCT

Optical diagnostics

Figure 10.37 shows an assembly that can be used for both passive and active optical diagnostics and for housing neutron detectors and foils or wires to be activated for integrated neutron flux measurements. Two rows of five small-diameter tubes pass through the main shield so that radiation can pass to and from the integrated assembly. The water-cooled, shielded assembly is vertically oriented and supported by a 24-in. port and flange. An optical table is supported by the integrated assembly.

ORNL-DWG 83-3477 FED

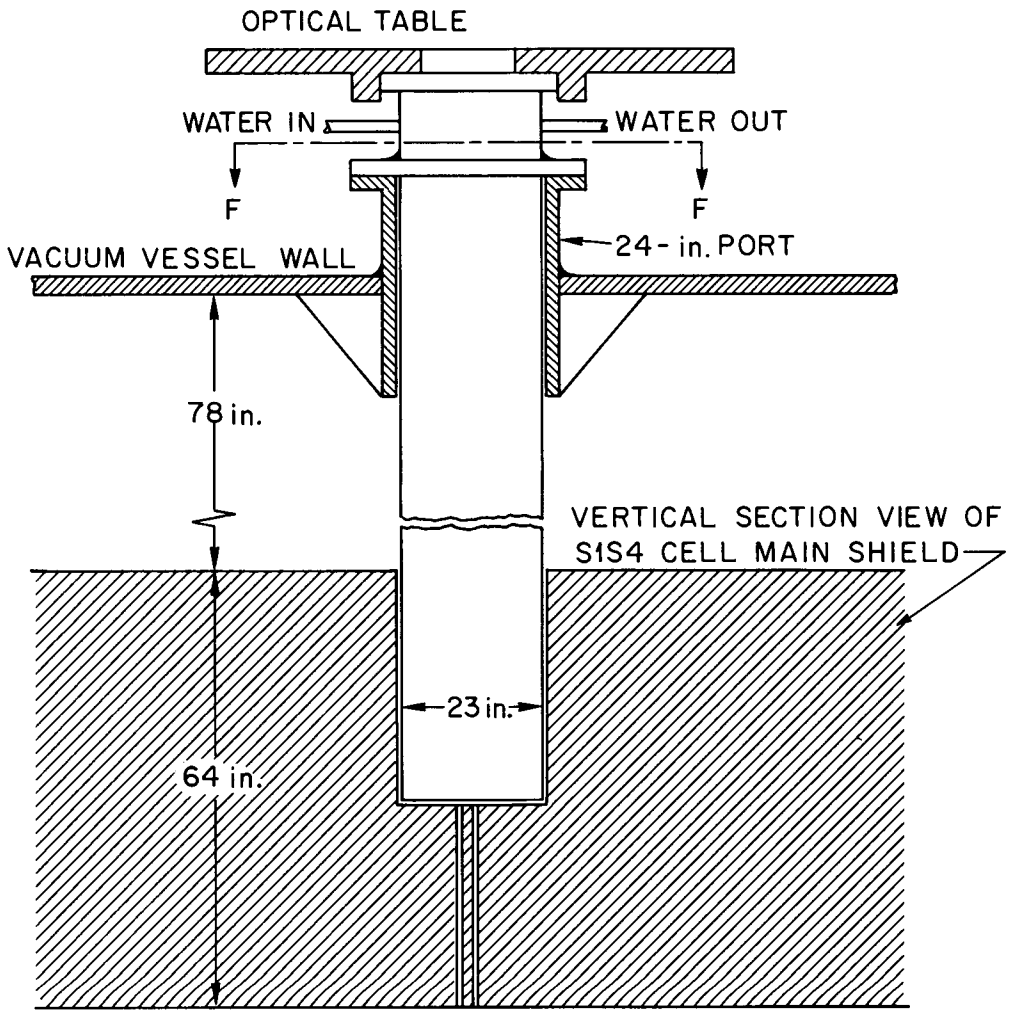

Fig. 10.37. Optical interface assembly (side view).

A view looking down into the assembly with the steel ball shielding removed is shown in Fig. 10.38. The steel plates have milled slots to support the five tubes on each side. Four larger tubes along the vertical diameter are capped at their lower ends; they form the slender thimble housings for neutron detectors and activated wires. The heavy wall tubes (left and right sides of Fig. 10.38) are water passages to the lower header. Figures 10.39 and 10.40 show additional details. Figure 10.39 is a section view of the upper water header and the small optical tube penetrations. Quartz or sapphire windows form part of the vacuum boundary. Cooling water flows down the inlet tubes to the lower water header, shown in Fig. 10.40, and returns through the lower shield support plate and the steel balls used for shielding. Mirrors are attached to the bottom of the assembly to provide the offset for optical radiation. Three 45° prism mirror assemblies have polished metal surfaces to deflect the optical radiation through two 90° bends. These components are replaced by removing the diagnostic assembly.

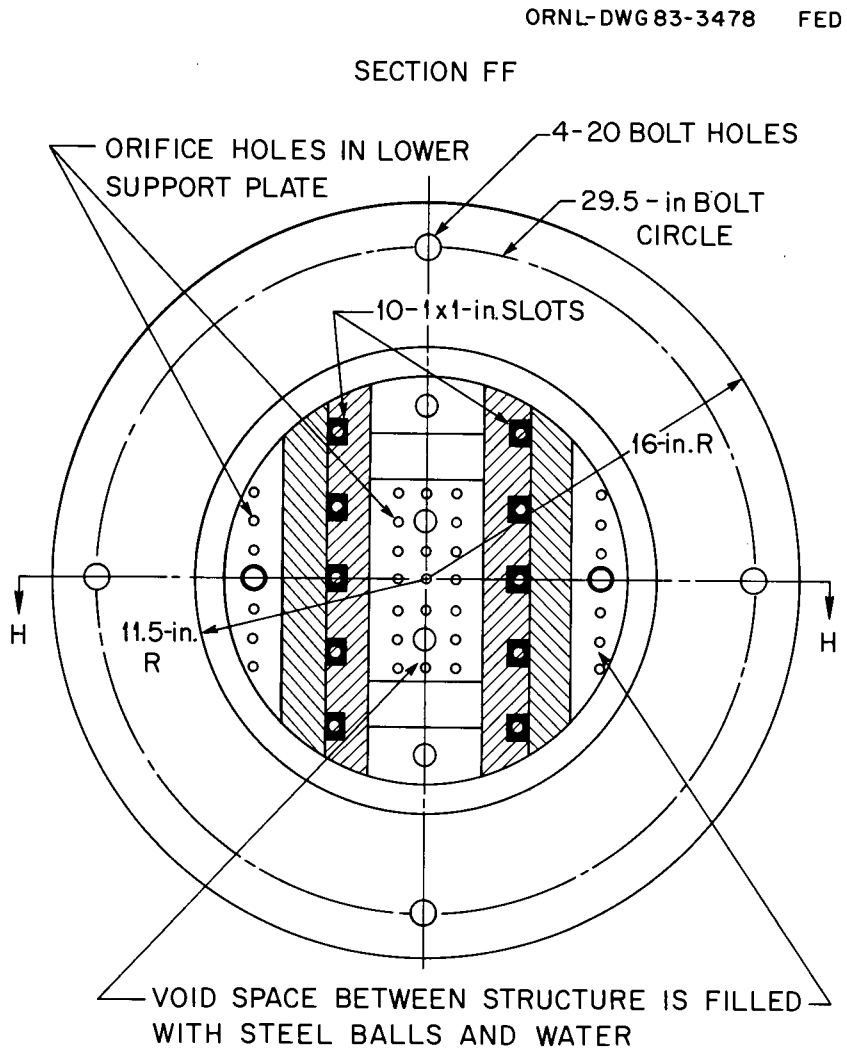

Fig. 10.38. Optical interface assembly (top view) with steel balls removed.

Line-of-sight diagnostics

For measurements that require line-of-sight penetrations, the assembly extends through the main shield, as shown in Fig. 10.41 for an assembly that can accommodate either collimated neutron or X-ray detectors. Two outside offsets prevent radiation streaming. Small line-of-sight penetrations pass through the shielded assembly to the detectors inside. Slab and steel-ball shielding collimates the radiation so that a number of measurements across the plasma can be made. This assembly is built to facilitate changes to less sensitive detectors during the transition from D-D to D-T operation.

A view looking down into the assembly with the steel ball shielding removed is shown in Fig. 10.42. Three pairs of steel plates support the 0.5-in. collimation tubes. The 11 tubes are staggered so that they are approximately equally spaced when projected along the diameter of the plasma. In the space between the plates are six internal tubes, capped

DRNL-DWG 83-3479 FED

UPPER PART OF SECTION HH

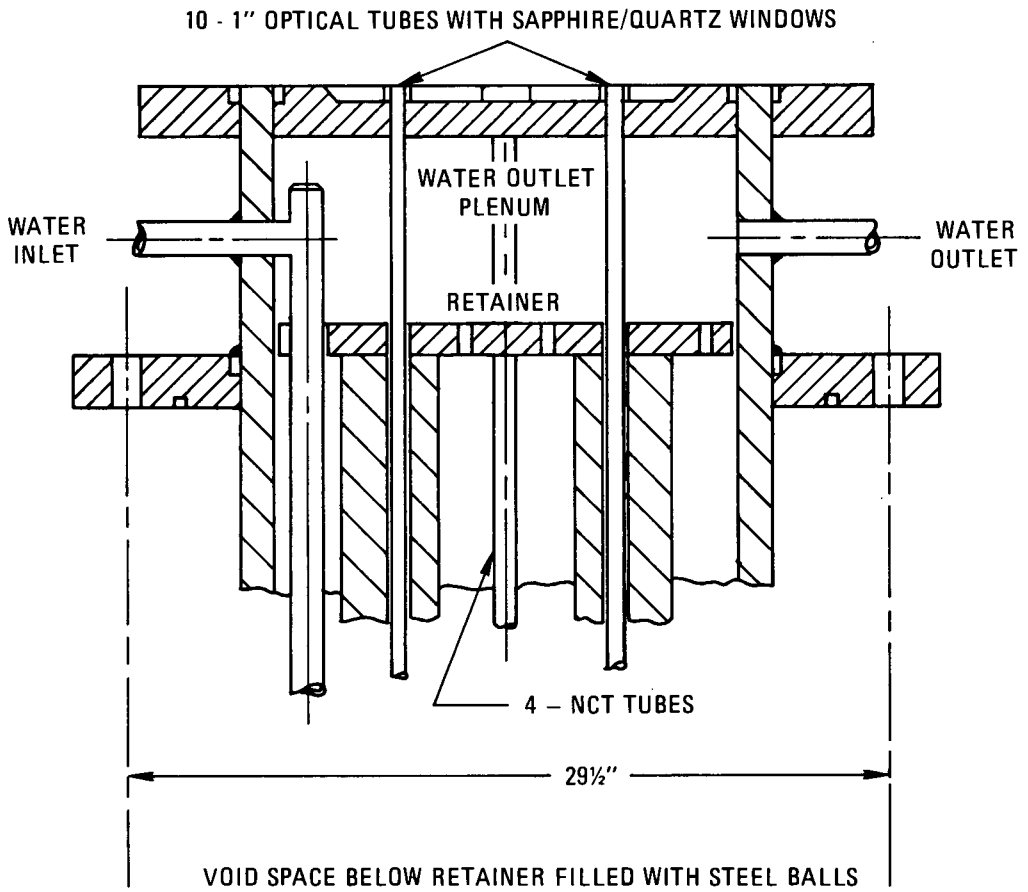

Fig. 10.39. Upper part of the optical interface assembly.

at their lower ends, for neutron detectors and activated wires. These tubes can be partially filled with shielding so that radial shielding measurements can be made. The lower inlet and upper outlet water headers are similar to those for the optical diagnostics assembly. The void space between the plates is filled with steel balls that provide cooling passages between the water headers. The upper ends of the 11 collimated tubes are capped with thin metal windows that are nearly transparent to both high-energy neutrons and X rays.

Microwave diagnostics

The microwave diagnostics also use an assembly that extends through the main shield, as shown in Fig. 10.43. (Losses across broken coaxial lines or waveguides prohibit the use of the optical assembly.) Electromagnetic fluctuation loops developed for MFTF-B are not water cooled and will not be useful in the central cell during D-T operation.

ORNL-DWG 83-3480 FED

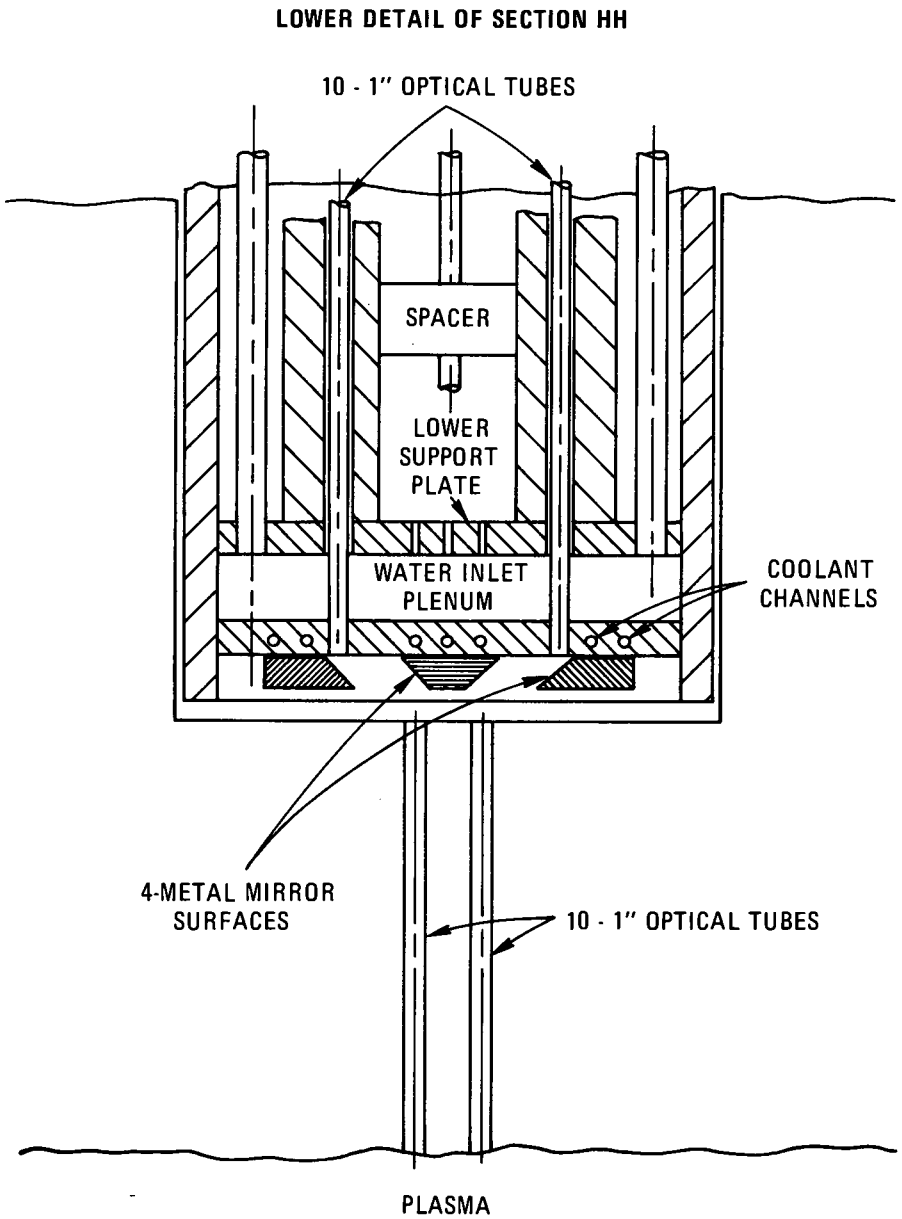

Fig. 10.40. Lower part of the optical interface assembly.

Water-cooled coaxial lines like those shown in Fig. 10.44 may be necessary. A half-turn coaxial pickup loop is made of a water-cooled tube grounded at the water inlet end. In the transition to the top header, the coaxial line has a double offset bend, as shown in Figs. 10.45 and 10.46. These bends may also be used for waveguides if a mitered 90° bend is used.

ORNL–DWG 83-3481 FED

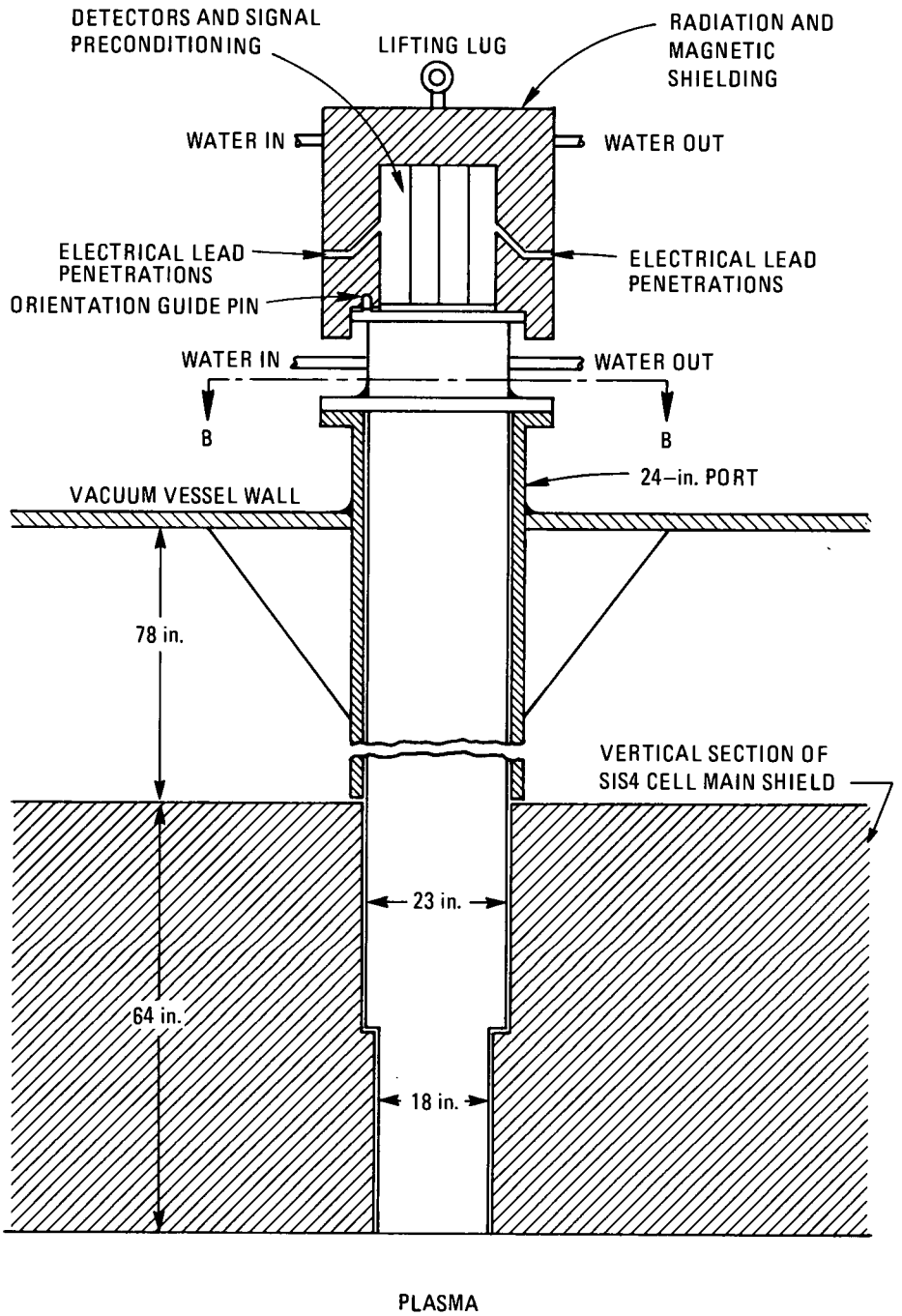

Fig. 10.41. Collimated neutron/X-ray interface assembly (side view).

ORNL-DWG 83-3482 FED

SECTION BB

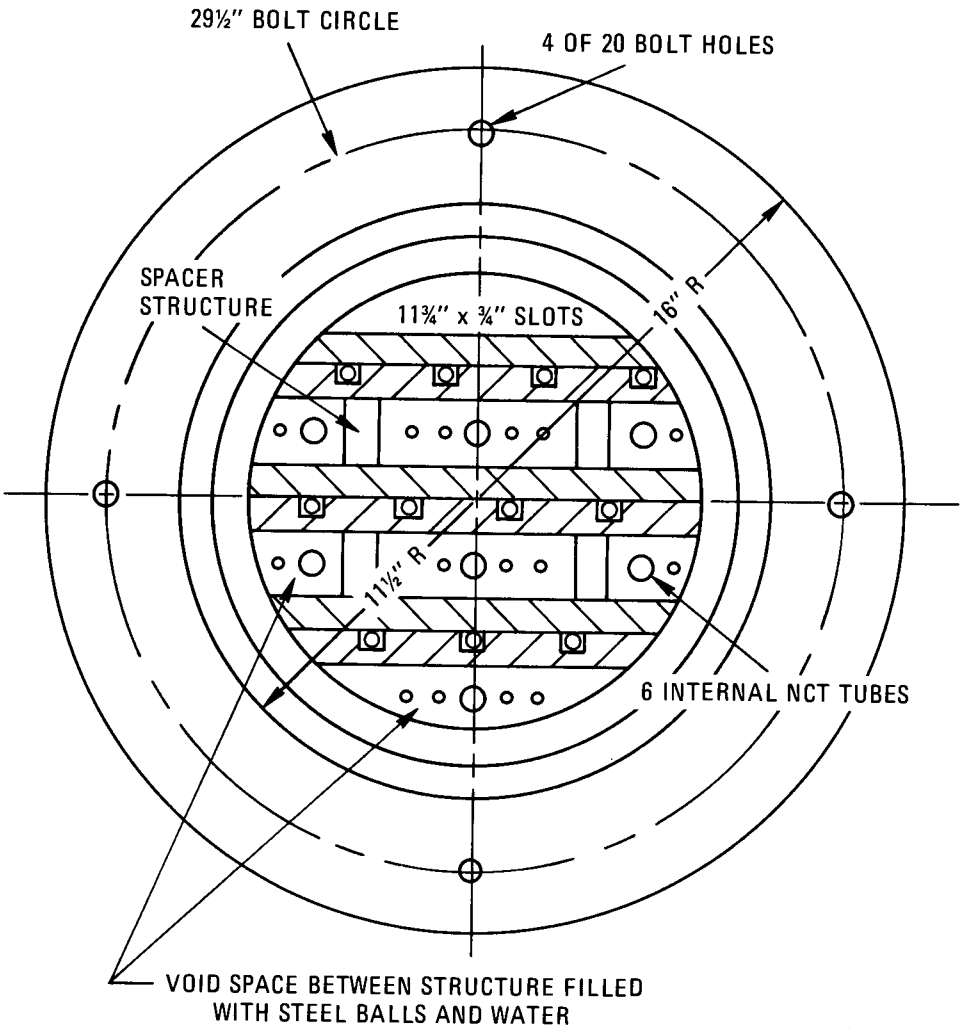

Fig. 10.42. Collimated neutron/X-ray interface assembly (top view) with steel ball shielding removed.

Figure 10.47 shows the microwave diagnostics assembly from the top. A number of slabs are milled to accommodate 11 pairs of coaxial or waveguide transmission lines. To maximize the effectiveness of the shielding, the pairs are alternated at the bends, as shown in Figs. 10.45 and 10.46. The assembly is water cooled with lower inlet and upper outlet headers similar to those for the optical assembly.

ORNL–DWG 83-3483 FED

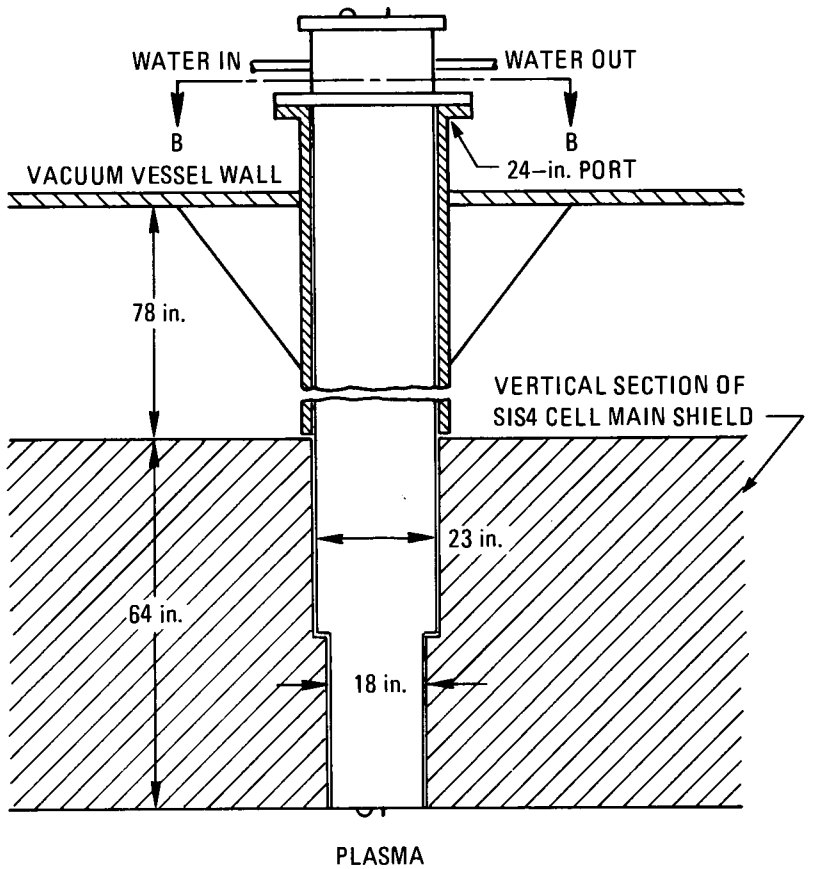

Fig. 10.43. Microwave interface assembly (side view).

Interface of diagnostics and data system

All of the diagnostics on MFTF-α+T interface with a data acquisition system. The MFTF-B data system is illustrated in Fig. 10.48. A typical diagnostic sends an electrical preamplifier signal to the CAMAC system. Fiber-optic links connect the CAMAC, the first-level computers, and the system timing. The supervisory control and processing system (SCPS) is equivalent to the SCDS of the machine process system.

One of the more complicated diagnostics on MFTF-α+T is the $E_{\parallel}B$ ion spectrometer, shown in Fig. 10.49. Six of these diagnostics are placed at each end of the machine. Each one is connected to the vacuum vessel through a 6-in. pipe with a vacuum isolation valve. The pipe is oriented along one of the magnetic field lines; one instrument is located to measure ion energies along the axis of the machine.

Only ions with energies greater than the potential barrier pass through a 6-in. opening in the direct converter and enter the ion spectrometer, where they encounter the force field of two parallel D-shaped magnets and two parallel electric plates. The radius of an ion trajectory in the magnetic field is directly proportional to the momentum of the ion,

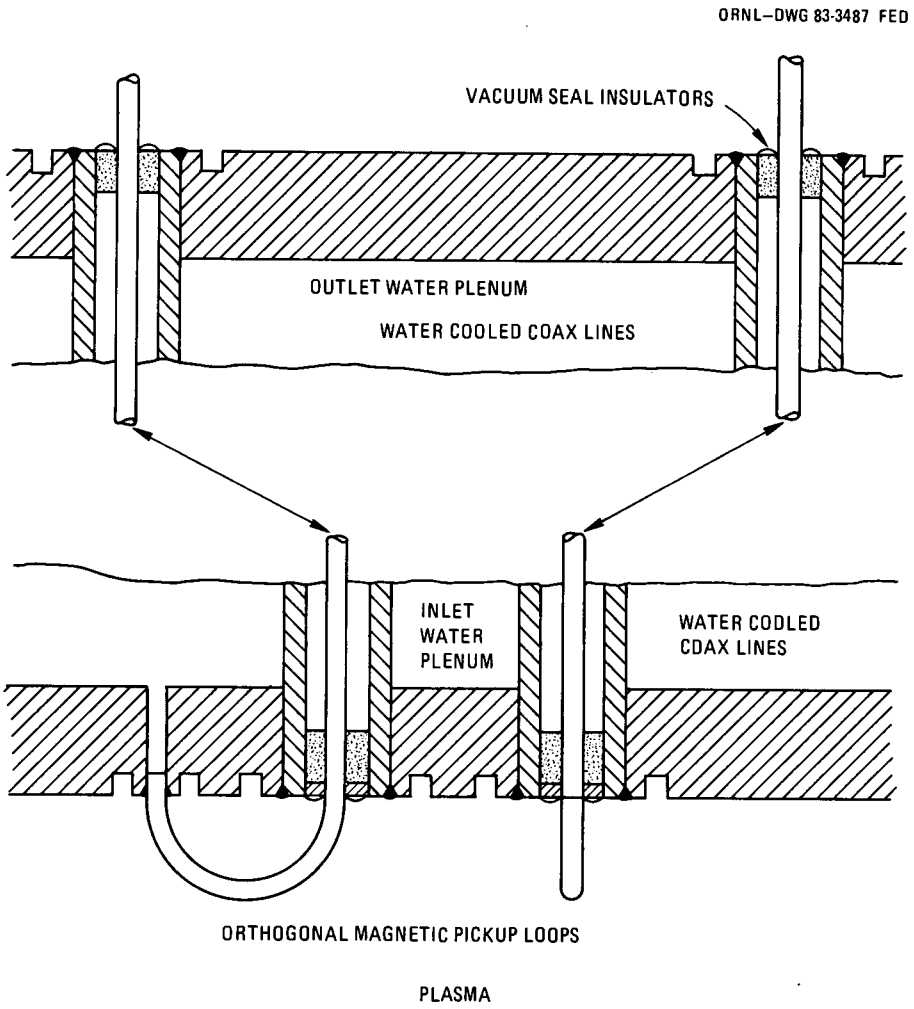

Fig. 10.44. Detailed view of water-cooled magnetic pickup loops.

$R = mv/qB$. The displacement s of the ion in the electric field is inversely proportional to the ion energy, $mv^2 = kqER^2/s$. Over 100 insulated collectors measure the number of ions per second within a collector domain. The energy spectrum of the ions can then be calculated from the collector position, the collector current, the electric field strength, and the magnetic field strength, assuming the ions are singly charged. The block diagram of the ion spectrometer in Fig. 10.50 indicates the large number of components and controls. Only half of some auxiliary components and power supplies are shown, and there are actually two magnets. This assembly also includes charged particle flux and bolometer diagnostics (not shown in the figure). The 12 systems require the data acquisition system to process about 1500 ion spectrometer points.

The ion spectrometry signal processing diagram for one instrument is shown in Fig. 10.51. The current-to-voltage (I/V) converters are located inside the vault; the rest of the equipment is in the local control area of Bldg. 431. The data acquisition system interfaces with the I/V converters.

ORNL–DWG 83-3485 FED

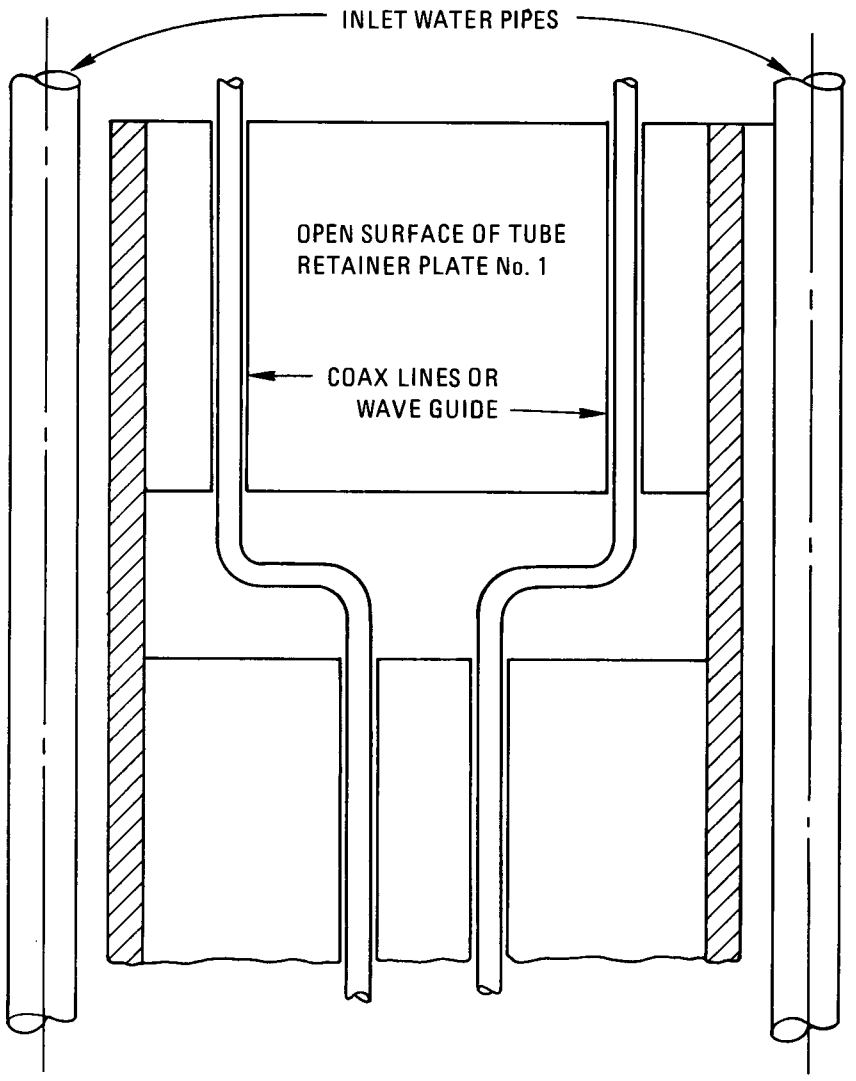

Fig. 10.45. Detailed face view of the waveguide/coaxial line offset for alternate plate 1.

10.6.3 Key Issues

The MFTF-B diagnostic penetrations and some of its sensors cannot be used for MFTF-α+T because the new machine requires a completely new interface with considerable shielding. In addition, the direct converters obstruct the views of the end-cover diagnostics unless there are large openings in the converters. Nevertheless, much of the MFTF-B diagnostic signal conditioning and data acquisition equipment outside the vacuum vessel can be used for MFTF-α+T. There are several major driving factors that influence the development and cost of MFTF-α+T diagnostics:

ORNL–DWG 83-3486 FED

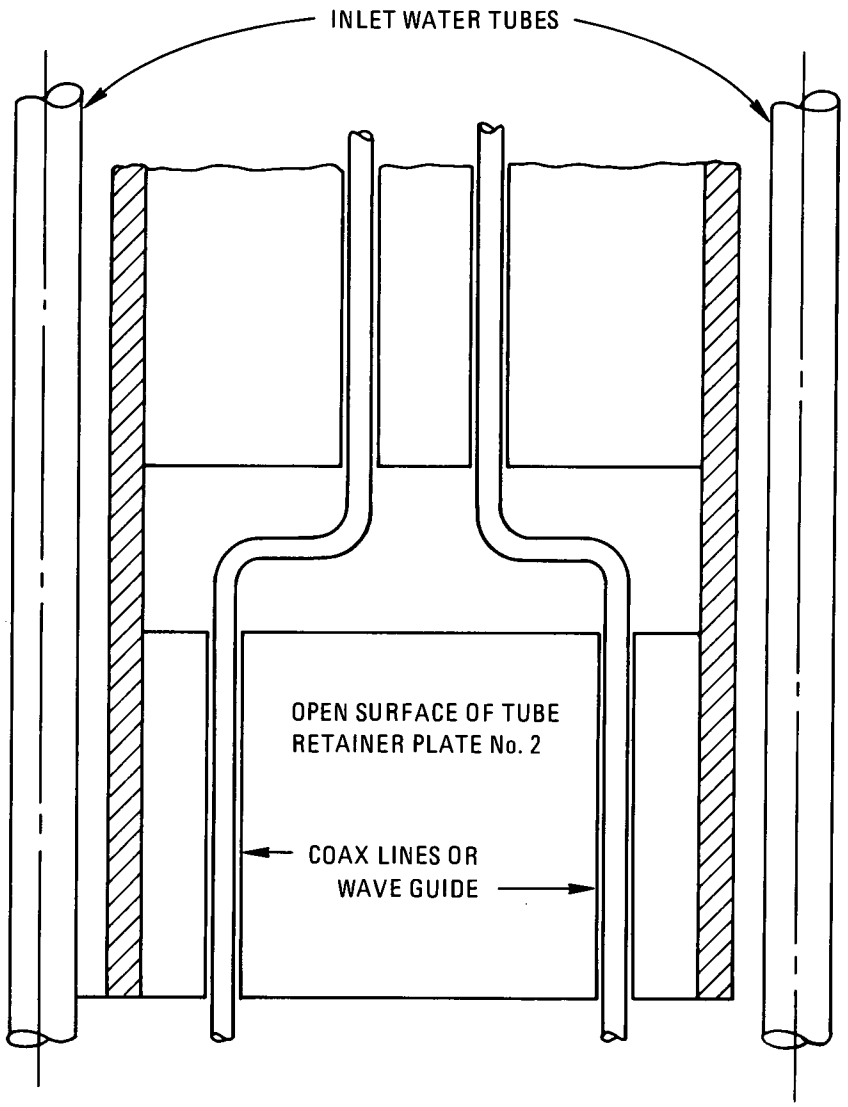

Fig. 10.46. Detailed face view of the waveguide/coaxial line offset for alternate plate 2.

1. Diagnostics will operate in a highly radioactive environment.
2. Access to the axicells, anchor cells, and plug cells is limited by neutral beam, ICRH, ECRH, and drift pumping equipment.
3. Real-time feedback control requires reliable plasma measurements with accuracy within $\leqslant 5\%$.
4. To meet the needs of both D-D and D-T operation, diagnostics must cover a wide range or must be easily removed and replaced with other diagnostics.
5. Tritium, neutron, and alpha particle diagnostics, which are not provided for MFTF-B, are required for MFTF-α+T.

ORNL-DWG 83-3484 FED

SECTION BB

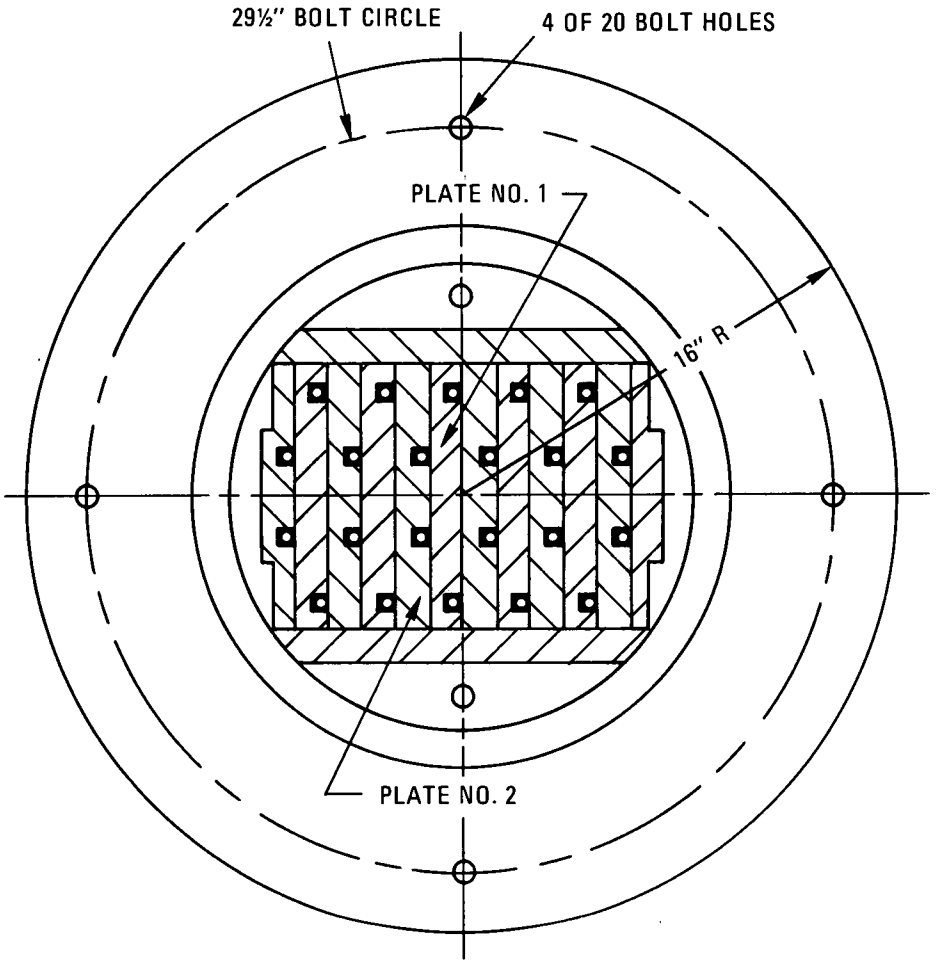

Fig. 10.47. Microwave interface assembly (top view) with steel ball shielding removed.

Because MFTF-α+T is expected to operate for up to 100 h at a time, some of the front-surface, metallized mirrors and directly viewing detectors will be subject to large radiation fluences. These components must be radiation hardened or easily replaced. Integrated diagnostic interface modules containing ten or more penetrations of a given kind can be constructed and shielded for convenient access and maintenance. Because of their size and weight, such modules should be oriented vertically so that they can be removed with an overhead crane. If they are mounted horizontally, they require rails and support structures that increase the size of the building. The ion spectrometers on the end covers must be mounted horizontally, and their guide rails and support structures extend about 4 m beyond the end covers.

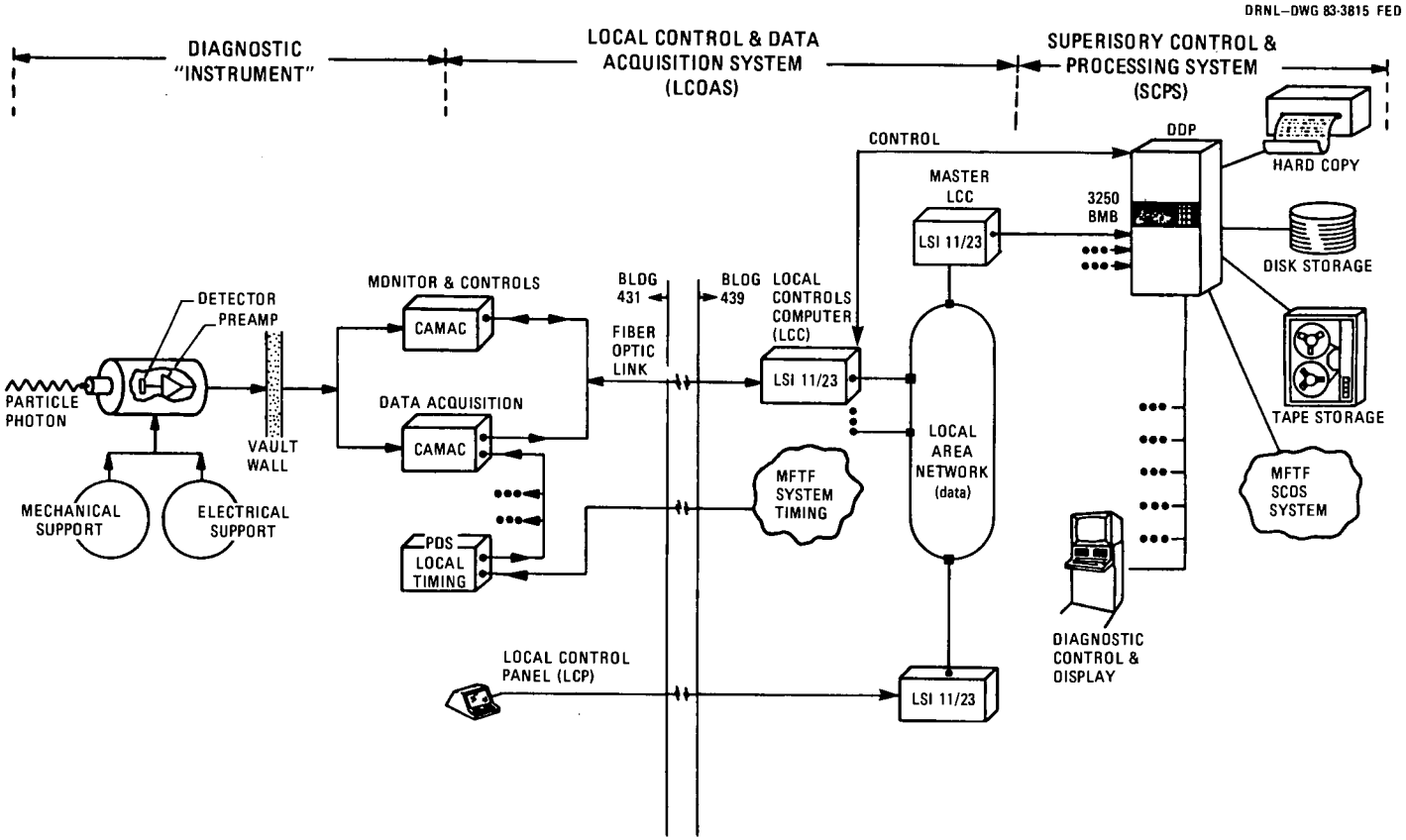

Fig. 10.48. Overview of plasma diagnostics systems for MFTF-B.

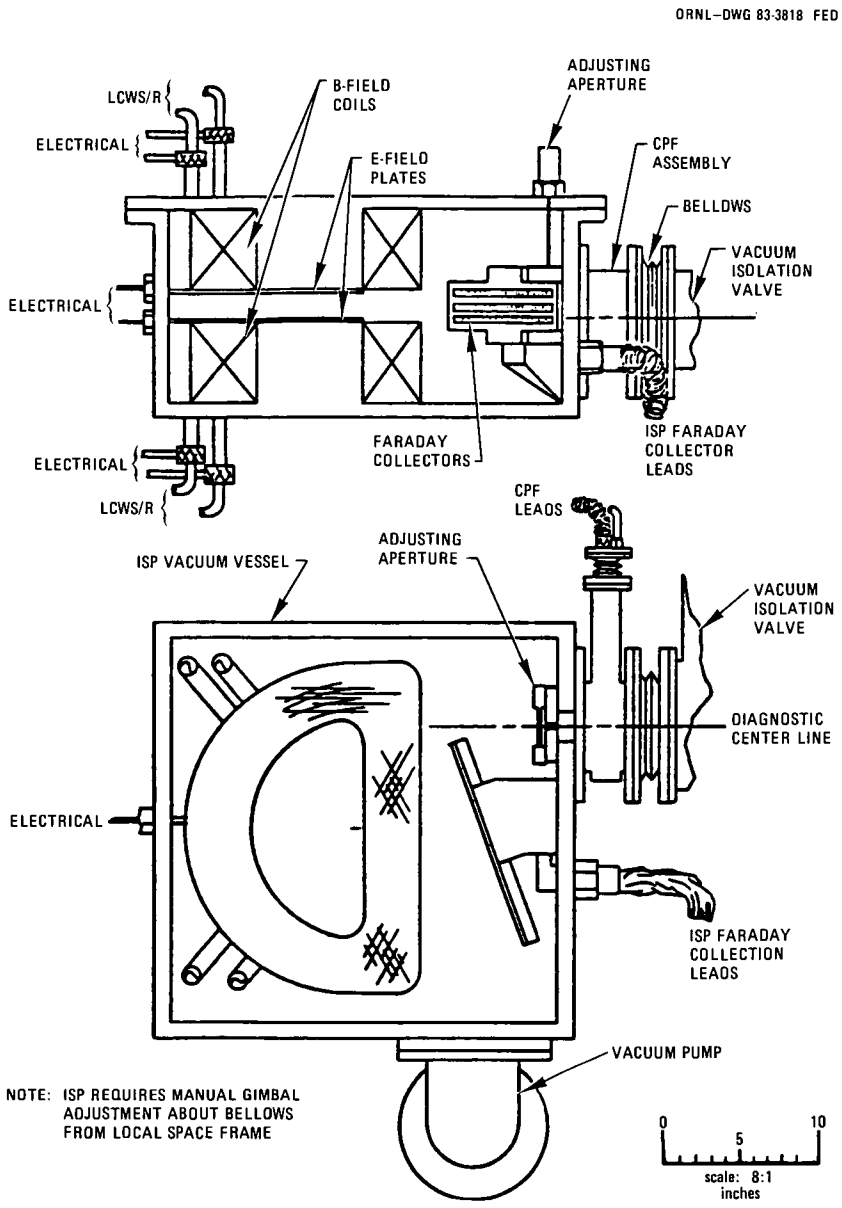

Fig. 10.49. Mechanical schematic of the ion spectrometer.

Required diagnostics and their locations must be reviewed. The locations and sizes of some diagnostics must be better defined to determine whether there are interface obstructions from other equipment and to determine the constraints imposed on remote maintenance equipment.

Preliminary studies indicate that MFTF-α+T should have some real-time diagnostics that can be used for feedback control development. Real-time diagnostics are desirable for the following measurements:

1. plasma density,
2. plasma temperature,

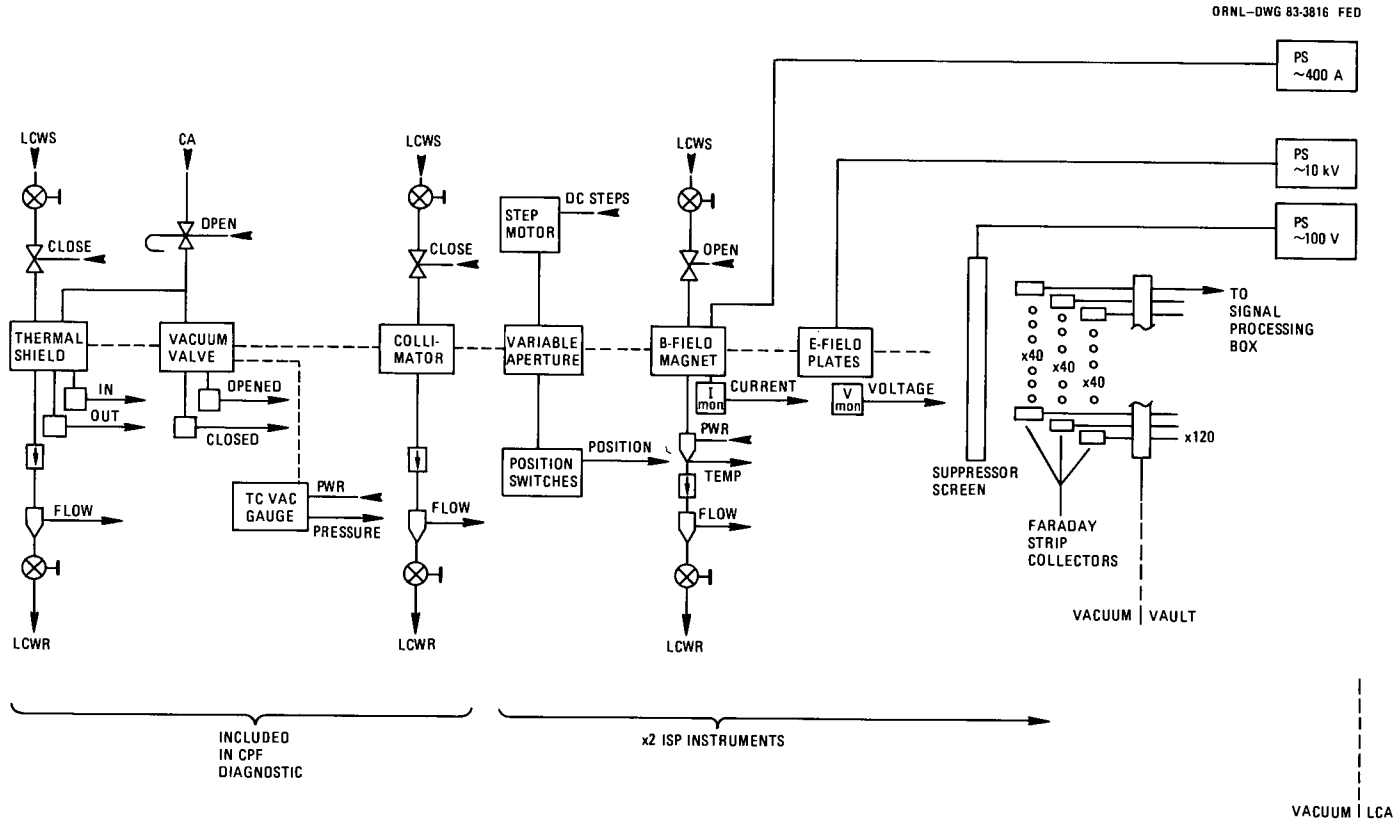

Fig. 10.50. Functional block diagram of the ion spectrometer.

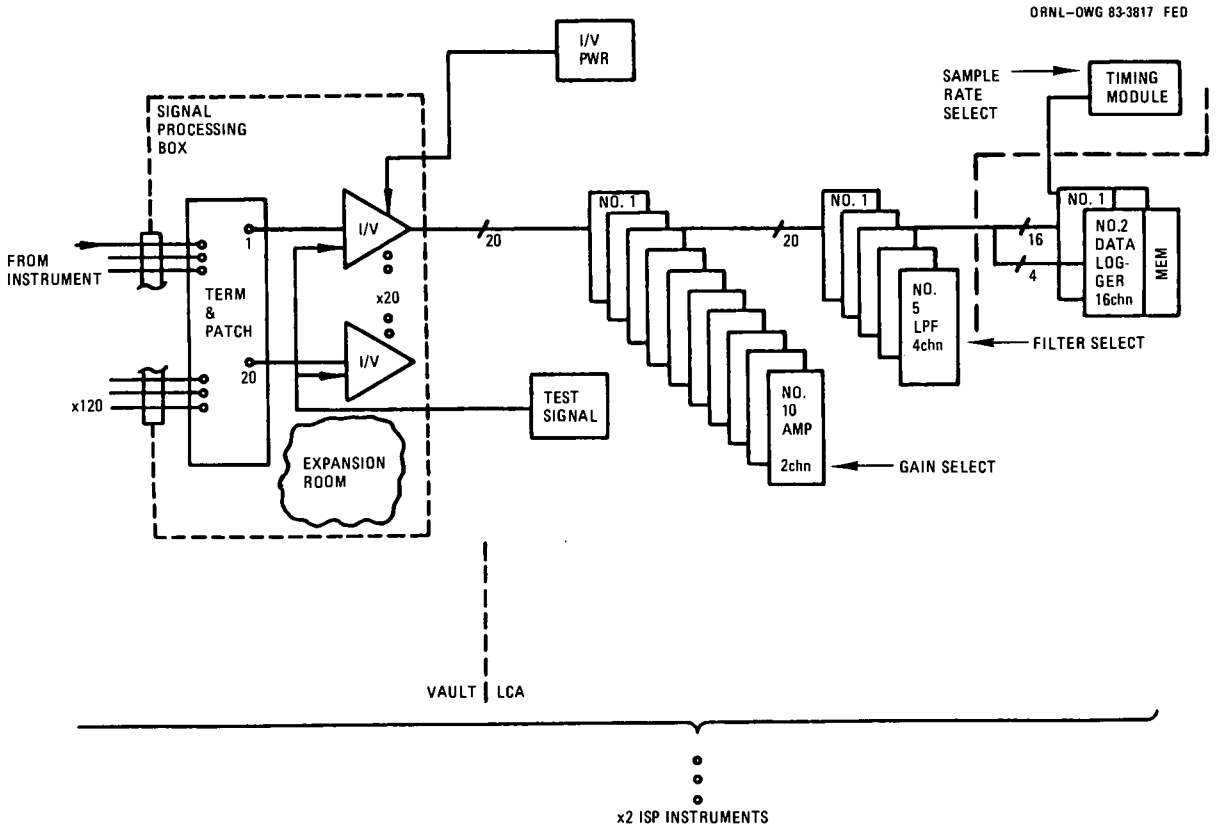

Fig. 10.51. Signal processing block diagram of the ion spectrometer.

3. neutron flux, and
4. maximum and minimum electrostatic potential in the plug cells, at least on the machine axis.

For control purposes, these diagnostics must be free of drift and of the need for extensive calibration, should be as accurate as typical industrial instrumentation, and must be highly reliable for significant periods of time (≥100 h). Diagnostic measurements require substantial real-time data processing, which will probably require a small, dedicated computer for each control diagnostic to alleviate the need for high-speed data links to a large, time-shared control computer.

10.7 DATA ACQUISITION SYSTEM

Data acquisition is defined as the sensors' signal conditioning, the analog-to-digital conversion, and the data control and transmission to the first-level processing computers. In this section, the process I&C data acquisition system is considered separately from the plasma diagnostics data acquisition system (discussed briefly in Sect. 10.6). Process data acquisition is divided into 13 groups:

1. the NBI group, for neutral beam injectors and their associated beam dumps;
2. the ECRH group, for ECRH power generation and launchers;
3. the ICRH group, for ICRH power generation and launchers;
4. the drift pumping group, for drift pumping rf power generation and launchers;
5. the magnet group, for SC and RC magnets and their power conversion and protection equipment;
6. the inner materials group, for first wall and inner shield materials subject to high radiation exposure;
7. the outer materials group, for the vacuum vessel, outer shield, and all support structures subject to lower radiation exposure;
8. the vacuum system group, for the vacuum system and ducting that remove fuel and impurities from the machine;
9. the fuel processing group, for the fuel recovery and reprocessing equipment that removes impurities and ash and restores fuel to its original state;
10. the water cooling group, for the machine water cooling systems (including heat exchangers, pumps, storage, and impurity removal equipment);
11. the cryogenic system group, for the cryogen recovery and liquefying equipment, insulated pumps, and valves;
12. the plasma collector group, for the direct converters, halo scrapers, and their support systems; and
13. the test module group, for test modules located in the axicell and their supporting cooling systems.

10.7.1 Requirements

NBI group

The data acquisition systems of the MFTF-B NBIs must be used as fully as possible. Some new sensors and transmitters will have to be mounted on the injectors and beam dumps for monitoring and control. Only eight of the existing 30-s neutral beam data acquisition systems are needed for the central-cell positive-ion sources. More of these systems may be used for the negative-ion neutral beams in the plug cells.

ECRH group

The existing 1600 kW of ECRH power generation on MFTF-B will be expanded to about 2400 kW for MFTF-α+T. The ECRH data acquisition system for MFTF-B will be expanded by about 60% to meet the ECRH monitoring and control data acquisition requirements for MFTF-α+T.

ICRH group

The existing 400 kW of ICRH power generation on MFTF-B will be expanded to about 2400 kW for MFTF-α+T. The ICRH data acquisition system for MFTF-B will be expanded by about five times to meet the ICRH monitoring and control data acquisition requirements for MFTF-α+T.

Drift pumping group

Because MFTF-B has no drift pumps, a new data acquisition system is needed to monitor and control the anchor and plug cells of MFTF-α+T. There are 24 drift pumping rf power generators for the anchor cells; each one can generate about 30 kW. There are two FM drift pumping rf generators for the plugs cells; again, each one can generate about 30 kW. Because there are so many rf generators and because the drift pumping control is so complex, this system may be more extensive than the ECRH and ICRH groups combined.

Magnet group

There are 24 SC magnet coils and no RC magnet coils on MFTF-B. On MFTF-α+T, there are 30 SC coils and 5 RC coils. The MFTF-B magnet data acquisition for monitoring and control must be expanded by about 50% to meet the requirements of MFTF-α+T. New magnet sensors for monitoring and control are needed for all magnets except the ten central-cell and two axicell magnets from MFTF-B that are being used on MFTF-α+T.

Inner materials group

There is very little nuclear radiation in MFTF-B because it uses deuterium fuel only; thus, it has no inner first wall or shield. A new data acquisition system with about 200 channels of instrumentation is required for monitoring the inner materials of MFTF-α+T.

Outer materials group

The support structure for the MFTF-B magnets and vacuum vessel must be heavily supplemented for the shielding, magnets, and vacuum vessel of MFTF-α+T, which also has an outer shield. The MFTF-B materials data acquisition system must be expanded to roughly double its existing capability to meet the outer materials monitoring requirements.

Vacuum system group

The data acquisition system used for the MFTF-B vacuum system should be adequate for MFTF-α+T. Some BGP sensors that are prone to failure should be replaced.

Fuel processing group

There is no fuel processing facility for MFTF-B. A facility comparable to the Tritium Systems Test Assembly (TSTA) will be required for MFTF-α+T. Data acquisition and processing for this facility will require at least 1500 channels of instrumentation.

Water cooling group

There is very little cooling water on MFTF-B compared with MFTF-α+T. Each cooling branch on MFTF-α+T must have enough instrumentation for heat flow balance, water treatment, and tritium monitoring. About 250 channels for monitoring flow, temperature, pressure, and radiation are needed. In addition, about 50 channels are needed for water treatment and control measurements.

Cryogenic system group

The MFTF-B cryogenic system must be expanded by 50% to 100% to provide the increased cryogenic load that results from nuclear radiation heating. The MFTF-α+T cryogenic data acquisition system will probably require 50% more channels of instrumentation than are provided for MFTF-B.

Plasma collector group

The plasma collector group has no equivalent on MFTF-B and requires a new data acquisition system for monitoring and control of the direct converters and halo scrapers. About 400 channels of instrumentation will be needed.

Test module group

Tests of engineering materials and blankets will be carried out in the MFTF-α+T axicell. Each test module, which has no equivalent on MFTF-B, will require about 200 channels of data acquisition. If there are two test modules, one on each side of the CS0 magnet, about 400 channels will be required.

10.7.2 Design Description

The existing MFTF-B data acquisition systems will be expanded to meet the requirements of MFTF-α+T. Two types of subsystems used for data acquisition are shown in Figs. 10.52 and 10.53. The type 1 CAMAC instrumentation is especially favored when most of the data come from monitoring sensors with very little control logic involved. The type 2 programmable controller is favored when free-standing logic control is required (e.g., for the magnet control and protection system).

NBI group

The neutral beam data acquisition system for MFTF-B can accommodate 24 NBIs, performing measurements of ion source parameters, beam diagnostics and calorimetry, beam power conversion control and monitoring, ion dump and beam dump coolant measurements, fuel injection control and monitoring, magnetic and nuclear shield measurements, cryogenic panel monitoring, monitoring of vacuum conditions, and monitoring of tritium leakage. Some existing neutral beam injection sensors may be used again, but many new ones will be needed. Cost of the new sensors will be about 80% of the cost of sensors for 16 of the MFTF-B sources and dumps.

ECRH group

There is one instrumented power supply on MFTF-B that is dedicated to eight gyrotron ECRH power generators. Another instrumented power supply will be assigned to the six additional gyrotrons needed for MFTF-α+T. The additional data acquisition to monitor and control the six gyrotrons, their waveguides, and their launchers will be provided; the cost should be about 60% of the MFTF-B ECRH data acquisition cost.

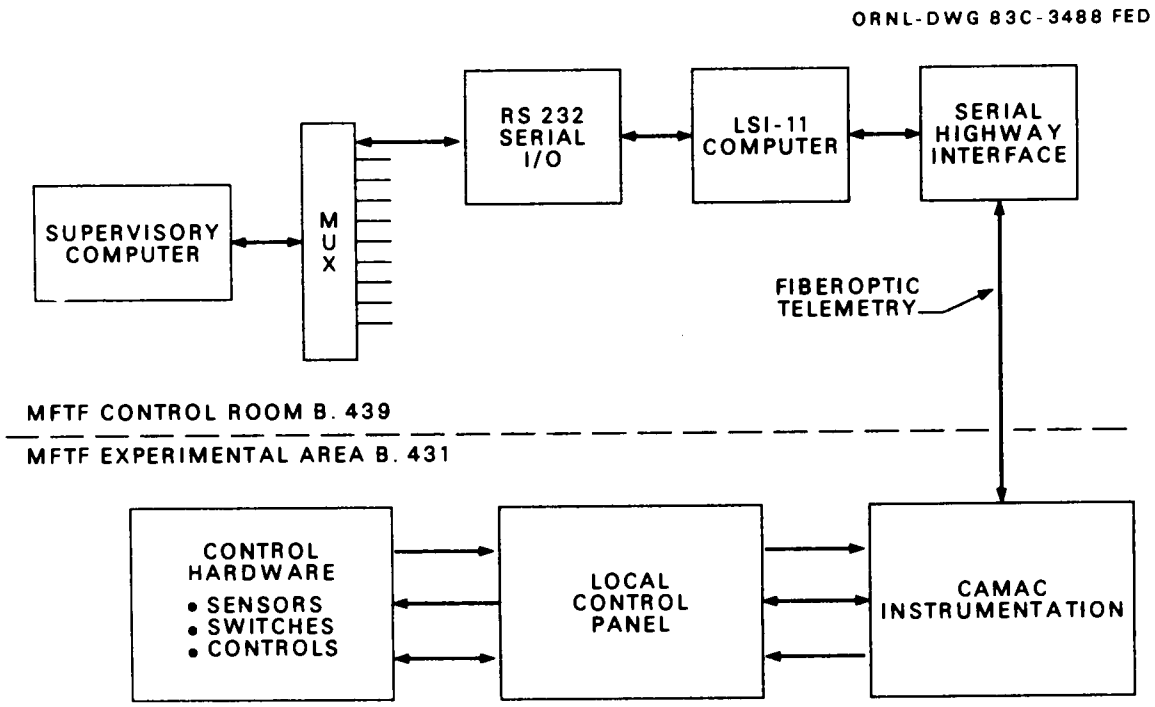

Fig. 10.52. Typical type 1 local control system.

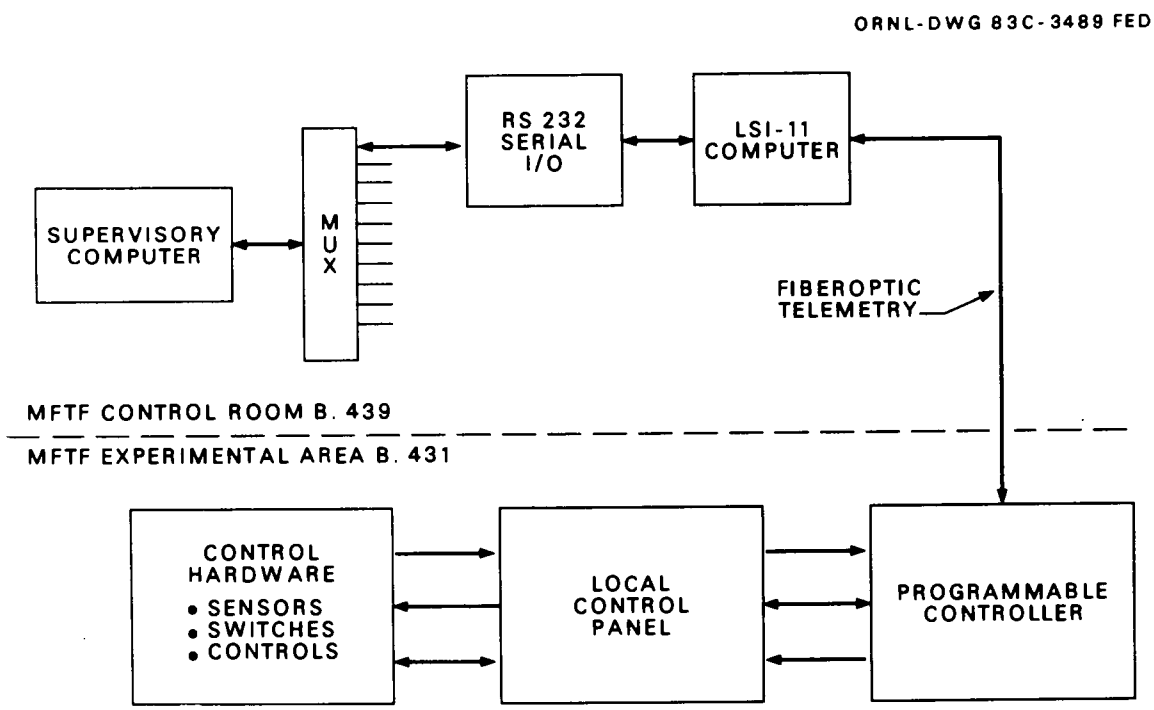

Fig. 10.53. Typical type 2 local control system.

ICRH group

The data acquisition needed for control and monitoring of the high-power ICRH tubes, circuits, transmission lines, and external launchers for 400 kW of ICRH power on MFTF-B will be expanded for control and monitoring of 2400 kW. Cost of the additional data acquisition is expected to be about five times the cost of the MFTF-B ICRH data acquisition.

Drift pumping group

New low-frequency rf power generation will be provided for drift pumping in MFTF-α+T. The necessary data acquisition systems for control and monitoring of 24 rf power generators, transmission lines, antenna loops, and associated power conversion will be provided. Data acquisition will also be provided for two low-frequency FM drift pumping power generators and their support systems. The cost of the drift pumping data acquisition system is estimated to be about the same as that of the ICRH system.

Magnet group

Data acquisition for 24 of the 30 SC magnet coils on MFTF-α+T will be provided by the MFTF-B magnet group data acquisition system. Additional data acquisition will be procured for the six additional SC coils and the five RC coils of MFTF-α+T and their supporting power conversion systems. The cost of the additional type 2 data acquisition is estimated to be about 50% of the cost of magnet data acquisition for MFTF-B.

Inner materials group

A new data acquisition system will be provided to monitor the first wall and shield throughout MFTF-α+T. About 200 channels of temperature, stress, and radiation monitoring instrumentation will be provided. The data acquisition cost is estimated to be about $1500 per channel.

Outer materials group

The MFTF-B outer materials group will be supplemented by an additional 150 channels of data acquisition to monitor the support structure, vacuum vessel, and outer shield of MFTF-α+T. The data acquisition cost is estimated to be about $1200 per channel.

Vacuum system group

The data acquisition system used for the MFTF-B vacuum system will be used for MFTF-α+T. About 20 new BGP sensors will be added. Cost of the vacuum system upgrade is estimated to be about $30,000.

Fuel processing group

About 1500 channels of data acquisition will be provided for the new fuel processing facility required for MFTF-α+T. The cost is estimated to be about $1200 per channel.

Water cooling group

Several additional cooling systems are needed for MFTF-α+T and will require about 300 new channels of data acquisition. The estimated cost is approximately $1200 per channel.

Cryogenic system group

The data acquisition for the MFTF-B 11-kW cryogen system will be expanded to about twice its existing capability to provide for the additional cryogen equipment of MFTF-α+T.

Plasma collector group

About 400 channels of data acquisition will be provided for the two direct converters and two halo scrapers of MFTF-α+T. Some of the instrumentation must be operated at the direct converter potentials. Cost of the data acquisition is estimated to be about $1500 per channel.

Test module group

About 400 channels of data acquisition will be provided for the test sections located on each side of the CS0 magnet of MFTF-α+T. Cost of this data acquisition is estimated to be about $1200 per channel.

10.7.3 Key Issues

The data acquisition needed for MFTF-α+T can be provided with a new, higher performance system procured when required. The new system must be compatible with the data processing computer interface of MFTF-B. Alternatively, the additional data acquisition can be provided by expanding the MFTF-B data acquisition system with standard modules like those procured for MFTF-B. Unless high-speed data acquisition is needed, which does not appear to be the case, expansion with standard modules is the better choice. Only one system must be understood and maintained, and existing software can be more readily used for the additional data acquisition needs of MFTF-α+T.

REFERENCE

1. K. E. Thomassen and J. N. Doggett, *Options to Upgrade the Mirror Fusion Test Facility*, UCID-19743, Univ. California, Lawrence Livermore Natl. Lab., Livermore, Calif., April 1983.

11. TESTING AND OPERATIONS

R. Mattas

Argonne National Laboratory

CONTENTS

11.1 INTRODUCTION 11-3
11.2 SYSTEM CHECKOUT 11-4
11.2.1 Preoperational Tests 11-4
11.2.2 On-Line Checkout Tests 11-4
11.2.3 Component Reliability and Improvement Tests 11-4
11.3 DEVICE PERFORMANCE EVALUATION 11-7
11.4 ADVANCED SYSTEMS TESTING 11-7
11.4.1 Neutronics 11-9
11.4.2 Magnetohydrodynamics 11-10
11.4.3 Materials Compatibility 11-11
11.4.4 Response to Off-Normal Events 11-11
11.4.5 Tritium Recovery and Reprocessing 11-11
11.4.6 Thermal Hydraulics 11-13
11.4.7 Tritium Permeation 11-13
11.4.8 Radiation Damage 11-13
11.5 TEST SCENARIO 11-14
REFERENCES 11-16

11. TESTING AND OPERATIONS

11.1 INTRODUCTION

The MFTF-α+T is envisioned to be one of the first fusion devices that can be used as both an engineering test facility and a nuclear test facility. The primary tests to be conducted are those that can only be carried out on MFTF-α+T. These tests will emphasize the systems integration aspects of the device, its unique plasma characteristics, its large volume for nuclear tests, and its relatively long burn times and high availability. In this section, a set of tests that may be performed on MFTF-α+T is described. The tests that will actually be performed will depend on the relation of MFTF-α+T to the rest of the fusion program, including other test facilities that become available in the future.

The tests can be divided into the categories shown in Table 11.1. The first category, system checkout, consists of tests aimed at determining the operational behavior and reliability of individual systems under actual reactor conditions. The second category, device performance, consists of tests to explore the integrated performance of the device in terms of plasma operation, neutron production, and impurity removal. The third category, advanced systems, consists of tests to explore the performance of systems that may be used in future reactors, such as the Engineering Test Reactor (ETR). Examples of advanced systems are tritium breeding blankets, impurity removal systems, and direct converter systems. For the purposes of test evaluations, the operating scenario shown in Table 11.2 is assumed. The parameters shown are most relevant to the nuclear systems tests, for which long burn times and high availability are desired.

Table 11.1. Testing categories

Category	Purpose
System checkout	Verify that original specifications are met Determine operating characteristics of individual components during operation Accumulate reliability data
Device performance	Determine plasma operation characteristics; neutron flux profiles; thermal and particle flux profiles to first wall, beam dumps, and end cells; impurity control behavior
Advanced systems	Test impurity control concepts and direct converter concepts Perform nuclear systems tests

Table 11.2. MFTF-α+T operating parameters

Lifetime, years	~10
Availability, %	10
Wall loading at 25 cm, MW/cm^2	2.0
Effective central-cell length, m	2.8
Integrated fluence (first wall), MW·year/m^2	2
Length of burn, h	$\lesssim$10

11.2 SYSTEM CHECKOUT

11.2.1 Preoperational Tests

Most individual systems can be tested before they are installed to determine if their operating specifications are met. However, in a few cases, system checkout tests can only be conducted after MFTF-α+T has been constructed. Tests in this category are verifications of the performance of the vacuum system, the cooling systems, the magnet system, and the maintenance system, as described in Table 11.3. The information obtained from these tests will also provide a significant addition to the engineering database.

Table 11.3. Preoperational checkout tests

System	Tests
Vacuum	Vessel leak detection, backout system operation, material outgassing characteristics, ultimate vacuum level, system pump rate
Cooling	Superconducting coils, cryopanels, normal conducting coils, first wall and shield, high-heat-flux components
Magnet	System energization and coil currents, stress or strains, system magnetic field, deenergization
Remote maintenance	In-vessel inspection system, component sensors

11.2.2 On-Line Checkout Tests

The integrated operation of some systems can only be determined during plasma operation. These are (1) the tritium fuel cycle, (2) the plasma heating systems, (3) the instrumentation and control systems, and (4) the heat removal systems.

With the exception of the tritium fuel cycle, most of the data required to ensure optimum operation can be obtained during the deuterium phase of operation. Final qualification of all systems will be made during the early stages of deuterium-tritium (D-T) operation. The times required to determine the operational characteristics are on the order of seconds to minutes of plasma operation.

11.2.3 Component Reliability and Improvement Tests

Long-term operation of MFTF-α+T is needed for analyzing component reliability. This information will be valuable in evaluating the remote maintenance needs and overall availability of an ETR that would use similar components. Analyses of component failures should also lead to design improvements that result in longer lifetimes. In general, achievement of a reasonably high availability and long operating lifetime is desirable so that

MFTF-α+T can accumulate statistically significant data on the mean time between failures (MTBF) and the mean time to repair (MTTR) for a wide range of components.

An assessment of component reliability has recently been performed for the Fusion Engineering Device/International Tokamak Reactor (FED/INTOR),[1] and much of that work is applicable to MFTF-α+T. The two areas where information is needed are confidence building and reliability growth. For confidence building, it is assumed that the MTBF of a particular component would be acceptable for use in an ETR. The purpose of testing in MFTF-α+T is then simply to reduce risks. The unknowns to be resolved are failure modes, failure distributions, and failure rates. Confidence-building data can be used for those systems that will be used as a basis for the design of an ETR.

To establish required test times, constant failure rates for components were assumed. This approach is commonly used to estimate equipment reliability and derive test plans for continuously operated equipment and is generally appropriate for large complex systems. The true failure rate distribution can only be determined by a test program, and variations from a constant failure distribution can have a substantial effect on the MTBF. However, if both the MFTF-α+T and the ETR components are similarly designed and experience similar environments, then the parts are likely to have the same failure distribution, with the exception of the nuclear system. This presumption of similar failure distributions helps to mitigate the shortcoming of the constant failure rate assumption. The Poisson curve (Fig. 11.1) indicates that a test time of 1.6 times the goal MTBF is appropriate for 80% confidence if no failures occur during the test; this factor increases to 3 and 4.3, respectively, for one and two failures of the component.[2] Therefore, in order to establish the lifetime of a component, it should be tested for ~3.5 times the MTBF. In the case of

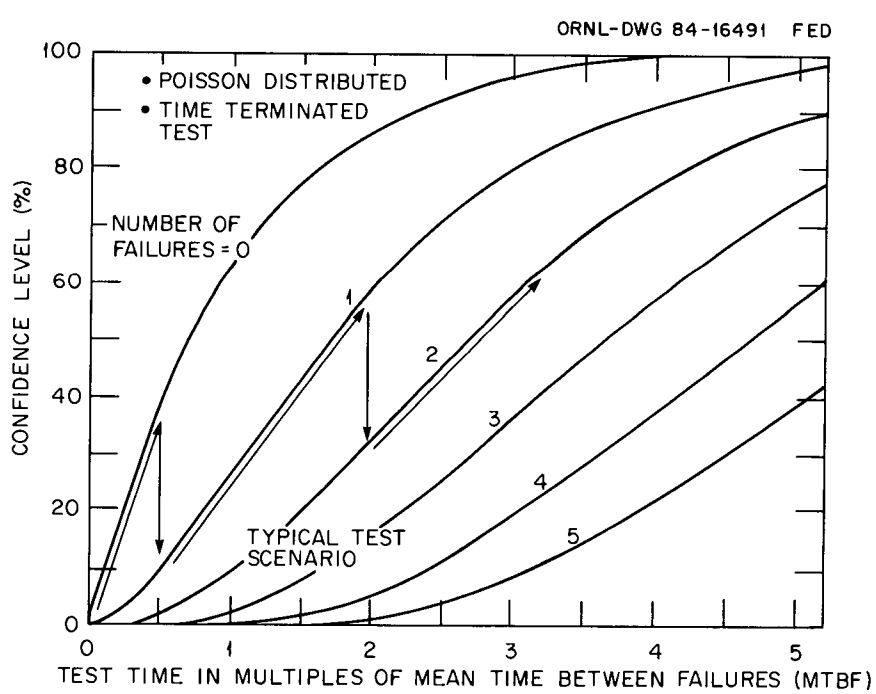

Fig. 11.1. Test time required to establish MTBF for various confidence levels.

relatively short-lived components (e.g., neutral beam sources), this criterion will easily be met, and the MTBF and MTTR can be established with a high degree of confidence. In the case of long-lived components (e.g., superconducting magnets), MFTF-α+T will not supply engineering data on the MTBF.

The other area for which engineering data are desired is reliability growth. During operation, components will undergo development to increase their reliability and to reduce their MTTR. Reliability growth data usually follow a distinctive pattern, as illustrated in Fig. 11.2, where the MTBF increases in a logarithmic fashion. The rate of growth is related to the program emphasis on reliability and ranges from 0.1 for programs with little emphasis on reliability to 0.6 for programs in which everything possible is done to improve reliability. As an example, U.S. Navy development programs experience reliability growth of ~0.4, whereas deployed systems experience a growth of 0.3 (ref. 3). Since MFTF-α+T is developmental in nature, a reliability growth rate of 0.4 is assumed. This indicates that a significant period of operation (~25 times the goal MTBF, if a reliability growth rate of 0.4 is assumed) may be required to meet availability goals. The actual amount of time required will depend on the desired availability for MFTF-α+T, the relative emphasis placed on developing components for ETR, and the actual reliability growth rate observed during the MFTF-α+T operating lifetime.

In summary, the objectives of the MFTF-α+T program should include identification of problems, implementation of improvements, and evaluation of the operational data to characterize the reliability, availability, and safety of the MFTF-α+T system. These findings and improvements will directly benefit the design and operation of a future ETR system if the reliability data are well documented and include proposed and implemented improvements. Ideally, proposed improvements should be incorporated into the MFTF-α+T system and their acceptable operation verified. In practice, incorporating changes based on proposed improvements in component design for ETR may be difficult, especially

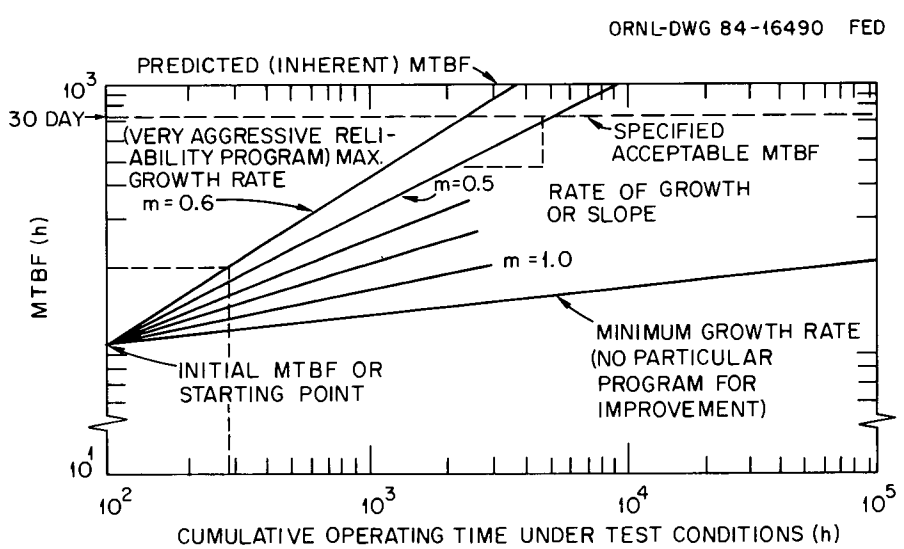

Fig. 11.2. Typical reliability growth plot.

where such changes have high costs. However, even where such proposed changes are not carried out in MFTF-α+T before use in ETR, the changes and expected improvements in performance and reliability should be well documented.

11.3 DEVICE PERFORMANCE TESTS

A significant portion of the early stages of operation will be devoted to determining the nominal plasma characteristics and the response of the device to the presence of the plasma and to the generation of neutrons. As shown in Table 11.4, the major areas of testing are plasma characteristics, impurity removal, and shielding response. The purpose of these tests is to verify that MFTF-α+T meets the plasma design goals and that the device can run for extended periods of time. The successful long-term operation of MFTF-α+T is largely dependent on the ability to fuel, to remove helium ash, and to provide adequate neutron shielding. These tests will probably be carried out in conjunction with the on-line system checkout tests.

Table 11.4. Performance tests

Performance area	Mode	Parameters evaluated
Plasma characteristics	High Q, high Γ	Temperature and density profiles in the central cell, end cell, and halo plasma; impurity behavior
Particle control	High Q, high Γ	Particle flux and temperature profiles at halo scraper, sputtering, heat removal capability, particle recycling, pumping rates, particle removal rates, tritium permeation
Shielding response	High Γ	Neutron flux profiles, shielding attenuation and nuclear heating, heat removal capability, neutron streaming, materials activation

The performance characteristics will be evaluated first in the high-Q mode and then in the high-Γ mode. If large deviations from predicted behavior of the plasma or impurity control systems are observed during testing in the high-Q mode, then modifications can be made more easily than in the high-Γ mode. Neutron flux profiles and shielding response can only be tested with D-D or D-T fuels. Major goals for these tests are to confirm that radiation levels during both operation and maintenance periods are in accordance with safety requirements.

11.4 ADVANCED SYSTEMS TESTING

A major goal for MFTF-α+T is to test advanced systems for future fusion devices. The major systems to be tested are the first wall/blanket/shield (FWBS) system, the impurity control system, and the direct converter system.

The extent of testing for the impurity control and direct converter system is not well defined at present, since these systems are only at the conceptual stage of development.

The emphasis to be placed on these tests in MFTF-α+T will depend on the successes in development between now and the time of construction. If acceptable solutions are found before construction, then little work will need to be done in these areas. Because of the uncertainties in performance, however, it is advisable at this stage to plan for testing and replacement of the impurity control and direct converter systems in MFTF-α+T. Testing of impurity control and direct converter systems is not discussed here since these systems are still developing. Assessment of the test needs for these systems will be required in the future.

Development of FWBS systems is under way. Many detailed designs are available from previous reactor design studies. A major study, designated the Blanket Comparison and Selection Study, has as its major objective the selection of a small number of the most promising designs for extensive research and development.[4] A number of experimental programs are studying various aspects of FWBS operation, including liquid-metal corrosion and magnetohydrodynamics (MHD), solid breeder tritium release, first wall response to surface heat fluxes, and radiation damage effects in materials.[5–7] As development proceeds, improvements in blanket design and reductions in the number of leading candidate designs are expected. Hence, by the time MFTF-α+T is constructed, blanket development will be well advanced, and the number of designs to be evaluated in MFTF-α+T blanket test modules will probably be limited.

Blanket systems testing covers the following areas:

- neutronics,
- MHD,
- materials compatibility,
- response to off-normal events,
- tritium recovery and reprocessing,
- thermal hydraulics,
- tritium permeation,
- radiation damage,
- lifetime performance, and
- system integration and operation.

Most of these tests are generic to both mirrors and tokamaks, although the details of the tests are likely to differ in the two systems. Summaries of the tests and the times required to perform them are presented in Fig. 11.3. Except for the neutronics tests, the tests should be run at wall loadings representative of advanced reactors (>0.5 MW/m^2). For the neutronics tests, the total fluence required is only $\sim$1 $MW \cdot s/m^2$, and the wall loading can be low. A representative range of times is shown for all tests. The time ranges come about because of uncertainties in the predicted effects, the type of component being tested, the size of the test module, or the range of fluences from which material properties begin to change to the point where the radiation effects saturate.

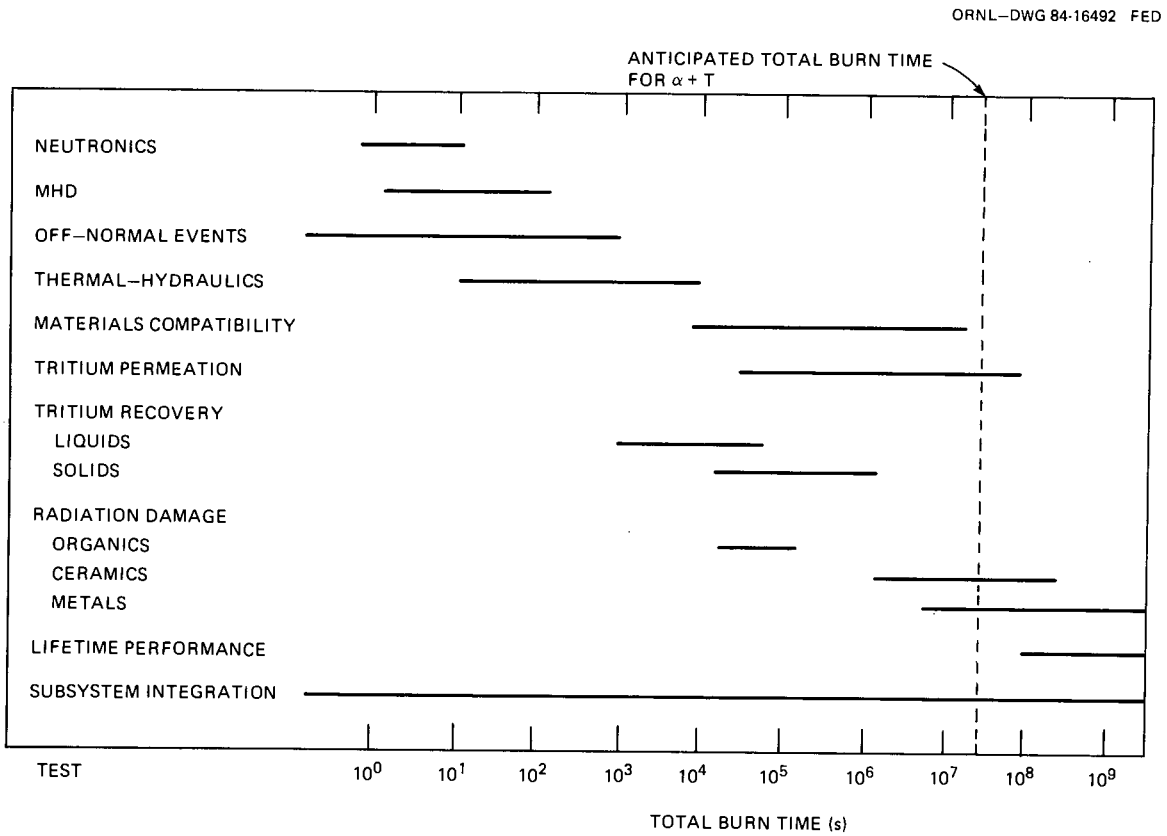

Fig. 11.3. Time required for advanced systems tests.

11.4.1 Neutronics

Neutronics testing includes the determination of tritium breeding ratios, nuclear heating levels, materials activation, and shielding efficiency.

To verify the predicted tritium breeding capability of the ETR blanket, the tritium production rate will be measured at different locations in the blanket module to obtain local tritium production rates. These measurements will then be compared with results of three-dimensional (3-D) neutronic analyses for the blanket. Several techniques are available to measure the tritium production rate: tritium radiochemistry, mass spectrometry, track recorders, and gas counters. The required fluence is ~ 1 MW·s/m^2, which is a fraction of the pulse. The expected uncertainty is $\sim 5\%$ for the radiochemical and mass spectrometry techniques. In these cases, the tritium breeding measurements can be performed during the early stage of operation with only a few pulses, each pulse having a few seconds of burn time.

Nuclear heating measurements are needed to validate the calculations used to predict nuclear heating profiles for heat removal and tritium inventory analyses. Calorimeters and thermoluminescent dosimeters (TLDs) have been considered for measuring the local heat deposition.

Calorimeters are used to measure neutron-plus-gamma energy deposition rates in fission reactor environments at different power levels. On the basis of the heating rates near the first wall, a calorimeter response time on the order of 1 s is expected. This response and burn times of 100 and 200 s allow the measurement to be made within one pulse with difficulty. The expected uncertainties are ~5%, based on the state of the art.

The TLD technique has been considered for measuring gamma heating in fusion blankets. The TLDs are small and do not perturb the radiation field, but they require a large correction factor for gamma heating due to their response to the hard spectrum of fusion neutrons. The expected uncertainty is less than 30% for gamma heating.

Two methods are considered to measure the neutron spectrum in the fusion environment: multimaterial activation and gas recoil proportional counters. The activation technique has been tested in a fusion-type spectrum where the uncertainty in the unfolded spectrum is 10% to 20%. The fluence required for this technique is a fraction of a pulse for good statistical counting. The proportional counter is capable of 5% accuracy but requires very low neutron wall loading (~1 W/m^2). This wall loading can be achieved by terminating the pulse during startup.

Calorimeters and TLD techniques can be used to measure the decay gamma heating with ~3% accuracy since the radiation field is free of neutrons after shutdown. The gamma-ray spectrum can be measured using sodium iodide scintillation detectors.

The fluence to which the test module has been exposed is determined by the activation of structural material used in the blanket. For the type 316 stainless steel of the reference blanket, the decay heat and the induced radioactivity after 1000 $MW \cdot s/m^2$ are 10% of the value after 20 $MW \cdot year/m^2$. After 0.03 $MW \cdot year/m^2$, steel attains 50% of the activation level at 20 $MW \cdot year/m^2$. Based on this analysis, a very small fraction of 1 $MW \cdot year/m^2$ is adequate to perform activation and decay heat testing.

11.4.2 Magnetohydrodynamics

A liquid metal moving across magnetic field lines is subjected to magnetic forces that affect flow behavior and pumping power requirements. The impact of these forces on blanket operation will depend on the size of the channel cross section, the flow path through the magnetic field, the flow rate, and the liquid metal and structural material. Several aspects of MHD can be examined in laboratory experiments, but MFTF-α+T offers the opportunity for integrated proof testing. The principal measurements are pumping power and heat removal efficiency; the times needed for these tests are on the order of 100 s.

For proper simulation of MHD effects in prototypical blankets, the coolant flow paths and the magnetic field strength should be close to those anticipated for advanced reactors. Simulating the flow paths will be difficult with the present MFTF-α+T design, which incorporates a circular normal conducting coil directly behind the blanket test module. Further evaluation of this problem is needed.

11.4.3 Materials Compatibility

The long-term operation of the blanket will depend on the interactions of the structural material, breeder, and coolant. Important aspects of materials compatibility include (1) integrity of the structural material, (2) transfer of activated material into the coolant, (3) flow blockage, and (4) safety issues related to the interactions of the coolant and breeder. The times required for tests of these factors are generally long, so testing can be expected to continue throughout the device life. During normal operation, data concerning the mass transfer characteristics of blanket systems will be collected. If an accident occurs, events such as total flow blockage or coolant channel rupture will provide additional information concerning materials compatibility. Other issues will be addressed in postirradiation destructive examinations to evaluate the condition of the structural components.

11.4.4 Off-Normal Events

Off-normal events include failure of structural material, loss of coolant accidents, and loss of flow accidents. The operation of MFTF-α+T will provide information on the frequency and severity of off-normal events. Loss of coolant accidents can be simulated during blanket tests and may be incorporated into the overall test plan in the latter stages of operation.

11.4.5 Tritium Recovery and Reprocessing

Testing of a fusion blanket includes demonstration of a tritium breeding ratio > 1.0 and the ability to easily remove and reprocess the tritium. A number of factors influence tritium breeding and recovery, as shown in Tables 11.5 and 11.6. In particular, there are significant differences between the recovery characteristics of solid and liquid breeders. With liquids, the breeder material can be circulated through the recovery system; with solid breeders, a purge gas is the preferred means of conducting the tritium to the recovery system. Solids are also subject to degradation of properties due to neutron damage. Therefore, tritium recovery from solid breeders is generally viewed as being more difficult than recovery from liquid breeders.

The times required to reach equilibrium in tritium recovery tests are also different for solid and liquid breeders. The time to equilibrium will depend, among other things, on the burn time, dwell time, and thickness of the blanket segment. During a tritium recovery test, essentially 100% reliability is desirable because tritium levels decrease as soon as the neutron source is removed, and long time periods are then needed to build up the tritium level in the blanket again. The test times indicated in Fig. 11.3 are those needed to reach an equilibrium concentration in the blanket and do not include long-term effects that could alter tritium recovery, particularly in the case of solid breeders. For liquid metals, the times to reach equilibrium tritium concentrations are calculated to be less than 15 h. Methods of tritium recovery from liquid metals have been demonstrated in laboratory experiments. Therefore, confirmation tests in MFTF-α+T, while desirable, are not critical. In solid breeders, the longer times to equilibrium (up to 300 h) are needed because these materials are calculated to retain higher tritium concentrations. It appears that with the present operating scenario of a 10- to 100-h burn, tritium recovery tests for liquid metals can be conducted, but recovery tests for solid breeders may be difficult.

Table 11.5. Factors affecting the demonstration of a breeding ratio > 1.0 in a breeder blanket

Bulk composition factors
Coolant volume fraction
Structural material volume fraction
Purge flow void fraction
Blanket thickness
Lithium enrichment
Neutron multipliers
Boundary factors
Material heterogeneities
Void penetrations
Secondary neutron spectra
Engineering factors
Extent of coverage around plasma
Special in-vessel and in-blanket components

Table 11.6. Factors affecting the demonstration of a low steady-state tritium inventory in the blanket system and the demonstration of tritium recovery

Solids	Liquids
Composition/configuration factors	
Choice of breeder material	Choice of breeder material
Breeder porosity	Choice of coolant
Breeder material microstructure	Choice of coolant channel geometry
Breeder pellet microstructure	
Purge path geometry	
Chemical factors	
Tritium recoil/combination chemistry	Vapor transport
Vapor transport	Impurities
Impurities (e.g., protium)	
Irradiation factors	
Lithium depletion	Lithium depletion
Sintering	
Physical property changes	
Dimensional changes	
Engineering factors	
Minimum breeder temperature	Maximum temperature
Maximum breeder temperature	Reactor power fluctuations
Purge flow characteristics	
Reactor power fluctuations	

11.4.6 Thermal Hydraulics

Meaningful tests of heat recovery require reaching quasi-steady-state conditions. For the first wall and high heat flux components, the time required to reach equilibrium is on the order of 10 s. However, the more massive blanket test sections require much longer times (up to 1 h). The actual amount of time needed depends on the blanket thickness, burn time, dwell time, and neutron wall loading. In general, a long continuous burn is more desirable than several consecutive short burns, since a shorter period of time is needed to reach a quasi-steady state. In any case, the maximum time required to reach these conditions is approximately 1 h of operation. The neutron wall loading should be greater than half the ETR wall loading to provide useful data.

It is anticipated that a significant amount of thermal hydraulics testing will take place in other facilities before MFTF-α+T is available. These tests should provide most of the information necessary to qualify component designs for heat removal. The primary purpose of such tests in MFTF-α+T would be to confirm the results from other facilities and to demonstrate heat recovery under actual fusion conditions.

11.4.7 Tritium Permeation

Components exposed to the plasma are subjected to tritium ion bombardment and injection. The increased concentration of tritium in the surface layer of plasma-side materials can lead to enhanced tritium permeation into the coolant. The degree of permeation depends on the temperatures and temperature gradients through the materials, the energy of the impinging particles, the tritium recombination rate on the surface, the diffusion characteristics of the material, the effect of neutron damage on tritium trapping, and the presence of a permeation barrier on the coolant-side surface. At present, the understanding of tritium permeation in a fusion environment is poor, and there is a large uncertainty in the times required for appreciable permeation to occur.[8] The level of understanding probably will not be adequate to permit accurate estimates of permeation rates when MFTF-α+T starts operation. Testing in MFTF-α+T will be the first opportunity to assess permeation rates under actual fusion conditions. The times required for permeation into the coolant can vary from $\sim 10^4$ s to 10^8 s. For mirror systems, tests can be made at the beam dumps, at the halo scraper, and at the direct converter collector, all of which are bombarded by high-energy ions.

11.4.8 Radiation Damage

Radiation damage testing will be performed for three classes of materials, (1) organic insulators, (2) inorganic insulators, and (3) metals. All of these materials are being tested in fission reactors, in which the radiation damage should be representative of that occurring in fusion reactors. Because of the long times involved in testing inorganic insulators and metals to end of life (EOL), any such tests in MFTF-α+T are likely to be for confirmation of the results of low-fluence experiments in fission reactors.

Nonmetallic materials are needed in fusion reactors for a variety of applications, including insulation for magnet systems and for plasma heating and diagnostic systems. Often, candidate materials to meet these needs have not been tested for their response to

neutron irradiation. Even for materials that have been tested, the test environment has often been a poor simulation of the fusion reactor service environment. The MFTF-α+T environment includes the appropriate neutron energy spectrum and the correct balance between energy deposited by the neutrons and gamma field. If rate effects can be adequately accounted for, tests in MFTF-α+T facility may provide EOL qualification of materials for service in lower flux regions of power reactors. Testing in MFTF-α+T will also establish the validity of the data obtained with simulation techniques and qualify these data for predictions of service in a fusion reactor.

Performance limits on organic insulators for use in superconducting magnets have not yet been established. Current experimental programs will establish the test environment and the critical property measurements required to qualify these materials. Testing in MFTF-α+T will probably require irradiation at 4 K, perhaps with periodic controlled warmup to simulate fusion reactor operations. In situ electrical measurements may be required to track possible degradation of insulating properties, and postirradiation mechanical property measurements may be required to determine life-limiting properties. The test volume to the west of the blanket test module is available to conduct these tests. Since superconducting magnets will operate only in low-flux regions of reactors, full-life testing may be possible in MFTF-α+T.

Inorganic materials, mainly ceramics, may be used in a variety of insulating applications. Candidate materials include Al_2O_3, SiC, BeO, C, MgO, and $MgAl_2O_4$ for insulation of normal magnets, neutral beam injectors, rf transmission and launching components, and diagnostic equipment. Testing of these materials will require irradiation at temperatures from 50°C to 500°C or higher, to the maximum fluences that can be attained in MFTF-α+T. Measurement of the in situ electrical properties to predict the service of these components will be important. More complete characterization of postirradiation properties will include the electrical and mechanical properties critical to proposed applications.

The fluence required to measure appreciable changes in properties in metals is 10–100 dpa. At 10% availability and a wall loading of 2 MW/m^2, MFTF-α+T would generate a total neutron damage level of ~20 dpa at the first wall. Irradiation of metal specimens in MFTF-α+T is thus expected to yield significant changes in the base properties. However, since the full device lifetime is needed to achieve these fluences, only a limited number of test conditions can be evaluated. Therefore, metal irradiation experiments in MFTF-α+T will probably serve to confirm the applicability of fission reactor data for fusion design assessments.

11.5 TEST SCENARIO

The order and emphasis of testing in MFTF-α+T are not well defined at present. The test scenario presented here should therefore be viewed as only one of several possibilities; it represents the first step in defining a test strategy. Ultimately, the test strategy will combine data accumulated before construction, availability of other test facilities, and goals of the device to follow MFTF-α+T.

The test scenario is based on several assumptions, the most important of which for the blanket tests is that a full breeder blanket will be required for ETR. (If tritium breeding is not required for ETR, then blanket qualification will be performed using ETR rather than MFTF-α+T.) Other assumptions are a 10-year device lifetime and a goal availability of 10%.

The test scenario is shown in Table 11.7 by year of operation. The first year of operation will be largely spent on preoperational and on-line checkouts of individual systems. The device availability is expected to be $\lesssim 1\%$ for this stage of operation. The next two years of operation will be devoted to device performance tests. First, deuterium operation in the high-Q mode will be examined, followed by D-T performance tests. Burn times during this phase will only be long enough to acquire performance data. It is expected that, as reliability improvements are made, the availability will increase to $\sim 3\%$. Any needed modifications to remote maintenance equipment should be completed during this phase.

Once its performance meets expectations, MFTF-α+T will be ready for operation at high availability and wall loading. This phase of operation, the high-Γ mode, will last seven years. The main objectives are to qualify a blanket design for ETR and to collect

Table 11.7. Test scenario for MFTF-α+T

Year of operation	Availability, %	Tests	Milestones
1	1	Preoperational checkout On-line checkout	Complete preoperational checkout
2	3	High-Q mode performance (D-D) On-line checkout	Complete on-line checkout Complete high-Q mode performance tests
3	3	High-Q mode performance (D-T)	Complete D-T performance tests
4	10	Liquid-metal blanket 1 Reliability tests	
5	10	Liquid-metal blanket 2 Reliability tests	Complete liquid-metal tests
6	10	Solid breeder blanket 1 Reliability tests	
7	10	Solid breeder blanket 2 (midyear) Reliability tests	
8	10	Solid breeder blanket 2 Reliability tests	Complete solid breeder tests
9	10	ETR prototypical blanket 1 Reliability tests	
10	10	ETR prototypical blanket 2 Reliability tests	Select ETR blanket design

engineering reliability data. A maximum of four blanket designs will be tested (two liquid-metal and two solid breeder systems). In order to simulate ETR as closely as possible, blanket modules should be close to full size; therefore, it is expected that the entire blanket test volume will be occupied by a single module. Separate heat removal, tritium removal, and diagnostic systems will be needed for each module.

Liquid-metal systems will be examined first because several tests (e.g., thermal hydraulics and tritium recovery tests) can be performed in less time for liquid-metal than for solid breeders. Thus, less stringent burn time requirements are needed at the early stages of blanket testing when the availability may be less than 10%. Each liquid-metal blanket would be tested for ~1 year; each solid breeder blanket, for ~1.5 years. Variation of neutron flux levels, coolant flow rates, coolant temperature, purge gas flow rates (for solid breeders), and tritium recovery rates during blanket testing is desirable. Following the testing of all four modules, improved blankets will be designed and tested. These improved modules will represent prototypical ETR modules, and final selection of the ETR blanket design will be based on these tests.

REFERENCES

1. M. A. Abdou et al., Chap. 12 in *U.S. FED/INTOR Activity: Engineering Testing*, FED/INTOR/TEST/82-4, 1982.

2. A. Coppola, *Bayesian Reliability Tests Are Practical*, RADC-TR-81-106, 1981.

3. NAVORD OD44622, U.S. Navy.

4. M. A. Abdou et al., *Blanket Comparison and Selection Study: Interim Report*, ANL/FPP/TM-177, Argonne Natl. Lab., Argonne, Ill., 1983.

5. H. D. Michael and J. Lambert, *ASURF System Checkout with a Three-Tube, Thick-Wall Test Panel*, WAESD-TN-83-0048, Westinghouse Electrical Corp., Pittsburgh, Pa., 1983.

6. *Fusion Technology Development Plan*, DOE/ER-0166, U.S. Department of Energy, 1983.

7. See, for example, the proceedings of the 2nd Topical Meeting on Fusion Reactor Materials [*J. Nucl. Mater.* **103 & 104** (1981)].

12. MAINTENANCE

P. T. Spampinato

Fusion Engineering Design Center/Grumman Aerospace Corporation

CONTENTS

12.1 INTRODUCTION 12-3
12.2 MAINTENANCE PHILOSOPHY 12-3
12.3 MAINTENANCE APPROACH 12-4
12.3.1 Approaches to Component Removal and Replacement 12-4
12.3.2 Requirements for Component Removal and Replacement 12-7
12.3.3 Requirements for Device Vault 12-9
12.3.4 Required Operations During Downtime 12-10
12.4 MAINTENANCE OPERATIONS 12-12
12.4.1 Plan of Operations 12-12
12.4.2 Component Replacement 12-13
12.4.3 Test Program Activities 12-21
12.5 MAINTENANCE EQUIPMENT 12-22
12.5.1 Lifting Systems 12-22
12.5.2 Manipulator Systems 12-23
12.5.3 In-Vessel Inspection Systems 12-29
12.5.4 Mock-Up Systems 12-26
REFERENCES 12-28

12. MAINTENANCE

12.1 INTRODUCTION

The maintenance philosophy for MFTF-α+T was adopted early in the design process to guide the development of the configuration, with particular emphasis on shield requirements, locations of the components in the vault, and access. Aspects of this philosophy include a plan for contact (hands-on) operations supplemented by remote operations for component handling, an understanding of the design limitations imposed by the upgrade of the Mirror Fusion Test Facility (MFTF-B), and a preliminary analysis of component lifetimes.

On this basis, a viable design requiring minimal changes to the MFTF-B vault was developed. The maintenance philosophy is discussed further in Sect. 12.2, and the maintenance approach is described in Sect. 12.3. Section 12.4 addresses the maintenance operations to be carried out in MFTF-α+T. The necessary maintenance equipment is described in Sect. 12.5.

12.2 MAINTENANCE PHILOSOPHY

The maintenance philosophy for MFTF-α+T is based on earlier work for the Technology Demonstration Facility (TDF).[1] It incorporates a fourfold approach that takes into account the need for operational flexibility and the opportunity to accomplish many maintenance tasks during scheduled downtime. The four requirements of this approach are as follows.

1. Contact maintenance at the shield boundary is permitted 24 h after the device is shut down. This means that personnel may routinely perform hands-on inspection, disconnect connections, set up maintenance equipment, and supervise maintenance activities in the vault before any disassembly of the device. These capabilities are particularly desirable in light of the amount of time available between device startups.

2. Major maintenance and disassembly operations can be accomplished remotely under both normal and emergency conditions. When the device is disassembled, activation levels within the shield boundary are too high to permit hands-on operations, so remotely operated equipment is required.

3. Modularized components are arranged for independent disassembly wherever possible, and their sizes and weights are within the limits of the crane system.

4. Proven remote-equipment technology is used. It is not reasonable to assume that major breakthroughs in remote handling or robotics will occur in the near term (4 to 5 years), so maintenance operations must be based on currently available equipment only.

Three additional guidelines that influence the maintenance approach have been established. First, neither personnel nor maintenance equipment is permitted in the vault during device operation. The neutron environment would obviously compromise personnel safety and could cause neutron-induced activation of the maintenance equipment, which would then require remote maintenance. The exception is equipment that is permanently installed in the vault. The overhead crane is positioned at one end of the vault, away from the central-cell region; activation analyses showed that this location provides sufficient shielding. (The approach taken in the TDF study, parking the crane behind a shielded

appendage to the vault structure, proved costly.) Other maintenance equipment, such as transporters and manipulators, may be stored behind shadow shields.

Second, power supplies to the device are shut down and magnet coils are deenergized during maintenance operations near the device. This requirement is for the safety of personnel, maintenance equipment, and device systems. Each deenergization or reenergization of the superconducting coils will take about 4 h.

Third, superconducting coils may be held at cryogenic temperatures during maintenance of other components or systems. A beam line source, for instance, is replaced with power supplies down, all coils deenergized, and superconducting coils held at 4 K.

12.3 MAINTENANCE APPROACH

12.3.1 Approaches to Component Removal and Replacement

Approach to remote operations

Three approaches to entering the device for remote operations were investigated. Each of the three—entry through the sides, through the end domes, and through the top of the device—had a different impact on the end-cell design and, to a lesser extent, on the orientation of some components.

The range of floor-mounted operations for side access is restricted by the four support foundations for the end cells and for the central-cell beam lines and beam dumps. Overhead lifting of large components would be required in order to raise them to the shielded doors to the hot cells. Removal of the rf systems and the drift pumping coils requires combined vertical and horizontal extraction because of the 45° orientation of the magnets which they penetrate. Hence, fixtures to overcome gravity loads and provide alignment are required.

Removal of components through the end domes is conceptually possible but creates two logistical problems. Components must be removed serially (which means they are interdependent modules), and significant laydown area in the vault is needed. This method thus requires disturbance of functioning subsystems, increased downtime due to the additional component removals, and additional hot-cell storage.

Overhead access to the central-cell components is the only practical approach because of the beam lines and the vault support structure. In addition, overhead access takes advantage of the stabilizing effect of gravity during lifting operations, minimizes the requirements for special fixtures, makes use of the linear geometry of the tandem mirror configuration, and is not space-limited by the vault structure. The plan view of MFTF-α+T in Fig. 12.1 shows that a single crane has easy access to the entire length of the device. The elevation view in Fig. 12.2 shows the removal of the test module with its shield plug. Side removal of this component is marginally possible but would require the test module to be designed as several smaller pieces to avoid interference with the side wall. Entry through the top of the device is the preferred approach for design purposes.

Approach to contact operations

The device shielding is designed to allow personnel access to the vault 24 h after the device is shut down. During the 24-h waiting period, short-lived radionuclides will decay

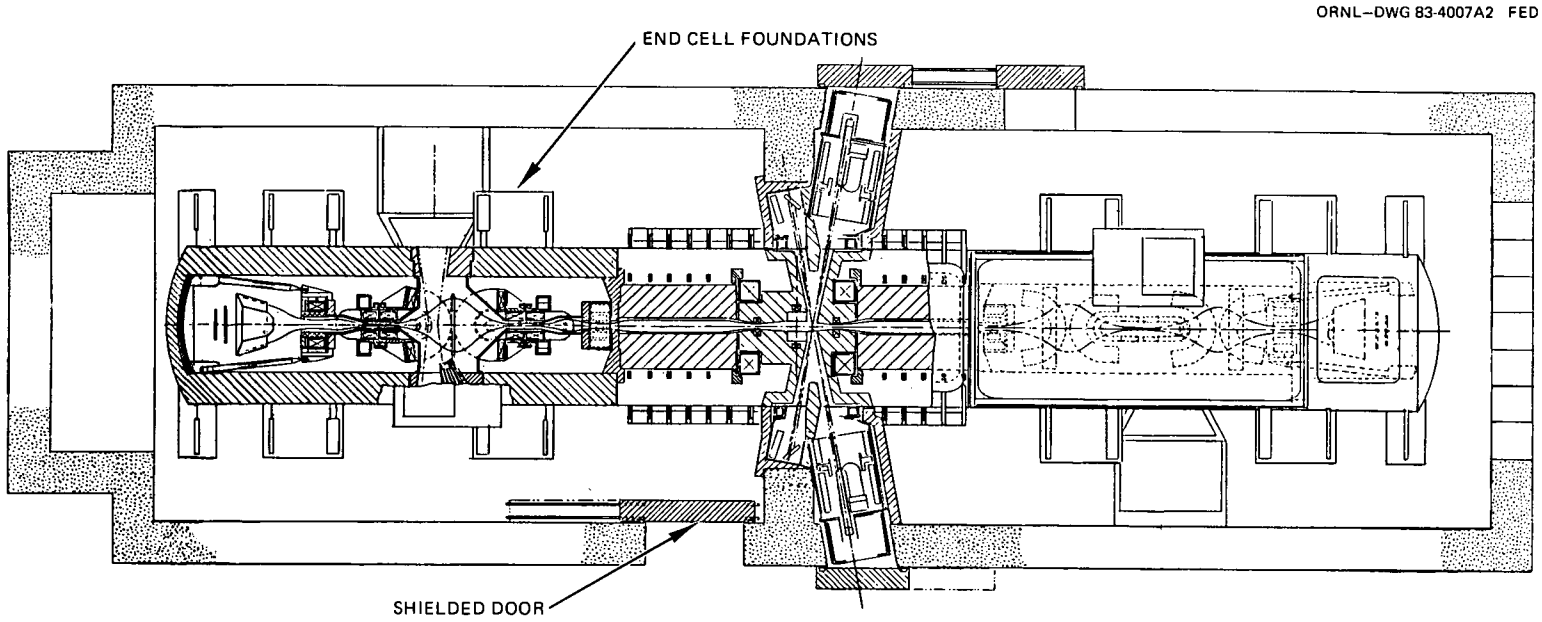

Fig. 12.1. Overhead access for handling device components.

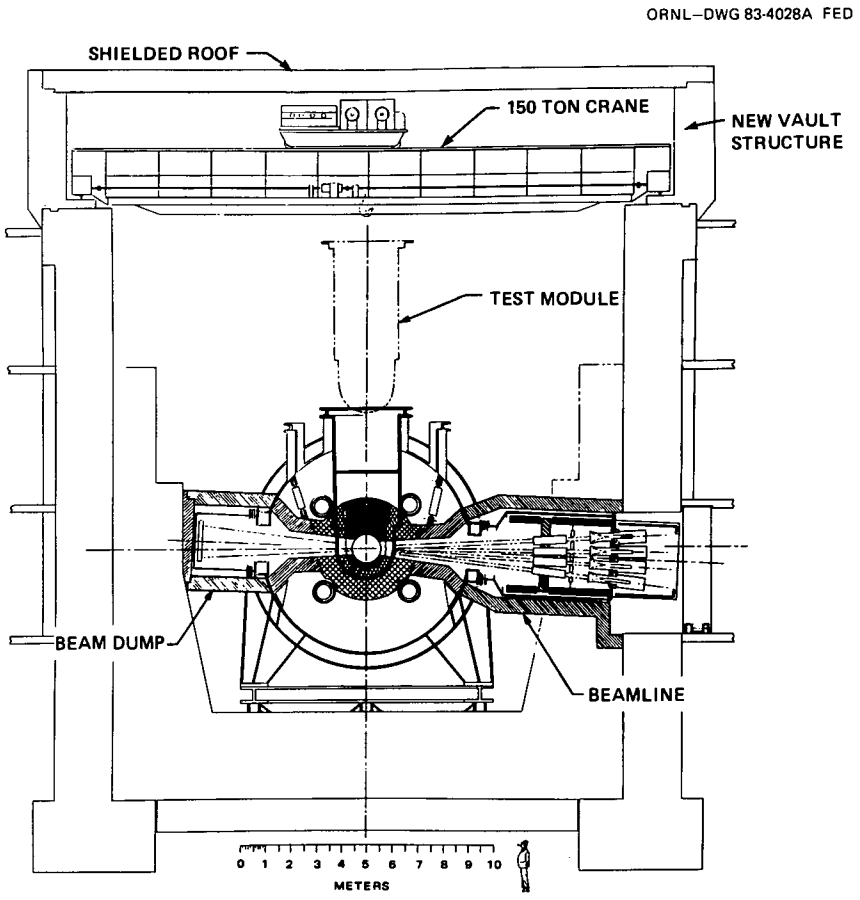

Fig. 12.2. Removal of test module and shield plug.

to low levels, so that the dominant activation levels are from long-lived isotopes, such as those of cobalt. (Further appreciable reduction in dose rate levels would require months of downtime.) The 24-h waiting period will be used for in-vessel and out-of-vessel remote inspection, for preparing maintenance equipment and personnel, and for deenergization of the coils.

After health physicists have verified that a safe operating environment exists, personnel outfitted with protective suiting will be permitted to enter the vault. Their main activities will be disconnecting electrical and coolant joints and unfastening flanged interfaces. Since many of the device components that require scheduled replacements are too large and heavy for manual handling, the remaining activities for personnel consist of setting up maintenance equipment, supervising procedures, and making visual inspections before remote operations are begun.

It has been shown that the protective suiting for personnel will reduce productivity to approximately 50% of "normal" operations.[2] Obviously, it is unrealistic to make such comparisons in light of the highly activated, tritiated environment in a fusion device, which is not a "normal" energy source. An analogous comparison of productivity might be how

much more quickly astronauts could perform extravehicular activities without their space suits. A further discussion of safety is presented in Chap. 14.

12.3.2 Requirements for Component Removal and Replacement

Access to components

The MFTF-α+T configuration is arranged to provide access to all major components and to use overhead lifting wherever possible. Components not accessed from overhead are the lower ion sources for the sloshing-ion beam lines, the structural supports for the end-cell magnets, and the ion sources for the central-cell beam lines.

In the end cells, large port covers provide for vertical removal of all of the coils, the halo scraper, and the direct converter. Figure 12.3 shows the access to the halo scraper and direct converter modules. Most of the sloshing-ion beam line components also have vertical access. The upper ion sources are reached by lifting a shield cover and removing the sealed HF_6 compartment cover. The ion dump and the beam dump are accessed by lifting smaller shield covers located at the top of the vessel. The lower ion sources are located behind a movable shield door and must be moved with floor-mounted handling

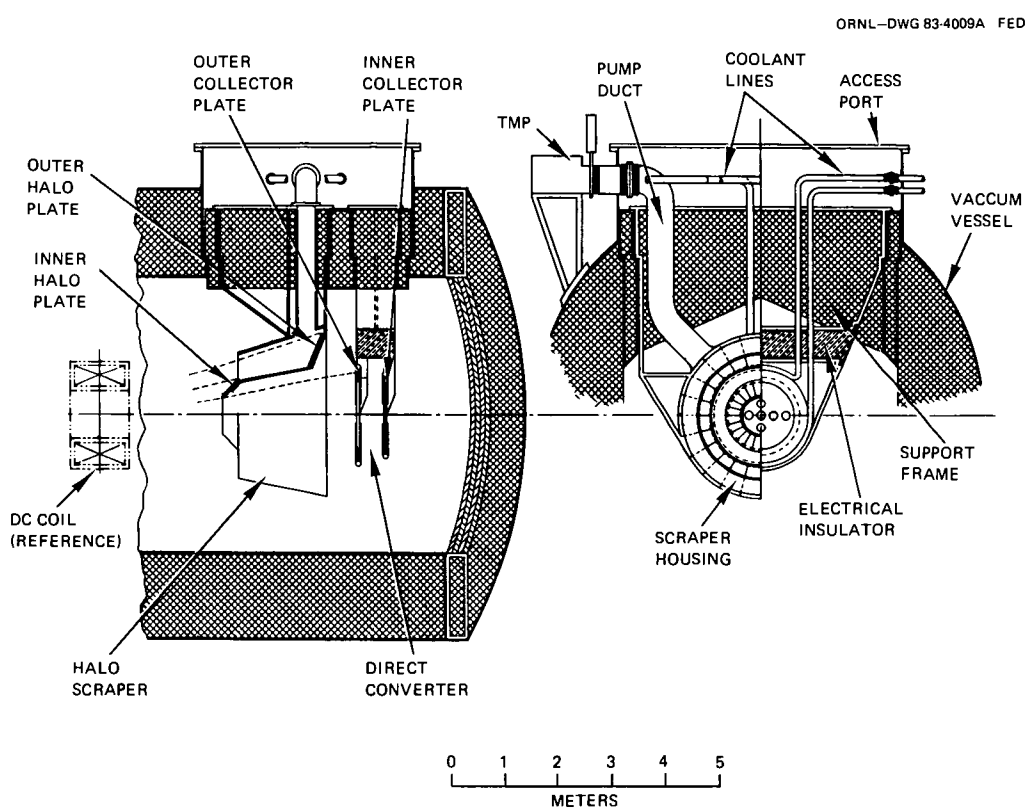

Fig. 12.3. Access to the halo scraper and the direct converter.

equipment. Figure 12.4 shows the access to the sloshing-ion beam lines and to the attachment pins for the C coil support structure.

In the central cell, operations on the solenoid coils, the beam dumps, the choke coils, and the test module are from overhead, as shown in Figs. 12.2 and 12.5. The ion sources, however, are reached through the movable shield door shown in Fig. 12.1 and in more detail in Fig. 12.6.

In addition to the global access requirements, which establish basic component locations, there are requirements for electrical and coolant connections, welded seals, bolted flanges, etc., that affect maintainability and access. In most cases, the MFTF-α+T configuration has not yet reached this level of development; however, where such detail has been included, access is considered to facilitate component replacement. The turbomolecular pump (TMP) in Fig. 12.3 is an example.

Modularization of components

Component designs are modularized as completely as possible to minimize handling requirements and, consequently, device downtime. Modularization is clearly an advantage for components that require frequent replacement. The most notable example is the ion sources, which may require as many as seven scheduled changes. Any source is easily replaced with a spare, and sources are repaired in the hot cell by replacing submodules (e.g., filaments, grids, insulators). To further reduce the downtime associated with source replacement, ion sources are isolated from the primary vacuum in the vessel with vacuum valves. The main requirements for modular design are simple interfaces and minimal connections.

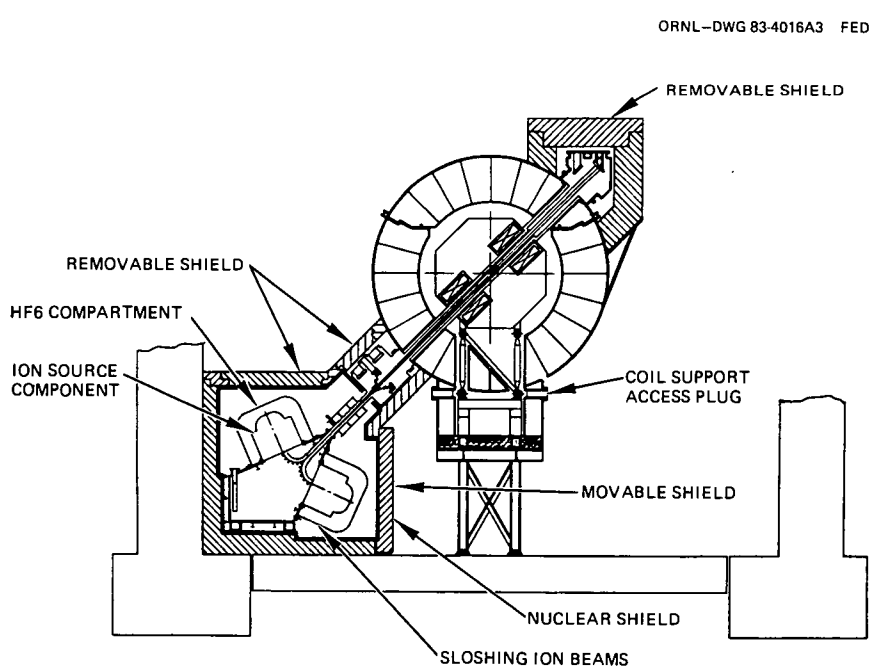

Fig. 12.4. Access to the sloshing-ion beam line components.

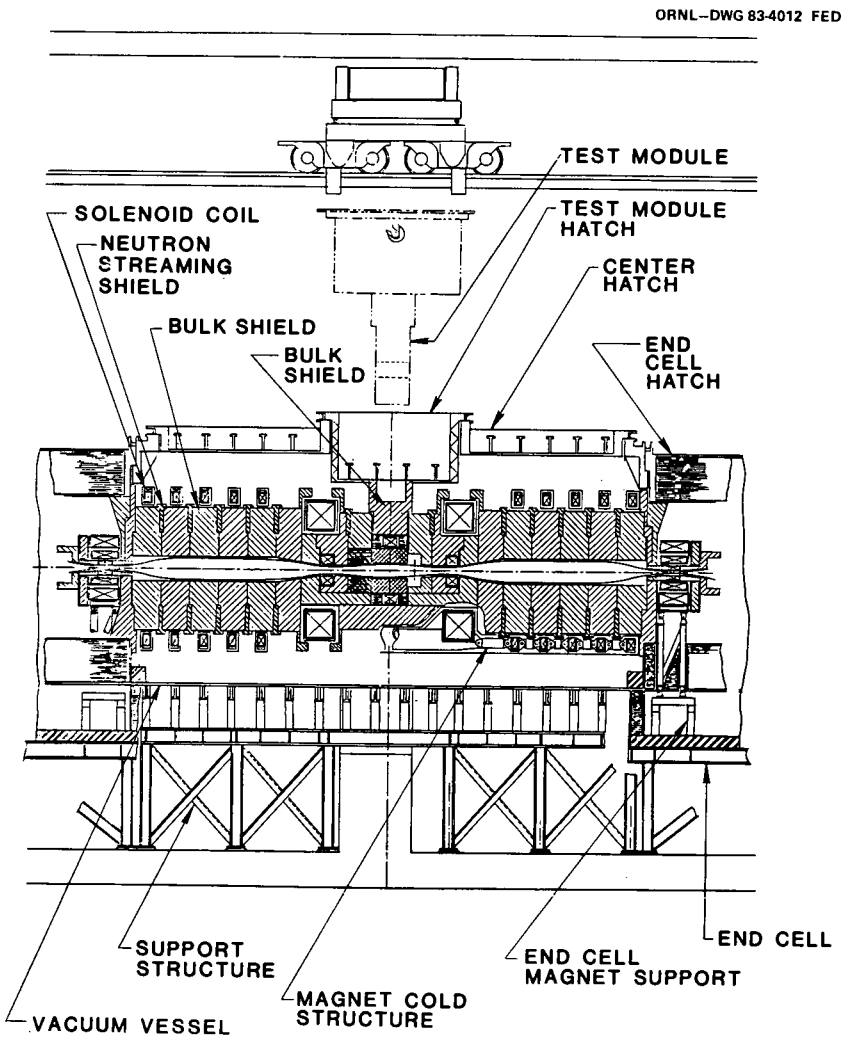

Fig. 12.5. Access to the central-cell components.

12.3.3 Requirements for Device Vault

The MFTF-α+T device is designed to occupy the MFTF-B vault, which is 75 m long, 25 m wide, and 22 m high. The major modification required to accommodate MFTF-α+T is raising the vault roof by about 5 m, as shown in Fig. 12.2, to provide overhead crane clearance above the device.

Other required modifications are shown in Fig. 12.1. A portion of the vault wall behind the central-cell beam injectors is modified to accommodate the ion sources and their magnetic shield. These openings are fitted with vacuum-tight, shielded doors that provide access to the beam lines. Neutronic analysis of this region has not been completed, so it is not clear if any contact operations are permitted for these beam lines.

ORNL–DWG 83-4028A2 FED

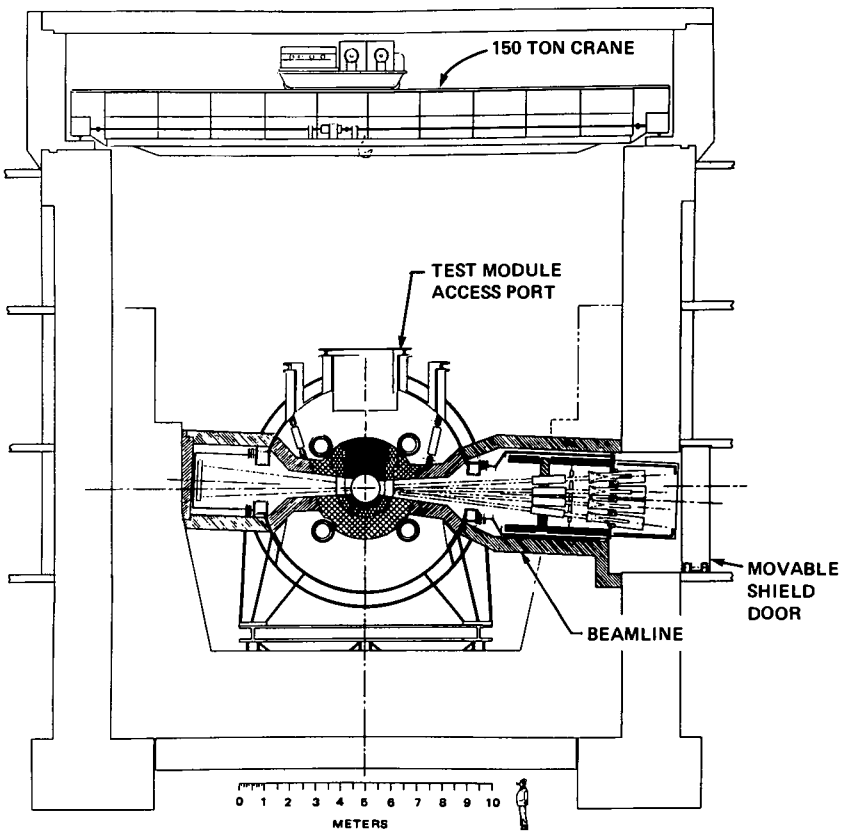

Fig. 12.6. Access to the central-cell ion sources.

The main shielded door, shown on the west side of the central cell, provides the primary access to the vault. This opening is sized for the largest modular components, the axicell solenoid coils, and the plug coil set.

Laydown area in the vault is limited to the 6-m clearance between the vault wall and the vessel, as shown in Fig. 12.1; even this is restricted by the central-cell beam lines, the main shield door, and the end-cell foundations. The area at the west end of the vault is not available because the crane bridge stops approximately 1 m short of this alcove and because the alcove is 6.5 m above the main floor. As noted in Sect. 12.3.1, limited laydown area was one factor in the choice of overhead access for component modules.

12.3.4 Required Operations During Downtime

Downtime (time when the device is not operable) consists of four major activities:

1. initial shutdown to reduce activation to levels allowing personnel access,
2. thermal cycling of the superconducting coil systems if maintenance activities require in-vessel operations (e.g., coil or rf antenna replacement),

3. maintenance operations during which components are removed and replaced (using both contact and remote technology), and
4. pumpdown of the vessel and reconditioning of the internal surfaces.

The approach to shutting down the device to begin maintenance-related operations depends on the nature of activities. If a maintenance activity can be accomplished remotely, then the 24-h waiting period after shutdown can be waived. Only the time required to deenergize the coils must pass before remotely operated equipment is introduced. This approach is not considered here, since MFTF-α+T is based on contact operations for initiating many maintenance-related activities.

During the 24-h period of waiting for dose rates at the shield boundary to decay to acceptable levels for personnel access to the device, the coils are deenergized (in approximately 4 h), the vessel could be brought up to atmospheric pressure (also in about 4 h), and maintenance equipment is prepared for use in the reactor cell.

Thermal cycling of the coil systems has the most impact on device downtime, since an estimated two to three weeks is required for both coil warmup and cooldown. These estimates are based on extrapolations from the Large Coil Program (LCP). Even though they essentially duplicate experience at Lawrence Livermore National Laboratory (LLNL) for the technology demonstration of yin-yang coils, no detailed analysis that includes the economic consideration of refrigeration has been done. Where it is appropriate to do so, it is assumed that six weeks is required for any operations that affect coil replacements. Coil cycling for scheduled component replacements is discussed in Sect. 12.4.2.

Similarly, the pumpdown time required for the plasma chamber after extended maintenance operations has not been analyzed in any detail. It has been estimated that under ideal conditions approximately 10 h of pumping using the TMPs in the end cells and the cryopanels in the beam line drift ducts may be sufficient to achieve the base operating vacuum. A more appropriate estimate may be in the range of three to six days, for two reasons. First, the operating experience for the Tandem Mirror Experiment (TMX) indicates that, although a three-day pumpdown is achievable, often six days are needed due to numerous unforeseen problems in operating large, complex vacuum systems. It appears reasonable to assume (at least for the time being) that experiences on MFTF-α+T will be similar. Second, the operating experience for tokamaks also indicates that several days of pumpdown are required, particularly if the vessel is open to atmospheric conditions for extended periods (days to weeks) and if replacement components such as limiters have not been "conditioned" before installation. Dylla discusses three conditioning techniques for tokamaks: bakeout, discharge cleaning, and gettering.[3] In one example, 100 h (4 days) of glow discharge conditioning was necessary for the Poloidal Divertor Experiment (PDX) to achieve acceptable levels of cleanliness for operation. Since one of these methods will be required for MFTF-α+T, it seems prudent to assume that pumpdown and wall conditioning will have an impact on downtime. Of the three techniques, gettering may be the most efficient; however, because of tritium inventory buildup, it does not appear appropriate in a deuterium-tritium (D-T) device. Hence, in light of the uncertainty for pumpdown, the assumed requirement is six days.

It should be noted here that pessimistic estimates for coil cycling and pumpdown are used to test their impact on achieving the 10% operating availability of the device. Clearly, if the availability objective can be achieved under these conditions, the uncertainties will not be a factor.

12.4 MAINTENANCE OPERATIONS

Maintenance operations are primarily concerned with activities that contribute to device downtime. For MFTF-α+T, these activities fall into two categories:

- component replacements, both scheduled and unscheduled, and
- test program activities, including replacement of blanket test modules, impurity control components, and diagnostics.

Component replacements comprise the usual perception of maintenance activities. The impurity control and diagnostics replacements are included in the test program activities even though their effects have not yet been quantified because they will almost certainly have an impact on the test program. (For example, several prototype designs for the halo scraper may be needed, and each one will require downtime for changeouts; diagnostics will be installed, tested, redesigned, and replaced, also requiring downtime.) Both component replacements and test program activities have an impact on the plan of operations.

12.4.1 Plan of Operations

The plan shown in Table 12.1 is based on the test program discussed in Chap. 11. The 10-year device lifetime is divided into four phases.

Table 12.1. Plan of operations

Phase	Duration, years	Description	Operating guidelines[a]	Full-power operation, hours per month	Average availability,[b] %
I	1	Integrated systems checkout	6 days per week, 2 shifts per day	7	1
II	1	High-performance deuterium operation and checkout	6 days per week, 2 shifts per day	22	3
III	1	High-performance D-T operation and checkout	5 days per week, 2 shifts per day, down 2 weeks per month	22	3
IV	7	High-availability nuclear testing	5 days per week, 2 shifts per day, down 2 weeks per month (on average)	72	10

[a]During Phases I and II, there is no scheduled downtime since the device is expected to be operational for less than an hour during any shift; during Phases III and IV, two weeks per month of downtime is scheduled.

[b]Availability is defined as the time during which the device is actually operated to create plasmas divided by the total calendar time, including planned shutdown.

Phase I (the first year) consists of an integrated systems checkout to verify the performance characteristics of all systems and to establish operating capabilities. Two shifts per day of active operations will probably be scheduled for at least six days per week. No distinction is made between maintenance activities and device operation, since this shakedown phase will consist of an intermingling of both. The expected operating availability goal is about 1% (7 h per month) to evaluate system performance. Certain systems will be operational for considerably longer periods, such as the TMPs and the cryogenic magnets.

Phase II (the second year) consists of high-performance deuterium plasma operations. The operating schedule is the same as that of phase I, except that the expected availability is 3%. During this phase, remote maintenance equipment is tested on the device. (Earlier development and testing of this equipment is accomplished on the device mock-ups.)

Phase III (the third year) is the start of the high-Q mode and represents high-performance D-T operations and checkout. In this phase, the device is activated, and subsequent operations will routinely require the use of remote handling equipment. Two shifts per day of device operations are scheduled for five days per week; two weeks out of every month, the device is down for scheduled maintenance operations. Two weeks per month of downtime should allow for several of the 24-h waiting periods needed to allow personnel access. If the superconducting coils require thermal cycling, two weeks down is not sufficient. On the other hand, if the device operates without major problems, operation could be continued and "scheduled" downtime would be waived. An availability of 3% is assumed to be achievable; this translates to approximately 1 h of D-T operation during each shift when the device is not shut down.

Phase IV (the last seven years) involves high-Γ operation for the blanket testing program. The operating schedule is the same as in phase III, except that the availability is up to 10% and the two weeks of downtime per month is an average for scheduled maintenance activities. Clearly, in a month when no test module or ion source replacement is scheduled, the device will be kept operating.

12.4.2 Component Replacement

Scheduled replacement

Ideally, scheduled component replacement should coincide with mandatory downtime. To determine the impacts of life-limited components on the device operating availability, an estimate of component lifetimes was compiled. Table 12.2 lists system and subsystem components on the device island. (Related items, such as power supplies, refrigerators, and rf drivers, that are outside the vault have not been considered.) Subunits of the halo scraper, the direct converter, the beam line dumps, and the test module (which contains a high-field resistive coil) are not considered separately because their failure requires removing the entire module. All component lifetimes must be regarded as estimates, since no precedent exists for the components of a D-T fusion reactor. Many of these estimates are based on numbers derived for the TDF study.[1]

Of the components listed in Table 12.2, about half are expected to require at least one replacement during the operating lifetime of the device. The others are mainly components that are expected to operate for many full-power years, such as the superconducting coils, and life-limited components with operating lifetimes longer than the full-power operating lifetime of the device, such as the halo scraper and the direct converter.

Table 12.2. Estimated component lifetimes

System	Number of modules	MTBF, h	MTTR, days	Lifetime, FPY
Test modules				
LM1	1			0.10
LM2	1			0.10
SB1	1			0.15
SB2	1			0.15
LM prototype	1			0.10
SB prototype	1			0.10
Test module coil (CC0)	1	≫8,800	>47	L[a]
Solenoid coils (CS)	2	≫8,800	≫47	L
Choke coils (CC1)	2	~2,200	47	0.25
Solenoid coils (S)	10	≫8,800	≫47	L
Choke coils (CC2)	2	~2,200	47	0.25
C coils	12	≫8,800	≫47	L
DC coils	2	≫8,800	>47	L
Drift pumping coils	4	≫8,800	47	L
Halo scraper	2	~8,800	47	1
Direct converter	2	~8,800	47	1
Central-cell beam lines				
Ion source	16	<900	10[b]	<0.1
Ion dump	2	~1,800	47	0.2
Cryopanels	2	~4,400	47	0.5
Bending magnets	2	≫8,800	47	L
Sloshing-ion beam lines				
Ion source	8	<900	10[b]	<0.1
Ion dump	2	~4,400	47	0.5
Cryopanels	2	~4,400	47	0.5
Central-cell beam dumps	2	~1,800	47	0.2
Sloshing-ion beam dumps	2	~4,400	47	0.5
ECRH windows	4	~1,600	47	0.25
ICRH	8	≫8,800	>47	L
Turbomolecular pumps	4			
Oil changeout[c]		~4,000	2	
Bearing changeout[c]		~25,000	3	

[a]L = lifetime component.
[b]Replacement of all sources.
[c]Scheduled maintenance.

The total full-power operating lifetime t_{FP} of the device is calculated by taking the availability for each phase of operation, multiplying it by the number of hours of operation per year H and by the number of years N_x in that phase, and adding the products,

$$t_{FP} = 0.01HN_{I} + 0.03HN_{II} + 0.03HN_{III} + 0.10HN_{IV} ,$$

which yields a total of 6652 h or 0.77 full-power year (FPY), where $H = 8640$; N_{I}, N_{II}, and $N_{III} = 1$; and $N_{IV} = 7$. To obtain the total D-T operating lifetime t_{DT}, the first two terms are omitted,

$$t_{DT} = 0.03HN_{III} + 0.10HN_{IV} ,$$

which yields 6307 h or 0.72 FPY. Obviously, components with lifetimes of $\geqslant 1$ FPY should not need to be replaced during the lifetime of MFTF-α+T.

The column in Table 12.2 that lists the number of modules indicates the component replacement in its modular form. For example, the number of modules for the electron cyclotron resonance heating (ECRH) system is listed as four. In fact, the ECRH system comprises 14 waveguides (7 in each end cell), but they are installed as modules, with one module consisting of 6 waveguides and another consisting of 1 waveguide for each end cell. Hence, replacing the ECRH system (because of damaged windows) requires 4 separate removals, not 14.

The mean time between failures (MTBF) is the number of hours that the component is expected to operate. The MTBF and the availability distribution can be used to calculate the replacement schedule. For example, the 18-T choke coil (CC2) has a lifetime of 0.25 FPY, which corresponds to 2160 h of operation. From the availability in Table 12.1, the annual hours of operation for the device are

- year 1: 86 h,
- years 2 and 3: 259 h each,
- years 4–10: 864 h each.

Thus, the CC2 coil must be replaced 4.8 calendar years after startup and every 2.5 years after that, as shown in Fig. 12.7.

Listed in Table 12.2 are four systems that must be evaluated differently: the TMPs, the CC0 coil, the CC1 coils, and the CC2 coils.

The oil and bearing changeouts[4] for the TMPs represent scheduled maintenance, not component replacement; however, these operations require shutdown of the device, so they are included here. Calendar-year equivalents of FPYs are not applicable because the TMPs operate whenever the machine is not down for maintenance (to sustain vacuum integrity). As shown in Fig. 12.7, 4,000 h corresponds to approximately 1 year; 25,000 h, to approximately 5.7 years.

The MTBF for the choke coils is indirectly related to several other components. The CC0 coil is an integral part of the test module, and even though it is estimated to be a lifetime component, it will be removed when blanket test modules are changed, which occurs

ORNL-DWG 83-3958 FED

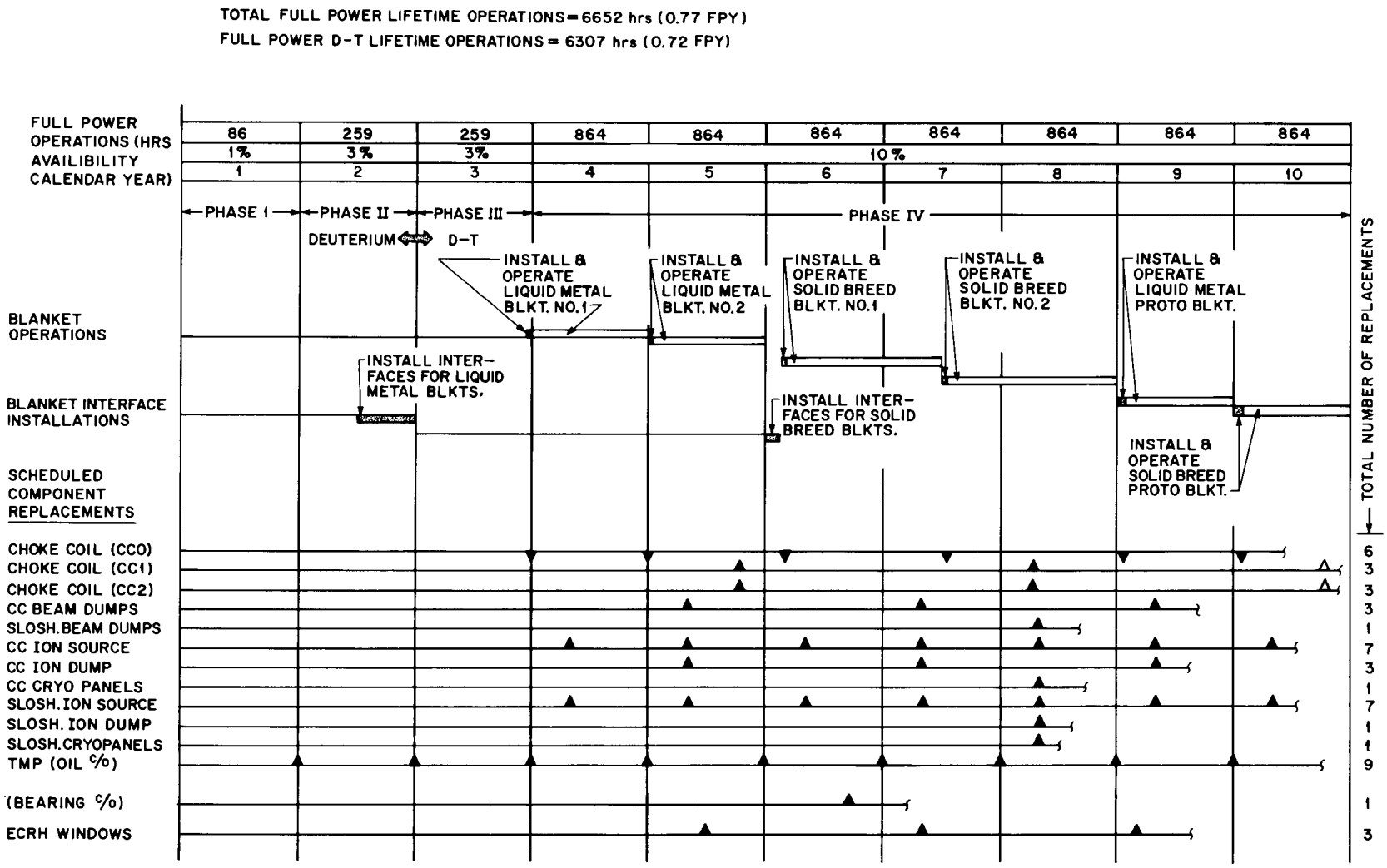

Fig. 12.7. Centerline elevation through end cell showing alcove.

six times in the 10-year life of the device. It might be possible to use the same coil for all blanket modules by remotely removing it from the used blanket module and installing it in the new module in the hot cell. However, this could increase the downtime estimated for blanket installation because of the extra handling and integrity testing operations that would be required. In addition, it could compromise the design features and reliability of the blanket design. It appears more reasonable at this time to assume that a new CC0 coil will be built into each blanket module at the manufacturer's facility, so that it will be an integral part of a test module. This approach is based on the modularity concept, which is the basis for the development of the device configuration. Therefore, in the 10-year lifetime, seven CC0 coils are required: one for initial operations during the first three years and six to be furnished to the manufacturers of the test blankets. Figure 12.7 indicates these replacements using inverted triangles to indicate that they are not required by component failures. Also, these triangles are aligned with the blanket installations for the purpose of discussion. Clearly, these components must be delivered to the blanket manfacturer many months before a test module assembly is completed.

The 12-T normal copper (CC1) choke coils have a limited life. They are attached to their supporting shield segments, which are lifetime components, and their service connections are routed through the shield segments. When a CC1 coil must be replaced, the entire coil/shield module is removed as a unit through the blanket access hatch. The old coil is removed and a new coil is mated to the shield segment in the hot cell. Each 18-T (CC2) choke coil set composes two subassemblies: the outer superconducting coil, which is a lifetime component, and the inner normal copper insert coil, which has a limited life. The coil set is removed as a unit, and the insert coil is replaced in the hot cell. These two situations are the only exceptions to the modular independence of components with different lifetimes. Removal of the CC1 and CC2 coils will have an impact on device downtime since their replacement requires more than simply the installation of spare choke coils; in addition to the remote handling operations in the hot cell, an integrated systems checkout must be performed when the assemblies are reinstalled.

The mean time to repair (MTTR) for each scheduled component replacement is the number of hours required to remove and replace a module and includes the following general procedures:

- 24-h device shutdown period,
- removal/replacement operations,
- repair time, where applicable (choke coils, TMP),
- thermal cycling of the superconducting coils, where applicable,
- testing and checkout, and
- vacuum pumpdown (except for TMP and ion source replacements).

Except for blanket module replacements, for which round-the-clock maintenance operations are assumed, MTTRs are based on two 8-h shifts of maintenance per day, six days per week. The MTTR is a strong function of the time required to thermally cycle the superconducting coils. Values in Table 12.2 are first approximations taken from Fig. 12.8.

Figure 12.7 presents simplified operating data for the device and the relationship of these data to blanket test operations and installations (discussed in Sect. 12.4.3) and component replacements.

Virtually all component replacements occur during D-T operation and will thus require the use of remote handling equipment. The first maintenance operation shown during D-T operation is replacement of oil in the TMPs at the end of phase III. Since the opportunity to accomplish this remotely (as a learning process) is likely during phases I and II, oil changeouts should not present any unforeseen problems. (In fact, this task is one that may be easily automated, considering its frequency.) The initial challenge is expected to be replacement of the central-cell and sloshing-ion beam line ion sources. These and all other scheduled replacements will be handled routinely since the maintenance equipment and the operators will have had ample opportunities for procedure development and experience using the mock-up systems described in Sect. 12.5.

To assess the impact of all of the scheduled replacements on the device operating availability, the 14 replacements listed in Table 12.2 were studied to evaluate required downtimes. Figures 12.8 and 12.9 are timeline charts that show to first order the procedures and the estimated time required. Three categories for components were established.

- Group 1 consists of components with similar replacement procedures for which the vessel must be brought up to atmospheric pressure, which entails warming the superconducting coils. Figure 12.8 shows that these operations require 47 days of device shutdown, primarily because of the need to thermally cycle the superconducting coils.

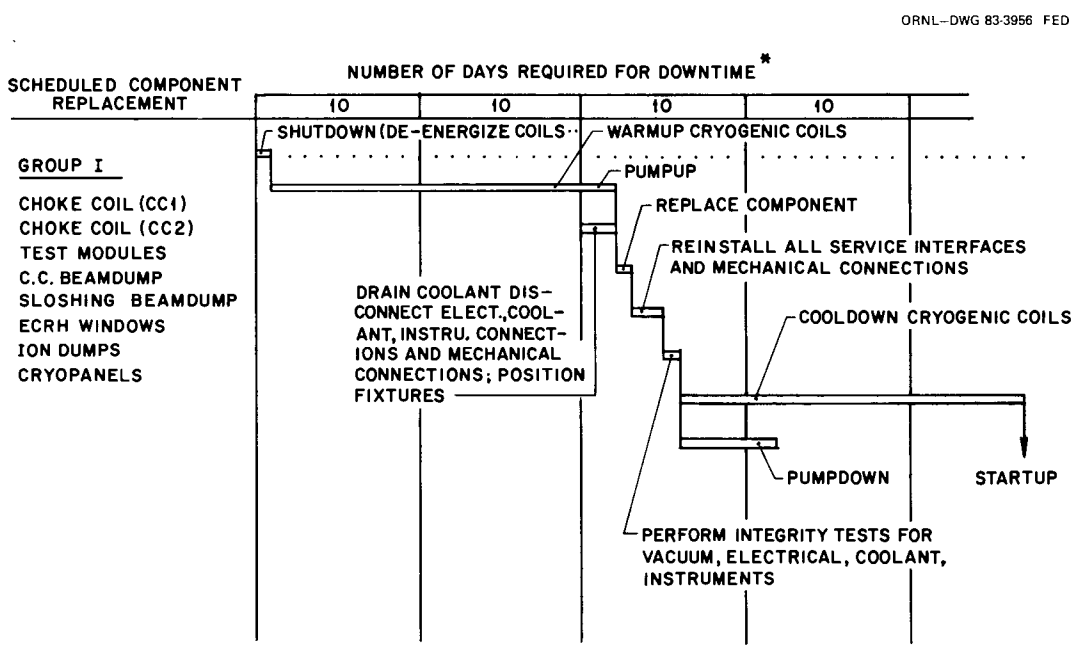

*MAINTENANCE OPERATIONS ARE ASSUMED TO OCCUR 6 DAYS PER WEEK, 2 SHIFTS PER DAY EXCEPT FOR COIL WARMUP/COOLDOWN AND VESSEL PUMPDOWN WHICH OCCUR 24 HOURS PER DAY.

Fig. 12.8. Plan of operations, showing component replacement schedules.

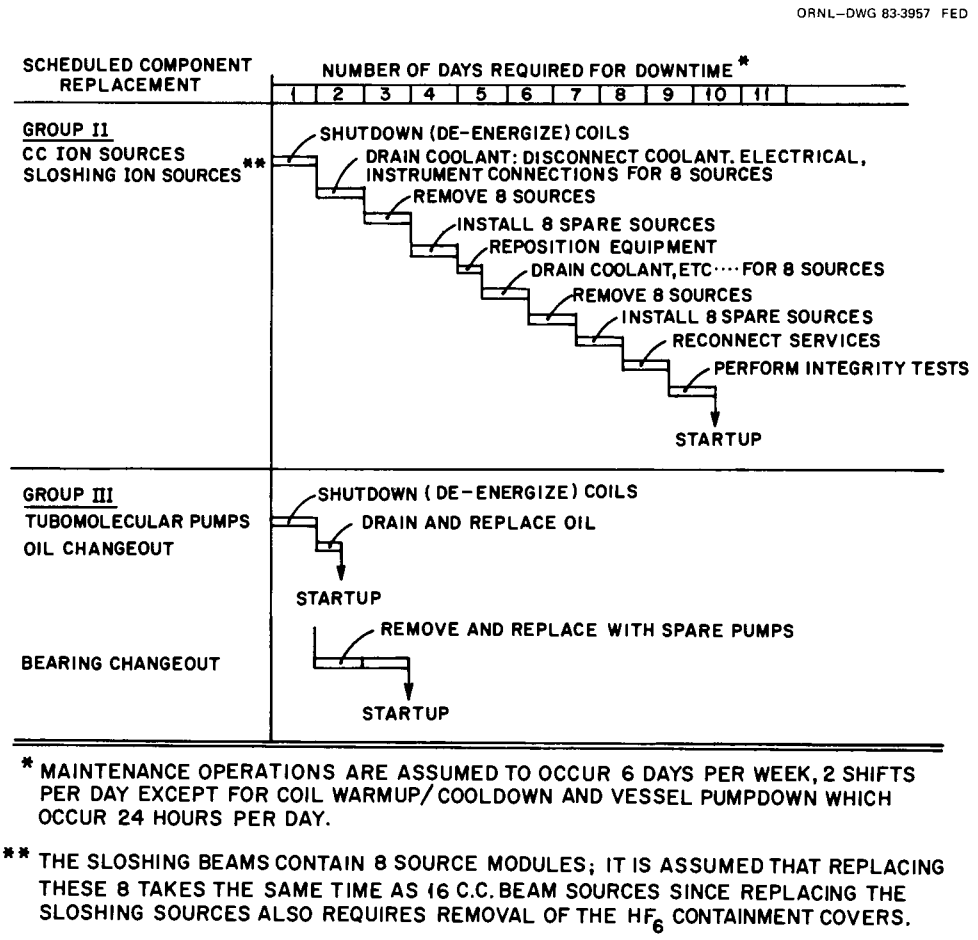

Fig. 12.9. Schedule for replacement of group 1 components (thermal cycling of superconducting coils required).

- Group 2 consists of the beam line ion sources. Their replacement does not affect the vacuum of the plasma chamber because each source has a vacuum-tight valve. Replacement of a Group 2 component is estimated to require 9.5 days of device downtime.
- Group 3 consists of two maintenance activities for the TMPs. Because of the vacuum valves, these do not affect the vacuum of the plasma chamber. Oil changeouts are annual but require only 1.5 days of downtime. The bearing changeout after 5.7 years can be accomplished as hot-cell repair, which would be time-consuming because of remote operations, or the pumps can simply be replaced. The latter is assumed to be the maintenance mode.

By applying the downtime required for each group (from Figs. 12.8 and 12.9) to the schedule of Fig. 12.7, the downtime for each calendar year can be derived. The very conservative assumption that no component replacements are done in parallel can be used to

establish an upper bound on achieving device availability and acts as a test for the feasibility of attaining a 10% operating availability. The results of this compilation are shown below.

Calendar year:	1	2	3	4	5	6	7	8	9	10
Total downtime (days):	1.5	1.5	15.5	34.5	255.5	37.5	175.5	302.5	161.5	127

The plan of operations (Table 12.1) shows two weeks of scheduled downtime per calendar month. This is 144 days per year (if maintenance is scheduled for six days per week). The calculated downtime for years 5, 7, 8, and 9 exceeds this value. However, even in year 8, with the most scheduled serial downtime (302.5 days), the desired operating availability can still be achieved:

$$\frac{365 - 302.5}{365} = 17\% \ .$$

Although this demonstrates that, theoretically, the upper bound on achieving 10% availability has not been reached, the assumption of serial component replacements is unreasonable for several reasons. It places unnecessary cycling on the cryogenic structures, is an inefficient use of manpower and equipment, and uses up time that could be allocated for unscheduled occurrences. Consequently, component replacements are scheduled as parallel operations wherever possible.

As an example, the scheduled replacements during year 8 can be accomplished as follows:

• Shutdown and coil warmup	~3 weeks
• Serial replacement of all group 1 components (8 operations requiring 1 week each)	~8 weeks
• Coil cooldown and vessel pumpdown	~3 weeks
Total downtime	~14 weeks (~100 days)

Therefore, approximately 200 days are gained for other activities.

No analysis of the need for an inventory of replacement components was undertaken for this study; however, it appears that having some spare components on hand is necessary. Figure 12.7 lists the total number of replacements for components over the device lifetime. Clearly, it is not necessary to keep all of these spares in inventory at one time, since components are cycled in intervals of one to several years.

Unscheduled replacement

In general, unscheduled maintenance operations were not considered in developing the details of this study. However, considerations for unscheduled replacements have been factored into the configuration development. The unscheduled replacement with the greatest

potential impact on device availability is that of the superconducting coils. Figure 12.10 shows the large access covers provided for both initial coil installation and any subsequent replacement.

Although no time studies for unscheduled replacements were developed, some judgments can be made about their impact on the operating availability of the device. During the device lifetime, approximately 1100 days of total downtime is reserved for scheduled component replacements. Two weeks per month (approximately 1700 days in 10 years) is assumed to be devoted to scheduled shutdowns. The difference of 600 days between these two amounts is potentially scheduled downtime that can be allocated to unscheduled component replacements. Clearly, a limited number of unforeseen component replacements can be accommodated during the device lifetime.

12.4.3 Test Program Activities

One of the major missions of MFTF-α+T is a successful blanket testing program. The test results from this device will be the basis for future devices with full-scale breeding

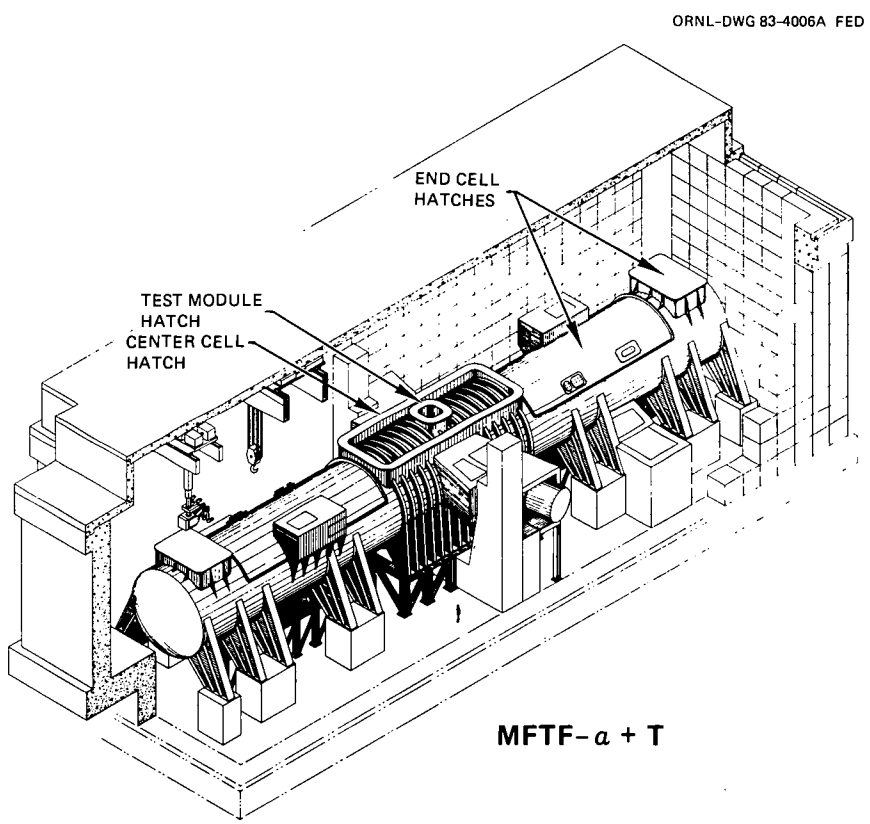

Fig. 12.10. Schedule for replacement of group 2 and group 3 components (thermal cycling of superconducting coils not required).

blanket designs. The MFTF-α+T program requires six blanket module replacements during the last seven years of operation, and the downtime for these is expected to vary according to the particular module being installed. A detailed discussion of the test program is given in Chap. 11. A brief discussion of its relationship to device downtime follows.

During years 4 and 5, two different liquid-metal modules will be tested, followed by two different solid breeders in years 6 through 8. The evaluations of the test results for these four designs will be used to develop one prototype for each concept; these prototypes will be operated during years 9 and 10. Figure 12.7 shows the four phases of device operation and the blanket tests.

It is estimated that two weeks of round-the-clock remote operations will be needed after the vessel is opened to install the liquid-metal blankets (LM1 and LM2). This estimate is based on the assumption that necessary interface connections, piping, device modifications, etc., are carried out before D-T operations begin (i.e., during the last six months of year 2), using a combination of contact and remote operations. Assuming that these modifications are sufficient, LM1 will be installed in two weeks at the end of year 3; LM2 in two weeks at the beginning of year 5.

Before the first solid breeder module (SB1) can be installed, an interface modification period of six weeks of round-the-clock operations is necessary. These operations will essentially be fully remote and will be made easier by practice with the full-scale mock-up system. Once these modifications are made, SB1 can be installed and checked out in two weeks at the middle of year 7.

The prototype modules are expected to use some of the original interface equipment and should be designed to require minimal device modifications for their installation. One month of downtime for each module appears reasonable at the beginning of year 9 and year 10.

12.5 MAINTENANCE EQUIPMENT

12.5.1 Lifting Systems

The MFTF-α+T configuration is designed to take advantage of the linear geometry of the device and of the overhead access afforded by the vault structure. Hence, most components are positioned above the midplane of the device. This permits efficient use of the overhead manipulator system for disassembly and the crane system for lifting and minimizes the need for special handling fixtures. Figures 12.1 and 12.2 show the device arrangement for overhead access and the lifting systems.

The only components that do not require some form of direct lifting for removal are the central-cell beam line ion sources, the lower sloshing-ion beam line sources, the two central-cell solenoid (S5) coils, the two 12-T choke coils, and the structural attachments for the superconducting coils. All other components are removed through access covers, either by straight vertical lifting or by a skewed lift at 45°. Table 12.3 summarizes the component lifting criteria and the required handling fixtures.

The main crane in the vault has a lifting capacity of 150×10^3 kg and is initially used to install components into the vessel. A secondary crane has a lifting capacity of 20

Table 12.3. Component lifting requirements

Component	Type of lift	Special equipment	Weight[a] (10^3 kg)
Test module	Vertical	Rigging[b]	
Beam dump	Vertical	Rigging	
18-T choke coil	Vertical	Rigging	
12-T choke coil	Vertical	Translation fixture	
Solenoid coils	Vertical	Rigging	11/50
C coils	Vertical	Rigging	130
DC coil	Vertical	Rigging	11
Halo scraper	Vertical	Rigging	
Direct converter	Vertical	Rigging	
Ion dump	Vertical	Rigging	
Cryopanels	Vertical	Rigging	
Drift pumping coils	Skewed	Alignment fixture[c]	
ECRH system	Skewed	Alignment fixture	
ICRH system	Skewed	Alignment fixture	

[a]Component weights not listed were not calculated but are estimated to be well within the maximum component lifting requirement.

[b]Cables and spreader bars.

[c]Guiderail-type device.

$\times 10^3$ kg. The bridge for the second crane is also used to transport the overhead manipulator system along the length of the vault.

Both cranes can be preprogrammed to travel to within a few centimeters of a target. Crane operators in the control room must perform only the final precision "inching" operations needed before contact is made with a component. Collision avoidance sensors to avoid crane-to-crane accidents and crane-to-component accidents are provided in two ways. The software controls for crane positioning are designed with interlock modes, and the crane trolleys and hooks are fitted with either optical or acoustical sensing devices.

The sensitivity of the controls for the trolley and crane hook is critical to precise alignment and positioning of components. A precision of several millimeters is envisioned, similar to that required of the crane for the Joint European Torus (JET). Accurate positioning may also entail the ability to rotate the crane hook, although this has not been established as necessary for MFTF-α+T because of its linearity.

12.5.2 Manipulator Systems

A bridge-mounted servomanipulator, similar to the Advanced Manipulator System (AMS) under development in the Fuel Recycle Division at Oak Ridge National Laboratory (ORNL), is proposed for use in MFTF-α+T. The AMS and its operating counterpart, the M-2, have numerous features that are applicable to tandem mirror maintenance

operations. Force reflection is adjustable to a maximum of 8:1 m, meaning that an operator can exercise the maximum 23-kg lift with one of the arms and only feel approximately 3 kg of force. The threshold of force reflection is approximately 2 kg; it is a gear-driven mechanism (rather than tape- or cable-driven) and can be remotely disassembled and maintained. It has integral closed-circuit television (CCTV), lighting, and audio equipment; the arms have a short-duration 45-kg lift capacity; and the system includes a 500-kg lifting hook.

In addition to the overhead manipulator, mobile, floor-mounted manipulator systems are required for remote operations on ion sources, diagnostics, and the equipment and connections in the lower midplane of the device. These are also bilateral, force-reflecting machines that can be positioned in the vault either with the crane or by remotely piloting them to a destination. At least two of these machines are required to handle the sloshing-ion source replacements. In addition, each central-cell ion source cell requires a manipulator system for these replacements.

Like the crane systems, the manipulators can be programmed to travel automatically to a defined position, except that they must first be indexed to some reference point in the vault or on the device. For mobile operations, the manipulator can sight targets using low-energy laser emissions; for fixed operations, the manipulator can be mechanically engaged (locked) into a known position on the device or on the vault floor.

12.5.3 In-Vessel Inspection System

Because of the experimental nature of MFTF-α+T, the ability to routinely "look into" the plasma chamber and view internal components will provide a distinct advantage for assessing component behavior and impending problems. For these investigations to be routine, a device must be introduced into the vessel under vacuum conditions. A schematic representation of an in-vessel inspection system (IVIS) is shown in Fig. 12.11. It consists of an evacuated cylinder that houses a rack-driven extension tube. On this tube is mounted a miniature television camera with a rotatable prism and mirror system. The motorized drive moves the tube into the vessel for viewing or back into the cylinder for storage during device operations. A vacuum valve is provided so that the IVIS can be removed without affecting the vacuum of the plasma chamber. This system is similar in principle to that of JET.

During device operations, the IVIS must be protected from neutrons and gamma radiation, or its operating life will be so short that the system will be useless. Figure 12.11 shows a concept for a movable shield plug that is in front of the viewing system when the device is operating but can be moved aside for inspection. It has a tapered, stepped surface geometry that allows it to slide to a clearance position for introducing the tube-mounted camera. An externally actuated mechanism is required for this movement. With the shield plug in place during plasma operations, it is estimated that the inspection system will have a useful operating life of several hundred hours, assuming a threshold damage level of 10^8 rad for the camera system and operation at a field of 10^5 to 10^6 rad/h.

The installed height of the IVIS is approximately 4.5 m, assuming a penetration into the vessel of 2.5 m to the centerline. A resolution of 4 mm at 2.5 m appears reasonable, since the IVIS for JET is designed to achieve that resolution at 5 m.

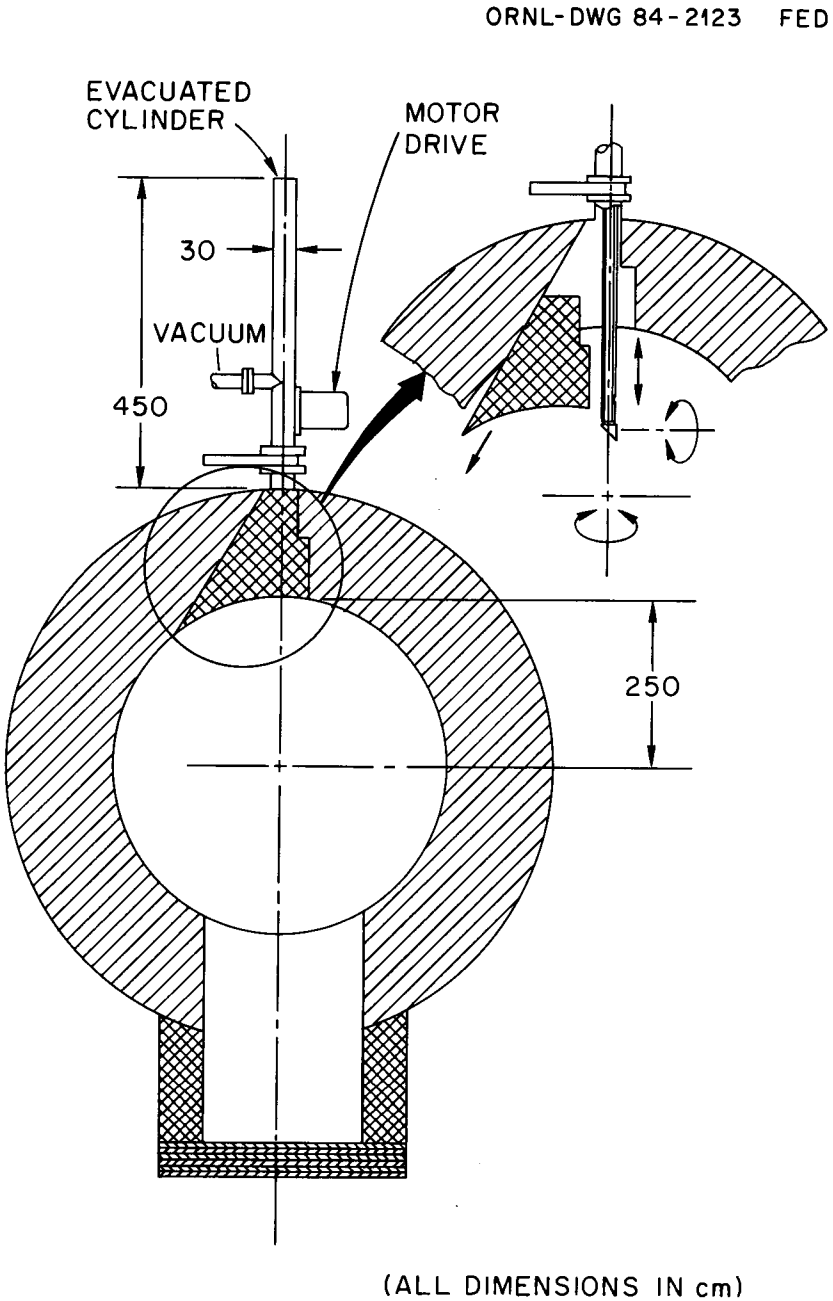

Fig. 12.11. Large access covers that permit unscheduled replacement of components.

A number of devices will be needed along the length of the device to allow inspection of key components and first wall surfaces. An initial estimate is 14 units, 7 on each side of the test module and located as follows:

1. between the test module and the 12-T choke coil,
2. between the 12-T and 18-T choke coil,
3. between the 18-T coil and the T1 coil,
4. between the T1 coil and the A1 coil,
5. between the T2 coil and the DC coil,
6. between the DC coil and the halo scraper, and
7. between the halo scraper and the direct converter.

Units 1, 2, and 6 are oriented vertically; units 3, 4, and 5 are oriented 45° from vertical. Both orientations are indicated in Fig. 12.11.

12.5.4 Mock-Up Systems

Mock-up systems are required to ensure that MFTF-α+T will be a maintainable device. They are used during the design phase to verify the maintainability of the machine and to facilitate the development of maintenance equipment. After the device is built, the mock-up systems serve several functions.

1. They are used for training maintenance personnel and for developing maintenance procedures.
2. They are used to check out installation procedures for equipment added to the device after it begins operating (e.g., the liquid-metal blanket interfaces).
3. They are used to verify the fit of the blanket test modules and the procedures for installing them. This use is similar to using the space shuttle mock-up to certify new pay loads before their installation for launch.
4. They are used as a development fixture to verify the design of components developed during the device lifetime (e.g., a new halo scraper module).

The MFTF-α+T mock-up systems are located in the staging area building, approximately 150 m from the reactor vault. The mock-up facility requires a minimum floor area of 30 by 20 m and sufficient height for overhead lifting simulations. This area represents about half of the staging building and is adequate to duplicate about half of the actual device. Since the device is essentially symmetrical, the length of the mock-up will probably include everything from the test module to the end dome, except that only one of the five solenoid coils needs to be included. The 20-m depth includes one vault wall to the other. All device components and their access ports are included in the mock-up. This includes components identified for scheduled replacements, as well as the direct converter system and the halo scraper system. It is not yet clear if the lifetime coil system (i.e., the C and DC coils) should be included for simulated handling operations, since these could be fabricated, installed, and tested while a real coil was being fabricated. A cost/benefit analysis is required to support such a decision.

Some major device components will require separate mock-up systems because of their arrangement on the device. The central-cell ion sources are one example. Access to these

components is actually outside the vault in a separate cell. In addition, mock-up of the repair operations for these sources and those of the sloshing beam lines requires a simulated repair shop where refurbishing and conditioning of sources can be simulated, particularly for any new designs that may be developed.

The mock-up facility requires a duplicate set of the manipulator systems and other equipment used in the vault. These include the bridge-mounted manipulator, a floor-mounted manipulator, and all of the handling rigs and alignment fixtures. Also needed is a replica of the control room used for remote operations. It is anticipated that the overhead crane need not be duplicated exactly since very large components will only be mocked up in terms of size, shape, and center of gravity, and not in terms of actual mass. For example, a mock-up of C coil can be fabricated at approximately one-tenth of its actual weight, requiring a lifting capacity of 13×10^3 kg. The necessary overhead crane capacity, therefore, is estimated to be $<20 \times 10^3$ kg for the mock-up facility.

REFERENCES

1. *A Tandem Mirror Technology Demonstration Facility*, UCID-19328, Univ. California, Lawrence Livermore Natl. Lab., Livermore, Calif., October 1983.

2. W. M. Stacey, Jr., et al., eds., *U.S. FED-INTOR Activity and U.S. Contribution to the International Tokamak Reactor Phase-2A Workshop*, TD-202/USA-82, Commission European Communities, Brussels, October 1982, Appendix D, p. 176.

3. H. F. Dylla, "A Review of the Wall Problem and Conditioning Techniques for Tokamaks," *J. Nucl. Mater.* **93 & 94**, 61–74 (1980).

4. C. A. Flanagan, D. Steiner, and G. E. Smith, eds., *Fusion Engineering Device Design Description*, ORNL/TM-7948/V1, Oak Ridge Natl. Lab., December 1981, p. 3-50.

13. PLANT FACILITIES

S. Ghose

Lawrence Livermore National Laboratory

CONTENTS

13.1 INTRODUCTION 13-3
13.2 REQUIREMENTS AND CRITERIA 13-3
13.2.1 Functional Requirements 13-3
13.2.2 Design Criteria 13-3
13.3 DESIGN DESCRIPTION 13-4
13.3.1 Mechanical Systems 13-4
13.3.2 Buildings and Structures 13-7

13. PLANT FACILITIES

13.1 INTRODUCTION

The facilities of the Mirror Fusion Test Facility (MFTF-B) at Lawrence Livermore National Laboratory (LLNL) are to be used as fully as possible to support the housing, installation, operation, and maintenance of the MFTF-α+T device. Major upgrades to the existing facilities are dictated by the requirements for safe operation of the device. The radioactive tritium used as fuel must be confined, and shielding is needed to protect personnel and equipment from neutron and gamma radiation. Additional upgrades are needed to allow remote maintenance and remote handling of activated components. Facilities are needed for on-site handling and processing of tritium gas. The heat removal system must be upgraded because MFTF-α+T rejects more heat on a steady-state basis than does MFTF-B. The preconceptual studies described in this section indicate that there should be no major obstacles to accomplishing these upgrades.

13.2 REQUIREMENTS AND CRITERIA

Functional requirements and design criteria were applied to studies of the upgrade of plant facilities for MFTF-α+T.

13.2.1 Functional Requirements

The plant facilities for MFTF-α+T must provide

- housing and structural support for all equipment, components, and services;
- protection against excessive release of radiation to the environment (see Chap. 14);
- protection against natural phenomena (e.g., tornado, missile, and seismic events) for the public and for plant personnel;
- safe and efficient movement of material, personnel, and equipment as needed for operation and maintenance; and
- services needed to ensure safe functioning of the plant (e.g., cooling water supply, electricity, radioactive waste handling facilities).

13.2.2 Design Criteria

There are many design requirements for the plant facilities, but most apply only to a detailed design. For the present conceptual design effort, only a few major design criteria were applied.

- The internal surfaces of the reactor building, hot cell, and tritium building must present a barrier to tritium permeation, so that these surfaces do not become sources of radioactivity release.
- The reactor building, hot cell, and tritium building must be reasonably leaktight (leakage < 24 vol %/d) to limit the leakage of radioactive gases (primarily tritium).
- The internal surfaces of the reactor building and the hot cell must provide shielding adequate to limit on-site dose rates from neutron and gamma radiation to less than 100 mrem/year.

- The cooling systems must be able to remove the 140-MW thermal power load from the reactor, its support systems, and miscellaneous plant facilities during normal operation and must also remove the estimated <1-MW emergency cooling load (for the atmospheric tritium cleanup units, diesel generators, and control building) needed when the normal cooling water supply is disrupted.

13.3 DESIGN DESCRIPTION

13.3.1 Mechanical Systems

Heat transport system

The MFTF-B heat transport system (HTS) is shown in Fig. 13.1. The HTS is only one part of the LLNL plant cooling water supply system. Its continuous heat removal capacity is about 10 MW. This is adequate for the 30-MW heat removal requirement of MFTF-B only because this device operates on 30-s pulses, and the thermal capacitance of the reactor components is high enough that they can cool over an extended period without exceeding the allowable temperature rise. In contrast, MFTF-α+T will operate in a steady state and will have a continuous heat removal requirement of 140 MW. The "upgrade" of this system will essentially entail installation of a completely new system. However, as much existing equipment (e.g., piping, valves, instrumentation) as possible will be used in the MFTF-α+T system.

The HTS proposed for MFTF-α+T provides equipment and facilities to supply high-purity demineralized and deionized cooling water as needed to remove heat from the reactor and the auxiliary components of the plant during normal operation. The components served by the system and the cooling loads are listed in Table 13.1.

The HTS is shown in Fig. 13.2. There are three primary heat transport loops and a heat rejection loop that disposes of the heat to atmosphere through a mechanical draft wet cooling tower. Separating the primary heat transport into three loops has two advantages. First, it separates components operating in a tritium and neutron environment (those in the reactor cooling and power absorption loops) from other components. Second, it allows

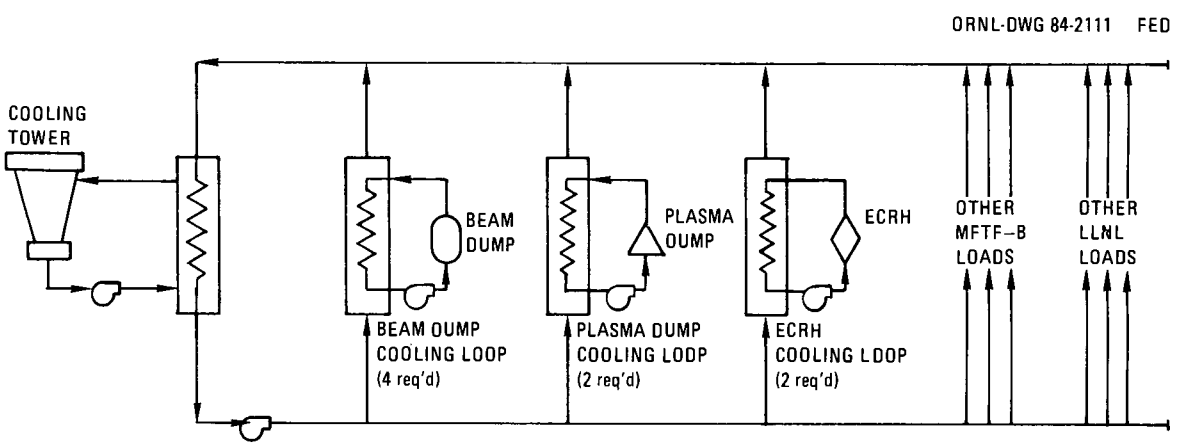

Fig. 13.1. Heat transport system for MFTF-B.

Table 13.1. Major plant cooling loads

Systems and components	Cooling load (MW)
Power absorption surfaces	
Neutral beam dump	7
Neutral beam (internal)	33
End-cell dump	18
Total	58
Reactor components	
Copper coils	38
Shield	15
Electron cyclotron resonance heating	5
Fuel processing and cleanup	4
Total	62
Facilities and other systems	
Cryogenic system	12
Power conversion	2
External vacuum	1
HVAC and miscellaneous	5
Total	20
Grand total	140

operation of the power absorption loop at a high coolant pressure to avoid boiloff (which may result from high surface heat loads). The peak coolant pressure in this loop is 2.4 MPa; that in both the reactor and facility cooling loops is 1 MPa. Hot and cold leg temperatures in the cooling loops are 60°C and 43°C, respectively; those in the heat rejection loop, 45°C and 28°C.

Emergency cooling water system

The emergency cooling water system provides cooling primarily to the atmospheric tritium cleanup units (ATCUs); the solid waste system; the diesel generators; and the control building heat, ventilation, and air conditioning (HVAC) systems during abnormal operating conditions (e.g., during an incident when the reactor has been shut down, there is a large tritium leak, and the diesel generators are supplying power). The ATCUs are the major components requiring emergency power, and it is assumed that no more than one ATCU will be operating at full capacity under abnormal conditions. The largest cooling water load occurs when the reactor ATCU is in emergency operating mode.

The system is shown in Fig. 13.3. It consists of a closed cooling loop with a forced draft water-to-air heat exchanger to reject heat to the atmosphere.

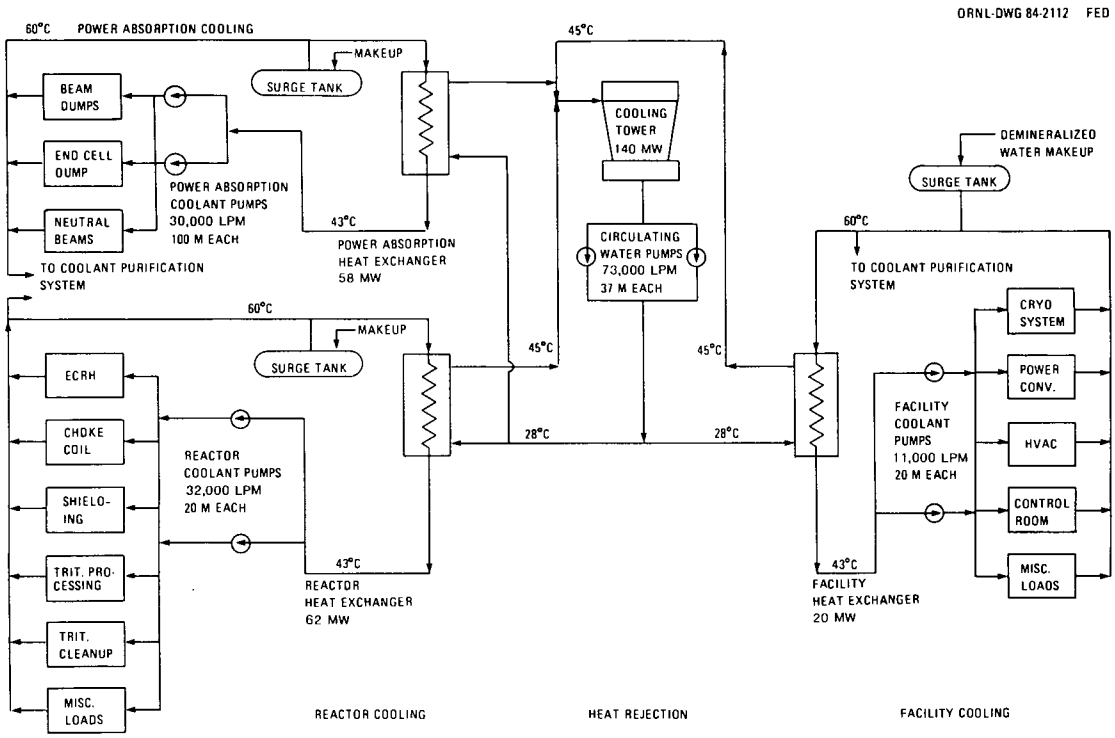

Fig. 13.2. Heat transport system for MFTF-α+T.

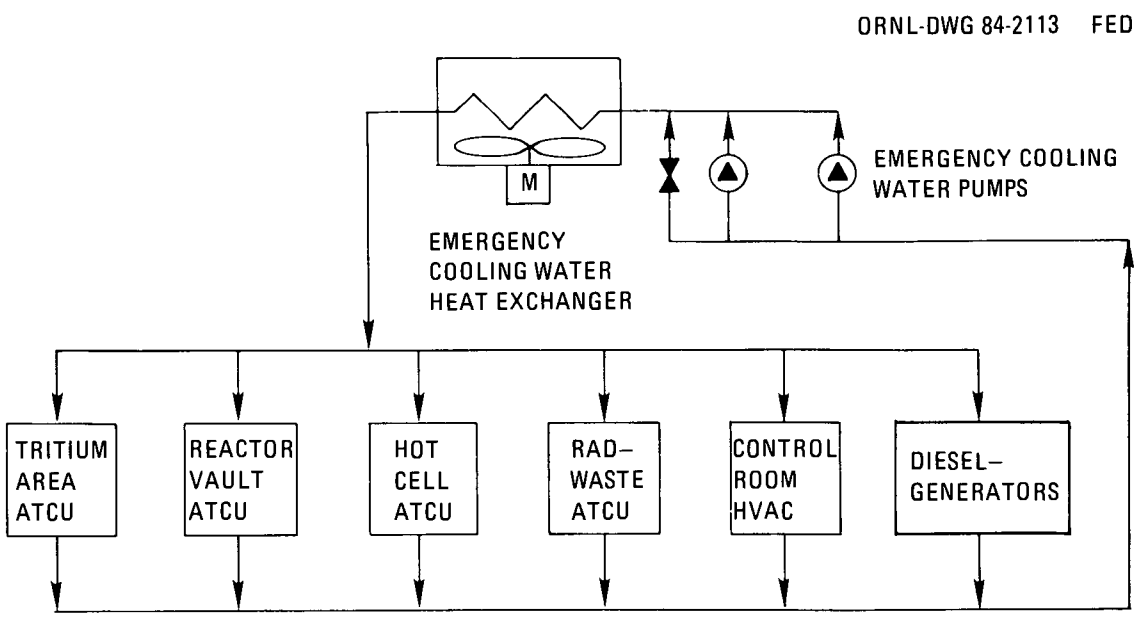

Fig. 13.3. Emergency cooling water system.

13.3.2 Buildings and Structures

Upgrades of major buildings and structures to accommodate the MFTF-α+T device are briefly discussed in this section. Figure 13.4 shows the locations of major buildings and structures, and Fig. 13.5 shows a plan view of the existing MFTF-B reactor vault in Bldg. 431.

Reactor vault

The existing reactor vault generally meets the functional requirements and design criteria discussed in Sect. 13.2. However, preconceptual studies have identified several areas in which some upgrading will be needed.

The vault must be modified to accommodate

- wall openings for the central-cell neutral beam injectors,
- a wall opening for removal and replacement of the test module and activated components,
- wall openings for viewing windows, and
- the addition of an overhead crane.

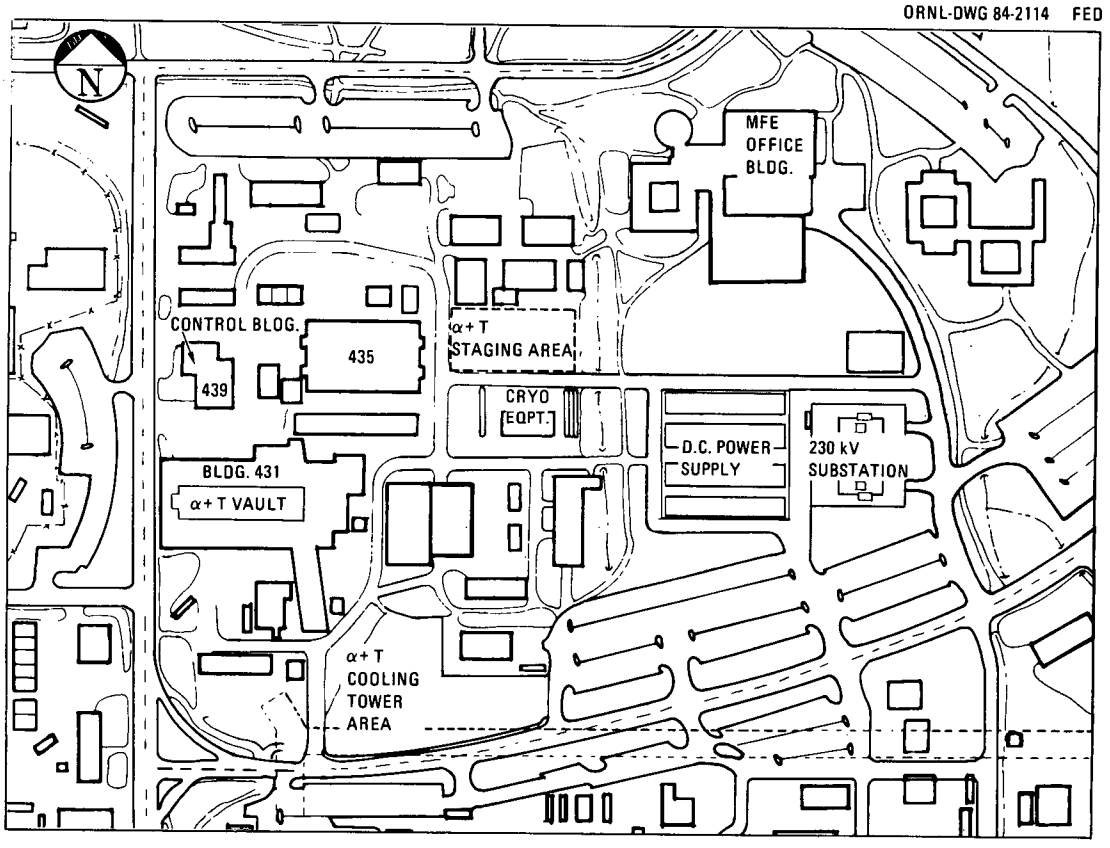

Fig. 13.4. MFTF-α+T site plan.

ORNL-DWG 84-2115 FED

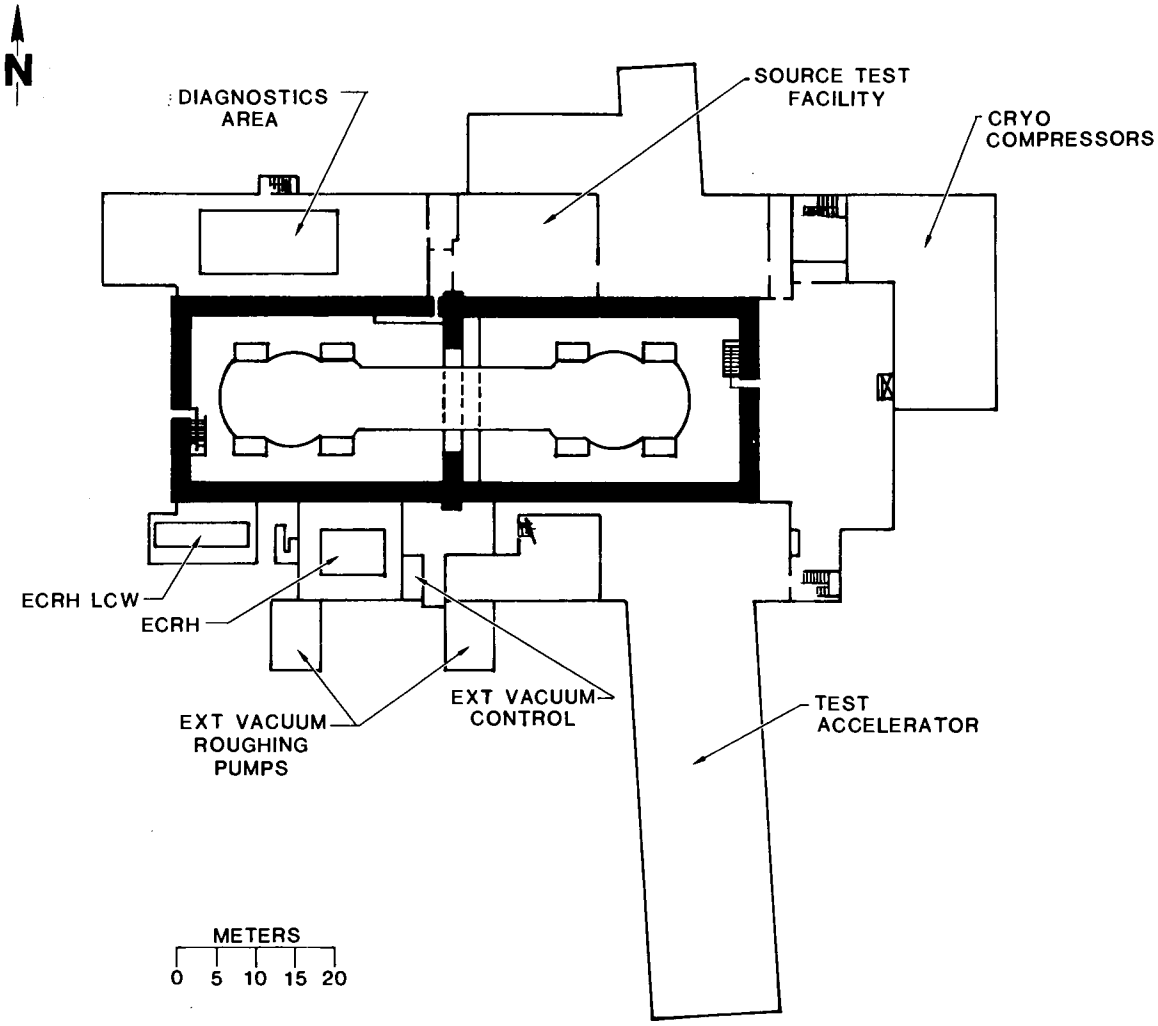

Fig. 13.5. First floor of Bldg. 431 with MFTF-B in vault.

Because the central-cell beam lines project into the north and south vault walls and to facilitate removal of beam line components into the hot cells for maintenance, two openings are required, one in the north wall and one in the south wall (see Fig. 13.6). Another opening on the south wall is needed for transferring test modules and activated components into the hot cell. Four wall openings are required for viewing windows that permit direct observation of remote maintenance operations. There is no crane in the MFTF-B vault, but one will be needed for installation and remote maintenance on MFTF-α+T. To accommodate an overhead crane within the vault and to provide headroom for lifting components, the vault roof is raised about 5 m, as shown in Fig. 13.7. The effect of this modification on the seismic capability of the vault has not been investigated. (The possibility of supporting a crane from the vault walls was investigated by the Bechtel Group, Inc.; details are given in Appendix A. The overhead crane is the reference design.)

ORNL-DWG 84-2116 FED

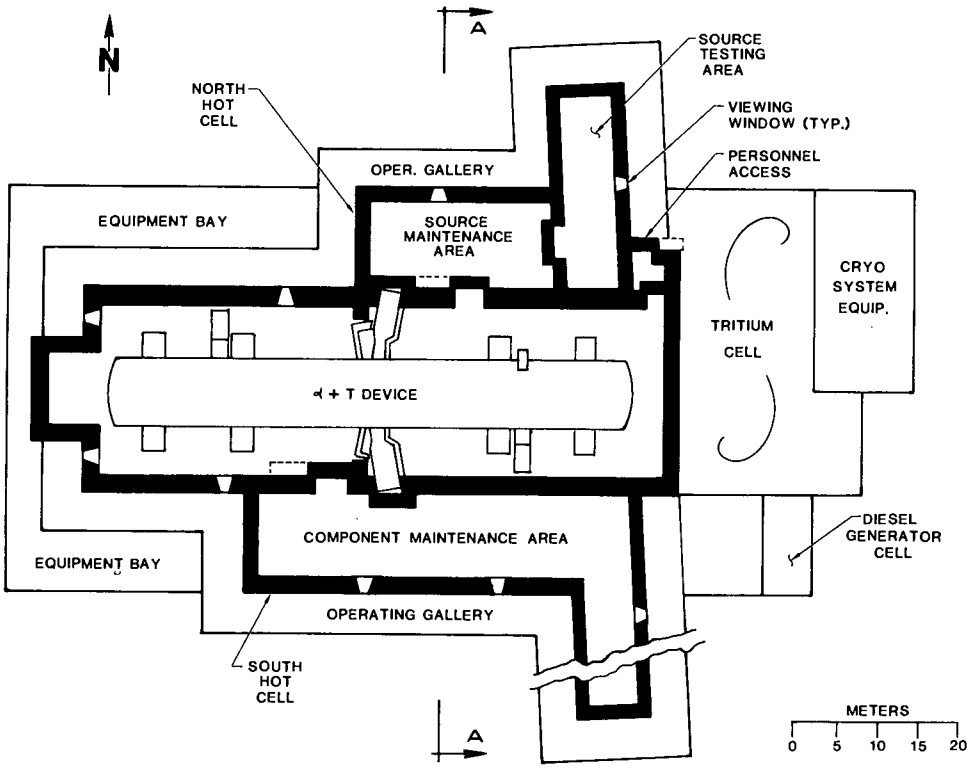

Fig. 13.6. First floor of Bldg. 431 with MFTF-α+T in vault.

ORNL-DWG 84-2117 FED

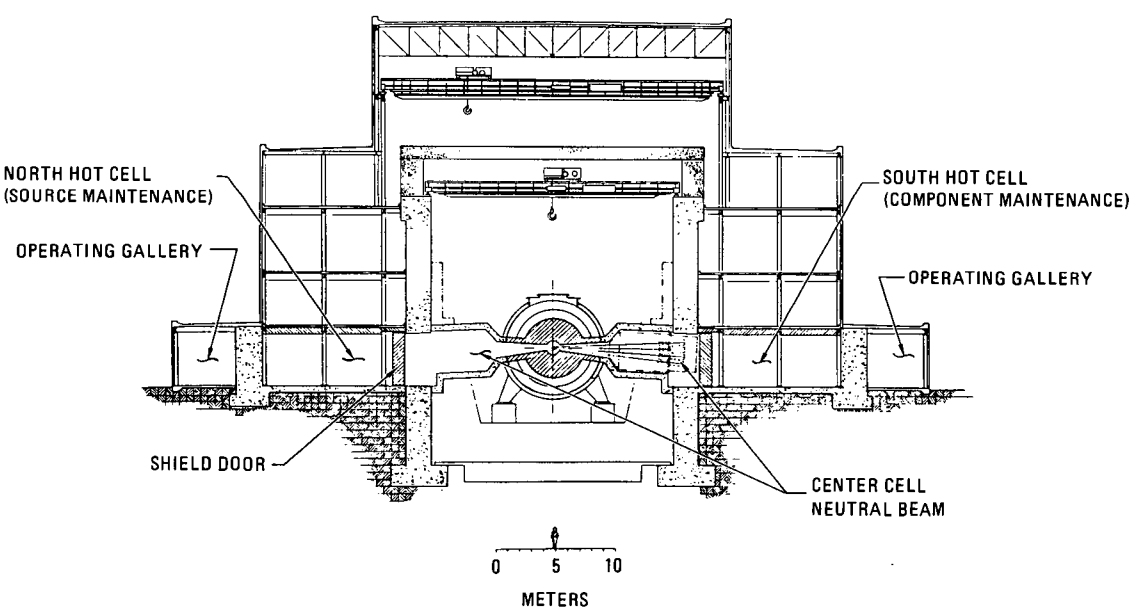

Fig. 13.7. Cross section of Bldg. 431 with MFTF-α+T in vault.

The reinforcement of the vault must be upgraded to meet the seismic accelerations specified for MFTF-α+T. The standards established by LLNL are an operating basis earthquake (OBE) of 0.4 g and a design basis earthquake (DBE) of 0.8 g. A preconceptual assessment of the vault's seismic capability was made by the Bechtel Group, Inc. The block wall strength was calculated, and the results showed that the prestressing at the center of the walls is not adequate to resist bending moments due to earthquakes. In addition, the reinforcement of the existing cast-in-place walls appears inadequate to develop resisting moments (additional calculations are needed to confirm this conclusion). Several methods of upgrading the reinforcement were considered. These included

- providing a rigid connection between roof and wall, which would reduce bending moments at the base of the wall for lateral loads;
- providing outside reinforcement by using steel plates attached to wall surfaces with drilled anchors;
- installing additional vertical prestress tendons; and
- removing the blocks and replacing them with monolithic reinforced concrete (a detailed assessment of this option is presented in Appendix A).

For this study, the reference method of reinforcement is providing a rigid connection between roof and wall.

The vault must also be sealed to minimize adsorption of tritium and subsequent release of radioactivity within the vault, which would make it difficult to maintain allowable dose rates for maintenance personnel. At the Tritium Systems Test Assembly (TSTA), an epoxy coating is being used as a protective lining for internal surfaces. Use of such a coating is proposed for MFTF-α+T, with the expectation that TSTA operation will confirm the suitability of this material.

A further tritium-related concern is the leakage of radioactive gas from the vault. The vault must be made leaktight so that the radiation dose to both on-site and off-site personnel can be kept well below allowable limits. The east wall of the reactor vault is made of concrete blocks, which are more likely to leak than the cast-in-place west wall. Leaky areas between blocks and electrical, mechanical, and control penetrations in the walls must be sealed. No method has been identified, but the necessary extent of sealing will depend on the degree of leakage that is acceptable and achievable at a reasonable cost.

Hot cells

The hot cells provide space and facilities for remote maintenance of activated components. Very rapid repair of failed components will not be as important for MFTF-α+T, which has an availability goal on the order of 10%, as it will be for a device with higher availability goals (e.g., a power reactor). Thus, general-purpose (rather than highly specialized) facilities are proposed for the MFTF-α+T hot cells.

Two hot cells are provided, one on the north and one on the south side of the vault. These cells use existing facilities—a shielded source testing facility on the north and shielded space formerly occupied by the Advanced Test Accelerator Facility on the south. The north hot cell is dedicated to the maintenance and testing of beam line sources. The south hot cell, which is larger, is used for the maintenance and testing of test modules and

other activated components. Both hot cells have operating galleries to facilitate local control of maintenance operations.

Tritium processing facility

The tritium facility for MFTF-α+T is a highly reliable, full-scale processing plant based on TSTA prototypes. The facility is separate from the reactor building but adjacent to it to minimize the length of tritium feedlines (and thus the tritium accident potential). The tritium facility is designed for contact maintenance; it has an air environment and is free of gamma and neutron radiation. Atmospheric tritium levels are maintained at 5 μCi/m^3. The total enclosed volume of the tritium facility is about 12,000 m^3, and it is designed to the same seismic criteria as the reactor building.

The tritium storage area is located within the tritium facility and consists of a shielded, barricaded vault in which an inert cover gas is used for fire protection. Most of the tritium is stored as UTX, but some low-pressure storage in tanks is provided. Storage space is also provided for nontritiated gaseous deuterium and hydrogen and for helium and nitrogen.

All tritium handling units are under remote, independent, hardwired computer control, and the computer is equipped with an uninterruptible power supply. A slight negative pressure is maintained by a self-contained HVAC system that is interfaced to the atmospheric tritium cleanup system to minimize tritium leakage.

The first floor of the tritium processing facility (Fig. 13.8) contains the ATCUs and the two airlocks that provide personnel access to the facility. One airlock is designed for routine use and connects the tritium cell with the health physics area; the other is designed for equipment transfer and emergency use.

On the second floor (Fig. 13.9), the tritiated water recovery unit, the gaseous tritium waste treatment unit, and the solid waste treatment and disposal unit (which generate and/or process tritiated waste) are located to provide easy waste removal. The isotope separation unit (ISS) is tall (Figs. 13.9 and 13.10); the 4-m-high vacuum shell around each unit must be removed vertically (Fig. 13.11).

The third floor contains the HVAC system (Fig. 13.12) and three service areas. The chemistry laboratory is used for routine analyses on catalysts, molecular sieves, etc. Nonactivated tritium monitors are serviced and tested in the radiation monitoring laboratory, and tritium units are repaired in the maintenance area.

Safety procedures are followed to minimize worker contact with tritium. Normal hydrogen fire prevention practices are followed.

ORNL-DWG 84-2118 FED

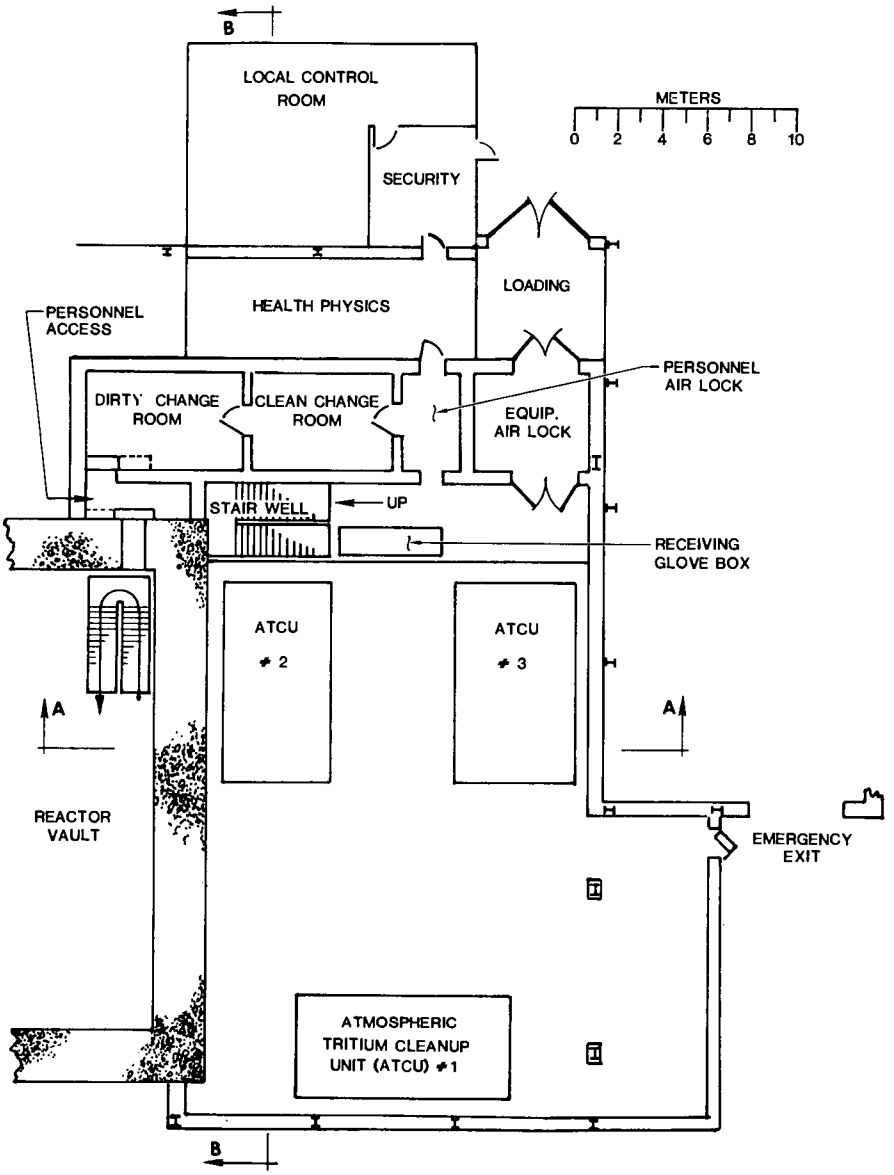

Fig. 13.8. First floor of tritium processing facility.

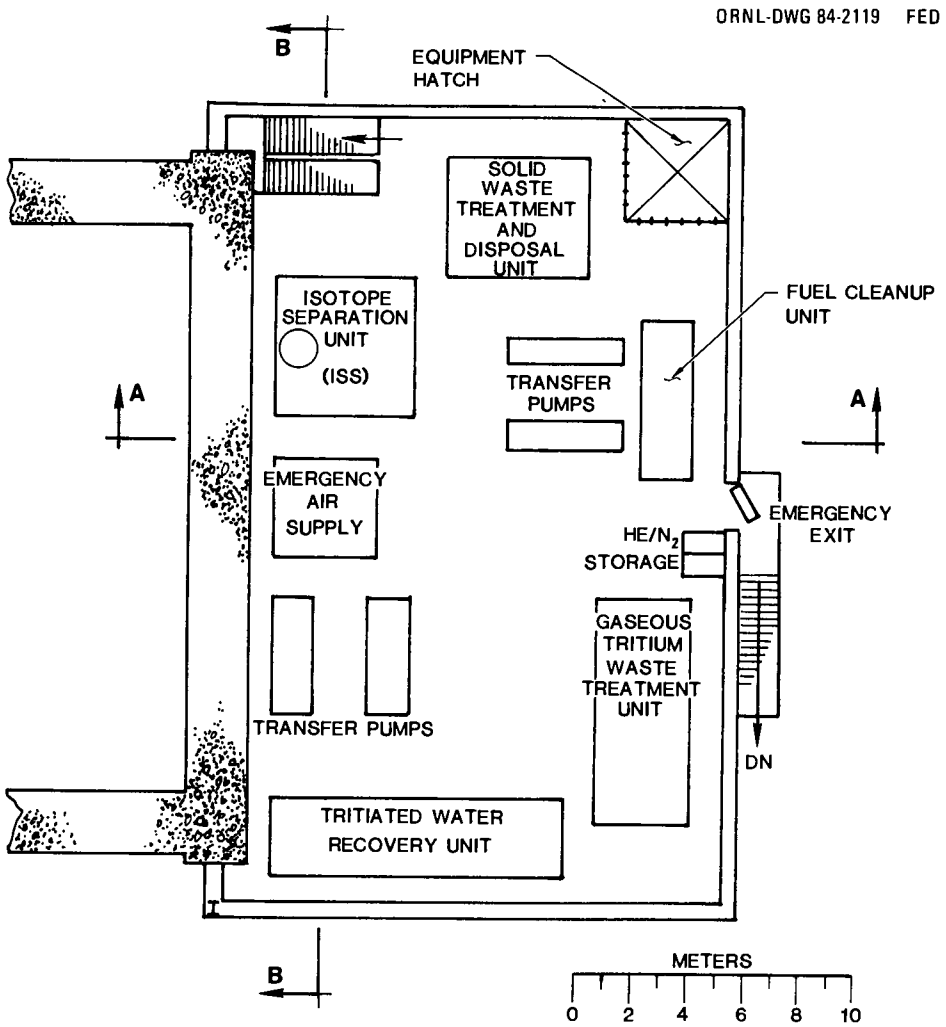

Fig. 13.9. Second floor of tritium processing facility.

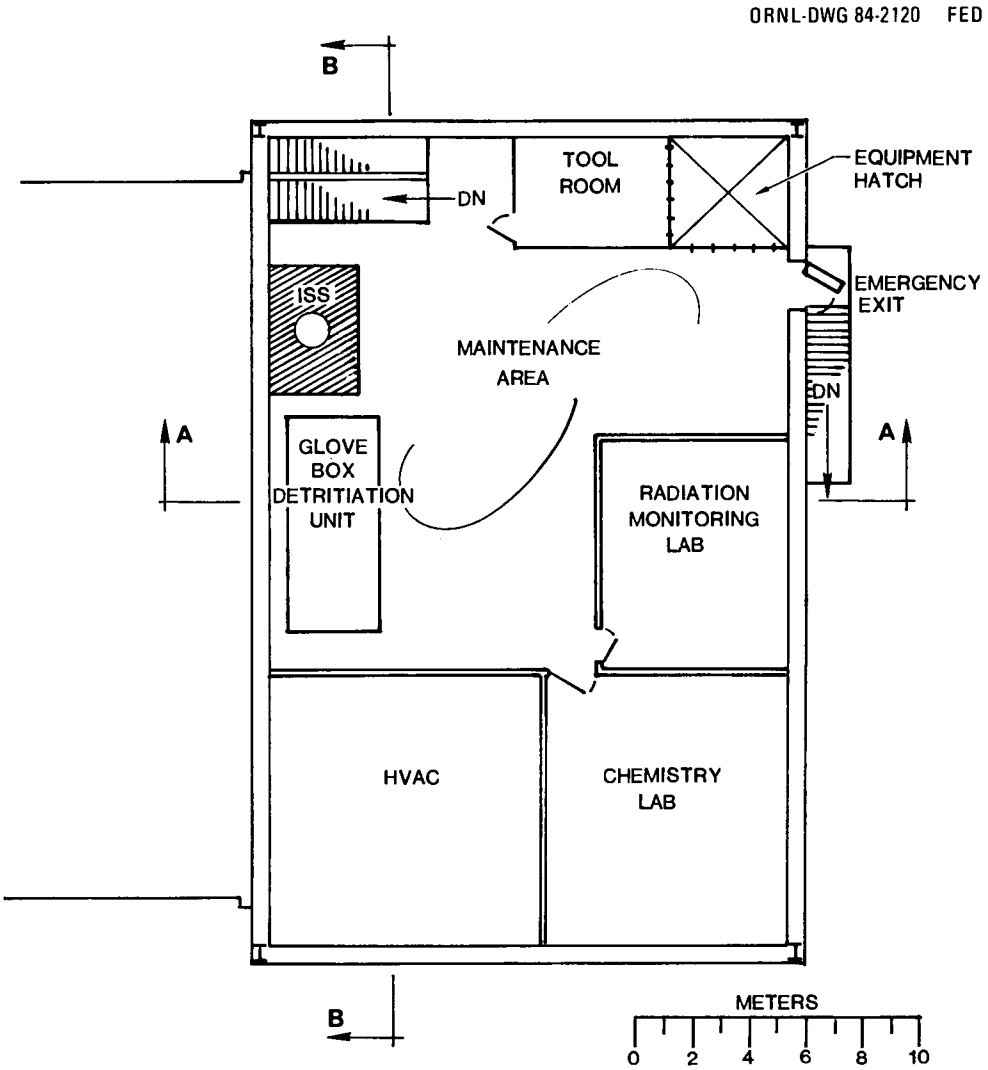

Fig. 13.10. Third floor of tritium processing facility.

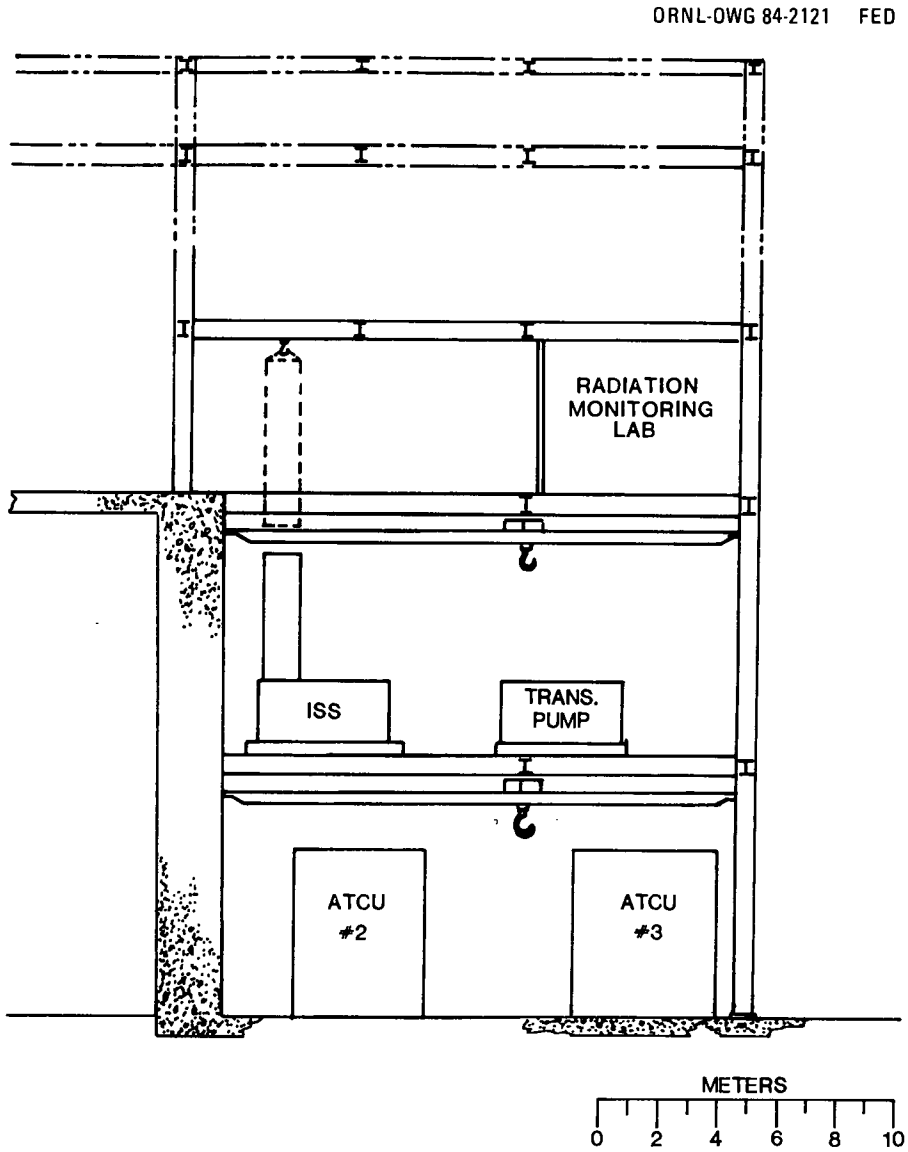

Fig. 13.11. Cross section of tritium processing facility (A-A).

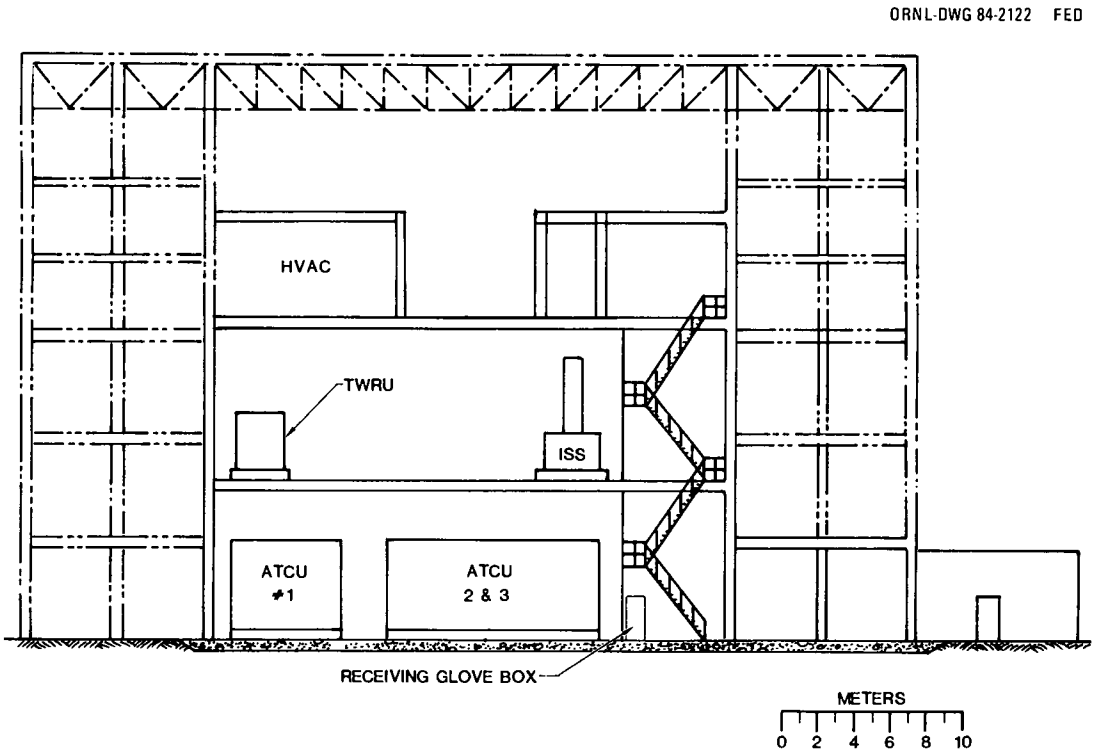

Fig. 13.12. Cross section of tritium processing facility (B-B).

14. SAFETY AND SITING

S. Ghose

Lawrence Livermore National Laboratory

CONTENTS

14.1 INTRODUCTION 14-3
14.2 SAFETY CRITERIA AND REQUIREMENTS 14-3
14.3 POTENTIAL RADIOLOGICAL HAZARDS AND CONSEQUENCES .. 14-6
14.3.1 Releases During Normal Operation 14-6
14.3.2 Releases During Off-Normal Conditions 14-7
14.4 SAFETY FEATURES 14-10
14.5 SITING 14-11
14.6 SUMMARY 14-11
REFERENCES 14-12

14. SAFETY AND SITING

14.1 INTRODUCTION

A preliminary assessment of the safety aspects of MFTF-α+T was carried out. The objectives of the assessment were to identify the safety issues for MFTF-α+T, to estimate the potential radiological hazards and consequences, and to describe the safeguards in the design of the device and supporting facilities.

The approach of the design studies for the Fusion Engineering Device (FED)[1] and for STARFIRE[2] was used in performing the assessment. Safety standards, criteria, and radiological guidelines are based on Department of Energy (DOE) orders and procedures.[3–8]

Potential safety hazards in MFTF-α+T and their results are shown in Table 14.1. The major safety issues involve tritium, neutron activation of reactor components, and corrosion products carried by the reactor coolant. Tritium is by far the most important of these issues, and tritium-related safety was the only issue addressed during this study period. The remaining issues will be addressed as the study progresses.

A discussion of safety criteria and requirements is presented in Sect. 14.2. Potential radiological hazards and consequences are discussed in Sect. 14.3, and safeguards incorporated into the MFTF-α+T device are outlined in Sect. 14.4. The safety aspects of the siting of MFTF-α+T are addressed in Sect. 14.5, and a summary is given in Sect. 14.6.

14.2 SAFETY CRITERIA AND REQUIREMENTS

The safety criteria used for this assessment are based on refs. 3 and 4, which give several applicable guidelines. The DOE policy is to limit radiation exposure of individuals and population groups to levels "as low as reasonably achievable (ALARA)." For DOE-sponsored projects, interpretation of the ALARA policy is carried out under the safety

Table 14.1. Sources of safety hazards in MFTF-α+T design

Potential hazard	Possible result
Tritium inventory	Tritium release
Induced radioactivity in the shield, magnet, structural material, and building structures	Release of activated structural materials
Corrosion products in the primary coolant	Loss of coolant flow to the heat dumps
Cryogenics	Release of liquid helium
RF heaters	RF heater failure
Lithium in test modules	Lithium fire

analysis and review system described in ref. 5, which determines whether a proposed design meets the intent of the policy. The DOE guidelines suggest that, under normal operating conditions, the radiation dose to an individual at the site boundary should be limited to <10 mrem/year; under off-normal or accident conditions, to <1 rem in a 2-h period.

Operating conditions for MFTF-α+T and suggested safety guidelines are presented in Table 14.2. Proposed radiation exposure guidelines for these conditions are listed in Table 14.3. The guidelines proposed in Table 14.3 are to be interpreted as minimum guidelines to protect health and safety. They apply only to MFTF-α+T and should not be construed as applying to other present or future fusion test facilities, research facilities, or reactor projects. The values quoted are for whole-body exposures; DOE values for organs (e.g., hand, arm, bone) and other time periods (e.g., quarterly totals) are also applicable.

Table 14.2. Safety guidelines for MFTF-α+T operating conditions

Operating conditions[a]	Description	Probability of occurrence P, year^{-1}	Safety guidelines
I	Regular planned events (e.g., normal facility operations)	$P = 1$	Normally operating modes should provide health and safety protection
II	Events that may occur several times during life of facility (e.g., minor incidents)	$1 > P > 10^{-1}$	Facility should be able to return to operation without extensive corrective action
III	Events that may occur infrequently during life of facility (e.g., more severe incidents)	$10^{-1} > P > 10^{-3}$	Facility should be able to return to operation following extensive corrective action
IV	Limiting fault events that are not expected during life of facility but are postulated because of potential significant radioactive release and because they represent upper bounds on failures or accidents with sufficient probability ($>10^{-7}$ per year) to require consideration in design	$10^{-3} > P > 10^{-7}$	Facility damage may preclude return to operation
V[b]	Events of extremely low probability that do not require consideration in design	$P < 10^{-7}$	

[a]Definitions for conditions I–IV are taken from *Nonreactor Nuclear Facilities: Standards and Criteria Guide* (draft), U.S. DOE, Washington, D.C., 1981.

[b]Definition adopted for MFTF-α+T.

Table 14.3. Dose limits and guidelines for MFTF-α+T

Operating condition[a]	Off-site Description	Off-site Limit	Off-site Design objective	On-site Description	On-site Limit	On-site Design objective
I	Dose per individual, mrem/year	500	≤10	Dose in uncontrolled area, mrem/year	500	≤100
II	Dose per individual, mrem/year		≤100	Dose in controlled area, mrem/year	500	≤1000
	Dose per average population member, mrem/year	170	≤35			
III	Dose, rem	5	≤1	Dose, rem	5	≤5
IV	Dose, rem	25	≤5	Dose, rem	25	≤25

[a]As defined in Table 14.2.

The nuclear shielding of MFTF-α+T is designed to ensure that the dose rate in the vault is 0.5 mrem/h 24 h after device shutdown. This meets the existing LLNL requirement for radiation zones accessed by personnel. The Fusion Engineering Design Center (FEDC) carried out a scoping study[9] that assessed biological dose rate guidelines as a function of device availability and worker availability. For devices with a high availability (≫10%), the time that a worker may spend near the device is limited by the amount of downtime available for maintenance. Therefore, dose rate levels may be higher than the current device designs assume. For example, if contact maintenance operations require only 100 h per worker annually, then even with a dose rate at the shield as high as 10 mrem/h the ALARA guideline of 1 rem/year can be met. This example is greatly oversimplified, since it does not account for background radiation from the vault or other structures, but it does demonstrate an alternative for establishing a dose rate limit.

For devices with low availability (<10%), the time that a worker may spend near the reactor is limited by his hours of availability. Table 14.4 shows that a worker is available to work in the radiation area for about 1400 h/year. Thus, the 1-rem/year ALARA guideline can be met with a dose rate at the shield of approximately 0.7 mrem/h. This example is also an oversimplification, since it does not account for background radiation sources and assumes that all operations take place at the shield boundary. Further, it does not account for the fact that a large percentage of component replacement operations on MFTF-α+T will be carried out remotely, which may reduce the number of contact maintenance hours needed to <1400. Nevertheless, since operating data for D-T fusion

Table 14.4. Summary of maintenance worker availability

	Hours
Total hours available (40 hours per week, 52 weeks per year)	2080
Holidays	−80
Vacation (minimum 2 weeks)	−80
Training and requalification (minimum 2 weeks)	−80
Clothing change and checkout (≈1 h/d)	−240
Medical examinations and tests (≈1 d per quarter)	−32
Administrative time (reviews, group meetings, etc.)	−50
Safety meetings (2 hours per month)	−24
Task reviews and dry runs	−100
Hours available for work in radiation area	1394

reactors are nonexistent and since experimental flexibility is required for MFTF-α+T and its successors, it seems appropriate to use a guideline that is based on the maximum possible time that workers could be available to work on the device. Since the amount of shielding neeeded to reduce the dose rate from 0.7 to 0.5 mrem/h is small and since the cost is negligible, the MFTF-α+T device should be designed to the existing LLNL requirement.

14.3 POTENTIAL RADIOLOGICAL HAZARDS AND CONSEQUENCES

In performing an overall safety assessment, the total fuel cycle must be examined. During part of its operating period, MFTF-α+T will use a deuterium-tritium (D-T) cycle, and a small quantity of lithium is used in the test modules. The deuterium and lithium are not radioactive. Only a small quantity of tritium (about 20 g per month when device availability is 10%) must be shipped to the plant; the rest of the fuel cycle, with an inventory of <0.5 kg, is contained within the plant. Thus, the radioactive hazard associated with fuel shipment is minimal and can be disregarded.

The radiological aspects of tritium release are discussed in ref. 10. Since our primary concern is the impact of released tritium on the public, the potential concentration and dose rate at the site boundary are the most important parameters. These parameters will depend on distance to the site boundary; wind, atmospheric, and topographical conditions; building and ventilation designs; and other variables, all of which make the calculation of dose rates quite complex.

14.3.1 Releases During Normal Operation

During normal operation, tritium can be released from the device as liquid or as gas. Gaseous releases to the atmosphere originate from permeation through components and

from leaks in valves and pumps within the plant. These releases eventually exit to the atmosphere through the ventilation systems. Gaseous and liquid releases to the atmosphere could originate from radioactive waste treatment systems if radioactive waste water and cooling water are mixed at the cooling tower blowdown before discharge into the receiving body of water. The doses from liquid release will be small because both the quantity available and the potential for such releases are small. Therefore, only the consequences of gaseous release were considered.

Airborne releases of tritium are carried by and diluted in the atmosphere. Portions of the released tritium can be inhaled by humans, and some is deposited on vegetation and works its way through the food chain. The methodology used in the Technology Demonstration Facility (TDF) study[11] was used to calculate doses from normal gaseous release. The site boundary was assumed to be 500 m from the plant. It is estimated that a maximum of about 11 Ci/d of tritium may be released from the plant at ground level without exceeding the acceptable dose (<10 mrem/year) at the site boundary. Higher release rates are acceptable if tritium is released from a tall stack. The allowable rate can be used to determine the ventilation flow rates from the plant buildings.

The predominant hazard to personnel in the tritium processing facility is exposure that may result from using and handling tritium and components contaminated with tritium. Glove boxes used for maintenance of contaminated components have an inert atmosphere to reduce oxidation and permeation to the cell atmosphere if the boxes should leak. Special protective suits will be worn as needed by maintenance personnel. The risk of personnel exposure to tritium in the reactor vault is minimal, because most of the vulnerable tritium is transferred to the tritium cell before personnel enter the vault.

14.3.2 Releases During Off-Normal Conditions

A preconceptual analysis of failure modes and consequences was carried out to identify potential accidents and their impact on worker and public safety. The TDF methodology[11] and the results of the Tritium Systems Test Assembly (TSTA) safety analysis[12] were used in the analysis. Confinement barriers were defined as follows.

- Primary confinement: innermost pressure boundary (e.g., plasma vacuum boundary, single-walled pipes and pressure vessels).
- Secondary confinement: vacuum jackets around equipment, glove boxes, double-walled pipes and pressure vessels).
- Tertiary confinement: confinement building (e.g., reactor vault, tritium processing facility).

Several accidents were postulated and categorized (intuitively, without benefit of a probability analysis) as condition III, IV, or V accidents, using the definitions of Table 14.2. These accidents and their (qualitative) consequences are listed in Tables 14.5 (accidents in reactor vault) and 14.6 (accidents in tritium cell).

Failure of the primary confinement in a system provided with secondary confinement (e.g., release into glove boxes) does not result in exposure to workers or in release to the environment, since the tritiated waste treatment (TWT) system processes the secondary

Table 14.5. Postulated accidents in reactor vault

Condition[a]		Accident	Form of release	Releasable inventory, g	Mitigation method[b]	Worker dose, rem/min[c]	Off-site dose, rem
III	1A.	Rupture of transfer line (reactor end cell to tritium cell) into secondary containment	T, DT	5	TWT	None	Negligible
IV	1B.	1A + breach of secondary containment	T, DT	5	ATC	None	$O(10^{-7})$[d]
IV	1C.	1B + fire	HTO, T_2O	5	ATC	None	$O(10^{-7})$
IV	2A.	Large leak from reactor end cell into the vault	T, DT	5	ATC	None	$O(10^{-7})$
IV	2B.	2A + fire	HTO, T_2O	5	ATC	None	$O(10^{-7})$
III	3A.	Rupture of supply line to injector into secondary containment	T, DT	10	TWT	None	Negligible
IV	3B.	3A + breach of secondary containment	T, DT	10	ATC	None	$O(10^{-6})$
IV	3C.	3B + fire	HTO, T_2O	10	ATC	None	$O(10^{-6})$
V	4.	Aircraft crash into facility; breach of primary, secondary, and tertiary containment; and fire	HTO, T_2O	21	Not considered; $P \leq 10^{-7}$ year^{-1}		
V	5.	Earthquake; breach of primary, secondary, and tertiary containment; and fire	HTO, T_2O	21	Not considered; $P \leq 10^{-7}$ year^{-1}		

[a]As defined in Table 14.2.
[b]TWT = tritiated waste treatment, ATC = atmospheric tritium cleanup.
[c]No worker entry is permitted until all releasable tritium has been transferred into tritium cell.
[d]O = on the order of.

Table 14.6. Postulated accidents in tritium cell

Condition[a]		Accident	Form of release	Releasable inventory, g	Mitigation method[b]	Worker dose, rem/min	Off-site dose, rem
III	1A.	Rupture of transfer line (reactor end cell to tritium cell) into secondary containment	T, DT	5	TWT		Negligible
IV	1B.	1A + breach of secondary containment	T, DT	5	ATC	$O(10^{-4})$	$O(10^{-7})$
IV	1C.	1B + fire	HTO, T_2O	5	ATC	O(10)	$O(10^{-7})$
III	2A.	Breach of fuel cleanup unit primary containment	T, DT	50	TWT		Negligible
IV	2B.	2A + breach of secondary containment	T, DT	50	ATC	$O(10^{-3})$	$O(10^{-6})$
IV	2C.	2B + fire	HTO, T_2O	50	ATC	$O(10^{2})$	$O(10^{-6})$
III	3A.	Rupture of isotope separation unit primary containment	T, DT	250	TWT		Negligible
IV	3B.	3A + breach of secondary containment	T, DT	250	ATC	$O(10^{-2})$	$O(10^{-5})$
IV	3C.	3B + fire	HTO, T_2O	250	ATC	$O(10^{3})$	$O(10^{-5})$
V	4.	Aircraft crash into facility; breach of primary, secondary, and tertiary containment; and fire		Not considered; $P \leqslant 10^{-7}$ year^{-1}			
V	5.	Earthquake; breach of primary, secondary, and tertiary containment; and fire		Not considered; $P \leqslant 10^{-7}$ year^{-1}			

[a]As defined in Table 14.2.
[b]TWT = tritiated waste treatment, ATC = atmospheric tritium cleanup.

confinement atmosphere. However, a failure of primary confinement in a system without secondary confinement (e.g., the plasma chamber) or a failure of both primary and secondary confinement may result in a tritium release in the vault or in the tritium processing facility. This could involve exposure of workers to tritium; the extent of the exposure depends on the amount of tritium released, its form (oxide or elemental), and the time required for workers to leave the building. Worker exposures for all credible accidents of this type can be kept below the design goal of 25 rem.

A minimum of two failures must occur for tritium to be accidentally released to the environment. This situation requires a release from a component with no secondary confinement (e.g., plasma chamber, TWT components) followed by a failure of the atmospheric tritium cleanup (ATC) system or a failure of the tertiary confinement. Since the amount of tritium in systems with no secondary confinement is small (<5 g), exposures to the general public at the site boundary from releases of this nature are several orders of magnitude below the allowable limit.

A minimum of three failures must occur for a large quantity of tritium to be released to the environment. This situation requires the failure of both primary and secondary confinement systems, followed by a failure of the ATC system or a failure of the tertiary confinement. The probability of this situation is considered to be extremely low ($<10^{-7}$ year^{-1}), so it is not considered a credible accident.

No credible accident in the reactor vault can cause exposure in excess of the allowable dose to either a worker or the public, and no credible accident in the tritium processing cell can cause exposure in excess of the allowable dose to the public. A number of postulated accidents in the tritium processing facility could cause worker exposure in excess of the allowable dose. However, several mitigating methods exist to prevent this. First, the ATC units come on line immediately following any release. Second, radiation monitors will almost instantly signal any release, and workers can reach for protective masks in a matter of seconds. Third, emergency exit doors are accessible in a matter of seconds. Additional safeguards are discussed in Sect. 14.4.

14.4 SAFETY FEATURES

Many features can be incorporated in the design of MFTF-α+T to reduce the consequences of potential safety-related problems. The most important features are those that provide safe housing for the reactor and the tritium processing equipment. Others include reducing vulnerable tritium by partitioning tritium flow systems and providing a vent stack to disperse effluents over a larger area. Only the features to ensure safe housing of the reactor and the tritium equipment were evaluated during this phase of the design study. As discussed in Chap. 13, the reactor vault now has or will be modified to have

- the capability to resist some overpressure (up to about 120 kPa),
- a leakage rate that does not exceed 1 vol %/h,
- an epoxy coating on the inside surfaces of the vault to reduce absorption of tritium into the concrete,

- the capability to resist the peak seismic acceleration expected at the site, and
- the capability to resist natural phenomena (missiles and tornados) of the intensity expected at the site.

The tritium processing facility will have similar leakage rate, tritium absorption barrier, seismic resistance, and protection from natural phenomena.

14.5 SITING

Siting of the MFTF-α+T project at LLNL appears feasible from the point of view of safety. Although the LLNL site (in common with much of the western part of the United States) is subject to earthquakes, extensive earthquake-fault mapping and analysis indicate that the maximum credible seismic accelerations can be accommodated by careful design of the facility. Severe tropical storms, hurricanes, and tornados are unknown in the area. The site is 400 ft above mean sea level, has good local drainage, has no upslope water reservoirs, and is more than 50 miles from the ocean.

The assessment of tritium hazards in this chapter provides confidence that proper design of the facility will allow adequate containment. The neutron and gamma radiation generated during and after typical operating scenarios for MFTF-α+T is projected to fall within acceptable limits. Calculations of neutron-induced activation are proceeding; results to date indicate that the facility can be designed and constructed to operate within existing guidelines and can be decommissioned after its useful life.

14.6 SUMMARY

An accidental release of tritium in the reactor vault or in the tritium processing facility may result in tritium leakage to the environment because the buildings are not 100% leaktight. Thus, the leakage rate and the site boundary distance determine the upper limit on the amount of tritium that can be released inside a building without exceeding the dose limit at the site boundary.

A preliminary assessment of the potential radiological consequences of tritium release indicates that to keep the tritium leakage rate to the environment $\leqslant$ 10 Ci/d under normal operating conditions, the exclusion area boundary should be 450 m from the building. The MFTF-α+T site boundary is 500 m away from the device.

A preliminary study indicates that the entire MFTF-α+T operation, including the tritium hazard, will fall within the bounds of the existing approved LLNL site environmental impact statement.

REFERENCES

1. *Fusion Engineering Device Design Description*, vol. 2, ORNL/TM-7948/V2, Oak Ridge Natl. Lab., 1981.
2. *STARFIRE: A Commercial Tokamak Fusion Power Plant Study*, vol. II, ANL/FPP-80-1, Argonne Natl. Lab., Argonne, Ill., 1980.
3. "Safety of Non-Reactor Nuclear Facilities," DOE Order 5480.1, Chap. V, Washington, D.C., 1981. Establishes requirements for an enviromental safety and health program.
4. "Standards for Radiation Protection," DOE Manual, Chap. 0524 (from ERDA Manual, Chap. 0524, approved Mar. 30, 1979).
5. "Safety Analysis and Review System," DOE Order 5481.1, Washington, D.C., 1979. Establishes uniform requirements for the preparation and review of safety analyses for all DOE operations.
6. *Nonreactor Nuclear Facilities: Standards and Criteria Guide* (draft), U.S. DOE, Washington, D.C., 1981.
7. *Tritium Systems Test Assembly: Preliminary Safety Analysis Report*, Los Alamos Scientific Lab., Los Alamos, N. Mex., 1979.
8. *Tokamak Fusion Test Reactor: Preliminary Safety Analysis Report*, Princeton Plasma Physics Lab., Princeton, N.J., 1976.
9. R. J. Barrett and P. T. Spampinato, *Assessment of Biological Dose Rate Guidelines for Use in Fusion Device Design*, FEDC-M-83-SE-003, Fusion Engineering Design Center, Oak Ridge Natl. Lab., Sept. 9, 1983.
10. P. S. Rohwer and W. H. Wilcox, "Radiological Aspects of Environmental Tritium," *Nucl. Safety* **17(2)**, 216–23 (1976).
11. *A Tandem Mirror Technology Development Facility*, UCID-19328, Univ. California, Lawrence Livermore Natl. Lab., Livermore, Calif., October 1983.
12. R. V. Carlson, "Safety Analysis Report for the Tritium Systems Test Assembly," presented at the Fifth Topical Meeting on the Technology of Fusion Energy, Knoxville, Tenn., 1983.

Appendix A

ASSESSMENT OF MFTF-α+T VAULT SEISMIC CAPABILITY

Bechtel Group, Inc.

Fifty Beale Street
San Francisco, California
Mail Address: P.O. Box 3965, San Francisco, CA 94119

September 29, 1983

To: Livermore Lawrence National Laboratory
P.O. Box 5012
Livermore, CA 94550

Attention: James N. Doggett, Project Manager

Reference: P.O. No. 3041805, Bechtel Job No. 16187

Subject: Seismic Review of Vault for
MFTF Upgrade Project

Gentlemen:

This letter report was prepared in accordance with the scope of work for the preconceptual seismic evaluation of the (α+ T) Tandem Mirror Fusion Machine concrete vault. The scope of work was developed with the assistance of the Bechtel site representative Dr. Sunil Ghose. The report contains comments and preconceptual recommendations on wall upgrading for a 150-ton crane installation, concrete vault seismic capability for (α+ T) conditions, and recommendations for future work.

1. Vault Upgrade for a 150-Ton Crane

A general view of the crane and vault is shown in Sketches 1 & 2. Crane parameters such as weight and height were selected using the "Whiting Crane Handbook" and were determined using extrapolation of the values presented in the above reference, shown in Sketch 3.

Predicted parameters of the crane concept are: estimated weight of the crane is 170 kips; span is 64'-4"; trolley height is about 6'; height from top of trolley to the bottom of crane girder is approximately 14 feet; hook can be raised to approximately 11' from the top of the crane.

As can be seen from Sketch 1, two possible types of crane girder supports were considered. They were either brackets attached to the upper wall faces or columns from the vault floor.

The bracket supports consist of anchor plates and stiffened web ledges (Sketches 4 and 5) attached to the walls by 1 1/4" Ø HVA type anchor bolts manufactured by Hilti Inc.. Anchor bolt embedment into the concrete is about 15". Brackets are spaced at 18'-0" on centers. Additional smaller upper anchor plates are provided for the lateral restraint of the top chord of the crane rail girder (Sketch 6).

The column type of support consists of W14x90 columns with a cover plate. They are spaced at 18' -0" on centers and supported by new foundations. Columns are laterally restrained each vertical 10 feet by anchors to the wall (Sketch 7).

The crane girder concept consists of a W36x230 beam with added top flange cover plate and angles (Sketch 8). Equivalent plate girder sections may be used instead of the W36x230. Nominal span of the crane girder over its supports is 18' -0".

2. Seismic Capability for (α+ T) Specification

Simplified dynamic analysis was used to compute the preliminary dynamic forces required to design the vault wall for the (α+ T) condition. A schematic view of the concrete vault is shown in Sketch 9. The entire building was modeled as a single degree of freedom system. The final forces were computed using the following procedure:

1. Compute the weight of the walls, roof and crane for a one foot strip. For OBE analysis the weight of the crane and its maximum load (live load) were distributed over 28 feet length of the wall - twice the distance spanned by the end trucks. For DBE analysis, live load was not included.

2. Compute the longitudinal, transverse and vertical stiffness of the wall based on a 7 ft. thick wall.

3. Compute the natural frequencies of this simplified system.

4. Select the spectral accelerations from spectral curves provided in Foster Engineering Inc's report for the maximum accelerations and dampings shown in Table 1. The values of spectral accelerations for the computed frequencies of the structure used for force calculations were 1.1g and 1.9g for OBE and DBE forces respectively. These values are higher than the ground input values 0.4g and 0.8g due to structural amplification.

5. Compute maximum forces and moments resulting in the wall, per lineal foot, which are listed in Tables 2 and 3. Computed forces were increased by a factor of 1.5 to account for the contribution of higher modes.

Although the results obtained from this simplified approach are approximate, the results compared reasonably well with values reported by Foster Engineering. However, for the final design we recommend that 3-D finite element dynamic analysis be performed to compute the required forces. In the simplified approach used, coupling effects and additional forces due to torsion were neglected.

The calculations of the strength of the walls showed that they would not be adequate to resist the bending moments due to the (α+ T) earthquake forces and therefore an upgrading of those walls would be required. Somewhat less reinforcement would be added to the monolithic walls compared to the block walls.

One of the upgrade possibilities is to provide a rigid connection between roof and wall. This would reduce bending moments at the base of the wall for lateral loads. Another possibility is to provide outside reinforcement of the wall using steel plates attached to the surfaces by drilled anchors (Sketch 10), although this will be visually unattractive. Still another possibility is to install additional vertical prestress tendons as shown in Sketch 11.

Order-of-magnitude preconceptual estimates of materials for upgrading the vault are as follows:

Crane Support Systems

Bracket-type supports: Steel-150 tons. The amount of drilling into concrete is about 20,000 inches

Column-type supports: Steel-225 tons; concrete - 200 cu. yd, reinforcing steel - 25 tons. It should be noted that the length of drilled anchor bolts for column-type supports is expected to be less than for bracket-type supports. (approximately 7,000 inches)

Seismic Upgrading of Walls: For the steel plate concept only, steel - 1500 tons. It is expected that this quantity may be reduced as a result of more detailed analysis and design.

3. Recommendations For Future Work

The work reported herein was necessarily of a preconceptual nature using quite approximate methods to scope the structural influence of the (α + T) seismic specification.

Below are some suggestions for future work:

a) Perform a preliminary design for each of two methods of upgrading the walls to meet requirements of (α+ T) seismic events. Investigate the quantities of materials and cost aspects of upgrading.

b) Investigate the performance and reliability of HVA 1 1/4" Ø anchor bolts (which use epoxy grout) for heavily-loaded crane girder bracket supports.

Bechtel Group, Inc.

c) Perform a preliminary design of support members for the 150-ton crane.

d) Perform a computer seismic analysis of the vault considering new crane loads.

e) Investigate geometry parameters of the crane concept and propose criteria for the crane design.

f) Investigate crane/load clearance requirements and influences on the vault layout.

Submittal of this letter report completes all technical work under the above purchase order.

H. A. Franklin
Project Manager
Bechtel Job No. 16187
Research and Engineering

HAF:dmc

cc: H. A. Pitkin

Case	Damping	ZPGA(H)	ZPGA(V)
OBE	4%	0.4g	0.27g
DBE	7%	0.8g	0.53g

Table 1 Maximum Design Accelerations and Damping Values

Case	Fx (k/ft)	Fy (k/ft)	Fz (k/ft)
OBE	50	97	27
DBE	81	137	48

Table 2 Shear Forces Per Linear Foot of Wall

Case	Mx (k•ft/ft)	My (k•ft/ft)
OBE	5150	2650
DBE	7260	4300

Table 3 Bending Moments Per Linear Foot of Wall at Elevation 0.0

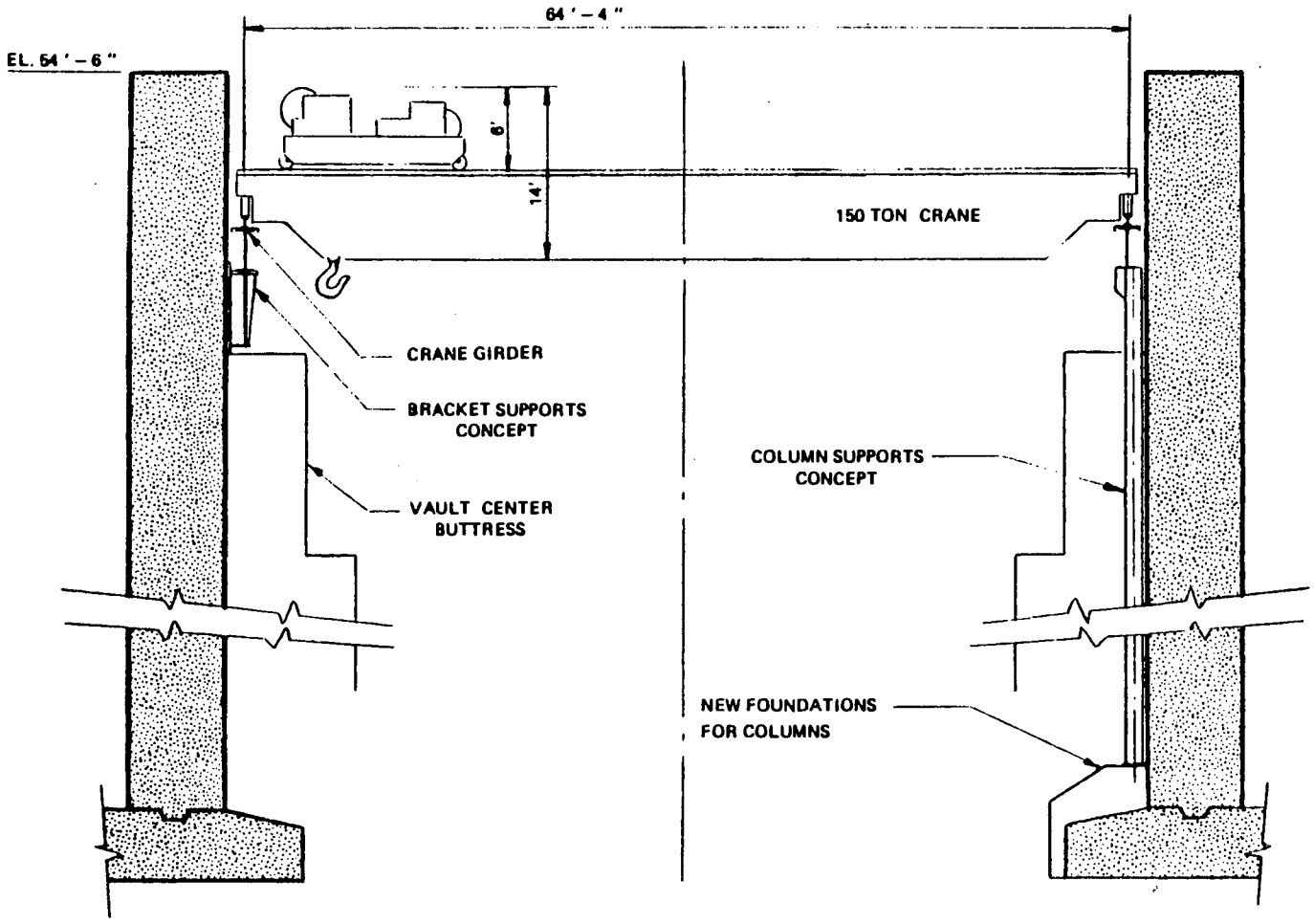

2 TYPES OF CRANE GIRDER SUPPORTS:
BRACKETS & COLUMNS

SKETCH 1 DP'11'

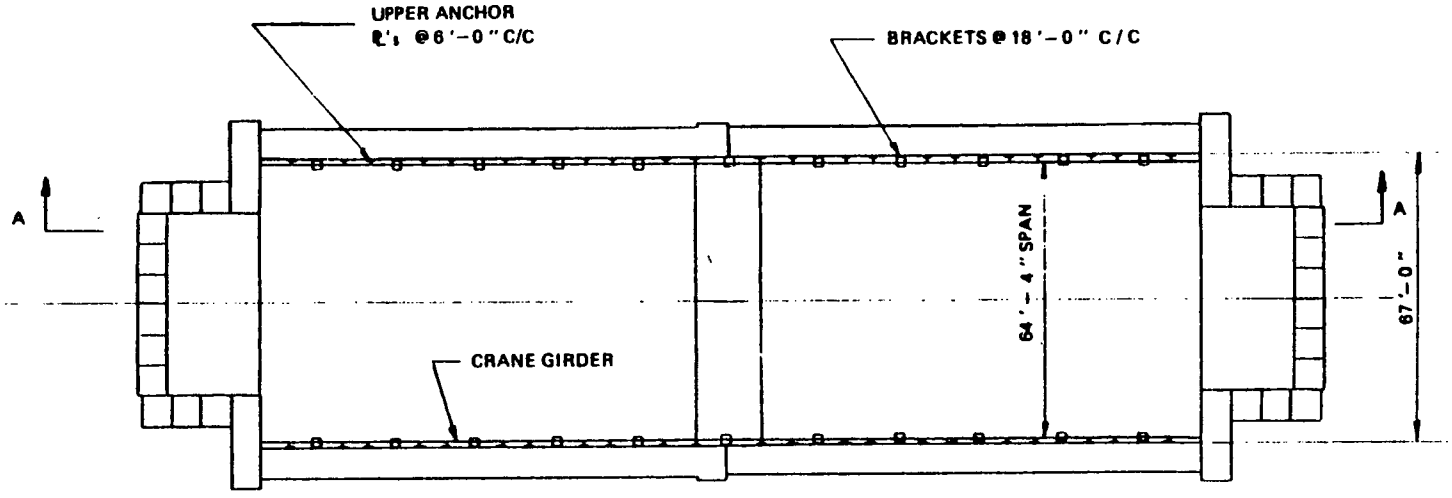

VAULT PLAN

SKETCH 2 OF 11

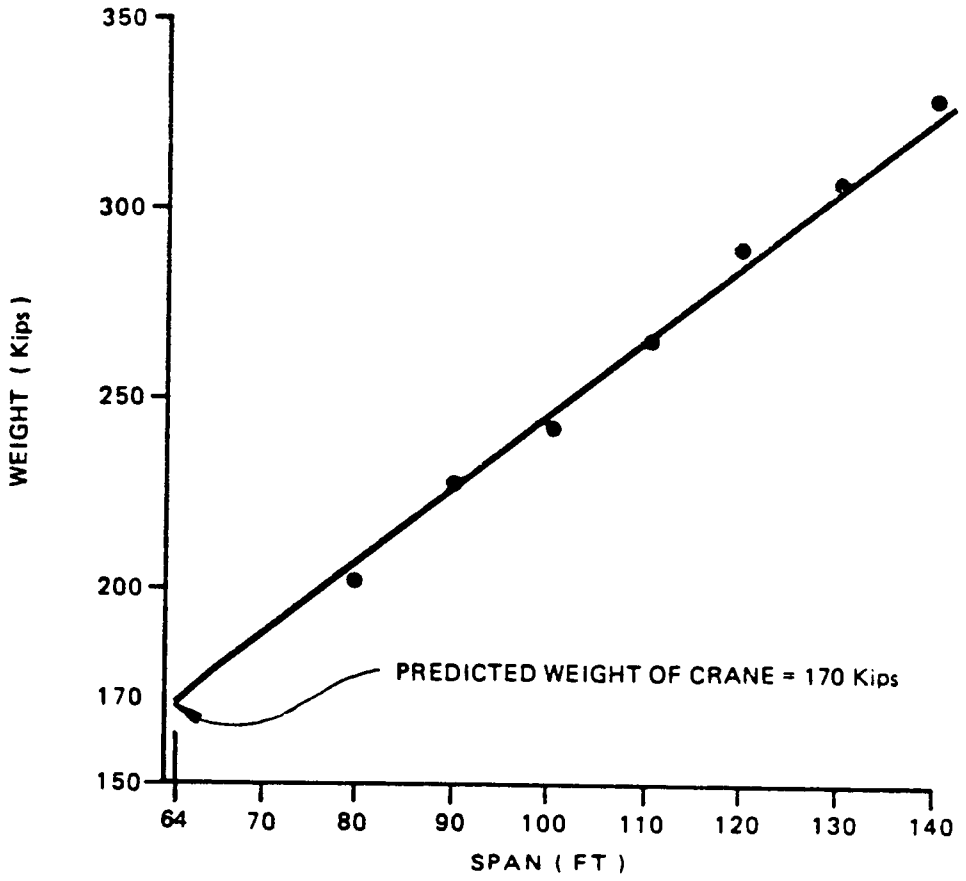

THIS CHART IS BASED ON DATA PRESENTED IN WHITING CRANE HANDBOOK

PREDICTED WEIGHT OF CRANE (Kips)

SKETCH 3 OF 11

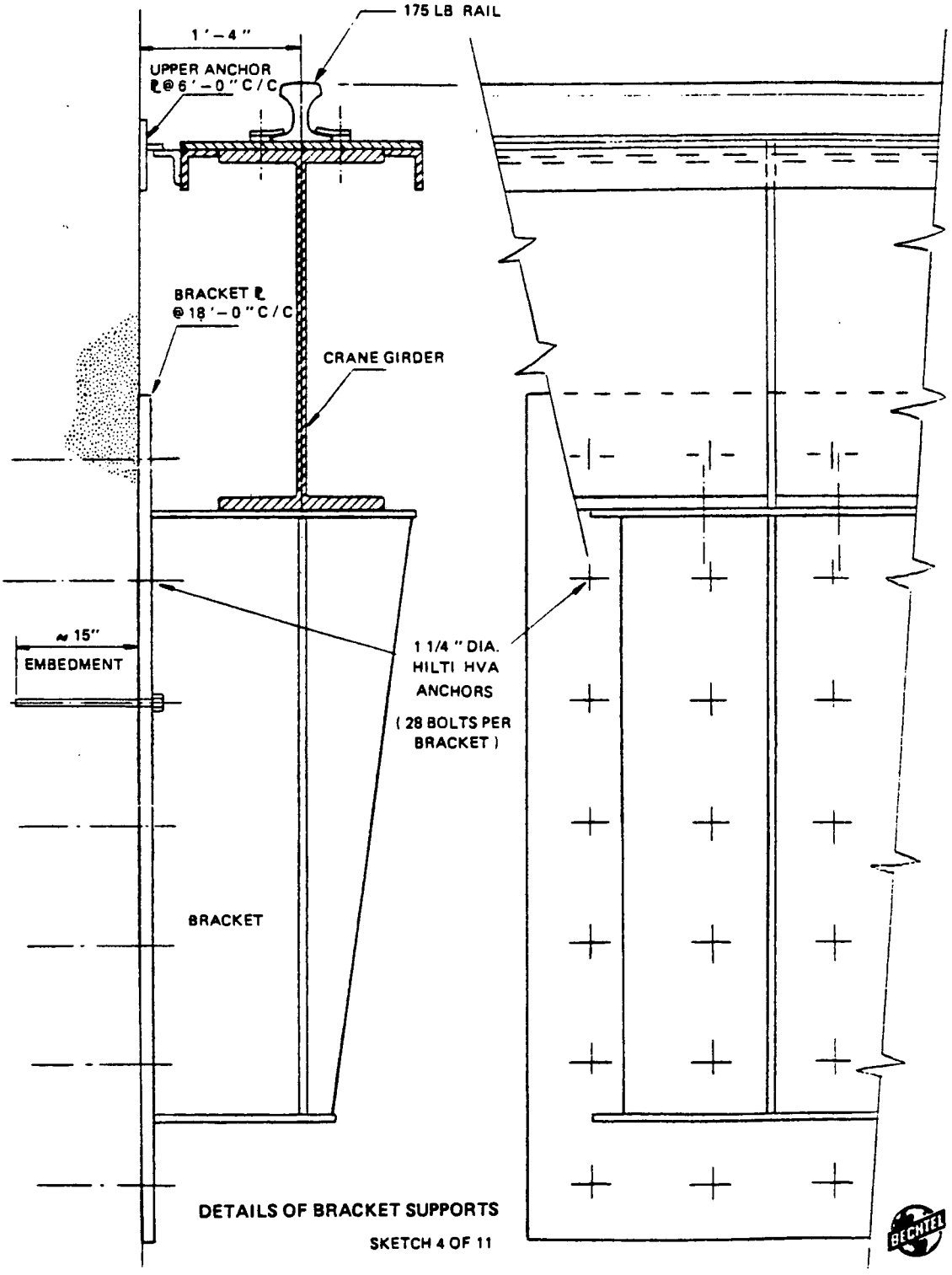
175 LB RAIL
1'-4"
UPPER ANCHOR
℄ @ 6'-0" C/C
BRACKET ℄
@ 18'-0" C/C
CRANE GIRDER
~ 15"
EMBEDMENT
1 1/4" DIA.
HILTI HVA
ANCHORS
(28 BOLTS PER
BRACKET)
BRACKET
DETAILS OF BRACKET SUPPORTS
SKETCH 4 OF 11
BECHTEL

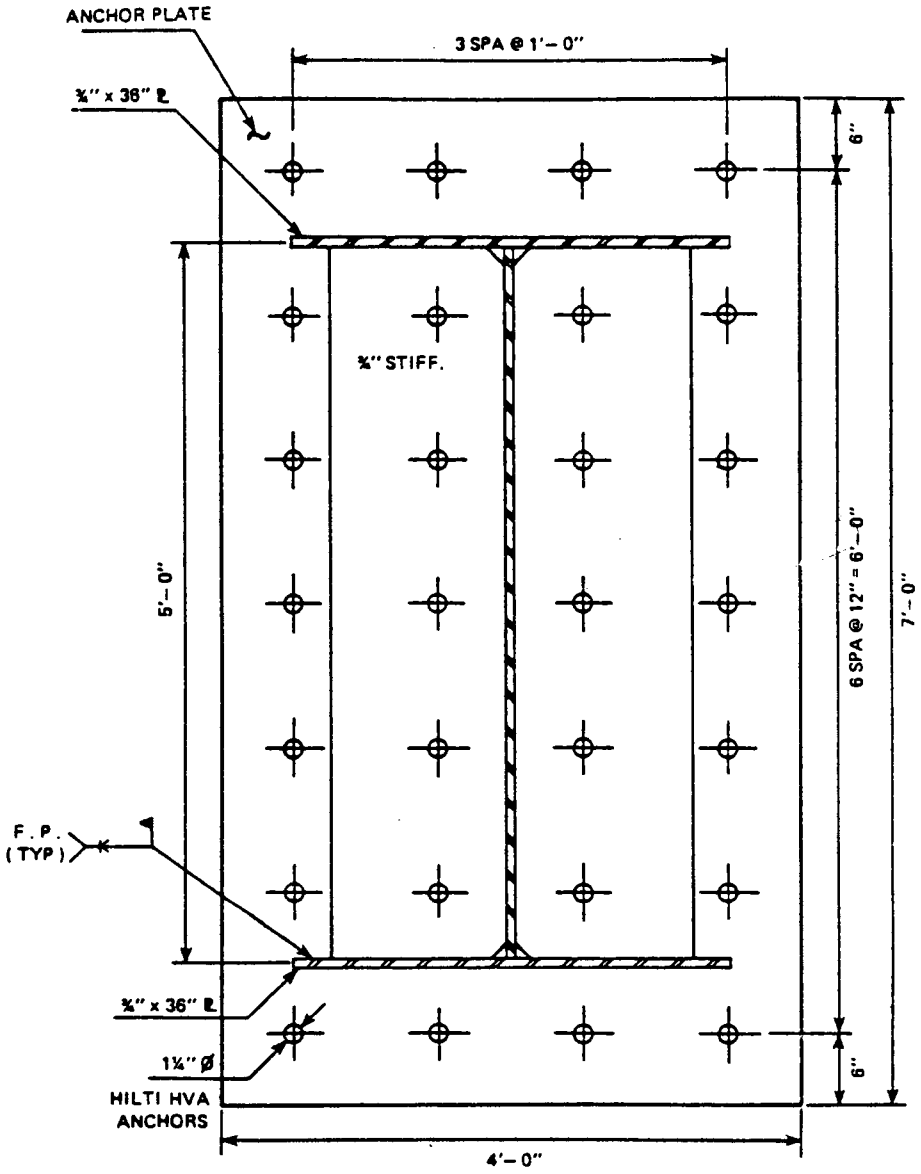

ANCHOR PLATE & BRACKET

SKETCH 5 OF 11

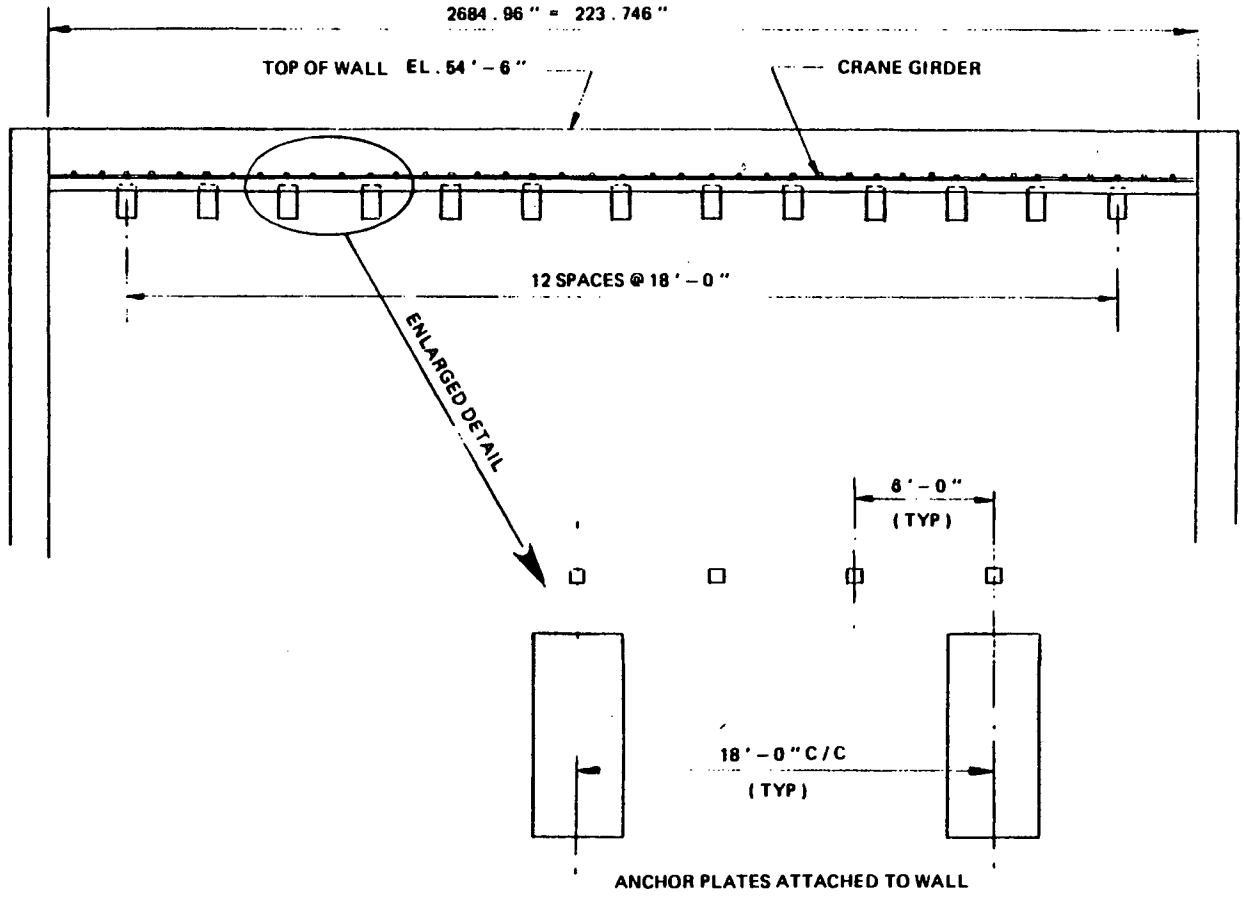

SECTION A – A (SEE SKETCH 2)
BRACKET TYPE SUPPORTS

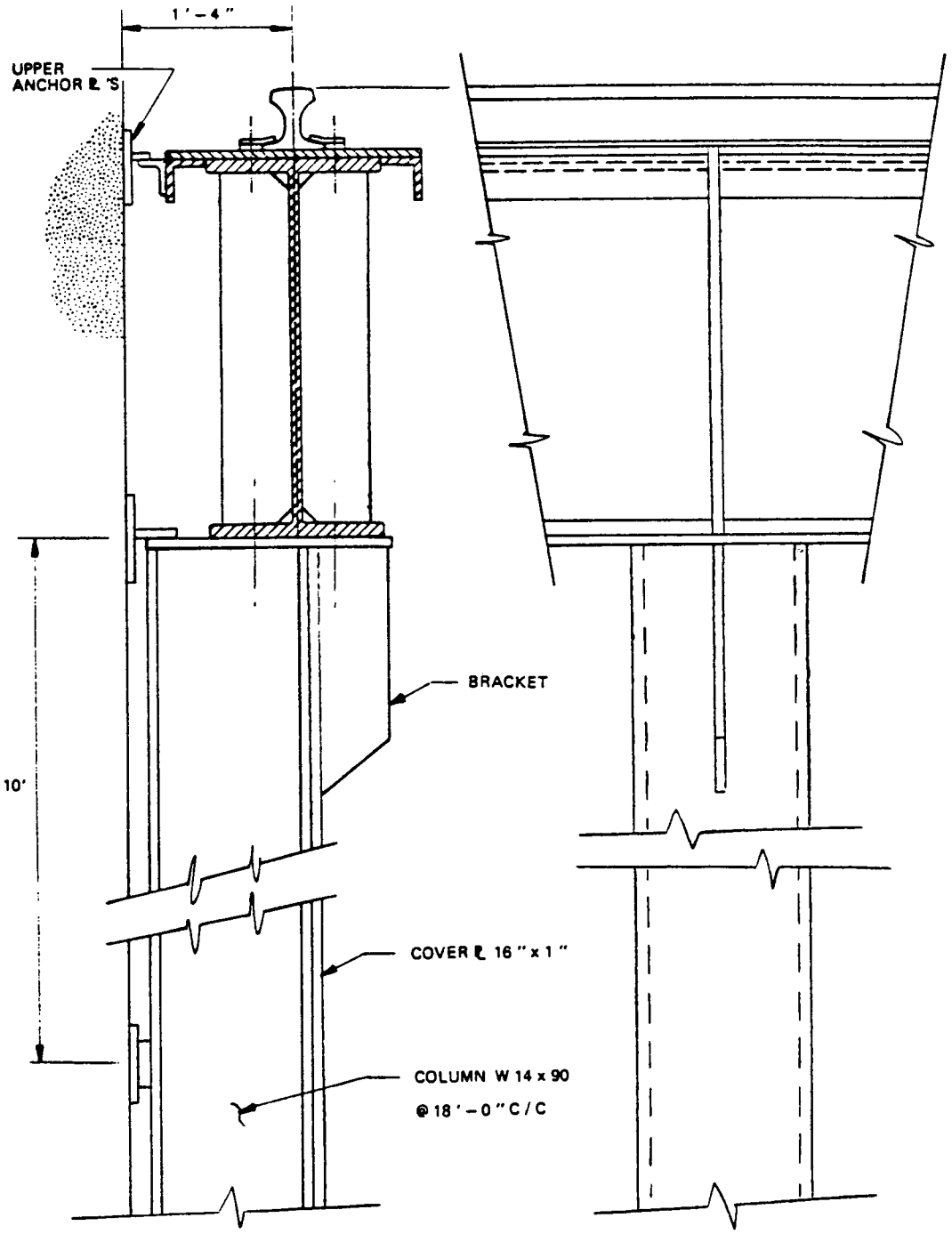

DETAILS OF COLUMN SUPPORTS

SKETCH 7 OF 11

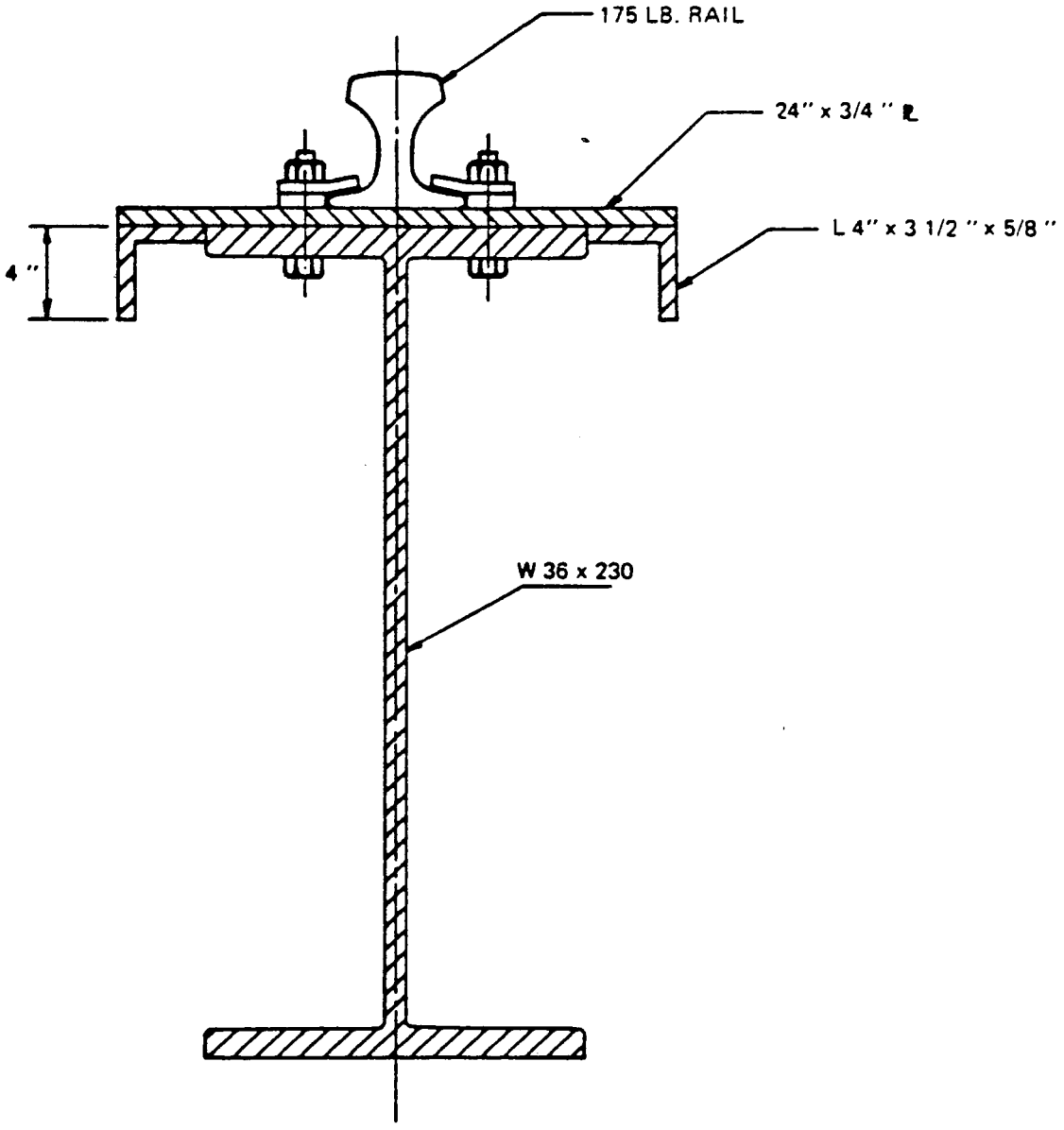

TYPICAL CRANE GIRDER CONCEPT

SKETCH 8 OF 11

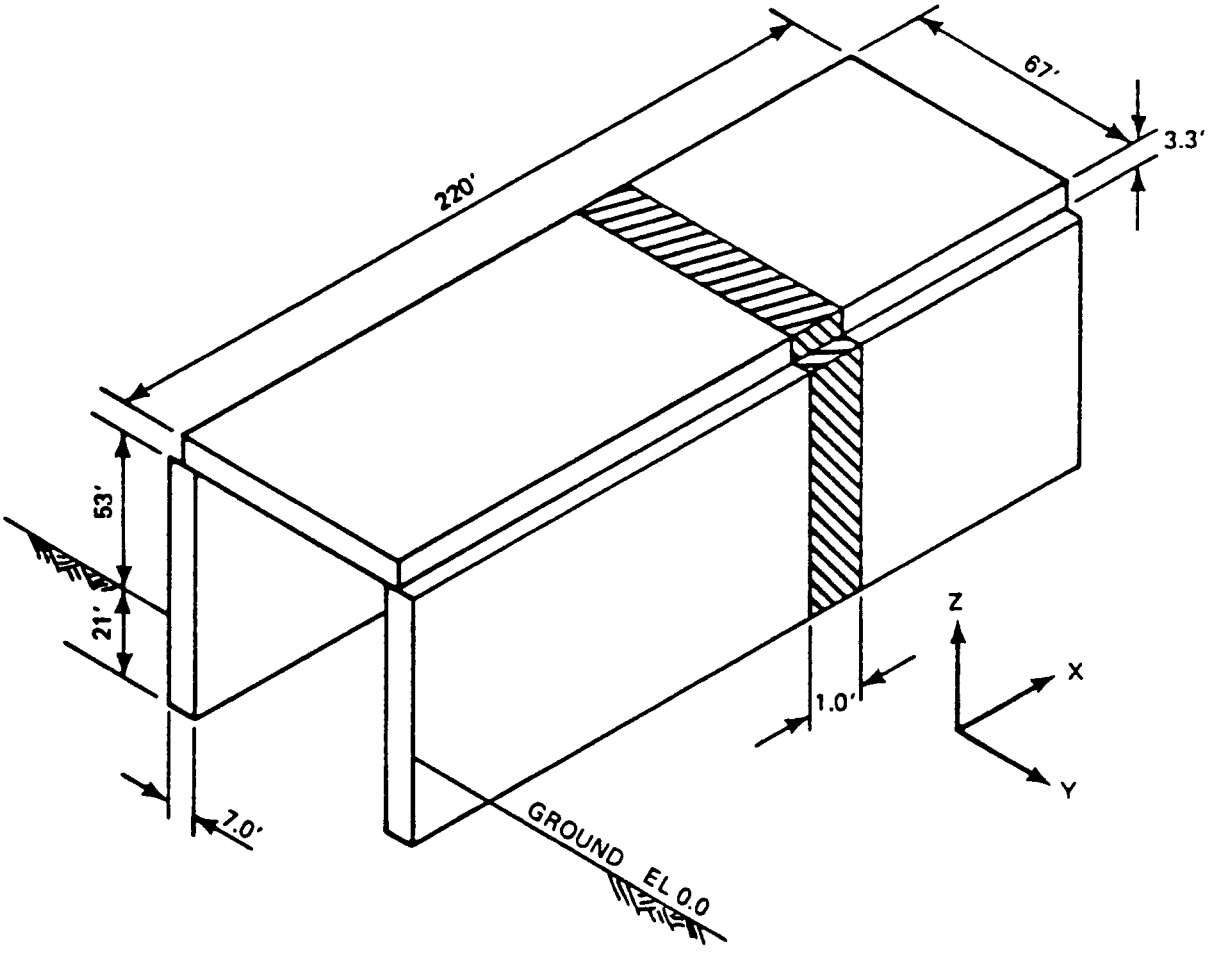

SCHEMATIC DRAWING OF CONCRETE VAULT

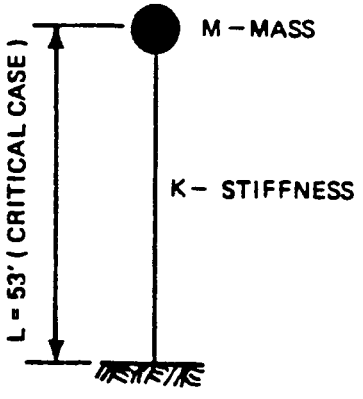

SIMPLIFIED MODEL

SKETCH 9 OF 11

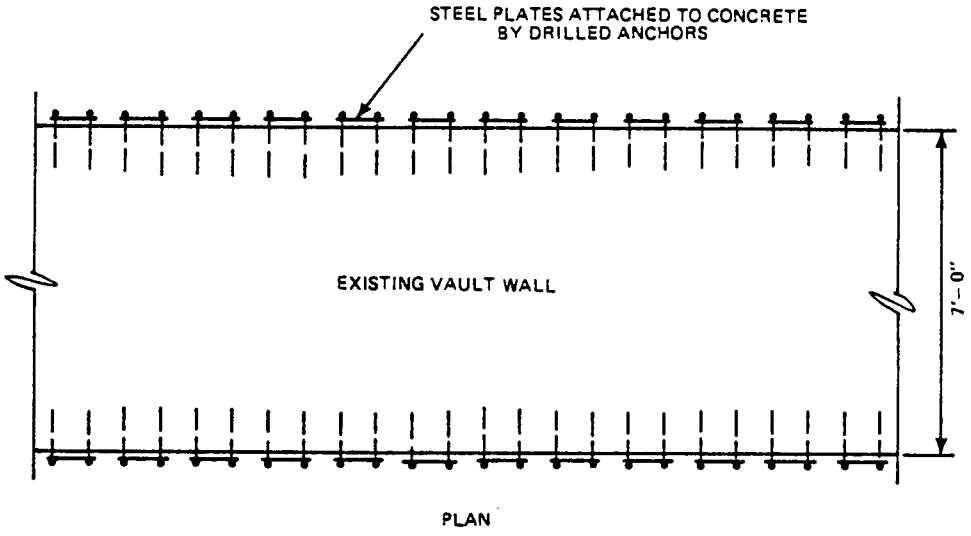

VAULT UPGRADING
PRECONCEPTUAL SCHEME

SKETCH 10 OF 11

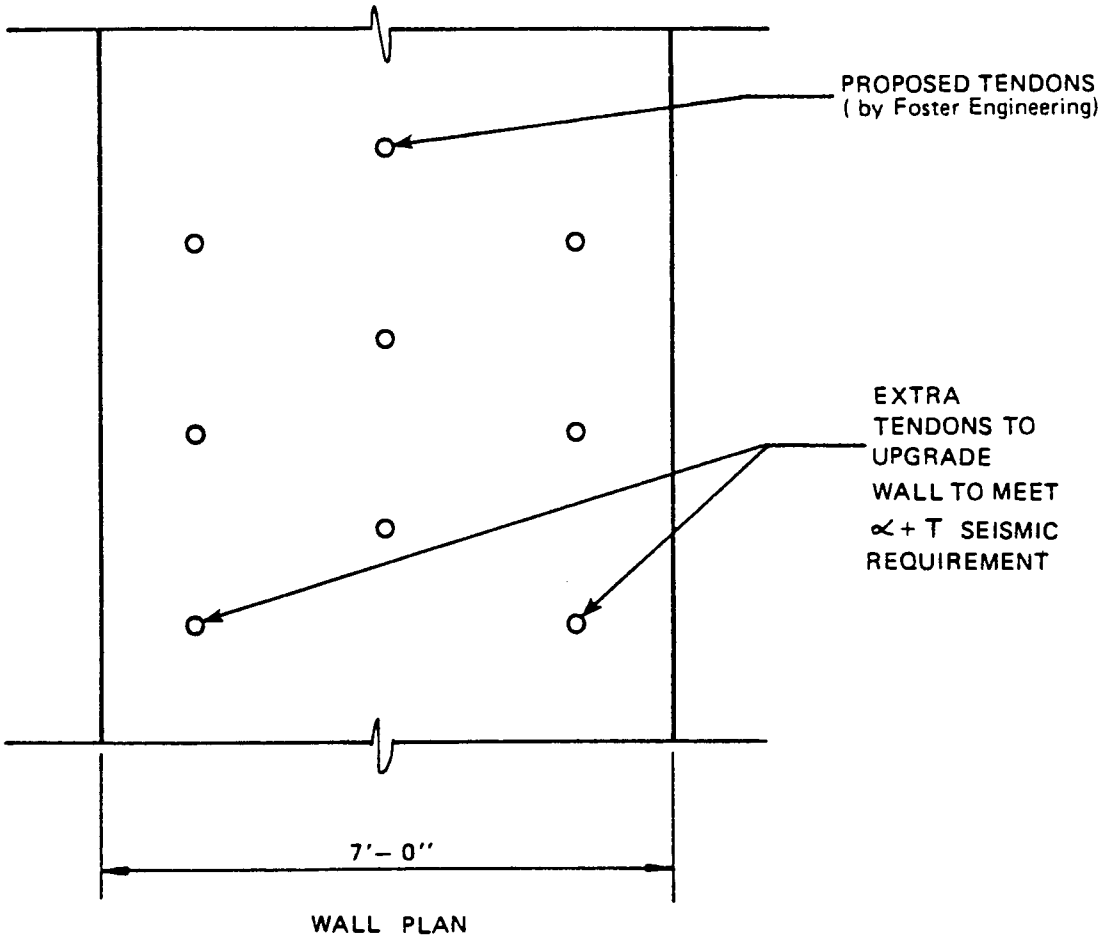

VAULT UPGRADING

PRECONCEPTUAL SCHEME

SKETCH 11 OF 11

ABBREVIATIONS AND ACRONYMS

ALARA	as low as reasonably achievable
AMS	Advanced Manipulator System
ATC	atmospheric tritium cleanup
ATCU	atmospheric tritium cleanup unit
BGP	background gas pressure
BHP	biological hazard potential
CCTV	closed-circuit television
D	deuterium
DBE	design basis earthquake
dc	direct current
DC	direct converter
DOE	Department of Energy
dpa	displacements per atom
DIII	Doublet III
D-D	deuterium-deuterium
D-T	deuterium-tritium
EBT	ELMO Bumpy Torus
ECE	electron cyclotron emission
ECRH	electron cyclotron resonance heating
EMF	electromagnetic fluctuation
EOL	end of life
EPA	Environmental Protection Agency
ETR	Engineering Test Reactor
FCU	fuel cleanup unit
FED	Fusion Engineering Device
FEDC	Fusion Engineering Design Center
FIR	far-infrared
FPD	Fusion Power Demonstration
FPY	full-power year
FWBS	first wall/blanket/shield
HPA	high-power amplifier
HTS	heat transport system
HVAC	heating, air conditioning, and ventilation
I&C	instrumentation and control
ICRH	ion cyclotron resonance heating
INTOR	International Tokamak Reactor
IPA	intermediate power amplifier
ISS	isotope separation system (or unit)
IVIS	in-vessel inspection system
JET	Joint European Torus
LBL	Lawrence Berkeley Laboratory
LCIS	local control and instrumentation system
LCP	Large Coil Program
LCTF	Large Coil Test Facility
LDS	local data system
LHe	liquid helium
LLNL	Lawrence Livermore National Laboratory
LN_2	liquid nitrogen
MARS	Mirror Advanced Reactor Study
MFTF-α+T	upgrade of MFTF-B
MFTF-B	Tandem Mirror Fusion Test Facility
MHD	magnetohydrodynamic
MIT	Massachusetts Institute of Technology
MTBF	mean time between failures
MTTR	mean time to repair
NBI	neutral beam injector
NRC	Nuclear Regulatory Commission
OBE	operating basis earthquake
ORNL	Oak Ridge National Laboratory
PDX	Poloidal Divertor Experiment
PLT	Princeton Large Torus
Q	ratio of fusion power produced to power input
rf	radio frequency
RRR	relative resistance ratio
SC	superconducting
SCDS	supervisory control and data system
SCPS	supervisory control and processing system
SCR	silicon-controlled rectifier
STP	standard temperature and pressure
T	tritium
TASS	Thermal Analysis for Safety and Stability
TDF	Technology Demonstration Facility
TFF	transverse field focusing
TFTR	Tokamak Fusion Test Reactor
TLD	thermoluminescent dosimeter
TMP	turbomolecular pump
TMR	tandem mirror reactor
TMX	Tandem Mirror Experiment
TMX-U	Tandem Mirror Experiment Upgrade
TSTA	Tritium Systems Test Assembly
TWRU	tritiated water recovery unit
TWT	tritiated waste treatment
1-D	one-dimensional
3-D	three-dimensional

ORNL/FEDC-83/9
Dist. Category UC-20 c,d

INTERNAL DISTRIBUTION

1. G. E. Gorker
2. J. R. Haines
3. S. S. Kalsi
4–8. W. D. Nelson
9. P. A. Powell
10. T. E. Shannon
11. P. T. Spampinato
12. V. C. Srivastava
13. F. W. Wiffen
14. S. A. Freije
15. J. Sheffield
16–17. Laboratory Records Department
18. Laboratory Records, ORNL-RC
19. Central Research Library
20. Document Reference Section
21. ORNL Patent Office
22. Fusion Energy Division Library
23–24. Fusion Energy Division Publications Office

EXTERNAL DISTRIBUTION

Lawrence Livermore National Laboratory, P.O. Box 808, Livermore, CA 94550

25–29. J. N. Doggett
30. B. G. Logan
31. J. D. Lee
32. W. S. Neef
33. V. N. Karpenko
34. D. E. Baldwin
35. R. Campbell
36. R. H. Bulmer
37. R. S. Devoto
38. W. L. Barr
39. L. J. Perkins
40. S. Ghose
41. M. Fenstermacher

TRW Defense and Space Systems, 1 Space Park, Redondo Beach, CA 90278

42. D. H. Berwald
43. J. D. Gordon
44. K. Kleefeldt, Kernforschungszentrum Karlsruhe GmbH, Postfach 3640, D-7500 Karlsruhe 1, Federal Republic of Germany
45. M. A. Abdou, 6288 Boelter Hall, University of California, Los Angeles, CA 90024

46. C. A. Anderson, Westinghouse Electric Corporation, Advanced Energy Systems Division, P.O. Box 158, Madison, PA 15663
47. J. L. Anderson, CMB-3, Mail Stop 348, Los Alamos National Laboratory, P.O. Box 1663, Los Alamos, NM 87545
48. C. C. Baker, FPP/208, Argonne National Laboratory, 9700 South Cass Avenue, Argonne, IL 60439
49. D. S. Beard, Office of Fusion Energy, Office of Energy Research, Mail Station G-256, U.S. Department of Energy, Washington, DC 20545
50. K. L. Black, Department E452, McDonnell Douglas Astronautics Company, P.O. Box 516, St. Louis, MO 63166
51. R. Botwin, C47-05, Grumman Aerospace Corporation, P.O. Box 31, Bethpage, NY 11714
52. W. B. Briggs, McDonnell Douglas Astronautics Company, P.O. Box 516, St. Louis, MO 63166
53. J. N. Brooks, FPP/207, Argonne National Laboratory, 9700 South Cass Avenue, Argonne, IL 60439
54. S. C. Burnett, GA Technologies, Inc., P.O. Box 81608, San Diego, CA 92138
55. J. D. Callen, Department of Nuclear Engineering, University of Wisconsin, Madison, WI 53706
56. D. R. Cohn, MIT Plasma Fusion Center, 167 Albany Street, Cambridge, MA 02139
57. J. W. Coursen, C36-05, Grumman Aerospace Corporation, P.O. Box 31, Bethpage, NY 11714
58. R. W. Conn, School of Chemical, Nuclear, and Thermal Engineering, Boelter Hall, University of California, Los Angeles, CA 90024
59. J. G. Crocker, EG&G Idaho, P.O. Box 1625, Idaho Falls, ID 83401
60. G. R. Dalton, Department of Nuclear Engineering Science, Nuclear Science Center, University of Florida, Gainesville, FL 32611
61. R. C. Davidson, Massachusetts Institute of Technology, 77 Massachusetts Avenue, Cambridge, MA 02139
62. N. A. Davies, Office of Fusion Energy, Office of Energy Research, Mail Station G-256, U.S. Department of Energy, Washington, DC 20545
63. S. O. Dean, Director, Fusion Energy Development, Science Applications, Inc., 2 Professional Drive, Suite 249, Gaithersburg, MD 20760
64. J. F. Decker, Office of Fusion Energy, Office of Energy Research, Mail Station G-256, U.S. Department of Energy, Washington, DC 20545
65. D. DeFreece, E451, Building 81/1/B7, McDonnell Douglas Astronautics Company, P.O. Box 516, St. Louis, MO 63166
66. H. Dreicer, Division Leader, CTR, Los Alamos National Laboratory, P.O. Box 1663, Los Alamos, NM 87545
67. D. Ehst, Argonne National Laboratory, 9700 South Cass Avenue, Argonne, IL 60439
68. F. Farfaletti-Casali, Engineering Division, Joint Research Center, Ispra Establishment, 21020 Ispra (Varese), Italy
69. P. A. Finn, Fusion Power Program, Argonne National Laboratory, 9700 South Cass Avenue, Argonne, IL 60439

70. H. K. Forsen, Bechtel Group, Inc., Research & Engineering, P.O. Box 3965, San Francisco, CA 94119
71. J. S. Foster, Jr., Building R4-2004, TRW Defense and Space Systems, 1 Space Park, Redondo Beach, CA 90278
72. T. K. Fowler, Associate Director for MFE, L-436, Lawrence Livermore National Laboratory, P.O. Box 808, Livermore, CA 94550
73. J. W. French, EBASCO Services, Inc., Forrestal Campus, CN-59, Princeton University, Princeton, NJ 08544
74. H. P. Furth, Director, Princeton Plasma Physics Laboratory, P.O. Box 451, Princeton, NJ 08544
75. J. G. Gavin, Jr., President, A01-11, Grumman Aerospace Corporation, P.O. Box 31, Bethpage, NY 11714
76. G. Gibson, Westinghouse Electric Corporation, Advanced Energy Systems Division, P.O. Box 158, Madison, PA 15663
77. J. R. Gilleland, Manager, Fusion Project, GA Technologies, Inc., P.O. Box 81608, San Diego, CA 92138
78. M. Y. Gohar, Argonne National Laboratory, 9700 South Cass Avenue, Argonne, IL 60439
79. R. W. Gould, Department of Applied Physics, California Institute of Technology, Pasadena, CA 91109
80. M. W. Griffin, Department E236, McDonnell Douglas Astronautics Company, P.O. Box 516, St. Louis, MO 63166
81. R. A. Gross, Plasma Research Laboratory, Columbia University, New York, NY 10027
82. C. R. Head, Office of Fusion Energy, Office of Energy Research, Mail Station G-256, U.S. Department of Energy, Washington, DC 20545
83. C. D. Henning, Lawrence Livermore National Laboratory, P.O. Box 808, Livermore, CA 94550
84. J. J. Holmes, Westinghouse-Hanford Engineering Development Laboratory, P.O. Box 1970, Richland, WA 99352
85. D. Hwang, Princeton Plasma Physics Laboratory, P.O. Box 451, Princeton, NJ 08544
86. J. B. Joyce, Princeton Plasma Physics Laboratory, P.O. Box 451, Princeton, NJ 08544
87. R. A. Krakowsi, CTR-12, Mail Stop 641, Los Alamos National Laboratory, P.O. Box 1663, Los Alamos, NM 87545
88. G. L. Kulcinski, University of Wisconsin, Department of Nuclear Engineering, Engineering Research Building, Room 439, 1500 Johnson Drive, Madison, WI 53706
89. D. L. Kummer, McDonnell Douglas Astronautics Company, P.O. Box 516, St. Louis, MO 63166
90. D. G. McAlees, Exxon Nuclear Company, Inc., 2101 Horn Rapids Road, Richland, WA 99352
91. W. Marton, Office of Fusion Energy, Office of Energy Research, Mail Station G-256, U.S. Department of Energy, Washington, DC 20545

92. L. G. Masson, EG&G Idaho, Idaho National Engineering Laboratory, P.O. Box 1625, Idaho Falls, ID 83401
93. D. M. Meade, Princeton Plasma Physics Laboratory, P.O. Box 451, Princeton, NJ 08544
94. A. T. Mense, Building 107, Post B2, McDonnell Douglas Astronautics Company, P.O. Box 516, St. Louis, MO 63166
95. R. W. Moir, Lawrence Livermore National Laboratory, P.O. Box 808, Livermore, CA 94550
96. D. B. Montgomery, MIT Plasma Fusion Center, 167 Albany Street, Cambridge, MA 02139
97. A. E. Munier, Grumman Aerospace Company, P.O. Box 31, Bethpage, NY 11714
98. R. E. Nygren, FPP/207, Argonne National Laboratory, 9700 South Cass Avenue, Argonne, IL 60439
99. T. Ohkawa, GA Technologies, Inc., P.O. Box 81608, San Diego, CA 92138
100. J. A. O'Toole, Plasma Physics Laboratory, Building I-P, Room 8A, James Forrestal Campus, P.O. Box 451, Princeton, NJ 08544
101. R. R. Parker, Francis Bitter National Magnet Laboratory, 170 Albany Street, Cambridge, MA 02139
102. B. Pease, Culham Laboratory, Abingdon, Oxfordshire OX14 3DB, United Kingdom
103. M. Pelovitz, Princeton Plasma Physics Laboratory, P.O. Box 451, Princeton, NJ 08544
104. F. W. Perkins, Princeton Plasma Physics Laboratory, P.O. Box 451, Princeton, NJ 08544
105. M. Porkolab, Massachusetts Institute of Technology, 77 Massachusetts Avenue, Cambridge, MA 02139
106. D. E. Post, Princeton Plasma Physics Laboratory, P.O. Box 451, Princeton, NJ 08544
107. L. K. Price, Department of Energy, Oak Ridge Operations, P.O. Box E, Oak Ridge, TN 37831
108. R. E. Price, Office of Fusion Energy, Office of Energy Research, Mail Station G-256, U.S. Department of Energy, Washington, DC 20545
109. F. A. Puhn, GA Technologies, Inc., P.O. Box 81608, San Diego, CA 92138
110. J. Purcell, GA Technologies, Inc., P.O. Box 81608, San Diego, CA 92138
111. R. V. Pyle, University of California, Lawrence Berkeley Laboratory, Berkeley, CA 94720
112. J. M. Rawls, GA Technologies, Inc., P.O. Box 81608, San Diego, CA 92138
113. H. P. Furth, Princeton Plasma Physics Laboratory, P.O. Box 451, Princeton, NJ 08544
114. M. Roberts, Office of Fusion Energy, Office of Energy Research, Mail Station G-256, U.S. Department of Energy, Washington, DC 20545
115. J. D. Rogers, Los Alamos National Laboratory, P.O. Box 1663, Los Alamos, NM 87545
116. M. L. Rogers, Monsanto Research Corporation, Mound Laboratory Facility, P.O. Box 32, Miamisburg, OH 45342
117. M. N. Rosenbluth, RLM 11.218, Institute for Fusion Studies, University of Texas, Austin, TX 78712

118. P. H. Rutherford, Princeton Plasma Physics Laboratory, P.O. Box 451, Princeton, NJ 08544
119. J. A. Schmidt, Princeton Plasma Physics Laboratory, P.O. Box 451, Princeton, NJ 08544
120. J. Schultz, MIT Plasma Fusion Center, 167 Albany Street, Cambridge, MA 02139
121. F. R. Scott, Electric Power Research Institute, P.O. Box 10412, Palo Alto, CA 94304
122. G. Sheffield, Princeton Plasma Physics Laboratory, P.O. Box 451, Princeton, NJ 08544
123. D. Smith, Materials Science Division, Argonne National Laboratory, 9700 South Cass Avenue, Argonne, IL 60439
124. L. Southworth, GA Technologies, Inc., P.O. Box 81608, San Diego, CA 92138
125. W. M. Stacey, Jr., Georgia Institute of Technology, School of Mechanical Engineering, Atlanta, GA 30332
126. D. Steiner, Rensselaer Polytechnic Institute, Nuclear Engineering Department, NES Building, Tibbets Avenue, Troy, NY 12181
127. E. Stern, Grumman Aerospace Corporation, CN-59, Forrestal Campus, Princeton, NJ 08544
128. P. M. Stone, Office of Fusion Energy, Office of Energy Research, Mail Station G-256, U.S. Department of Energy, Washington, DC 20545
129. I. N. Sviatoslavsky, Room 33, Engineering Research Building, 1500 Johnson Drive, University of Wisconsin, Madison, WI 53706
130. R. E. Tatro, Manager, Energy Systems, M.Z. 16-1070, General Dynamics–Convair Division, P.O. Box 80847, San Diego, CA 92138
131. F. Thomas, B-20-5, Grumman Aerospace Corporation, Bethpage, NY 11714
132. K. I. Thomassen, Lawrence Livermore National Laboratory, P.O. Box 808, Livermore, CA 94550
133. R. J. Thome, Francis Bitter National Magnet Laboratory, 170 Albany Street, Cambridge, MA 02139
134. C. Trachsel, McDonnell Douglas Astronautics Company, P.O. Box 516, St. Louis, MO 63166
135. A. W. Trivelpiece, Office of Fusion Energy, Office of Energy Research, Mail Station G-256, U.S. Department of Energy, Washington, DC 20545
136. L. R. Turner, Fusion Power Program, Argonne National Laboratory, 9700 South Cass Avenue, Argonne, IL 60439
137. E. H. Valeo, Princeton Plasma Physics Laboratory, P.O. Box 451, Princeton, NJ 08544
138. R. Varma, Physical Research Laboratory, Navrangpura, Ahmedabad, India
139. K. E. Wakefield, Princeton Plasma Physics Laboratory, P.O. Box 451, Princeton, NJ 08544
140. J. C. Wesley, GA Technologies, Inc., P.O. Box 81608, San Diego, CA 92138
141. H. Willenberg, Mathematical Sciences Northwest, Inc., P.O. Box 1887, Bellevue, WA 98009
142. J. E. C. Williams, Francis Bitter National Magnet Laboratory, 170 Albany Street, Cambridge, MA 02139

143. H. H. Yoshikawa, W/A-62, Hanford Engineering Development Laboratory, P.O. Box 1970, Richland, WA 99352
144. K. M. Young, Princeton Plasma Physics Laboratory, P.O. Box 451, Princeton, NJ 08544
145. N. E. Young, EBASCO Services, Inc., Princeton Plasma Physics Laboratory, P.O. Box 451, Princeton, NJ 08544
146. Bibliothek, Max-Planck-Institut fur Plasmaphysik, D-8046 Garching bei Munchen, Federal Republic of Germany
147. Bibliothek, Institut fur Plasmaphysik, KFA, Postfach 1913, D-5170 Julich, Federal Republic of Germany
148. Library, Centre de Recherches en Physique des Plasmas, 21 Avenue des Bains, 1007 Lausanne, Switzerland
149. Bibliotheque, Service du Confinement des Plasmas, CEA, B.P. No. 6, 92 Fontenay-aux-Roses (Seine), France
150. Documentation S.I.G.N., Department de la Physique du Plasma et de la Fusion Controlee, Association EURATOM-CEA, Centre d'Etudes Nucleaires, B.P. 85, Centre du Tri, 38041 Grenoble, Cedex, France
151. Library, Culham Laboratory, UKAEA, Abingdon, Oxfordshire, OX14 3DB, England
152. Library, FOM Instituut voor Plasma-Fysica, Edisonbaan 14, 3439 MN Nieuwegein, Netherlands
153. Library, Institute for Plasma Physics, Nagoya University, Nagoya 464, Japan
154. Library, International Centre for Theoretical Physics, Trieste, Italy
155. Library, JET Joint Undertaking, Abingdon, Oxfordshire, OX14 3DB, England
156. Library, Laboratorio Gas Ionizzati, CP 56, 00044 Frascati, Italy
157. Plasma Research Laboratory, Australian National Laboratory, P.O. Box 4, Canberra, ACT 2000, Australia
158. Thermonuclear Library, Japan Atomic Energy Research Institute, Tokai, Naka, Ibaraki, Japan
159. Library, Plasma Physics Laboratory, Kyoto University, Gokasho, Uji, Kyoto, Japan
160. Office of the Assistant Manager for Energy Research and Development, Department of Energy, Oak Ridge Operations, Oak Ridge, TN 37830

161–350. Given distribution as shown in TID-4500, Magnetic Fusion Energy (Category Distribution UC-20 c,d: Reactor Materials and Fusion Systems)